



**TECHNISCHE  
UNIVERSITÄT  
WIEN**

**VIENNA  
UNIVERSITY OF  
TECHNOLOGY**

## DISSERTATION

### **Species concentration measurements by laser diagnostics characterizing combustion and ignition processes up to high pressures**

ausgeführt zum Zwecke der Erlangung des akademischen Grades eines Doktors der  
technischen Wissenschaften unter der Leitung von

a.o.Univ. Prof. Dipl.-Ing. Dr. techn. Franz Winter

Institut für Verfahrenstechnik, Umwelttechnik und Technische Biowissenschaften

eingereicht an der Technischen Universität Wien  
Fakultät für Technische Naturwissenschaften und Informatik

von

Dipl.-Ing. Maximilian Lackner  
Mat. Nr. 9725350  
Langegasse 8/30  
2540 Bad Vöslau

Wien, am 1. Juli 2003

A handwritten signature in black ink, appearing to read 'Maximilian Lackner', is written over a horizontal line.

# Species concentration measurements by laser diagnostics characterizing combustion and ignition processes up to high pressures

Dipl.-Ing. Maximilian Lackner

2003



## Abstract

This PhD thesis uses tunable diode laser absorption spectroscopy (TDLAS) for species concentration measurements to characterize combustion and ignition processes. The experiments are based on an FFF funded project on laser-induced ignition of gaseous fuel/air mixtures at high pressures. The author's part in the project was to characterize the quality of laser-induced ignition.

In TDLAS, the resonant attenuation of a near infrared diode laser beam with the wavelength matched to a rovibrational transition of the gaseous target species is used to determine the concentration of this species. By tuning the wavelength over the absorption peak (this can be achieved by varying the laser injection current or its temperature), resonant absorption which is proportional to the concentration of the target species (Lambert Beer's law) can be discerned from unspecific effects like scattering, partial blocking of the laser beam or beam steering as they occur in harsh environments. TDLAS enables fast, accurate and spatially resolved *in-situ* (i.e. right at the spot) measurements (concentration, temperature and pressure) and is therefore suited well to the investigation of laser-induced ignition.

The laser ignition tests were conducted in a constant volume vessel (0.9 l, 473 K) using a Q-switched Nd:YAG laser (pulse duration 10 ns, 1-50 mJ pulse energy). The beam of a tunable diode laser (room temperature continuous wave InGaAsSb/AlGaAsSb quantum well ridge diode laser emitting at 2.55  $\mu\text{m}$  ( $3922\text{ cm}^{-1}$ )) was sent through this vessel perpendicularly to the Nd:YAG laser at the location of the igniting laser spark and frequency tuned at 5 kHz. By doing so, the formation of  $\text{H}_2\text{O}$  (strong absorption at 2.55  $\mu\text{m}$ ) in the vicinity of the developing flame kernel could be tracked with 0.2 ms time resolution (detection limit approx. 50 ppm\*m) in a semi-quantitative manner. The initial pressure in the laser ignition tests with fuel lean to fuel rich  $\text{CH}_4$ /air mixtures was up to 30 bar. Also, laser-induced ignition of biogas/air and vaporized higher hydrocarbon/air mixtures (gasoline and several key aliphatic and aromatic constituents) was investigated. Besides the formation of  $\text{H}_2\text{O}$ , the emissions of the flame (1-10  $\mu\text{m}$ ) and the variations in the transmission of the diode laser beam through the combustion vessel onto the detector (caused by beam steering due to temperature induced refractive index gradients) were used to characterize the ignition process.

Before being used in ignition diagnostics, the InGaAsSb/AlGaAsSb laser at 2.55  $\mu\text{m}$  ( $\text{H}_2\text{O}$  detection) and a similar device emitting at 2.3  $\mu\text{m}$  ( $4348\text{ cm}^{-1}$ , simultaneous  $\text{CH}_4$  and  $\text{CO}$  detection, detection limit approx. 500 ppm\*m for both species) were deployed to investigate solid fuel combustion in the freeboard of a laboratory-scale fluidized bed combustor (tuning coefficients for both lasers 0.07 nm/mA and 0.2 nm/K, used tuning frequency 300 Hz). The concentration histories of  $\text{CO}$ ,  $\text{CH}_4$  and  $\text{H}_2\text{O}$  were measured *in-situ* directly above the surface of the suspended single fuel particles (biomass and coal, distance laser beam to particle 4-31 mm, investigation on the influence of the  $\text{O}_2$  partial pressure and the bed temperature on emission characteristics during devolatilization and char combustion) and compared to chemical kinetic modeling results (good agreement).

Because of the shortcomings of the 2.3 and 2.55  $\mu\text{m}$  lasers especially in high pressure environments (narrow wavelength tuning range), novel, promising diode lasers were tested in different setups.

A DFB GaAs-based quantum cascade laser (QCL) emitting at 11.4  $\mu\text{m}$  ( $877\text{ cm}^{-1}$ , simultaneous  $\text{NH}_3$  and  $\text{C}_2\text{H}_4$  detection, detection limit approx. 2200 ppm\*m for  $\text{C}_2\text{H}_4$ , 220 ppm\*m for  $\text{NH}_3$ ) was used to record the absorption spectra of product gas from a biomass steam gasification plant and biogas. The biomass steam gasification gas was found to contain 2% of  $\text{C}_2\text{H}_4$ .  $\text{NH}_3$  could not be detected. The laser was operated at 5 kHz in a pulsed mode (tuning coefficient 0.71 nm/K, tuning range 886.76 - 889.16  $\text{cm}^{-1}$  (30.4 nm) from 185 to 225 K).

Novel vertical-cavity surface-emitting lasers (VCSELs) in the 1.54 to 1.81  $\mu\text{m}$  wavelength range ( $6494 - 5525\text{ cm}^{-1}$ ) had just become available and were tested for their use in absorption spectroscopy. During a research stay at Munich University of Technology single mode lasers at 1.54  $\mu\text{m}$  ( $\text{NH}_3$ ), 1.68  $\mu\text{m}$  ( $\text{CH}_4$ ), and 1.81  $\mu\text{m}$  ( $\text{H}_2\text{O}$ ,  $\text{CH}_4$  and  $\text{HCl}$  simultaneously) were characterized with respect to their temperature and current tuning properties. Compared to conventional diode lasers of similar wavelength (edge emitting DFB lasers), VCSELs can be wavelength tuned by injection current modulation much faster (up to 5 MHz). The total continuous current tuning range was found to be one order of magnitude larger than for comparable lasers. High resolution spectra were recorded at pressures ranging from 10 mbar to 1.5 bar and temperatures between 298 and 1173 K. Good agreement with the HITRAN2000 database was observed. The lower detection limit was calculated (based on a minimum detectable absorbance of 0.01) to yield 17500 ppm\*m for  $\text{NH}_3$ , 2200 ppm\*m for  $\text{CH}_4$ , 320 and 290 ppm\*m for  $\text{HCl}$  and  $\text{H}_2\text{O}$ , respectively. The tuning properties of the 1.68  $\mu\text{m}$

VCSEL were 0.86 nm/mA, 0.11 nm/K, maximum continuous current tuning range  $> 16 \text{ cm}^{-1}$  (4.5 nm), peak tuning rate  $5.2 \text{ cm}^{-1}/\mu\text{s}$  (1.5 nm/ $\mu\text{s}$ ). The tuning range at 1 MHz tuning frequency was  $2.6 \text{ cm}^{-1}$  (1.5 nm) and still  $0.36 \text{ cm}^{-1}$  (0.21 nm) at 5 MHz.

A  $0.761 \mu\text{m}$  ( $13140 \text{ cm}^{-1}$ ) VCSEL ( $\text{O}_2$  detection) was used to demonstrate measurements in flames (up to 1.0 m long) and particle laden gas streams. Absorption spectra were recorded up to 10 bar. The range of operation of TDLAS with respect to pressure is reassessed for VCSELs. Wavelength modulation spectroscopy (WMS) was also conducted.

Due to their fast and far wavelength tuning properties, VCSELs were found to be best suited for the investigation of high pressure, transient environments like laser-induced ignition.

VCSELs at  $1.69 \mu\text{m}$  ( $5917 \text{ cm}^{-1}$ ,  $\text{CH}_4$  detection) and  $2.015 \mu\text{m}$  ( $4963 \text{ cm}^{-1}$ ,  $\text{CO}_2$  detection) were used to conduct *in-situ* species concentration measurements in an internal combustion engine. During a research stay at the Optical Engine Facility at the Lund Institute of Technology, these lasers were used in an internal combustion engine (modified Volvo TD 100) with optical access operating in HCCI mode (HCCI = homogeneously charged compression ignition) running on  $\text{CH}_4$  and isooctane (25 -  $1200^\circ\text{C}$ , 1 - 50 bar). Laser aided HCCI was also investigated. These tests showed the limitations of VCSEL based optical diagnostics and the potential of laser aided HCCI.

In this thesis, transient phenomena in hot, multi-phase environments at elevated pressures were investigated successfully by *in-situ* laser spectroscopy using novel diode lasers in newly developed measurement systems.

## Kurzfassung

Das Thema dieser Doktorarbeit befasst sich mit Laserspektroskopie mittels durchstimmbarer Diodenlaser (englisch: *tunable diode laser absorption spectroscopy*, TDLAS) zur Charakterisierung von Verbrennungs- und Zündprozessen. Die durchgeführten Experimente basieren auf einem FFF Projekt zur Laserzündung von gasförmigen Brennstoff/Luft-Gemischen bei hohen Drücken. Die Aufgabe des Autors in diesem Projekt war es, die Qualität der Laserzündung zu charakterisieren.

Bei der eingesetzten Technik TDLAS wird die resonante Abschwächung des Strahls eines Infrarotlasers, dessen Wellenlänge mit einem rovibronischen Übergang der gasförmigen Zielsubstanz zusammenfällt, zur Bestimmung der Konzentration derselben herangezogen.

Über das Durchstimmen der Wellenlänge des Lasers über den Absorptionsspeak (verwirklicht durch Verändern des Laserstroms oder seiner Temperatur) lässt sich die resonante Strahlabschwächung, welche proportional zur Konzentration der Zielsubstanz ist (Gesetz von Lambert Beer), von unspezifischen Effekten unterscheiden, zu denen Streuung, teilweise Blockade des Lichts und Beam Steering, wie sie alle in rauen Umgebungen vorkommen, zählen. TDLAS ermöglicht rasche, genaue und räumlich aufgelöste *in-situ* (d.h. direkt am Ort des Geschehens) Messungen (Konzentration, Temperatur, Druck) und eignet sich daher zur Untersuchung der Laserzündung.

Die Versuche zur Laserzündung wurden in einem Druckbehälter (konstantes Volumen von 0,9 l, 473 K) mit einem gütegeschalteten Nd:YAG Laser (Pulsdauer 10 ns, Pulsenergie 1-50 mJ) durchgeführt. Der Strahl eines durchstimmbaren Diodenlasers (bei Raumtemperatur betriebener, InGaAsSb/AlGaAsSb Quantum Well Dauerstrich-Diodenlaser bei  $2,55 \mu\text{m}$  ( $3922 \text{ cm}^{-1}$ )) wurde durch diese Druckkammer geführt, und zwar senkrecht zum Strahl des Nd:YAG Lasers am Ort des Zündfunken. Der Laser wurde mit einer Repetitionsrate von 5 kHz durchgestimmt.

Auf diese Weise war es möglich, die Bildung von  $\text{H}_2\text{O}$  (starke Absorption bei  $2,55 \mu\text{m}$ ) in der Nähe des sich entwickelnden Flammenkerns mit einer Zeitauflösung von 0,2 ms semiquantitativ zu verfolgen (Nachweisgrenze etwa  $50 \text{ ppm}\cdot\text{m}$ ). Der Fülldruck bei den Laserzündversuchen mit brennstoffarmen bis -reichen  $\text{CH}_4$ /Luft-Gemischen lag bei bis zu 30 bar. Auch die Laserzündung von Biogas/Luft-Gemischen sowie verdampfter, höherer Kohlenwasserstoffe (Benzin und einige aliphatische und aromatische Hauptbestandteile davon) wurde mit dieser Technik untersucht.

Neben der Bildung von  $\text{H}_2\text{O}$  wurden die Emissionen der Flamme ( $1-10 \mu\text{m}$ ) sowie die Schwankungen in der Transmission des Diodenlaserstrahls auf den Detektor (hervorgerufen durch Beam Steering des Laserstrahls aufgrund von temperaturinduzierten Brechungsindexgradienten) zur Charakterisierung des Zündprozesses herangezogen.

Vor dem Einsatz in der optischen Diagnostik der Laserzündung wurden der InGaAsSb/AlGaAsSb Diodenlaser (Wellenlänge  $2,55 \mu\text{m}$ , geeignet zur Messung von  $\text{H}_2\text{O}$ ) sowie ein ähnlicher Laser (Wellenlänge  $2,3 \mu\text{m}$  ( $4348 \text{ cm}^{-1}$ ), geeignet zur gleichzeitigen Messung von  $\text{CH}_4$  und  $\text{CO}$ , Nachweisgrenze für beide Spezies etwa  $500 \text{ ppm}\cdot\text{m}$ ) verwendet, um die Verbrennung fester Brennstoffe in einer Wirbelschichtanlage (Freeboard) im Labormaßstab zu untersuchen (Durchstimmkoeffizienten für beide Laser  $0,07 \text{ nm}/\text{mA}$  und  $0,2 \text{ nm}/\text{K}$ , eingesetzte Durchstimmrate  $300 \text{ Hz}$ ).

Die Konzentrationsverläufe von  $\text{CO}$ ,  $\text{CH}_4$  und  $\text{H}_2\text{O}$  wurden gemessen, und zwar *in-situ* direkt über der Oberfläche von suspendierten Einzelpartikeln (Biomasse und Kohle, Abstand Laserstrahl zu Partikel  $4 - 31 \text{ mm}$ , Untersuchung des Einflusses von  $\text{O}_2$  Partialdruck und Betttemperatur auf das Emissionsverhalten während der Phase der Entgasung und des Koksabbrands) und mit Modellrechnungen verglichen (gute Übereinstimmung).

Aufgrund der Unzulänglichkeiten der Diodenlaser bei  $2,3$  und  $2,55 \mu\text{m}$  speziell zur Untersuchung von Systemen unter hohen Drücken (enger Bereich, in welchem sich die Wellenlänge durchstimmen lässt), wurden neue, vielversprechende Diodenlaser in verschiedenen Aufbauten getestet.

Ein DFB Quantenkaskadenlaser (englisch: *quantum cascade laser*, QCL) auf GaAs Basis mit einer Emissionswellenlänge von  $11,4 \mu\text{m}$  ( $877 \text{ cm}^{-1}$ , geeignet zur gleichzeitigen Messung von  $\text{NH}_3$  und  $\text{C}_2\text{H}_4$ , Nachweisgrenzen etwa  $2200 \text{ ppm}\cdot\text{m}$  für  $\text{C}_2\text{H}_4$  und  $220 \text{ ppm}\cdot\text{m}$  für  $\text{NH}_3$ ) wurde eingesetzt, um Absorptionsspektren vom Produktgas einer Biomasse-Vergasungsanlage sowie von Biogas aufzunehmen. Im Vergasergas wurden  $2\%$   $\text{C}_2\text{H}_4$  festgestellt,  $\text{NH}_3$  konnte nicht nachgewiesen werden. Der Laser wurde gepulst ( $5 \text{ kHz}$ ) betrieben (Durchstimmkoeffizient  $0,71 \text{ nm}/\text{K}$ , Durchstimmbereich  $886,76$  bis  $889,16 \text{ cm}^{-1}$  ( $30,4 \text{ nm}$ ) im Temperaturintervall von  $185$  bis  $225 \text{ K}$ ).

Neue, unmittelbar verfügbar gewordene, oberflächenemittierende Diodenlaser (englisch: vertical-cavity surface-emitting lasers, VCSELs) im Wellenlängenbereich von 1,54 bis 1,81  $\mu\text{m}$  ( $6494 - 5525 \text{ cm}^{-1}$ ) wurden auf ihre Einsatzfähigkeit in der Absorptionsspektroskopie hin getestet. Während eines Forschungsaufenthalts an der TU München wurden diese monomodigen Laser bei 1,54  $\mu\text{m}$  ( $\text{NH}_3$ ), 1,68  $\mu\text{m}$  ( $\text{CH}_4$ ) und 1,81  $\mu\text{m}$  (simultane Messung von  $\text{H}_2\text{O}$ ,  $\text{CH}_4$  und  $\text{HCl}$ ) in Hinblick auf ihr Verhalten beim Durchstimmen der Wellenlänge mit der Temperatur und mit dem Strom charakterisiert.

VCSEL lassen sich im Vergleich zu konventionellen Diodenlasern derselben Wellenlänge (kantenemittierende DFB Laser) durch Modulation des Laserstroms in ihrer Wellenlänge viel schneller (bis zu 5 MHz) und um etwa eine Größenordnung weiter (über den Strom) durchstimmen.

Hochaufgelöste Spektren in den Druck- und Temperaturbereichen von 10 mbar bis 1,5 bar bzw. 298 K bis 1173 K wurden aufgezeichnet. Gute Übereinstimmung mit berechneten Spektren (basierend auf der HITRAN2000 Datenbank) wurde festgestellt. Die Nachweisgrenze wurde, unter Zugrundelegung einer gerade noch detektierbaren Absorbanz von 0,01, zu 17500 ppm\*m für  $\text{NH}_3$ , 2200 ppm\*m für  $\text{CH}_4$  und 320 sowie 290 ppm\*m für  $\text{HCl}$  bzw.  $\text{H}_2\text{O}$  ermittelt. Die Durchstimmeigenschaften des 1,68  $\mu\text{m}$  VCSEL waren 0,86 nm/mA, 0,11 nm/K, maximaler Durchstimmbereich mit dem Strom  $> 16 \text{ cm}^{-1}$  (4,5 nm), maximale Durchstimrate 5,2  $\text{cm}^{-1}/\mu\text{s}$  (1,5 nm/ $\mu\text{s}$ ). Der Durchstimmbereich bei 1 MHz Durchstimmfrequenz betrug 2,6  $\text{cm}^{-1}$  (1,5 nm) und 0,36  $\text{cm}^{-1}$  (0,21 nm) bei 5 MHz.

Ein weiterer, bei 0,761  $\mu\text{m}$  ( $13140 \text{ cm}^{-1}$ ) emittierender VCSEL (geeignet zur Messung von  $\text{O}_2$ ) wurde eingesetzt, um die Durchführbarkeit von absorptionsspektroskopischen Messungen in Flammen (bis 1,0 m Länge) und partikelbeladenen Gasströmen zu demonstrieren. Ferner wurden Absorptionsspektren bei Drücken bis zu 10 bar aufgenommen und Wellenlängenmodulationsspektroskopie (WMS) durchgeführt. Der Einsatzbereich von TDLAS bezüglich hoher Drücke wurde neu definiert.

Aufgrund der sehr raschen und sehr weiten Wellenlängendurchstimmbareit der VCSEL wurden diese Laser als besonders geeignet erkannt zur Untersuchung von Systemen, welche transientes Verhalten und hohen Druck aufweisen, so wie etwa die Laserzündung.

VCSEL mit Emissionswellenlängen von 1,69  $\mu\text{m}$  ( $5917 \text{ cm}^{-1}$ , geeignet zur Messung von  $\text{CH}_4$ ) und 2,015  $\mu\text{m}$  ( $4963 \text{ cm}^{-1}$ , geeignet zur Messung von  $\text{CO}_2$ ) wurden schließlich dazu verwendet, *in-situ* Konzentrationsmessungen in einem Verbrennungsmotor durchzuführen. Während eines Forschungsaufenthaltes an der TU Lund wurden diese Laser an einem Motor (modifizierter Volvo TD 100) mit optischem Zugang, welcher im HCCI Modus betrieben wurde (Treibstoff  $\text{CH}_4$  und Isooktan), im Bereich von 25 - 1200°C und 1 - 50 bar eingesetzt (HCCI = homogeneously charged compression ignition; Selbstzündung eines homogenen Gemisches). Die „lasergestützte“ HCCI Verbrennung wurde ebenfalls untersucht. Die Motorenversuche verdeutlichten die Grenzen der auf VCSELn basierenden optischen Diagnostik sowie das Potential der lasergestützten HCCI.

Im Rahmen dieser Doktorarbeit wurden instationäre Phänomene in heißen, mehrere Phasen enthaltenden (d.h. feststoffbeladenes Gas) Umgebungen bei erhöhten Drücken erfolgreich untersucht. Zum Einsatz kam *in-situ* Laserspektroskopie mittels neuer Diodenlaser in neu entwickelten Meßsystemen.

## Acknowledgements

An extensive piece of work is seldom the achievement of a single person, but rather stems from the contributions and the support of many people. This also holds true for the thesis at hand.

This doctoral thesis comprises the digest of the author's studies at Vienna University of Technology from 03/2001 to 06/2003 in tunable diode laser absorption spectroscopy (TDLAS) applied to combustion and ignition diagnostics.

Prof. Dr. Franz Winter is the head of the Reaction Engineering and Combustion (RE&C) work group at the Institute of Chemical Engineering, Vienna University of Technology. He gave me the opportunity to do this work in an interesting and demanding area that started as a diploma thesis for me. I am especially grateful to Prof. Dr. Franz Winter for being able to pursue my own ideas, but also for fruitful discussions, guidance and support. Prof. Dr. Franz Winter helped me to develop my working style and a broader perception. He was always open for discussions and shared his thoughts and knowledge, which was very valuable. The personal ambition and interest that he showed in the progress of the work was very encouraging.

Dr. Gerhard Totschnig started TDLAS investigations in the RE&C work group. As one of his diploma students, I not only learned from him how to work with diode lasers, but also how to do scientific research in general. He helped me to get started in many aspects of experimental work, ranging from handicrafting, data acquisition and electronics to the presentation of our results. The laser measurement systems that were devised and built by and together with him were used in many ongoing experiments. Working with Gerhard was very instructive and also good fun. I would therefore like to express my thanks to Gerhard.

Dipl.-Ing. Christian Forsich was an eager diploma student and later on a good co worker. We completed several interesting measurement campaigns. It was also good fun to work together with Christian, and I am grateful for his contributions.

I am also indebted to my other diploma students Herwig Nier, Wilhelm Kräftner, Martin Tesch, Martin Weinrotter, Barbara Klatzer and Harald Holzapfel for their ambitiousness and eagerness in our research.

Prof. Dr. Ernst Wintner and Dipl.-Ing. Herbert Kopecek were excellent partners in a joint FFF funded research project (grant 803050) on laser-induced ignition. Their project rendered possible most of the research work presented here.

I would like to personally thank Prof. Dr. Ernst Wintner. Apart from enabling our diode laser based laser ignition diagnostics he always showed a strong personal interest in our work and provided valuable help. We had many interesting and fruitful discussions where he provided excellent insight and impulses to us. I would also like to thank Prof. Dr. Ernst Wintner for being the opponent in my PhD examination.

My thanks also go to Dipl.-Ing. Herbert Kopecek. It was him who did the first laser ignition tests. He offered a lot of help in our work and questions related to optics. Working together with Herbert was good fun, especially on our joint research stay at the optical engine laboratory at the Lund Institute of Technology, Sweden.

Also, I would like to thank our numerous cooperation partners, especially Prof. Dr. Gottfried Strasser and Dr. Solveig Anders from Vienna University of Technology (joint quantum cascade laser measurements), Prof. Dr. Markus-Christian Amann, Dr. Markus Ortsiefer and Dipl.-Phys. Robert Shau from Munich University of Technology, Germany (joint experiments

using novel vertical-cavity surface-emitting lasers), Dr. Wolfgang Kreutner from the Paul Scherrer Institute, Switzerland (valuable discussions for a research proposal building up on the work in this thesis).

I would further like to thank Prof. Dr. Anders Hultqvist and Bertil Andersson from the Lund Institute of Technology, Sweden, for their contributions to our joint measurements at an optical engine.

Dr. Günter Herdin and Dipl.-Ing. Johann Klausner from our industrial project partner Jenbacher AG also deserve being mentioned here.

Also, my thanks go to many others not mentioned here by name.

I would like to thank my girlfriend Astrid for the wonderful time that we have spent outside the laboratory.

I would like to sincerely thank my parents for all the support that they have provided me through the years.

This work is dedicated to my parents.



## Table of Contents

<b>I</b>	<b>Introduction</b>	<b>10</b>
<b>II</b>	<b>Fundamentals</b>	<b>13</b>
II.1	Absorption spectroscopy	13
II.2	Semiconductor lasers	25
II.3	Tunable diode laser absorption spectroscopy	39
II.4	Combustion	51
II.5	Ignition	58
II.6	Laser-induced ignition	66
II.7	High pressure combustion and internal combustion engines	81
II.8	High pressure combustion control	90
<b>III</b>	<b>Laser systems</b>	<b>94</b>
III.1	Edge emitting lasers at 2.3 and 2.55 $\mu\text{m}$ for CO, CH <sub>4</sub> and H <sub>2</sub> O	94
III.2	Quantum cascade laser at 11.4 $\mu\text{m}$ for NH <sub>3</sub> and C <sub>2</sub> H <sub>4</sub>	101
III.3	Vertical-cavity surface-emitting laser (VCSEL) at 0.761 $\mu\text{m}$ for O <sub>2</sub>	103
III.4	VCSELs at 1.54, 1.68, 1.80 and 2.04 $\mu\text{m}$ for NH <sub>3</sub> , CH <sub>4</sub> , H <sub>2</sub> O and HCl	106
III.5	Summary of all laser systems	115
<b>IV</b>	<b>Applications</b>	<b>116</b>
IV.1	<i>In-situ</i> measurements close to the surface of burning fuel particles	116
IV.2	Characterisation of laser ignition: CH <sub>4</sub> , biogas and liquid fuels	133
IV.3	Trace gas sensing in biogas and biomass steam gasification gas	165
IV.4	Rapid absorption spectroscopy using VCSELs	169
IV.5	Absorption spectroscopy at elevated pressures using VCSELs	199
IV.6	Rapid absorption spectroscopy in an internal combustion engine	206
IV.7	Summary of all applications	238
<b>V</b>	<b>Conclusions</b>	<b>239</b>
<b>VI</b>	<b>Outlook</b>	<b>242</b>
<b>VII</b>	<b>Publications and Patents</b>	<b>244</b>
<b>VIII</b>	<b>Collaborations</b>	<b>248</b>
<b>IX</b>	<b>Nomenclature</b>	<b>250</b>
<b>X</b>	<b>References</b>	<b>253</b>
<b>XI</b>	<b>Appendix 1: Pictures</b>	<b>270</b>
<b>XII</b>	<b>Appendix 2: Drawings of the high pressure static cell</b>	<b>276</b>
<b>XIII</b>	<b>Curriculum vitae</b>	<b>279</b>

## I. Introduction

The task of an analytical chemist is to obtain qualitative (e.g. species, functional groups) or quantitative (e.g. concentration, pH) information on a sample by developing and applying suitable methods, instruments and strategies. The deployed methods can be classified as “classical” and “instrumental” methods.

Classical methods involve wet chemical analysis. For quantitative analysis, the traditional way was by a gravimetric or titrimetric approach. For qualitative analysis, the compound of interest was judged by its reaction with special reagents. Both types require a preceding separation of the compound of interest.

Instrumental methods comprise techniques of sophisticated sample separation from the matrix (e.g. chromatography, electrophoresis), but also measurements of physical properties (e.g. light absorption, mass/charge ratio), and have been replacing classical methods continuously. The following Fig. I-1 (modified from [1]) shows a general instrumental measurement.



Fig. I-1: Scheme of an instrumental measurement (modified from [1]).

The Federation of European Chemical Societies (FECS) has listed future needs for analytical chemistry (see table I-1 (Modified from [2])).

#	Future needs in analytical chemistry
1	Greater sensitivity/selectivity
2	More innovative combinations of analytical methods
3	Advanced three-dimensional micro, nano, and subsurface analysis
4	More sophisticated understanding of measurement science
5	Ability to analyze under more rigorous <i>in-situ</i> situations
6	Direct probes of energy localization in molecules, transient states, and reaction dynamics
7	Interpretation of analytical raw data via expert systems

Table I-1: Future needs in analytical chemistry according to the Federation of European Chemical Societies (FECS), 1998 (Modified from [2]).

Point (5) in table I-1, the ability to analyze under more rigorous *in-situ* situations, is a vital concern in many respects. “*In-situ*” denotes “right at the spot”, which means that all detours like sampling, sample preparation and final *ex-situ* analysis are avoided by directly determining the measurand in the unaltered matrix. Sampling and sample preparation are prone to errors and are often laborious. Also, they introduce a time delay.

By performing an *in-situ* determination instead, fast sensor response is obtained besides less likelihood for experimental errors. For example, a pH electrode mounted in a chemical process plant will yield better results than drawing samples for manual analysis.

Even worse than failed timeliness, ex-situ determinations might easily lead to false results. This is especially true for reactive and intermediate species.

Species concentrations in flames are conventionally determined by sampling with a suction probe. A hollow metallic tube is introduced into the sample volume and used to convey a sample to the analyser.

In the literature [3], the discrepancy in the concentration values for sampled and directly determined CO in a flame has been found to reach one order of magnitude for different designs and conditions. It was suggested that the conversion of CO to CO<sub>2</sub> inside the suction probe according to  $\text{CO} + \text{OH} \rightarrow \text{CO}_2 + \text{H}$  accounts for the non-representativeness of conventional methods.

By applying a non-invasive technique like optical diagnostics, the probed system is not influenced and faulty results are avoided.

Optical diagnostics are predestined for industrial process control applications, since no plugging of sampling ports, corrosion or fouling can deteriorate the performance of and ultimately destroy the sensor, hence guaranteeing long maintenance intervals and satisfactory reliability. They are also apt for research purposes, scale-up and optimization issues, and for the determination of unstable and intermediate species in general.

It is often desired to obtain information in real-time mode, for instance in order to optimize or control a chemical process. This is the area of process analytics.

Fig. I-2 presents sampling methods that are used for process analytical purposes (modified from [2]).

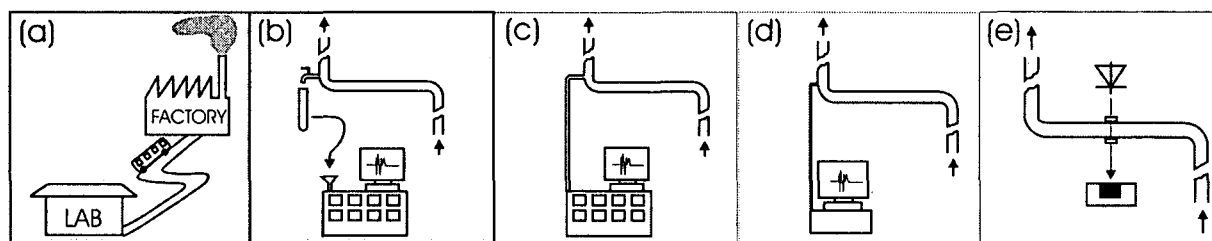


Fig. I-2: Different degrees of maturity in process analytical applications (Modified from [2]). Off-line (a), at-line (b), on-line (c), in-line (d) and non-invasive (e) measurements are possible.

Measurements in a chemical plant can be performed off-line (a), at-line (b), on-line (c), in-line (d) and in a non-invasive way (e).

For off-line analysis the sample has to be taken to a laboratory where highly sophisticated equipment and qualified personnel are available. In at-line analysis, the analyser is on site. Qualified personnel are still required. In on-line analysis, the instrument has been interfaced with the process for automated sampling and discontinuous measurements. Generally, this method is more robust and less versatile than its laboratory counterpart. In-line sensors provide measurement data continuously. Non-invasive, optical methods finally allow continuous measurements directly in the supervised process (see Fig. I-3).

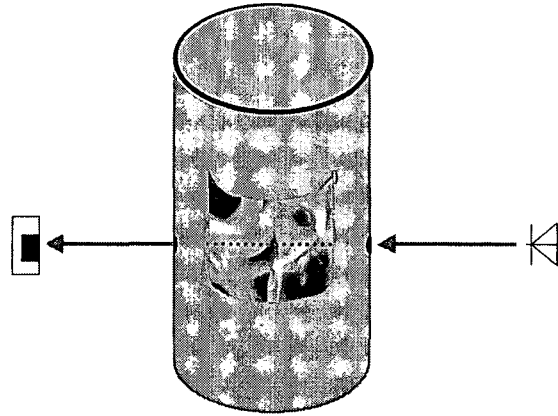


Fig. I-3: Non-invasive *in-situ* measurements under rigorous conditions by TDLAS.

The inherent advantages of *in-situ* measurements, some of which have been touched on above, are numerous. However, the implementation of an *in-situ* sensor is not always a trivial task. As point (5) in table I-1 puts it, there is an unfulfilled need for *in-situ* analysers capable of operating under rigorous conditions.

*In-situ* tunable diode laser absorption spectroscopy (TDLAS) deploys a (near infrared) diode laser as a spectrally narrow light source with the emission frequency being matched to a rovibronic transition of the target species to be analysed. The laser wavelength is scanned fully over the chosen absorption peak in order to determine the absorbance at the center (quantitative information) and in the wings (for proper background subtraction) simultaneously. This enables the determination of species concentrations, temperature and pressure under rigorous conditions. The repetition rate of this procedure, i.e. scanning the laser wavelength over the chosen absorption peak, determines the time resolution in the TDLAS experiment. A hot, multi phase environment (e.g. a flame with soot and ash particles passing through the laser beam) can hence be probed. Fast wavelength scanning enables the investigation of transient phenomena.

In this thesis, species concentration measurements under difficult conditions were performed.  $\text{H}_2\text{O}$ ,  $\text{CO}$  and  $\text{CH}_4$  were measured close to the surface of single burning fuel particles in a laboratory-scale fluidized bed combustor.  $\text{O}_2$  was measured in liquid fuel flames of up to 1 m path length.

Also, transient phenomena were investigated. Laser induced ignition of gaseous mixtures was observed by measuring the  $\text{H}_2\text{O}$  vapour generated close to the position of the igniting spark.

As the pressure in the probed system increases, the absorption peaks tend to broaden, and the diode laser cannot scan over the entire peak any more. The background signal hence cannot be determined any more, and the TDLAS technique can no longer be used. In this thesis, experiments with novel near infrared diode lasers, so called vertical-cavity surface-emitting lasers (VCSELs), were conducted. It was discovered that these lasers can be wavelength scanned extraordinarily far, hence pushing the limit of sensors based on conventional diode lasers further towards higher pressures. It was also discovered that these lasers can be wavelength scanned faster than conventional diode lasers, thus enabling measurements of pressure, temperature and concentration in gases with extremely transient behaviour.

In this thesis, TDLAS was applied to *in-situ* combustion and ignition diagnostics. Laser measurement systems were constructed and tested for their use in hostile environments.

The test runs started with laser characterisation, moved on to tests in static cells and were finally carried out in an internal combustion engine.

## II. Fundamentals

### II.1 Absorption spectroscopy

In a generalizing approach, spectroscopy is the interaction of electromagnetic radiation (light) with matter. An arbitrary sample can be characterized by its state of matter (liquid, solid, gas, plasma), its composition, the spatial distribution of certain "building blocks" (atom, molecule, phase), and its chemical properties. This results in a set of energy states that are all determined by the properties of the sample. The states are quantized (cf. elementary quantum mechanics). So each sample is defined by a set of energy states. Now one can turn this statement around and argue: When information about these energy states is obtained, information about the sample itself is won. This is the principle of physical analysis.

Photons, electrons and ions can serve as agents or probes, the energy ranges from  $10^4$  to  $10^7$  eV ( $1 \text{ eV} = 1.602 \cdot 10^{-19} \text{ J}$ ). The signal is characterized by its type, energy and intensity. The information can be quantitative, qualitative, structural, etc.

The electromagnetic spectrum can be divided into several regions (the boundaries are not fixed by nature, so the following tables II.1-1 and II.1-2 show arbitrary -but common-subdivisions).

Spectral region	Wavelength $\lambda$
X-ray	< 10 nm
UV (ultra violet)	10 nm - 400 nm
VIS (visible)	400 nm - 800 nm
IR (infra red)	0.8 $\mu\text{m}$ - 100 $\mu\text{m}$
Microwave	0.1 mm - 100 mm
RF (radio frequency)	0.1 m - 10 m

Table II.1-1: Arbitrary division of the electromagnetic spectrum.

Tables II.1-2 shows the subdivisions of the infrared spectral region.

Spectral region	Wavelength $\lambda$
Near IR	0.8 $\mu\text{m}$ - 2.5 $\mu\text{m}$
Mid IR	2.5 $\mu\text{m}$ - 25 $\mu\text{m}$
Far IR	25 $\mu\text{m}$ - 100 $\mu\text{m}$

Table II.1-2: Subdivision of the IR spectrum.

Light can interact with matter in different ways: Absorption, emission, refraction, interference, diffraction, scattering and rotation. This thesis deals with absorption spectroscopy, thus the focus of this chapter will be on the theoretical background of this phenomenon. This restriction is also justified by the outstanding importance of this technique (e.g. uncomplicated setup, quantitative results, high sensitivity and selectivity).

A typical experimental setup for absorption measurements is depicted below in Fig. II-1.1.

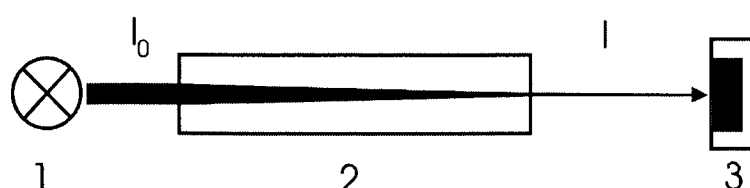


Fig. II.1-1: Basic absorption spectroscopy setup. 1: Monochromatic light source; 2: sample volume; 3: detector;  $I_0$  is the initial and  $I$  the transmitted light intensity.

(In Fig. III-1 and Fig III-2 the setup with a laser based measurement system can be seen in more detail).

A phenomenological description of absorption is illustrated in the following Fig. II.1-2. Light is radiated through a sample (solid, liquid and gaseous) and the transmitted light is recorded to yield a spectrum. The intensity of transmitted light is plotted over its wavelength. One can see that solids and liquids absorb light in broad bands, whereas sharp lines are encountered in gases (right part of Fig. II.1-2).

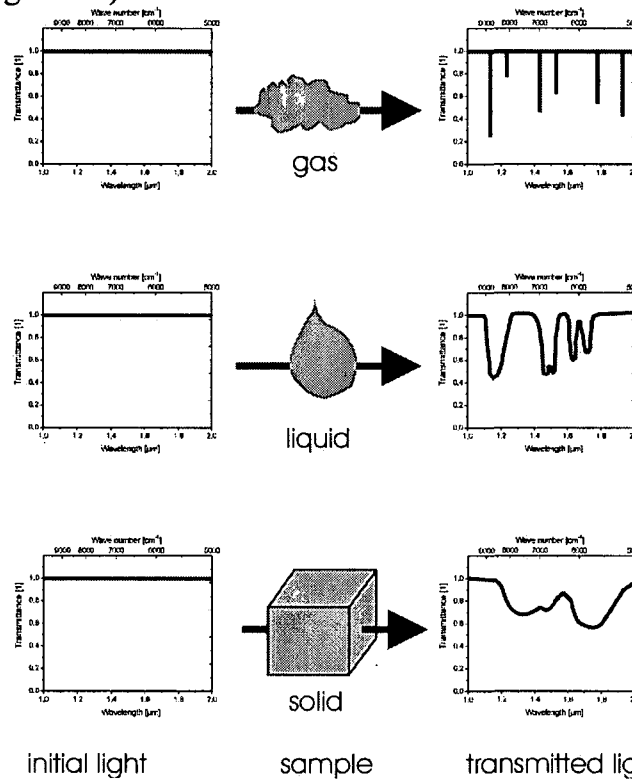


Fig. II.1-2: Qualitative appearance of spectra in the three states of matter. In a gaseous sample, discrete, sharp absorption lines are encountered. In liquids, absorption takes place in bands. Solids show even broader absorption bands.

The emission or absorption of a photon when a molecule changes its energy causes the typical lines in spectra to appear. By definition, a spectrum is a plot of intensity versus wavelength. The energy levels in a molecule are called terms. The internal energy, which excludes kinetic energy, is stored in three modes: rotation, vibration and electronic (Equation II.1-1).

$$E_{\text{tot}} = E_{\text{rot}} + E_{\text{vib}} + E_{\text{elec}}$$

(Eq. II.1-1)

E... Energy [J]

The discreteness of energy states leads to discrete changes in energy when molecules change quantum states. These energy differences are associated with the emission or absorption wavelengths in discrete spectra. Planck's law (Eq. II.1-2) links the properties of a photon as a particle and a wave:

$$\Delta E = E_1 - E_2 = h\nu$$

(Eq. II.1-2)

h... Planck's constant ( $6.63 \cdot 10^{-34}$  Js)

v... frequency [ $s^{-1}$ ]

Eq. II.1-1 and Eq. II.1-2 give

$$\Delta E = E_{\text{rot}} + E_{\text{vib}} + E_{\text{elec}}$$

(Eq. II.1-3)

So in order for an energy exchange and a transition to occur, the energy of the photon has to match any combination of  $E_{\text{rot}} + E_{\text{vib}} + E_{\text{elec}}$ .

The energy level separation is roughly 400kJ/mol ( $\sim 4\text{eV}$ ,  $33400\text{ cm}^{-1}$ ) for electronic transitions, 20 kJ/mol ( $\sim 0.2\text{ eV}$ ,  $1670\text{ cm}^{-1}$ ) for vibrational and 0.04 kJ/mol ( $\sim 4 \cdot 10^{-4}\text{ eV}$ ,  $3.3\text{ cm}^{-1}$ ) for rotational changes. Accordingly, in the near and mid IR ( $0.8 - 25\text{ }\mu\text{m}$ ,  $\sim 12500 - 0.0025\text{ cm}^{-1}$ ), a molecule can absorb light by increasing its vibrational or its vibrational and rotational energy simultaneously. An electronic transition requires too much energy and is out of reach. A purely rotational energy change is too small and thus out of reach, too.

Since the average thermal energy of a molecule at room temperature is on the order of 4 kJ/mol ( $\sim 0.04\text{ eV}$ ,  $330\text{ cm}^{-1}$ ), most molecules will be in the lowest vibrational and electronic levels (the ground state), but will be distributed over several rotational levels.

This is described by the Boltzmann distribution (see Eq. II.1-4 and II.1-6 below).

All possible transitions following absorption may start from any of these occupied rotational levels within the vibrational ground state and may end on any rotational level within the vibrational first excited state, with selections rules imposing some limitations on allowed transitions.

To summarize, it can be concluded that

$\Delta E_{\text{rot}}$  leads to microwave transitions (rotational spectroscopy)

$\Delta E_{\text{rot}} + \Delta E_{\text{vib}}$  lead to IR transitions (vibrational spectroscopy)

$\Delta E_{\text{rot}} + \Delta E_{\text{vib}} + \Delta E_{\text{elec}}$  lead to UV/VIS transitions

Atoms can only undergo electronic transitions, whereas molecules also exhibit vibrational and rotational changes. The spectra contain a wealth of information, e.g. clues to the dipole moment or bond angles. Vibrational spectra in the gas phase are always superimposed by rotational transitions, since their excitation energy is one order of magnitude smaller. Whether a sample is probed by absorption or emission techniques does not affect the information that is obtained (A big advantage of measuring emission is that a strong signal and a weak background are encountered. In absorption spectroscopy, one generally has to determine a small attenuation of a strong signal). The transitions depend on which energy levels are occupied and which transitions are possible. The latter is dealt with by selection rules, the former by the Boltzmann distribution. The Boltzmann equation gives the fraction of molecules  $F_i$  in an energy level  $i$ :

$$F_i = \frac{n_i}{n} = \frac{g_i \cdot \exp\left(-\frac{E_i}{kT}\right)}{Q}$$

(Eq. II.1-4)

Q... partition function [1]

n... number

$g_i$ ... degeneracy of level  $i$  (number of individual states with a common energy  $E_i$ )

T... temperature [K]

n... number [1]  
 k... Boltzmann constant ( $1.38 \cdot 10^{-23}$  J/K)  
 E... energy [J]

The partition function  $Q$  is given by Eq. II.1-5.

$$Q = \sum_i g_i \cdot \exp\left(-\frac{E_i}{kT}\right) = Q_{rot} \cdot Q_{vib} \cdot Q_{elec}$$

(Eq. II.1-5)

The Boltzmann distribution function yields the distribution of species (molecules or atoms) over all allowed quantum states.

(Eq. II.1-5) shows that  $Q$  can be written as a product of partition functions for the different types of internal energy  $Q_{rot}$ ,  $Q_{vib}$  and  $Q_{elec}$ .

For a two level system 1 and 2 (or in simplification for a multi level system with other states being far out of reach), (Eq. II-1-4) can be written as

$$\frac{N_1}{N_2} = \frac{g_1}{g_2} \cdot \exp\left(-\frac{(E_2 - E_1)}{kT}\right)$$

(Eq. II.1-6)

$N_1, N_2...$  number populations [1]  
 $g...$  degeneracy [1]

When  $E_2 - E_1$  is on the order of  $kT$  (which is well the case for two adjacent vibrational levels at room temperature), the upper level will be significantly populated.

The properties of a photon can be quoted in terms of its wavelength  $\lambda$  [ $\mu\text{m}$ ], its wave number  $\bar{\nu}$  [ $\text{cm}^{-1}$ ] or its energy  $E = h\nu$  [eV].

The conversion of these different dimensions is as follows:  $1 \text{ eV} = 1.602 \cdot 10^{-19} \text{ J} = 8044 \text{ cm}^{-1} = 0.413 \mu\text{m}$ .

Another important equation in this respect is the connection between wavelength and wave number:

$$\lambda = \frac{c}{\nu} = \frac{1}{\bar{\nu}}$$

(Eq. II.1-7)

$c...$  speed of light ( $3 \cdot 10^8 \text{ m/s}$ )

To convert  $\lambda$  [ $\mu\text{m}$ ] to  $\bar{\nu}$  [ $\text{cm}^{-1}$ ], one has to divide  $10^4$  by the other variable. The preferred use of the wave number results from the fact that it is directly proportional to the energy. A conversion table between these two units is given in the appendix. When light passes through a sample that contains an absorbing species, the beam will be attenuated. This phenomenon can be described by the following differential equation:



$$dI = -\kappa[J]I dl$$

(Eq. II.1-8)

- dl... differential path length  
 [J]... concentration of the absorbing molecule  
 I... intensity [W/m<sup>2</sup>]  
 κ... some constant

If the absorbing species is distributed uniformly, [J] is no function of the path length. Separation of the variables transforms (Eq. II.1-8) to

$$\frac{dI}{I} = -\kappa[J] dl$$

(Eq. II.1-9)

$$\int_{I_0}^I \frac{dI}{I} = -\kappa \int_0^l [J] dl$$

(Eq. II.1-10)

$$\ln \frac{I}{I_0} = -\kappa[J]l$$

(Eq. II.1-11)

One obtains Lambert Beer's law:

$$A = \alpha_{\nu} l = -\ln \frac{I}{I_0} = \ln \frac{I_0}{I}$$

(Eq. II.1-12)

- A... absorbance [1]  
 α<sub>ν</sub>... spectral absorption coefficient [cm<sup>-1</sup>]  
 l... path length [cm]  
 I<sub>0</sub>... incident light intensity [W/m<sup>2</sup>]  
 I... transmitted light intensity [W/m<sup>2</sup>]

The transmittance T is defined as

$$T = \frac{I}{I_0}$$

(Eq. II.1-13)

The absorption Abs is defined as

$$\text{Abs} = 1 - T$$

(Eq. II.1-14)

Neither the absorption nor the transmittance is directly proportional to the concentration of the absorber.

The absorbance  $A$  fulfils this practical requirement and is therefore the often preferred. It is also termed optical depth.

The following Fig. II.1-3 illustrates the relationship between transmittance, absorption and absorbance.

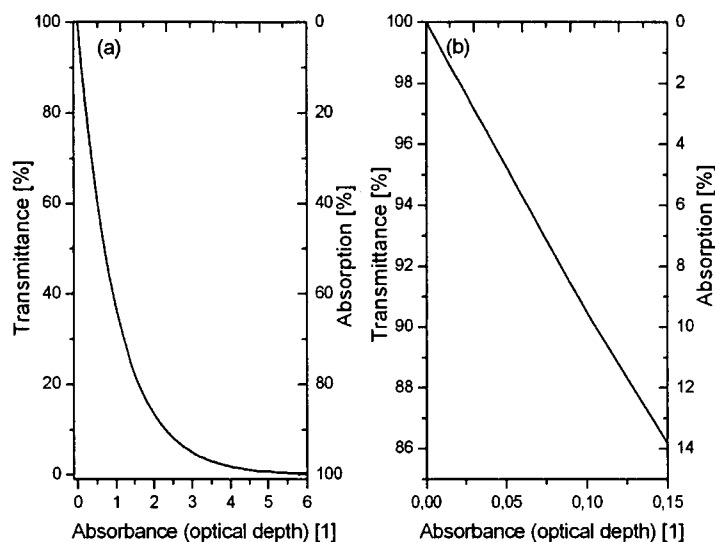


Fig. II.1-3: Relationship between absorbance, transmittance and absorption. Depicted are the transmittance (left vertical axis) and the absorption (right vertical axis) as a function of absorbance (= optical depth). (b) is a magnification of (a) to show that for low absorbances, there is an approximately linear relationship.

Requirements for the derivation of Lambert Beer's law are:

- Monochromatic light
- Collimated beam
- No stray light
- Parallel entrance and exit planes
- No molecular interaction

As mentioned and derived above, the absorbance can be related directly to the concentration of a compound in the sample. In the case of quantitative gas analysis, the partial pressure is used instead of the concentration.

The spectral absorption coefficient  $\alpha_\nu$  is given by

$$\alpha_\nu = S_i \Phi_\nu P_i$$

(Eq. II.1-15)

- $S_i$ ... "strength" of the transition  $i$  [ $\text{cm}^{-2}\text{atm}^{-1}$ ]  
 $\phi$ ... line shape function [cm]  
 $P_i$ ... partial pressure of the absorbing species  $i$  [atm]

The "strength" of the transition  $S$  is also termed spectral line intensity. In HITRAN, it is tabulated for 296K in [ $\text{cm}^{-1}/\text{molecule} \cdot \text{cm}^{-2}$ ]. To convert  $S$  from [ $\text{cm}/\text{molecule}$ ] to [ $\text{cm}^{-2}/\text{atm}^{-1}$ ], one has to multiply by  $2.48 \cdot 10^{19}$ .

HITRAN [4] is a spectroscopic database. It is a tabular compilation of line parameters of 38 gaseous species (e.g. H<sub>2</sub>O, CO, CO<sub>2</sub>, CH<sub>4</sub>, OH, NH<sub>3</sub>, HCN, O<sub>2</sub>). Another important spectroscopic database is GEISA [5]. The data contained in such databases can be used for spectra calculation [6] (see later).

The absorption coefficient is related to the absorption cross-section  $\sigma_\nu$  by:

$$\alpha_\nu = \sigma_\nu N$$

(Eq. II.1-16)

N... number density of molecules [molecules/cm<sup>3</sup>]

$\sigma_\nu$ ... absorption cross-section [cm<sup>2</sup>/molecule]

The number density can be obtained from the ideal gas law:

$$N = 2.687 \cdot 10^{19} \cdot (273/T) \cdot (p/1013)$$

(Eq. II.1-17)

p... pressure [mbar]

T... temperature [K]

From what has been said above, one might think that all transitions found in a spectrum are sharp. However, perturbation effects blur the energy levels so that they are not completely the same for each molecule any more.

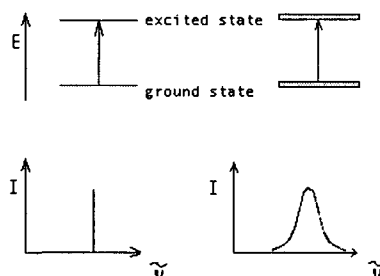


Fig. II.1-4: Spectral broadening. On the left, sharp ground and excited state (top) lead to a sharp absorption line (bottom). On the right, ground state and excited state have no infinitely sharp energy. Therefore, the absorption line will also show broadening.

Depending on whether the perturbation is the same for all molecules or not, the underlying broadening mechanism is called homogeneous (the interaction for all molecules being the same) or inhomogeneous, respectively. Broadening of absorption lines is caused by perturbation of the energy levels.

This is expressed in terms of the line shape function  $\phi$ .

So-called lifetime broadening will be considered first.

Heisenberg's uncertainty principle states that

$$\delta E \sim \frac{h}{2\pi \tau}$$

(Eq. II.1-18)

$\delta E$ ... energy uncertainty [J]

The lifetime  $\tau$  of any excited state is first and foremost determined by the rate of spontaneous emission and hence causes an intrinsic broadening, the natural line width. Typical life times in the excited state are listed in table II.1-3.

$t_{\text{electronic}}$	$\sim 10^{-16}$ s
$t_{\text{vibrational}}$	$\sim 10^{-13}$ s
$t_{\text{rotational}}$	$\sim 10^{-10}$ s

Table II.1-3: Life times. The typical life time of an excited electronic state is  $10^6$  times shorter than of a rotational state.

The uncertainty of a transition is given by the lifetimes of the upper and lower state  $\tau_{\text{upper}}$  and  $\tau_{\text{lower}}$  by

$$\Delta\nu = \frac{1}{2\pi} \left( \frac{1}{\tau_{\text{lower}}} + \frac{1}{\tau_{\text{upper}}} \right)$$

(Eq. II.1-19)

So any transition will occur in a more or less sharp frequency interval  $\Delta\nu$ . Lifetime broadening is a homogeneous broadening mechanism.

Lifetime broadening is partly natural in its origin, since the intrinsic lifetime of an excited state is limited by the rate of spontaneous emission. The line width is negligible.

Another important broadening mechanism is Doppler broadening. The Doppler effect describes the changes in frequency when a source of electromagnetic or acoustic waves moves relatively to the observer. When source and observer are approaching, more peaks than normally hit the observer, resulting in a seemingly higher frequency.

The shift can be described as:

$$\nu_{\text{approaching}} = \nu_0 \sqrt{\frac{1 + \frac{s}{c}}{1 - \frac{s}{c}}}$$

(Eq. II.1-20)

$$\nu_{\text{receding}} = \nu_0 \sqrt{\frac{1 - \frac{s}{c}}{1 + \frac{s}{c}}}$$

(Eq. II.1-21)

s... speed of the observer [m/s]

In gases, the molecules move fast in all directions at different speeds  $v$ . According to Maxwell, the fraction between  $\nu_{\text{lower}}$  and  $\nu_{\text{upper}}$  is given by

$$\int_{\nu_{lower}}^{\nu_{upper}} f(\nu) d\nu$$

(Eq. II.1-22)

with

$$f(\nu) = 4\pi \left( \frac{M}{2\pi RT} \right)^{\frac{3}{2}} \nu^2 \exp\left(-\frac{M\nu^2}{2RT}\right)$$

(Eq. II.1-23)

- T... temperature [K]  
 M... molar mass [amu]  
 R... gas constant (8.314 J\*K<sup>-1</sup>mol<sup>-1</sup>)

$e^{-x^2}$  denotes a Gaussian function. Therefore the Doppler broadened absorption feature will exhibit a line shape function with a Gaussian form. The Doppler broadened line half width (measured at half maximum, FWHM, full width at half maximum, or HWHM, half width at half maximum) is on the order of 0.02 cm<sup>-1</sup> (5\*10<sup>-3</sup> nm at 1.5 μm). Doppler broadening is inhomogeneous. It is dominant at pressures below 1 bar.

Perturbations through collisions lead to so-called pressure broadening. This effect dominates at pressures above approximately 1 bar. Pressure broadened spectra are much broader than Doppler broadened ones.

There are several other mechanisms that lead to the broadening of spectral lines. Charged particles in plasmas exert long-range Coulomb forces that can perturb the energy levels of especially light atoms. This effect is called Stark broadening. Instrument broadening is an artifact due to a bad monochromator or a broadly emitting light source. Power broadening is an artifact, too; In this case, the laser is so strong that the initial population distribution is perturbed.

The pressure broadened line half width  $\gamma(p,T)$  for a gas at pressure  $p$  [atm], temperature  $T$  [K] and partial pressure  $p_s$  [atm] is given by the following equation:

$$\gamma(p,T) = \left(\frac{T}{T_{ref}}\right)^n (\gamma_{air}(p_{ref}, T_{ref})(p - p_s) + \gamma_{self}(p_{ref}, T_{ref})p_s)$$

(Eq. II.1-24)

- $\gamma$ ... line half width [cm<sup>-1</sup>]  
 n... coefficient of the temperature dependence of the air-broadened half width [1]

The pressure shift of the transition frequency results in a shifted frequency  $\nu^*_{\eta\eta'}$ ,

$$\nu^*_{\eta\eta'} = \nu_{\eta\eta'} + \delta(p_{ref})p$$

(Eq. II.1-25)

## Line shape functions

Not taking into account the natural life time of a quantum state, the shape of a spectral line of a molecule is determined by the perturbing influences stemming from neighboring species and the thermal motion of the absorber/emitter itself.

There are three main constituents contributing to the overall shape of a single rotational line:

- a Gaussian line shape component due to Doppler broadening
- a Lorentzian contribution due to collisional broadening (pressure broadening)
- an instrumental line shape function

Each free line will be a convolution of the inherent natural line shape (of negligible width) with the above functions. The different pressure regimes govern the mechanism driving the shape of the line. At sub atmospheric pressures, the spectral line profile depends only upon the velocity distribution of the molecules. If the expression for the kinetic energy  $E=mv^2/2$  is combined with the Boltzmann equation, a Gaussian function is obtained. It exactly describes the line profile below a few mbar. At higher pressure, molecular collisions broaden the line so that the profile has to be described by a Lorentzian function. So the absorption line shape in the gas phase is usually a convolution of a Doppler-broadened Gaussian function and a pressure-broadened Lorentzian function that can be described by a Voigt profile. At low pressures (below a few mbar), the Voigt profile transforms to a Gaussian one, and at high pressures (towards 1 atm and above) the Lorentzian profile is obtained. The pressure at which neither Gaussian line width nor Lorentzian line width can be neglected is around 30 mbar. At pressures around a few mbar, the Gaussian profile will correctly describe the line shape, whereas at atmospheric pressures and above, the Lorentzian profile will yield the best fit. Thus the Voigt line shape function incorporating both parts offers a good description for all pressures. A visual comparison of the major line shape functions is presented in Fig. II.1-5.

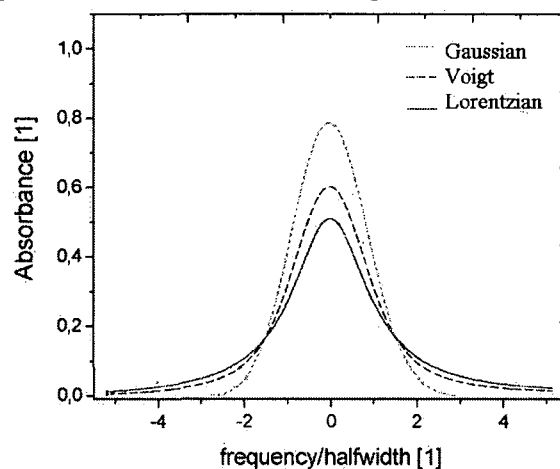


Fig. II.1-5: Spectroscopic functions: The Gaussian line shape has a peak value that is ~50% higher than the Lorentzian counterpart, but it drops off faster towards the wings, the Voigt profile being the convolution of both is situated in the middle. (The line shape function  $S$  and the half width (FWHM or HWHM, respectively) are the same. The Voigt profile has been calculated for the pressure where  $\gamma_L = \gamma_D$ ) (Modified from [7]).

The area under the curves in Fig. II.1-5 is always the same.

The Lorentzian line shape  $S_L$  is given by

$$S_L = \pi \sigma_L(\nu) \frac{(\nu - \nu_0)^2 + \gamma_L^2}{\gamma_L}$$

(Eq. II.1-26)

$\gamma_L$ ... HWHM of the line shape (L stands for Lorentz)

$\nu_0$ ... center frequency

$\gamma_L$  depends on the pressure and the temperature according to

$$\gamma_L = \gamma_{L0} \frac{p}{p_0} \sqrt{\frac{T_0}{T}}$$

(Eq. II.1-27)

$\gamma_{L0}$ ... HWHM of the line shape at  $T_0, p_0$  (STP)

The Gaussian line shape  $S_G$  is given by

$$S_G = \sigma_D(\nu) \sqrt{\frac{\pi}{\ln 2}} \gamma_D \exp\left(-\frac{(\nu - \nu_0)^2 \ln 2}{2 \gamma_D^2}\right)$$

(Eq. II.1-28)

$\gamma_D$ ... HWHM of the line shape (D stands for Doppler)

The Doppler HWHM  $\gamma_D$  is given by Eq. II.1-29 and II.1.30:

$$\gamma_D = \sqrt{\frac{8kT \ln 2}{m}} \frac{\nu_0}{c}$$

(Eq. II.1-29)

A simplification is obtained by replacing the constants by their numerical values:

$$\gamma_D = 7.1623 \cdot 10^{-7} \nu_0 \sqrt{\frac{T}{m}}$$

(Eq. II.1-30)

m... mass [amu]

T... temperature [K]

$\gamma$ ... half width [ $\text{cm}^{-1}$ ]

For the more complicated Voigt profile, several approximations exist, one of which is the following:

$$\gamma_V = 0.5346\gamma_L + \sqrt{0.2166\gamma_L^2 + \gamma_D^2}$$

(Eq. II.1-31)

$\gamma_V$ ... HWHM of the line shape (V stands for Voigt)

The height of the absorption peak/the area below it (in absorbance units) is directly proportional to the number density (i.e. concentration times path length) of the target species. This brings us back to Lambert Beer's law (Eq. II.1-12).

The following Fig. II.1-6 presents a compilation of absorption lines of several species in the infrared (taken from [4]). Only the fact that the individual lines and the line width of the probing diode laser are extremely narrow enable the recording of single absorption lines (see chapter II.3, especially Fig. II.3-3).

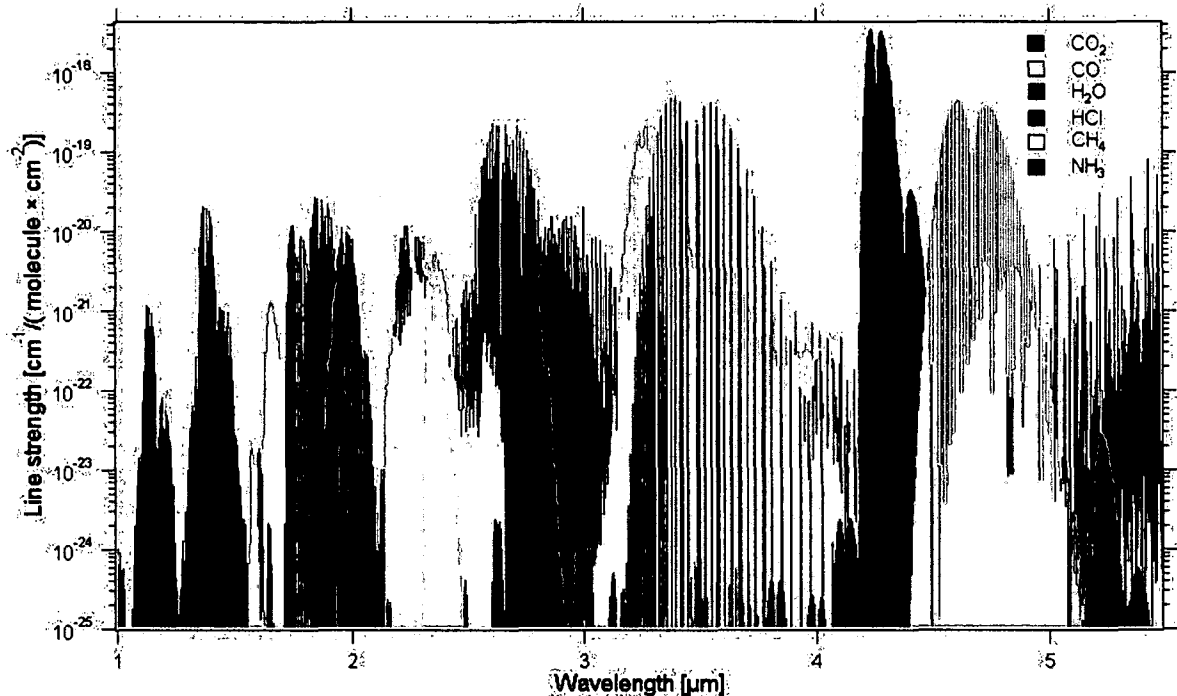


Fig. II.1-6: Absorption lines of CO<sub>2</sub>, CO, H<sub>2</sub>O, HCl, CH<sub>4</sub> and NH<sub>3</sub> in the infrared (Taken from [4]). The individual lines are very sharp so that a narrow light source (e.g. a laser) can be used to access one of them separated from the others.

More information on absorption spectroscopy in gases can be found in [8] to [12].



## II.2 Semiconductor lasers

This chapter presents some introductory concepts on diode lasers. A laser consists of two mirrors forming a resonance cavity and a gain medium between them. This basic principle that holds true for single laser is illustrated below in Fig. II.2-1:

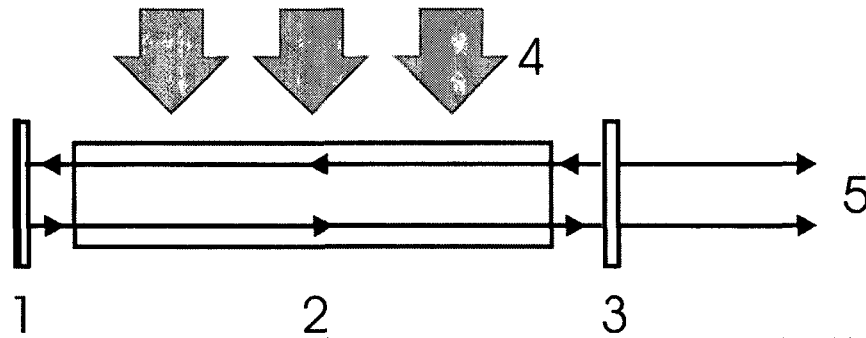


Fig II.2-1: Every laser has got a resonator (2) between two mirrors (1, 3) and a gain medium (4). The light (5) is coupled out at the semi transparent mirror (3).

The key issue in constructing a laser is getting population inversion. Thermodynamics prohibit an inverted state, since it would correspond to a negative absolute temperature. To understand this, simply recall the Boltzmann distribution:  $N_{upper}/N_{lower} = g_{upper}/g_{lower} \cdot \exp([E_{upper}-E_{lower}]/kT) < 1$  (Eq. II.1-6). By resorting to a three level system where the upper level has got a much shorter lifetime than the lower excited state, pumping can bring about inversion between the ground state and the lower excited state. In a four level laser, inversion can be accomplished easier; for population inversion between levels 2 and 3, far less than half of the atoms have to be excited. This idea is shown graphically in Fig. II.2-2.

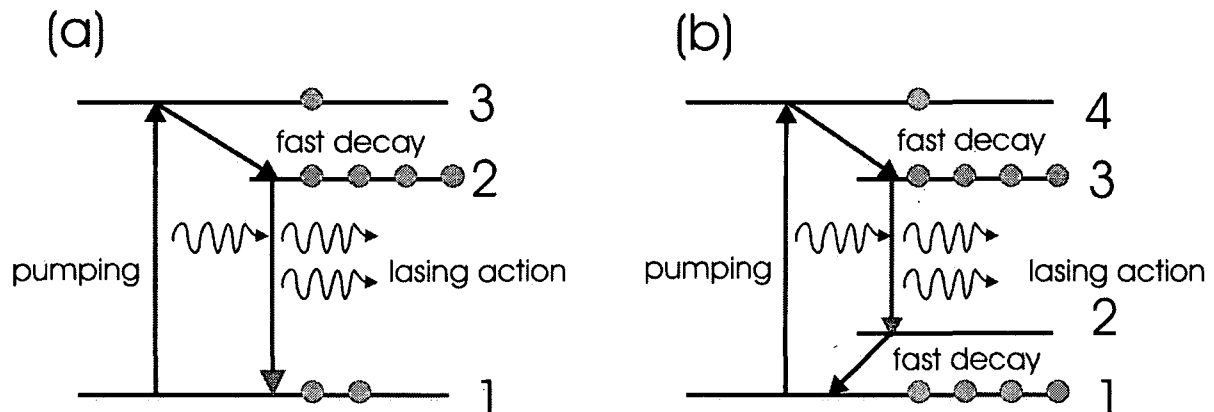


Fig. II.2-2: Schemes of a three-level (a) and four-level (b) laser. Population inversion can be achieved more easily in a four level system.

The resonator dimensions determine the wavelength. For a standing wave to form, an integral multiple of  $\lambda/2$  has to fit into the cavity. As shown below in Fig. II.2-3, this is possible for an infinite number of wavelengths  $\lambda_i$ . However, the gain profile determines which of these will be amplified. LASER is an acronym for light amplification by stimulated emission of radiation.

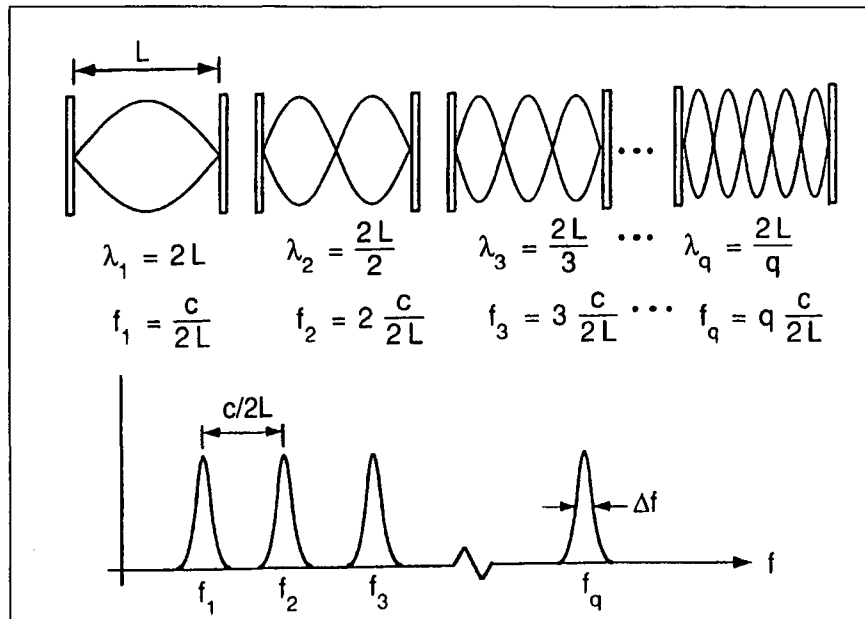


Fig. II.2-3: Possible standing waves (wavelengths  $\lambda_i$ , frequencies  $f_i$ ) in a laser resonator (Taken from [13]). The frequency spacing is  $c/2L$  with  $c$  being the speed of light and  $L$  the resonator length.

The cavity can have different shapes. Stable resonators need not necessarily be composed of two plane parallel facets. Concentric (spherical), confocal, hemifocal or hemispherical cavity setups are also possible. The easiest cavity design has got two plane parallel mirrors, also known as Fabry Perot (FP) resonator. One of the two mirrors is partly transparent so that light can be coupled out of the laser.

### Semiconductor lasers

The main difference between semiconductor lasers and other types of lasers is that the relevant energy levels are bands rather than discrete states. In conventional solid-state lasers, dopants within a host material have got well-defined, sharp energy levels because they are unperturbed. The splitting of atomic energy levels as the atoms in a solid start interacting with each other is rooted in Pauli's exclusion principle. In a conducting material like metals the valence and conduction band overlap. As for insulators, the band gap is several eV (5.45 eV for diamond). Semiconductors have got a much smaller spacing of the two bands (1.17 eV for Si and 0.744 eV for Ge). At  $T = 0$  K, the energy levels are all filled up to a maximum energy which is called the Fermi level. No states above the Fermi level are filled.

The following Fig. II.2-4 illustrates the band theory of solids. In (a), the molecular orbital energy level diagram for  $O_2$  is shown (molecular orbital theory, Mullikan, Hund, 1928 [14]).

Two atoms combine ( $N = 2$ ). In (b), the energy level splitting for  $N = 1, 2, 3, \dots, \infty$  atoms in a solid is shown. For  $N \rightarrow \infty$ , an energy band is obtained. Fig. II.2-4 (c) illustrates the

simplified band structure of Si (1). The valence band (VB) is filled with electrons, the conduction band (CB) is empty. CB and VB are separated by the band gap. At  $T > 0$  K, electrons from the VB can be thermally excited into the CB. For this reason, the resistance of semiconductors decreases with temperature. In (2), the doping of silicon (Si) with indium (In) is shown, in (3), the doping with arsenic (As). In has got fewer electrons than the host material (Si) and can therefore accept electrons from the VB. As has got more and can supply electrons to the CB. (6) and (7) show the modification of the band structure. Doping alters the electronic properties of the material (introduction of donor or acceptor levels, see Fig. II.4-4 (c)).

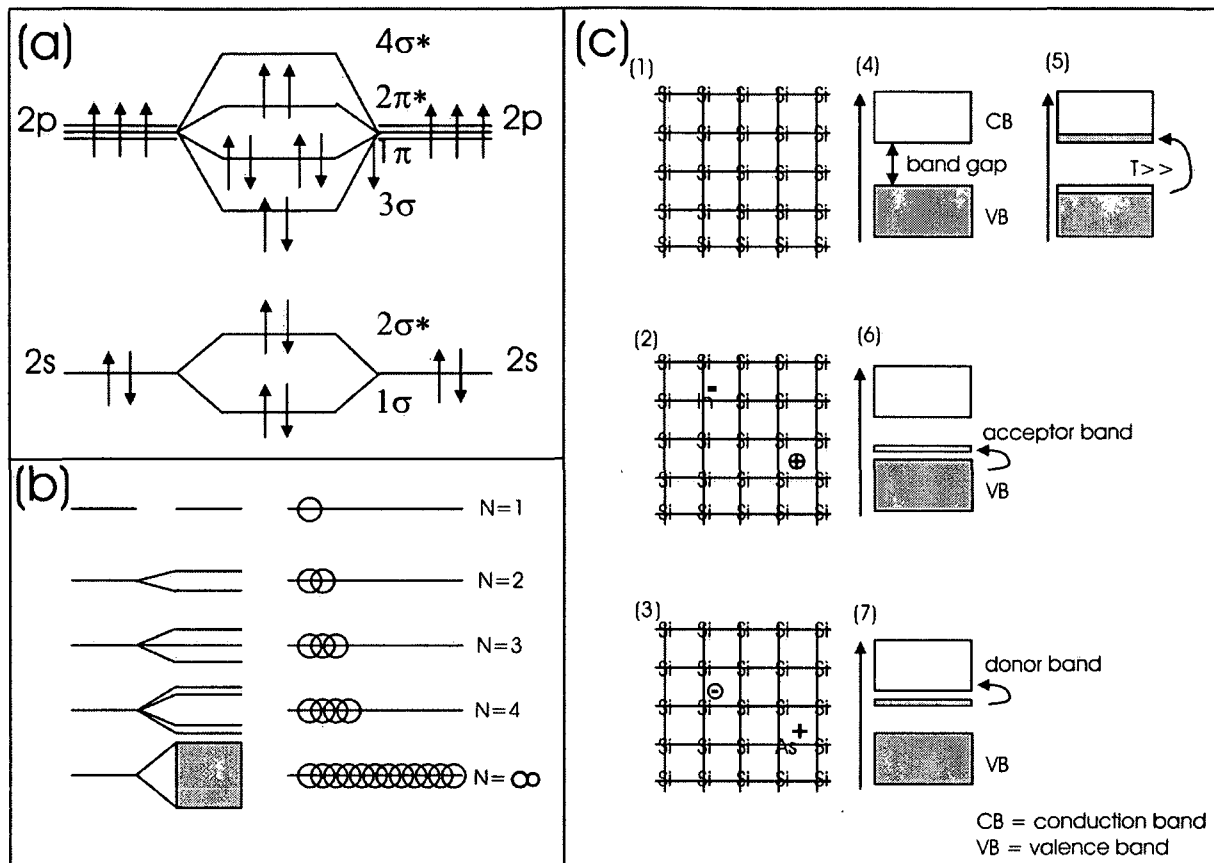


Fig. II.2-4: Energy bands in semiconductors; (a): molecular orbital energy diagram of  $O_2$ ; (b): molecular orbital energy diagram of a metal; (c): Influence of dopants on the band structure. Depicted are undoped, n-doped and p-doped Si (Modified from [8] and [14]). In (p-doping) introduces holes, As (n-doping) electrons. Compare the periodic table of elements below (Fig. II.2-5) for the location of elements. See text for details.

The periodic table of elements in Fig. II.2-5 is to illustrate the location of suitable elements for p doping (group 13) and for n doping (group 15).

1																		18																	
Atomic number																		Atomic weight																	
1	H	2	He															3	B	4	C	5	N	6	O	7	F	8	Ne						
3	Li	4	Be															9	Al	10	Si	11	P	12	S	13	Cl	14	Ar						
5	Na	6	Mg															13	Al	14	Si	15	P	16	S	17	Cl	18	Ar						
7	K	8	Ca	9	Sc	10	Ti	11	V	12	Cr	13	Mn	14	Fe	15	Co	16	Ni	17	Cu	18	Zn	19	Ga	20	Ge	21	As	22	Se	23	Br	24	Kr
19	Rb	20	Sr	21	Y	22	Zr	23	Nb	24	Mo	25	Tc	26	Ru	27	Rh	28	Pd	29	Ag	30	Cd	31	In	32	Sn	33	Sb	34	Te	35	I	36	Xe
37	Cs	38	Ba	39	La	40	Hf	41	Ta	42	W	43	Re	44	Os	45	Ir	46	Pt	47	Au	48	Hg	49	Tl	50	Pb	51	Bi	52	Po	53	At	54	Rn
55	Fr	56	Ra	57	Ac	58	Th	59	Pa	60	U	61	Np	62	Pu	63	Am	64	Cm	65	Bk	66	Cf	67	Es	68	Fm	69	Md	70	No	71	Lr	72	Uuo

Fig. II.2-5: Periodic table of elements. Si is in group 14. Group 13 elements can be used for p-doping (+), group 15 elements for n doping (-). The periodic table was taken from [15].

In semiconductors, the vital population inversion can be generated in three different ways:

- Excitation by optical pumping
- Excitation by electron bombardment
- Excitation by injection of charge carriers over a pn junction (= diode lasers)

Semiconductor lasers belonging to the last subset are called diode lasers. They are the most important semiconductor lasers.

### **Epitaxial growth techniques for semiconductor lasers**

Electronic devices are usually produced by erecting different structural layers on top of a monocrystalline substrate. These structures also have got to be monocrystalline. The lattice of the grown layers must be matched to the one of the substrate. This is important for a perfectly conducting contact. Such layers are called epitaxial. There are four methods of epitaxial growth:

- Liquid phase epitaxy (LPE)

Solutions of molten group III (13) and group V (15) elements are brought into contact with appropriate substrates where, upon lowering the temperature, deposition takes place very close to thermal equilibrium.

- Vapor phase epitaxy (VPE)

The constituents are introduced into the reacting zone either as chlorides or hydrides. The deposition zone is held at a slightly lower temperature. The stoichiometry is determined by the respective flow rates.

- Metal organic chemical vapor deposition (MOCVD)

Stemming from VPE, group III alkyls and group V hydrides are introduced into the reaction chamber where the substrate is contained on a graphite holder heated by radio frequency.

The relevant process before deposition is thermolysis (which is far away from equilibrium).

- Molecular beam epitaxy (MBE)

The substrate is contained in an ultrahigh vacuum chamber where it is hit by vapors of the elements to be deposited. Very high purities are needed for this process that even enables the growth of monoatomic layers.

For details the reader is referred to [16].

## Diode lasers

The first diode lasers were constructed in 1962. They had to be cooled with liquid nitrogen (77K) and could only be operated in a pulsed, multi mode manner with a very limited lifetime. Driven by a demand in communications engineering, today cheap, industrially produced diode lasers for cw (continuous wave, as opposed to pulsed) operation at room temperature for more than  $10^6$  hours at many different wavelengths have become available. Their main advantages over conventional (bulky, solid state) lasers are their compact, robust design and the unmatched quantum efficiency ( $\sim 50\%$ ). Generally speaking, it is the III-V compounds that are most important. The ternary compound GaAlAs is used for  $\lambda \sim 0.8 \mu\text{m}$ , the quaternary system InGaAsP for  $\lambda \sim 1.3 \mu\text{m}$  and  $\lambda \sim 1.5 \mu\text{m}$ , and GaInP for  $\lambda \sim 0.67 \mu\text{m}$ . Basically a diode laser is a diode. Fig. II.2-6 shows the characteristic curve of a diode.

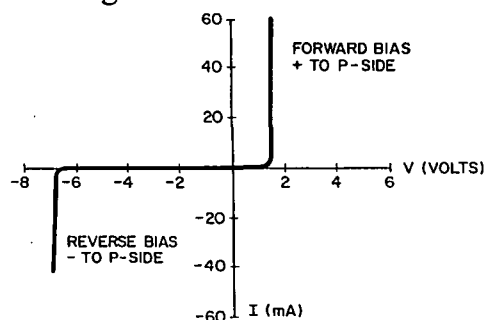


Fig. II.2-6: Characteristic curve of a diode (current as a function of applied voltage, taken from [13]). A diode is a non linear device.

The recombination of an electron from the conduction band with a hole in the valence band leads to the emission of a photon. In the case of a direct semiconductor (like GaAlAs), the energy minimum of the conduction band is localized directly over the energy maximum of the valence band (plotted on the energy/momentum chart).

For the recombinations to take place the diode has to be biased (i.e. a voltage has to be applied in forward direction) so that the charge carriers from the n-doped and p-doped GaAlAs layers are forced into the layer between them to recombine. The energy of the photon is equivalent to the band gap energy.

As for indirect semiconductors (e.g. Si from group IV), the minimum of the conduction band and the maximum of the valence band are not exactly located over each other. Since momentum has to be conserved, the emission of a photon must be accompanied by the emission of a phonon (a quantum of vibrational energy in a crystal).

This requirement decreases the probability of stimulated emission by several orders of magnitude. For this reason, direct semiconductors (e.g. the III-V compound GaAs) are used for lasers.

A further prerequisite for lasing action is that stimulated emission outweighs spontaneous emission.

To obtain the necessary high photon density for this to happen, the active region is bordered by two reflective mirrors to form a resonator, also called cavity.

Because of the high difference in the refractive index of air and the laser medium ( $n_{\text{GaAs}} = 3.6$ ), it is sufficient to simply cleave the facets of the crystal for  $\sim 32\%$  reflectivity (Fresnel formula, see Eq. II.3-3 in the following subchapter). Compared to other lasers, this may not sound much, but the mediocre reflectivity is compensated for by a higher amplification.

The resonator length  $L$  is on the order of 0.6 mm, giving rise to a typical free spectral range (FSR, i. e. the spacing of two adjacent longitudinal modes) of  $c/2L = 250 \text{ GHz} \sim 0.08 \text{ cm}^{-1}$  ( $3 \cdot 10^{-2} \text{ nm}$  at  $1.5 \mu\text{m}$ ).

The output wavelength and line width of diode lasers depend on various factors. Usually, the frequency is determined by the cavity length of the laser chip and the band gap providing the gain by carrier injection. By changing the temperature and current, the laser frequency can be moved slightly, since this changes the refractive index, the cavity length and the gain curve. However, the line width of such laser diodes (FP type) is broad and the laser may be operating with multiple longitudinal modes (see below for advanced laser structures). To stabilize the frequency it is very important to stabilize the diode's temperature. It is also necessary to stabilize the injection current because fluctuations change the output frequency. A scheme of a semiconductor laser is shown below in Fig. II.2-7.

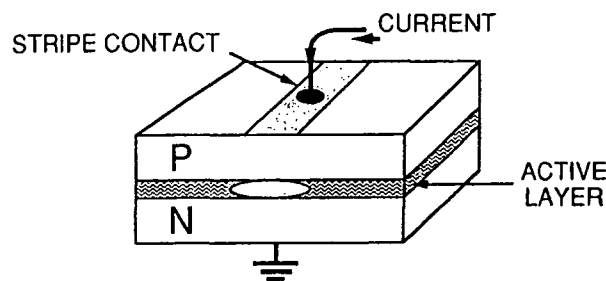


Fig. II.2-7: Generic scheme of a semiconductor laser (Taken from [13]). The active layer is contained between the p and n doped slabs (pn junction).

The active region typically measures  $0.1\text{-}0.3 \mu\text{m}$  in the parallel and  $3\text{-}5 \mu\text{m}$  in the perpendicular dimension to the pn junction. Since the electrons are much more mobile than the holes, the depth of the active region is determined by the mobility of the electrons. Diffraction phenomena at the facets make the beam diverge.

The elliptical beam profile results from the fact that the smaller dimensions in line with the active layer cause more diffractive widening perpendicularly to it than horizontally.

The laser intensity is strongly dependent on the injection current. Above the threshold current  $I_{\text{thres}}$ , there is a steep slope in the characteristic curve (see Fig. III.3-1 and Fig. III.4-2 later).

Below  $I_{\text{thres}}$ , spectrally broad spontaneous emission comparable to LEDs (light emitting diodes) is dominant.

The maximum output power is limited by the thermal destruction of the facets (initiated via crystal defects).

To obtain a wave-guide by total reflection, the index of refraction of the active region has to be higher than outside. This can, for instance, be achieved by lowering the content of Al in GaAlAs structures.

The wave guide reduces losses and suppresses other modes than the so-called fundamental mode  $\text{TEM}_{00}$ .

### Ordinary diode lasers

Two heavily doped p and n semiconductor slabs ( $>10^{18} \text{ atoms/cm}^3$ ) are brought into contact to form what is known as a diode.

If the diode is biased in forward direction with a voltage  $V$  on the order of magnitude of the energy gap  $E_g$  ( $V \sim E_g/e$ ), electrons from the n region and holes from the p region are driven towards the pn junction where population inversion is obtained ( $e$  is the elementary charge:

$1.602 \cdot 10^{-19}$  C). Electromagnetic radiation with  $E_g/h < \nu$  will be amplified when passing through this zone.

The thickness of this region can be estimated by assessing how far the electrons can diffuse in the p region before they recombine with a hole.

This distance  $d$  is given by  $d = (D\tau)^{1/2}$  where  $D$  is the diffusion coefficient [ $s^{-1}$ ] and  $\tau$  the lifetime [s] of the electrons.

Typical values of  $d$  are  $\sim 1 \mu\text{m}$  in GaAs.

### Homojunction lasers

In this early type of diode lasers, both the p and the n region were made of the same semiconductor material. The resulting high threshold current density ( $\sim 100 \text{ kA/cm}^2$ ) prohibited cw operation at room temperature ( $I_{\text{thres}}$  decreases exponentially with  $T$ ).

### Double heterostructure (DH) diode lasers

#### (a) Gain guided DH diode lasers

The threshold current density does not only depend on the temperature, but also on the spatial dimensions of the active region or the laser beam, respectively. By reducing the size of the active laser and also of the laser beam, losses in the bordering p and n regions are minimized. This concept can be achieved by building a so-called double heterostructure device as illustrated below in Fig. II.2-8.

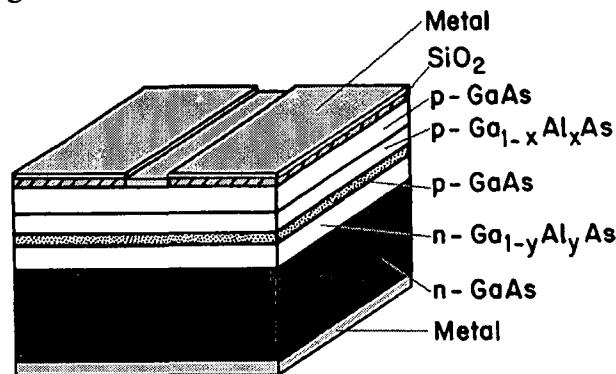


Fig. II.2-8: Gain guided GaAs-GaAlAs laser with double hetero structure (Modified from [17]). Compare the original setup in Fig. II.2-7 (no current and beam confinement).

This laser diode has got two junctions between different materials, that is one in p-Ga<sub>1-x</sub>Al<sub>x</sub>As/GaAs and one in GaAs/n-Ga<sub>1-y</sub>Al<sub>y</sub>As ( $x$  and  $y \sim 0.3$ ).

Electrons and holes are injected on both sides and conveyed to the active GaAs layer ( $0.1 - 0.5 \mu\text{m}$  thick) in between. Upon recombination there, light around  $\nu = E_g/h$  is amplified.

This sandwich structure has got two important implications:

- The energy gap in Ga<sub>1-x</sub>Al<sub>x</sub>As rises alongside with  $x$ . This means that a potential barrier for the injected electrons at the GaAs/p-Ga<sub>1-x</sub>Al<sub>x</sub>As junction and likewise for the holes at the GaAs/n-Ga<sub>1-y</sub>Al<sub>y</sub>As junction has been established that way. This hinders diffusion of the charge carriers away from the active GaAs zones. So the active layer has been downsized.

- The difference in the refractive indices between  $\text{Ga}_{1-x}\text{Al}_x\text{As}$  and GaAs increases alongside with  $x$  ( $\Delta n \sim 0.4x$ ). The resulting profile of the refractive index inside the structure forms a dielectric wave-guide so that the light, too, is effectively confined.

To reduce the lateral extensions of the active zone, the area of the upper electrode is restricted to a narrow strip not broader than  $10 \mu\text{m}$ . The lower contacting area is kept unchanged (stripe geometry laser).

The considerable confinement of both the active zone and the laser mode lower the threshold current density from  $\sim 100 \text{ kA/cm}^2$  to  $\sim 1 \text{ kA/cm}^2$ . This enables cw operation of DH lasers at room temperature.

#### (b) Index guided DH diode laser

Double heterostructure diode lasers as presented above have got two shortcomings: neither the pumping current nor the light waves are guided effectively in the lateral direction.

Index guided DH diode lasers like the buried heterostructure semiconductor laser circumnavigate this problem.

Below a constructive scheme is presented:

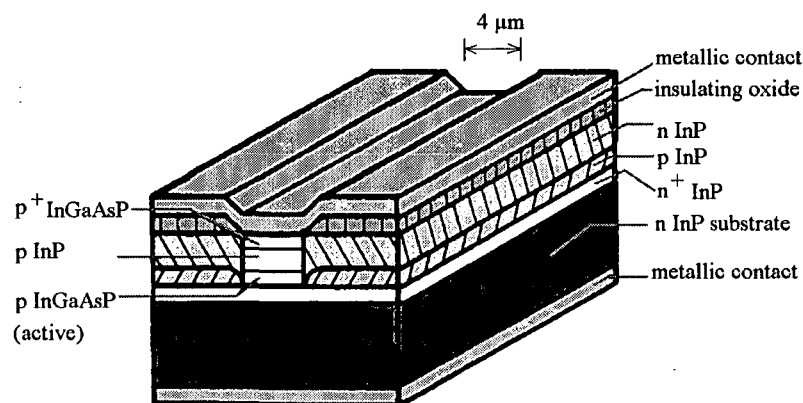


Fig. II.2-9: A buried heterostructure diode laser (Modified from [17]). Compare the original setup in Fig. II.2-7 (no current and beam confinement).

On both sides of the active p-InGaAsP channel an adjacent InP diode in reverse bias has been placed so that the pumping current is forced solely through the active zone in the middle. This further confinement allows the threshold current to drop below 10 mA. It goes without saying that the epitaxial growth processes involved here are quite sumptuous.

#### Vertical-cavity surface-emitting lasers (VCSELs)

VCSEL is an acronym for vertical-cavity surface-emitting laser, as opposed to conventional edge-emitting lasers (EELs). Today, 75% of all manufactured communication lasers are of this type. They are said to be the most reliable lasers. A potential replacement of the electronic picture tube by VCSELs has been discussed. Conventional lasers are known as "edge emitters" because their laser light comes out from the edges in a horizontal direction. As the name implies, a vertical-cavity surface-emitting laser, radiates perpendicularly from its surface and has a laser cavity that is vertical (i.e. parallel to the flow of the injection current). VCSELs have become commercially available in 1996. They offer many advantages over conventional diode lasers like low threshold current, small beam divergence and easy fiber coupling.



The most important issue, however, is that VCSELs can be industrially manufactured using well-established standard microelectronic fabrication methods. The entire fabrication and, even more important, the testing can be done directly on the wafer in contrast to conventional edge-emitting lasers.

When manufacturing edge emitters, they need to be cut out of the material they are formed on before being packaged for testing. This stage of packaging is quite an expensive process, and if the laser then fails, the tests it has been subjected to were wasted effort. Because VCSELs emit light from their surface, they can be tested while they are still on the wafer that they were made on.

Completion and testing at the wafer level mean tremendous cuts in manufacturing costs. Besides, this enables the integration with other IC (integrated circuit) components without pre-packaging.

The low threshold current enables high-density two dimensional array configurations.

Low power consumption and lower temperature sensitivity than edge emitters are further advantageous features. The main drawbacks are low output power ( $< 1\text{mW}$ ), limited wavelength availability (especially higher wavelengths) and the higher resistance (50-100 Ohms compared to 0.5 –2 Ohms). For data communications, the wavelengths of 1.3 and 1.55  $\mu\text{m}$  (lowest loss in silica fibers) are most interesting. Nowadays low-power VCSELs at 850 nm are widely used for short-distance networks, but high-power 1550 nm products will be needed for widespread use in large-scale optical networks.

The principles involved in the fabrication of a VCSEL are very similar to those of regular lasers. There are two semiconductor materials sandwiched together to yield an active layer. The cavity length is very short, typically 1-3 wavelengths. In a single pass at low carrier density, a photon is very unlikely to trigger stimulated emission, so for low threshold currents highly reflective mirrors are needed, that is greater than 99.9% as compared to 30% with edge emitters. Such a high reflectivity cannot be achieved by metallic mirrors (~98% at the most). Instead, Distributed Bragg Reflectors (DBRs) are used. They are composed of alternating layers of dielectric materials with differences in their refractive indices with a thickness appropriate to give maximum reflectivity at the desired lasing wavelength. The upper stack usually comprises 20 periods, the lower DBR reflector 40 alternating layers. Suitable combinations of materials should have a high contrast in their refractive index and exhibit small optical losses. Si/SiO<sub>2</sub>, GaAs/AlAs, AlAsSb/GaAsSb and GaAs/Al<sub>2</sub>O<sub>3</sub> are good material combinations for the epitaxial layers.

Current confinement is done by reducing the area where the gain occurs. This helps to reduce the threshold current (typically 0.5 mA,  $< 20\ \mu\text{A}$  at the lowest) for VCSELs as opposed to 15 mA for edge emitting lasers, EELs). Vertically, current confinement is achieved by the Bragg mirrors. In the horizontal direction, the shape of the electrodes and the current path determine the confinement. Layers with high Al content that are subsequently oxidized help confine the current to the desired areas (i.e. the center). Another common approach to narrow the current path is ion implantation. This procedure turns the bombarded regions of the semiconductor material into an insulator. Apart from ion implantation and selective oxidization, the current path can also be narrowed by etching away the surrounding substrate. This setup exhibits inferior performance, however. The buried heterostructure approach is demanding but gives good results. Fig. II.2-10 shows a simplified cross section of a VCSEL.

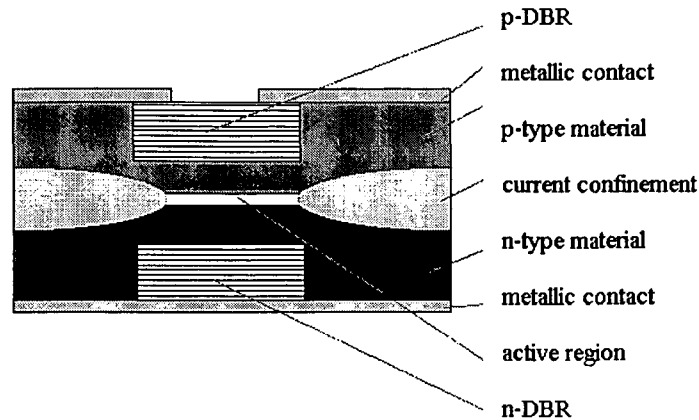


Fig. II.2-10: Generic scheme of a VCSEL (vertical-cavity surface-emitting laser). DBR stands for distributed Bragg reflector. In contrast to edge emitting diode lasers (compare Fig. II.2-7, Fig. II.2-8 and Fig. II.2-9, the light emission takes place perpendicularly to the carrier injection (hence the term “vertical”).

The mirrors are composed of 20 to 40 pairs of e.g. GaAs/AlAs layers.

It has already been mentioned that the cavity length is very short in VCSELs, typically 1-3 wavelengths. This has advantageous implications: Since fewer modes fit under the gain profile (free spectral range, FSR, compare Fig. II.2-3), single mode emission can be achieved more easily.

As it was discovered during the work presented in this thesis, VCSELs are interesting for laser spectroscopy because they can be tuned over a wide range at very high frequencies (see chapter III.3 and III.4).

### Quantum cascade lasers (QCLs)

The quantum cascade laser (QCL) [18] is the only semiconductor laser that does not contain a pn junction. In an ordinary diode laser, the emission of a photon is caused by the recombination of an electron in the conduction band with a hole in the valence band. The energy of the photon is the net energy difference, i. e. approximately the bandgap energy of the material. In order to change the emission wavelength, the bandgap has to be altered. Since the energy bandgap is an intrinsic property of the material, only a change in the composition of the semiconductor material can achieve a different wavelength. A QCL, on the other hand, is designed or even “tailored” by bandstructure engineering. It is predominantly the layers’ thickness of the active region rather than the bandgap of the material deployed that determines the wavelength. Molecular beam epitaxy (MBE) [16] enables the growth of thin layers over a very wide range using the same heterostructure material and is hence the basis for QCL production. QCLs can be designed to operate at any wavelength from 3.5  $\mu\text{m}$  to  $> 50 \mu\text{m}$ .

There are two approaches of realizing a QCL. The first one (original design) is based on an active region comprised of three quantum wells. The second design uses a superlattice as the active region.

Resonant tunneling is used as a pumping mechanism. Intersubband transitions between excited states of the coupled quantum wells cause light emission. Population inversion is designed by tailoring the electrons’ intersubband scattering times. In a QCL, the thickness of the active layer is reduced to approximately 100 nm resulting in the quantization of the valence and conduction band energy levels. Rather than being subjected to a single recombination (cf. conventional diode lasers), the electron which was injected into an excited state in a quantum well in the conduction band relaxes to a lower energy level in the quantum

well by stimulated emission of a photon. At this point, the electron can exit the quantum well via tunneling which brings it to another active region where the process repeats itself. A typical QCL has got more than 20 of such alternating active and injection regions than an electron can “travel” through.

The difference between an ordinary diode laser and a QCL is depicted in Fig. II.2-11 below in a simplified band structure diagram.

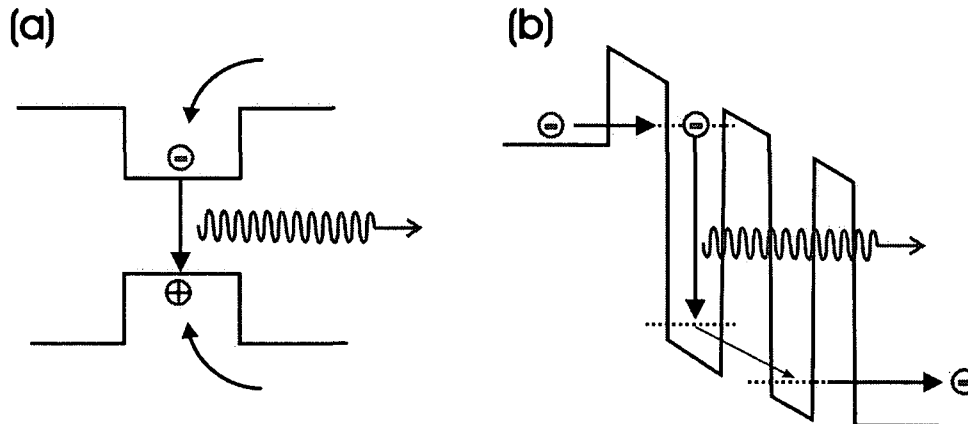


Fig. II.2-11: Illustration of an ordinary diode laser (a) and a quantum cascade laser (b) in terms of valence and conduction band profiles. In (a), interband transitions occur. In (b), it is intersubband transitions.

At longer wavelengths (i.e.  $> 3 \mu\text{m}$ ) diode lasers (=lasers based on interband transitions) suffer from the strong increase of non-radiative relaxation (Auger recombination). The unipolar QCL also overcomes these fundamental limitations of the classical bipolar diode laser.

Single mode emission can be obtained by incorporating a DFB structure in the QCL device. Despite their favourable wavelengths, the in-field use of QCLs has been limited due to cryogenic cooling requirements. Pulsed operation at room temperature has been obtained, and many groups are striving to achieve room temperature operation in cw mode.

More information on QCLs can be found in [18] and chapter III.2.

### Tunable lasers

When the gain curve of the active medium covers a broad range, the laser wavelength can be pinned down to a narrow interval or even a single mode by inserting a wavelength selective element into the resonator. By simultaneously changing the transmission maxima of these parts the wavelength can be tuned continuously under the gain curve. This method is used in dye lasers, color center lasers and vibronic solid state lasers. Another possibility to active wavelength tuning is to shift the energy levels in the active medium. This can be done by applying an external magnetic field (Raman spin flip laser) or by changing the temperature or pressure (semiconductor lasers). Yet another possibility to tune the emission wavelength is frequency mixing. Nonlinear processes enable the generation of the sum and difference frequencies of two lasers, one of which must be tunable. So-called optical parametric oscillators (OPOs) can achieve very large tuning ranges. KTP ( $\text{KTiOPO}_4$ ) is a material that can be used for these purposes. Nonlinear techniques are important for obtaining tunable laser sources in the UV and the far IR. Dye lasers are most important for the VIS range. In Fig. II.2-11, a compilation of operating ranges of tunable laser sources is presented.

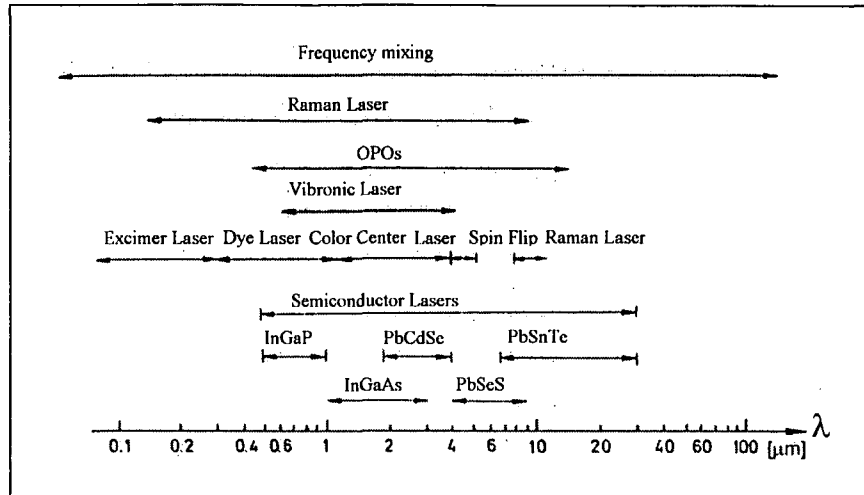


Fig II.2-11: Spectral coverage of tunable lasers (Modified from [10]). In the near infrared, compact, robust diode lasers are available (weak overtone and combination bands). In the mid infrared, quantum cascade and lead salt lasers (cryogenic cooling requirements) are available to probe the strong fundamental bands.

Semiconductor lasers dominate in the mid IR region, thus their tuning properties shall be considered in the following section.

### Tuning of diode lasers

A coarse wavelength selection is made by choosing the laser material. The bandgap has to be varied in order to generate the desired wavelength. Fig. II.2-12 shows bandgaps versus lattice constants for III-V compounds (plus Si and Ge). The dots represent binaries. Ternaries are located on the connecting lines. The even more complicated quaternaries are situated within the four connecting lines of the respective binary compounds. Quaternary compounds allow full flexibility with respect to both bandgap and lattice constant. One can therefore match the material to a given substrate and nevertheless independently choose the wavelength.

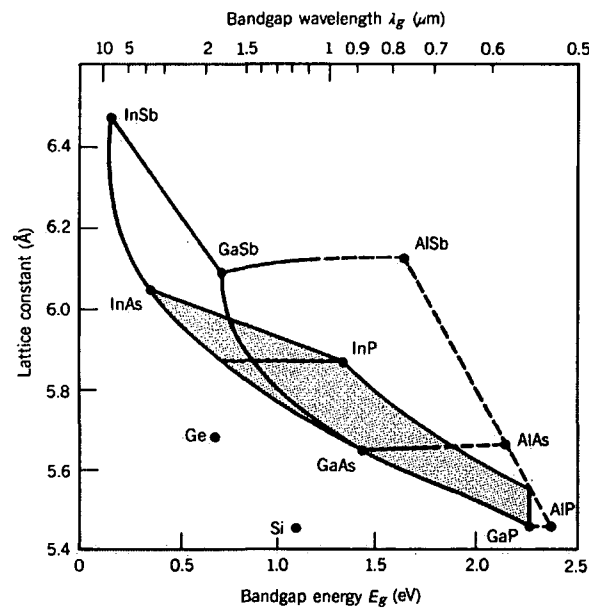


Fig. II.2-12: Lattice constants, bandgap energies and bandgap wavelength for Si, Ge and nine III-V binary compounds. The ternary compounds are the lines connecting the points. Solid and dashed lines represent direct-gap and indirect-gap compositions, respectively. The quaternary compounds are the area in-between these lines. For example  $In_{1-x}Ga_xAs_{1-y}P_y$  is represented by the shaded area (Taken from [19]).

Diode lasers can be tuned by temperature and/or injection current. Actually, both methods change the temperature of the active region. According to Ohm's law, higher currents heat up the laser. Direct variation of the temperature allows tuning over a wide range but is comparatively slow. Typical tuning rates are 0.1 nm/K (both for DFB lasers and VCSELs).

DFB stands for distributed feed back. DFB and DBR lasers are special edge emitting lasers (EEL). A grating serves as a wavelength selective element. DFB and DBR lasers show single mode emission and are therefore suitable for spectroscopic applications.

Variation of the drive current can only access a smaller range but allows rapid tuning (up to MHz for spectroscopic applications). Typical rates are 0.05 nm/mA for DFB lasers and 0.1 nm/mA for VCSELs (compare Table III.4-1). Tuning can be done discontinuously to select a desired wavelength or continuously to e. g. sweep over an absorption feature. Mode hops are always undesirable. In the continuous tuning mode the emission wavelength of the laser diode is a smooth function of the driving current. It enables one to unambiguously access any wavelength within the tuning range. Tuning of semiconductor lasers by current modulation can be done at kHz to MHz over several  $\text{cm}^{-1}$  (see chapter III.4).

The frequencies at which lasing action can take place are predetermined by the length of the cavity: eigenfrequencies  $\nu = mc/(2nL)$ , ( $m=1,2,3\dots$ ).

The natural frequencies can be shifted according to

$$\Delta\nu = \frac{\partial\nu}{\partial n} \frac{dn}{dT} \Delta T + \frac{\partial\nu}{\partial L} \frac{dL}{dT} \Delta T = -\nu \left( \frac{1}{n} \frac{dn}{dT} + \frac{1}{L} \frac{dL}{dT} \right) \Delta T$$

(Eq. II.2-1)

n... index of refraction [1]

L... resonator length [m]

T... temperature [K]

Generally the first term is much bigger than the second one. The maximum of the gain profile experiences a much faster shift than  $\nu$  itself. As soon as the maximum of the gain curve has "overtaken" the oscillating mode and reached a new, formerly inactive mode, the laser "jumps" to this frequency and the new mode starts lasing. This phenomenon is known as mode hopping. In between these hops, the frequency can be tuned continuously as shown below in Fig. II.2-13.

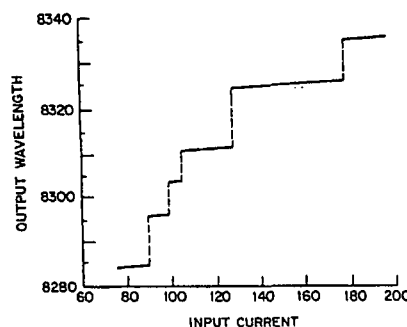


Fig. II.2-13: Mode hopping and tuning of a Fabry Perot type diode laser (Taken from [20]). To prevent spurious mode hopping, one has to switch to a DFB or DBR device (or a VCSEL, see later).

The figure above shows the spectral output [ $\text{cm}^{-1}$ ] of a tunable diode laser as a function of its input current [mA]. The overall slope (i.e. the tuning coefficient  $\Delta\lambda/\Delta I$  ( $\lambda$  being the wavelength,  $I$  the injection current)) is due to the band gap change with temperature. The rise in temperature can be explained by the fact that not the whole energy is converted to light. The resistance of a diode laser is on the order of 0.5 to 2 Ohms (for VCSELs, it is on two

orders of magnitude bigger because the two Bragg reflectors are in series with the active volume). For AlGaAs,  $\Delta\lambda/\Delta I$  is  $\sim 0.3$  nm/mA, and for InGaAsP  $\sim 0.5$  nm/mA. The slope in between, that is in the single mode regime, is caused by a change of the refractive index of the material with temperature. The implication is about  $\Delta\lambda/\Delta I = 0.05$  nm/mA. Only single mode tuning can be exploited in tunable diode laser absorption spectroscopy (see the following chapter II.3).

### **Wavelength tuning with external resonators**

The use of an external resonator pursues two chief interests: stabilization and wavelength tuning. The line width of a diode laser is on the order of 100 MHz ( $0.0033$  cm<sup>-1</sup>). The use of an external resonator can narrow the line width to several MHz or even a few kHz. Outside the diode laser, a wavelength is selected and partly sent back into the laser. This feedback mechanism allows the selection of a single wavelength. One can choose all modes that fit under the gain profile; They are spaced by  $c/2L$  (FSR).

External cavity lasers allow very far, single mode wavelength tuning. Since they involve mechanical components (grating), tuning is rather slow.

More information on tunable diode lasers can be found in [21].

### II.3 Tunable diode laser absorption spectroscopy (TDLAS, TDLS)

Spectroscopic techniques operate in non-contact mode. They allow the *in-situ* investigation of processes and phenomena without perturbing the probed system.

Measuring *in-situ* means that the experimental data are gathered right “at the spot”. Before *in-situ* laser spectroscopic techniques have been known, intrusive suction probes were used for measuring species concentrations in flames. Extractive probe measurements of CO yielded concentrations ten times less than the authentic values obtained from *in-situ* laser spectroscopic techniques [3]. The reasons for these deviations are quite obvious. Quenching of reactive species occurs before “freezing” them (this cannot be achieved fast enough). Before the external (“ex-situ” or “extra-situ”) analyzer is reached, the reactive species have changed their concentrations because of continued reactions.

Spectroscopic techniques have become the most important investigation method in physical analysis (see Introduction). Absorption spectroscopy can deliver quantitative, path averaged results with high sensitivity and selectivity.

Quantification is not a trivial task for competing optical sensing techniques like laser-induced fluorescence (LIF). As a line of sight technique, absorption spectroscopic measurements yield path averaged results. This is not necessarily a disadvantage, since one is often interested in the overall performance of a process or the mean pollutant concentration.

Usually, quantification is done by calibration procedures. If Lambert Beer’s law is fulfilled, the calibration function will be linear. Ideally, the component of interest absorbs at a frequency where there are no interferences from other present species. When interferences do occur, there are three possible ways to circumnavigate the problems:

- Spectra subtraction
- Multi component analysis
- Measuring a single rotation-vibration line (high resolution spectroscopy)

For the first approach, spectra subtraction, reference spectra of all present species  $i$  have to be recorded prior to or after the actual test runs. A computer can subsequently subtract multiples  $m$  of these from the sample spectrum to determine the concentration of all species.

$$A_{sample} - \sum_i m_i A_{i,reference} = 0$$

(Eq. II.3-1)

A... absorbance [1]

Measuring a single rotation-vibration (= rovibrational) line is possible in gases of small molecules (compare Fig. II.1-6). To resolve the rovibrational fine structure of molecular spectra in the gaseous or vapor phase, the recording has to be done at high resolution. This is illustrated below in Fig. II.3-1 with a spectrum of CO around 2.35  $\mu\text{m}$  for different resolutions.

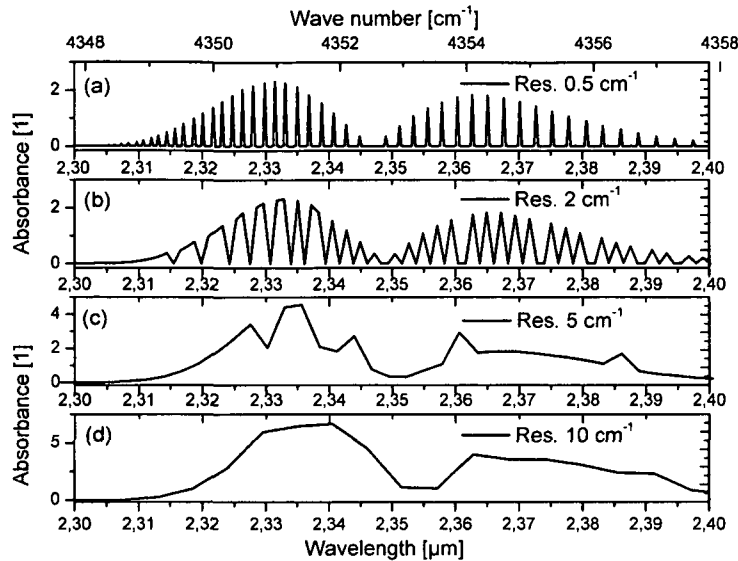


Fig II.3-1: Absorption spectra of CO, calculated with resolutions of  $0.5 \text{ cm}^{-1}$  (a),  $2.0 \text{ cm}^{-1}$  (b),  $5.0 \text{ cm}^{-1}$  (c) and  $10.0 \text{ cm}^{-1}$  (d). At  $2.35 \text{ } \mu\text{m}$ ,  $1 \text{ cm}^{-1}$  corresponds to  $0.55 \text{ nm}$ . A high spectral resolution is needed for single line recording.

Species with more than four atoms generally have complex rovibrational spectra where the assignment of individual spectral lines is not possible any more.

In order to resolve the individual lines, a resolution (of the monochromator in a spectrometer) of better than  $0.5 \text{ cm}^{-1}$  is needed. At  $2.35 \text{ } \mu\text{m}$ ,  $1 \text{ cm}^{-1}$  corresponds to  $0.55 \text{ nm}$ .

The typical line width of a single mode diode laser (VCSEL, DFB, DBR or external cavity laser) is on the order of  $10 \text{ MHz}$ , whereas it is around  $200 \text{ MHz}$  ( $0.02 \text{ cm}^{-1}$ ) for absorption lines at atmospheric pressure.

Therefore, a diode laser can be used for the recording of high resolution spectra.

In tunable diode laser absorption spectroscopy (TDLAS or TDLS), a diode laser with an emission frequency (or wavelength) matched to a suitable absorption line is used. The laser wavelength is scanned over the entire absorption peak in order to record the full feature. This is illustrated in the following Fig. II.3-2. The experimental setup essentially consists of the laser and the detector with a probed absorption volume that contains the target species as illustrated in Fig. II.1-1.

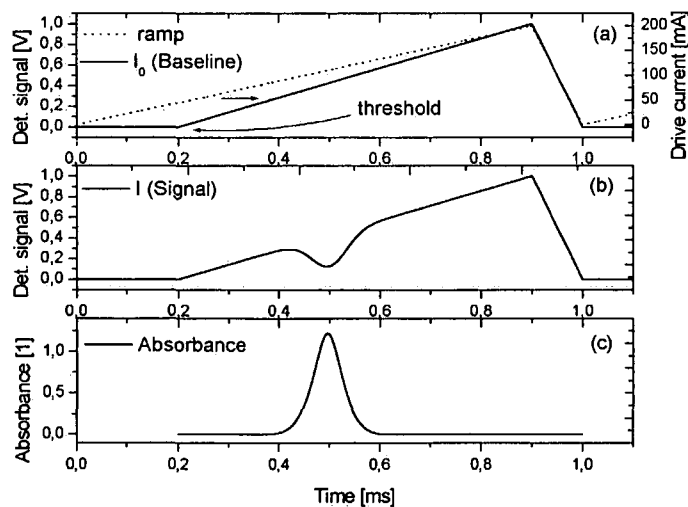


Fig II.3-2: Recording of an individual absorption line. (a) shows the current ramp applied to the laser and the baseline ( $I_0$ ), (b) gives the transmitted signal ( $I$ ). In (c), the absorbance  $A = \ln(I_0/I)$  is shown.



Diode lasers can be frequency tuned in a narrow range by either varying the temperature or the injection current. Usually, the temperature is adjusted so that the laser wavelength coincides with the wavelength of the transition in the target molecule. The injection current is then modulated. This modulation causes a repetitive change in the laser wavelength.

It has proven convenient to apply a linearly rising current ramp to the laser as shown in Fig. II.3-2 (a) (dotted line). As soon as the threshold current at the given temperature is reached, the device starts lasing. The output power then scales approximately linearly with current. At the same time, the emission wavelength shifts. In (b), an absorption peak can be seen as a dip on the transmitted light intensity at the resonance wavelength. In (c), the absorbance has been plotted. The width of the absorption peak is determined by the ambient temperature and pressure, the area by the number density (concentration times path length) of the absorbing species.

The frequency of the current ramps applied to the laser determines the time resolution of the absorption spectroscopic measurements.

Signal  $I$  and baseline  $I_0$  can be recorded simultaneously (using a beam splitter), but also consecutively. It is also possible to determine the baseline mathematically by applying a fitting procedure.

The following Fig. II.3-3 illustrates the need for recording the absorbance not only at the center of the absorption peak, but also in the wings where no resonant absorption occurs.

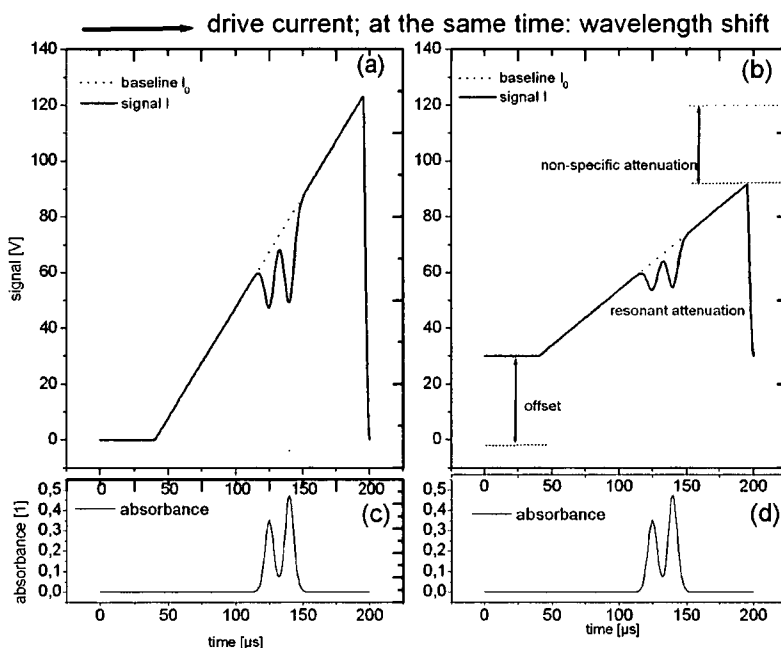


Fig II.3-3: TDLAS without (a) and with (b) interferences. The absorbance (c, d) is the same. Non-specific attenuation and the offset can be removed by scanning over the entire absorption feature (here: double peak). The wavelength scan of the line is achieved by tuning the laser current (temperature held constant).

In Fig. II.3-3, a double peak was recorded (calculated curves). In the left frame (a), there are no interferences. One can see the baseline  $I_0$  (no absorption by the target species) and the transmitted signal  $I$ . In (c) the absorbance is shown. The right frame (b) incorporates several interferences. (a) might be a laboratory measurement, (b) might have been recorded in a furnace or chimney. The whole signal has been reduced in its intensity, and has also lifted off. The reduction in intensity stems from non-specific beam attenuation.

The laser light beam traveling through the sample volume might be subjected to partial blocking (e.g. by soot and ash particles passing the beam path), scattering (particles and particulates like smoke) and beam steering. In non homogeneous media where strong

temperature gradients are encountered (such as in turbulent, non premixed flames), the laser beam will not travel along a constant path, but instead be constantly redirected by refractive index gradients.

The offset might stem from emissions caused by the flame, thermal radiation emitted by hot walls or luminosity of glowing soot particles.

The specific absorption of the laser light by the target molecule is extremely dependent of the wavelength (narrow peaks). The non-specific attenuation and the luminosity hitting the detector, on the other hand, are far less wavelength specific. This is the reason why resonant absorption can be measured in adverse environments.

The following Fig. II.3-4 shows the data evaluation process in an illustrative way:

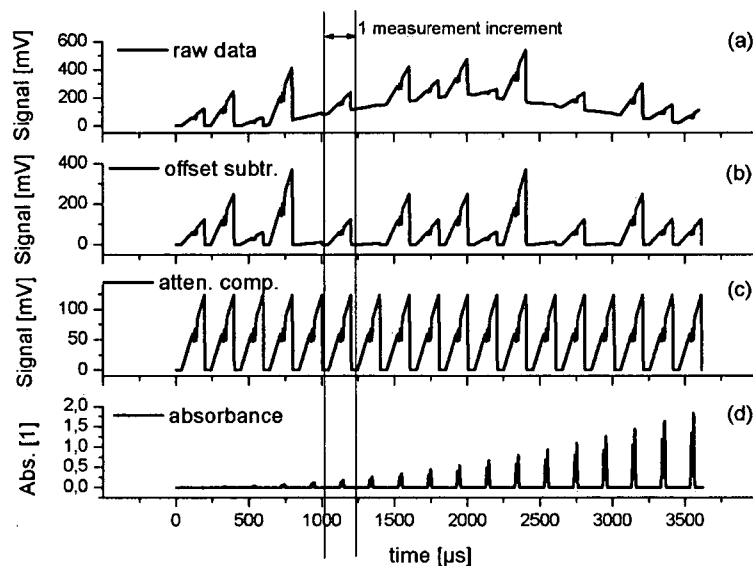


Fig II.3-4: Illustration of how the absorbance is extracted from the raw data (a). In (b), the offset was removed, in (c), the individual ramps were rescaled (removal of beam steering and similar effects). In (d), the absorbance is shown (double peak from Fig. II.3-3).

One can see four curves where (a) represents the raw data (laser ramps + offset). In (b), the offset was removed. In (c), all ramps were rescaled and in (d), the extracted absorbance can be seen. In a final step, one would have to convert it into concentration.

Another prerequisite is that the frequency of the current ramp applied to the laser, that is the duration of an individual measurement, be shorter than the time scale of the fluctuations. Neither the amount of light from flames or glowing soot particles hitting the photodetector nor the extent of non-specific beam attenuation by partial blocking of the beam and scattering are constant. They fluctuate strongly in time. So in order to probe the system and to obtain undistorted absorption peaks, the tuning of the laser must be faster than these transient processes.

### Characterization of the wavelength tuning properties

The wavelength tuning properties of a diode laser can be characterized using an etalon. An etalon (Fabry Perot type) is essentially composed of two parallel surfaces. If a light beam is sent through an etalon, as illustrated in Fig. II.3-5 below, the different transmitted beams (main beam and higher order beams from back reflections) will be subject to constructive or destructive interference, depending on the wavelength. The transmission is high when an integral multiple of  $\lambda/2$  ( $\lambda$  being the wavelength) fits into the etalon cavity.

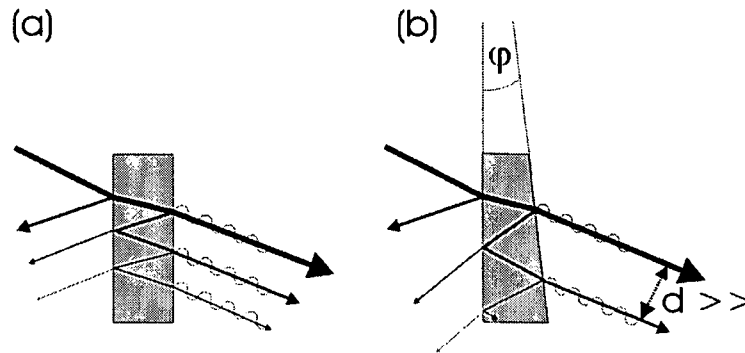


Fig II.3-5: Illustration of the etaloning effect. (a) is a plane parallel plate, (b) is a wedged window ( $\varphi \sim 1-3^\circ$ ). Wedged windows are commonly used in spectroscopy to avoid etaloning.

The transmission of the laser light beam through a window with plane parallel surfaces will be subjected to a periodic, comb like modulation as shown in the next Fig. II.3-6.

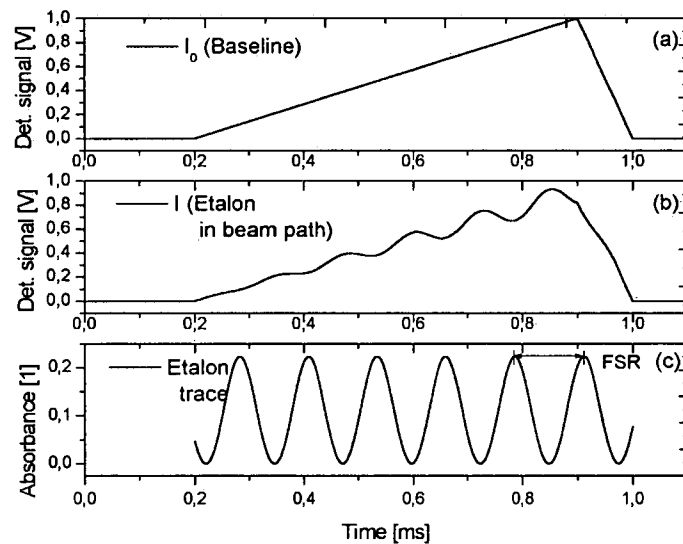


Fig II.3-6: Etaloning effect. The spacing between the transmittance maxima is constant (termed the free spectral range (FSR)).

The spacing between the transmittance peaks is constant. It is called the free spectral range (FSR). It can be calculated according to

$$\text{FSR [s}^{-1}] = c/(2ln)$$

(Eq. II.3-2)

c... speed of light ( $2.99 \cdot 10^{10}$  cm/s)

l... thickness [cm]

n... index of refraction [1]

The intensity of the modulation in transmission is determined by the reflectivity R [1] of the material. It can be calculated by the Fresnel formula as

$$R = (n-1)^2/(n+1)^2$$

(Eq. II.3-3)

with  $n$  being the index of refraction [1] of the material. Eq. II.3-3 is valid for light incidence perpendicularly to the surface.

In this thesis, a 5.0 mm thick sapphire window ( $n=1.744$  at  $1.68 \mu\text{m}$ ) was used (see chapter III.4). The FSR can be calculated as  $\text{FSR} = (2.99 \cdot 10^{10}) / (2 \cdot 0.5 \cdot 1.744) = 1.71 \cdot 10^{10} \text{ s}^{-1} = 0.574 \text{ cm}^{-1} = 0.16 \text{ nm}$ . The reflectivity  $R = (1.744-1)^2 / (1.744+1)^2 = 7.4 \%$ .

The etaloning effect can be used to characterize the wavelength tuning properties of a diode laser.

On the other hand, if the laser beam traverses two parallel, reflecting surfaces in an experimental setup, one will encounter unwanted etaloning.

This is depicted schematically below (Fig. II.3-7).

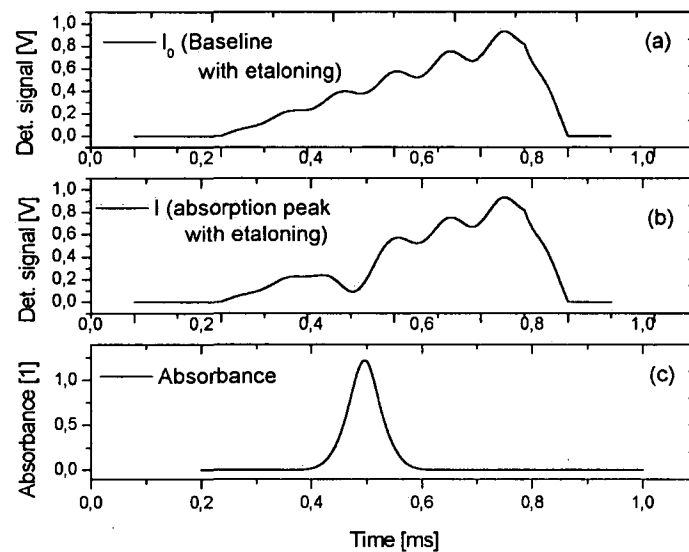


Fig II.3-7: Unwanted etaloning, e.g. introduced by reflections between parallel surfaces in the setup, can be removed (since the etaloning is both on the signal and on the reference, the calculation of the absorbance cancels it out). However, since it deteriorates the detection limit, etaloning should be avoided right away.

In any experimental setup using TDLAS, one will therefore strive to avoid plane parallel surfaces. Wedged windows are commonly used. The advantage of wedged in comparison to plane windows is that the reflected beams of higher orders are spatially displaced and that interference is therefore less effective. This is shown in Fig. II.3-5 (b).

If the use of wedged windows is not possible, one might try to pass through the plane parallel surface at an angle or to use an iris. Both reduce the efficiency of the unwanted etaloning.

### Choice of an absorption line

The choice of a suitable absorption line for a planned measurement has to incorporate the following considerations:

- The transition must have an appropriate line strength  $S$ . Normally,  $S$  should be strong in order to be able to detect low concentrations. However, for monitoring abundant species, it might also be necessary to move to a weaker line in order to avoid non-linear responses. TDLAS has a dynamic range of  $10^4$ .
- The laser has to be able to sweep over the line. Therefore, the line must be situated within a single mode regime of the diode laser in use.

- It is advisable to choose a region where several adjacent lines are accessible by the laser. When the laser emission changes over time, the chances are good that there is still at least one tunable line for measurements.
- The line must be separated from interfering lines. There is little or no concern from trace gases, but all the more from abundant, omnipresent constituents such as CO<sub>2</sub> or H<sub>2</sub>O. The latter poses the biggest problems, since the atmospheric concentration of water changes considerably over time.
- When conducting measurements at high temperatures, the temperature dependence of the line should be weak (or at least be known).

The procedure of choosing an appropriate transition is vastly simplified by the existence of spectral databases such as HITRAN [4].

Usually, one calculated spectra of all expected species for the appropriate pressure and temperature conditions. Evaluation of these data determines which laser to use. The choice might well be limited by the fact that of course only existing lasers can be used.

In practice, one often does not have to know exactly which line is measured. It is completely sufficient to select a laser for a region where transitions occur. The sample volume is filled with a calibration gas. Then the temperature of the laser heat sink and/or the drive current are varied until a strong signal is found. This approach is very simple and effective. It was pursued with the 2.3  $\mu\text{m}$  laser (CO and CH<sub>4</sub> detection) as used in chapter IV.1.

### Achieving higher sensitivity

In direct absorption spectroscopy as shown above, the attenuation of the light beam is determined directly by calculating the absorbance. Tunable diode lasers are readily available in the near infrared where the needs of the telecommunication industry have provided spectroscopists with small and robust devices that show good performance (e.g. room temperature operation, several mW cw output). Unfortunately, as the following Fig II.3-8 illustrates for HCl, the fundamental absorption bands of most small gases are situated in the mid and far infrared. Between 1 and 2  $\mu\text{m}$  where diode lasers are available, there are only overtone and combination bands that are by several orders of magnitude weaker.

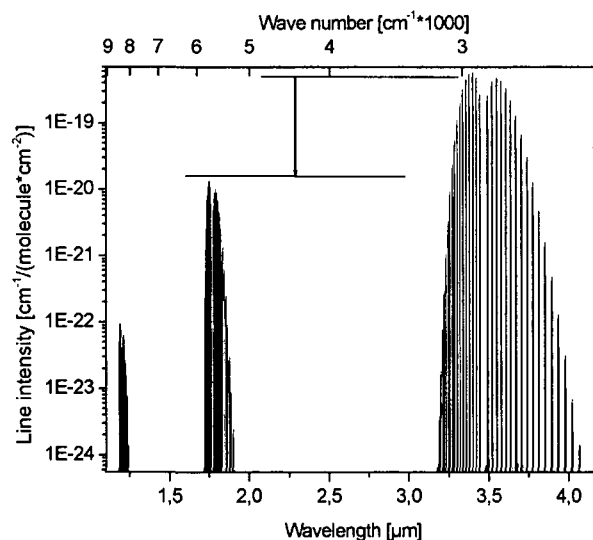


Fig II.3-8: Overtone and combination bands in the near infrared where diode lasers are readily available contain weaker transitions than the fundamental bands in the mid and far infrared (depicted for HCl).

The detection limit in TDLS is often quoted in terms of ppm\*m because doubling the path length with double the sensitivity (e.g. if 100 ppm can be detected by using a 1 m path length, the detection limit will be approximately 1000 ppm for a 0.1 m path length).

Long multi pass cells make a TDLS experiment much more sensitive because strong absorbencies can be reached. Most frequently, a multi pass absorption cell based on the design of White (1942) or Herriott (1964) is employed as the sampling cell. Using base paths of 0.3 to 1.5 m, such cells result in total absorption path lengths ranging between 10 and 200 m. Whenever multi pass setups cannot be used and weakly absorbing species at low concentrations have to be measured, the ratio  $I/I_0$  almost remains unity, and it is complicated to detect small changes in large signals. For single scan measurements, an absorption of the laser light beam on the order of 5 % can be readily detected and evaluated. By averaging, the minimum detectable absorbance can be lowered to approximately  $10^{-3}$ .

For short path lengths or trace gas sensing, this might not be sufficient.

By deploying ultra sensitive modulation techniques (see below), viz. WMS (wavelength modulation spectroscopy) [22] and FMS (frequency modulation spectroscopy) [23] minimum absorbencies of  $10^{-9}$  can be measured. Cavity ring-down spectroscopy (CRD) [24] is a slight modification of direct absorption spectroscopy where long path lengths are obtained. Cavity enhanced absorption spectroscopy (CEAS) [25] and integrated cavity output spectroscopy (ICOS) [26] are similar techniques. The Hobbs' Auto balancing technique [27] is an electronic circuit where  $I$  and  $I_0$  are divided before amplification. This prevents uncorrelated noise in  $I$  and  $I_0$  from being amplified and hence lowers the minimum detectable absorbance. The lowest absorbencies can be determined by combining the advantages of FMS and CRD. This can be done in a technique called noise-immune cavity enhanced-optical heterodyne molecular spectroscopy (NICE-OHMS) [28]. Minimum absorbencies of  $\sim 10^{-14}$  (!) can be detected. However, the setup for NICE-OHMS is very sophisticated.

### Modulation spectroscopy

Modulation spectroscopic detection techniques exploit the fact that laser noise shows a  $1/f$  tendency ( $f$  stands for frequency) by shifting the detection to higher frequencies. This significantly lowers the sensitivity or the time required for averaging. WMS (wavelength modulation spectroscopy) and FMS (frequency modulation spectroscopy) are the two techniques. Since wavelength and frequency denote the selfsame thing ( $c=\lambda/\nu$ ), the terms are somewhat confusing. The difference is as follows: For FMS the modulation frequency ( $\sim 500$  MHz) is equal to or greater than the absorption feature. As for WMS, the modulation frequency ( $\sim 50$  kHz) is much narrower than the absorption line width. Since there is no physical difference between WMS and FMS, intermediate frequencies (1-50 MHz) have also been used successfully. In modulation techniques, an ac (alternating current) component is added to the injection current of the diode laser. A comparison on WMS and FMS can be found in [29]. Basically, the experimental setup is the same for WMS and FMS. It is depicted below in Fig. II.3-9.

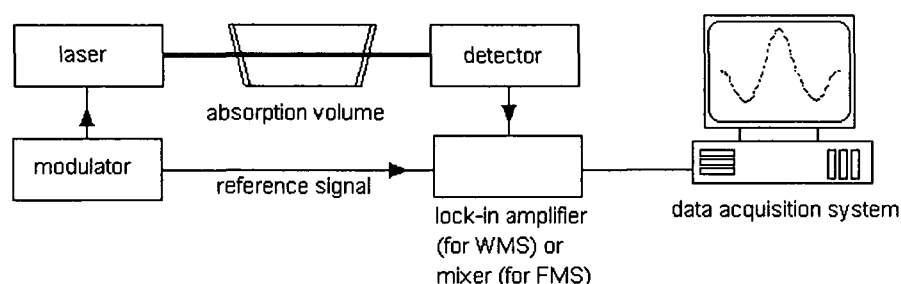


Fig II.3-9: Scheme of the experimental setup for modulation spectroscopy. See text for details.

The laser frequency is modulated around its center through the drive current. A lock-in amplifier is needed for frequency selective amplification of the signal. Because of significantly lower costs, WMS is more commonly used than FMS although it is two orders of magnitude less sensitive. FMS is used when a fast response time is needed.

A special approach in FMS is two tone frequency modulation spectroscopy (TTFM) [30].

The lock-in technique is used to detect and measure very small ac (alternating current) signals. The capabilities are well beyond those of passive electronic filters and most of the unwanted noise can be effectively suppressed. Basically, a lock-in is a filter with an arbitrarily narrow bandwidth that is tuned to the frequency of the signal to be measured. In addition to filtering, a lock-in also provides gain of up to  $10^9$ . The technique requires that the signal to be detected be at a fixed frequency in a relatively quiet part of the noise spectrum. The response of the experiment in a very narrow bandwidth of this frequency is then detected. A lock-in detector has to be provided with two signals: Detector signal and reference signal. The latter could be a sine wave with a frequency  $\omega_r$ . The purpose is to tell the device the exact frequency of the signal in question. A special circuit, the Phase-Lock Loop (PLL), will track this input signal frequency. The output may be phase shifted. In this case, the output can be given by  $\cos(\omega_r t + \phi)$ . The signal coming from the sample is amplified by a high gain ac coupled differential amplifier. The output of this amplifier is then multiplied by the PLL output in a circuit called the Phase-Sensitive Detector (PSD). This multiplication shifts each frequency component of the input signal,  $\omega_s$ , by the reference frequency,  $\omega_r$ , so that the output of the PSD is given by

$$V = \cos(\omega_r t + \phi) * \cos(\omega_s t) = \frac{1}{2} \cos[\omega_r + \omega_s]t + \phi + \frac{1}{2} \cos[\omega_r - \omega_s]t + \phi$$

(Eq. II.3-4)

$\omega \dots$  angular frequency [ $s^{-1}$ ]

The sum frequency component is attenuated by a low pass filter, and only those difference frequency components within the low pass filter's narrow bandwidth will pass through the subsequent dc (direct current) amplifier to yield the output signal. A good lock-in can reject noise which is more than  $2.5 * 10^{-3}$  Hz away from the reference frequency input.

### WMS (Wavelength modulation spectroscopy)

Upon modulation, the laser frequency is given by:

$$v = 2 v_c + \delta v \cos(\omega t)$$

(Eq. II.3-5)

$v \dots$  optical frequency [ $s^{-1}$ ]

$v_c \dots$  center frequency [ $s^{-1}$ ]

$\omega \dots$  modulation frequency [ $s^{-1}$ ]

$\delta v \dots$  modulation amplitude (on the order of the line width) [ $s^{-1}$ ]

The intensity  $I(v_c)$  of the transmitted light can be developed into a Fourier series:

$$I(v_c, t) = \sum_{n=0}^{\infty} A_n(v_c) \cos(n\omega t)$$

(Eq. II.3-5)

$A_n$  are the individual harmonic components. They can be measured with a lock-in amplifier.

By substituting  $\omega t$  against  $\theta$  the following analytical expression can be derived:

$$A_n(\nu_c) = \frac{2}{\pi} \int_0^\pi I_0(\nu_c + \delta\nu \cos\theta) \exp[-\alpha(\nu_c + \delta\nu \cos\theta)L] \cos n\theta d\theta$$

(Eq. II.3-6)

The transmitted light intensity in the empty cell  $I_0(\nu)$ , the absorption coefficient  $\alpha(\nu)$  and the path length  $L$  have to be known for evaluation of (Eq. II.3-6).

If  $I_0$  is constant, that is  $I_0$  is no function of  $\nu$  as in an ideal light source, (Eq. II.3-6) can be simplified to

$$A_n(\nu_c) = \frac{2I_0}{\pi} \int_0^\pi \exp[-\alpha(\nu_c + \delta\nu \cos\theta)L] \cos n\theta d\theta$$

(Eq. II.3-7)

For low gas concentrations and short path lengths,  $\alpha(\nu)L \ll 1$ .

We know that

$$\alpha(\nu) = \sigma(\nu)N$$

(Eq. II.1-16)

Thus (Eq. II.3-7) can be rewritten to

$$A_n(\nu_c) = -N \frac{2I_0 L}{\pi} \int_0^\pi \sigma(\nu_c + \delta\nu \cos\theta) \cos n\theta d\theta$$

(Eq. II.3-8)

(Eq. II.3-8) demonstrates that the harmonic components  $A_n(\nu_c)$  are directly proportional to the concentration  $N$ .

If the modulation amplitude  $\delta\nu$  is much smaller than the absorption feature, the absorption cross section  $\sigma(\nu)$  can be expanded into a Taylor series and truncated after the first term:

$$A_n(\nu_c) = \frac{2^{n-1} I_0 LN}{n!} \delta\nu^n \left. \frac{d^n \sigma}{d\nu^n} \right|_{\nu=\nu_c}$$

(Eq. II.3-9)

The  $n^{\text{th}}$  harmonic component  $A_n(\nu_c)$  is proportional to the  $n^{\text{th}}$  derivative of  $\sigma(\nu)$ . This technique is called *derivative spectroscopy*.



### Operating WMS TDLAS systems

The laser center frequency  $\nu_c$  is scanned over the total absorption feature repetitively at  $\sim 100\text{Hz}$ . A lock-in amplifier is used to measure  $A_n(\nu_c)$ . The amplitude of the harmonic spectrum is proportional to  $N$ .

Alternatively,  $\nu_c$  is fixed to where  $A_n(\nu_c)$  has got a maximum. The lock-in amplifier now yields a dc voltage that is directly proportional to  $N$ . The latter method is faster but rather prone to errors.

From equation (II.3-9) we can see that  $A_n$  is proportional to  $\delta\nu_n$  for small  $\delta\nu$ .

However, as  $\delta\nu$  is increased  $A_n$  reaches a peak value soon after  $\delta\nu$  reaches the line width. After that, with further increase of  $\delta\nu$ ,  $A_n$  decreases again. The value of  $\delta\nu$  for which  $A_n$  is biggest is known as the optimum modulation. It is characterized by the parameter  $m$ .

$$m = \frac{\delta\nu}{\text{HWHM line}}$$

(Eq. II.3-10)

For the second, fourth and sixth harmonic, the optimum value for  $m$  is 2.2, 4.3 and 5.6 respectively.

To obtain high sensitivities, the modulation amplitude is set close to the optimum value.

Since all harmonics are proportional to the species concentration, basically any of them may be used.

However, some practical considerations influence the choice:

- $A_n$  (and in row with  $A_n$  the sensitivity) decreases with increasing  $n$ .  $A_2$  is  $\sim 2$  times stronger than  $A_4$ .
- In contrast to odd harmonics, even harmonics (2, 4, 6, ...) have got a maximum at the line center.
- Only first and second harmonics can easily be measured with commercially available lock-in amplifiers.
- Higher harmonics are less sensitive to residual amplitude modulation (RAM). Modulation of the laser drive current not only modulates the laser frequency but also its intensity. This effect is known as RAM. Note that the expressions above assume that  $I_0$  is not a function of  $\nu$ .

Normally, the second harmonic is used.

Fig. II.3-10 below shows the line shape of a direct absorption signal (a), the first harmonic (b) and the second harmonic (c) of the absorption line.

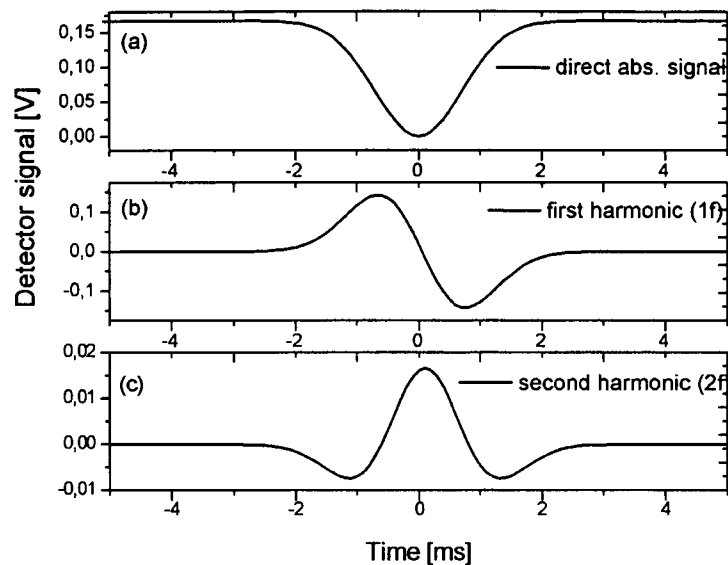


Fig. II.3-10: Original (a), 1f (b) and 2 f (c) signal of an absorption peak (calculated). See text for details.

A review on WMS can be found in [31].

Within the scope of this thesis, TDLAS is used for combustion and ignition diagnostics. The range of operation is much broader:

A review can be found in [32]-[34].

[35] to [44] list “showcase” examples of what TDLAS is capable of.

The determination of isotope ratios was reported in [35]. In [36], eddy correlation measurements in the atmosphere were carried out using TDLAS, [37] reported species concentration measurements in the atmosphere at sub ppb levels, [38] an airborne spectrometer for the stratosphere. Chemical rate constants were determined by TDLAS in [39]. Intermediate species were measured in [40], investigations in atmospheric pressure plasma in [41]. Temperature distribution measurements were carried out in [42] and [43]. In [44], a detection limit for atmospheric peroxy radicals of 1 ppt ( $10^{-12}$ ) was attained.

Tunable diode laser absorption spectroscopy can be used for quantitative measurements of

- species concentrations (number densities)
- temperature (and temperature distributions)
- pressure (total and partial)

In this thesis the following “corner stones” using TDLAS were attained (examples):

- multiple species concentration measurements using a single laser ( $\text{H}_2\text{O}+\text{HCl}$ ,  $\text{CO}+\text{CH}_4$ )
- extremely fast species concentration measurements (0.2  $\mu\text{s}$ )
- investigation of transient phenomena (ignition)
- measurements in hostile multi phase environments (particle laden gas streams and flames, fluidized bed combustor)
- measurements at high pressures ( $\gg 1$  bar) and high pressures ( $>1000^\circ\text{C}$ )
- *in-situ* measurements in an internal combustion engine

See also tables III.5-1 and IV.7-1.

## II.4 Combustion

Combustion is said to be the oldest technology of mankind. Fire has been used in numerous ways. Today approximately 90% of the energy we produce stems from combustion processes. This is not expected to change in the near future, either. The burning of fossil fuels has reached such an extent that we are now facing issues like global warming, depletion of natural resources and pollution with large implications. Apart from a mere academic interest in combustion processes that sprouts from the widespread use, a profound knowledge is needed to improve efficiency and to reduce emissions from the use of combustion. Traditionally, research was limited to fluid mechanics. Chemical reactions were assumed to be infinitely fast, with nothing but the global heat release to be considered. For the design of a combustion apparatus as such, this was sufficient. However, pollutant formation and other transient processes like ignition have to take the coupling of fluid flow with chemical kinetics into account. Intrusive suction tubes have been widely replaced by laser spectroscopic tools to gain a deeper insight into the processes involved. A satisfactory treatment of the processes responsible for combustion phenomena requires a basic understanding of the underlying concepts and principles.

### Flame types

In combustion processes, there is always a fuel (e.g. gaseous, liquid) and an oxidizer (e.g. air,  $O_2$ ). Flames can be divided into the two categories premixed (the fuel and its oxidizing agent are mixed and burned afterwards) and non-premixed (combustion and mixing occur simultaneously). In Fig. II.4-1, a premixed flame (methane/air) is shown on a McKenna flat flame burner (now Holthuis and Associates, Sebastopol, CA).

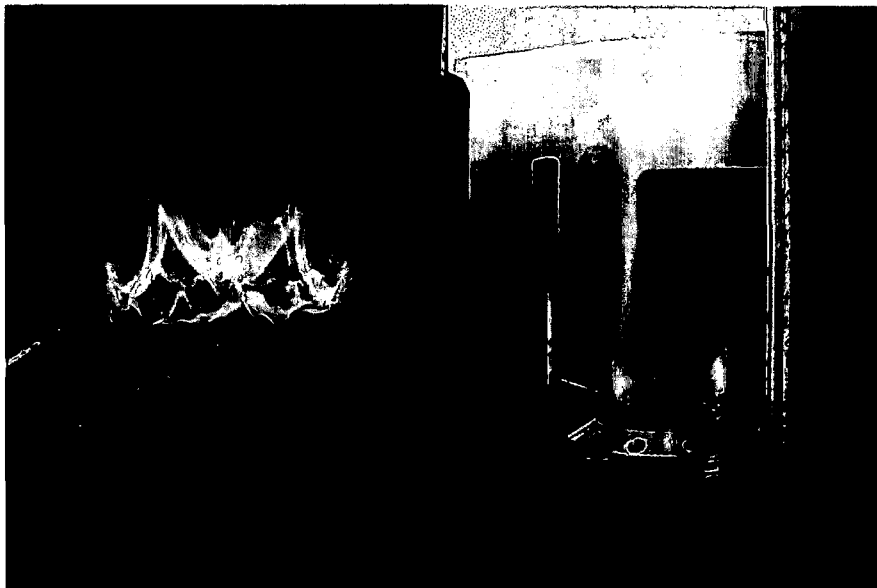


Fig. II.4-1: Premixed methane/air flame on a McKenna flat flame burner. The right picture shows the determination of the laminar flame velocity.

In Fig. II.4-2, a non premixed (diffusion) flame (methane/air) is shown.

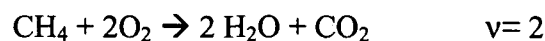


Fig. II.4-2: Non premixed methane/air flame on a McKenna flat flame burner. The flow is higher in the picture on the right, therefore more turbulence occurs.

Each of these types can be further subdivided based on whether the flow is laminar or turbulent.

The Bunsen flame constitutes a well-known example of laminar premixed flames.

In Eq. II.4-1, an easy reaction equation is given:



(Eq. II.4-1)

$\nu$ ... mole number of  $\text{O}_2$  for a complete reaction [1]

In the reaction the equation is written down for 1 mole of fuel. The mole fraction of the fuel  $x_{\text{fuel}}$  in a stoichiometric mixture is obtained by the following equation:

$$x_{\text{fuel, stoichiometric}} = \frac{1}{1 + \nu}$$

(Eq. II.4-2)

For  $\nu=2$

$$x_{\text{fuel, stoichiometric}} = \frac{1}{1 + 2} = 0.33$$

(Eq. II.4-3)

If air is used as an oxidizer, it has to be considered that  $x_{\text{oxygen}}$  is 0.21 ( $x_{\text{N}_2} = 3.76 x_{\text{O}_2}$ ). In this case, the mole fractions in a stoichiometric mixture with air are

$$x_{\text{fuel, stoichiometric}} = \frac{1}{4.76\nu + 1}$$

(Eq. II.4-4)

$$x_{\text{oxygen, stoichiometric}} = \nu x_{\text{fuel, stoichiometric}}$$

(Eq. II.4-5)

The so-called air equivalence ratio  $\lambda$  (air number, lambda) is defined as

$$\lambda = \frac{\frac{x_{air}}{x_{fuel}}}{\frac{x_{air,stoich}}{x_{fuel,stoich}}}$$

(Eq. II.4-6)

The fuel equivalence ratio  $\Phi$  is given by

$$\Phi = 1/\lambda$$

(Eq. II.4-7)

A flame can be stoichiometric, fuel-rich or fuel-lean (see table II.4-1).

The latter case guarantees lower flame temperatures and thus lowered emissions, but also exhibits a reduced burning velocity.

	fuel equivalence ratio $\Phi$	air equivalence ratio $\lambda$
(Fuel) rich combustion	$\Phi > 1$	$\lambda < 1$
Stoichiometric combustion	$\Phi = 1$	$\lambda = 1$
(Fuel) lean combustion	$\Phi < 1$	$\lambda > 1$

Table. II.4-1: Premixed combustion.  $\lambda = 1/\Phi$ .

The flame speed  $v_L$  (laminar burning velocity, flame velocity) characterizes the propagation of the flame front into the unburned mixture. The flame velocity depends on the mixture composition, the pressure and the initial temperature (see Figures II.4-3 and II.4-4, taken from [45]).

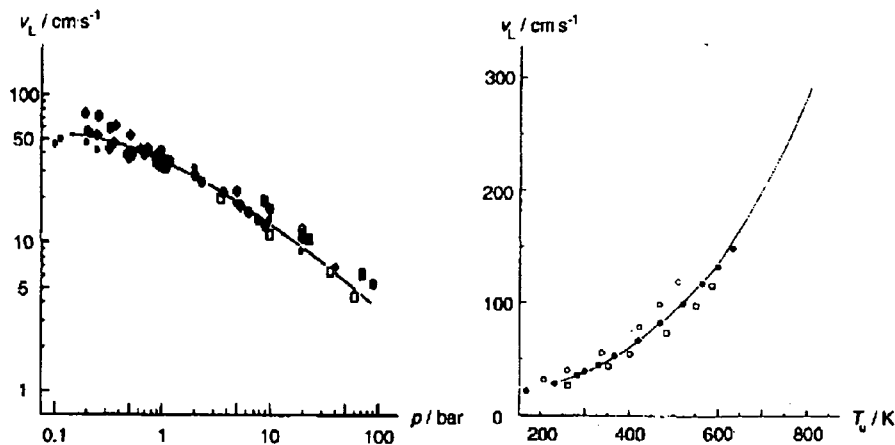


Figure II.4-3: Pressure dependence of the flame speed  $v_L$  at 298 K(left) and temperature dependence of  $v_L$  at 1 bar (right) in stoichiometric  $\text{CH}_4/\text{air}$  mixtures (Taken from [45]).

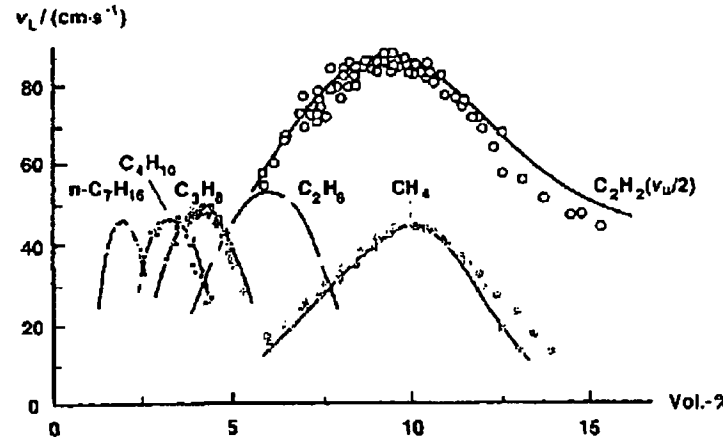


Figure II.4-4: Dependence of the flame speed  $v_L$  (298 K, 1bar) on the composition of the gas mixture shown for various hydrocarbon/air mixtures. For  $\text{CH}_4$ , 10 vol% correspond to  $\lambda = 1$  (Taken from [45]).

Because of the lurking risk of explosion of the premixed reactants, special care has to be taken when working with premixed flames. Turbulent premixed flames are encountered in the Otto engine with spark plugs. They are theoretically modeled using the so-called flamelet concept [46]. Laminar non-premixed flames (also called diffusion flames) do not propagate and cannot be characterized by a laminar flame speed. Burning candles constitute an example for this type. Modeling is more difficult, since  $\Phi$  goes from 0 (air) to  $\infty$  (fuel). The flame front occurs in regions of stoichiometric mixture, since the temperature is highest there. There is a further subdivision into counter-flow and co-flow laminar non-premixed flames. Turbulent non-premixed flames are the dominant flame type in the Diesel engine. Again the flamelet concept can be used. The typical yellow color stems from glowing soot particles in the rich combustion domain.

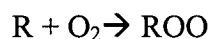
Internal combustion engines are treated in chapter II.7.

### Hydrocarbon combustion chemistry

The combustion chemistry of the different hydrocarbons varies very little. It is characterized by complete fragmentation. A mixture of  $\text{C}_2\text{H}_4$ ,  $\text{CH}_4$ ,  $\text{CH}_2\text{O}$ ,  $\text{H}_2$  and  $\text{CO}$  is the fuel that actually burns. Only methane constitutes an exception (This will be discussed later). There are, however, pronounced mechanistic differences between combustion at low (several 100 K) and high (>1000K) temperatures. There are also significant mechanistic changes in oxidation processes at high pressures. Below 10 atm, no appreciable effects on the relative significance of major oxidation routes could be observed [47].

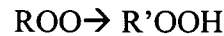
### General features

When hydrocarbons are oxidized, self-acceleration is observed. The induction periods suggest that there must be some form of chain reaction involved (In fact, it is degenerate branching). Prior to significant energy release, large amounts of the fuel are converted to stable partially oxidized intermediates. The core mechanism of hydrocarbon oxidation at low temperatures involves the formation of peroxide radicals according to



(Eq. II.4-8)

Isomerization to the hydroperoxy radical follows.



(Eq. II.4-9)

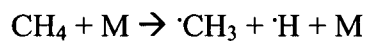
R,R' ... organic rest (hydrocarbon chain)

The hydroperoxy radical subsequently decomposes according to



(Eq. II.4-10)

This reaction constitutes the chain branching reaction. At higher temperatures, thermal decomposition is the chain initiation step:



(Eq. II.4-11)



(Eq. II.4-12)

As the C-C bond is substantially weaker than the C-H bond, chain fission is more important than the loss of an H-atom. For more details, see [48].

#### CH<sub>4</sub> combustion

Methane, CH<sub>4</sub>, is the simplest organic fuel (see Fig. II.4-5 below). Its calorific value is 39.8 MJ/m<sup>3</sup> (55.3 MJ/kg).

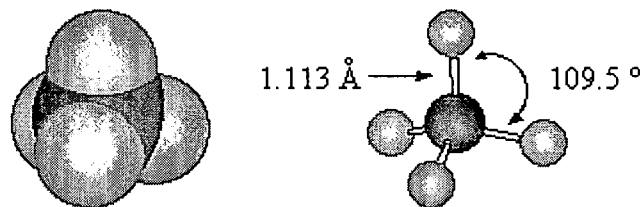
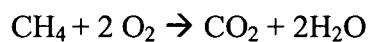


Figure II.4-5: Depiction of the methane molecule (left: calotte; right: dimensions).

The oxidation of a fuel as simple as methane is very complex. The gross chemical reaction is formulated as:



(Eq. II.4-13)

According to [49], the reaction rate can be formulated as

$$d[\text{CH}_4]/dt = -k \cdot [\text{CH}_4]^a \cdot [\text{O}_2]^b \cdot [\text{Diluent}]^c \cdot \exp(-E/RT)$$

(Eq. II.4-14)

[ ]... molar concentrations [molL<sup>-1</sup>]

k... velocity constant [L<sup>2</sup>mol<sup>-2</sup>s<sup>-1</sup>]

a, b, c... constants [1]

E... activation energy [Jmol<sup>-1</sup>]

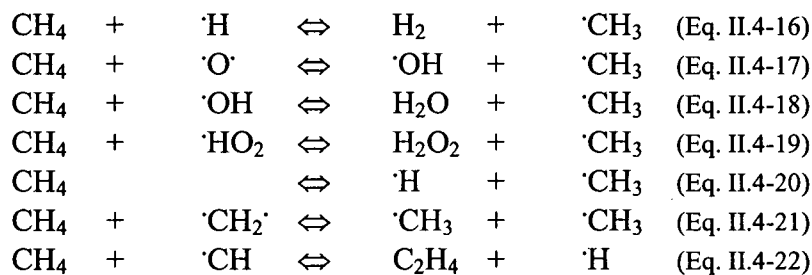
The GRI (Gas Research Institute) mechanism for the oxidation of methane [50] consists of 279 reactions of 49 species. The Leeds methane oxidation mechanism [51] lists 351 reactions of 57 species. More sources for detailed hydrocarbon combustion mechanisms can be found in [48]. The general sequence of the oxidation of methane is given by



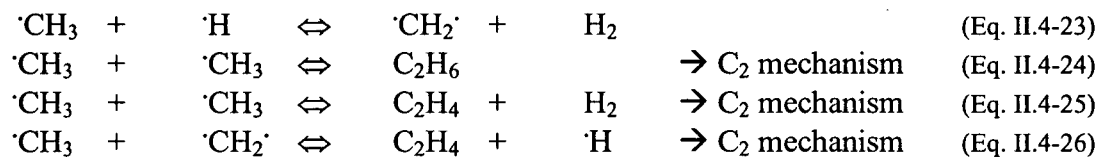
(Eq. II.4-15)

Some elementary reactions are listed below:

Consumption of CH<sub>4</sub>

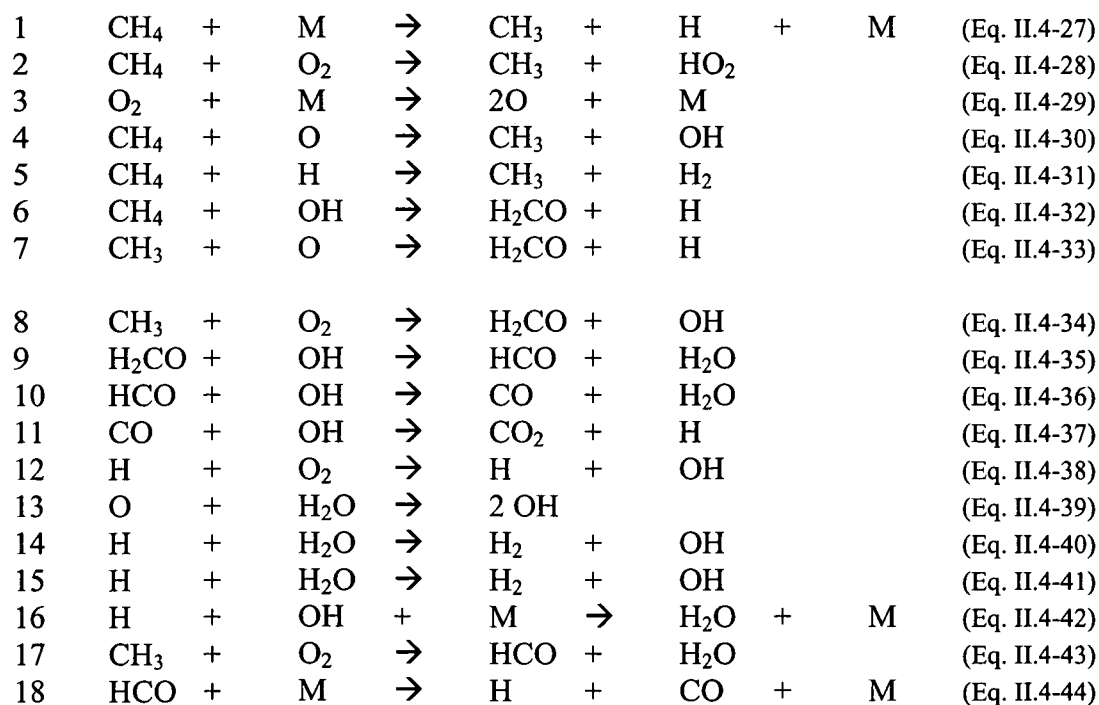


Consumption of ·CH<sub>3</sub>



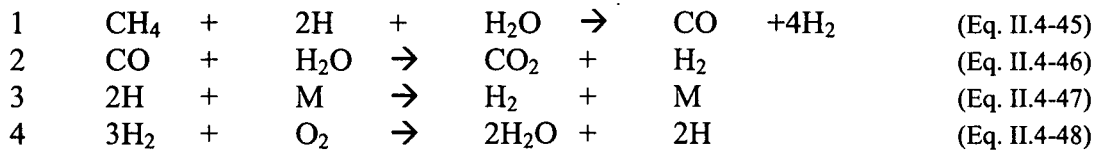
...

As one can see, dimerization leads to the formation of higher hydrocarbons. Recombination reactions are very important for high-temperature combustion. At high temperatures, the oxidation of methane is assumed to consist of 18 governing elementary reactions involving 14 species [52].





A four step skeletal (reduced) mechanism is used by [53].



The dissociation energy of the C-H bond in  $\text{CH}_4$  is 440 kJ/mol. This value is much higher than the C-C and C-H bond strength in higher hydrocarbons (C-H bond in ethane: 410 kJ/mol; C-C bond in ethane: 377 kJ/mol). Therefore, the oxidation of methane differs strongly from other hydrocarbons. It is also more difficult to ignite methane than its homologues. Small additions of ethane or hydrogen produced a dramatic improvement of the ignitability of methane. [54] and [55]. The primary attack of  $\text{CH}_4$  by  $\cdot\text{O}$ ,  $\cdot\text{OH}$ ,  $\text{H}$  and  $\cdot\text{HO}_2$  as shown above produces  $\cdot\text{CH}_3$  radicals. In contrast to heavier radicals,  $\cdot\text{CH}_3$  does not decompose significantly to yield other radicals ( $\cdot\text{CH}_2$  or  $\cdot\text{CH}$ ). The chemistry of the methane flame is mainly determined by  $\cdot\text{CH}_3$ . The total concentration of radicals is lower, the ignition and all reactions take place more slowly. In the case of  $\text{CH}_4$ , large amounts of the fuel are consumed only towards the end of the induction period. This is not the case for higher hydrocarbons. Mechanistic changes in the oxidation of methane were found to occur above 476 atm [56] and 1780 K [49]. Nitrogen chemistry in the combustion of methane is considered in [53]. Reaction flow analysis is done when combustion is numerically simulated. A spreadsheet lists the percentage contributions of all reactions  $r_i$  ( $r_1, r_2, r_3, \dots, r_n$ ) to the formation or consumption of a chemical species  $s_j$  ( $s_1, s_2, s_3, \dots, s_m$ ). Visualization makes it easier to distinguish between main and minor reaction paths. Such a visualization is depicted below. Fig. II.4-6 (a) shows the reaction flow for a stoichiometric  $\text{CH}_4/\text{air}$  flame at 1 atm and 298 K, (b) belongs to a fuel rich flame (all other parameters being equal). There are some noticeable differences in the adopted reaction paths; As for the stoichiometric flame, the biggest part of the methane is oxidized directly, whereas in the fuel rich flame, the methyl radicals are prone to recombination to ethane prior to oxidation.

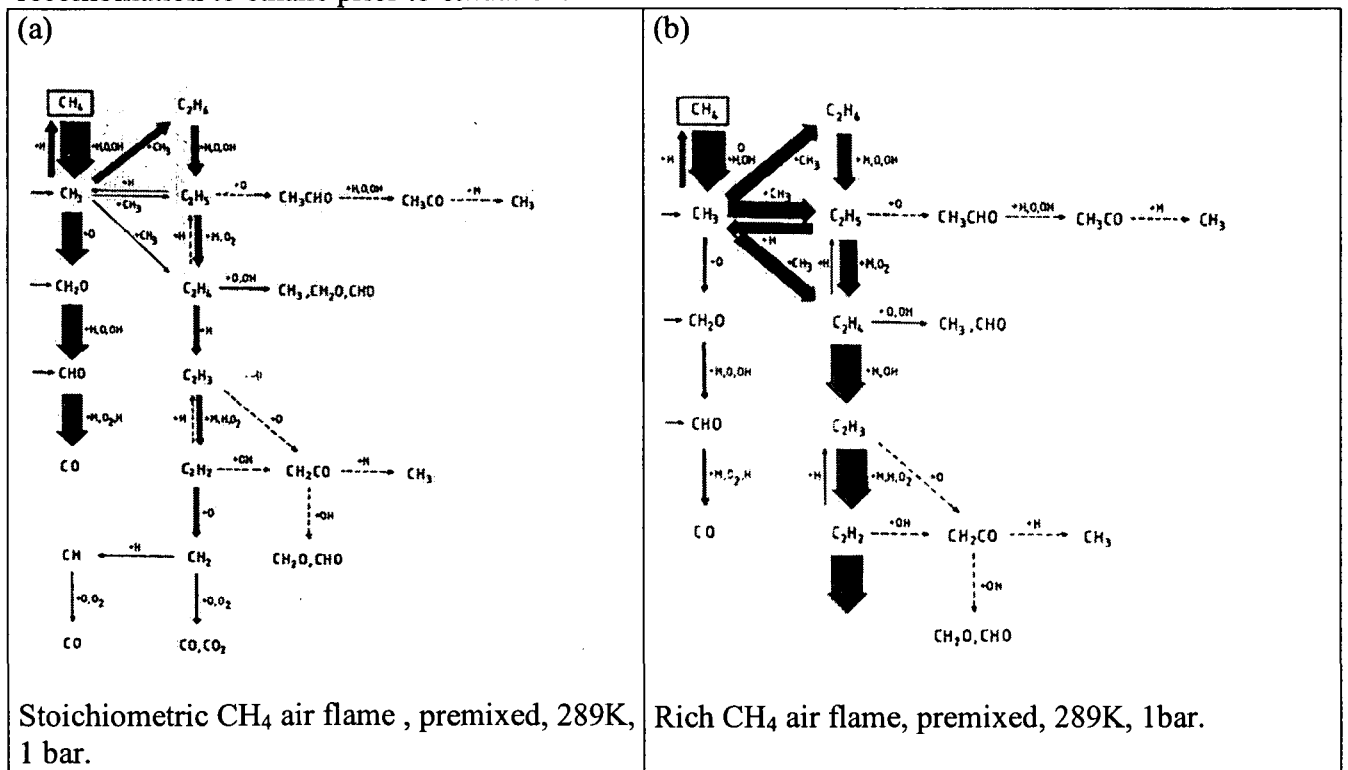


Figure II.4-6: Integral reaction flow analysis of the combustion of  $\text{CH}_4$  (Taken from [46]).

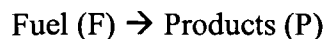
## II.5 Ignition

In this chapter, some aspects related to ignition will be described. Differences between ignition, detonation and explosion are elaborated.

### Homogeneous and inhomogeneous ignition

Ignition is the process of starting radical reactions until a self-sustaining flame has developed. In contrast to ideal premixed and non-premixed flames, ignition obviously has to be described as a time-dependent phenomenon. Examples of ignition processes include auto ignition, induced ignition and photo-ignition caused by photolytic generation of radicals. For a merely qualitative description, two models have been developed: Homogeneous ignition (Semenov) and inhomogeneous ignition (Frank-Kamenetskii) [46].

If the heat exchange in the reaction system is fast compared to the heat exchange with the surrounding (vessel wall) the theory of Semenov is suitable. In his analysis of thermal explosion, Semenov considers a spatially homogenous system (temperature, pressure, mole fractions). Further simplification approximated the chemistry by a one-step reaction



(Eq. II.5-1)

with a reaction rate  $r$  [1] of

$$r = -M_F c_F A e^{\frac{-E}{RT}}$$

(Eq. II.5-2)

- R.... universal gas constant [ $\text{JK}^{-1}\text{mol}^{-1}$ ]
- E.... activation energy [ $\text{Jmol}^{-1}$ ]
- $c_F$ .... concentration of fuel [ $\text{molL}^{-1}$ ]
- $M_F$ .... molar mass [ $\text{kgmol}^{-1}$ ]
- A.... pre-exponential factor [ $\text{Lkg}^{-1}$ ]

The temperature dependence of the reaction rate  $r \sim k \cdot \exp(-E/RT)$  (see Eq. II.5-2) is termed "Arrhenius' law". Because the fuel consumption is small at the beginning of the ignition, it can be neglected ( $c_F = c_{F,0}$ ;  $\rho = M_F c_{F,0}$ ). This simplification leads to

$$r = -\rho A e^{\frac{-E}{RT}}$$

(Eq. II.5-3)

$\rho$ ... density [ $\text{kgL}^{-1}$ ]

To describe the heat flux  $j_P$  to the surroundings Newton's law of heat exchange is used (Eq. II.5-4):

$$j_P = \chi S (T - T_W)$$

(Eq. II.5-4)

- $T, T_W$ ... temperature in the system; wall temperature [K]
- $S$ ... surface area of the system [ $\text{m}^2$ ]
- $\chi$ ... heat transfer coefficient [ $\text{Wm}^{-2}\text{K}^{-1}$ ]

The time behavior of the temperature can be determined considering the heat production (P) and the heat loss (L) in the system.

$$\rho c_P \frac{dT}{dt} = P - L = (h_f - h_p) \rho A e^{\frac{-E}{RT}} - \chi S (T - T_w)$$

(Eq. II.5-5)

The heat production term and the heat loss term are depicted in Fig. II.5-1. The heat loss term represented by the dotted line increases linearly with the temperature. Three curves with different activation energies and pre-exponential factors show the dependence on temperature.

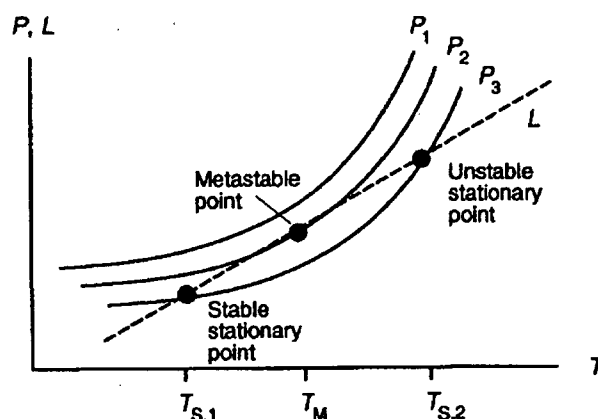


Fig. II.5-1: Dependence of temperature on heat production P (solid line) and heat losses L (dotted line, taken from [46]). See text for details.

Kamenetskii's theory is an extension of Semonov's analysis. Newton's heat transfer law is replaced by the law of Fourier allowing a diffusion of energy to the wall. As a consequence, the temperature in the system is inhomogeneous. This results in a formation of a temperature gradient. Kamenetskii's theory is suitable for such cases where the heat exchange with the surroundings is faster than the heat exchange within the system. A shortcoming is the assumption of no reactant consumption which has been overcome by more sophisticated approaches.

## Auto ignition

### Ignition limits (explosion limits)

The question within which ranges of temperature, pressure and composition a mixture can ignite is of utmost importance. At certain values of temperature and pressure the mixture will ignite spontaneously and at other conditions only a slow reaction is observed. These phenomena are illustrated in Fig. II.5-2 by a p-T-diagram, where a region in which ignition takes place is separated by a curve from the region where no ignition occurs. The curve represents the spontaneous ignition temperature as a function of the pressure.

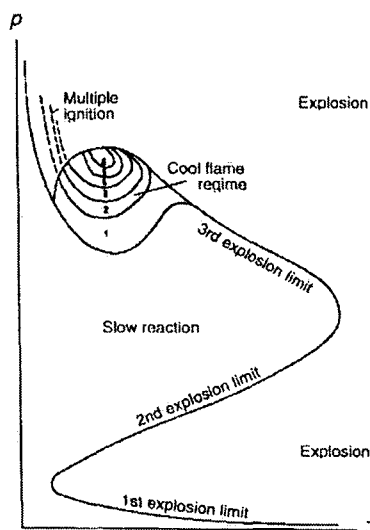


Fig. II.5-2: Schematic p-T explosion diagram for hydrocarbons ( $p$ =pressure,  $T$ =temperature, taken from [46]). The cool flame phenomenon is described later.

At low pressure radicals that are able of inducing ignition diffuse to the vessel wall where they recombine to stable species. Due to low pressure conditions the diffusion coefficient  $D$  is very high, since the diffusivity is inversely proportional to the pressure ( $D \sim 1/p$ ). Thus, the mixture does not ignite and only a slow reaction takes place. When the pressure is raised above the so-called first explosion limit, the radical production rate in the gas phase outweighs the reduced diffusion rate of the radicals to the vessel wall and an ignition is observed. Since the first explosion limit is a result of the competition between radical generation and chain branching in the gas phase and the termination step (due to recombination) at the vessel surface, it strongly depends on the material composition of the vessel surface. It was found in [57] that coating a stainless steel vessel with boric acid reduces its wall termination efficiency which lowered the ignition temperature of methane by about 20 K. It was also observed that metal surfaces are more efficient terminators than glass ones. By further increasing the pressure the second ignition limit is reached. One does not observe ignition. It is determined by the competition of chain branching and chain termination in the gas phase. Since the chain termination requires a third molecule to dissipate the recombination energy (three-body reaction) it increases faster and exceeds the rate of the competing two-body branching reaction. This competition is the explanation for the second explosion limit.

At even higher pressures the third explosion limit is observed. This third explosion limit is also called thermal explosion limit and results in the competition of heat production by chemical reactions and heat losses to the surroundings (vessel wall). The heat production increases with increasing pressure, which explains the transition to explosion. As for ignition of hydrocarbon/air mixtures things are rather complicated due to additional chemical processes involved (e.g. formation of peroxides). This is especially pronounced in the region of the third explosion limit, where ignition after the emission of short light pulses (multiple ignition) takes place or where combustion at low temperature (cool flames) is observed.

### Ignition delay time (induction time)

When an ignitable hydrocarbon/air mixture is brought to supplied with sufficient energy, it still will not ignite until an induction time (ignition delay time) has passed. This ignition delay time can be as long as several hours or as short as microseconds and is characteristic for radical-chain explosions. During this time span, the radical population increases

exponentially. These chemical reactions (radical formation) do consume fuel but the temperature remains nearly constant. As soon as the radical pool has grown enough to consume a significant fraction of the fuel, ignition occurs and the temperature starts to rise. In contrast, in a purely thermal ignition processes there is not induction time and the temperature increases immediately.

The temperature rise of a thermal and a radical-chain explosion is depicted in Fig. II.5-3.

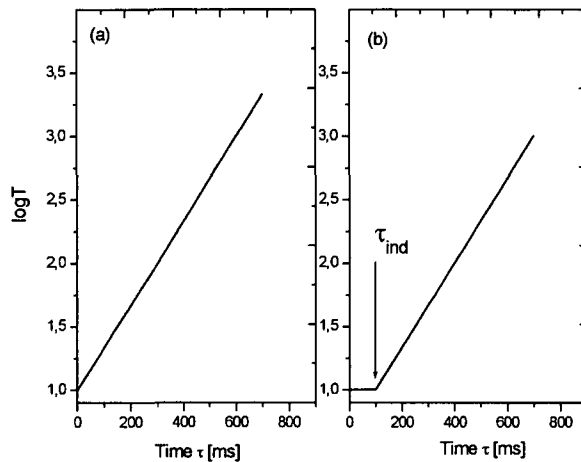


Fig. II.5-3: Simplified time behavior of a thermal explosion (a) and chain reaction (b) in an adiabatic system ( $\tau$ =time,  $T$ =temperature, taken from [46]). In thermal explosions, there is no ignition delay time  $\tau_{ind}$  (ind=induction).

The underlying reactions depend exponentially on the reciprocal temperature  $T$  (Arrhenius' law, Eq. II.5-2). The induction time can hence be written as

$$\tau = Ae^{\frac{B}{T}}$$

(Eq. II.5-6)

B... constant [K]

A... constant [s]

Fig. II.5-4 illustrates the induction time dependence on the temperature for several hydrocarbon/air-mixtures at a pressure of 3 bar.

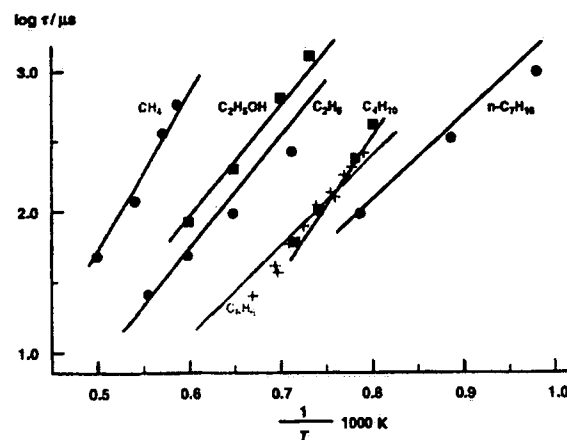


Fig. II.5-4: Induction times  $t$  in hydrocarbon/air mixtures (Taken from [46]).  $t$  decreases with temperature.

Different fuel concentrations and initial pressures also lead to a variation of the induction time [58]. Fig. II.5-5 (left side) shows the decrease of induction time with the increase in methane concentration for two different initial pressures at a temperature of 410°C. The concentration dependence of the induction time can be expressed as

$$\tau = C_1 \frac{1}{[c]^{k_1}}$$

(Eq. II.5-7)

$C_1$ ... constant [s]  
 $k_1$ ... constant [1]  
 $[c]$ ... concentration [vol%]  
 $\tau$ ... induction time [s]

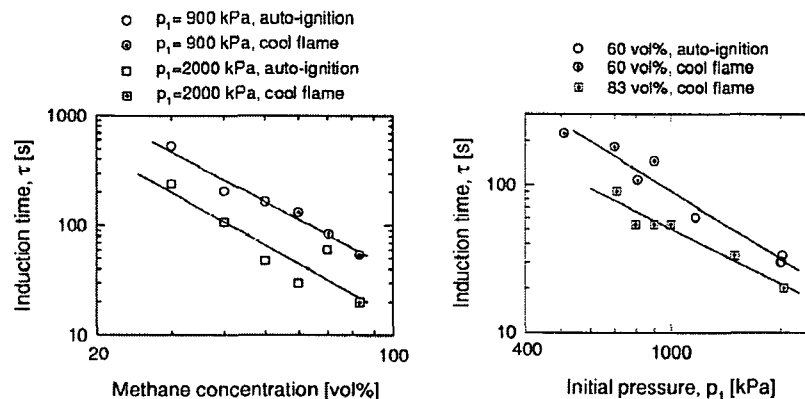


Fig. II.5-5: Dependence of induction time  $t$  on methane concentration and initial pressure at 410°C (taken from [58]).  $\tau$  decreases both with increasing fuel concentration and pressure.

In Fig. II.5-5 (right side) the induction time as a function of initial pressure for two methane concentrations (60 and 83 vol%) is presented at a temperature of 410 °C. The decrease of the induction time with increasing pressure  $p$  is given by

$$\tau = \frac{C_2}{p^{k_2}}$$

(Eq. II.5-8)

$C_2$ ... constant [ $\text{sPa}^{k_2}$ ]  
 $k_2$ ... constant [1]

[57] investigated ignition delays of methane/air mixtures, which lasted seconds or even minutes depending on the fuel concentration.

[56] studied the influence of surface to volume ratio of non-catalytic surfaces (tabular alumina and activated alumina,  $\text{Al}_2\text{O}_3$ ) on the ignition delay. It was found in general that high surface/volume conditions lengthened ignition delay considerably. Additionally several catalytic materials were chosen to investigate the effect of catalysts on ignition delay. Catalysts included silica-alumina, silica magnesia, cobalt molybdate and nickel oxide. In general, the catalysts shortened the ignition delay. With the nickel catalyst, no ignition delay was observed at all.

### Auto ignition temperature and cool flame temperature

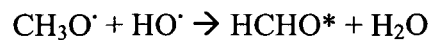
The ignitability of a flammable gas/air mixture is characterised by its minimum ignition energy (MIE) (see later) and its auto ignition temperature also called spontaneous ignition temperature (SIT). The auto ignition temperature (AIT) is the lowest temperature to which a mixture must be heated to ignite spontaneously without the presence of an ignition source. AIT is not a constant and depends on the fuel concentration, flow condition, the initial pressure and volume of the mixture as well as the geometry of the combustion vessel.

In [58] experimental results are presented investigating the pressure dependence and the concentration dependence of AIT. Besides explosion processes cool flames have been observed where a mixture reacts only partially. These flames emitting a pale blue light take place at temperatures below AIT. These phenomena result in a small pressure rise and limited temperature rises.

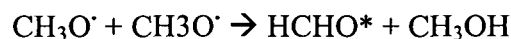
The cool flame temperature (CFT) is defined as the lowest temperature at which a mixture is able of generating cool flames.

The cool flame phenomenon (compare Fig. II.5-2) was observed both within and outside the flammable range of fuel-rich fuel/air and fuel/oxygen mixtures at temperatures below AIT. It manifests itself as a weak flame with low heat release and it favored at high pressures and was observed for CH<sub>4</sub>, saturated and unsaturated hydrocarbons, alcohols, ethers and others. They were encountered both in static vessels and internal combustion engines (knock). The hazard in cool flames lies predominantly in the potential spontaneous transition to a subsequent "hot" ignition. For the initiation of cool flames, given correct temperature, pressure and mixture composition, no ignition source is needed.

The reactions are accompanied by a slight temperature rise and a pale blue flame (luminescence originating from an excited state (\*) of formaldehyde [59]):



(Eq. II.5-9)



(Eq. II.5-10)

In cool flames, among many other products, it is CO and aldehydes that are formed instead of CO<sub>2</sub> and H<sub>2</sub>O as in ordinary combustion. Cool flames never bring about full fuel conversion. More information on cool flames can be found in [59].

In Fig. IV.5-6 the initial pressure  $p_1$  as a function of the methane concentration is plotted to yield the cool flame and the auto ignition region.

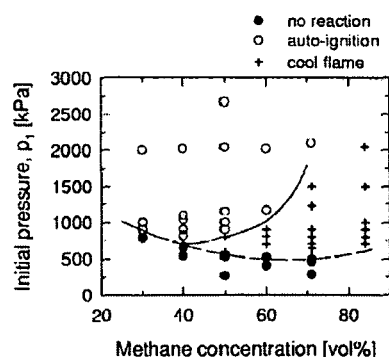


Fig. II.5-6: Concentration versus initial pressure within the cool flame and the auto ignition region at 410°C (Taken from [58]).

The solid line marks the pressure limit beyond which ignition occurs while the dashed line represents the pressure limit beyond which cool flames occur. No cool flame reactions were observed for methane concentrations below 40 %vol. By increasing the methane concentration the cool flame area becomes wider.

Fig. II.5-7 presents the dependence of AIT and CFT on the initial pressure  $p_1$  determined at 60 vol% methane.

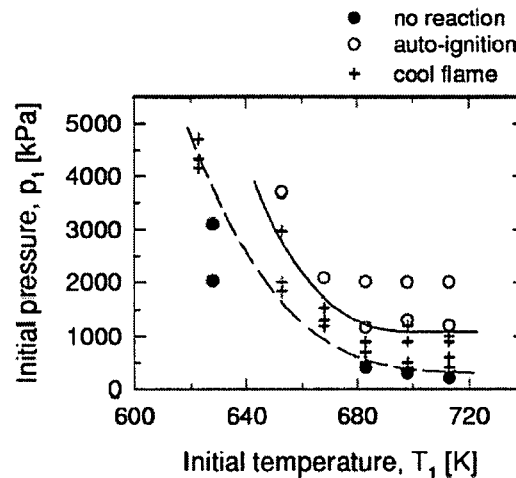


Fig. II.5-7: Initial pressure vs. initial temperature diagram for the cool flame and the auto-ignition region (Taken from [58]).

The solid curve illustrates the pressure above which auto-ignition occurs while the dashed line represents the pressure above which cool flames are observed. Higher initial pressure results in a lower AIT and CFT.

In [57] spontaneous ignition temperatures were determined by enclosing a methane/air-mixture in a heated combustion vessel under stirred and unstirred conditions. Spontaneous ignition temperatures (SIT) are presented in Fig. II.5-8 over a range of equivalence ratios  $\Phi$ , for both the stirred and static reaction conditions. The temperature trace exhibits a minimum at an equivalence ratio of about 0.7. This unusual result was only observed for methane experiments.

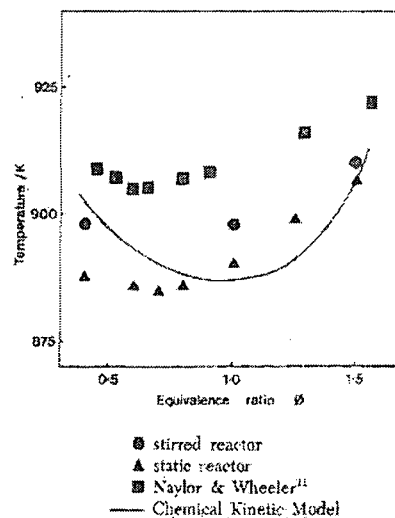


Fig. II.5-8: Spontaneous ignition temperature of methane/air mixtures (Taken from [57]). There is an increase both towards the fuel lean and fuel rich side.



### Induced ignition

A process where a mixture, which would not ignite by itself, is ignited locally by an ignition source (i.e. spark plug, pulsed laser, microwave ignition source) is called induced ignition. During induced ignition, energy is deposited, leading to a temperature rise in a small volume of the mixture, where auto ignition takes place or the energy is used for generation of radicals. In both cases a subsequent flame propagation occurs and sets the mixture on fire.

Diffusion and recombination reactions compete with the generation of new radicals by chemical reactions, and radiative heat losses might overcome the heat generation. So a critical amount of energy is needed to bring about ignition. The smallest amount of energy that results in a successful ignition is known as the minimum ignition energy (MIE). The knowledge of this parameter for a given combustible mixture is of importance for safety purposes and for more efficient internal combustion engines. Besides MIE, the minimum laser pulse energy (MPE) is often used in context with laser-induced ignition.

MPE has to be discerned from MIE. Whereas MIE is the energy necessary to bring about ignition inside the combustion vessel, MPE is the total pulse energy necessary to cause ignition.

MPE is greater than MIE because of incomplete absorption. Not until the plasma spark has fully developed can it absorb all incoming laser energy.

MPE also includes losses such as reflections and scattering at the entrance window of the combustion vessel.

Since MIE is prone to experimental errors and uncertainties, MPE is a much more robust parameter than MIE.

Ignition can take place directly or indirectly. Indirect ignition denotes the initiation of a conventional deflagration (propagation velocity  $< 1000$  m/s) that speeds up to a detonation by itself. Deflagration is caused by chemical reactions that sustain a gradient and molecular transport process that propagate the gradient. Direct initiation of a detonation requires much less energy than deflagration to be started. Experience shows that detonations are only stable when their speed is equal to the local sound velocity (Chapman-Jouget detonation). In contrast, the propagation of detonations is caused by a pressure wave which is sustained by the chemical reaction and the corresponding heat release.

Laser-induced ignition is treated in the following chapter II.6.

## II.6 Laser-induced ignition

For the ignition of especially fuel lean gas mixtures, alternatives to conventional electric spark ignition systems have been devised: high-energy spark plugs, plasma jet ignitors, rail plug ignitors, torch jet ignitors, pulsed-jet ignitors, exhausted gas recirculation ignition systems, laser-induced ignition and flame jet ignitors. Among these, laser-induced spark ignition has been widely investigated as an alternative to conventional electric spark ignition.

Generally, there are four basic mechanisms by which laser radiation is able to ignite a combustible mixture:

- thermal initiation (thermal ignition)
- photochemical ignition
- resonant breakdown
- non-resonant breakdown

### Ignition mechanisms

#### 1) Thermal initiation

In laser-induced thermal ignition there is no electrical breakdown of the gas. The laser radiation is used to heat up and increase the temperature of the gas. Molecular bonds are cleaved and chemical reactions can take place.

#### 2) Photochemical ignition

In resonant photochemical ignition laser photons generally in the UV are absorbed by the target molecules and cause them to dissociate into reactive radicals (photolysis). If the radical production rate surpasses the recombination rate chain branching reactions lead to ignition and finally to combustion. The energy necessary for a photochemical ignition is in the order of  $<1\text{mJ}$  [60]. This process does not lead to direct heating or photo ionization and so it does not involve breakdown. In fact, the technique can be used to ignite a combustible mixture if a sufficient amount of reactive radicals (in the order of  $10^{17}$  atoms/cm<sup>3</sup>) within a sufficient large volume is produced. The crucial factor for a successful ignition process is the radical concentration produced by absorption, and the volume in which the radicals are contained.

There are several disadvantages of photochemical ignition. The main drawback is the necessity of a tunable laser to provide the wavelength that matches the absorption wavelength of the molecule to enable dissociation. Second, since the photon energy in the visible and near-IR range is smaller than the dissociation energy of most gases, this ignition mode is most effective using UV-laser sources which are very expensive.

#### 3) Resonant breakdown

In resonant breakdown, a target molecule is dissociated by a non-resonant multi photon dissociation process. The atoms produced are then ionized by a resonant multi photon ionization process. This is depicted in the following (Fig. II.6-1). Electrons that are generated in this second step (i.e. by resonant multi photon absorption) absorb photons at any wavelength (continuum absorber). This leads to the formation of a plasma.

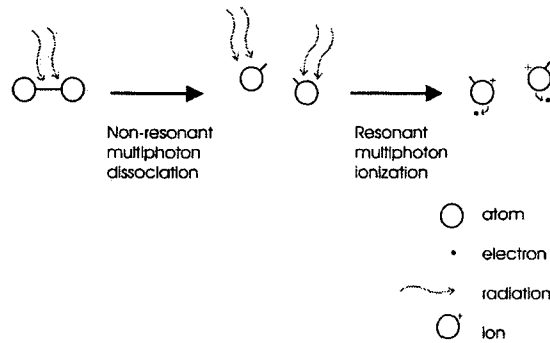


Fig. II.6-1: Principle of the resonant breakdown process. First, gas molecules are dissociated by a non-resonant multi photon process into atoms. These atoms are then ionized by a resonant multi photon process to yield free electrons. These electrons are continuum absorbers and lead to the formation of a spark.

#### 4) Non-resonant breakdown

This type is most similar to conventional spark ignition. Non-resonant breakdown is the most frequent ignition mode and is generally termed laser-induced spark ignition. In laser spark ignition a focused laser beam of irradiance in the order of  $10^{10}$  W/cm<sup>2</sup> (or laser photon flux in the order of  $10^{29}$  photons/(cm<sup>2</sup>s)) is sufficient to generate a plasma spark either by multi photon ionization or electron cascade process.

In the multi photon ionization process a gas molecule or atom simultaneously absorbs a number of photons. If the photon energy absorbed is higher than the ionization potential of the molecule, the gas molecule is ionized. This process is important only at very short wavelengths (<1 $\mu$ m) or at very low pressure (<13 mbar), where collision effects are negligible. It becomes insignificant at visible and NIR-wavelengths because the photon energy at these wavelengths is much smaller than the ionization potentials of most gases.

The electron cascade process requires the existence of initial electrons also called seed electrons. The electrons then absorb photons via the inverse bremsstrahlung process increasing their kinetic energy. If the electrons gain sufficient energy, they ionize other gas molecules on impact, leading to an electron avalanche and breakdown of the gas. At high pressure (>132 mbar) and long wavelengths (>1  $\mu$ m) this process usually dominates the generation of the plasma spark. The initial electrons necessary for the initiation of the electron cascade process can be generated by the multiphoton ionization process, if the laser irradiance is high enough. The presence of impurities, such as low-ionization-potential organic vapors or aerosol particles, can significantly facilitate the formation of the initial (seed) electrons.

The generated plasma spark of high temperature (in the order of  $10^6$  K) and pressure (in the order of  $10^3$  atm) leads to the formation of a rapidly expanding shock wave [60] (see Fig. II.6-2 (calculation) for a laser-induced spark in a CH<sub>4</sub>/air mixture at 1 atm:

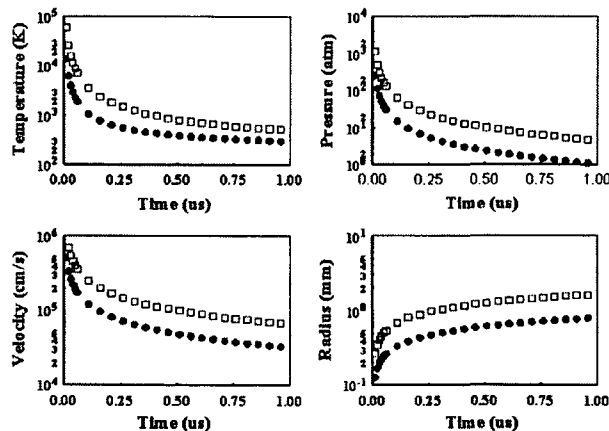


Fig. II.6-2: Properties of an expanding laser-induced spark for a stoichiometric mixture of methane and air at 1 atm. Input energies are 0.4 mJ (solid circle) and 10 mJ (open squares, taken from [60]).

[61] investigated the initial flame kernel development for methane/air mixtures numerically. It has been reported that an asymmetric deposition of laser energy takes place in direction of the laser, such that the laser-produced flame kernels have two distinct segments: a torus-like flame kernel that propagates radially and a front lobe that expands towards the laser source (see Fig. II.6-19).

Focusing a laser beam causes breakdown of the gas and produces plasma with high temperature and pressure. The high pressure region induces a nearly spherical shock wave propagating away from the plasma kernel. A rarefaction wave characterized by a pressure smaller than the ambient pressure is generated. This leads to a complex flow pattern, and further vortical motions are developed. These vortical motions deform the flame kernel leading to a torus-like shape kernel and to the formation of the front lobe as illustrated in Fig. II.6-3. The front lobe was found to be separated from the torus for lean mixtures, while the front lobe and torus were connected for the stoichiometric mixture.

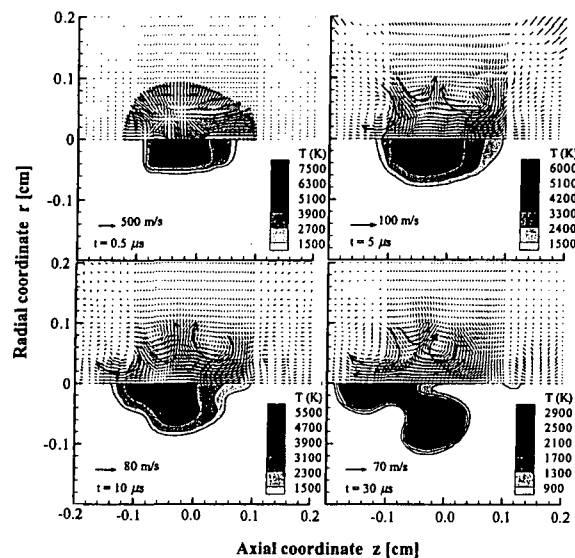


Fig. II.6-3: Formation of the torus and the front lobe obtained from model calculations (Taken from [52]).

Flame kernel development including torus and front lobe formation was also investigated by [62]. This is shown in Fig. II.6-4.

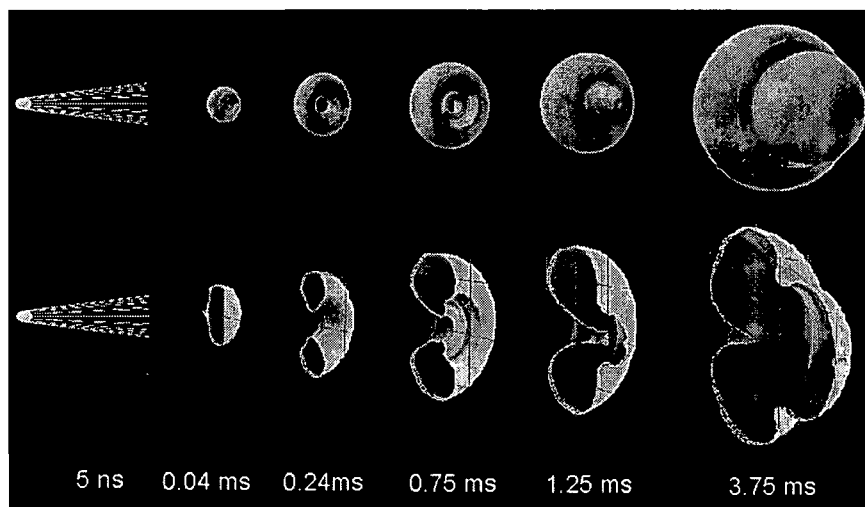


Fig. II.6-4: Flame kernel development of the torus and front lobe after laser energy deposition received from LIF-measurements of OH radicals (Taken from [62]).

In [62], laser-induced fluorescence (LIF) and subsequent rendering were deployed. [60] and [63] present research work on the pressure dependence of the breakdown threshold laser energy and the breakdown threshold laser intensity respectively for the generation of the spark plasma. [60] investigated the threshold laser energy in air and methane using a Nd:YAG laser (1064 nm wavelength, 5.5 ns pulse duration) as illustrated in Fig. II.6-5 (left graph).

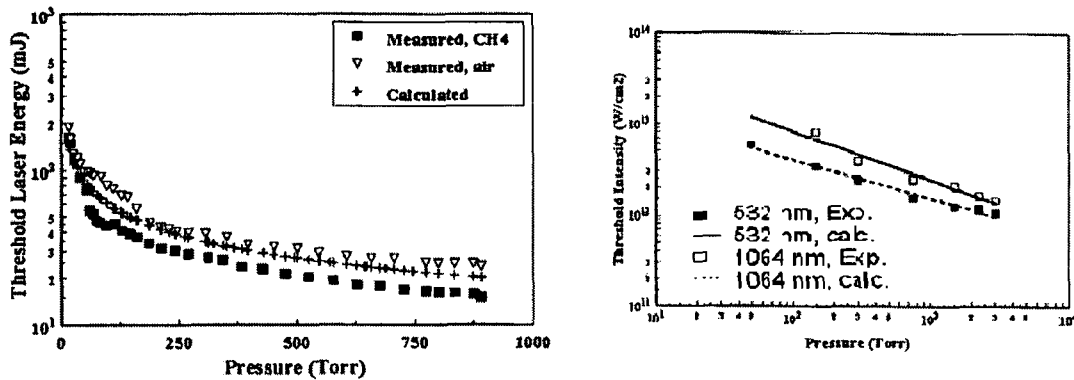


Fig. II.6-5: Comparison of measured and calculated breakdown threshold laser energy as a function of pressure for air and methane [60] (left side). Breakdown threshold intensity in CH<sub>4</sub> [63] (right side).

The present data on breakdown threshold laser energies at various pressures are incompatible with the multiphoton ionization process which predicts a very weak pressure dependence but in good agreement with the cascade theory according to

$$E_{thr} \propto p^{-n}$$

(Eq. II.6-1)

$E_{thr}$ ... breakdown threshold laser energy [mJ]  
 $p$ ... pressure [Pa]

$n$  is 4 for gases with ionization potential of 12 eV (CH<sub>4</sub>).

[64] demonstrated that a laser intensity in the range of 10<sup>12</sup> to 10<sup>14</sup> W/cm<sup>2</sup> was sufficient to create a breakdown spark plasma in several gases (197 mbar to about 3947 mbar). In air, oxygen and nitrogen the spark plasmas are very bright, while those produced in methane and hydrogen have a pinkish color. Fig. II.6-5 (right graph) shows that the breakdown threshold laser intensity decreases rapidly as the pressure increases. The dependence of the threshold intensity on the pressure  $p$  can be expressed as

$$I_{thr} \propto p^{-n}$$

(Eq. II.6-2)

$I_{thr}$ ... breakdown threshold laser intensity [Wcm<sup>-2</sup>]

$n \sim 0.4$  for methane at 1064 nm.

The degree by which the threshold depends on the pressure was found to be stronger at shorter wavelengths. The laser used for these experiments was a Q-switched Nd:YAG laser operating at 532 nm and 1064 nm and with a pulse duration of 5.5 ns. The breakdown threshold laser energies and laser intensities at 197 mbar and 4000 mbar are tabulated in table II.6-1.

By comparing CH<sub>4</sub> to the other gases it was found that the threshold in CH<sub>4</sub> is consistently lower. This was expected since methane has got a lower ionization potential (12.51 eV) than nitrogen (15.58 eV) or hydrogen (15.425 eV).

Breakdown threshold laser energy,  $E_{thr}$  (mJ), and laser intensity,  $I_{thr}$  (W/cm<sup>2</sup>), in gases (75 mm focal length)

Gas	Pressure	$E_{thr}$ (mJ)		$I_{thr}$ (W/cm <sup>2</sup> )	
		532 nm	1064 nm	532 nm	1064 nm
Air	156	20.14	32.31	$1.08 \times 10^{13}$	$4.35 \times 10^{12}$
	3040	3.06	10.53	$1.65 \times 10^{12}$	$1.40 \times 10^{12}$
CH <sub>4</sub>	150	14.97	25.09	$8.05 \times 10^{12}$	$3.37 \times 10^{12}$
	3040	2.67	7.83	$1.44 \times 10^{12}$	$1.05 \times 10^{12}$
H <sub>2</sub>	150	42.00	60.00	$2.26 \times 10^{13}$	$8.07 \times 10^{12}$
	3040	3.76	8.29	$2.03 \times 10^{12}$	$1.12 \times 10^{12}$
N <sub>2</sub>	150	26.37	38.13	$1.42 \times 10^{13}$	$5.13 \times 10^{12}$
	3040	3.34	10.74	$1.80 \times 10^{12}$	$1.45 \times 10^{12}$
O <sub>2</sub>	150	18.88	51.60	$1.02 \times 10^{13}$	$6.94 \times 10^{12}$
	3040	3.45	10.50	$1.85 \times 10^{12}$	$1.41 \times 10^{12}$

Table II.6-1: Breakdown laser energy and breakdown laser intensity for the formation of a plasma spark in gases (Taken from [64]).

### Minimum ignition energy (MIE)

The minimum ignition energy (MIE) is one of the most interesting questions related to laser-induced ignition. It has been demonstrated by [55] that excessive pulse energy does not contribute to ignition enhancement. There was no significant difference in the ignition delay time or pressure rise of the combustion process using different high laser energies. The extra pulse energy can only be added in the form of plasma heat, but there is no advantage in using higher laser energy. Therefore, a practical laser ignition system deploying excessive energy would be more costly due to a stronger laser that in the end, serves no purpose. For the determination of MIE not only the laser output power has to be considered. Losses at the windows of the optical setup, reflections and scattering of the transmitted laser beam have to be taken into account. Pyroelectric energy meters can be used to determine the energy of the transmitted beam.

The minimum ignition energies obtained by laser-induced spark ignition are consistently larger than the corresponding data from electrical sparks (remember the difference between MPE and MIE at the end of the preceding chapter). Electrodes experience losses from heat transfer to the metal. As for laser-induced ignition, only a portion of the laser energy is absorbed by the gas in the vicinity of the focal point. In [65] it is reported that the losses in laser ignition due to the shock wave formation and scattering are bigger than the losses at the electrodes of spark plugs, thus increasing MIE.

For hydrocarbons ranging from methane to heptane, MIE at 1 atm is in the order of  $\sim 0.6$  mJ when igniting a combustible mixture by a photon source. Fig. II.6-6 illustrates the experimental results of laser energy observed for propane/air mixtures at various fuel equivalence ratios  $\Phi$  and pressures. Compared to the data obtained for electrical sparks [66], there is a factor of two discrepancy in MIE. The theoretical MIE was calculated to be even lower. An explanation might be found in the short time duration of the laser pulse and the small focal spot size. The thermal energy tends to rapidly dissipate due to high thermal gradients in comparison to electrode sparks.

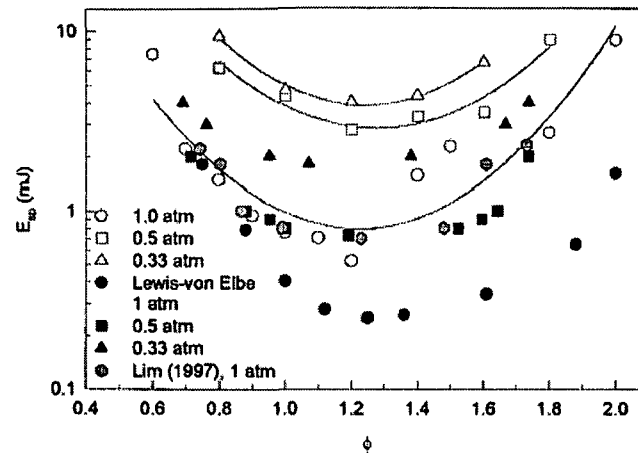


Fig. II.6-6: Ignition energies for propane/air mixtures at various equivalence ratios and pressures (Taken from [67]).

Mechanistically, there are also several fundamental differences between laser and electrical spark ignition leading to different minimum ignition energies. Electrical sparks are generated when the electrical field strength (applied voltage potential  $U$  divided by the distance  $r$  between the electrodes) surpasses a certain threshold level. Electrons are accelerated from the cathode to the anode gaining a high kinetic energy ( $E=e*U$ ,  $e$  = elementary charge). The collisions of these energetic electrons with the gas molecules generate the high-temperature and high-pressure plasma. The energy deposition takes place in the order of 100  $\mu$ s.

In contrast, laser sparks are initiated by the presence of free electrons (seed electrons) created by multi photon ionization. These electrons become energetic through the absorption of photon energy (this phenomenon is called inverse bremsstrahlung process). Upon collision of these energetic electrons with other gas molecules, an electron avalanche process starts generating a spark plasma.

Fig. II.6-6 shows that this difference of MIE between laser and electrode ignition also exists at lower pressures of 0.5 and 0.33 atm. At lower pressures higher energy is required for a successful ignition of fuel/air mixtures due to the decrease in collisional frequency and number density of the molecules. Similar results were obtained by [68] also for methane/air mixtures (see Fig. II.6-7).

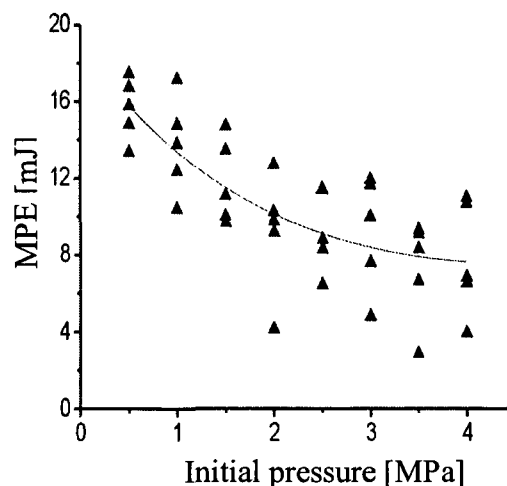


Fig. II.6-7: Minimum laser pulse energy (MPE) in  $\text{CH}_4/\text{air}$  mixtures as a function of initial pressure at  $70^\circ\text{C}$  and a fuel equivalence ratio  $\Phi$  of 0.77. A Nd-YAG laser emitting at 1064 nm and a pulse duration of 8 ns was deployed (Taken from [68]).

In Fig. II.6-6 it can also be observed that the minimum in the ignition energy of propane/air mixtures occurs at the equivalence ratio of 1.25 and not at  $\Phi=1$  as expected. For hydrocarbon fuels the equivalence ratio at which the ignition energy is lowest moves further towards the fuel rich side with increasing carbon number. For methane, MIE has been found to be situated in the fuel lean regime at  $\Phi=0.9$ . The corresponding values for the higher hydrocarbons are 1.15 (ethane), 1.25 (propane), 1.5 (butane), 1.75 (hexane) and 1.8 (heptane). In Fig. II.6-8 these MIE-values are illustrated for electrical spark ignitions and atmospheric pressure.

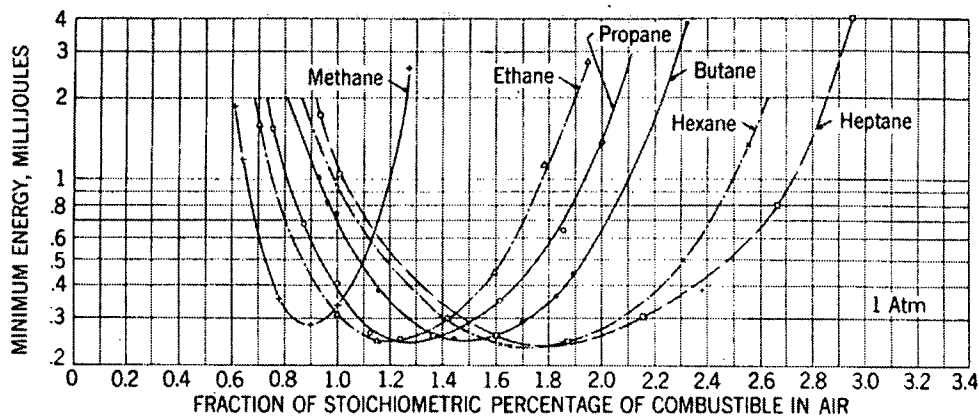


Fig. II.6-8: Ignition energies for hydrocarbon/air mixtures as a function of  $\Phi$  at 1 atm (Taken from [66]).

These results have been attributed to the rapid depletion of the fuel at the ignition point and relatively slow diffusion of new fuel molecules towards this region. Heavier molecules tend to have smaller diffusion coefficients.

Laser ignition is capable of igniting extremely fuel lean mixtures. This has been demonstrated by [68]. Mixture compositions down to  $\Phi=0.56$  (5.56 vol% methane in air) could be ignited in these experiments (Fig. II.6-9).

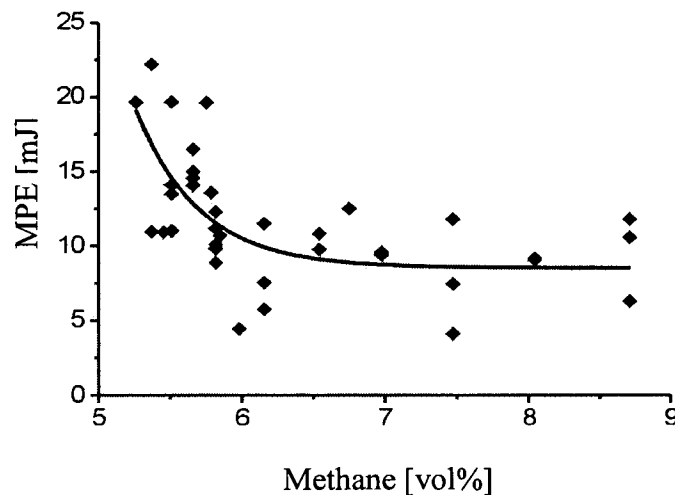


Fig. II.6-9: Minimum laser pulse energy for methane/air mixtures vs. percentage of methane by volume at 70°C and an initial pressure of 3 MPa. The wavelength of the Nd-YAG laser was 1064 nm, the pulse duration 8 ns. At a methane concentration below a value of 6% a steep increase of minimum laser pulse energy (MPE) was observed (Taken from [68]).

The size of the excited volume also influences MIE. Electric spark plugs exhibit an optimum distance  $d_g$  of the electrodes with regard to MIE. Fig. II.6-10 illustrates MIE as a function of spark gap for propane/air mixtures. The lowest points of the curves represent the minimum ignition energy. The corresponding electrode gap  $d_g$  is also called quenching distance.



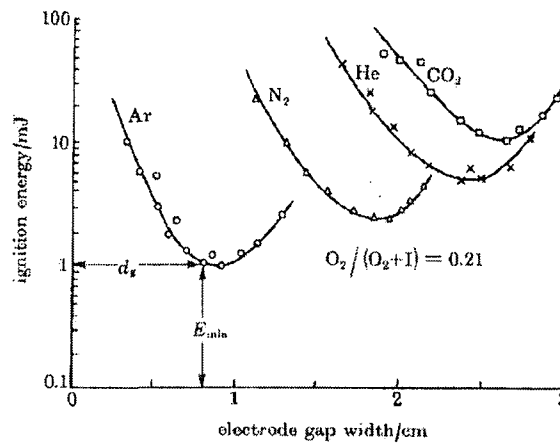


Fig. II.6-10: MIE as a function of electrode gap width [cm] (Taken from [69]).

For  $d > d_g$  an increase in MIE occurs. This can be explained by the fact that a larger volume of the mixture than actually required is heated. For  $d < d_g$  MIE also increases due to the energy is being deposited in a small volume, the peak temperatures and temperature gradients are higher, thus there will be greater radiative loss from the gas and greater conductive heat loss to the electrodes. This results in a larger portion of the deposited energy being dissipated in ways that are not useful for ignition. Also, the higher temperatures imply the formation of stronger shock waves from the ignition source, which additionally carry away energy that would otherwise be available for ignition. [70] also investigated electric spark ignition. The effect of the ignition parameters (spark gap and spark duration) on MIE is performed for stoichiometric methane/air mixtures at 298 K and 1 atm. Fig. II.6-11 shows MIE as a function of ignition time for different ignition radii. All curves look similar except for  $r_{ig} = 63.5 \mu\text{m}$  where a shallow minimum is seen.

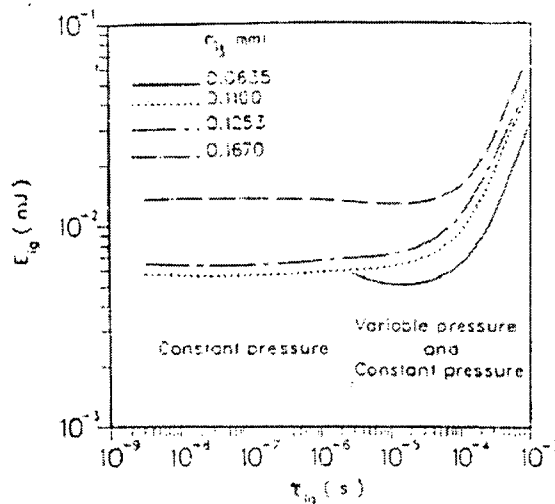


Fig. II.6-11: Variation of MIE with ignition time for different kernel radii in the range between 63.5 and 167  $\mu\text{m}$  (Taken from [70]).

Longer ignition times lead to an increase in MIE due to heat losses by diffusion. The dependence of MIE on the kernel radius (source radius) for several ignition times is depicted in Fig. II.6-12. By decreasing the kernel radius MIE was found to reach a constant value for  $\tau = 2.75 \mu\text{s}$  and  $27.5 \mu\text{s}$ , and to approach the same value for  $\tau = 100 \mu\text{s}$ . An increase of the

kernel radius resulted in a steep rise in MIE, because more energy is needed to heat up a bigger ignition volume.

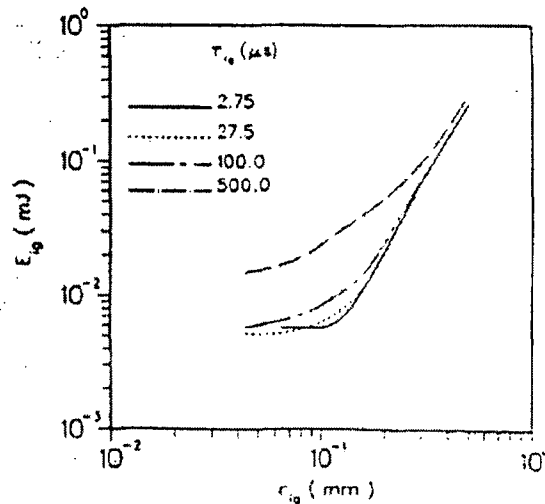


Fig. II.6-12: Variation of MIE with kernel radius for different ignition times (Taken from [70]).

Comparing the ignition parameter of spark plugs with laser sources several parallels can be found. If an oversized volume is heated, more energy has to be provided than necessary. A very small volume (corresponding to a short electrode gap) where diffusion and radiative losses carry away most of the laser energy quickly will need more heating, too. In laser ignition, the focal spot size is in the order of 200 to 500  $\mu\text{m}$ . For the duration of the energy deposition, again there is an optimum with respect to MIE. If energy is deposited during a long time interval, the flame front already starts propagating away from the ignition spot, the excess energy only increases MIE. If the time is too short, a higher temperature will have to be reached, leading to higher radiative heat losses and a stronger shock wave formation due to the higher pressure rise. This issue is particularly worthwhile discussing with laser-induced ignition, where the energy deposition takes place in a very short time. It has to be noted that any laser pulse has got time scales much shorter than the kinetic time scale and the chemical induction time. (Q-switched) nanosecond pulses yield a lower MIE than (mode-locked) picosecond laser pulses. With ps pulses, shock waves that propagate much faster than deflagration waves withdraw energy and increase MIE.

The ignition source is another important factor governing MIE. Glow discharge devices are less effective than arc discharge appliances. Electric spark plugs that cause an air breakdown are even more effective. This order is due to heat losses and the distribution of energy in the plasma channel. AC (alternative current) and DC (direct current) operation also cause different plasma shapes, thus influencing MIE. Laser sources can ignite flames by either creating radicals directly or by providing thermal energy that is subsequently used by the gas to form radicals. In fact, each ignition source contributes both heat and direct radicals. Quite surprisingly, computational studies reveal that MIE is only slightly lower when the radicals are produced directly, since the overabundant active radicals quickly recombine liberating thermal energy. Because of these recombination reactions, the net difference in MIE between thermal and chemical sources is small.

Turbulence also affects the value of MIE. MIE always coincides with the maximum burning velocity. Turbulence promotes the burning velocity and this tends to reduce MIE. However, it also increases the rate of heat loss from the spark kernel to the surrounding fresh mixture, thereby increasing MIE. The net effect of increasing turbulence and flow velocity is increasing MIE. However, turbulence is needed in fast running engines because otherwise combustion would be too slow, especially with lean mixtures.

By comparing the figures in Fig. II.6-13 the effect of flow velocity on MIE can be seen. The influence of flow velocity on various stagnant methane/air and propane/air mixtures was investigated in these experiments. In some test runs the nitrogen in the air was replaced by various inert gases such as  $\text{CO}_2$ , He or Ar. The conditions for these two figures are identical except for flow velocity which is zero in the first case and 15.3 m/s in the other. One can see, as expected, that an increase in flow velocity leads to an increase of MIE due to heat dissipation to the surroundings.

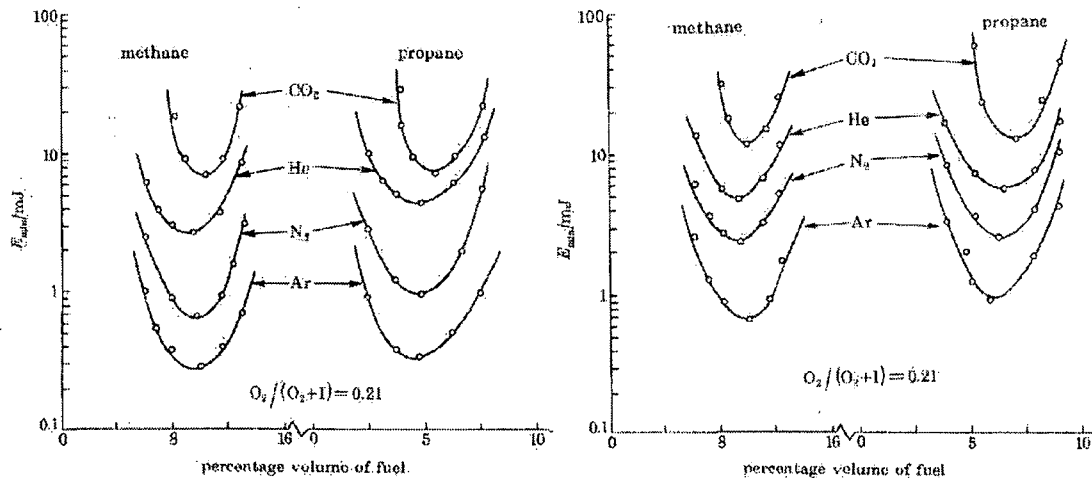


Fig. II.6-13: Influence of mixture composition and inert gas substitution on MIE for stagnant (left) and flowing (15.3 m/s, right) mixtures (Taken from [70]).

Due to variations in the physical and chemical properties of the constituents, namely thermal conductivity, density, specific heat, laminar flame speed, flame temperature and activation energy, a significant variation of MIE was achieved. The variation of the ignition location does not have a great influence on MIE, but as the ignition spot approaches a surface, quenching effects due to heat losses occur leading to an increase in MIE.

### Multi-point ignition

Lasers have got several advantages including the capability of providing multi-point ignition that can be used to ignite the combustible mixture either sequentially or simultaneously. This could be potentially important for fuel-lean combustion applications. [64] compared single-point versus multi-point laser ignition using three different ignition configurations: multi-point ignition, single-wall ignition and single-center ignition. With center-ignition, the flame had a nearly spherical shape and the combustion time was about 36% shorter than with wall-ignition. In the two-point ignition case the time required for complete combustion was 50% shorter than required for the wall-ignition and about 25% shorter for the center-ignition case. The combustion time was defined as the time duration between firing the laser and the time when the maximum chamber pressure was reached. With multi-point ignition the distance over which the flame must propagate to complete the combustion process is shortened, therefore the combustion time is reduced. Because the combustion times are short, the flame can not lose so much heat, resulting in higher temperature and higher pressure rises, respectively. The total laser energy was the same in the single-point and in the multi-point ignition experiments. For single-point ignition the laser energy was about 18 mJ. For two-point ignition, each laser beam had an energy of 9.25 mJ. The effect of two-point ignition was most evident in the fuel-lean and fuel-rich regimes and less in the near-stoichiometric region. [71] studied two-point ignition using a different approach. It is known that one of the main drawbacks of laser-induced ignition is the fact that only a portion of the laser energy is

deposited in the ignition spot. The rest of the energy is transmitted and scattered at the vessel wall. A new technique called laser-induced cavity ignition has been proposed which uses almost the entire energy for the ignition process. A single-shot laser is utilized in a multi-point ignition setup in which laser-induced spark ignition is followed by laser-induced cavity ignition.

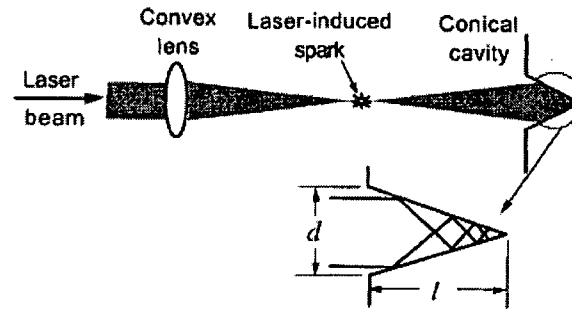


Fig. II.6-14: Principle of a two-point ignition system (Taken from [71]).

A conical cavity is frequently adopted as a beam dump. The incident energy is absorbed at the surface of the cavity. The rest is reflected and directed towards the apex, while the multiple reflections almost trap all of the incident energy. If the conical surface has a high reflectivity, the focusing effect will be more pronounced. Aluminum is a highly reflective material and was therefore used. The two-point ignition system, laser-induced spark ignition and laser-induced cavity ignition is illustrated in Fig. II.6-14.

The advantage of two-point ignition is depicted in Fig. II.6-15 in terms of flame initiation period and total combustion time. The flame initiation period is defined as the time interval between laser shot and 5% mass burned, the total combustion time as the time to 90% mass burned. In comparison to single-spark or single-cavity ignition, it was found that the reduction in the flame initiation time by the two-point spark/cavity ignition was about 45-69%. The total combustion time for the two-point ignition case was also reduced by about 28-45% depending on the initial pressure. It was also reported that the center of the combustion vessel is the optimum location for obtaining minimum flame initiation time and combustion time, respectively.

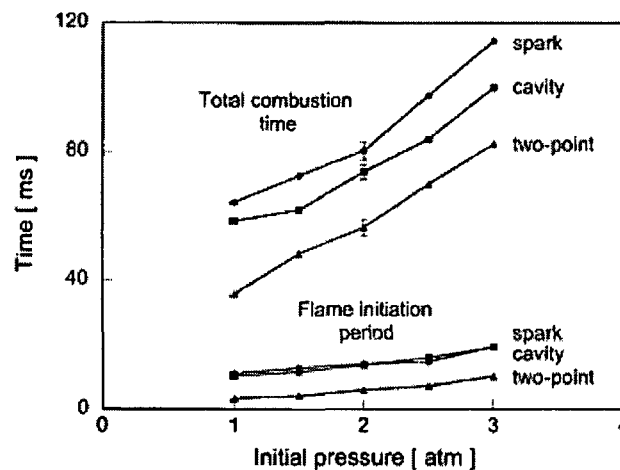


Fig. II.6-15: Flame initiation period and total combustion time as a function of initial pressure for an equivalence ratio  $\Phi$  of 0.7 (Taken from [71]).

### Potential benefits of a laser ignition system

Interest in laser ignition has increased in recent years because of its many potential benefits over conventional ignition systems. In general, laser ignition is capable of providing multiple ignition sites that can be controlled to ignite a gaseous combustible mixture either sequentially or simultaneously. Multi-point applications are suggested to enhance combustion efficiency and prevent possible misfire and could be useful especially for fuel-lean mixtures. One of the main advantages is the choice of the optimum ignition location which is not easy in conventional ignition systems. Further, precise ignition timing as well as the ignition energy and the deposition rate can be controlled easily. Laser-ignition is non-intrusive, so that heterogeneous effects and wall heat loss can be eliminated. It was found that leaner mixtures could be ignited using laser sources which are not ignitable with electric sparks.

Another aspect in this respect is radiation-assisted combustion. Apart from replacing conventional ignition systems such as spark plugs, laser radiation may also be used to promote combustion processes. This can either be achieved by photochemical preconditioning of the gas mixture or directly by irradiating the flame with appropriate light. Radiation assisted combustion reduces soot formation and allows the use of lower grade fuels. It might also be useful for non automotive use. Radiation to promote combustion can be:

- electric fields and microwaves
- VIS and IR (lasers)
- UV
- Nuclear radiation

Although vastly investigated, the concept of the usage of electric fields has not been successful so far. Nuclear radiation involves substantial safety questions and is thus not suitable for most applications. The irradiation with VIS and IR light provides stimulation by thermal means and requires a lot of power. Microwaves are difficult to couple to the flame. UV can stimulate and even initiate combustion by generating highly reactive oxygen atoms. One proposed extension of this concept, called "preconditioning", is to irradiate the fuel-air mixture with UV light prior to combustion. The problems associated with this technique are that UV in the range from 160 – 200 nm is needed (there are not many sources), and that the windows have to be made of special materials (ZnSe, LiF, sapphire). It can also be questioned whether the highly reactive radicals have a sufficiently long lifetime. One of the drawbacks, however, are the comparatively high costs involved in setting up a reliable system.

A critical element in a laser ignition system is the optical window where the laser beam is coupled in. Fouling due to carbonaceous or mineral deposits (e.g.  $\text{CaSO}_4$  from motor oil residues) on the one hand and destruction due to material fatigue on the other hand are the chief difficulties in this respect. In [55], laser ignition was tested in an Otto cycle single cylinder engine. The engine ran 1.25 h before it was necessary to remove combustion product build-up from the interior of the optical window. The window was made of ZnSe. Sapphire windows were utilized by [68]. It is supposed that ablation has a self cleaning effect on the interior of the window.

Another disadvantage of laser-induced ignition is that only a portion of laser energy is used for ignition process while the rest of the laser energy is lost since the unabsorbed laser beam passes through the ignition location so that it cannot be utilized in the ignition process.

Spark plugs which serve as ignition sources in internal combustion engines are associated with several problems:

- accumulation of carbonaceous deposits on the surface of the insulating parts → malfunction and inefficient operation due to this fouling
- wear of the electrodes by erosion and oxidation → higher losses
- the best position for ignition shortens its durability → compromise necessary
- periodic maintenance of the engine to replace the spark plugs → costly
- preignition due to retained heat of the electrode or static electricity on it
- ineffective for ignition of extremely lean fuel-air mixtures, thus fuel rich operation is necessary → more consumption and pollutants (unburned hydrocarbons)
- resistance (transformer!) and discharge losses
- generation of radio frequency that has to be shielded
- spark plugs are prone to the ingress of moisture
- thermal quenching effect by the metal (electrodes)

One of the main drawbacks of spark plugs is the periodic maintenance of the engine (especially for big, stationary devices). It leads to short service life times. In comparison to spark plugs, laser systems are contactless therefore quenching effects due to heat losses can be avoided. As mentioned before multi-point ignition can be performed and ignition locations moved easily. Furthermore ignition timing and energy deposition can be controlled and programmed exactly. An important fact is the ability to ignite leaner mixtures with a laser source than with a spark plug. Another benefit of laser-induced ignition is to modify the combustion chamber to obtain lower turbulence [72]. All practical combustion engines employ turbulence to accelerate mixing and/or burning. However, this turbulence also increases heat losses to walls and pressure drops. If the need for acceleration of combustion by turbulence could be reduced by using multi-point laser ignition, it is possible to reduce heat loss and pressure drops.

### Time scale of laser ignition

In the following Fig. II.6-16 a time scale of the major processes involved in laser-induced ignition in the pressurized combustion bomb is presented which covers several orders of magnitude in time. The ignition process starts with a 5 ns pulse of a focused Q-switched Nd:YAG laser operating at 1064 nm with an irradiance in the order of  $10^{10}$  W/cm<sup>2</sup>. A number of photons are simultaneously absorbed by a gas molecule or atom leading to ionization if the energy of the photons exceeds the ionization potential. This so called multi photon ionization generates seed electrons necessary for the following electron cascade process. The electrons absorb photons via the inverse bremsstrahlung process increasing their kinetic energy. Due to the absorption electrons gain sufficient energy to ionize other gas molecules on impact, leading to an electron avalanche and finally to the spark plasma with high temperature (in the order of  $10^6$  K) and pressure (in the order of  $10^3$  atm). The plasma shape is more blunt in the front region facing the laser source than in the rear region due to a higher absorption rate of the electrons. The high pressure region of the plasma develops to a spherical shock wave propagating away from the plasma kernel. Pressure gradients lead to complex flow patterns and finally vortical motions are developed. These vortical motions are the reason for the development of two distinct flame kernel segments: a torus-like shape propagating radially and a front lobe propagating back toward the laser source. The front lobe formation can be attributed to the asymmetric deposition of laser energy in the direction of the laser. The time for flame kernel development lasts in the order of ms. The following ignition delay can be in the order of hundreds of ms depending on the composition of the combustible mixture. During

induction time and already during the flame kernel development radical chain reactions may take place which lead to combustion if the radical production rate surpasses the recombination rate. The combustion process of a fuel-rich mixture lasts about 1 second, whereas a fuel-lean mixture needs several seconds for a complete combustion. The pressure rise also depends on the mixture composition and lasts in the order of ms and seconds.

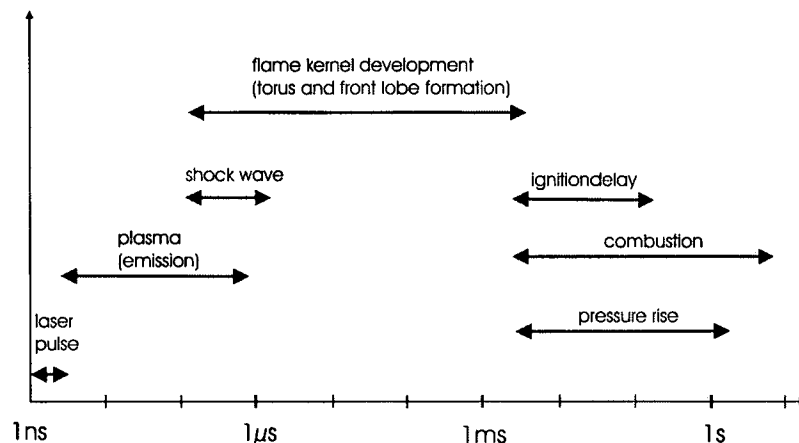


Fig. II.6-16: Time scale of different processes involved in laser-induced ignition.

### Laser ignition versus conventional spark plug ignition

Comparing laser-induced ignition with an ignition process that utilizes a spark plug fundamental differences can be found. Electric sparks develop when the electrical field (potential  $U$  between the two electrodes divided by their distance) surpasses a certain threshold value. For typical electrode sparks, the streaming of the electrons is produced by a potential in the order of kV. Electrons are accelerated from the cathode to the anode and gain a high kinetic energy ( $E=e*U$ ;  $e$ =elementary charge). These electrons collide with mixture molecules in the surrounding leading to the plasma generation. Fig. II.6-17 illustrates a completely different flame kernel development during spark plug ignition process in comparison to the ignition process using a laser source.

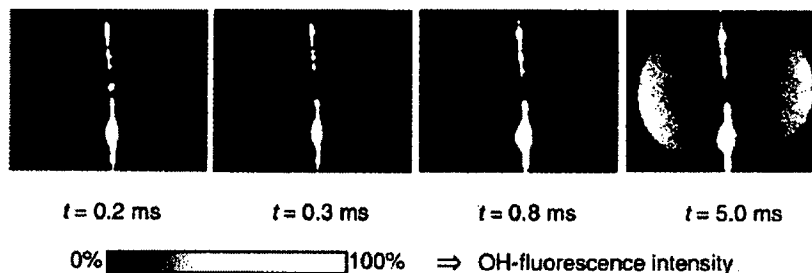


Fig. II.6-17: Development of the flame kernel during spark plug ignition in a 11% methanol/air mixture with an ignition energy of 1.6 mJ and an energy deposition time of 35  $\mu$ s (2D-LIF of OH radicals, taken from [46]).

Typical duration of the electrical energy deposition is in the order of 100  $\mu$ s to ms and the spark plasma diameter is in the order of the electrode diameter having a life time up to ms. For laser spark generation initial electrons (seed electrons) are needed. They have to be produced by some kind of absorption process, possibly by multi-photon ionization, when the laser power density is above the threshold level of  $\sim 10^{10}$  W/cm<sup>2</sup>. After the generation of seed electrons, they absorb laser light and simultaneously their kinetic energy increases. Gaining sufficient energy, they ionize other gas molecules upon impact, leading to an electron cascade and final breakdown of the gas (spark plasma). In contrast to electrical energy deposition the laser releases its energy in a few nanoseconds onto a small focal spot size of  $\sim 0.5$  mm. This different energy deposition step is also responsible for the higher minimum ignition energy

(MIE) of the laser source because the small focal spot size tends to rapidly dissipate the thermal energy due to high thermal gradients induced by the laser spark in comparison to electrode sparks. It is seen that due to these differences in the initial conditions in the respective sparks, different ignition behavior results. Further differences are found concerning pressure dependence of the ignition energy. The minimum laser pulse energy (MPE) decreases with increasing pressure. Ignition energy of a spark plug depends on the applied voltage, pressure and temperature as well as the electrode gap. The break through voltage is obtained according to the law of Paschen or Lau [73]:

$$U = 2.03 \cdot 10^6 \cdot p \cdot d + 59.3 \cdot 10^3 \cdot \sqrt{(p \cdot d)}$$

(Eq. II.6-3)

U... break through voltage [V]

p... pressure [Pa]

d... electrode gap [mm]

In Fig. II.6-18, one can see a spark plug designed for operation in an automotive engine (left) and in an industrial engine that operates at higher pressures (right).

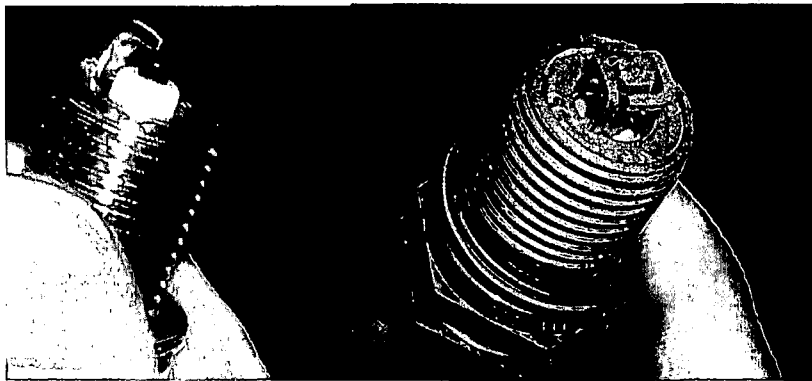


Fig. II.6-18: Image of a spark plug for use in automotive (left) and gas (b) engines.

Fig. II.6-19 depicts a spark in room air generated by a Q-switched Nd:YAG laser (10 ns, 1064 nm, 50 mJ, focal length of the lens 150 mm).

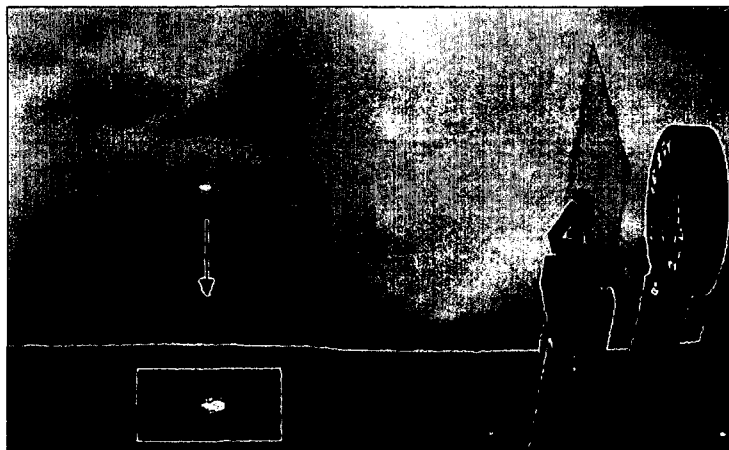


Fig. II.6-19: Image of a laser spark produced in air. The laser pulse comes through the lens on the right. The lower picture is a magnification.

The insert shows a magnification. One can see the asymmetric, drop like shape. The front lobe of the plasma kernel propagates towards the laser source.



## II.7 High pressure combustion and internal combustion engines

Most combustion appliances work at or near atmospheric pressure; However, several applications demand compactness. High-load combustors operating at elevated pressure to benefit from smaller unit size, increased efficiency (see Fig. II.7-1) and increased power output are common e.g. in transport. Internal combustion engines, rocket motors and an increasing number of power plant burners are operated at increased pressure [74] in order to obtain high energy densities. The maximum pressure in recent gas turbine combustors is as high as 4 MPa [75]. Fig. II.7-1 shows that combustion efficiency increases with pressure.

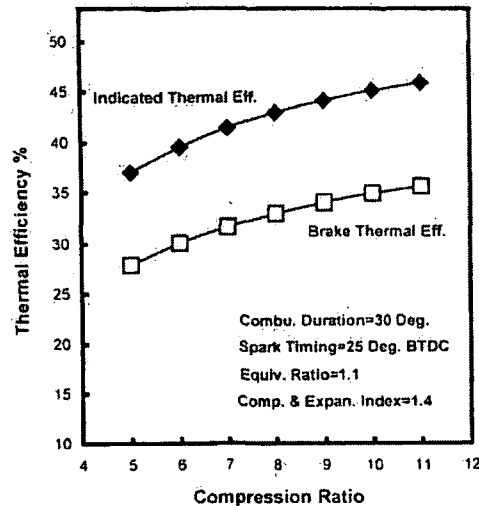


Fig. II.7-1: Increased pressure not only reduces the unit size of a combustor, but also its efficiency (Taken from [76] for a four stroke engine, calculated curves). The indicated thermal efficiency ( $\blacklozenge$ ) is the amount of heat energy converted into work within the cylinder head. The brake thermal efficiency or overall thermal efficiency ( $\square$ ) is the amount of heat energy turned into useful work.

Depicted are calculated curves for a four stroke engine (taken from [76]). The indicated thermal efficiency ( $\blacklozenge$ ) is the proportion of the total heat of combustion which appears as work done by the explosion and expansion of the piston. Brake thermal efficiency or overall thermal efficiency ( $\square$ ) is the proportion of the total heat of combustion which appears as work provided by the engine and is hence smaller than the indicated thermal efficiency.

A vast array of studies concentrating on different aspects of combustion has been carried out at or near ambient pressure. The use of low pressure kinetics to describe high pressure phenomena is questionable both in terms of rate constants and kinetic path ways that can be quite different at higher pressures [77]. The extrapolation of results obtained at slightly above ambient conditions to high pressure regimes should be verified by experiments carried out at pressures relevant to e.g. internal combustion engines. This procedure is necessary in order to provide computer models with representative data or to check the reliability of computer models. In Fig. II.7-1, OH-PLIF (planar laser-induced fluorescence) images of a turbulent premixed methane/air flame are shown [75]. (a) shows a flame at 0.1 MPa, (b) at 1.0 MPa.

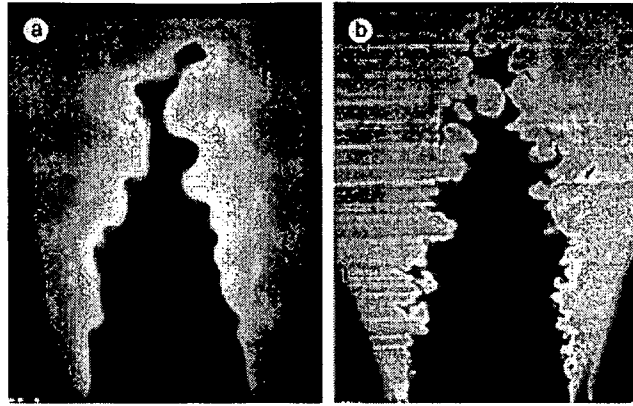


Fig. II.7-1: OH-PLIF images of turbulent premixed flames for  $\text{CH}_4/\text{air}$  mixture: (a): pressure 0.1 MPa, velocity 2.3 m/s; (b): pressure 1.0 MPa, velocity 3.4 m/s (Taken from [75]). One can see marked differences in the shape of the flame.

One can see that in the high pressure flame in Fig. II.7-1 (b), the flame front is much more wrinkled. This picture is to plainly show one phenomenological difference between high and ambient pressure combustion.

The purpose of a combustion engine is to convert the chemical energy contained in the fuel into mechanical or electrical energy. In contrast to external combustion engines like steam engines, internal combustion engines burn the fuel inside the engine. They are more efficient than external combustion engines, however, they are more restrictive as far as the fuel is concerned. Internal combustion engines can be grouped in spark ignition (SI) engines (Otto engines) and compression ignition (CI) engines (Diesel engines; a glow plug might be contained for cold starting). Another classification can be made according to the basic engine design: reciprocating (e.g. radial, V, W) or rotary engines (e.g. Wankel). Based on the work cycle, one can distinguish between four stroke cycle and two stroke cycle. The main advantages of these engine types are high power/weight ratio, efficiency, reliability and robustness with applications in transport (land, sea and air) and power generation (stationary and mobile).

In Fig. II.7-2, the core of an internal combustion engine is depicted in a very basic way.

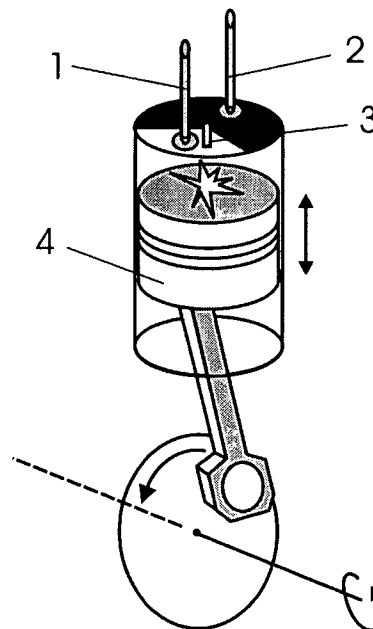


Fig. II.7-2: Simplified scheme of an internal combustion engine (one cylinder); 1: inlet valve; 2: outlet valve; 3: spark plug; 4: piston;

In a reciprocating engine, the piston-driven by the expansion of the hot pressurized combustion products- travels up and down in a cylinder and transmits the power through a connecting rod to the shaft. The four strokes are (a) intake, (b) compression, (c) expansion and (d) exhaust. For each power stroke, two crankshaft revolutions are required. In order to obtain a higher power output for a given engine, the two stroke engine was developed. The two strokes are (a) compression stroke and (b) power or expansion stroke. Both four stroke and two stroke engines can be operated as SI and CI engines. In two stroke engines, the intake air is precompressed in order to displace the exhaust gas. The advantage of the two stroke engine, higher power to weight ratio, is offset by the loss of a fraction of the unburnt fuel which is swept out during the intake of fresh air and hence reduces the efficiency. The two stroke engine is therefore restricted to some applications where low cost and weight are more important than fuel economy (e.g. small boat engines, lawnmowers).

There are inherent advantages in the SI and CI concept. Numerous attempts have been taken in order to combine the best features of each. The goal has been to operate the engine at the best compression ratio (12 -15). The compression ratio is defined as the ratio of maximum volume/minimum volume in the cylinder. Typical values are 8-12 for SI engines and 12 – 24 to CI engines.

Direct injection of fuel in SI engines (fuel stratified injection, FSI) is a recent development. In stratified charge engines [78]-[80], the fuel is not charged homogeneously. One strives to place an easily ignitable mixture at the location of the spark plug at the time of ignition.

The prechamber concept [81] is similar from the basic idea: safe initiation of the combustion process, fuel lean conditions in the main part of the cylinder.

Gas engines [82], as the name implies, run on gaseous fuel (e.g. natural gas or producer gas). Generally, gas engines are stationary industrial engines for (remote) power generation. Compared to automotive derivative engines, these engines are designed for longer life time operation and longer maintenance intervals. They also tend to run at lower speeds and at constant load conditions.

There are also approaches to dual fuel engines running on gaseous and liquid fuels [83].

A gas turbine [84] utilizes a different approach than reciprocating engines. It normally consists of a compressor, a combustion area and a turbine (compressor and turbine are connected by a shaft). Another vital piece is the flameholder (cañ). This is a hollow, perforated cylinder. As its name implies, it is used to prevent the flame from being blown out. The expansion of the hot combustion gases is used to propel a turbine to produce work. The useful work developed by the turbine can either be used directly as mechanical energy or may be converted into electricity by adding a generator. Aircraft jet engines are essentially gas turbines, the work here is produced as thrust. Most aero turbines are turboprop engines. They have got a large fan at the front of the engine (an ordinary gas turbine) to create more thrust through bypass air. A turboprop engine is similar to a turboprop engine, only that there is a conventional propeller for the creation of the bypass air.

There are two types of land based gas turbines: heavy frame engines (compression ratio < 15) and the more compact aero derivative engines (compression ratio > 30).

The exhaust heat from land based gas turbines may be recovered to generate steam for additional energy production in a steam turbine (= cogeneration plant) or to provide process or district heating (= cogeneration plant).

The main advantage of reciprocating internal combustion engines over electric energy accumulators is the ease of refuelling. Over gas turbines, it is predominantly acquisition costs. Gas turbines prefer constant load and tend to use more fuel upon idling. Therefore, they are well suited for transcontinental aircraft but not for stop and go car traffic.

Gas turbines, on the other hand, have got a better power/weight ratio and are smaller. Micro turbines [85] might rise in importance in the near future.

### Homogeneously Charged Compression Ignition (HCCI)

A novel engine concept is homogeneously charged compression ignition or homogeneous charge compression ignition (HCCI) [86] - [88]. It is a hybrid concept between SI and CI engines. The fuel is thoroughly premixed with air (as in SI engines), but is ignited through compression (as in CI engines). The mixture is very fuel lean (compared to SI engines). Therefore, combustion peak temperatures are low, and so are  $\text{NO}_x$  emissions. The potential of HCCI is to provide diesel like efficiencies at very low emission levels of  $\text{NO}_x$  and particulates. A major goal in future engine development is depicted qualitatively in the following Fig. II.7-3.

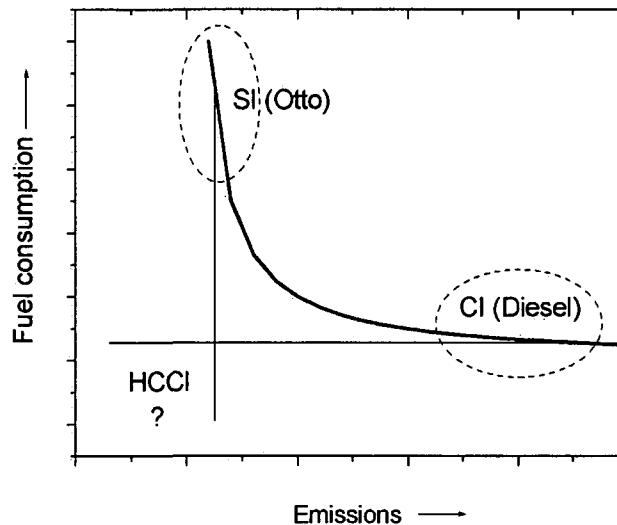


Fig. II.7-3: HCCI is capable of combining the advantages of SI and CI engines, that is low emissions at high efficiencies.

The major problems of HCCI engines comprise hydrocarbon and CO emissions, smooth response (rapid cycle operation, compare knocking in SI engines!) and reliable cold starting. Also, the timing of the ignition is a critical issue, as it is not externally controlled.

In SI engines, the mixture flow (fuel/air) to the engine is controlled by a throttle plate to change the engine load (torque). The mixture ratio between air and fuel is kept constant at  $\lambda = 1$  at all loads.

In CI engines, pure air is compressed and the fuel is injected under high pressure at the end of the compression stroke. The fuel is vaporized and mixes partially before self-ignition takes place. The load is adjusted by varying the amount of injected fuel.

In HCCI, varying the amount of fuel controls the load. The HCCI engine is always unthrottled, a high compression ratio is used and the combustion is fast. This gives a high efficiency at low loads compared to an SI engine that has low efficiency at partial load.

HCCI combustion is not yet well understood.

The following Figures II.7-4 and II.7-5 (taken from [89]) illustrate HCCI test runs with n-heptane (cetane number 56, diesel surrogate) and isooctane (octane number 100, gasoline surrogate). The temperature has been plotted as a function of crank angle (CA) [ $^\circ$ ] for different compression ratios (CR).

The compression ratio (CR) is defined as the volume above the piston at bottom dead center (BDC) position divided by the volume above the piston at top dead center (TDC) position.

Generally speaking, both the pressure and the temperature trace are a good measure of the ignition start. Temperature plots contain more information on the ignition chemistry, whereas pressure plots illustrate efficiency advantages.

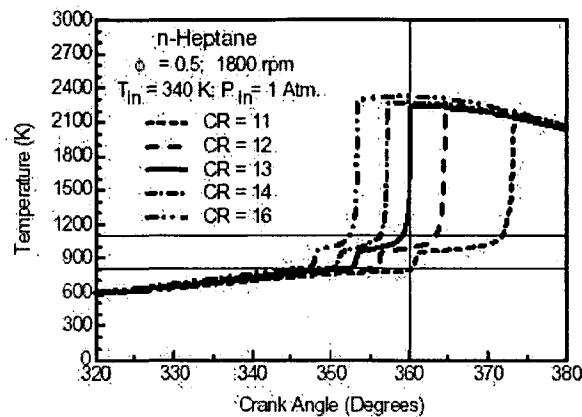


Fig. II.7-4: HCCI test runs with n-heptane for varying compression ratios (CR). Note the two step ignition characteristic (Taken from [89]).

In Fig. II.7-4, one can see a two step ignition procedure. The first step occurs within 1 ms at 800K which is a relatively low temperature, the second step starts at 1100K (main “ignition”). The two steps are marked by horizontal lines. There is a “cool” combustion chemistry that initiates the “hot” combustion chemistry. As the compression ratio is raised, the ignition takes place earlier. This effect prevents the use of high compression ratios and results in a loss in efficiency.

In Fig. II.7-5, similar tests were conducted with iso-octane.

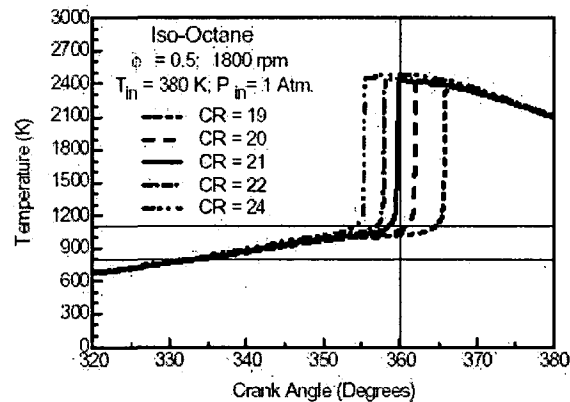


Fig. II.7-5: HCCI test runs with iso-octane for varying compression ratios (CR, taken from [89]).

With gasoline fuel, the “cool” chemistry is minimal, and there is no two step reaction as in Fig. II.7-4 for the diesel surrogate fuel. The induction time is approximately 8 ms (compare 1 ms for n-heptane). At 1800 rpm (= 30 revolutions/second), 1 degree crank angle corresponds to 93  $\mu$ s. With iso-octane, high compression ratios and resulting high (diesel like) efficiencies are possible.

The HCCI engine might bridge the time gap until the fuel cell becomes economically mature. A means of stimulating self ignition (e.g. by laser radiation or a magnetic field) might help overcome the timing problem in future HCCI engines (see also chapter IV.6, last part, for preliminary results on laser aided HCCI).

### Pollutant formation in internal combustion engines

Urban air pollution is vastly caused by automotive SI and CI engines, both direct emissions and secondary pollutants (e. g. smog).

Table II.7-1 lists major constituents of exhaust gas from SI engines and typical concentrations.

Pollutant	Concentration range
NO <sub>x</sub>	500 -1000 ppm
CO	1-2 %
HC	3000 ppm (C <sub>1</sub> ) + evaporating HC from standing engine

Table II.7-1: NO<sub>x</sub>, CO and HC are the most important pollutants from SI engines (taken from [90]).

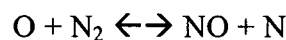
In the following table II.7-2, pollutants from CI engines are listed.

Pollutant	Concentration range
NO <sub>x</sub>	~ 500 -1000 ppm
CO	<<
HC	~600 ppm (C <sub>1</sub> ), may also condense to white smoke
particulates	0.2 – 0.5 % of fuel mass

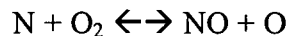
Table II.7-2: Pollutants from CI engines (taken from [90]).

Since CI engines always operate on the fuel lean side, CO emissions are by far not as high as those from SI engines. HC emissions and NO<sub>x</sub> emissions exhibit comparable levels. Particulates are another important issue in CI engines.

Nitric oxide and nitrogen dioxide are combined generically to NO<sub>x</sub>. It is NO that is predominantly formed inside the combustion cylinder. Since common fuels only contain negligible amounts of N, the principal source for NO emissions is N<sub>2</sub> which is oxidized in the Zeldovich mechanism (Eq. II.7-1 and II.7-2):



(Eq. II.7-1)



(Eq. II.7-2)

NO is formed both in the flame front and behind. Post flame NO dominates since the high pressures make the flame front rather thin (~100 μm).

According to chemical equilibrium considerations, the ratio of NO<sub>2</sub>/NO ought to be negligible. This holds true for SI engines, but not for their CI counterparts.

In diesel engines, 10 – 30 % of all NO<sub>x</sub> can be NO<sub>2</sub>.

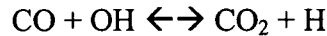
CO emissions are significant in SI engines and can be more or less neglected in CI engines.

Since the emissions of CO downstream the exhaust pipe are lower than the concentrations measured *in-situ* inside the combustion chamber, but yet above equilibrium values, kinetic control can be assumed. The main formation step is an integral part of hydrocarbon combustion chemistry and can be written as (compare Fig. II.4-5)



(Eq. II.7-3)

The main CO oxidation reaction under engine conditions is the following



(Eq. II.7-4)

Hydrocarbon emissions can be judged by the absolute amount of C emitted, however, breaking down different classes seems useful since some HC constituents are physiologically practically inert, while others cause smog or induce cancer.

Oxygenated constituents in the fuel such as alcohols substantially increase the emissions of aldehydes both in SI and CI engines. Depending on the sulphur content of the fuel, emissions of  $\text{SO}_2$  and  $\text{SO}_3$  will arise. Diesel tends to contain more S than gasoline.

Generally speaking, the emitted pollutant concentrations are higher than chemical equilibrium calculations would predict.

In the following Fig. II.7-6, pollutant formation path ways in an SI engine are depicted qualitatively.

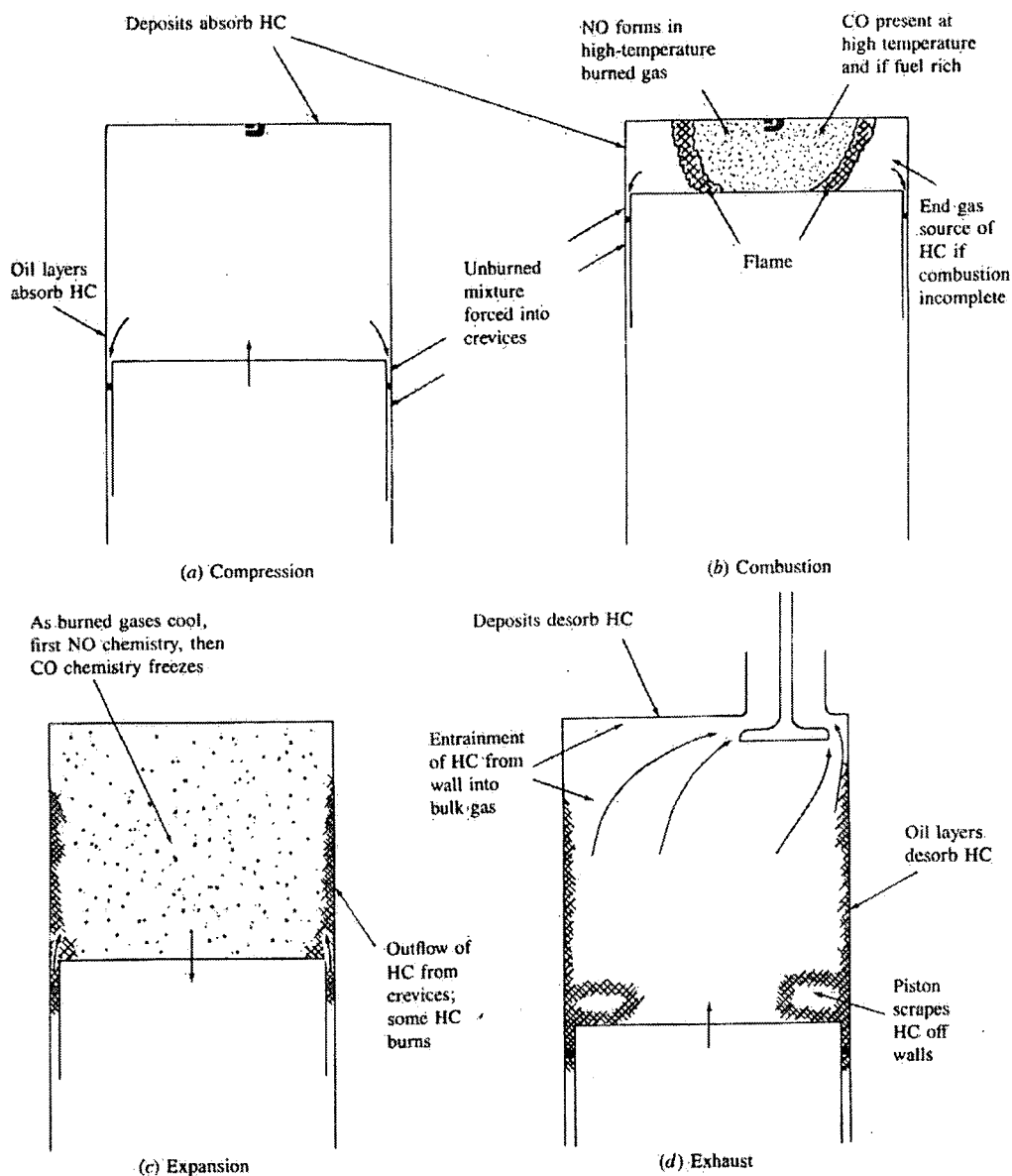


Fig. II.7-6: Pollutant formation path ways of HC, CO and  $\text{NO}_x$  in SI engines (taken from [90]).

(a) to (d) denote the four phases in the engine cycle: compression, combustion, expansion and exhaust. Nitric oxide (NO) forms in the high temperature post flame zone during the combustion stroke. In the expansion stroke, it is "frozen", leaving behind concentrations far

above chemical equilibrium. Likewise, CO is formed in the combustion stroke and “frozen” in the expansion stroke. CO is favoured under fuel rich conditions, however, at high temperatures dissociation will also yield significant amounts. As shown in Fig. II.7-6, the sources of HC are numerous. The most important contribution stems from unburnt mixture that was contained in small crevices too narrow for the flame to propagate. Another source are the combustion chamber walls where flame quenching occurs. Deposits facilitate the adsorption and later desorption of fuel molecules. A third source for HC emissions is located in the lubricating oil where the fuel partly dissolves. Incomplete combustion also increases HC emissions.

The air/fuel ratio is probably the most important parameter in engine emission optimization.  $\text{NO}_x$  formation is most expressed at stoichiometric mixture compositions (high peak temperatures leading to thermal  $\text{NO}_x$ ). Hydrocarbon (HC) and CO emissions increase towards the fuel rich side (HC also towards the fuel lean side due to incomplete combustion). In Fig. II.7-7, the conversion efficiency of a three way catalyst is shown.

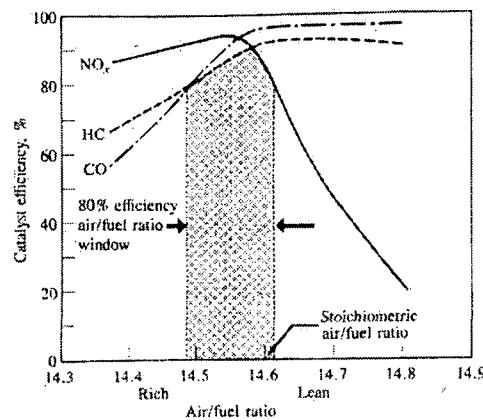


Fig. II.7-7: Main pollutants in SI engines are HC, CO and  $\text{NO}_x$ . The efficiency of a common three way catalyst (taken from [90]) is best around  $\lambda = 1$ .

One can see that for (close to) stoichiometric conditions, the emissions display a minimum (“lambda window”). Therefore, SI engines operate at  $\lambda = 1$  or at slightly fuel rich conditions (for safe and smooth engine run). Exhaust gas recirculation (EGR) [91], [92] is a popular concept of lowering  $\text{NO}_x$  emissions by diluting the fresh reactants, however, combustion quality generally deteriorates.

Diesel or CI engines operate differently, therefore, the emission governing conditions are different. The fuel is injected into the CI engine shortly before the onset of ignition, therefore the conditions in the combustion chamber are highly non uniform. The pollutant formation pathways are mainly determined by the fuel distribution. This is illustrated qualitatively in the following Fig. II.7-8.



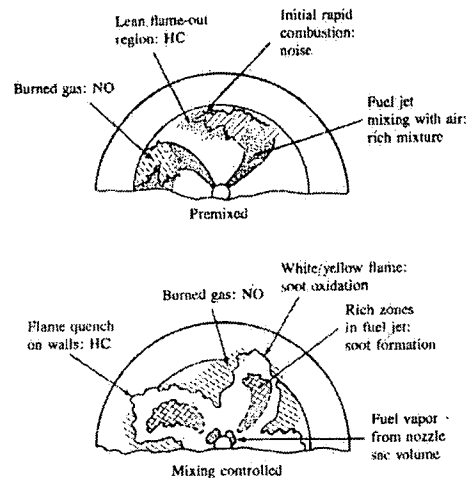


Fig. II.7-8: Pollutant formation path ways of HC, CO and  $\text{NO}_x$  in CI engines (taken from [90]).

In [90], premixed and mixing controlled phases are distinguished.

Soot forms in the fuel rich regions.

Hydrocarbon emission in diesel engines has to be considered separately from HC emissions from SI engines.

First, diesel contains hydrocarbons that are less volatile. Second, substantial pyrolysis of the fuel occurs. Therefore, the unburnt and partially oxidized, condensed hydrocarbons in diesel exhaust are much more complex than in SI engine exhaust. Small particulates, partly even respirable ( $< \sim 10\mu\text{m}$ ), that convey adsorbed carbonaceous species are one of the main problems associated with diesel engines. Particulates associated with SI engines have lost importance with the removal of leaded gasoline from petrol stations.

Tailpipe emissions can also be lowered by after treatment of the exhaust gases. Catalytic converters (reducing catalysts for  $\text{NO}_x$ , oxidizing ones for CO and HC, three way catalysts for  $\text{NO}_x$ , CO and HC) [93] (see also Fig. II.7-7), thermal reactors (HC and CO degradation, high temperatures required) [90] and particulate filters [94].

More information on pollutant formation in internal combustion engines can be found in [95].

## II.8 High pressure combustion control

With combustion catering for approximately 90% of the worldwide primary energy production, a lot of effort has been undertaken to reduce the amount of concurrent pollution. Active control of the combustion process is an efficient means of obtaining clean and efficient fuel conversion. Combustion control systems often demand timely data (e.g. temperature, pressure, concentration of key species) measured directly in the supervised process where harsh conditions like high temperatures prevail.

Combustion control has encountered an increased interest, the main objectives being optimization of the process in terms of pollutant emission and efficiency on the one hand and monitoring of the process to alleviate dangerous instabilities on the other hand.

One has to discern between open loop and closed loop control. The former does not deliver any feedback and is therefore not suitable for process optimization. The latter can already be found in automotive engines [96] where the lambda probe allows a fine tuning of operating conditions.

It is convenient to divide combustion control systems into two categories: operating point control (OPC) and active combustion control (ACC). In ACC, one can still distinguish between active combustion enhancement (ACE) and active instability control (AIC) [97]. Sensors can be divided into solid state sensors and optical sensors. A review of combustion control and sensors is given in [97].

The time scale in ACC spans 20 Hz to a few kHz whereas it ranges from 1 to 100 Hz in OPC. Fuzzy logic has also been tested for combustion control [98]–[101].

### Sensing techniques in combustion control

In Fig. II.8-1, sensing techniques and locations in a general combustion appliance are illustrated.

Upstream of the flame, i. e. at the inlet, one might be interested in the flow properties, the mixing quality, the air/fuel ratio, the composition of the fuel or the flow velocity. In [102], the moisture content of coal is measured by microwave absorption as a means for thermal power station combustion control. Sensors in the combustion chamber itself often observe the flame [103]. Classical devices such as thermocouples and pressure sensors are also used. Harsh conditions like high temperatures and high pressures quickly lead to sensor deterioration and aging. Automobile sensors are required to work for > 150,000 km, and sensors mounted in gas turbines are expected to work for about 25,000 hours [101]. Most sensors are located past the flame to analyse the flue gas, e.g. solid state sensors or exhaust gas analysers, depending on the application.

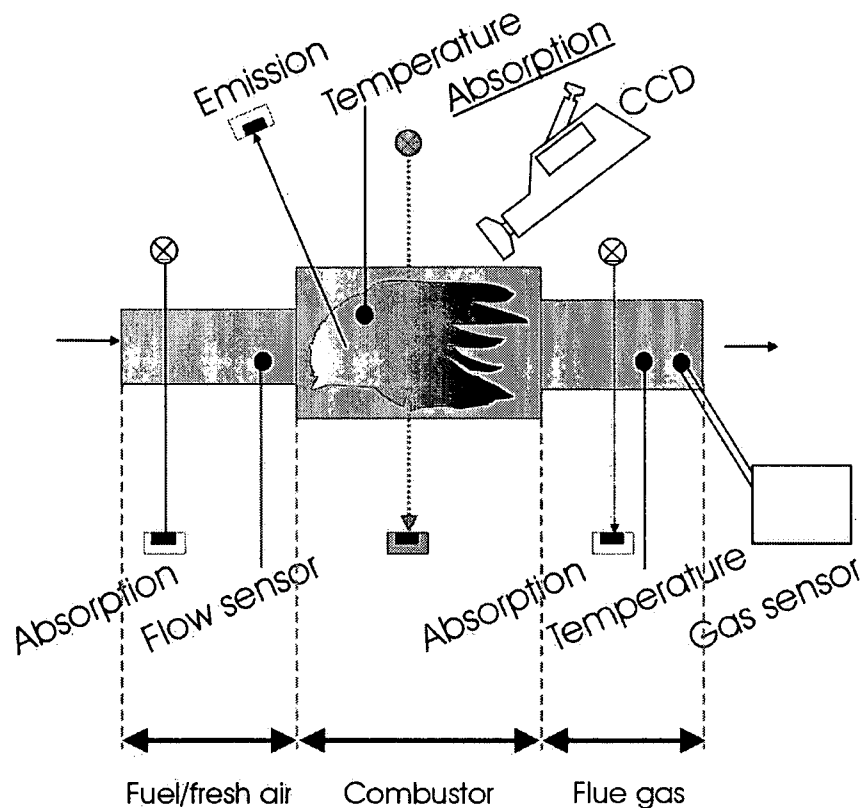


Fig. II.8-1: Scheme of a combustion process and illustration of sensing techniques. The fuel flow is from the left to the right. CCD stands for charged coupled device and denotes the part in a digital (video) camera that converts light into proportional current pixel by pixel (adapted from [97]).

Optical sensors can monitor emission, fluorescence, absorption or scattered light.

Optical techniques offer good spatial and temporal resolution and do not influence the system under investigation since they operate in non-contact mode. However, at least one (emission) or two (absorption) apertures for optical access are required which is not always a trivial task to achieve. Also, blockage of the windows by deposition of soot might pose a problem. Line of sight techniques might also not be representative in the case of highly non-homogeneous flows. Conventional analysis, on the other hand, generally relies on extractive sampling techniques, which suffer from slow response times due to long sampling lines and inherent delays from the analyser. Also, high maintenance is required because of probe degradation and failure due to plugging and corrosion. Frequent recalibration is yet another disadvantage. Absorption spectroscopy delivers quantitative results. It has been used to obtain species mole fractions, temperatures and pressures *in-situ*. Note, however, that for practical combustion control, a trend in the change of a variable might be sufficient in the place of accurate, absolute data.

Diode laser based combustion control concepts have been reported in the literature [104] – [107]. The main benefits are timeliness, low maintenance (no blocking of sampling heads), high sampling rate and representativeness of the results.

### Combustion control at high pressures

Most combustion appliances work at or near atmospheric pressure; However, several applications demand compactness. High-load combustors operating at elevated pressure to benefit from smaller unit size, increased efficiency and increased power output are common e.g. in transport. Internal combustion engines, rocket motors and an increasing number of power plant burners are operated at increased pressure [74] in order to obtain high energy densities. The maximum pressure in recent gas turbine combustors is as high as 4 MPa [75].

With increasing pressure, it becomes a demanding task to deliver fast and accurate data from a combustion process.

In Fig. II.8-1, a calculated absorption spectrum of H<sub>2</sub>O vapor (1 m path length, 296K, partial pressure 1 bar) is shown. The solid trace is for 1 bar total pressure, the dashed line for 10 bar total pressure. The tuning range of a conventional edge emitting laser (\*) and a VCSEL (\*\*) is shown.

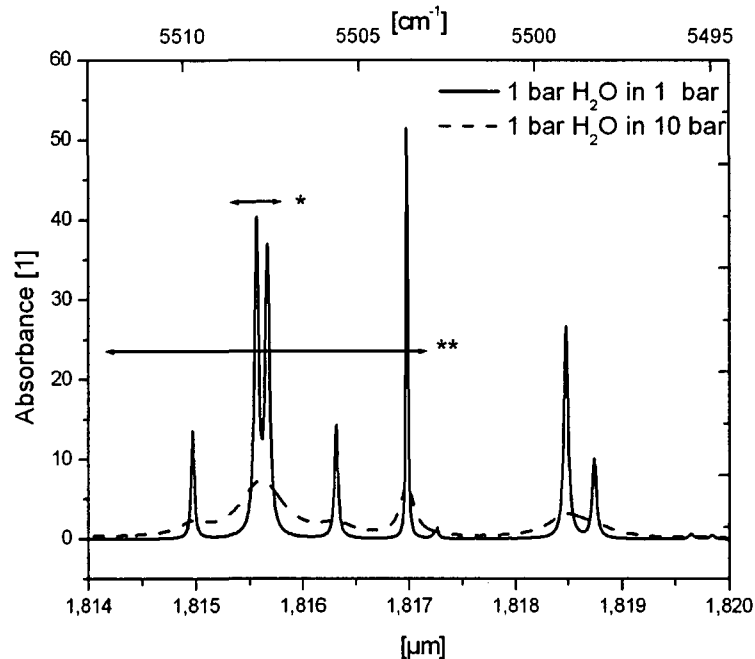


Fig. II.8-2: Tuning range of an edge emitting diode laser (\*) and a VCSEL (\*\*) compared graphically to two pressure broadened absorption spectra of gaseous H<sub>2</sub>O.

One can see that in order to determine the absorbance in the wings of the chosen absorption feature for proper background subtraction, that is in order to scan over the entire peak, the tuning range of an edge emitter is not sufficient at higher pressures.

VCSELs allow the determination of the absorbance at higher pressures. Depending on molecule and temperature, the upper limit of operation is different. This is illustrated graphically in the succeeding Fig. II.8-3.

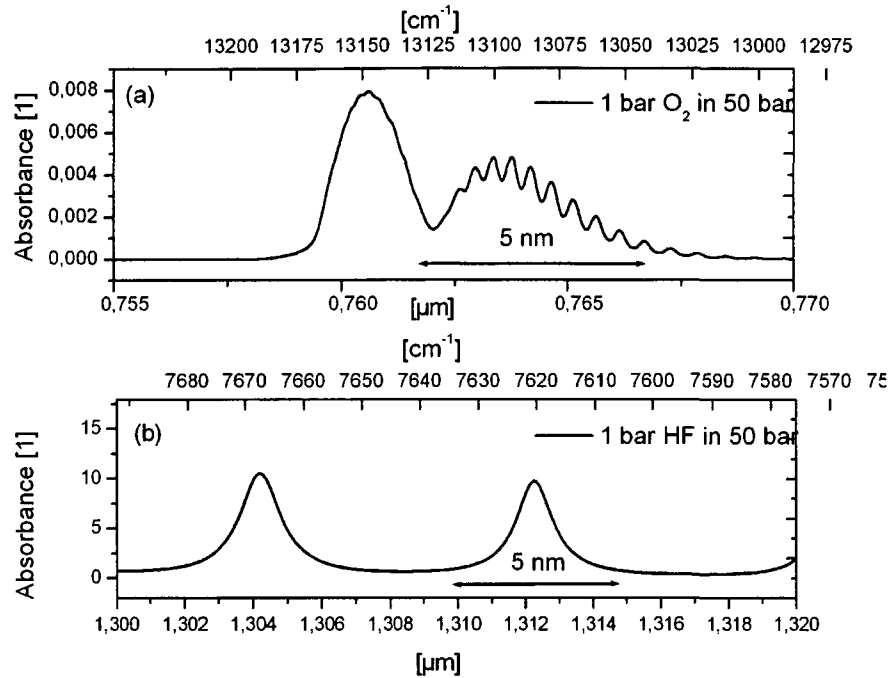


Fig. II.8-3: Pressure broadening leads to spectral interference that limits the range of operation of VCSELs at high pressures. In (a), a spectrum of O<sub>2</sub> is shown, in (b), one of HF. Since the HF lines are less close together, interference is not so strong. The assumed temperature is 296K.

Fig. II.8-3. (a) shows a calculated absorption spectrum of O<sub>2</sub>, Fig. II.8-3 (b) one of HF. The typical tuning range of a VCSEL has been marked. In contrast to the absorption peaks of HF around 1310 nm, the absorption peaks of O<sub>2</sub> in the A band around 761 nm are spaced rather closely. Therefore, the O<sub>2</sub> lines start interfering earlier.

(Since several O<sub>2</sub> absorption lines can be determined simultaneously, temperature and also temperature distribution measurements in gases can be measured using a 761 nm VCSEL [42]).

Although the VCSEL is able to tune over an individual peak, mixing of neighboring peaks leads to spectral congestion. The baseline (that is zero absorption) between the peaks is not reached any more so that there is a limit to the range of operation for VCSELs towards high pressures, depending of selected transition and temperature (see also chapter IV.5).

This work was accepted for oral conference presentation:

M. Lackner, G. Toschnig, F. Winter, M.-C. Amann, R. Chau, M. Ortsiefer, J. Roskopf, Pollutant reduction by *in-situ* combustion diagnostics at high pressures using a novel near infrared diode laser, the vertical-cavity surface-emitting laser (VCSEL), CleanAir 2003 (7<sup>th</sup> International Conference on Energy for a Clean Environment), Lisbon, Portugal, 7-10 July (2003).

### III. Laser systems

In this chapter, the laser measurement systems used in this thesis are described. The laser systems were designed and constructed "from scratch". Diode lasers were obtained from various national and international cooperation partners and integrated into custom measurement systems. These systems have evolved constantly, getting better and decreasing in size.

Fig. III-1 shows a generic scheme for a laser measurement system as used.

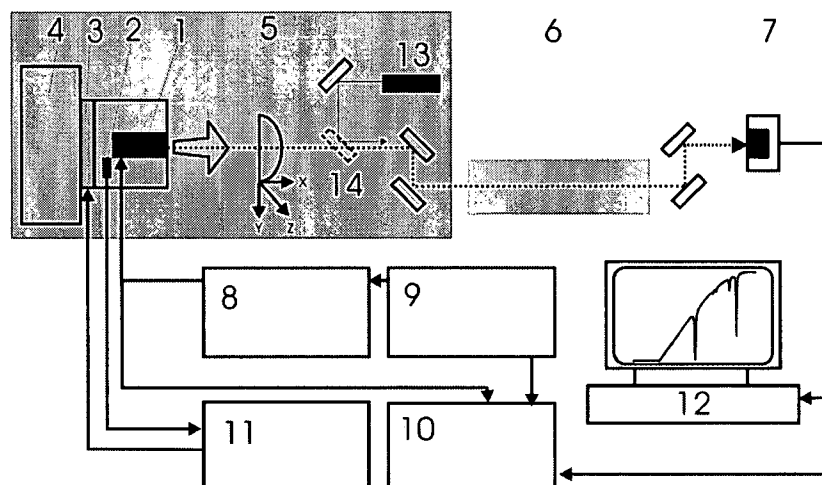


Fig. III-1: Setup for TDLAS experiments; 1: diode laser; 2: thermistor; 3: thermoelectric cooler; 4: heat sink; 5: planoconvex (aspheric) lens; 6: sample volume; 7: photo detector; 8: laser driver; 9: function generator; 10: oscilloscope; 11: temperature controller; 12: data acquisition; 13: alignment laser (visible laser diode module); 14: removable mirror.

The main parts are the thermo stated laser with the light collimation unit. A visible alignment laser that can be overlaid with the infrared laser by a removable mirror has proven very helpful. This basic unit (highlighted in grey in Fig. III.-1) can be placed in a protective box. A compact "launching box" protects the laser and might be necessitated by purging requirements. Apart from the "launching box" plus appropriate equipment (laser driver, temperature controller), the setup in Fig. III-1 has got a sample volume and a detector plus data acquisition equipment. It can be classified as a single beam setup.

The baseline can either be recorded between actual measurements (that is without absorbing species present) or determined mathematically by an appropriate fitting procedure. The single beam setup is easy to implement from the experimental point of view. A two beam setup where signal and baseline are recorded simultaneously often uses a beam splitter to divide the laser beam. Fig. III-2 presents an extended two beam setup for long term stability. Not only the baseline is measured in addition to the signal trace, the target species is also measured in a reference cell (this might be used for line locking purposes). Also, the tuning properties of the laser are observed using an etalon.

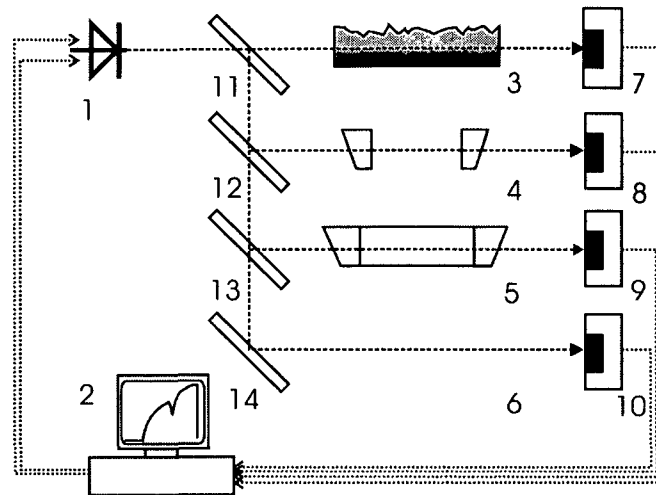


Fig. III-2: Setup for long term stability; 1: diode laser; 2: PC for data acquisition and laser current/temperature control; 3: probed sample value; 4: etalon (wide spacing for large FSR), 5: gas cell containing reference gas at low pressure (prevent drift, recalibration). 6: recording of the baseline; 7-10: photo detectors; 11-13: beam splitters; 14: mirror.

The following subchapters focus on characteristics of the various lasers. Basically, the same setup as described in Fig. III-1 was used. Diode lasers are sensitive devices. Electrostatic discharges are particularly dangerous. Information on diode laser protection strategies can be found in [108]. Details on thermoelectric temperature control systems for diode lasers are outlined in [109]. The main standards for the safe use of lasers are ANSI Z136.1 (USA) and IEC 60825-1 [110] (European Union). The following table III-1 presents a common classification of lasers related to safety issues:

Class	Description
Class 1	intrinsically safe
Class 2	low power devices emitting visible light - not completely safe, but the blink reflex will protect the eye
Class 3a	similar to Class 2, except that if the beam is focused onto the eye, it can be hazardous
Class 3b	either the blink reflex is not fast enough to prevent damage, or the beam is invisible and therefore the blink reflex cannot work
Class 4	high power devices capable of causing immediate injury to the skin or eye - even diffuse reflections may be hazardous

Table III-1: Classification of lasers according to health hazards.

The Nd:YAG laser (1064 nm, 1-50 mJ, 5 ns) used for the laser-ignition test runs (see chapter IV.2) is a class 4 device. The laser diode modules used as alignment lasers and most commercial laser pointers belong to class 3a (630-680 nm wavelength (red), maximum power output 1 - 5 mW). The duration of exposure to visible lasers is usually limited by the eye's blink reflex, which normally occurs within 250 ms. The hazards of laser pointers and low power diode lasers as used here are limited to the eye. The most likely effects from exposure to viewing the beam from a laser pointer are afterimage, flashblindness and glare. Damage to the retina is not likely.

Afterimage is the perception of spots in the field of vision and may last several minutes. Flashblindness is temporary vision impairment after viewing a bright light (compare looking directly into the sun). It may last several minutes. Glare is a reduction or complete loss of visibility in the central field of vision during exposure to the direct or scattered beam (compare looking into the headlights of an approaching car at night). Once the beam is out of the field of vision, the glare decreases. Glare can cause distraction, but does not pose a health hazard.

The near infrared diode lasers used in this thesis belong to class 3b.

### III.1 Edge emitting lasers at 2.3 and 2.55 $\mu\text{m}$ for CO, CH<sub>4</sub> and H<sub>2</sub>O

Two room temperature continuous wave InGaAsSb/AlGaAsSb quantum well ridge diode lasers in the near infrared spectral region were used for *in-situ* measurements of CO and CH<sub>4</sub>. The lasers were provided by Dr. M. A. Maiorov, Dr. D. Z. Garbuzov and Dr. J. C. Connolly from Princeton Lightwave, Inc. (USA).

One of the lasers emitted at 2.3  $\mu\text{m}$  (250  $\mu\text{m}$  long), the second one at 2.55  $\mu\text{m}$  (500  $\mu\text{m}$  long device).

The characteristic curves of the lasers are presented in Fig. III.1-1. In [111]–[112], more information on the device can be found.

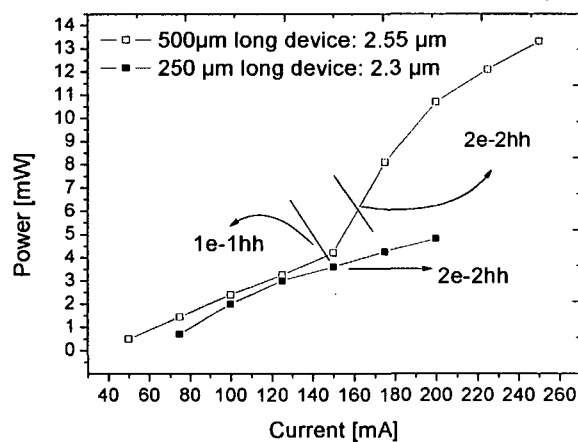


Fig. III.1-1: Output power versus injection current of the edge emitting diode lasers.

1e-1hh denotes the recombination of the ground state electron with the heavy hole, 2e-2hh the recombination between the second electron and the second heavy hole state.

Modulation of the injection current allows fast single mode tuning at about  $\Delta\lambda/\Delta I = 0.07\text{nm}/\text{mA}$  (with  $\lambda$  being the wavelength and  $I$  the injection current). By shifting the laser temperature the emission frequency can be changed at a rate of about  $\Delta\lambda/\Delta T = 0.2\text{nm}/\text{K}$ . Tuning by current is fast, but temperature tuning can access a broader frequency range. So usually the laser center frequency is determined by the temperature and tuning is done by current. The output power of diode lasers scales approximately linearly with the injection current. (2 mW at 100 mA and 4mW at 200 mA for the laser at hand at a temperature of 16°C). The whole wavelength shift region consisted of several alternating multimode and single mode regions. The distance between the single mode regions was about 6-12 nm.



Within a single mode area, the tuning range was about 0.5 - 2 nm. In the areas adjacent to the selected absorption lines for CO, CH<sub>4</sub> and H<sub>2</sub>O, no mode hops occurred.

In Fig. III.1-2, absorption spectra recorded with the 2.3  $\mu\text{m}$  laser are shown.

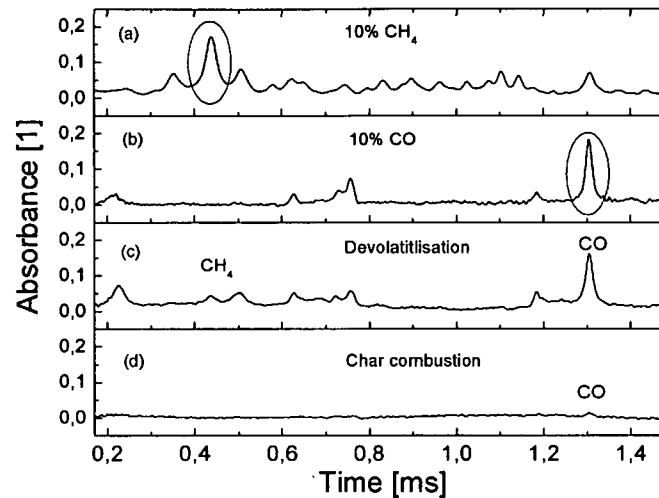


Fig. III.1-2: The 2.3  $\mu\text{m}$  long laser could be used to measure CH<sub>4</sub> and CO simultaneously. (a) and (b) show reference spectra of CH<sub>4</sub> and CO, respectively. (c) and (d) show spectra obtained during measurements close to the surface of a burning particle (see chapter IV.1).

It is a fortunate coincidence that a suitable absorption line both of CO and CH<sub>4</sub> falls into the narrow tuning range of the laser. Since the exact wavelength of the laser was not known, the spectral parameters could not be taken from a database, e.g. HITRAN [4]. Instead, the temperature dependence had to be determined experimentally.

In Fig. III.1-3, an absorption spectrum of water vapor recorded with the 2.55  $\mu\text{m}$  laser is shown.

The insert (b) shows a Lorentzian fit. The corresponding residual is given in (c).

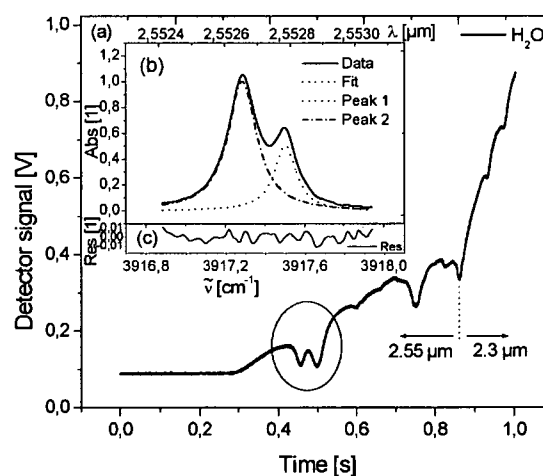


Fig. III.1-3: The 2.55  $\mu\text{m}$  long laser was used to measure the concentration of water vapor. (a) shows the absorption peak, (b) gives a fit with the residual shown in (c).

In Fig. III.1-4, the continuous tuning range of the 2.55  $\mu\text{m}$  laser is shown. The laser showed mode hops (Fabry Perot device). Care had to be taken that the absorption peak for species concentration measurements (H<sub>2</sub>O) was situated in a spectrally pure, mode hop free area.

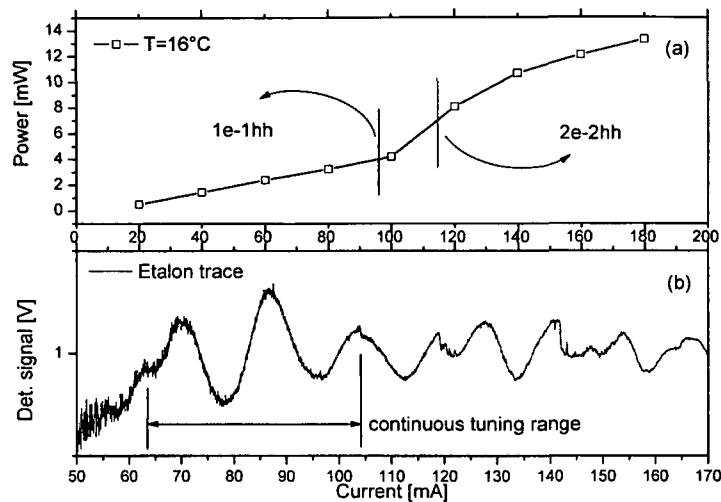


Fig. III.1-4: The 2.55  $\mu\text{m}$  long laser was used to measure the concentration of water vapor. (a) shows the absorption peak, (b) gives the etalon trace. One can see the continuous tuning range.

The following three figures Fig. III.1-5 to III.1-7 show the temperature dependence of the absorbance for the selected peaks of  $\text{CH}_4$ ,  $\text{CO}$  and  $\text{H}_2\text{O}$ .

Fig. III.1-5 illustrates the dependence for the chosen  $\text{CH}_4$  absorption line accessible with the 2.3  $\mu\text{m}$  laser (a). The exact wavelength was not determined, therefore the calibration had to be performed experimentally. The temperature dependence can be expressed as

$$A(T[\text{K}], \text{CH}_4) = 9\text{E-}07T^2 - 0.0028T + 2.154$$

(Eq. III.1-1)

A... absorbance [1]

T... temperature [K]

The polynomial fit is valid from 300 K to 1500 K.

In Fig. III.1-5 (b), the line intensities of  $\text{CH}_4$  in the range of 0.1 to 7  $\mu\text{m}$  are depicted (taken from [4]).

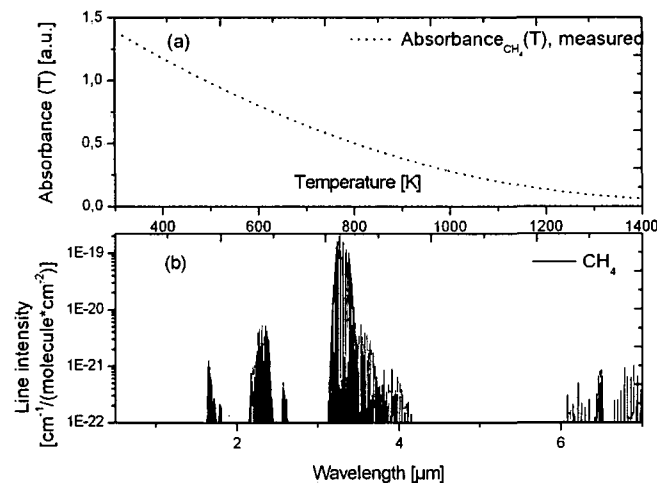


Fig. III.1-5: Temperature dependence of the chosen  $\text{CH}_4$  absorption line at 2.3  $\mu\text{m}$  (a) and depiction of strong absorption lines of  $\text{CH}_4$  in the near and middle infrared spectral region (b).

Likewise, Fig. III.1-6 illustrates the dependence for the chosen CO absorption line accessible with the 2.3  $\mu\text{m}$  laser (a). The calibration had to be performed experimentally. The temperature dependence can be expressed as

$$A(T[\text{K}], \text{CO}) = 2\text{E-}07T^2 - 0.0006T + 0.5078$$

(Eq. III.1-2)

A... absorbance [1]  
T... temperature [K]

The polynomial fit is valid from 300 K to 1500 K.

In Fig. III.1-6 (b), the line intensities of CO in the range of 0.1 to 7  $\mu\text{m}$  are depicted (taken from [4]).

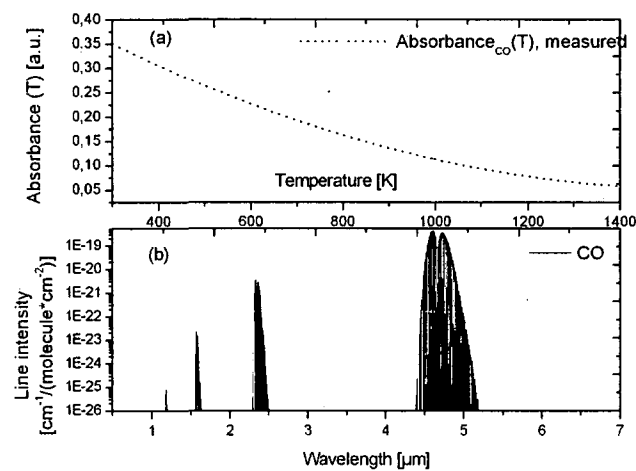


Fig. III.1-6: Temperature dependence of the chosen CO absorption line at 2.3  $\mu\text{m}$  (a) and depiction of strong absorption lines of CO in the near and mid infrared spectral region (b).

Likewise, Fig. III.1-7 illustrates the calculated temperature dependence of the chosen  $\text{H}_2\text{O}$  absorption line (double peak) accessible with the 2.55  $\mu\text{m}$  laser (a). It can be expressed as

$$A(T[\text{K}], \text{H}_2\text{O}) = -1\text{E-}12T^4 + 7\text{E-}09T^3 - 1\text{E-}05T^2 + 0.0087T - 1.0443$$

(Eq. III.1-3)

A... absorbance [1]  
T... temperature [K]

The polynomial fit is valid from 300 K to 1500 K.

In Fig. III.1-7 (b), the line intensities of  $\text{H}_2\text{O}$  in the range of 0.1 to 7  $\mu\text{m}$  are depicted (taken from [4]).

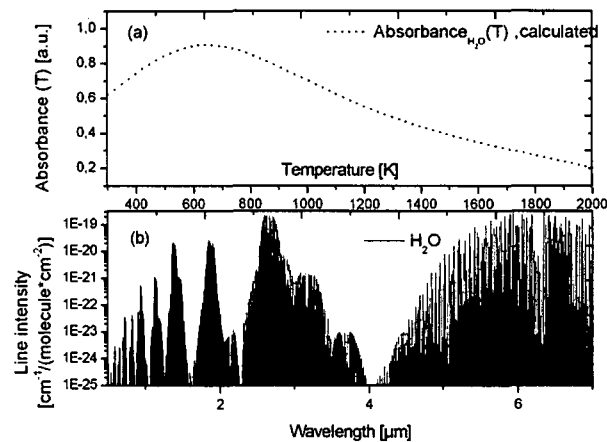


Fig. III.1-7: Temperature dependence of the chosen H<sub>2</sub>O absorption line at 2.55 μm (a) and depiction of strong absorption lines of H<sub>2</sub>O in the near and mid infrared spectral region (b).

In order to be able to supply the drive current to the laser, a mounting construction had to be devised. For proper thermostatisation, a copper heat sink was chosen.

In Fig. III.1-8, this is shown schematically.

In chapter III.3, the construction of VCSEL based laser measurement systems is explained in more detail. Many aspects are equally valid for the edge emitters presented here. Therefore, the reader is referred to that chapter for more information.

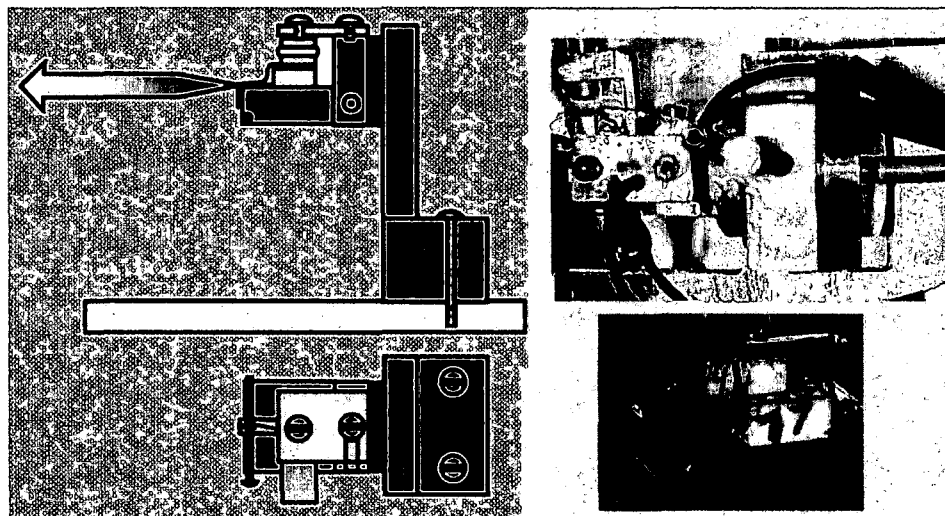


Fig. III.1-8: Mounting of the laser; The sketch on the left shows how the laser (cylindrical shape) is shunt in a copper block. The picture on the right is an actual photograph (top right: mounted laser; bottom right: two unmounted devices).

### III.2 Quantum cascade laser at 11.4 $\mu\text{m}$ for $\text{NH}_3$ and $\text{C}_2\text{H}_4$

Many interesting small molecules can be rovibrationally excited in the infrared and hence be detected by absorption spectroscopic techniques. Transitions in the near infrared (0.8-2.5  $\mu\text{m}$ ) have been extensively probed by semiconductor lasers. However, since only combination and overtone bands can be found in this spectral region, sophisticated techniques, e.g. modulation methods, have to be deployed in order to obtain acceptable detection limits (see chapter II.3). The fundamental absorption bands that are situated in the mid infrared (2.5-25  $\mu\text{m}$ ) are at least two orders of magnitude stronger than the transitions in the near infrared. Lead salt diode lasers emit at longer wavelengths but have to be kept at cryogenic temperatures. This restricts their use to controlled laboratory environments. Another type of laser, the quantum cascade laser (QCL), also emits in the mid infrared. The wavelength of a QCL can be specifically tailored to spectroscopic needs since it is not limited by the band gap of the material, but determined by the layer thicknesses of wells and barriers of the cascaded structure [113]. QCLs (not all of them, e.g. the one used here) can be operated at quasi-room temperature. (Quasi-room temperature means that thermoelectric temperature control by a Peltier element is sufficient, as opposed to liquid  $\text{N}_2$  (cryogenic) cooling). More information on QCLs can be found in chapter II.2 and [18].

A QCL emitting single mode around 11.3  $\mu\text{m}$  ( $888\text{ cm}^{-1}$ ) was used to obtain the absorption spectra of gaseous ethylene ( $\text{C}_2\text{H}_4$ ) and ammonia ( $\text{NH}_3$ ). The laser was provided by Prof. Dr. Strasser and Dr. Solveig Anders from the Institut für Festkörperelektronik, Vienna University of Technology. Joint experiments were carried out at our partners' institute. This work is presented in chapter IV.3.

The QCL consists of a  $\text{GaAs}/\text{Al}_{0.45}\text{Ga}_{0.55}\text{As}$  (50 periods) chirped superlattice structure. The growth and design of such superlattice QCLs have been described in [114], [115]. The ridge-shaped double plasmon waveguide has been defined by reactive ion etching. On top of the waveguide, a grating with a period of 1.78  $\mu\text{m}$  has been etched in order to provide distributed feedback. This results in a single mode-emitting QCL. The emission wavelength can be tuned by the temperature with a tuning rate of about 0.71 nm/K. The QCL used for this work was 1.5 mm long and 20  $\mu\text{m}$  wide. It was electrically driven with pulses of a repetition rate of 5 kHz. In order to obtain a narrow emission line width, a short pulse duration (20 ns) was chosen (cf. [116]). For the spectroscopy described here, the laser was mounted in a liquid nitrogen cooled cryostat. For the desired emission wavelength range, the laser temperature was adjusted between 185 and 225 K. The driving current density was kept constant at 10  $\text{kA}/\text{cm}^2$ . Fig. III.2-1 shows how the QCL emission wavelength can be tuned with temperature.

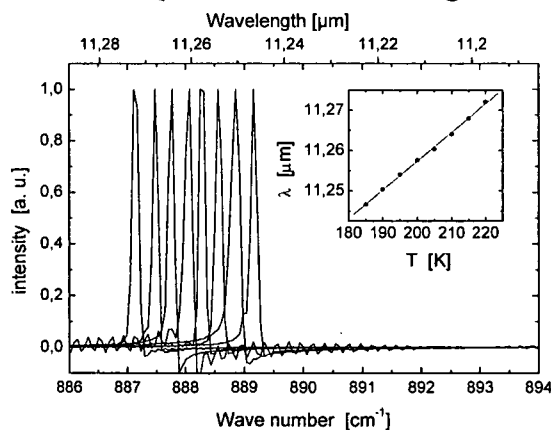


Fig. III.2-1: Emission characteristics of the quantum cascade laser. Single mode emission was observed in the whole temperature range needed for the gas spectroscopy. The bias current of the laser was 3 A, the pulse width 20 ns at 5 kHz. Inset: temperature dependence of the emission wavelength.

A Fourier transform infrared spectrometer with nominal resolution of  $0.125\text{ cm}^{-1}$  was used to determine the QCL emission wavelength and to check for single mode emission. For the work described here, the laser emission was tuned over  $2.4\text{ cm}^{-1}$  (30 nm) from  $886.76$  to  $889.16\text{ cm}^{-1}$  ( $11.277$  to  $11.247\text{ }\mu\text{m}$ ).

In Fig. III.2-2, two pictures of the QCL are shown. The picture on the left is a close-up of the laser mounted on a copper heat sink, the right picture depicts the housing of the QCL in a cryostat.

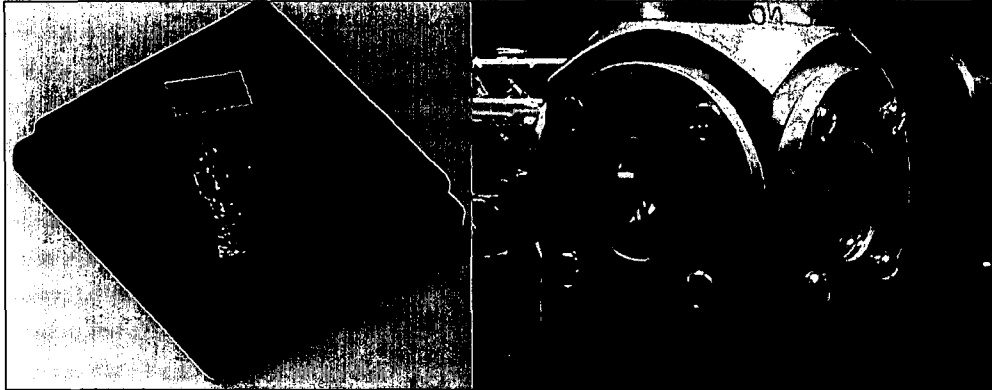


Fig. III.2-2: View of the QCL (left) and the cryostat.

The emission wavelength of the QCL in the middle infrared spectral region ( $11.4\text{ }\mu\text{m}$ ) is beneficial compared to telecommunication diode lasers in the near infrared ( $1\text{-}2\text{ }\mu\text{m}$ ) because strong fundamental molecular transitions can be excited. This results in an increased sensitivity by several orders of magnitude (see Fig. III.2-3). The biggest drawback of the laser, however, is that it requires cryogenic cooling which limits its use to laboratory-based applications.

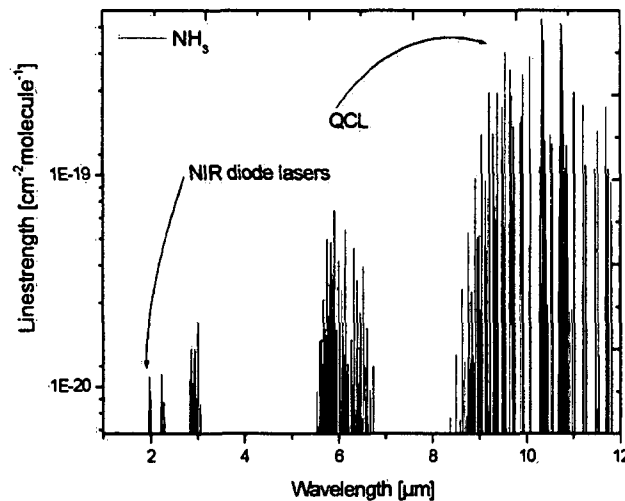


Fig. III.2-3: Illustration of the line strength of absorption lines ( $\text{NH}_3$ ) in the middle infrared (QCL) and in the near infrared (telecommunication diode lasers). QCLs allow increased sensitivity by two orders of magnitude.

### III.3 Vertical-cavity surface-emitting laser (VCSEL) at 0.761 $\mu\text{m}$ for $\text{O}_2$

A TO 39 case containing a small wafer section with four contacted VCSELs was supplied by CSEM SA (Centre Suisse d'Electronique et de Microtechnique), Switzerland. The VCSELs one of which was used had typical maximum output powers of 1 mW at threshold currents around 2.3 mA (25°C). The characteristic curves of the VCSEL that was used are shown in Fig. III.3-1.

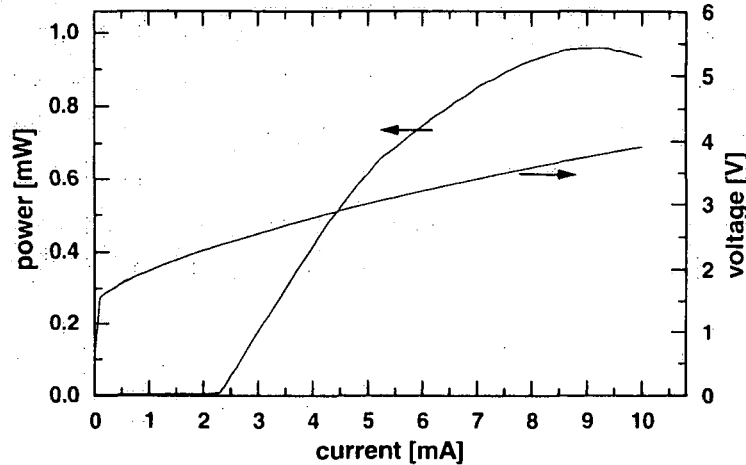


Fig. III.3-1: PIV curves of the VCSEL. The threshold current is approximately 2.3 mA (25°C).

The slope efficiency of the VCSEL was 0.2 mW/mA.

The slope efficiency, also differential efficiency, is the mean value of the incremental change in output power for an incremental change in injection current when the laser is operated above threshold.

The beam divergence was 12° (full width at half maximum, FWHM), the line width 5 MHz (at 0.5 mW). Fig. III.3-2 takes a look at the line width.

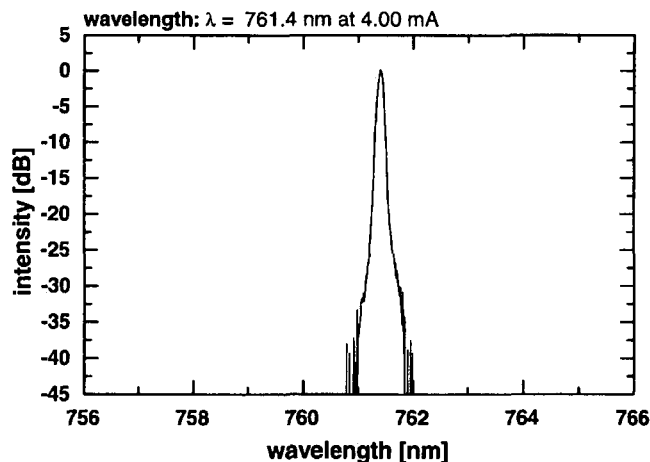


Fig. III.3-2: (Taken from CSEM data sheet provided with the VCSEL).

One can see that the laser operates in single longitudinal mode emission.

Temperature and current tuning coefficients of the VCSEL are summarized in table III.3-1 and compared to a typical DFB laser (data from [117]) of the same wavelength.

Laser	$\Delta\lambda/\Delta I$	$\Delta\lambda/\Delta T$	Threshold current
761 nm VCSEL	0.29 nm/mA ( $-5.0 \text{ cm}^{-1}/\text{mA}$ )	0.05 nm/K ( $-0.86 \text{ cm}^{-1}/\text{K}$ )	2.3 mA (298K)
Typical DFB laser (760 nm)	0.0047 nm/mA <sup>(a)</sup> ( $-0.081 \text{ cm}^{-1}/\text{mA}$ )	0,0597 nm/K <sup>(a)</sup> ( $-1.03 \text{ nm}/\text{K}$ )	~30 mA (298K)

Table III.3-1: Comparison of the tuning rates with injection current  $\Delta\lambda/\Delta I$  and with temperature  $\Delta\lambda/\Delta T$  plus the threshold current of the VCSEL to a standard DFB laser (data (a) were taken from [117]).  $\lambda$  denotes the wavelength [nm], T the temperature [K] and I the current [mA].

Fig. III.3-3 illustrates the tuning properties of the VCSEL. At moderate tuning frequencies, the continuous tuning range is as large as  $32 \text{ cm}^{-1}$  (at 1kHz), but decreases with higher tuning frequencies ( $8 \text{ cm}^{-1}$  at 500 kHz).

At 5 MHz tuning frequency, the tuning range was determined to be  $0.85 \text{ cm}^{-1}$  (0.05 nm). To put it another way, a single measurement can be performed in less than one microsecond. Such tremendous tuning frequencies are not possible with edge emitting diode lasers.

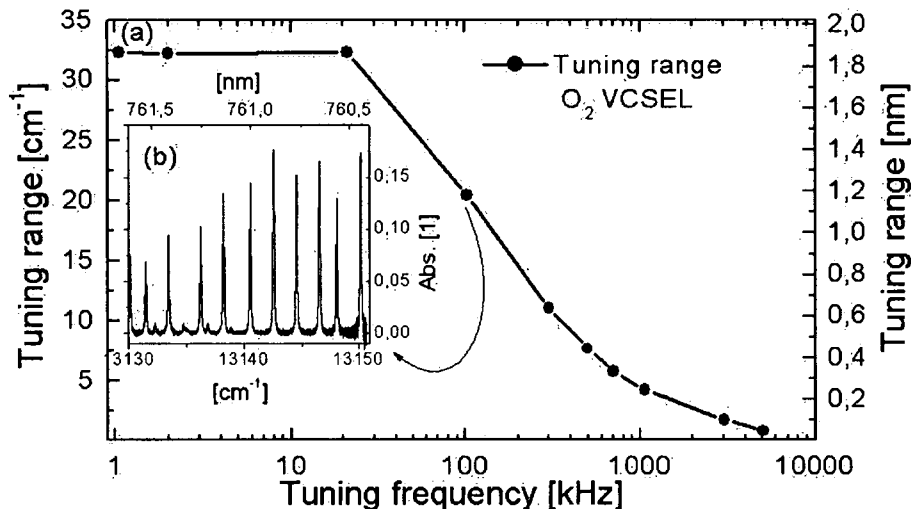


Fig. III.3-3: Tuning range of the VCSEL as a function of tuning frequency. At high (MHz) tuning frequencies, there is a tradeoff between fast measurement ability and far wavelength tuning.

Fig. III.3-4 depicts the position of oxygen absorption bands in the VIS and NIR spectral regions (a). The A band (shown as a magnification in (b)) around 765 nm contains the strongest transitions.



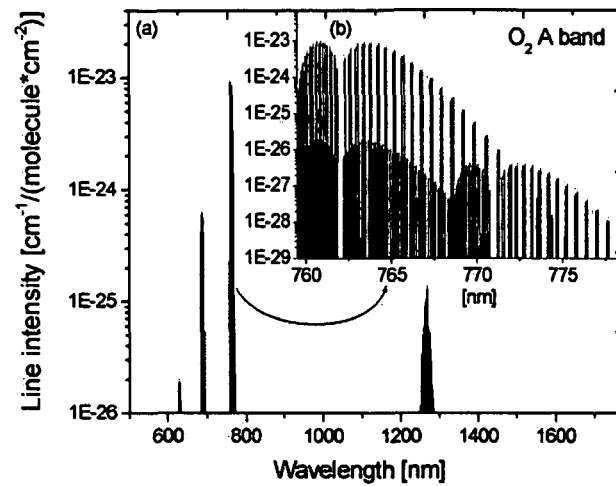


Fig. III.3-4: Absorption lines of molecular oxygen. The A band (insert (b)) contains the strongest transitions.

In Fig. III.3-5, a picture of the laser in its copper heat sink (right) and the collimating lens (left) is shown. An aspheric lens with 4.5 mm focal length (Geltech C230TM) was used.

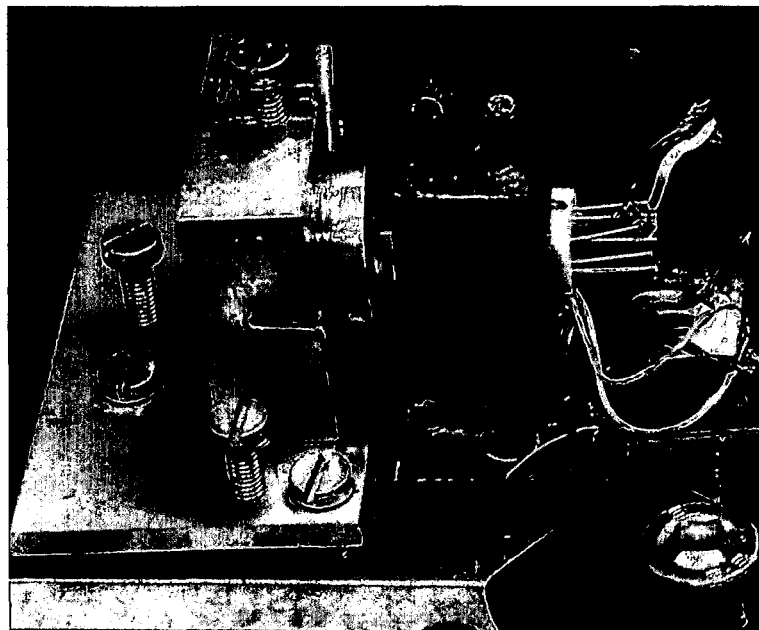


Fig. III.3-5: Picture of the 761 nm VCSEL for the detection of O<sub>2</sub>. The system is described in detail in [118].

### III.4 Long wavelength VCSELs at 1.54, 1.68, and 1.81 $\mu\text{m}$ for $\text{NH}_3$ , $\text{CH}_4$ , $\text{H}_2\text{O}$ and $\text{HCl}$

Vertical-cavity surface-emitting lasers (VCSELs) below 1.0  $\mu\text{m}$  have been available commercially for several years. A lot of research effort for the development of VCSELs in the near infrared, especially at the telecommunication wavelengths 1.3 and 1.55  $\mu\text{m}$  (lowest losses in silica fibers), has been taken. The Walter Schottky Institute, Munich University of Technology, has been engaged in long wavelength VCSELs and produced InP based devices in the 1 – 2  $\mu\text{m}$  wavelength range. An international cooperation was started in 2001. The long wavelength VCSELs were tested for their spectroscopic usefulness. As lined out in this chapter and in chapter IV.4, device characterization (e. g. tuning properties), demonstration experiments (e. g. high resolution molecular spectra) and species concentration measurements were carried out. Also, measurements were performed at high pressures (see chapter IV.5) and in an internal combustion engine (see chapter IV.6)

General information on VCSELs can be found in chapter II.2. Here, special and novel InP based long wavelength VCSELs are used.

Fig. III.4-1 shows a schematic cross section of these long wavelength InGaAlAs/InP VCSEL, which incorporates a buried tunnel junction (BTJ) as well as a dielectric layer stack which serves as a back mirror (described in detail in [119]).

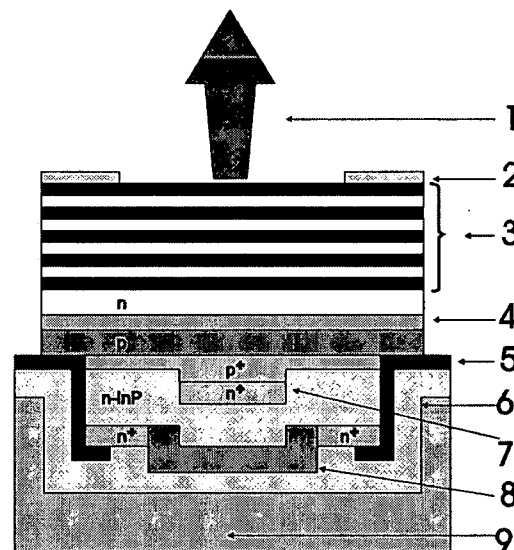


Fig. III.4-1: Schematic illustration of the BTJ VCSEL (BTJ= buried tunnel junction) emitting in the 1 – 2  $\mu\text{m}$  wavelength range. 1: Light emission perpendicularly to the surface; 2: n-contact; 3: epitaxial front mirror; 4: active region; 5: isolation; 6: p side contact; 7: BTJ; 8: dielectric back mirror; 9: integrated heat sink (Modified from [120]).

The BTJ technology provides the device with effective current confinement and wave-guiding, which are otherwise difficult to realize in InP-based material systems like (InGaAl)(As) or (InGa)(AsP) that are required for wavelengths in this region [121]. The current confinement ensures that the required current density in the active region can be obtained with an operating current as small as possible and therefore avoids excess heating. The strong wave-guiding associated with the BTJ allows the application of small BTJ diameters and therefore stable single frequency emission with side mode suppression ratios well exceeding 30 dB. The polarization of the laser can be controlled using an elliptically shaped BTJ to lift the polarization degeneracy. Moreover, the BTJ and the dielectric back mirror allow a significantly improved device design with respect to reduced resistivity and

heat generation in the conducting layers and optimized thermal conductivity between the active region and the heat sink, which is necessary to efficiently operate the active region to obtain a low threshold current as well as high output power.

The key features of VCSELs are

- closely-packed two-dimensional array configuration
- easy alignment and packaging (surface-normal emission)
- circular and low-divergence output beam
- high fiber-coupling efficiency
- low susceptibility to optical feed back
- low power consumption
- significant low-cost potential (selection and testing at the wafer level as demonstrated here)

### III.4.1 1540 nm VCSEL

1.55  $\mu\text{m}$  VCSELs fabricated in the buried tunnel junction technology have shown sub-mA threshold currents, 10-100  $\Omega$  series resistance, output powers up to 7 mW (20  $^{\circ}\text{C}$ , cw), differential efficiencies >25% and cw operation up to >110  $^{\circ}\text{C}$  [122]. The large current tuning range for BTJ-VCSELs is a result of the high current density in the active region and is not a consequence of the resistive heating in the epitaxial mirror. The VCSEL showed a mode-hop free continuous single frequency tuning over the whole laser driving current range. The concept of InP-based VCSELs using a BTJ and a dielectric mirror holds for a wavelength range from 1.3  $\mu\text{m}$  to at least 2  $\mu\text{m}$  [123]. Customizations concerning the different wavelengths determine the appropriate choice of dielectrics, recalculated layer thicknesses and appropriate alloy compositions in the active region.

In Fig. III.4-2 the diode laser voltage versus injection current and the output power versus injection current characteristics are shown. At 20 $^{\circ}\text{C}$  laser temperature the laser threshold was 0.93 mA, the peak output power was 0.58 mW (at 6.1 mA) and the series resistance was 60  $\Omega$ . The series resistance is very low compared to published data of other VCSELs [124]. This is a result of the Buried Tunnel Junction (BTJ) VCSEL technology [122]. The low series resistance and the current confinement reduce the unwanted device heating and therefore allow to operate the active region efficiently and to obtain a low threshold current as well as high output power even for long wavelength VCSELs. The current tuning rate was measured 0.7 nm/mA (-2.96  $\text{cm}^{-1}/\text{mA}$ ) and the temperature tuning rate was 0.11 nm/K (-0.46  $\text{cm}^{-1}/\text{K}$ ).

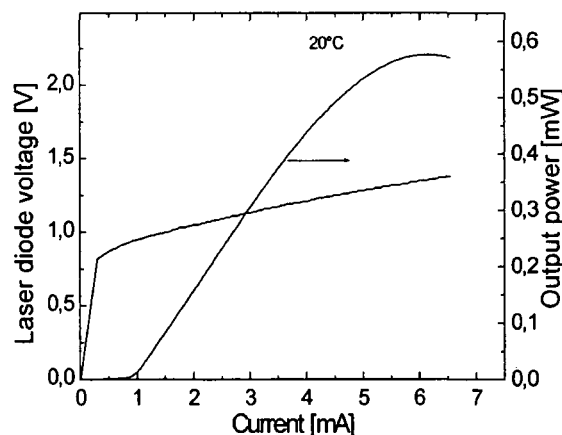


Fig. III.4-2: PIV curves of the 1.54  $\mu\text{m}$  VCSEL. The threshold current is below 1 mA (20 $^{\circ}\text{C}$ ), the maximum output power below 1 mW.

In Fig III.4-3 the tuning range of the VCSEL is shown as a function of the tuning frequency. In order to measure the tuning properties of the laser, a 5 mm thick sapphire window was placed in the beam path and the interference signal was detected. The free spectral range (FSR, the frequency difference between two neighboring transmission maxima) of the etalon was  $0.574 \text{ cm}^{-1}$  ( $0.136 \text{ nm}$  at  $1.54 \text{ }\mu\text{m}$ ). In the top window (b) of the inset the detector signal without the etalon (baseline) and the detector signal with the etalon inserted in the beam path are shown for a 120 kHz, 0-5.8 mA triangular current modulation. In the bottom window (c) of the inset the etalon trace defined as the negative logarithm of the ratio of etalon and baseline signals is shown in absorbance units. The point A indicates the turning point of the triangular 0-5.8 mA current modulation. As it can be seen from the etalon trace the laser tuning is continuing beyond the point A up to the point B. This means the laser still heats although the current already started to decrease. The tuning range is defined here as the wavelength tuning between the laser threshold and the point B. From the data shown in the main window (a) of Fig. III.4-3 it can be seen that the tuning range only slowly decreases with increasing tuning frequency from  $13.5 \text{ cm}^{-1}$  ( $3.2 \text{ nm}$ ) at 200 Hz to  $4.5 \text{ cm}^{-1}$  ( $1.1 \text{ nm}$ ) at a tuning rate of 200 kHz (see also Fig. IV.4-7 in chapter IV.4). For the 200 kHz triangular current modulation the time needed to scan over the  $4.5 \text{ cm}^{-1}$  range was only  $2 \text{ }\mu\text{s}$ . The tuning range could be increased if the 0-5.8 mA current modulation amplitude is increased close to the maximum possible current.

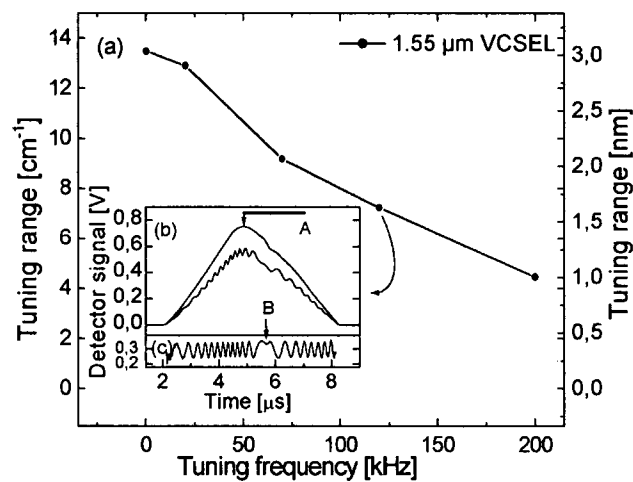


Fig. III.4-3: Wavelength tuning properties of the  $1.54 \text{ }\mu\text{m}$  VCSEL (0-5.8 mA triangular current modulation). The main window (a) illustrates the decrease in tuning range (left:  $[\text{cm}^{-1}]$ ; right:  $[\text{nm}]$ ) as a function of tuning frequency. The inserts (b) and (c) take a closer look at the tuning behavior. (b) shows the baseline (upper curve) and the etalon trace (lower, corrugated trace). The current ramp reverses at point A, however, the laser still continues tuning up to point B. In (c), the etalon trace ( $\text{FSR} = 0.574 \text{ cm}^{-1}$ ) is shown in terms of absorbance units.

## III.4.2

## 1680 nm VCSEL

The 1680 nm VCSEL used for the experiments emits light in a single longitudinal and transverse mode with a low-divergence beam vertically from the surface of a fabricated wafer. Due to their architecture, VCSELs are inherently single longitudinal mode. Multiple transverse mode lasing was not observed during the experiments. Details about the fabrication and the device characteristics can be found in [121] to [123].

Fig. III.4-4 presents typical output characteristics of the selected laser. The operating voltage as a function of the injection current at 15°C is depicted. Due to the small active region, the threshold current is considerably lower than for conventional edge emitting lasers and amounts to 750  $\mu\text{A}$  (15°C). The threshold voltage is as small as 0.86 V.

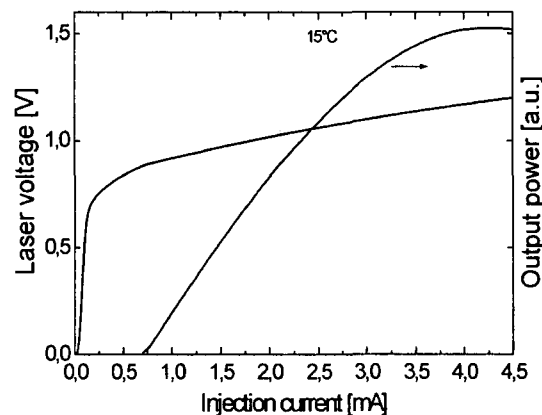


Fig. III.4-4: PIV curves of the 1.68  $\mu\text{m}$  VCSEL. The threshold current is below 1 mA (15°C), the maximum output power on the order of 1 mW.

Fig. III.4-4 also illustrates the output power as a function of injection current. As the threshold is reached, the power increases approximately linearly with the current. The output power is shown in terms of the detector voltage. It is on the order of sub-mW. The current heats up the active zone. One can see that around 4 mA, the loss of gain with increasing temperature overcomes the increase of gain with increasing current. As a result, the output power starts to roll over.

Similarly to edge emitters, VCSELs can be tuned by varying either the heat-sink temperature or the injection current.

Because of the small dimensions of the cavity, VCSELs can be tuned much faster than edge emitting diode lasers. Typical tuning rates are on the order of  $1 \text{ cm}^{-1}/\text{K}$  and  $5$  to  $10 \text{ cm}^{-1}/\text{mA}$  (compare  $-0.40 \text{ cm}^{-1}/\text{K}$  and  $-3.05 \text{ cm}^{-1}/\text{mA}$  for the device tested, see later).

Generally speaking, fast but narrow tuning of diode lasers can be achieved by varying the injection current, whereas wider emission frequency shifts are viable by changing the temperature of the heat sink.

Traditionally, temperature tuning has therefore been used for coarse wavelength selection and current tuning for matching a suitable absorption line. As for VCSELs, the overall wavelength variation that can be obtained by current modulation alone is approximately equal to the traditional temperature tuning range.

The main focus of this chapter is on rapid wavelength tuning of the VCSELs. To track the frequency tuning, an etalon (5.0 mm thick sapphire,  $\text{FSR} = 0.574 \text{ cm}^{-1} = 0.164 \text{ nm}$  at 1.680  $\mu\text{m}$ ) was used. The tuning range decreases with the modulation frequency as shown in Fig. III.4-5 ( $9.9 \text{ cm}^{-1}$  at 25 kHz to  $2.6 \text{ cm}^{-1}$  at 1000 kHz). The laser was ramped in the form of a symmetric triangle (0-4 mA). The figure shows the tuning properties in the range of 25 to

1000 kHz. The measured tuning rate was as high as  $5.2 \text{ cm}^{-1}/\mu\text{s}$  at a tuning frequency of 1 MHz.

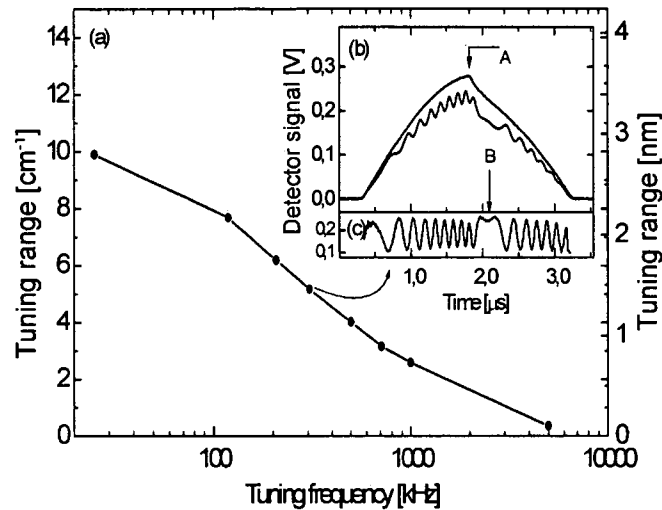


Fig. III.4-5: Tuning range of the VCSEL as a function of injection current modulation frequency. The main window (a) illustrates the decrease in tuning range (left:  $\text{cm}^{-1}$ ; right:  $\text{nm}$ ) as a function of tuning frequency. The inserts (b) and (c) take a closer look at the tuning behavior. (b) shows the baseline (upper curve) and the etalon trace (lower, corrugated trace). The current ramp reverses at point A, however, the laser still continues tuning up to point B. In (c), the etalon trace ( $\text{FSR} = 0.574 \text{ cm}^{-1}$ ) is shown in terms of absorbance units.

The insert in Fig. III.4-5 takes a deeper insight in the tuning behavior of the VCSEL at high frequencies, here 308 kHz. The upper triangular curves are the base line and the etalon trace, respectively. The lower corrugated line in the insert is the etalon trace plotted in terms of absorbance units. The peak to peak distance corresponds to an increment in frequency of  $0.574 \text{ cm}^{-1}$  (FSR). As the injection current is increased, the wavelength shifts. Point A denotes the reversal of the current ramp. However, the wavelength tuning overshoots the turning point of the injection current (the active region still heats up to point B) and finally starts to reverse. In Fig. III.4-6 the wide temperature tuning properties of the VCSEL are demonstrated. One can see two strong absorption features of methane at 136 mbar that are approximately  $12 \text{ cm}^{-1}$  ( $3.42 \text{ nm}$ ) apart.

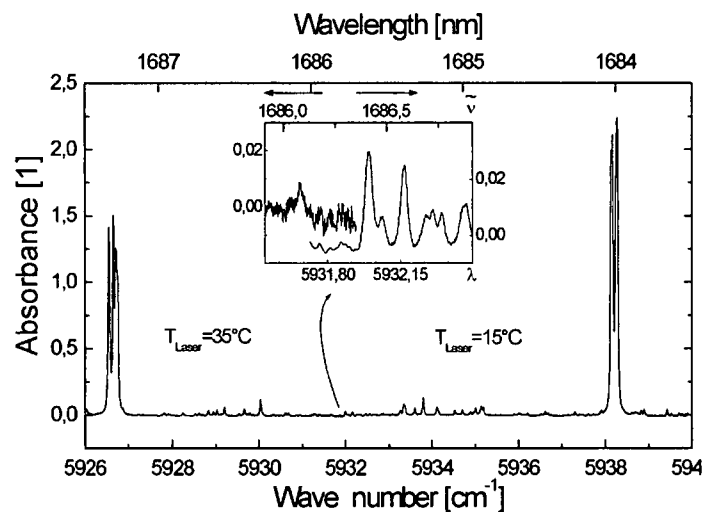


Fig. III.4-6: Temperature tuning of the VCSEL. This figure is composed of two spectra, one recorded at a laser heat sink temperature of  $15^\circ\text{C}$  (right), the other at  $35^\circ\text{C}$  (left). The laser current was 0-5.1 mA, the pressure 140.8 mbar (pure  $\text{CH}_4$ ) at 296 K, the path length 44 cm. The insert shows a magnification of the overlapping region.

The left part of the spectrum was covered by current tuning 0-5.1 mA of the VCSEL at a heat sink temperature of 15°C. The right part of the spectrum was obtained by current modulation from 0-5.1 mA at a heat sink temperature of 35°C. Since there was an overlap of the two scans (depicted in the insert of Fig. 4), it is possible to record both absorption features in a continuous scan using a single VCSEL. The temperature tuning coefficient was determined to be  $-0.40 \text{ cm}^{-1}/\text{K}$  ( $+0.11 \text{ nm}/\text{K}$ ).

Fig. III.4-7 shows the far wavelength tuning ability of the VCSEL. The laser was frequency tuned by raising the drive current from 0 to 6 mA at a fixed heat sink temperature (15°C).

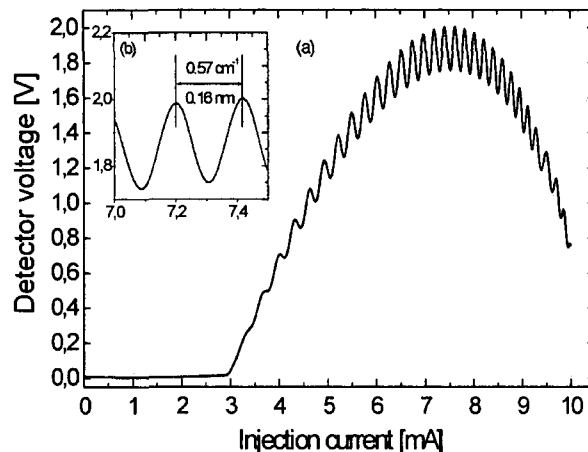


Figure III.4-7: Continuous (mode-hop free) tuning of the VCSEL. The FSR of the etalon (5.0 mm thick sapphire) was  $0.574 \text{ cm}^{-1}$ . The insert (b) is a magnification of (a) to illustrate that the spacing of two adjacent transmission maxima is the FSR.

One can see 29 etalon features, resulting in a tuning range of  $> 16 \text{ cm}^{-1}$  (4.5 nm). The tuning rate can be determined to  $-3.05 \text{ cm}^{-1}/\text{mA}$  ( $+0.86 \text{ nm}/\text{mA}$ ). One of the special features of VCSELs for spectroscopy is the ability to scan large wavelength ranges solely by current modulation. There is no need for an external cavity setup. Smaller wavelength ranges can be accessed at higher speeds with the modulation speed being much faster than it is possible with conventional diode lasers.

### III.4.3 1810 nm VCSEL

A detailed description of the used InGaAlAs/InP VCSEL device structure is given in [121] (schematic see Fig. III.4-1). The Buried Tunnel Junction (BTJ) VCSEL technology [123] enabled the realization of the first long-wavelength VCSELs at 1.8  $\mu\text{m}$ . These devices also show excellent lasing performance and stable single-frequency operation over the whole driving current range. The BTJ allows optimizing the thermal device design by achieving a low series resistance and effective current confinement. While the low resistance results from the substitution of high-resistive p-doped material by n-doped layers, the current confinement concentrates the laser injection current in the active region, so that the required current density there can be obtained with an operating current as small as possible. These measures are important to avoid excess heating, which is necessary to efficiently operate the active region to obtain a low threshold current as well as high output power. A strong index guiding associated with the BTJ allows the application of small BTJ diameters and therefore stable single frequency (single transverse mode) emission with side mode suppression ratios exceeding 30 dB. Operation temperatures up to 90°C and threshold currents as low as 190  $\mu\text{A}$  were demonstrated for devices at 1.8  $\mu\text{m}$  [123]. The large range for current tuning of BTJ-VCSELs stems from the high current density in the active region and is not a consequence of the resistive heating in the *n*-doped epitaxial mirror. The 1.8  $\mu\text{m}$  VCSEL used here had a threshold current of 0.9 mA at 30 °C and a 7  $\mu\text{m}$  BTJ aperture diameter. The temperature tuning rate was 0.125 nm/K (0.38  $\text{cm}^{-1}/\text{K}$ ). The current tuning rate was 0.9 nm/mA (2.75  $\text{cm}^{-1}/\text{mA}$ ). Fig. III.4-8 shows the characteristic curves of the VCSEL.

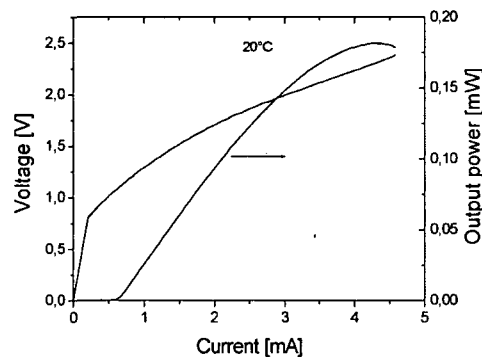


Fig. III.4-8: PIV curves of the 1.81  $\mu\text{m}$  VCSEL (7  $\mu\text{m}$  BTJ). The threshold current is below 1 mA (20°C).

In Fig. III.4-9, the multiple species measurement capability of the VCSEL is illustrated.

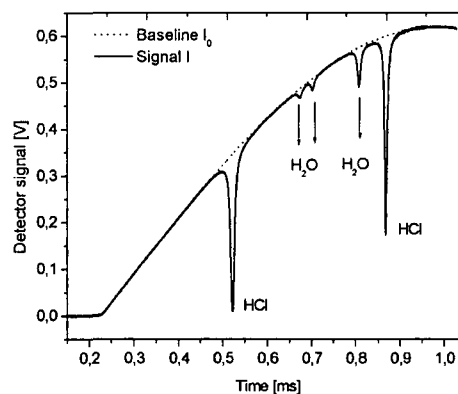


Fig. III.4-9: Simultaneous determination of HCl and H<sub>2</sub>O using a single 1810 nm VCSEL (path length for H<sub>2</sub>O (0.75 % by volume) 1.30 m, path length for HCl (29% by volume) 0.44 cm, pressure 1000 mbar, temperature 21 °C).



The path length for H<sub>2</sub>O was 1.30 m (0.75 % by volume), the path length for HCl was 0.44 cm (29% by volume) at 1000 mbar and 21 °C. The peaks have been labeled.

In table III.4-1, characteristics of the long wavelength InP based VCSELs are summarized and compared to an edge emitting device of comparable wavelength.

Laser	$\Delta\lambda/\Delta I$	$\Delta\lambda/\Delta T$	Threshold current
1540 nm VCSEL	0,11 nm/mA (-2,96 cm <sup>-1</sup> /mA)	0,11 nm/K (-0,46 cm <sup>-1</sup> /K)	0,93 mA (20°C)
1680 nm VCSEL	0,86 nm/mA (-3,05 cm <sup>-1</sup> /mA)	0,11 nm/K (-0,40 cm <sup>-1</sup> /K)	0,75 mA (15°C)
1810 nm VCSEL	0,9 nm/mA (-2,75 cm <sup>-1</sup> /mA)	0,125 nm/K (-0,38 cm <sup>-1</sup> /K)	0,90 mA (30°C)
Typical DFB laser 1580 nm	0,003 nm/mA <sup>(a)</sup> (-0,012 cm <sup>-1</sup> /mA)	0,15 nm/K <sup>(a)</sup> (-0,60 cm <sup>-1</sup> /K)	~30 mA (25°C)

Table III.4-1: Comparison of the current tuning rates  $\Delta\lambda/\Delta I$ , temperature tuning rates  $\Delta\lambda/\Delta T$  and the threshold current of the VCSELs and a typical DFB laser ( $\lambda$  denotes the wavelength, I the current, T the temperature). The data (a) were taken from [125].  $\Delta\lambda/\Delta T$  is comparable.  $\Delta\lambda/\Delta I$  is much larger for VCSELs which translates into a much larger total tuning range for VCSELs compared to DFB laser.

The larger current tuning coefficients  $\Delta\lambda/\Delta I$  of VCSELs translate into a larger maximum continuous current tuning range as opposed to standard DFB lasers.

In Fig. III.4-10, the line intensities of CH<sub>4</sub>, HCl and NH<sub>3</sub> in the infrared are shown.

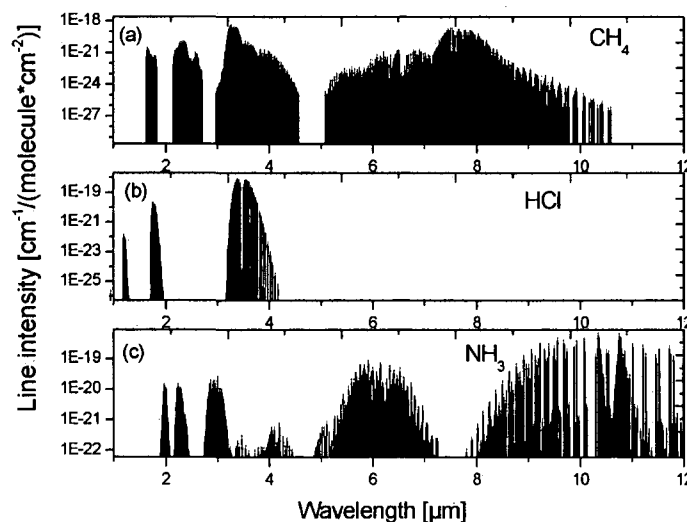


Fig. III.4-10: Line intensities of CH<sub>4</sub>, HCl and NH<sub>3</sub> in the infrared (Calculated for 296K from [4]).

Fig. III.4-10 to Fig. III.4-13 present some pictures of the VCSELs. A section of a wafer containing several 10 VCSELs is shown in Fig. III.4-11. The VCSEL is housed in a TO 46 case.

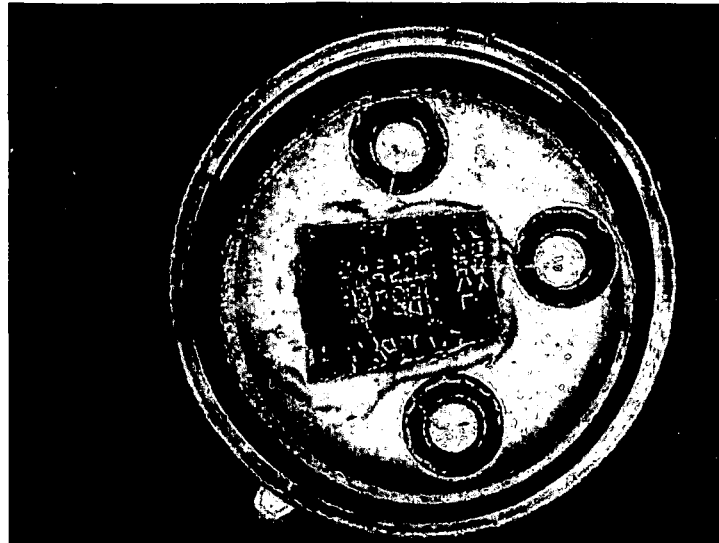


Fig. III.4-11: Section of a wafer containing several 10 1.5  $\mu\text{m}$  VCSELs three of which have been contacted.

Fig. III.4-12 shows a section of a 1680 nm VCSEL wafer under a microscope. The picture was taken during a research stay at Munich University of Technology).

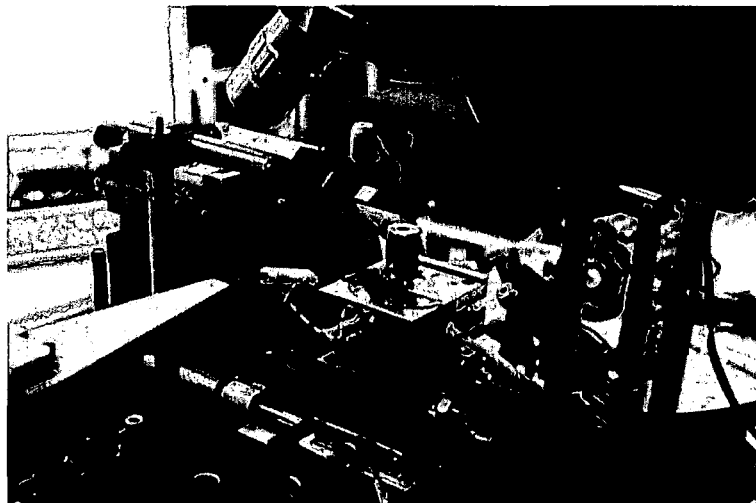


Fig. III.4-12: For the characterization of the VCSELs, a single laser was contacted directly on the chip under a microscope.

In Fig. III.4-13, a semi finished thermo stated mounting device for the VCSELs is shown.

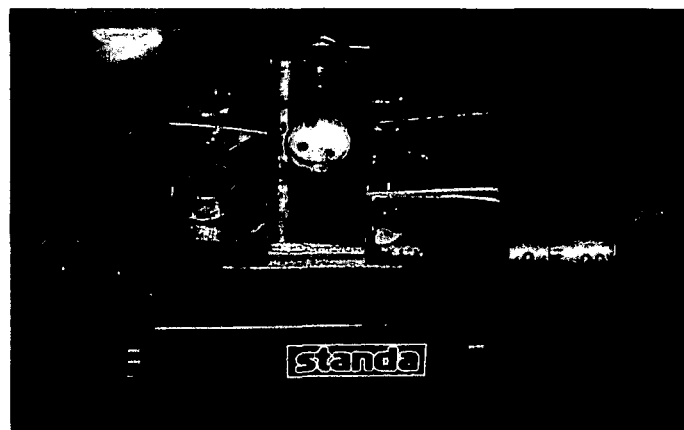


Fig. III.4-13: Half-finished mount for the VCSEL.

### III.5 Summary of all laser systems

The following table III.5-1 is a compilation of all laser systems that were used in this thesis. Two Fabry Perot type (i.e. neither DFB nor DBR structure) edge emitting lasers at 2.3 – 2.55  $\mu\text{m}$ , one quantum cascade laser at 11.4  $\mu\text{m}$  and several vertical-cavity surface emitting lasers at 761 nm and in the 1.54 to 2.015  $\mu\text{m}$  wavelength range were used.

Type	Wave-length	Detectable species	Detection limit (1 bar, 296K)	$I_{\text{thres}}$	Max. operating current	Tuning coefficient	Source
FP EEL	2.3 $\mu\text{m}$	CO, CH <sub>4</sub>	500 ppm*m	Approx. 40 mA (20°C)	200 mA	0.07 nm/mA, 0.2 nm/K	Dr. M. A. Maiorov, Dr. D. Z. Garbuzov and Dr. J. C. Connolly from Princeton Lightwave, Inc. (USA).
FP EEL	2.55 $\mu\text{m}$	H <sub>2</sub> O	50 ppm*m	Approx. 40 mA (20°C)	250 mA	0.07 nm/mA, 0.2 nm/K	Dr. M. A. Maiorov, Dr. D. Z. Garbuzov and Dr. J. C. Connolly from Princeton Lightwave, Inc. (USA).
QCL	11.4 $\mu\text{m}$	NH <sub>3</sub> , C <sub>2</sub> H <sub>4</sub>	2200ppm*m for C <sub>2</sub> H <sub>4</sub> , 220 ppm*m for NH <sub>3</sub>	Pulses (10 kA/cm <sup>2</sup> , 20 ns)	-	0.71 nm/K	Prof. Dr. Strasser and Dr. Solveig Anders from the Institut für Festkörperelektronik, Vienna University of Technology
VCSEL	0.761 $\mu\text{m}$	O <sub>2</sub>	~150000 ppm*m #	2.3 mA (23°C)	9.0 mA	0.29nm/mA, 0.05 nm/K,	CSEM SA (Centre Suisse d'Electronique et de Microtechnique), Switzerland
VCSEL	1.540 $\mu\text{m}$	NH <sub>3</sub>	~17500 ppm*m #	0.93 mA (20°C)	6.0 mA	0.11nm/mA, 0.11 nm/K	Prof. Amann, WSI (Walter Schottky Institute), Munich University of Technology, Germany
VCSEL	1.680 $\mu\text{m}$	CH <sub>4</sub>	~2200 ppm*m #	0.75 mA (15°C)	4.5 mA	0.86nm/mA, 0.11 nm/K	Prof. Amann, WSI (Walter Schottky Institute), Munich University of Technology, Germany
VCSEL	1.810 $\mu\text{m}$	H <sub>2</sub> O, HCl, CH <sub>4</sub>	~290 ppm*m, ~320 ppm*m, ~4400 ppm*m #	0.90 mA (30°C)	4.5 mA	0.9 nm/mA, 0.125 nm/K	Prof. Amann, WSI (Walter Schottky Institute), Munich University of Technology, Germany
VCSEL	1.690 $\mu\text{m}$ *	CH <sub>4</sub>	~2400 ppm*m #	0.48 mA (20°C)	4.0 mA	0.69 nm/mA, 0.11 nm/K	Prof. Amann, WSI (Walter Schottky Institute), Munich University of Technology, Germany
VCSEL	2.015 $\mu\text{m}$ *	CO <sub>2</sub>	~1500 ppm*m #	1.01 mA (20°C)	3.5 mA	0.7 nm/mA 0.14 nm/K	Prof. Amann, WSI (Walter Schottky Institute), Munich University of Technology, Germany

Table III.5-1: Summary of all laser systems used in this thesis ( $I_{\text{thres}}$  = threshold current, FP= Fabry Perot, EEL = edge emitting laser, QCL = quantum cascade laser, VCSEL = vertical-cavity surface-emitting laser).

\* Not described explicitly in chapter III.4; used in IV.6.

# Not determined experimentally; Calculated for a minimum detectable absorbance of 0.01.

## IV. Applications

### IV.1 *In-situ* species concentration measurements close to the surface of burning single fuel particles

#### Introduction

Combustion of coal and, to a lesser extent, biomass, contributes strongly to the production of thermal and electrical power, a status which is not likely to change in the near future. Among the array of methods for advanced (coal) combustion, that is low-cost at the least environmental impact, gasification [126] and fluidized bed combustion (FBC) [127] are two leading techniques. This work focuses on the latter.

The fluidized bed technology has gained wide acceptance in many fields of applications, e. g. catalytic cracking or mineral processing.

The appropriation of a nearly isothermal environment with high heat transfer efficiency to submerged objects and the fluid-like behavior which facilitates the mixing and handling of solids can also be exploited for combustion applications. A detailed assessment of criteria for and against fluidized bed firing is given in [128].

A fluidized bed combustor (FBC), pressurized or circulating, represents a multi-phase, hostile environment. Elevated pressures, high temperatures and soot, ash and bed material particles in the gas flow all pose severe problems for experimental investigations. Yet it is interesting to gather process parameters either for optimizing the performance or for controlling the process online [129]. Conventional techniques often use intrusive suction probes for species concentration determinations.

In this work, the authors deploy *in-situ* tunable diode laser spectroscopy to measure species concentrations directly in a laboratory fluidized bed combustor.

Two lasers are used to quantitatively determine the concentrations of carbon monoxide (CO), methane (CH<sub>4</sub>) and water (H<sub>2</sub>O) formed during pyrolysis, devolatilization and char combustion of a single fuel particle suspended in a laboratory-scale fluidized bed combustor.

Devolatilization and char combustion are the two consecutive phases in solid fuel combustion. Char is defined as the remaining substances from the fuel after all volatile matter has been removed. In the process of pyrolysis which takes place in the absence of oxygen the volatile components of the fuel are released.

#### Experimental

In this work, two edge emitting diode lasers were used for *in-situ* species concentration measurements of CO, CH<sub>4</sub> (2.3 μm) and H<sub>2</sub>O (2.55 μm).

*In-situ* species concentration measurements in multi phase, hostile environments were carried out. Some modelling work was also done (see later).

Details of the laser can be found in chapter III.1. This work was carried out in cooperation with Dr. M. A. Maiorov, Dr. D. Z. Garbuzov and Dr. J. C. Connolly from Princeton Lightwave, Inc. (USA) who provided the lasers.

The solid fuel combustion measurements were conducted in a laboratory-scale fluidized bed combustor depicted in Fig. IV.1-1.

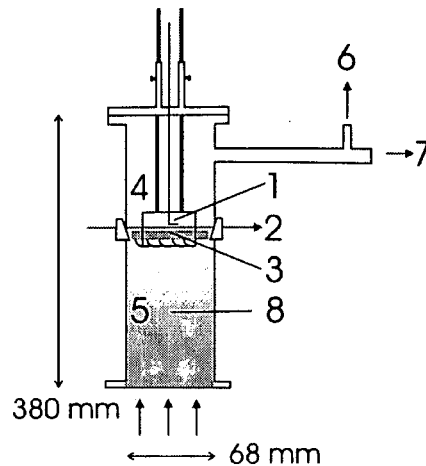


Fig. IV.1-1: Experimental setup. The laser beam passes directly above the particle surface to record species concentration histories of CO, CH<sub>4</sub> and H<sub>2</sub>O in the laboratory-scale fluidized bed combustor. (1: thermocouple; 2: laser beam; 3: single fuel particle; 4: freeboard section; 5: fluidized bed of sand; 6: to ex-situ determination; 7: exhaust; 8: thermocouple). See also Fig. IV.1-2 for a horizontal cross section.

The FBC consists of an upright tube of refractory steel (height 380 mm, inner diameter 68 mm) with a porous frit at the bottom and an exhaust duct 75 mm down from the top. The bed material was quartz sand (315-400  $\mu\text{m}$ ). The lid has got a downward extension of two rods with a basket made of wire at the bottom to hold a single fuel particle. The samples had the shape of a cylinder (diameter 4 and 6 mm) and a length of approximately 55 mm. The fuel samples were placed horizontally in the basket, their length was matched to the diameter of the fluidized bed combustor to ensure homogeneous conditions along the whole laser path length.

The fuel samples were attached to the basket by wire. The vertical position of the basket in the fluidized bed combustor was variable. At the position of the particle, about 170 mm from the bottom in the freeboard region of the bed, the fluidized bed combustor has got two opposite windows. They are wedged and made of fused silica. Wedged windows instead of parallel ones prevent optical interferences leading to fringes that limit the detection limit (see Fig II.3-5 in chapter II.3). The appearance of these unwanted fringes, known as the etalon effect, is caused by inadvertent multiple reflections between parallel optical surfaces. Because of the varying particle diameters, the distance is defined as and referred to as the spacing between the laser beam and the top of the particles. The fluidized bed combustor can be electrically heated up to 1000°C. Basically, a simple tube with a heated gas stream could also have been used. Instead, the freeboard region of a fluidized bed combustor was chosen. This was to demonstrate that laser measurements can be done in a multi-phase environment with sand particles passing the laser beam. The bed height is thus not relevant here.

Two mass flow controllers allowed the mixing of pressurized air and diluent (bottled N<sub>2</sub> in standard quality). Homogeneous mixing of the metered gas streams (+ 0.01 l/min) was ensured. The flow rate was always 20.0 l/min (at room temperature and atmospheric pressure). At temperatures of 700, 800 and 900°C, the corresponding superficial velocities were 29.97 cm/s, 33.05 cm/s and 36.13 cm/s respectively (uncertainty  $\pm$  0.02 cm/s). The superficial velocity is defined as the velocity of the gases in the fluidized bed combustor and was obtained by dividing the flow by the diameter of the reactor. There is only a slight influence on the volatile release rate due to convective heat transfer to the particle under varying superficial velocities.

The residence time inside the fluidized bed combustor for gases formed at the position of the solid particle as indicated in Fig. IV.1-1, approximately 170 mm above the distributor (entry), was between 600 and 800 ms. The temperature inside the fluidized bed combustor was measured in the particulate phase and approximately 10 mm above the solid particle using NiCrNi (type K) thermocouples. The time response of the upper thermocouple was

determined to be 2-3 s. The heat-up of the particles themselves was delayed by 14-24 s (at 900 and 700°C respectively) because of cooling effects by the metallic parts holding the particle. The oxygen partial pressure was varied between 5 and 21 kPa, the bed temperature between 700 and 1000°C. Three different fuels were investigated: pieces of bituminous coal and sticks of beech wood and fir wood. Supplemental data on the fuels obtained by proximate and ultimate analysis is provided in Table IV.1-1 (see later). Cylindrical rods of beech wood (4 mm and 6 mm diameter) and rectangular pieces (3\*5mm<sup>2</sup>) of fir wood were used. The samples were about 55 mm long. For the woods, the mass was 0.5 g, for the coal it was 1.0 g. For the coal, several small pieces aligned in a row in the basket were used. Obviously the surface to volume ratio is larger for chucks than for an individual stick. Heat-up is faster, too. For more comparable results, one could shape stick-like samples out of the coal. For sake of simplicity, this was not done in the scope of these experiments.

The swelling behavior of the different fuels and the fact that the fuel regresses with time were considered to be of minor importance here so that a constant distance of the laser beam to the surface could be assumed.

In the exhaust duct, approximately 300 mm from the lateral exit of the fluidized bed combustor (cf. Fig. IV.1-1), samples were continuously taken and analyzed in-line (cf. Fig. 2 in the introduction) for their content of CO, CO<sub>2</sub> and O<sub>2</sub> in addition to the *in-situ* measurements. A paramagnetic method was used for oxygen (absolute accuracy 0.1%). CO (range 0-6000 ppm, absolute accuracy 5 ppm) and CO<sub>2</sub> (absolute accuracy 0.1 %) were determined by a non-dispersive infrared technique. The delay introduced by the 7.5 m long plastic tube was 12 seconds. This delay was considered for data evaluation by shifting and superimposing the time scales correspondingly.

For the *in-situ* measurements of CO and CH<sub>4</sub>, a room temperature continuous wave InGaAsSb/AlGaAsSb quantum well ridge diode laser was used. The laser could be frequency-tuned around 2.3 μm in single mode emission and is described in detail elsewhere [111] – [112].

The laser was mounted in a heat sink. The temperature was held constant at 16.0 °C using a temperature controller (HTC 3000, Wavelength Electronics Inc.). The laser was tuned around 2.3 μm by providing a current ramp (0-160 mA) at 300 Hz. A laser diode precision current source (LDC 100, Profile Optische Systeme GmbH) providing 44mA/V was deployed. The laser light was collimated by an anti-reflection coated planoconvex ZnSe lens (focal length 5 mm).

A multi pass setup was used to increase the sensitivity. This is shown in Fig. IV.1-2.

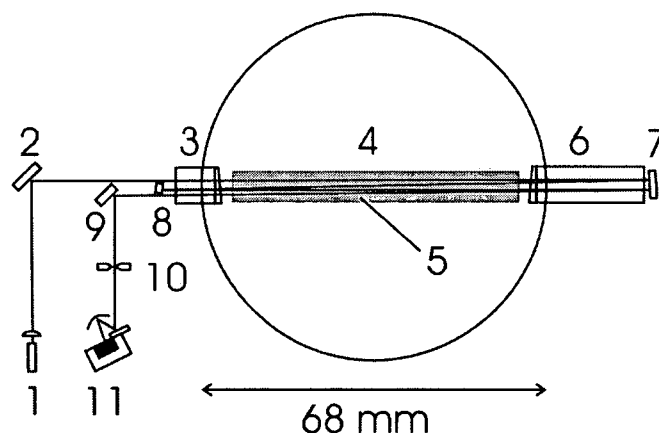


Fig. IV.1-2: Cross section of the laboratory-scale fluidized bed combustor showing the alignment of the laser beam. The beam passes above the sample four times in a horizontal alignment. A focusing mirror is placed before the detector, an iris is used to prevent the detector from being saturated by emissions of the flame and thermal radiation. (1: InGaAsSb/AlGaAsSb diode laser and planoconvex lens; 2: mirror; 3: wedged window; 4: FBC; 5: single fuel particle cylinder; 6: wedged window; 7, 8, 9: mirror; 10: iris; 11: detector with focusing mirror). See also Fig. IV.1-1 for a vertical cross section.

The laser beam was sent through the fluidized bed combustor four times. This resulted in a total path length of approximately 0.28 m. The beams were aligned horizontally with the least lateral distance possible. The maximum beam diameter was determined to be approximately 3 mm. Since the aperture of the detector was smaller than the beam diameter and since we used two irises in order to prevent the detector from being saturated by the emissions from the flame, the probed volume was smaller than it would result from the beam diameter.

Prior to the measurements, the laser emission characteristics with respect to single longitudinal mode emission were determined using an FTIR spectrometer (MIDAC Illuminator). An InSb semiconductor detector (EG&G Judson Technologies) was used in conjunction with a homemade amplifier and a focusing mirror. An iris was used to reduce the emissions from the flame (which would otherwise have lead to saturation of the detector). The detector signal was digitized using a data acquisition board (SignaTec PDA12A). Calibration over the entire temperature range was done using bottled gases of CO (10.0% in N<sub>2</sub>) and CH<sub>4</sub> (99.5%) The calibration was necessary to select suitable, strong absorption lines of CH<sub>4</sub> and CO. The temperature dependence of the line strength S(T) had to be recorded in order to correct the values for the actual temperature above the particle due to the flame.

The lower detection limit was 0.2 vol% (500 ppm\*m) for both species.

The experimental results obtained for the bituminous coal were compared to a detailed chemical kinetic model.

### Modeling

For the calculations a modified version of a model for a single fuel particle burning in a laboratory-scale fluidised bed [130] is used. In this work only the reactions ongoing in the freeboard downstream the fuel particle are considered. The freeboard is considered to be a plug flow reactor. The temperature profile within the freeboard is taken from measurements and given as input to the calculations. During devolatilization and char combustion respectively the measured release rates of carbon were applied for the model. All species were assumed to be released in proportion to the carbon.

In the pertinent literature very little is known about the composition of the volatiles. There are only a few devolatilization models describing the composition of the yields of volatiles, among those of Merrick [131], Loison and Chauvin [132], van den Bleek et al. [133], and Niksa and Kerstein [134]. Due to the easy implementation the model of van den Bleek et al. [133] was modified. For the calculation of the composition of the volatiles the following assumptions were made:

- all volatile S becomes H<sub>2</sub>S;
- all volatile N becomes NH<sub>3</sub> or HCN, the split between the two being characteristic of the fuel and the devolatilization conditions; for the bituminous coal a HCN/NH<sub>3</sub> ratio of 3 is assumed.
- 75 % of volatile H becomes CH<sub>4</sub>: if there is not enough C available, C is the limiting reactant, and all volatile C becomes CH<sub>4</sub>;
- all remaining volatile C, if any, becomes CO: if there is not enough O available, O is the limiting reactant, and all volatile O becomes CO;
- all remaining volatile O, if any, becomes H<sub>2</sub>O;
- all remaining volatile C, if any, becomes C<sub>2</sub>H<sub>4</sub>;
- all remaining volatile H, if any, becomes H<sub>2</sub>: if there is no H available, H is the limiting reactant, and if there was enough volatile O available, all volatile H becomes H<sub>2</sub>O;
- all remaining volatile O becomes O<sub>2</sub>.
- no tar is considered.

During char combustion it was assumed that the primary products are CO and H<sub>2</sub>O. Assuming a H/C ratio of 1 in the char H<sub>2</sub>O was released proportionally to the carbon. This ratio was varied within a reasonable range of 0.5 to 2 without any significant effect on the predicted emissions.

## Results and discussion

Figure IV.1-3 illustrates how the absorbance trace is converted into a concentration history; The absorbance is a function of temperature.

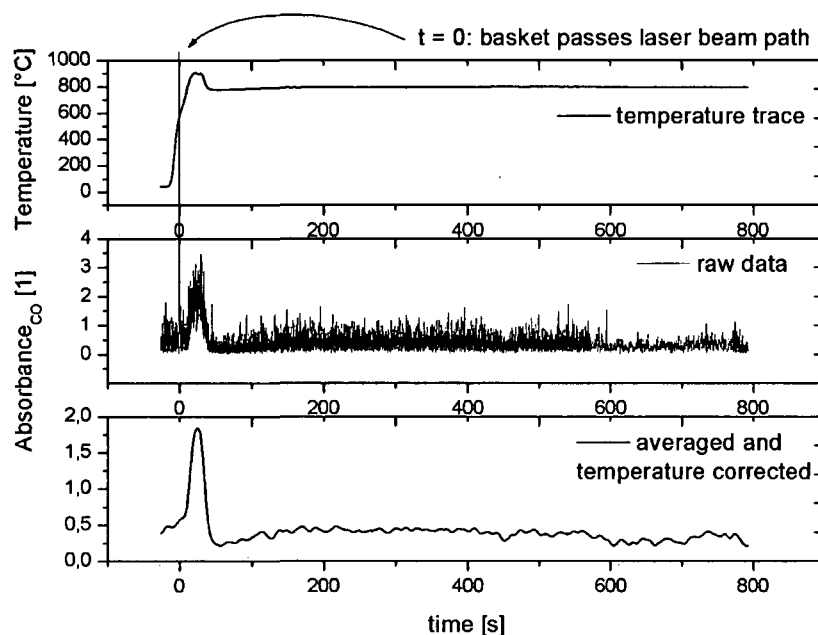


Fig. IV.1-3: Determination of the concentration from the raw absorbance data, depicted for CO (2.3  $\mu\text{m}$  laser). (a) shows the temperature 10 mm above the burning particle at the position of the laser beam. (b) gives the raw data in terms of the absorbance. In (c), the concentration of CO is shown. Depicted is the averaged concentration trace which has been temperature corrected (the absorbance decreases with temperature). The tuning frequency of the laser was 300 Hz.

In Fig. IV.1-3 (a), the temperature above the coal particles at the height of the traversing laser beam (i. e. 10 mm above the coal) is shown.

The relatively slow rise of the temperature curve is due to cooling by the basket and the two supporting metallic rods. One can see that the flame temperature exceeds the bed temperature by approximately 100°C.

Fig. IV.1-3 shows the data processing of a test run. In Fig. IV.1-3 (a), the temperature above the particle is shown. In Fig. IV.1-3 (b), the measured absorbance of CO has been plotted as a function of time.

The insertion process (which itself takes 1–2 s) provides a comfortable means of determining the start of the experiment. As the basket with the fuel sample traverses the laser beam path shortly before reaching its final position, the absorbance goes up sharply (no transmission). One can see that the absorbance is very noisy.

Besides the resonant absorption of laser light at the wavelengths of the molecular transitions, the transmission through the FBC fluctuates strongly over time. The hot interior of the FBC produces blackbody radiation. According to Planck's law, the peak intensity location at 800°C is at 2.70  $\mu\text{m}$  with the total intensity being approximately 24 kW/m<sup>2</sup>. The response curve of the detector ranges from 1 to 10  $\mu\text{m}$ . The fraction of radiation contained in this domain is



approximately 0.93. The fraction of radiation in the visible wavelength range (0.4 to 0.7  $\mu\text{m}$ ) is less  $10^{-5}$ . This explains the constant offset by the background radiation.

In addition, the emissions from the flame in the infrared region also fall onto the detector.

These preceding two effects increase the light intensity.

Several effects also reduce the transmission. Beam steering is the effect that (temperature gradients that translate into) refractive index gradients act as a lens for the probing laser beam and make it change its position. As a result, the laser light intensity hitting the detector will fluctuate. Also, solid particles passing the beam path will partly obstruct the laser and reduce the transmission. Sand particles that reach the freeboard region of the FBC where the experiments were conducted hence also cause fluctuations of the transmission.

It was observed that during combustion, especially under reduced oxygen partial pressures, soot caused blocking of the windows. This layer of soot brought the transmission several times close to zero. The minimum in transmission coincides with the maximum devolatilization rate. Subsequently, the slow burning of the soot in the hot gas stream reconstituted the full transmission of the windows.

All these effects are non-correlated and cause the laser light intensity falling onto the detector to vary vigorously.

As pointed out in chapter II.3 (see Fig. II.3-3), the laser has to tune over an entire absorption feature faster than the timescale on which experimental noise (flickering of the flame, sand particles passing the beam) occurs.

The reason why this approach works is that all major non-resonant effects described here do not show a strong dependence on the wavelength, but the absorption peaks do.

At scan rates of 300 Hz as used in these experiments, this requirement is not fulfilled. Therefore, as the beam gets deflected from the detector or partially blocked, an absorption value that is too high is obtained. However, by averaging the raw data (Fig. IV.1-3 (b)), one gets a smooth curve (Fig. IV.1-3 (c)). In order to directly obtain quantitative results without the need for averaging, it is necessary to tune over the selected absorption feature(s) faster than the time scale of the fluctuations. In Fig IV.1-3 (b), the shortest spikes in the transmission are on the order of 1 ms.

They stem from beam steering effects and solid particles passing the beam path. By scanning the laser wavelength over the absorption line with repetition rates faster than 1 kHz, the system seemingly comes to a standstill. All non-resonant effects only manifest themselves by a constant attenuation of the laser light plus an offset. Both can easily be subtracted as shown above. VCSELs possess the ability of extremely fast wavelength modulation (up to 5 MHz as demonstrated in this thesis, see chapter IV.4). Therefore, these devices are apt for probing extremely transient environments, for instance particle laden gas flows as encountered in this work.

The concentration history of CO measured *in-situ* closely above the coal as depicted in Fig. IV.3-1(c) has also been temperature corrected to display correct values.

Before devolatilization ended, flame extinction was observed. The lower detection limit at 800°C was determined to be 0.2 vol% (approximately 500 ppm\*m) for CO and CH<sub>4</sub>. It could have been improved by using a sensitive detection technique instead of simple absorption spectroscopy, the most common ones being wavelength modulation spectroscopy (WMS) and frequency modulation spectroscopy (FMS) [29] (see chapter II.3). At lower temperatures approaching room temperature, the detection limit improves due to the fact that the intensity of the selected absorption lines rises.

## Experimental findings

### 2.3 $\mu\text{m}$ laser for CO and CH<sub>4</sub>

CO and CH<sub>4</sub> species concentration measurements were conducted close to the surface of three different fuels in the freeboard of a fluidized bed combustor. Sand particles were passing the beam path.

Note that in absorption spectroscopy, non-resonant attenuation effects of the laser beam as caused by these grains of sand can only be discerned from molecular absorption by tuning the laser wavelength over an absorption feature.

Beech wood, fir wood and bituminous coal were investigated. All measurements inside the fluidized bed combustor were repeated at least three times to check for the reproducibility of the results. The temperature profile over the fluidized bed combustor was studied prior to the experiments and found to be homogeneous. Tunable diode laser absorption spectroscopy is based on line-of-sight absorption of targeted rovibrational transitions. The measurements present an average of the concentration profile over the entire pathway. For the current studies, however, this does not constitute a serious problem. The cylindrical sample (55 mm in length) almost filled the whole length of the fluidized bed combustor (68 mm) and the laser probe beam passed it in a parallel direction. The lower detection limit for the measurements was about 0.2 vol% (500 ppm\*m). This figure was derived by evaluating the noise in the base line signal according to the 3  $\sigma$  criterion ( $\sigma$ ... standard deviation). By deploying sensitive detection techniques (e.g. modulation spectroscopy [29]) or switching to absorption lines other than those originating from combination and overtone bands, the sensitivity could be significantly lowered. However, for the current investigations 0.2 vol% was considered sufficient.

The temperature close to the laser beam path above the particle was measured to correct the measured absorbances for the temperature. The line strength of the selected transitions for CO and CH<sub>4</sub> decreased with rising temperature. Therefore, if the calibrated values for the absorbances at the bed temperature had been used, the alleged concentration values would have been too low. As shown for a typical experiment in Fig. IV.1-4, the temperature above the solid fuel particle was found to exceed the bed temperature by up to 200 °C.

Since the thermocouple used for this was firmly attached to the basket, its position relative to the burning particle never changed. The particles themselves were attached by wire to prevent them from changing their position with respect to the laser beam. Time zero is defined by the basket passing through the laser beam when the fuel particle is introduced into the reactor. Since the heat-up and release of volatiles already start during this insertion process (which itself takes 1-2 seconds), the temperature curve starts rising before  $t = 0$ . However, this definition gives an accurate starting point that is not readily available with conventional methods. With an inner diameter of the fluidized bed combustor of 68 mm and the zone of volatile release being approximately 10 times 55 mm in cross section, the dilution of the species can be estimated to be 1:7.

In Fig. IV.1-4 typical results for the combustion of beech wood are presented. The dimensions of the wood were 55 mm in length, 4 mm in diameter and 0.5 g in mass. The bed temperature was 800°C, the oxygen partial pressure 10 kPa. The distance of the laser beam from the particle surface was 10 mm. For all measurements, CO, CO<sub>2</sub> and O<sub>2</sub> were also determined after the exhaust duct. Fig. IV.1-4 presents *in-situ* data on CO and CH<sub>4</sub>, the temperature and CO<sub>2</sub> (determined *ex-situ*). Because of the definition of time zero, the temperature has already risen approximately 300 °C before the wood reaches its final position inside the fluidized bed combustor. One can see that devolatilization lasts about 25 seconds. Char combustion takes more than 140 seconds to complete.

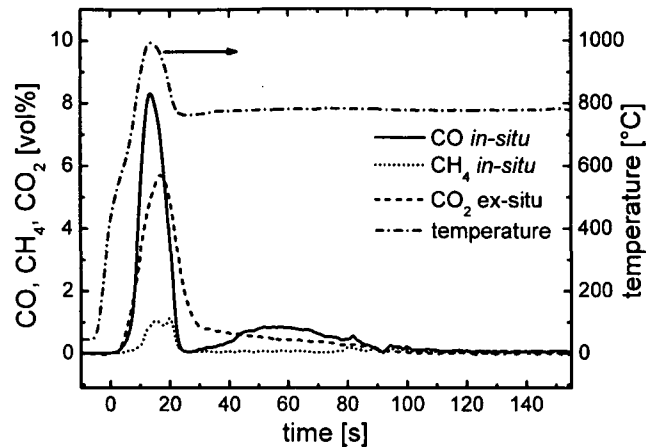


Fig. IV.1-4: *In-situ* species concentration measurements during carbon conversion of biomass. Experimental parameters: Bed temperature 800°C, oxygen partial pressure 15 kPa, distance from the surface 10 mm, 0.5 g beech wood,  $\phi$  4 mm.

During devolatilization, CO and CH<sub>4</sub> reach their peak values of 8.1 and 1.1 vol% respectively before CO<sub>2</sub>. The concentration of CO<sub>2</sub> measured *ex-situ* does not exceed 5.5%. The temperature curve is influenced by the two initially cold metallic rods holding the particle in the basket. The flame temperature can be seen to exceed the bed temperature by 200°C. The relatively slow rise of the temperature curve is due to cooling by the basket and the two supporting metallic rods. Before devolatilization ended, flame extinction was observed.

### Effect of oxygen

In Fig. IV.1-5 the influence of changing oxygen partial pressures is shown. The bed temperature was 800°C, the distance of the particle 155 mm from the bottom of the fluidized bed combustor. The distance of the laser beam from the surface was 10 mm (uncertainty  $\pm$  2 mm), the path length of the laser beam 0.28 m (4 horizontally aligned passes). Flow rates of the gas through the fluidized bed combustor were 20.0 l/min (at room temperature and atmospheric pressure, uncertainty 0.01 l/min). 0.5 g of beech wood (a cylindrical rod with 4 mm in diameter and 55 mm in length) was used as fuel. The oxygen partial pressure was varied between 5 and 20 kPa by diluting air with nitrogen. Four test points were measured. Fig. IV.1-5 shows that with decreasing amount of oxygen, the devolatilization lasts longer (20-25 seconds in total) and yields more CO. Peak values are 5.5 and 9.4 vol% for 20 and 5 vol% of oxygen respectively. This behavior is also observed during char combustion but not as markedly expressed as during devolatilization.

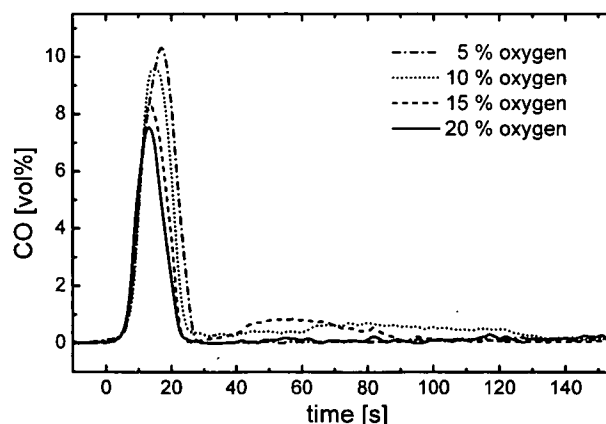


Fig. IV.1-5: CO measured *in-situ*, variation of the oxygen partial pressure. Experimental parameters: Bed temperature 800°C, distance from the surface 10 mm, 0.5 g beech wood,  $\phi$  4 mm.

When the oxygen content is reduced from 15 to 10 vol%, the char combustion phase almost lasts twice as long. For 5 vol% oxygen, char combustion is so slow that it is hardly recognizable by probing the generated CO with the sensitivity deployed. It is well known from the literature that higher oxygen partial pressures lead to higher combustion rates and higher concentrations of radicals [135]. Our measurements are consistent with these data.

### Effect of temperature

Fig. IV.1-6 outlines the influence the temperature has got on the CO formation characteristics. A fluidized bed reactor was chosen for the experiments to decouple the temperature from the actual burning process. All other parameters were kept constant (10 vol% oxygen, beech wood of the same dimensions in the same relative position). The higher the temperature, the faster the concentration of CO formed by devolatilization rises. For an ambient temperature of 700°C, devolatilization lasts from approximately 9 to 35 seconds after inserting the particle. For 900°C, the heat transfer from the fluidized bed is evidently faster. Devolatilization begins almost instantaneously and lasts for no longer than 20 seconds. The peak concentrations of CO reach 10%. Higher temperatures also accelerate char combustion.

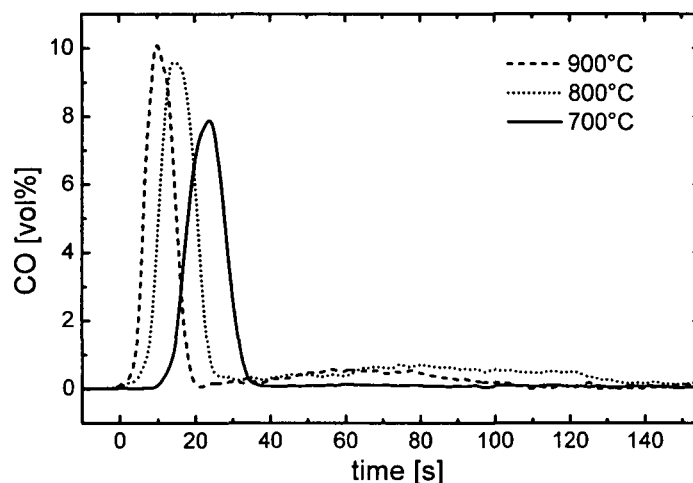


Fig. IV.1-6: CO measured *in-situ*, variation of the bed temperature. Experimental parameters: Oxygen partial pressure 10 kPa, distance from the surface 10 mm, 0.5 g beech wood,  $\phi$  4 mm.

### Effect of residence time and distance from the particle

In Fig. IV.1-7 results from the variation of the distance laser beam to particle surface are shown. Again 0.5 g of beech wood at 800°C and 10 vol% oxygen were used. Combustion takes place under diffusion control. One can see that the closer to the particle the measurement is conducted, the higher the concentration of the measured CO gets. This observation is obvious. For a distance of 4 mm, the peak concentration during the devolatilization phase is about 10%. When being measured 31 mm away from the surface, the CO has been diluted and converted by chemical reactions down to 3%. Note that for a distance greater than 20 mm, the trace of CO during char combustion cannot be resolved any more. These results are consistent with the curves presented in Fig. IV.1-5 and IV.1-6. For 700°C and 20 vol% oxygen (both at a distance of 10 mm), the CO curve cannot be resolved well any more. At the high amount of oxygen, the char reacts to CO<sub>2</sub> rather than CO. At 700°C, the reaction rate is too low to produce large amounts of CO.

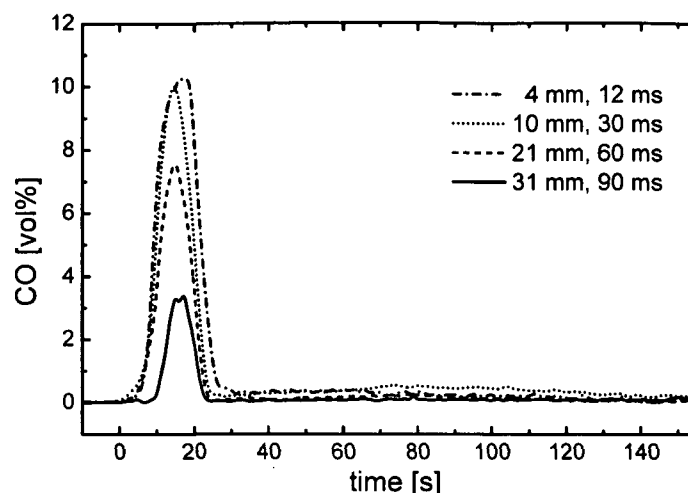


Fig.IV.1-7: CO measured *in-situ*, variation of the height/residence time. Experimental parameters: Bed temperature 800°C, oxygen partial pressure 10 kPa, 0.5 g beech wood,  $\phi$  4 mm.

An interesting question is the residence time of the CO evolving from the particles. To put it another way, the key question is how close the laser beam can approach the formation of CO at the surface before it is converted in consecutive reactions. The initial velocity was found to be well below the superficial velocity.

With the superficial velocity being roughly 0.30 m/s, the gases depart from the surface by 0.30 m in 1 second in a first approximation. At these flow rates, a distance of the laser beam to the surface of 31 mm corresponds to 90 ms, 21 mm correspond to 60 ms, 10 mm to 30 ms and a distance of 4 mm to 12 ms after the formation. The biggest uncertainty is the actual position of the laser beam relative to the particle with  $\pm 2$  mm. Therefore, the above mentioned times are affected by an uncertainty of 5 ms. At 700, 800 and 900°C, the calculated superficial velocities were 29.97 cm/s, 33.05 cm/s and 36.13 cm/s for 700°C, 800°C and 900°C respectively, uncertainty  $\pm 0.02$  cm/s).

By approaching the surface that close, the kinetics of primary and secondary devolatilization products can be investigated.

An interesting issue during char combustion is the CO to CO<sub>2</sub> ratio at the surface. A lot of discrepancy exists in the literature. For example, [136] claims that CO is the only primary carbonaceous product, whereas [137] found that CO<sub>2</sub> outweighed CO as the primary product in its studies. [138] quotes [CO]/[CO<sub>2</sub>] as 0.38 for the conditions encountered in our studies.

### Effect of particle size

The influence of the particle size was investigated using sticks of beech wood with 4 mm and 6 mm in diameter, both approximately 55 mm in length. In contrast to findings in the pertinent literature, it was found that the particle size does influence pyrolysis characteristics [139]. Pyrolysis-like conditions are encountered during devolatilization. The larger particles produce significantly less CO during char combustion, the peak values during devolatilization are higher. As expected, both the devolatilization and char combustion time increase with the size of the fuel particle. The heat-up process is prolonged. Because of the larger surface, the carbon release rates rise significantly. This behavior has been observed in the literature [140] and could be verified.

### Effect of fuel type

Fig. IV.1-8 presents a compilation of results for all fuels investigated. The CO concentration histories are compared. The bed temperature was 800°C, the oxygen partial pressure 10 kPa, the distance of the laser beam from the particle surface 10 mm. The mass was 0.5 g for beech wood and fir wood and 1.0 g for the coal. The biomass was investigated in the shape of 55 mm long rods.

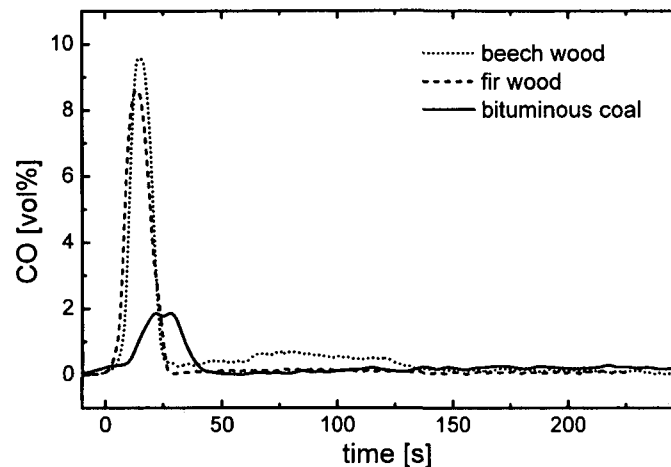


Fig.IV.1-8: CO measured *in-situ* for different fuels: Experimental parameters: Bed temperature 800°C, oxygen partial pressure 10 kPa, distance from the surface 10 mm. The mass of the bituminous coal was 1.0 g, for beech wood and fir wood it was 0.5 g.

The coal sample consisted of 4 lumps aligned in a row parallel to the laser beam. The two biomass fuels were found to behave very similarly during devolatilization. During char combustion beech wood emits significantly more CO than fir wood. This observation implies that the CO/CO<sub>2</sub> ratio at the surface of beech wood must be higher than for fir wood since all carbon was found to have reacted. It is assumed in a first approximation that the CO/CO<sub>2</sub> ratio is about five times higher for beech wood than for fir wood. Devolatilization of char starts later and lasts longer than devolatilization of the wood samples. The measured peak concentrations of CO were 2% for coal and approximately 10% for the biomass. The measured CO values are four times higher for biomass than for coal. The elemental composition of the fuels is presented in table IV.1-1.

		Beech wood	Fir wood	Bituminous coal
<b>Proximate analysis</b>				
Volatile matter	[wt%]	80.7	80.8	30.6
Moisture	[wt%]	6.8	6.8	1.6
Ash content	[wt%]	0.4	0.2	15.2
Fixed carbon	[wt%]	12.1	12.2	52.6
<b>Ultimate analysis</b>				
(Water, ash free)				
Carbon	[wt%]	46.4	45.7	66.0
Hydrogen	[wt%]	6.3	6.3	4.1
Nitrogen	[wt%]	0.0	0.0	1.3
Oxygen (by diff.)	[wt%]	47.3	48.0	28.6

Table IV.1-1: Results from proximate and ultimate analysis of the fuels under investigation.

### Comparison of *in-situ* to conventionally obtained results

Depicted in Fig. IV.1-9 are the concentration histories of CO measured *in-situ* by laser spectroscopy and analyzed conventionally from the exhaust gas by a commercial gas analyser deploying non-dispersive infrared spectroscopy. Experimental conditions were 15 kPa oxygen, 800°C bed temperature, 0.5 g beech wood and a distance of 10 mm. One can see that the conventional method generally yields higher concentrations during char combustion and lower values during devolatilization compared to the *in-situ* method. From the relative height of the peaks it can be inferred that this effect is no artifact caused by dilution. The dilution factor was estimated to be approximately 7. This figure was derived by using the combustor's cross section and the cross sectional area where the volatile release occurred.

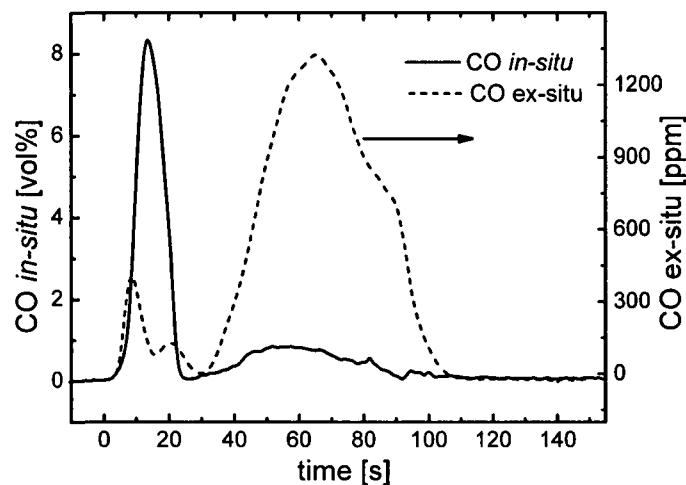


Fig.IV.1-9: Comparison of the CO concentration histories measured *in-situ* and in the exhaust gas. Experimental parameters: Bed temperature 800°C, oxygen partial pressure 15 kPa, distance of the laser from the surface 10 mm. Note that the conversion of CO is more effective during devolatilization. 0.5 g of beech wood were used.

The measurements were repeated several times to check for the reproducibility. Obviously the degradation mechanism of CO to CO<sub>2</sub> works more efficiently during devolatilization due to the high content in volatiles. One can also see that diffusion causes some broadening of the conventionally determined concentration profile.

### 2.55 $\mu\text{m}$ laser for water vapor

In Fig. IV.1-10 (a) the concentration history of water vapor 10 mm above the fuel particles (measured at 2.55  $\mu\text{m}$ ) is shown for all three fuels. In Fig. IV.1-10 (b) tests with beech wood (a 55 mm long cylindrical particle, 3 mm diameter, mass 0.25 g) are shown. The gas flow was 20.0 l/min at room temperature or 72.5 l/min at 800°C inside the reactor. For the combustion test, pure air was used, the oxygen partial pressure being 20 kPa. For the pyrolysis test, an identical sample was exposed to a pure nitrogen gas flow. After 90s, the gas flow was changed to 10 % oxygen (also 20 l/min). This subsequent combustion is shown by the third (the lowest) curve. There is no double peak observable. It can therefore be assumed that the first peak in the combustion test stems from drying, whereas the second results from chemical reactions forming water. In [141] the effect of drying, devolatilization and char combustion was investigated by intra-particle temperatures.

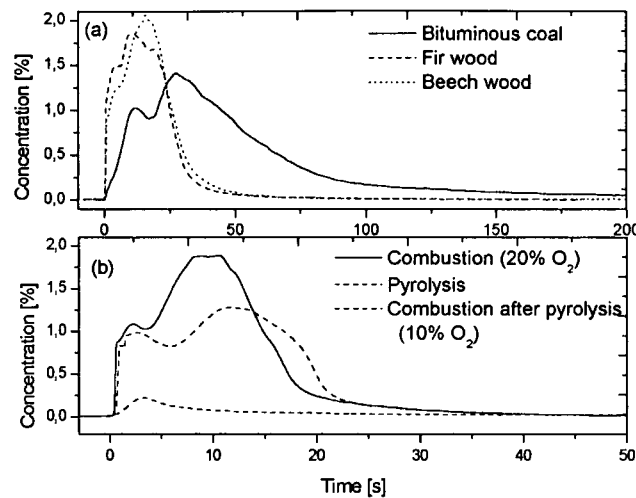


Fig. IV.1-10: Experimental data of a typical test run with the  $2.55 \mu\text{m}$   $\text{H}_2\text{O}$  laser (bed temperature  $800^\circ\text{C}$ , oxygen partial pressure  $10\text{kPa}$ , distance  $10 \text{ mm}$ ). (a) shows the  $\text{H}_2\text{O}$  concentration histories of the different fuels. The double peak might stem from drying and subsequent water generation. (b) shows two fuel samples. One (solid curve) was burned right away. The second (dashed curves) was first pyrolyzed and subsequently burned in oxygen (lowest curve, no double peak).

The lower detection limit for  $\text{H}_2\text{O}$  at  $800^\circ\text{C}$  was  $0.02\%$  for a path length of  $0.28\text{m}$ . This corresponds to  $50 \text{ ppm}\cdot\text{m}$ . Since the absorbance of the selected peak also decreases from room temperature to  $800^\circ\text{C}$ , the detection limit at ambient conditions would also be higher.

### Comparison of experimental results and modeling

In Fig. IV.1-11, the concentration histories of the main species, i.e.  $\text{CH}_4$ ,  $\text{CO}$ , and  $\text{CO}_2$ , are shown during the first  $100 \text{ s}$  of bituminous coal combustion (experimental parameters: bed temperature  $1073 \text{ K}$ ,  $10\text{vol}\%$  oxygen. The distance of the laser beam to the surface of the particles was  $10 \text{ mm}$ ). *In-situ* measurements demonstrate that  $\text{CO}$  is the main volatile species. Also significant amounts of  $\text{CH}_4$  are released during devolatilization, especially during the later stages the proportion  $\text{CH}_4$  gains equivalent importance compared to  $\text{CO}$ . However, since the measured  $\text{CH}_4$  was close to the detection limit, no reliable conclusions can be drawn.

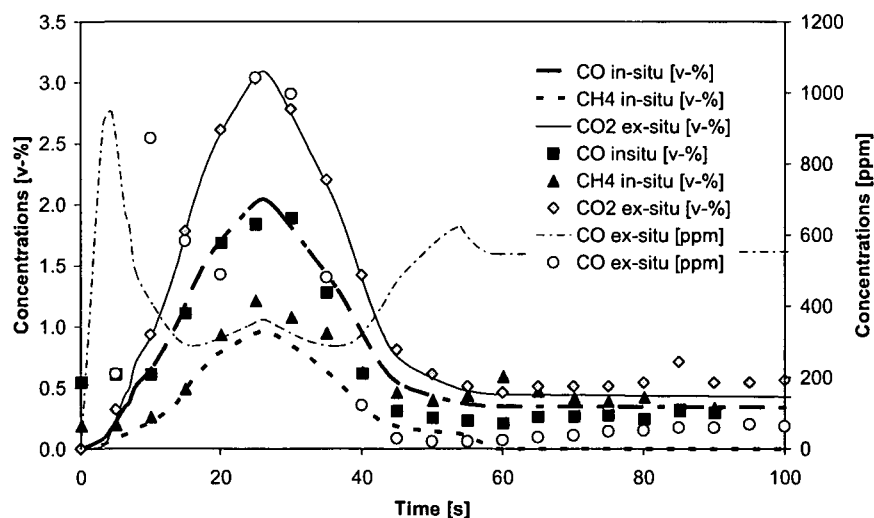


Fig. IV.1-11: Measured and calculated concentration histories during bituminous coal combustion, bed temperature  $1073 \text{ K}$ ,  $10\text{vol}\%$  oxygen. The distance of the laser beam to the surface of the particles was  $10 \text{ mm}$ .



The simple model for the volatile composition applied here, captures well the measured release of the main volatile species, though it does not account for any change of the composition during the devolatilization time. The model also well predicts the conversion of the volatiles in the freeboard. While  $\text{CH}_4$  is converted completely, up to 1000 ppm CO can be found in the off-gas of the laboratory scale fluidized bed. The CO emissions increase rather steeply at the beginning of devolatilization, decrease then to a minimum concentration of 500 ppm after 20 s and increases again afterwards. The model predicts this general behavior correctly, however with an earlier maximum and minimum concentration. After the minimum CO emissions the model fails in predicting the rapid concentration increase. From the modeling results we found that the reason for this observed behavior is the radical mechanism of CO oxidation. Higher CO concentrations lead to higher radical concentrations during ignition and thus to a higher conversion rate of CO to  $\text{CO}_2$ . For this reason CO emissions are lower for high CO release rates and vice versa. The reason for the significant deviations between predictions and measured CO emissions after the minimum was passed, may be the change in volatile composition in the later stages of devolatilization. As stated before, the *in-situ* measurements indicate that the  $\text{CH}_4$  content in the volatiles increases with devolatilization time, while the CO content decreases. By taking the volatile composition from the *in-situ* measurements, fine agreement between the measured and calculated emissions of CO as shown in Fig. IV.1-11 was found. This has also significant impacts on the nitrogen chemistry during devolatilization, as is known that CO increases the selectivity of HCN and  $\text{NH}_3$  oxidation, while  $\text{CH}_4$  favors  $\text{N}_2\text{O}$  formation especially from HCN [142]. Thus, knowledge on the volatile composition versus devolatilization time is significant for the prediction of emissions in solid fuel combustion.

After 55 s devolatilization ends, defined by a minimum in CO emission as shown in Wartha [143].

The following Fig. IV.1-12 to IV.1-14 graphically depict measured and calculated results. Since the model was developed for coal, it could not be applied to the biomass test runs. In Fig. IV.1-12 and IV.1-13, concentration profiles are plotted as a function of time for two given times (viz. 10 and 24 seconds). Fig. IV.1-14 presents concentration histories of the major species as a function of time at a fixed position (10 mm above the fuel particle).

Fig. IV.1-12 shows the concentration profiles of  $\text{CH}_4$ , CO,  $\text{CO}_2$ , O, H, and OH versus height above the fuel particle after 10 s. 10 s after the insertion process of the sample, the particle is in the devolatilization phase. The symbols indicate measured values (Experimental parameters: bed temperature 1073 K, 10vol% oxygen). All measured data ( $\text{CO}_2$  and  $\text{O}_2$  from ex-situ measurements,  $\text{CH}_4$  and CO *in-situ*) agree well with the model predictions.

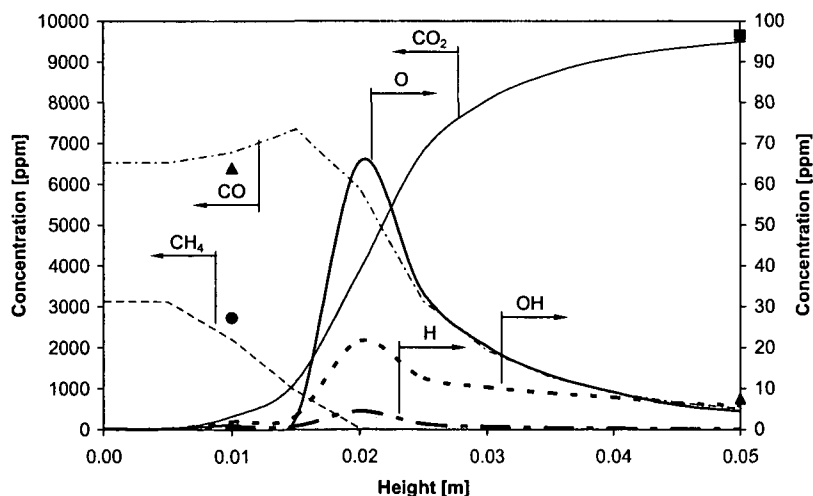


Figure IV.1-12: Concentration profiles of  $\text{CH}_4$ , CO,  $\text{CO}_2$ , O, H, and OH versus height above the fuel particle after 10 s. Symbols indicate measured values:  $\blacktriangle$  CO,  $\bullet$   $\text{CH}_4$ ,  $\blacksquare$   $\text{CO}_2$ ; bed temperature 1073 K, 10vol% oxygen.

Fig. IV.1-13 shows concentration profiles of  $\text{CH}_4$ ,  $\text{CO}$ ,  $\text{CO}_2$ ,  $\text{O}$ ,  $\text{H}$ , and  $\text{OH}$  versus height above the fuel particle 24 s after the insertion process. The symbols indicate measured values (Experimental parameters: bed temperature 1073 K, 10vol% oxygen). As in Fig. IV.1-12, measured and calculated data for  $\text{CO}$ ,  $\text{CO}_2$ ,  $\text{O}_2$  and  $\text{CH}_4$  agree well with each other. The simple devolatilization model applied here can therefore well describe the release rates of  $\text{CH}_4$  and  $\text{CO}$  from the coal.

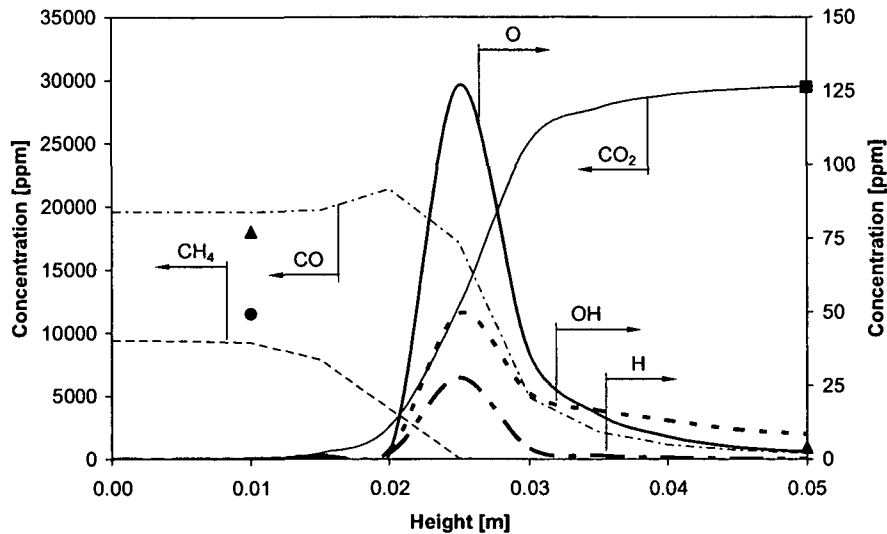


Figure IV.1-13: Concentration profiles of  $\text{CH}_4$ ,  $\text{CO}$ ,  $\text{CO}_2$ ,  $\text{O}$ ,  $\text{H}$ , and  $\text{OH}$  versus height above the fuel particle after 24 s. Symbols indicate measured values:  $\blacktriangle$   $\text{CO}$ ,  $\bullet$   $\text{CH}_4$ ,  $\blacksquare$   $\text{CO}_2$ ; bed temperature 1073 K, 10vol% oxygen.

Fig. IV.1-14 depicts measured and calculated concentration histories during bituminous coal combustion at 10 mm above the fuel particle (Experimental parameters: bed temperature 1073 K, 10vol% oxygen). The volatile composition is taken from *in-situ* measurements. The lines represent the model, the symbols give measured concentration data. One can see adequate resemblance. Only  $\text{CO}$  is overestimated in the model by a factor of three during char combustion. Devolatilization is predicted too early. All other species can be predicted correctly by the model.

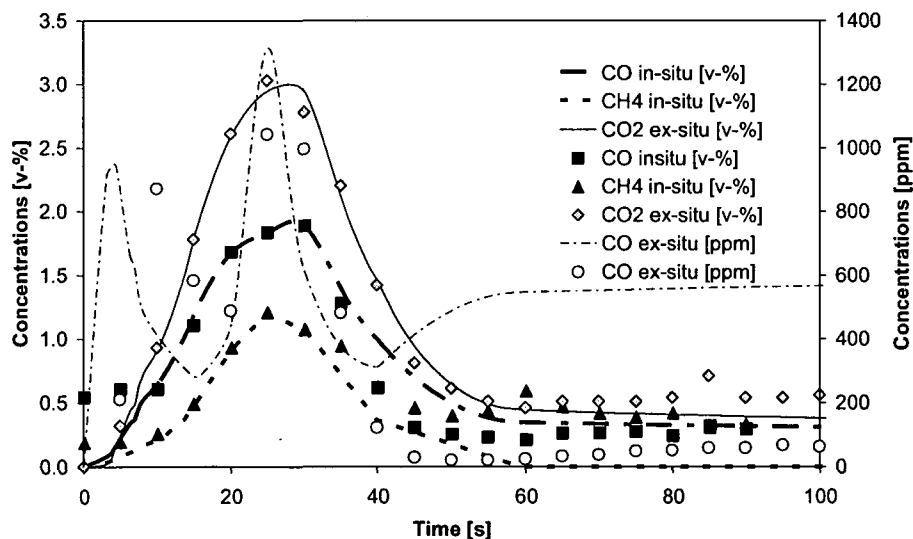


Figure IV.1-14: Measured and calculated concentration histories during bituminous coal combustion, bed temperature 1073K, 10vol% oxygen (volatile composition taken from *in-situ* measurements).

The following Fig. IV.1-15 shows a series of twelve pictures that were taken from a stick of beech wood in the FBC. The first (upper left) picture shows one of the two openings of the FBC. In the second picture (adjacent to the right), one can see the laser beam (spot) of a 760 nm VCSEL. In the third picture (upper right corner), the particle is introduced into the FBC. The next pictures show how it catches fire, enters the stage of char combustion and finally starts shrinking. On the last three pictures, one can see the laser beam again.

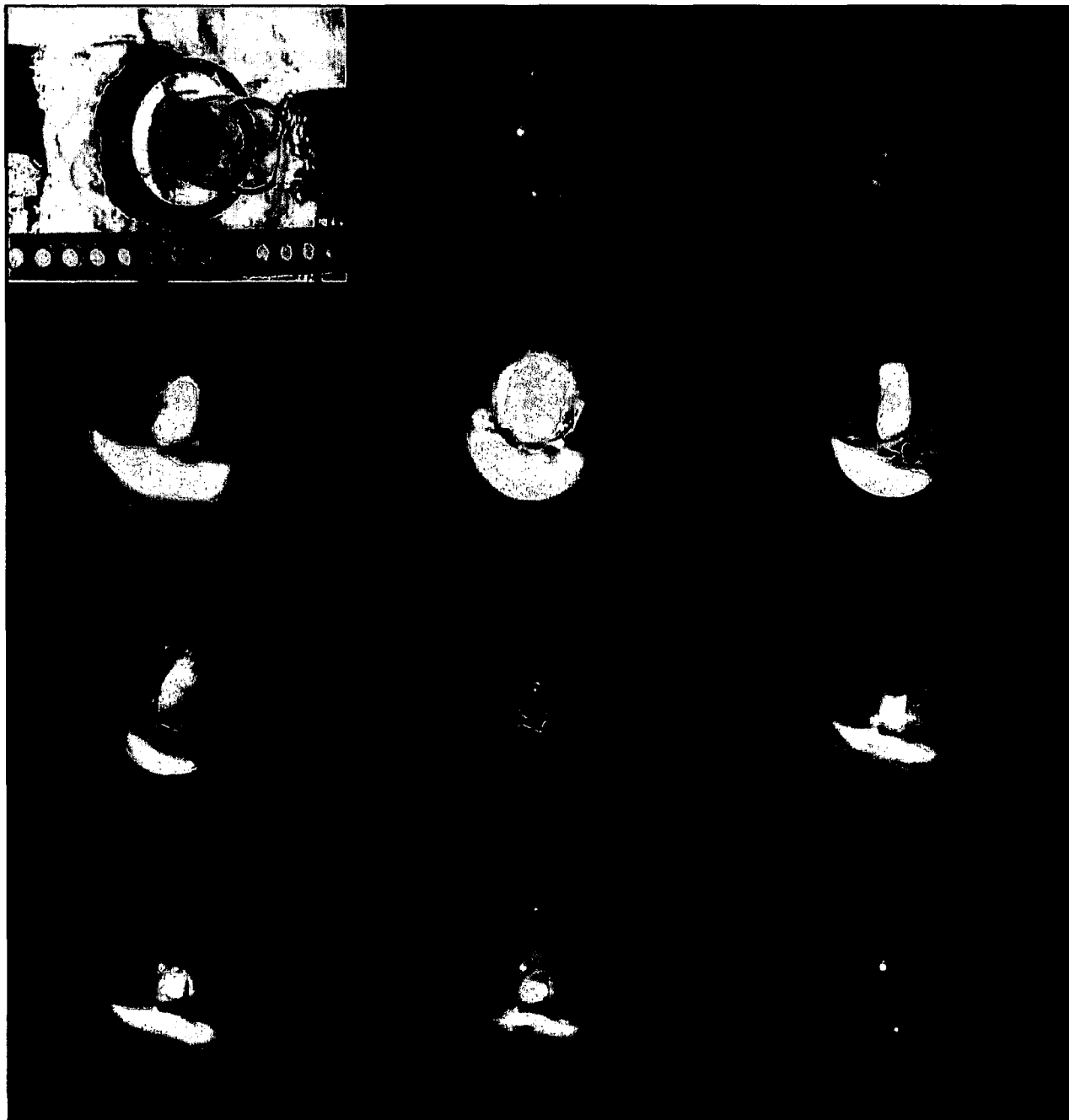


Fig.IV.1-15: View into the FBC along the laser path; The 12 pictures were taken in consecutive order from top left to bottom right. One can see the insertion of the particle, the devolatilization and char combustion phase (note the shrinking of the particle). Experimental conditions:

### Conclusions (CO, CH<sub>4</sub> and H<sub>2</sub>O laser measurements and modeling)

For the first time, concentration histories of CO, CH<sub>4</sub> and H<sub>2</sub>O were measured *in-situ* close to the surface of burning particles in conjunction with accompanying conventional determinations of CO<sub>2</sub> and O<sub>2</sub>. CO, CH<sub>4</sub> and H<sub>2</sub>O could be measured *in-situ* and real-time in the freeboard section of a laboratory-scale fluidized bed combustor (superficial velocity 0.3 m/s) in a distance of 4, 10, 21 and 31 mm to the surface of burning particles. The corresponding residence times were 12, 30, 60 and 90 ms. Tunable diode laser absorption spectroscopy deploying an InGaAsSb/AlGaAsSb diode laser at 2.3 and 2.55  $\mu\text{m}$  was used to probe the two species simultaneously at 300 Hz in line-of-sight absorption spectroscopy with a lower detection limit of 0.2% (CO, CH<sub>4</sub>, 500 ppm\*m) and 0.02% (H<sub>2</sub>O, 50 ppm\*m). Bituminous coal, fir wood (softwood) and beech wood (hardwood) were investigated. The oxygen partial pressure was 5, 10, 15 and 21 kPa, the bed temperature 700, 800 and 900°C. Biomass was found to produce four times as much CO as coal. The CO/CO<sub>2</sub> ratio was found to be about five times higher for beech wood than for fir wood. The *in-situ* results of CO were compared to data obtained by conventional methods. It was found that conventional methods overestimate the concentrations during char combustion and underestimate those during devolatilization.

Benefits of the developed *in-situ* laser measurement technique for applications to solid fuel combustion are: absence of broadening effects due to diffusion as encountered with conventional methods using transport lines and filters, timeliness and the possibility of performing species concentration measurements close to the surface of burning particles (on the order of mm and ms respectively). The point of time when inserting the particle into the fluidized bed combustor is an accurate trigger of the start of the experiment.

This study demonstrates the feasibility of *in-situ* concentration measurements close to the surface of burning particles in a multi-phase environment with quantitative data evaluation.

The experimental results obtained for the bituminous coal were compared to a detailed chemical kinetic model.

The *in-situ* measurements proved to be advantageous compared to conventional ex-situ concentration measurements. The calculations confirm that it was possible in this way to determine the primary products of solid fuel combustion during devolatilization and char combustion, respectively. A rather simple model for the devolatilization products was proven to well describe the release rates of CH<sub>4</sub> and CO for the bituminous coal.

The lower detection limit at 800°C was determined to be 0.2 vol% (500 ppm\*m) for CO and CH<sub>4</sub>. For H<sub>2</sub>O, it was determined as (50 ppm\*m).

This work was published:

M. Lackner, G. Totschnig, G. Loeffler, H. Hofbauer, F. Winter, *In-situ* laser spectroscopy of CO, CH<sub>4</sub> and H<sub>2</sub>O at 2.3 - 2.55  $\mu\text{m}$  in a particle laden laboratory-scale fluidized bed combustor (FBC), *Thermal Science* 6 (2), 13-27 (2002).

M. Lackner, G. Totschnig, F. Winter, *In-situ* laser measurements of CO and CH<sub>4</sub> close to the surface of a burning single fuel particle, *Measurement Science and Technology* 13 (10), 1545-1551 (2002).

M. Lackner, G. Totschnig, F. Winter, *In-situ* Laser Measurements of CO and CH<sub>4</sub> Close to the Surface of a Single Fuel Particle in a Fluidized Bed Combustor, oral presentation at 44<sup>th</sup> IEA-FBC Meeting, Vienna, Austria, May 27<sup>th</sup> (2002).

M. Lackner, G. Totschnig, G. Löffler, H. Hofbauer, F. Winter, *In-situ* laser spectroscopy and modeling of bituminous coal in a laboratory-scale FBC, oral presentation at 45<sup>th</sup> IEA-FBC Meeting, Prague, Czech Republic, November 18<sup>th</sup> (2002).

## IV.2 Characterisation of laser-induced ignition using tunable diode laser absorption spectroscopy: CH<sub>4</sub>, biogas and liquid fuels

### IV.2.1 Laser ignition of methane/air mixtures

#### Introduction

Most combustion appliances work at or near atmospheric pressure; However, several applications demand compactness. High-load combustors operating at elevated pressure to benefit from smaller unit size, increased efficiency and increased power output are common e.g. in transport. Internal combustion engines, rocket motors and an increasing number of power plant burners are operated at increased pressure [74] in order to obtain high energy densities.

A vast array of studies concentrating on different aspects of combustion has been carried out at or near ambient pressure. The use of low pressure kinetics to describe high pressure phenomena is questionable both in terms of rate constants and kinetic path ways that can be quite different at higher pressures [144]-[146]. The extrapolation of results obtained at slightly above ambient conditions to high pressure regimes should be verified by experiments carried out at pressures relevant to e.g. internal combustion engines. This procedure is necessary in order to provide computer models with representative data.

Combustion environments are challenging for the experimentalist, because high temperatures are involved. High pressures, particle load, high luminosity and limited optical access as encountered in engines result in further complications [147]. For this reason, experimental work at high pressures has lagged behind the needs.

Gas sampling is an established technique to obtain species concentrations. A suction probe is inserted into the system and samples are drawn for analysis. Though the method is prone to errors, especially when high temperatures and unstable and reactive species are involved, it is generally recognized as a very reliable method. A major problem associated with sampling is the time delay that is always introduced. Also, flow field disturbance, heat loss and catalytic effects have to be considered [76].

Spectroscopic techniques are intrinsically non-intrusive. Hence they do not disturb the system under investigation and allow measurements *in-situ*, that is right at the spot. Time delays or sampling error are no issues to be dealt with any more. Quantification and calibration of the signal, on the other hand, often become very sophisticated tasks.

Raleigh scattering has been used to obtain concentrations in diesel engines [148], Raman scattering to determine air/fuel ratios in engines [149]. Laser induced fluorescence (LIF) is based on selectively exciting a target molecule and subsequently detecting the emission signal. The method generally delivers significant signals and reveals two-dimensional information such as in [150]. It is possible to track the flame front (OH radical) or to observe fuel concentrations by using fluorescence doping agents. Quantification is not a trivial task with LIF, yet the two dimensional images provide useful information, e.g. on the flame front propagation.

Laser absorption spectroscopy on the other hand allows quantification in a relatively easy way. As a line-of-sight technique, one obtains path-averaged results along the beam path.

Ignition processes are particularly difficult to investigate and not yet fully understood, because they occur on a short time scale with harsh experimental conditions.

Yet ignition is extremely important to understand, because slight differences in the early stages of combustion might lead to a significantly different final combustion result. In internal combustion engines, the main combustion is determined by the preceding development of the flame kernel and the initial combustion to a very strong degree.

In [151] it was found that successful ignitions appear virtually identical to failed ignitions during the first 100  $\mu\text{s}$ . Significant differences were found to appear between 100 and 500  $\mu\text{s}$  following the spark.

Internal combustion engines that are operated in a fuel lean regime are desirable because they show reduced  $\text{NO}_x$  emissions due to lower peak temperatures. However, cycle to cycle variations tend to increase as the air/fuel ratio is increased. These non-advantageous variations are assumed to stem from fluctuations at the location of the ignition, e. g. inhomogeneities in the equivalence ratio. Therefore a lot of the research related to ignition is concerned with determining the fuel concentration in the vicinity of the location of the ignition (e.g. by a laser absorption technique in [152] and [153] and by a variant of laser induced breakdown spectroscopy in [154]).

A method of sampling hydrocarbons by a special valve in the spark plug was developed in [155].

Optical fibers have also found widespread use to detect flames and failed ignitions [156], [157] with emissions in different wavelength regions.

When investigating ignition phenomena, laser ignition lends itself as the ignition type of choice. The location of the ignition can be chosen freely, that is undisturbed by electrodes that bring about cooling and quenching. Furthermore, the amount of deposited energy can be selected easily, and the reproducibility is very good.

In laser-induced ignition, a powerful pulsed laser beam is normally focused to a high laser light intensity in the focal region.

Irradiance in the order of  $10^{14}$   $\text{W}/\text{m}^2$  [63], [154] is necessary to obtain gas break-down leading to multi photon ionization and an electron avalanche process [158].

A review on alternative ignition systems such as laser ignition is presented in [159]. Information on the ignition of methane in general can be found in [66] and [160] - [162].

Experimental studies on laser ignition, first and foremost laser-induced spark ignition of gaseous mixtures have been carried out extensively using different complementary techniques.

In [60], a high speed digital video camera was used to obtain images of the spark. In [59], [61] and [163] shadowgraphs and in [55] streak camera photographs were recorded.

Schlieren streak photographs using a flash lamp and a rotating mirror camera were made by [65]. [71] presents shadowgraphs from two-point ignition, and [63] used a 30 frames/s CCD camera for studies of laser-induced multi-point ignition.

In [151] the shape and structure of developing flame kernels in laser-induced spark ignited hydrogen/air mixtures was investigated using planar laser-induced fluorescence (PLIF).

In [164] LIF spectroscopy is used to study the relative concentrations of NO and CN with a time resolution better than 1  $\mu\text{s}$ . Also, the vibrational temperature was measured. OH emission was detected in [151] and [154] measured time-resolved OH-emission.

The pressure trace was recorded and evaluated inside a constant volume vessel [68] and a laser ignited internal combustion engine [165].

In [166] laser ignition of an explosive (1,3,5-trinitrohexahydro-1,3,5-triazine (RDX) was tracked by a mass spectroscopic technique.  $\text{N}_2\text{O}$ , HCN,  $\text{NO}_2$ ,  $\text{H}_2\text{CO}$ , NO and  $\text{CO}_2$  were determined quantitatively up to 5 MPa.

In [167] plasmas were generated in low pressure direct current hollow cathode flowing discharges. It was concluded that it would be necessary to detect and quantify all species produced, including radical and reactive intermediate species that play the key roles in the plasma chemistry. Stable end-products were considered to give a trustful indication of the intermediate chemical species formed in the plasmas and to provide valuable data for unraveling the mechanisms involved. Therefore, *in-situ* FT-IR (Fourier Transform IR) spectroscopy was chosen for the simultaneous determination of 13 species in that study.

[168] was able to detect radical intermediate species: methyl radicals were produced in a hollow cathode discharge cell from  $\text{CH}_4$ . The  $\text{CH}_3$  absorption decay with time was monitored in a multipass cell in White configuration. A laser amplitude double modulation spectroscopic technique with a difference frequency laser spectrometer and a double phase sensitive detection method was used. The time constant of the whole system was 1 ms.

In this work, a tunable diode laser was used to investigate the laser-induced ignition of methane/air mixtures at high pressures. Some of the above-mentioned experimental methods provide an insight into the very first phenomena, that is on a time scale of ns where the laser pulse interacts with the gas. Other techniques focus on later stages of the combustion onset. Here, a method of tracking the ignition for almost four orders of magnitude in time, starting with ignition and ending after approximately 1 s with total conversion, at a 0.2 ms time resolution is presented.

### Experimental

The experimental setup is depicted in Fig. IV.2-1. Information about the equipment related to laser ignition itself can be found in [68]. A pressurized combustion vessel in cylindrical shape was used (internal length 223 mm, internal diameter 71.6 mm). The volume was constant ( $0.9 \cdot 10^{-3} \text{ m}^3$ ). The vessel could be thermo-stated from room temperature to 473K. The first experiments were carried out with methane/air mixtures. The vessel could withstand rated peak pressures of up to 30 MPa. Given a pressure increase of approximately a factor of 5-6 upon combustion, the maximum filling pressure was 3 MPa. There were four windows made of sapphire, two of which were mutually opposite each other in the lateral and transverse direction (along the axis and perpendicularly to it). A Q-switched Nd:YAG laser was deployed for igniting the combustible mixture inside the vessel. The pulses (10 ns duration) could be attenuated using a polarizer from 50 to 1 mJ. The experiments were conducted in single-shot mode (the maximum laser repetition frequency was 15 Hz). The exhaust gas was analyzed for the content of  $\text{CH}_4$ ,  $\text{CO}$ ,  $\text{CO}_2$  and  $\text{O}_2$  to determine the extent of conversion after combustion. A pressure transducer in conjunction with a precision charge amplifier was used to determine the pressure inside the vessel. The pressure trace was recorded on an oscilloscope (100 MHz, 1GS/s) and read from the RS232 interface into a personal computer using a PCI I/O card.

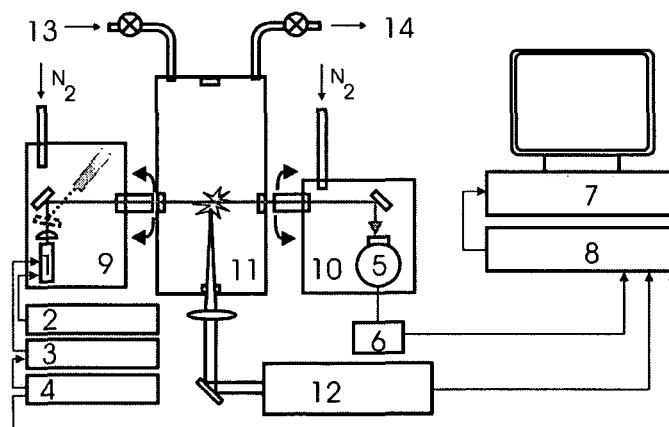


Fig.IV.2-1: Schematic diagram of the experimental setup. A constant volume vessel is used. The near infrared diagnostic laser system deploys two parallel windows that are arranged perpendicularly to those used for the ignition laser. The focus of the ignition laser is placed close to the passing diagnostic laser beam. 1: diode laser at  $2.55 \mu\text{m}$ ; 2: temperature controller; 3: laser driver; 4: function generator; 5: detector; 6: amplifier; 7: PC; 8: oscilloscope; 9, 10: boxes purged with  $\text{N}_2$ ; 11: pressurized combustion vessel; 12: pulsed Nd:YAG laser; 13: fuel and air inlet; 14: exhaust gas analysis;

As shown in Fig. IV.2-1, the pulsed Nd:YAG laser beam was focused through one of the windows on the axis of the cylindrical vessel in a way that the focal point was on the height of

the two remaining opposing windows. The window behind the one to couple in the Nd:YAG laser pulse was used to visually observe the occurrence of plasma sparks and combustion.

For the spectroscopic measurements, the above-mentioned opposing windows at the height of the focal point were used. It would have been equally possible to use the transverse direction for the pulsed laser and the longitudinal direction for the diagnostic probing laser.

A tunable diode laser (emission wavelength  $2.55 \mu\text{m}$ ) traversed the pressurized combustion vessel in the vicinity of the focal point (i. e. the location of the laser spark) as a diagnostic or probe laser (see later). An anti-reflection coated plano-convex lens was used to collimate the light. The laser was housed in a heat sink made of copper and thermo stated at  $291.15 \text{ K}$  using a commercial laser diode temperature controller in conjunction with a Peltier element and an NTC temperature sensor ( $10\text{k}\Omega$ ). A commercial laser diode precision current source with a transfer function of  $44 \text{ mA/V}$  was used to tune the emission wavelength of the laser. The laser driver was operated by a function generator. An asymmetric triangular ramp ( $0$  to  $4 \text{ V}$ ) was imposed on the laser driver to yield a current output of  $0$  to  $174 \text{ mA}$ .

The laser driver and temperature controller were protected against the line voltage by an overvoltage protector and an automatic voltage regulator in order to prevent damage to the laser diode caused by surges or brownouts.

A liquid  $\text{N}_2$  cooled infrared InSb photo detector in conjunction with a home-made transimpedance amplifier was used to detect the transmitted signal.

The laser and the detector were housed in a transparent plastic box purged with nitrogen. Since ambient room air contains approximately  $0.5 - 1 \text{ vol\%}$  of humidity and the selected wavelength of  $2.55 \mu\text{m}$  is strongly absorbed by water, the surrounding water vapor was removed in order to enable sensitive measurements of water vapor generated inside the combustion vessel upon ignition.

The detector signal was visualized on an oscilloscope ( $20\text{MS/s}$ ,  $20 \text{ MHz}$ ) and digitized using a data acquisition board which had a maximum sampling rate of  $125 \text{ MS/s}$ ,  $60 \text{ MHz}$  bandwidth and  $12$  bit vertical resolution.

The combustion vessel was charged with the combustible mixture using an automated filling procedure. Methane and air were supplied from pressurized gas bottles (standard technical quality).

Methane was filled in first. The stoichiometry of the mixture was calculated from the partial pressures of methane and air. Methane is a relatively compressible gas, however, the error was found to be negligible. The partial pressures were determined by two digital manometers (pressure range  $0-0.7$  and  $0-7 \text{ MPa}$ ) and read into a personal computer. Fuel rich to fuel lean mixtures were investigated.

The trigger signal provided by the Nd:YAG laser was used to start the data acquisition. A sampling rate of  $0.98$  to  $0.39 \text{ MS/s}$  was chosen. Since the on-board memory of the data acquisition board was  $512 \text{ kB}$ ,  $256,000$  data points per channel were available for data recording. The time span for which each ignition event could be tracked was therefore  $39$  to  $256 \text{ ms}$ . With the repetition rate of the current ramp being  $5 \text{ kHz}$ , the number of data points on the x-axis was  $300$  to  $500$  for each ramp.

The vertical resolution was  $12$  bit on a  $3 \text{ V}$  scale, which was sufficient even when transmission became low. Typically, the detector voltage ranged from  $0$  to  $800 \text{ mV}$ . Values as high as  $2.5 \text{ V}$  were registered when a high offset caused by luminosity from the inside of the combustion was overlaid with the diode laser signal.

The frequency of the current ramps was  $5 \text{ kHz}$ , so new information was obtained every  $0.2 \text{ ms}$ . The ramps were not averaged.



## Results and discussion

In this study, a tunable diode laser was used to investigate the laser-induced ignition of methane/air mixtures.

The beam of the tunable diode laser was sent through the combustion vessel perpendicularly to the pulsed Nd:YAG laser. The Nd:YAG laser was used to ignite the mixture at the position of the focal spot (spot size approximately 20  $\mu\text{m}$ ). The diode laser was frequency tuned around 2.55  $\mu\text{m}$  to detect water that was generated close to the ignition spark at initial pressures of up to 4 MPa. Additional information was obtained from the evaluation of the detector signal.

Previously described comparable studies are:

[169] observed the absorption of UV light perpendicularly to the cell axis during laser ignition of  $\text{O}_2/\text{O}_3$  mixtures.

In [152], the fuel concentration in the vicinity of a spark plug of a four-stroke-cycle, single-cylinder research engine fuelled with methane and propane was determined using a NeHe laser at 3.39  $\mu\text{m}$ .

In [153], the fuel concentration in the vicinity of a spark plug of a four-stroke cycle spark-ignition engine with four cylinders was determined using a fiber optic system linked to an optical sensor installed in the spark plug. The fuel used in that study was octane.

In [170] and [171] water was measured by a sensor based on TDLAS in a static cell at 10 atm. In this study, laser ignition, an inherently fast phenomenon, at high pressures was investigated by in-situ laser spectroscopy.

Fig IV.2-2. presents typical raw data from an ignition experiment. One can see the detector signal, i.e. the time-varying offset plus the transmitted laser beam intensity (Fig. IV.2- 2(a)). The insert (Fig. IV.2- 2(b)) shows a close-up of the detector signal where the individual ramps are resolved.

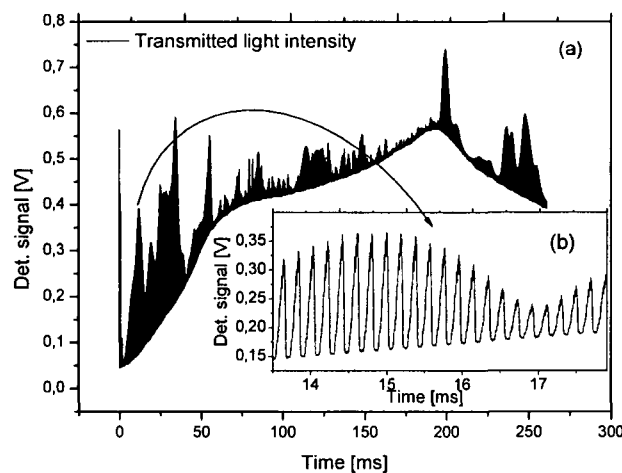


Fig. IV.2-2: Raw data obtained during a single measurement (signal at the photo detector). The latter is a superimposition of emissions from the flame and the laser signal. The transmission of the laser signal fluctuates strongly over time. The insert shows a magnification from the indicated location of the curve. One can see the induced combustion of a stoichiometric methane/air mixture (air equivalence ratio = 1.06, initial pressure 3 MPa, initial temperature 200°C, laser pulse energy 20 mJ). The repetition rate of the diagnostic laser was 5 kHz (corresponding to a 0.2 ms time resolution). The total recorded time is 264 ms, the insert is 4.6 ms long ( 23 times 0.2 ms).

A single pass arrangement was used. In sensitive tunable diode laser absorption spectroscopic measurements, beam splitters are often deployed to simultaneously record signal, baseline and tuning properties using an etalon (compare Fig. III-2). This more complicated setup was not considered useful for the experiments presented here.

Since the entrance windows of the combustion vessel (5.0 mm thick sapphire) caused severe etaloning, a dual beam arrangement for simultaneous baseline recording would not have yielded the expected increase in sensitivity.

In Fig. IV.2-3 the information gathered from the probing laser at  $2.55 \mu\text{m}$  as shown in Fig. IV.2-2 (raw data) is illustrated:

Fig. IV.2-3(a) shows the absorbance of water as a function of time.

Fig. IV.2-3(b) shows the emissions of the flame as a function of time.

Fig IV.2- 3(c) shows the gas inhomogeneity index (see later).

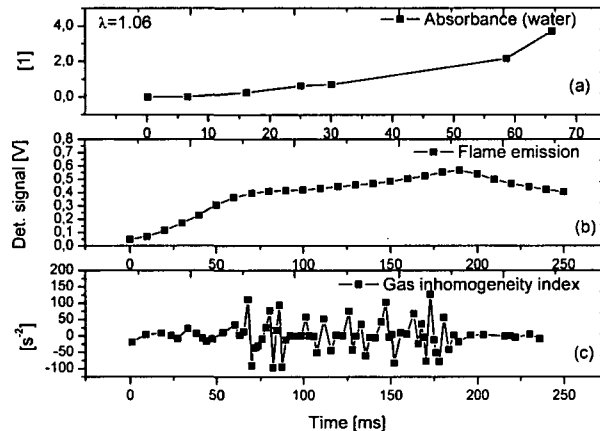


Fig. IV.2-3: Stoichiometric combustion and data obtained during an ignition measurement (confer raw data in Fig. IV.2-2). (7a) shows the absorbance of water as a function of time. (7b) is the trace of the emissions of the flame. (7c) is the gas inhomogeneity index (derivation of the frequency of the upper envelope curve, see later). After 70 ms, the absorbance became too high.

The ignition event shown in Fig. IV.2-2 (raw data) depicts a stoichiometric mixture of methane in air at an initial chamber filling pressure of 3 MPa. The temperature was 473K. The laser pulse energy was 20 mJ.

In Fig. IV.2-3 (a), the absorbance of water is shown. An absorbance of 4 corresponds to a transmittance of 1.8 %. The gas inhomogeneity index in (c) is described later.

The following figures show fuel rich (Fig. IV.2-4, Fig. IV.2-5), fuel lean (Fig. IV.2-6, Fig. IV.2-7) and failed (Fig. IV.2-8, Fig. IV.2-9) ignition. As in Fig. IV.2-3 for a stoichiometric mixture, the absorbance, the emissions of the flame and the gas inhomogeneity index have been extracted and plotted.

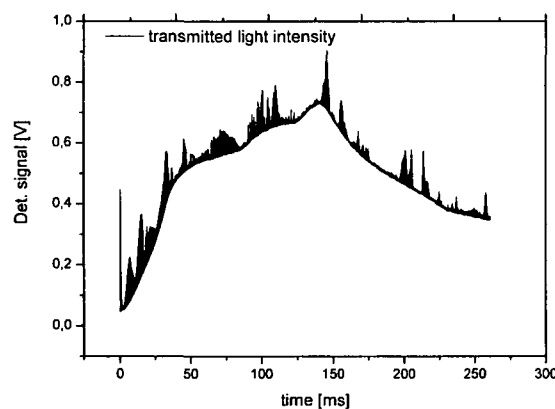


Fig. IV.2-4: Laser-ignition of a fuel rich methane/air mixture, raw data. Experimental parameters were initial pressure 3 MPa,  $200^{\circ}\text{C}$ , air equivalence ratio 0.89.

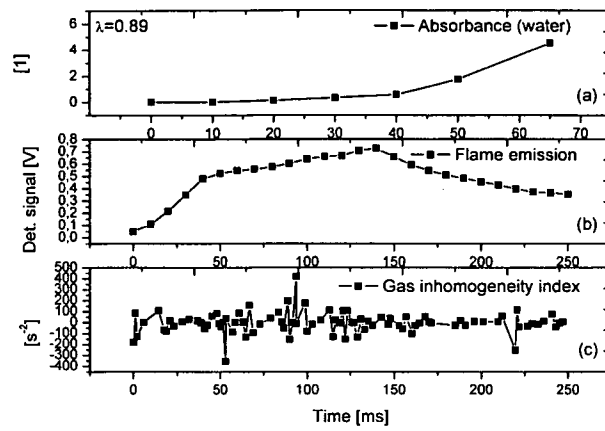


Fig. IV.2-5: Data obtained from the fuel rich ignition experiment in Fig. IV.2-4. Fig. IV.2-5 (a) shows the absorbance of water vapor, Fig. IV.2-5(b) the emissions from the flame, and Fig. IV.2-5(c) the gas inhomogeneity index (derivation of the frequency of the upper envelope curve, see later). After 70 ms, the absorbance became too high.

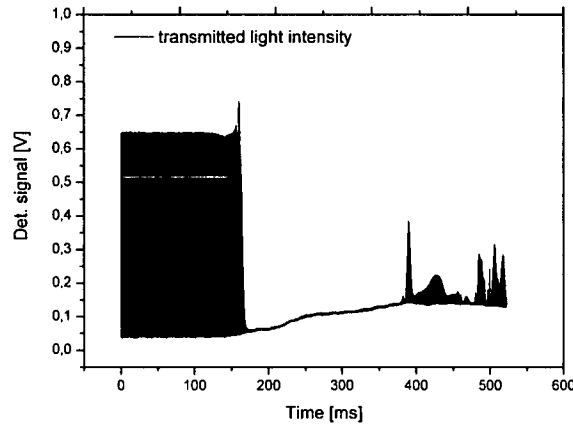


Fig. IV.2-6: Laser-ignition of a fuel lean methane/air mixture, raw data. Experimental parameters were initial pressure 3 MPa, 200°C, air equivalence ratio 1.42.

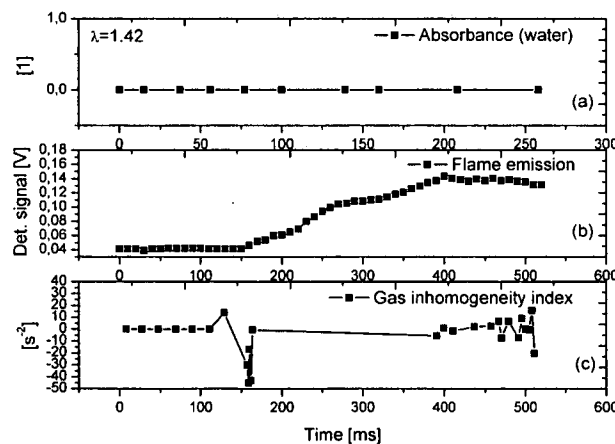


Fig. IV.2-7: Data obtained from the fuel lean ignition experiment in Fig. IV.2-6. Fig. IV.2-7(a) shows the absorbance of water vapor, Fig. IV.2-7(b) the emissions from the flame, and Fig. IV.2-7(c) the gas inhomogeneity index (derivation of the frequency of the upper envelope curve, see later). No absorbance could be detected at 2.55  $\mu$ m up to 500 ms (duration of the measurement).

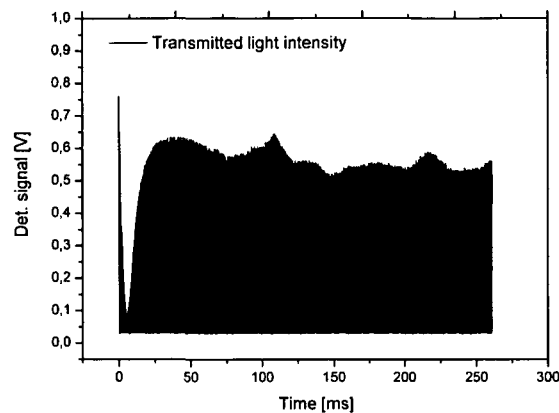


Fig. IV.2-8: Failed laser-ignition experiment. Experimental parameters were initial pressure 3 MPa, 200°C, air equivalence ratio 2.50 (beyond limit of flammability).

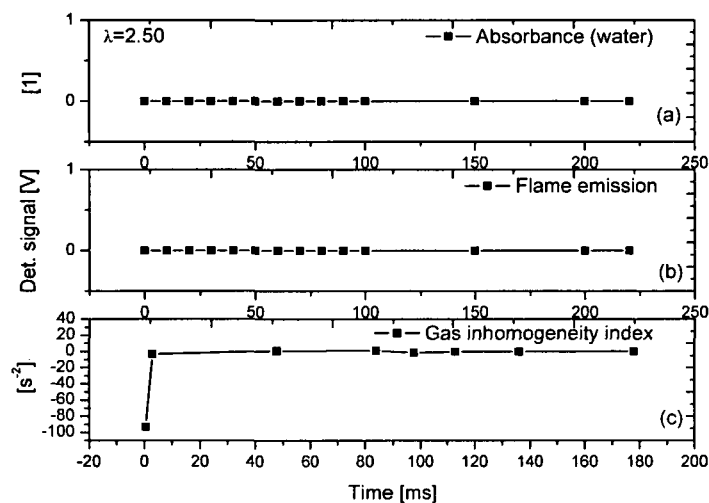


Fig. IV.2-9: Data obtained from the failed ignition experiment in Fig. IV.2-8. Fig. IV.2-9(a) shows the absorbance of water vapor, Fig. IV.2-9 (b) the emissions from the flame, and Fig. IV.2-9(c) the gas inhomogeneity index (derivation of the frequency of the upper envelope curve, see later).

### Absorbance of water as a measure for concentration

The absorbance  $A = \ln(I_0/I)$  is directly proportional to the concentration of the absorber (cf. Eq. II.1-12). There are several limitations, however, that were encountered in the present work, so that quantification is not a trivial task.

First, absorption spectroscopy is an inherently integrative technique. It delivers path averaged results. When water is formed close to the ignition spot, one will see a signal that stems from absorption in both very hot and rather cold regions. The line strength is a function of the temperature, which is neither known exactly nor a constant. In the early stages of combustion, which are most interesting, one can assume a homogeneous temperature in the growing flame ball to address and simplify this problem.

Second, the pressure inside the vessel rises steeply, so that significant pressure broadening will occur (not, however, in the very beginning during the flame development phase). Pressure broadening limits the use of tunable diode lasers because as soon as the wings of the absorption feature cannot be recorded properly any more, the method resembles very much the fixed-wavelength technique with all its problems (compare Fig. II.3-3).

In this study, a tunable diode laser with a continuous tuning range of approximately

$1.71 \text{ cm}^{-1}$  ( $1.11 \text{ nm}$ ) is used. The broadening coefficient  $\gamma_{\text{AIR}}$  was determined to be on the order of  $0.3 \text{ cm}^{-1}\text{atm}^{-1}$ . The temperature dependence of  $\gamma_{\text{AIR}}$ , taken from [4], is  $T_C = 0.6$ . Therefore, the pressure-broadened absorption lines become smaller at higher temperatures so that the range of operation of the laser can be extended towards higher pressures.

If the peak becomes broader than the tuning range, a non-linear dependence of the concentration on the measured absorbance will be observed.

These two drawbacks, the obscure temperature and linearity aspects, are relevant for quantitative modeling purposes. For judging the ignition at an early stage, as it is presented here, this does not constitute a major problem, yet one has to be aware of it.

Water that is formed by reactions of methane in the vicinity of the laser spark can hence be determined merely in a semi-quantitative manner.

In this study, the absorbance was obtained from  $A = \ln(I_0/I)$  at the center of the peak. The area of the water peak might turn out to be a more robust parameter. For sake of simplicity, the first method was chosen.

Let us assume that at 3 MPa initial pressure, the flame ball has grown to  $10^{-2} \text{ m}$  in diameter (compare [60]). The concentration of water vapor is 10% in this example (at  $\lambda = 2$ , the concentration of  $\text{CH}_4$  is 5%. 1 mole  $\text{CH}_4$  yields 2 moles  $\text{H}_2\text{O}$ ). At an estimated mean temperature of 1300 K, the absorbance at  $2.55 \mu\text{m}$  is 0.8, and at an alleged 1800K, it is 0.44. Without any sophisticated detection schemes, absorbances above 4 become difficult to measure, since the transmission approaches zero (an absorbance of 4 corresponds to a transmission of approximately 1.8 %).

As shown in Fig. IV.2-3(b) for the stoichiometric and in Fig. IV.2-5(b) for the fuel rich mixture, the absorbance of water at  $2.55 \mu\text{m}$  increases sharply with time. After approximately 70 ms, it could not be determined any more because the transmission became too low. The burning velocity in the (stagnant as in all experiments) fuel lean mixture was too slow as to detect any water absorbance within the first 500ms of the ignition test. The duration of the measurement was limited by the memory of the data acquisition card. As for the failed ignition (Fig. IV.2-9(b), evidently no water absorbance could be detected either.

### Emissions from the flame

The emissions caused by the flame were captured by the detector as an offset to the voltage caused by the transmitted laser radiation.

The InSb photodetector used in these studies has a response from approximately 1 to  $10 \mu\text{m}$ . Therefore, most of the infrared radiation (stemming from the flame and the inner walls of the hot combustion vessel) contributes to the signal.

One can deduct the ignition delay time from the difference of the start in emissions to the trigger signal of the Nd:YAG laser pulse.

The flame emissions for the stoichiometric (Fig. IV.2-3(b)) and fuel rich (Fig. IV.2-5(b)) case resemble each other very much, except for the fact that in the fuel rich mixture, the peak value is reached sooner. One can see that the emissions from the flame in the fuel lean case (Fig. IV.2-7(b)) do not emerge before approximately 150 ms. This is caused by the extraordinarily long ignition delay time. The failed ignition experiment (Fig. IV.2-9(b)) obviously does not produce any emissions from the flame either.

### Variation of the transmittance (gas inhomogeneity index)

In the experimental setup used, the infrared probe beam traverses the combustion vessel before hitting the photo detector situated in a purged box behind. The transmitted signal fluctuates strongly over time.

The non-resonant variation of the transmittance is caused by several effects: The beam can be partially blocked, e. g. by soot particles, or partly be deflected from the detector by refractive index gradients inside the vessel, e. g. due to flames. The latter effect is dominant in this study. A collimating mirror (which would have reduced the amplitude of these fluctuations) was not used because this would have increased the unwanted etaloning.

In [172] and [173] the initial formation process of the laser-induced plasma shock wave was studied based on detecting beam deflection: When the detection beam interacts with the shock front it is deflected with respect to its undisturbed direction due to the effects of density, temperature and ionization on the refractive index of the shock region. By measuring the deflection angle, it is possible to determine the shock arrival time, shock location and strength. A continuous HeNe laser beam (632.8 nm, 2mW, diameter 1mm) mounted on a micrometer translator was passed near the spark breakdown region 0.4, 0.8, 1.2 and 1.6 mm above the spark center. At 0.4 and 0.8 mm, the laser-induced shock-wave and plasma front and at 1.2 and 1.6 mm, only the shock wave were detected.

In the present study, the laser beam can be deflected from the detector by the influence of the plasma and the shock wave as in [172] and [173], depending on the relative position to the plasma spark. It can also be deflected by refractive index gradients caused by the propagating flame, which is relevant during the whole ignition experiment. The faster the flame develops, the stronger the transmitted signal will fluctuate. The fluctuations can be illustrated as the envelope curve that is measured directly (cf. raw data in Fig. IV.2-2, Fig. IV.2-4, Fig. IV.2-6 and Fig. IV.2-8). The refractive index gradients that alter the light intensity falling onto the detector can either increase or decrease the detected light intensity. Some of the fluctuations may also stem from artifacts, such as influences from the line voltage (e. g. introduced by capacitive coupling). The fluctuations can also be expressed in terms of a frequency [ $s^{-1}$ ] or the derivation thereof. This was done in the present study. The (sometimes vigorous) fluctuations themselves do not lend themselves for easy, direct conclusions. Therefore, the frequency can be shown. This was done by hand in this study. Each deflection (or dip) was considered for itself. The reciprocal of the time duration  $\Delta t_i$  (start: valley of the ascending  $i^{\text{th}}$  dip; ending: valley of the descending  $i^{\text{th}}$  dip) times 0.5 was calculated to yield a frequency  $f_i$ :  $f_i = 1/(0.5 \cdot \Delta t_i)$ , with  $\Delta t_i$  being the difference between the time at the end of the  $i^{\text{th}}$  dip  $t_{i+1}$  and the time at its beginning  $t_i$ . This frequency [ $s^{-1}$ ] was attributed to the mean time  $t_{i,m} = (t_i + t_{i+1})/2$ . The amplitude is not considered at all. One is interested in the variation of the transmittance rather than the fluctuations themselves. Therefore, the derivation  $D$  of the frequency  $f$  can be formed according to  $D = df/dt \sim \Delta f/\Delta t = (f_{i+1} - f_i)/(t_{i+1,m} - t_{i,m})$ .

By doing so, it is possible to introduce a new so-called "inhomogeneity index" [ $s^{-2}$ ] (compare to Fourier transformation). This index allows to easily spot the start of combustion, follow the combustion and to discern failed or stopped combustion experiments. Turbulence introduced by the flame into the stagnant air of the constant volume vessel also dominates this inhomogeneity index. Before the ignition is launched, the inhomogeneity index can be used to obtain information on the homogeneity in the gas phase at the location of ignition.

When the combustion vessel was filled, it took approximately two minutes for the transmitted laser signal to stop fluctuating. These variations were caused again by refractive index gradients, possibly by temperature and mixture inhomogeneities. The influence of the plasma can be seen very well in Fig. IV.2-8. The marked dip downwards in the transmission signals that the probing laser beam is strongly deflected by refractive index gradients introduced by the plasma (cf. [172] and [173]).

### Duration of the measurements

The time resolution of the measurements is given by the repetition rate of the current ramp applied to the tunable diode laser, that is 5 kHz or 0.2 ms. The first data point is hence obtained 200  $\mu$ s after the Nd:YAG pulse. The total measurement time, limited by the memory of the data acquisition card, was up to 600 ms.

The events leading to laser-induced ignition occur on very different time scales:

The pulse duration and energy deposition happen during the first 10 ns (several ps for studies with ps pulses), the initial plasma and the following shock wave live for approximately 1  $\mu$ s. Speaking in orders of magnitude, ignition delay lasts approximately 10-100 ms, combustion itself 1 - 5 s. An overview of the different time scales that are encountered in laser ignition is presented in chapter II.1.6.

As shown in this work, it is possible to track ignition over more than four orders of magnitude of time (0.2 ms to 1 s) and to cover several key events associated with ignition.

The majority of competing techniques concentrate on a shorter time scale at a resolution better than or equal to ours, or exhibit a much worse time resolution.

### Frequency of the current ramp

The frequency of the current ramp was fixed at 5 kHz. This corresponds to a time resolution of 0.2 ms. 5 kHz is a kind of compromise; Evidently, the higher the frequency of the current ramp is, the better the time resolution becomes. However, the tuning range of diode lasers decreases with increasing modulation frequency (see chapter III.4).

Because of the severe pressure broadening, the highest possible tuning range is desirable. Also, bandwidth limitations of the detection system, especially, the home-made amplifier, had to be considered.

5 kHz was found to be the optimum frequency. The most limiting parameter was the bandwidth of the detector in conjunction with the home-made amplifier which led to considerable smoothing at higher frequencies.

The following Fig.IV.2-10 and Fig.IV.2-11 show consecutive images of two ignition events. In Fig. IV.2-10,  $\lambda$  was 1.3, in Fig. IV.2.-11, it was 2.0. Note that these values might not be totally accurate since  $\lambda$  was obtained from the partial filling pressures without taking into account the compressibility of methane (so the true  $\lambda$  might be slightly below the given values, i.e. "fatter").

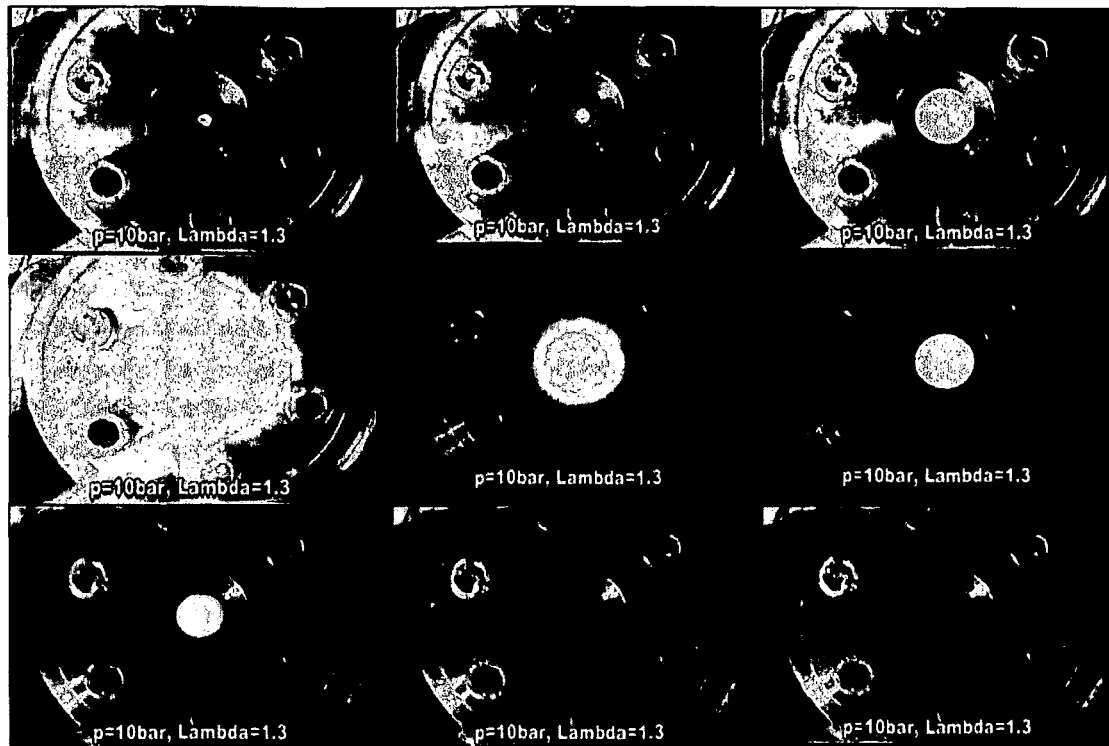


Fig.IV.2-10: Laser-induced ignition of methane/air mixture ( $\lambda$  1.3). The pictures were recorded by Dipl.-Ing. Herbert Kopecek.

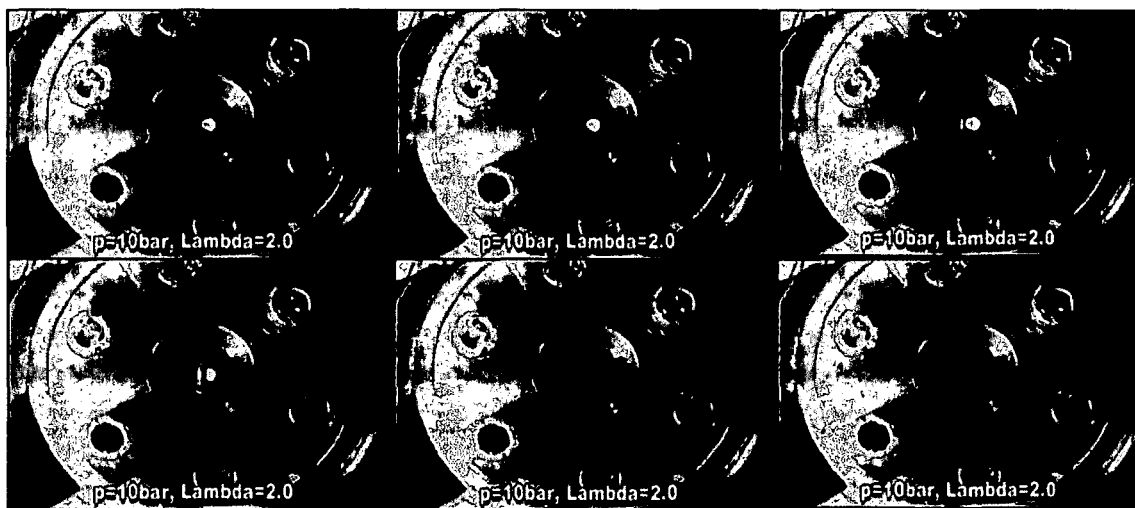


Fig.IV.2-11: Laser-induced ignition of a methane/air mixture ( $\lambda$  2.0). The pictures were recorded by Dipl.-Ing. Herbert Kopecek.



### Conclusions (laser ignition of CH<sub>4</sub>/air mixtures)

The processes involved in laser-induced ignition occur on a time scale that spans several orders of magnitude. A method based on tunable diode laser absorption spectroscopy was developed to track and characterize laser-induced ignition over four orders of magnitude in time with a time resolution of 0.2 ms. Fuel rich to fuel lean methane/air mixtures were ignited in a constant volume vessel at high pressures. A tunable diode laser emitting in the near infrared at 2.55  $\mu\text{m}$  ( $3920\text{ cm}^{-1}$ ) was used. The probing laser beam traversed the combustion vessel at the height of the ignition spark perpendicularly to the radiation of the pulsed Nd:YAG laser for ignition.

In this study, a tunable diode laser is applied to investigate hostile environments (high pressures, elevated temperatures) as encountered in several practical combustion appliances such as engines. *In-situ* species concentration measurements are performed at initial pressures of 3 MPa.

Water was determined as a combustion product. The formation of water in the vicinity of ignition is used as an indicator of the combustion process.

In addition, the emissions from the flame were recorded. They allow the determination of ignition delay time, flame growth and flame quenching.

The fluctuations in the transmission over time of the probing diode laser beam onto the detector were found to result mainly from refractive index gradients inside the combustion vessel. These can be correlated with properties of the developing flame and the effect the plasma and the shock wave have generated. A gas inhomogeneity index is introduced by extracting a frequency variable from the envelope curve in the raw data and performing its derivation.

The developed technique based on the three parameters (i.e. water absorption, flame emissions, gas inhomogeneity index) was found to adequately characterize fuel rich, stoichiometric, fuel lean and failed ignition attempts of methane/air mixtures in the constant volume vessel.

Limitations include the adverse effect of pressure broadening on the quantification of the absorbance signal and the ignorance of temperature.

The following effects can be determined by the absorption spectroscopic method:

- Formation of water in the vicinity of the laser spark (semi-quantitative);
- Characterization of ignition (ignition delay time, incomplete ignition, failed ignition, ignition termination by flame emission measurements);
- Homogeneity of the gas phase in the vicinity of ignition and progress of combustion;

The importance of representative *in-situ* species concentration measurements at high pressures for the design and development of high-load combustors is described.

## IV.2.2 Laser ignition of biogas/air mixtures

### Introduction

Having the limitation of conventional fossil fuel reserves in mind, intense research for alternative fuels for use in internal combustion engines is going on. Several reports dealing with the utilization of renewable fuels for energy generation are presented in [174] – [182]. Biogas is CO<sub>2</sub>-neutral and constitutes a promising alternative fuel with high availability. The two most common sources of biogas are digester gas and landfill gas. Bacteria form biogas in an anaerobic fermentation process from organic matter. The degradation is a very complex process and requires certain environmental conditions. Biogas is primarily composed of CH<sub>4</sub> (50-70%) and CO<sub>2</sub> (25-50%). Digester gas is produced at sewage plants from municipal and industrial sewage. Landfill gas is obtained from the decomposition of organic waste in sanitary landfills. The gas, unless flared for better alternatives, serves as fuel in gas engines to drive a generator producing electricity which is fed into the municipal power supply network. Additionally, thermal energy can be generated which is used for heating purposes (cogeneration plant).

In Vienna, landfill gas from the largest sanitary landfill (Rautenweg) is burnt in gas engines to produce electricity.

Electric spark plugs are common ignition sources in internal combustion engines. Though spark plug technology is being improved continuously, one can not get rid of some intrinsic drawbacks. Laser sources for initiating combustion have encountered increased interest recently (see e.g. [59]-[64]) because of several potential benefits over conventional ignition systems. In general, laser ignition is capable of providing multiple ignition sites [71] that can be controlled to ignite a gaseous combustible mixture either sequentially or simultaneously. One of the main advantages is the choice of the optimum ignition location which is not easy in conventional ignition systems. Further, precise ignition timing as well as the amount of energy and the deposition rate can be controlled easily. Laser ignition is non-intrusive so that quenching effects on electrodes and walls can be prevented.

In internal combustion engines the air to fuel equivalence ratio  $\lambda$  shows a great influence on NO<sub>x</sub>-formation in the exhaust gas, leading to reduced NO<sub>x</sub> emissions with increasing  $\lambda$ -values due to lower combustion temperatures. On the other hand unburned hydrocarbon emissions in the exhaust gas have to be considered as well as the thermal efficiency and the power output of the engine when operating in fuel lean regimes. Too lean fuel/air mixtures cause harsh and irregular running of the engine due to incomplete combustion and slow burning velocities, respectively. When using biogas as fuel one must also pay attention to several harmful ingredients such as H<sub>2</sub>S polluting the catalytic converter of the engine.

The biogas used for the test runs was provided from the municipal sewage plant in Bad Voeslau, Lower Austria. The composition of biogas varies, depending on its origin. The composition of the biogas used in this work is given in table IV.2-1.

Compound	Concentration
CH <sub>4</sub>	50.5 %
CO <sub>2</sub>	31.7 %
O <sub>2</sub>	0.5 %
CO	375 ppm
H <sub>2</sub> S	80 ppm

Table IV.2-1: Composition of the biogas used for the investigation of laser-induced ignition (all values +/-5%).

## Experimental

The experimental setup used for the experiments is similar to the one used on the methane test runs (see previous chapter IV.2.1). In Fig. IV.2-12 and Fig. IV.2-13 a picture of the laboratory and a close-up of the laser measurement system are shown.

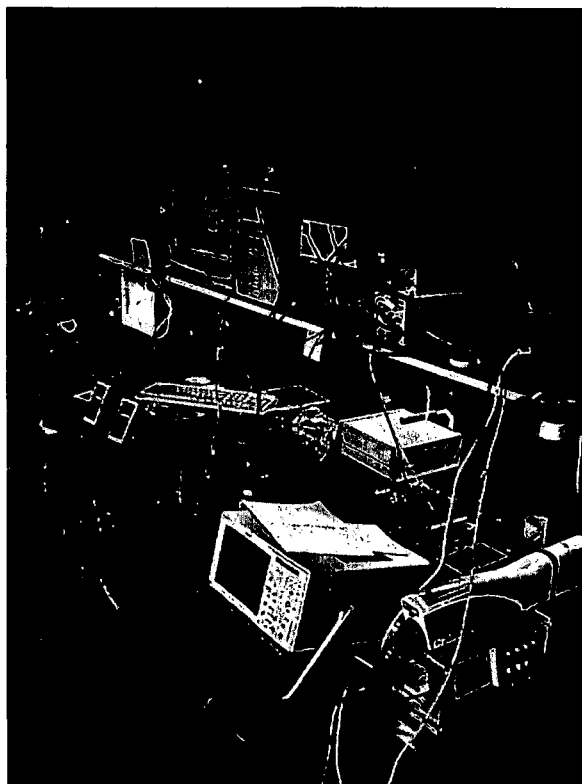


Fig. IV.2-12: Installations in the laser ignition laboratory. The Q-switched Nd:YAG laser can be seen on the right hand side at the bottom (lower level desk). The upper level desk houses the equipment for the spectroscopic measurements.

Fig. IV.2-13 shows a picture of the setup. The box on the left contains the diode laser, the one behind the combustion bomb the photo detector. The pulsed Nd:YAG laser enters through the window on the right (see the mirror and the two lenses).

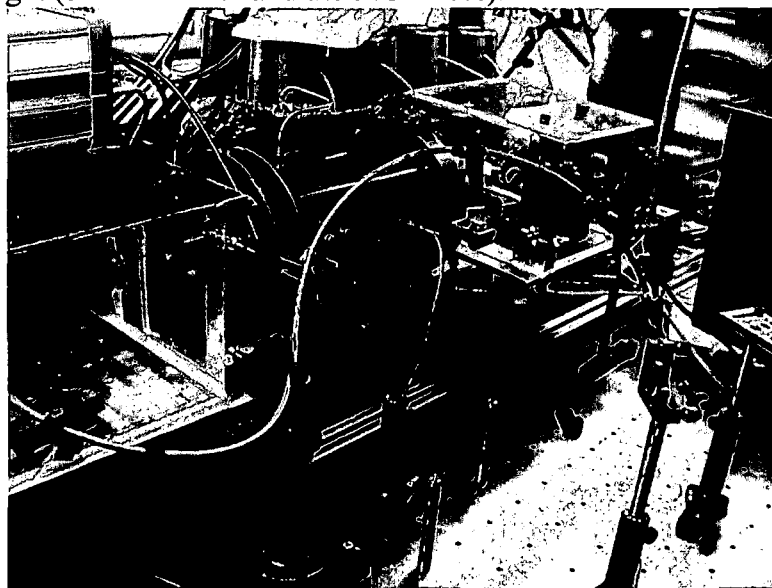


Fig. IV.2-13: Laser measurement system. The  $N_2$  purged box on the left contains the laser, the box on the right the detector. The combustion bomb for the test runs can be seen in the middle between the boxes.

Detailed information concerning the ignition laser and the optical setup can be found in [68]. The pressure vessel is constructed to withstand pressures up to 30 MPa. Since there is a factor of about 7 between the initial pressure and maximum combustion pressure, the ignition of gas mixtures can be investigated up to 4 MPa filling pressure. This is particularly important because in stationary gas engines, pressures are in the order of this magnitude.

The cylindrical combustion chamber of  $9 \times 10^{-4} \text{ m}^3$  volume is composed of a metallic tube made of refractory steel (internal length 0.223 m, internal diameter 0.0716 m). The combustion vessel can be heated by heating rods situated outside the metal cylinder between room temperature and 473 K. To allow the entry of the ignition laser beam and the semiconductor laser the chamber is equipped with 4 windows of sapphire. Two windows located on the transverse opposite sides of the chamber admit the laser beam for the ignition process, while the other two, situated in the longitudinal direction on opposite sides, serve as the entrance and exit windows for the diagnostic  $2.55 \mu\text{m}$  laser beam. The cell has several ports that were used for gas inlets, gas outlet and for mounting a pressure sensor. This piezoelectric pressure sensor is utilized in combination with a charge amplifier to determine the pressure inside the chamber. The pressure trace was recorded on an oscilloscope (100 MHz, 1GS/s) and read from an interface into a personal computer. A Q-switched Nd-YAG laser (Quantel Brilliant) operating at 1064 nm (pulse duration 5 ns) is focused into the combustion chamber to initiate ignition. The laser energy can be attenuated using a polarizer from 50 to 1 mJ per pulse.

An InGaAsSb/AlGaAsSb quantum well ridge diode laser tunable around  $2.55 \mu\text{m}$  was employed to track the generation of water close to the ignition spark. The spectroscopic device was thermo-stated at 291.15 K using a laser diode temperature controller in conjunction with a Peltier element and a NTC temperature sensor (10 kOhm thermistor). The laser was frequency tuned utilizing a laser driver. A voltage ramp of 0-4 V with a repetition rate of 5 kHz was applied to the laser driver by a function generator. There is a slow rise from 0-4 V and a steep decrease to 0 again (asymmetric triangle). One entire sweep is achieved in 1/5000 seconds, accordingly one scan takes 0.2 ms, thus a time resolution of 0.2 ms can be obtained. Corresponding to the voltage function the laser driver tuned the laser by varying the injection current between 0-176 mA while keeping the temperature of the heat sink constant.

The laser driver and temperature controller were fed by a 15V current source protected against the line voltage. An anti-reflection coated plano-convex ZnSe lens (focal length 5 mm) was utilized to collimate the laser beam. The two boxes containing the semiconductor laser and the spectroscopic setup situated on both sides of the combustion reactor had to be purged with nitrogen to remove the water vapor of the ambient atmosphere (0.5-1 vol%) along the path length outside the bomb. This was necessary to allow the detection of the very small amount of initially formed water. An infrared InSb photo detector (EG&G Judson, Inc.) cooled by liquid nitrogen was utilized to track the transmitted laser radiation. The signal of the detector was amplified and visualized on the oscilloscope. The detector signal was transferred to a personal computer and digitized using a high speed data acquisition board (SignaTec PDA 12A).

All experiments were carried out at elevated pressures up to 3 MPa and at a temperature of 473 K to prevent condensation of water on the inner surface of the chamber and especially on the (colder) windows. Fuel (methane, biogas) and pressurized air (standard technical purity) from pressurized gas bottles were delivered automatically to the ignition cell using a purpose-built gas handling system. Before each ignition event, the combustion cell was first sucked and purged with air in order to remove all residual products of the previous combustions. For achieving the desired fuel to air ratio the partial pressure method was used. The compressibility of methane was not considered. To prevent spatial inhomogeneity the calculated partial pressure of the fuel was filled first and the fuel pressure inside the ignition cell was monitored using a high resolution pressure meter. Next, air was injected and in this

way, the homogeneity was achieved easily by the turbulence of the incoming air stream. The mixture inside the cell was given some time to settle (no concentration and temperature gradients) before igniting. The trigger signal provided by the flash lamps of the Nd:YAG laser was used to start the data acquisition.

The investigated methane/air and biogas/air mixtures contained similar methane concentrations but in the case of biogas additionally  $\text{CO}_2$  was present.

## Results and Discussion

### Fuel rich ignition

In this work a tunable diode laser was utilized to characterize laser-induced ignition of biogas/air and methane/air mixtures by evaluating the three parameters water absorbance, luminosity and gas inhomogeneity index (see previous chapter IV.2.1). The laser beam traversed the combustion vessel in the vicinity of the plasma spark which was generated by a Nd:YAG-laser to ignite the hydrocarbon/air mixtures.

The spectroscopic data of water vapor were used to judge the quality of ignited hydrocarbon/air mixtures by a laser source. In Fig. IV.2-14 a typical detector signal of a fuel rich biogas/air mixture is depicted.

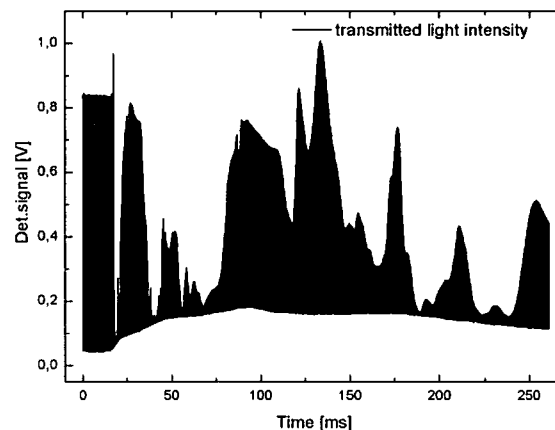


Fig. IV.2-14: Raw data (detector signal) obtained during laser-induced ignition of a fuel rich biogas/air mixture (air to fuel equivalence ratio  $\lambda$  0.76; initial filling pressure 3 MPa; temperature 473 K) with a 5 kHz repetition rate, corresponding to a time resolution of 0.2 ms. The transmitted laser light intensity fluctuates over time.

The absorbance of water vapor at 2.55 was measured. Due to the effects of severe pressure broadening at high pressures and the ignorance of the exact temperature distribution after ignition, the concentration (derived from the absorbance) could only be determined in a semi-quantitative manner (see previous chapter IV.2.1). In this way one obtains the first characterizing parameter, viz. the water absorbance. The flame emission was also evaluated. The gas inhomogeneity index was the third parameter.

Fig. IV.2-15 depicts the absorbance and the flame emission evaluated from the original data in Fig. IV.2-14.

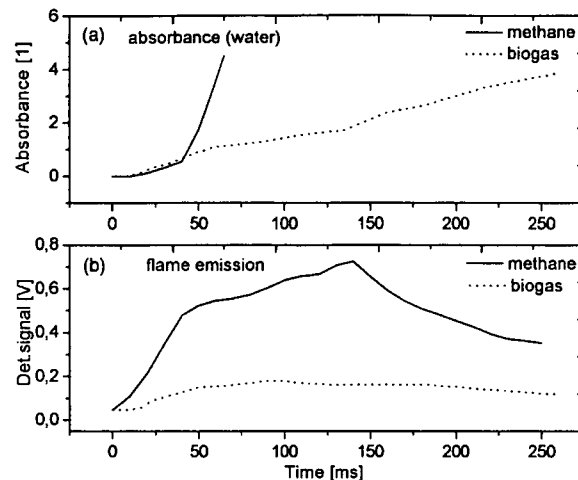


Fig. IV.2-15: Evaluated water absorbance (a) and flame emission (b) of the fuel rich biogas/air mixture depicted in Fig. IV.2-14 and comparison to a methane/air mixture of similar composition (air to fuel equivalence ratio 0.82; initial filling pressure 3 MPa; temperature 473 K). In a) the water absorbance in methane rises faster than in biogas due to  $\text{CO}_2$  decelerating the combustion process. In (b) the flame emission intensity of a methane/air mixture is by a factor 3 higher than in the biogas test run.

Additionally the corresponding curves of a methane/air mixture are shown for visual inspection. For the fuel rich combustion process of biogas the water absorbance rises due to water production during the combustion process and reaches an absorbance of four within 250 ms (Fig. IV.2-15 (a)). In this work the absorbance of water vapor was evaluated up to four. Absorbances above four become difficult to measure because the transmission approaches zero (an absorbance of four corresponds to an absorption  $> 98\%$ ). The flame emission rises after approximately 15 ms and reaches a maximum after 100 ms and then falls off again (Fig. IV.2-15 (b)). The time span of 15 ms at the beginning of ignition is the ignition delay which can be easily deduced from the flame emission parameter.

In a fuel rich methane/air mixture the water absorbance at  $2.55 \mu\text{m}$  increases faster with time. After approximately 70 ms, it reached already a value of four (1.8 % transmittance) which implies an accelerated combustion process compared to the biogas/air mixture (Fig. IV.2-15 (a)). The maximum of the flame emission intensity in the rich methane mixture is by factor of 3 higher than for fuel rich biogas ignition and there is no significant ignition delay (Fig. IV.2-15 (b)). The reason for these results is the presence of  $\text{CO}_2$ , an incombustible diluent gas in the biogas which reduces the burning velocity due to obstructing the flame propagation during combustion. The small amount of  $\text{SO}_2$  which is formed during  $\text{H}_2\text{S}$  conversion may also affect the combustion process and the flame velocity, respectively. The ignition processes discussed in this work are radical-chain reactions involving reactive species such as  $\text{CH}_3$ ,  $\text{O}$ ,  $\text{OH}$ ,  $\text{H}$ .  $\text{SO}_2$  affects the radical pool in reducing mainly the  $\text{O}$ -radical concentration to equilibrium state due to the recombination of the  $\text{O}$ -radicals to  $\text{O}_2$  by the following steps (eq. IV.2-1 and IV.2-2) [183] and [184]:



As listed in table IV.2-1, the concentration of  $\text{H}_2\text{S}$  was 80 ppm ( $\pm 5\%$ ).

The gas inhomogeneity index (see corresponding section in the previous chapter IV.2.1) was obtained by evaluating the fluctuations of the transmitted signal. After the ignition delay

strong fluctuations are obtained during the whole combustion process as shown in Fig. IV.2-16 (a).

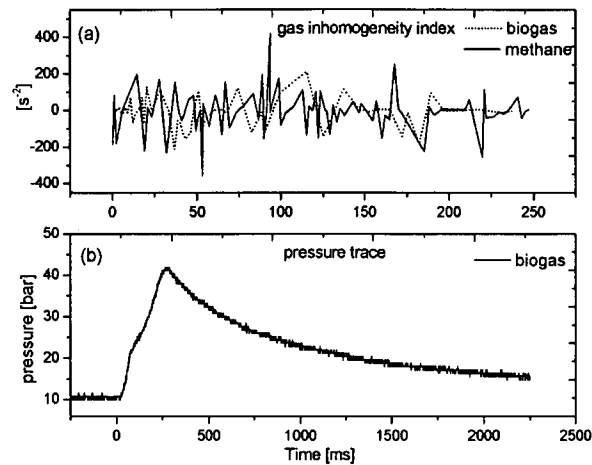


Fig. IV.2-16: Gas inhomogeneity index (a) and pressure trace (b) of the fuel rich biogas/air mixture. Note the different time scales.

The plasma spark ignites the fuel rich biogas/air mixture and the flame front starts to expand with a high velocity causing irregular transmission variations. The flame front generates temperature gradients which further lead to refractive index gradients inside the pressure vessel. These refractive index gradients partly prevent the laser light from falling onto the detector due to deflection and beam steering. The beam can also be partially blocked, e.g. by soot particles but the effect of the refractive index gradients is dominant. The gas inhomogeneity index of biogas does not depict significant differences to a methane/air mixture. In Fig. IV.2-16 b the pressure rise in the vessel after ignition of a biogas/air mixture is illustrated. The maximum pressure rise is reached after approximately 300 ms and decreases again due to heat losses at the chamber walls. In fuel rich methane/air mixtures with similar air to fuel equivalent ratio the pressure trace rises faster and reaches higher pressures because of the absence of  $\text{CO}_2$  resulting in a higher efficiency and power output.

### Fuel lean ignition

Comparing a fuel rich biogas/air mixture with a fuel lean one with respect to laser ignition, several differences can be observed. Fig. IV.2-17 shows the raw data obtained from a fuel lean biogas/air mixture.

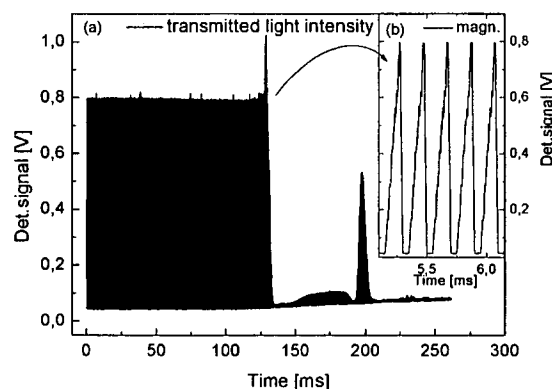


Fig. IV.2-17: Raw data (detector signal) obtained during laser-induced ignition of a fuel lean biogas/air mixture (air to fuel equivalence ratio  $\lambda$  1.21; initial filling pressure 3 MPa; temperature 473 K). The insert (b) shows the magnification of the applied laser ramps with a time resolution of 0.2 ms.

In Fig. IV.2-17 (b) an insert is shown where one can see the individual ramps. The corresponding characterization parameters are depicted in Fig. IV.2-18 (absorbance and flame emissions) and Fig. IV.2-19 (gas inhomogeneity index). By looking at the absorbance one can see that the combustion process is decelerated (slower water generation). In the fuel rich mixture water absorbance of 2 (corresponds to a transmission of 13.5%) is reached after approximately 125 ms, whereas in the fuel lean case the same value is not even obtained after 200 ms as shown in Fig. IV.2-18 a).

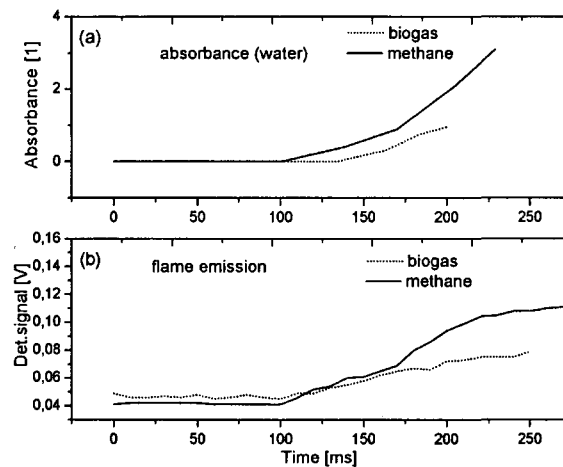


Fig. IV.2-18: Evaluated water absorbance and flame emission of the fuel lean biogas/air mixture depicted in Fig. IV.2-17 and comparison to a methane/air mixture of similar composition (air to fuel equivalence ratio  $\lambda$  1.31, initial filling pressure 3 MPa, temperature 473 K).

In a fuel lean methane/air mixture a steeper rise of the water absorbance is obtained which corresponds to a faster combustion process.

With regard to the flame emission signal in Fig. IV.2-18 (b) an ignition delay time of about 130 ms is observed prior the combustion process is initiated. The slow rise and the lower intensity of the flame emission compared to methane/air mixtures concludes a slow and incomplete combustion of the biogas/air mixture which is also consistent with the slower rise of the water absorbance.

During the ignition delay initiation reactions take place, generating mainly reactive methyl radicals, followed by chain propagation, chain branching and recombination processes. The main initiation steps that convert methane molecules to methyl radicals are depicted by the following reactions (Eq. IV.2-3 to IV.2-5, compare Fig. II.4-5):



If the radical production rate surpasses the recombination rate chain branching reactions lead to ignition and finally to combustion. During the long ignition delay time of the fuel lean biogas/air mixture no variations in the transmitted laser signal are apparent because the flame kernel refracting the laser beam is generated at the end of the induction time.

As shown in Fig. IV.2-19 (a) only slight fluctuations of the gas inhomogeneity index occur because the flame front propagates with decelerated velocity into the unburned mixture.



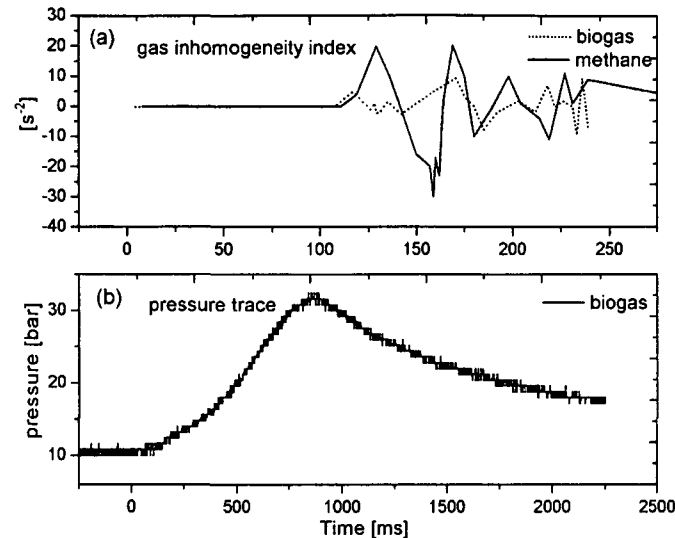


Fig IV.2-19: Gas inhomogeneity index (a) and pressure trace (b) of the fuel lean biogas/air mixture. The peak pressure is higher and reached later compared to the fuel rich case.

In Fig. IV.2-19 (b) the recorded pressure trace of the fuel lean biogas/air mixture is shown. The pressure curve exhibits a lower and later peak pressure compared to the fuel rich case in Fig. IV.2-16 (b). During laser-induced ignition of a fuel lean methane/air mixture the corresponding pressure trace shows again an accelerated combustion behaviour (higher peak pressures, higher temperatures).

Fuel rich methane/air mixtures show a higher burning velocity than fuel rich biogas/air mixtures due to the incombustible gas  $\text{CO}_2$  or even  $\text{SO}_2$ . The same results are obtained investigating fuel lean mixtures. In a stoichiometric mixture the burning velocity has its maximum. By changing the mixture composition into fuel rich or fuel lean regions a decrease is observed (compare Figure II.4-4). Below a certain burning velocity the flame extinguishes and the ignition of the mixture is not possible.

Fuel lean combustion results in lower peak temperatures and hence reduced  $\text{NO}_x$  emissions. In contrast, the total unburnt hydrocarbon emissions increase. Therefore a kind of compromise has to be found. A problem with fuel lean mixtures is a reduced burning velocity resulting in a harsh and irregular running of the engine (note that by generating turbulence, the combustion process is accelerated). Multi-point ignition might help in compensating the loss in flame speed. With multi-point ignition, the distance over which the flame must travel to complete the combustion process is shortened. The combustion times are, therefore, reduced. Because the combustion times are short, the flame does not have enough time to lose heat resulting in higher combustion temperature and pressure leading to a better thermal efficiency and increased power output in internal combustion engines.

### Failed ignition

Besides characterizing ignited biogas/air mixtures the evaluated parameters are also useful for the judgement of failed ignition processes. Fig. IV.2-20 shows a recorded detector signal and Fig. IV.2-21 the corresponding evaluated parameters of a measurement without successful ignition of the mixture. The reason for the failed attempt is that the mixture was too lean. A remarkable dip in the raw data signal at the beginning of the failed ignition event is depicted in Fig. IV.2-20 (compare [172] and [173]).

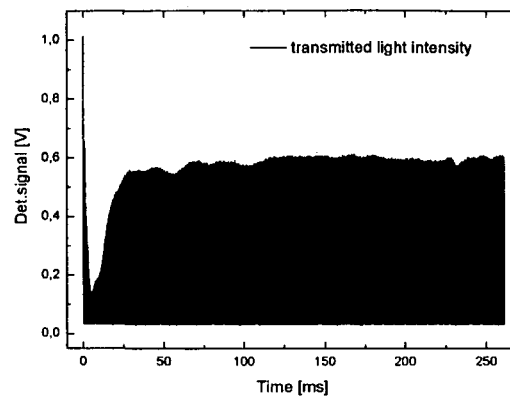


Fig. IV.2-20: Raw data (detector signal) obtained during failed laser-induced ignition measurement. Parameters: air to fuel equivalence ratio  $\lambda$  1.82; initial filling pressure 3 MPa; temperature 473 K (beyond limit of flammability)

The transmission of the laser beam steeply decreases and increases again turning into uniform values after approximately 20 ms. Considering the corresponding gas inhomogeneity index in Fig. IV.2-21 c) this effect results in a significant variation in the transmitted laser signal.

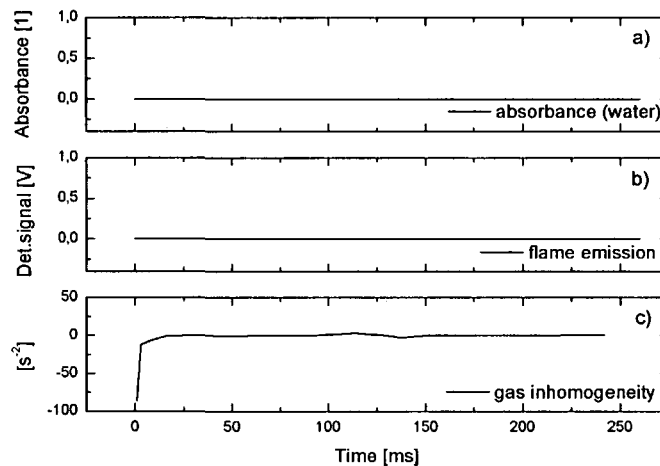


Fig. IV.2-21: Characterizing parameters obtained from the previous test run (failed ignition) in Fig. IV.2-20, namely water absorbance (a), flame emission (b) and gas inhomogeneity index (c).

The remarkable fluctuation at the beginning of the ignition experiment signals that the probing laser beam is strongly deflected by refractive index gradients introduced by the plasma. This plasma spark is a hot spot with temperatures in the order of  $10^6$  K and about 2 mm in diameter [63] which serves as a kind of lens refracting the optical beam path of the laser source. Though the plasma spark has a lifetime of several  $\mu$ s it affects the laser beam up to the ms regime. Because of the failed ignition, evidently no water absorbance and flame emissions were detected. This is a trivial finding, however, it might be useful for the design of an industrial sensor.

The characteristic dip in transmission of the laser beam due to the effect of the plasma spark could also be observed for a failed methane/air mixture with an air to fuel equivalence ratio  $\lambda$  of 2.5. The energy content of the laser pulse was too low to set the mixture on fire and further the generated plasma extinguished. The temperature gradient of the plasma spark deflected the laser beam from the detector causing the marked dip downwards in the laser signal within the first 25 ms of the measurement.

### Conclusions (laser ignition of biogas/air mixtures)

Laser ignition of biogas/air mixtures was investigated and compared to test runs with methane/air mixtures by TDLAS.

For combustion processes in engines fuel lean mixtures are desirable due to lower peak combustion temperatures that would lead to higher  $\text{NO}_x$  emissions (thermal  $\text{NO}_x$ ). It is very important to know the lean ignition limit of the fuel used. Compared to methane/air mixtures biogas/air mixtures show a slower combustion behavior. Because of this effect higher lambdas can be achieved with methane/air mixtures in internal combustion engines (e.g. stationary gas engines for power generation).

In the fuel rich case methane/air mixtures reached a water absorbance of four within 70 ms whereas the time for biogas/air mixtures to reach the same value lasted approximately 3 times longer. The maximum of the flame emission intensity in the rich methane mixture is by a factor of 3 higher than for fuel rich biogas ignition and there is no ignition delay. Fuel lean biogas/air mixtures exhibit a slower combustion behavior resulting in lower peak pressure and flame emission compared to methane/air mixtures of similar air to fuel equivalence ratio.

The reason for these results is the presence of  $\text{CO}_2$  in the biogas which reduces the burning velocity due to obstructing the flame propagation during combustion. By comparing failed ignition test runs of biogas and methane similar results were obtained.

### IV.2.3 Laser ignition of higher hydrocarbon/air mixtures

#### Introduction

The *in-situ* laser diagnostic technique that was applied to laser-induced ignition of methane/air and biogas/air mixtures in the two previous chapters IV.2.1 and IV.2.2 was also used in laser ignition test runs of vaporized liquid fuel/air mixtures.

These tests are to be understood as preliminary experiments. The maximum temperature of the combustion vessel ( $200^\circ\text{C}$ ) was too low to ensure full vaporization at the chosen pressures ( $\gg 1$  bar), and the method of injecting the fuel was not very advanced either. Ten different liquid fuels were used (grouped below according to chemical functionality):

- gasoline (ON 95, petrol station grade)
- pentane ( $\text{C}_5$ ), hexane ( $\text{C}_6$ ), heptane ( $\text{C}_7$ ) (homologous alkanes)
- isooctane (2,2,4-trimethylpentane) and n-octane (both  $\text{C}_8$ )
- cyclohexane (cycloalkane)
- toluene, xylene (aromatic hydrocarbons)
- MTBE (methyl tertiary-butyl ether)

#### Experimental

Fig. IV.2-22 gives a schematic illustration of the experimental setup. It was similar to the preceding tests except for the fuel delivery system (liquid instead of gaseous).

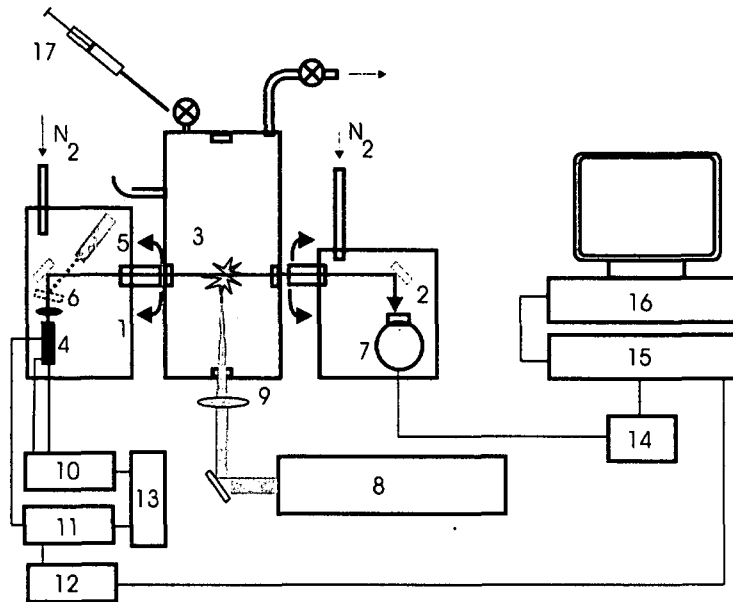


Fig. IV.2-22: Illustration of the setup for laser ignition of higher hydrocarbon/air mixtures. 1,2: purged box; 3: combustion bomb; 4: laser (2.55  $\mu\text{m}$ ); 5: alignment laser; 6: removable mirror; 7: photo detector; 8: ignition laser; 9: focusing lens; 10: temperature controller; 11: laser driver; 12: function generator; 13: 15 V DC power supply; 14: amplifier; 15: oscilloscope; 16: personal computer for data acquisition; 17: syringe;

The experimental setup is similar to the one used in the preceding tests for gaseous fuels except for the fuel delivery system. A port on the top of the chamber was mounted with a ball valve and a septum. The liquid fuels were introduced with a syringe equipped with a long needle able to reach the interior of the chamber heated at 423 K. The syringe is depicted in the following Fig. IV.2-23 (close-up on the right).

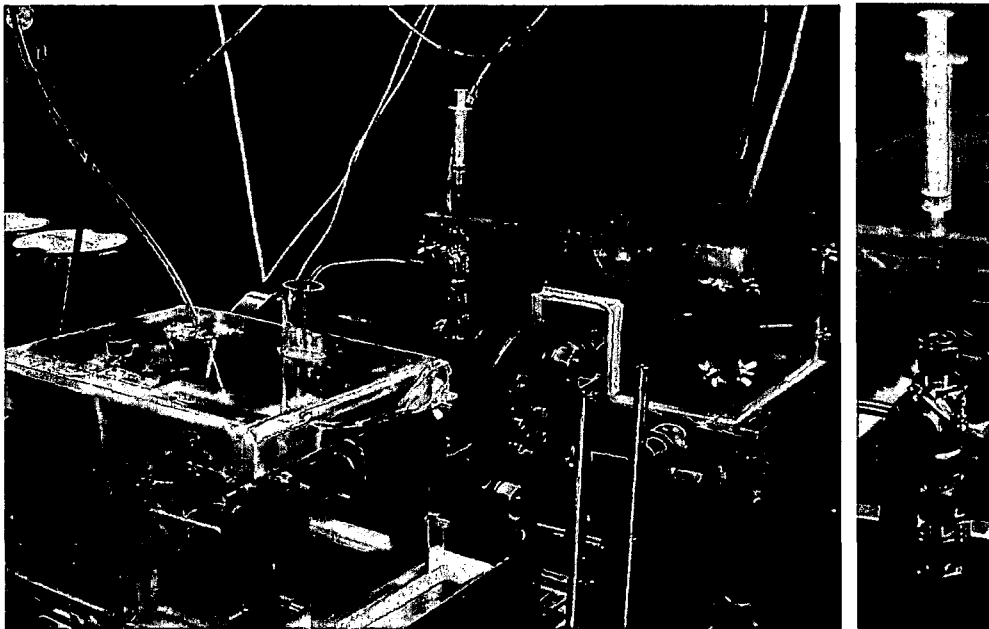


Fig. IV.2-23: Syringe for the introduction of liquid fuels into the combustion chamber.

Next, air was manually fed to reach an initial filling pressure of 1 MPa. Complete vaporization of the fuel could not be ensured at 423 K due to the increase of the boiling point with higher pressure.

The laser measurement system was also the same (InGaAsSb/AlGaAsSb quantum well ridge diode laser at 2.55  $\mu\text{m}$ )

## Results and Discussion

Two parameters namely water absorbance and flame emission were utilized to judge the quality of laser-induced ignition of the vaporized fuel/air mixtures. None of the species produced during ignition and combustion ( $\text{CO}_2$ ,  $\text{CO}$ ) significantly absorb light at  $2.55 \mu\text{m}$  besides  $\text{H}_2\text{O}$ . The formulae used in the following section were taken from [185].

### Gasoline

Fig. IV.2-24 (a) depicts the raw data of a test-run with a fuel rich gasoline/air mixture (the individual ramps are not resolved).

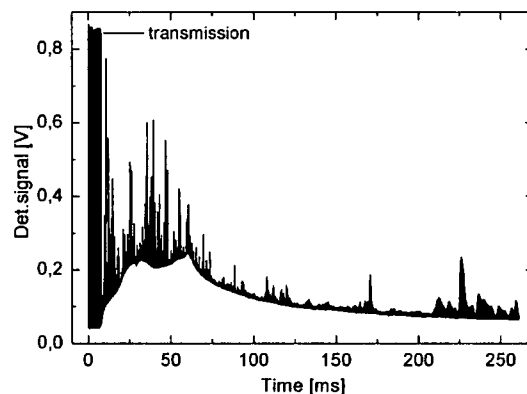


Fig. IV.2-24: Laser-induced ignition of a fuel rich gasoline/air mixture (air to fuel equivalence ratio  $\lambda$  0.59; initial filling pressure 1 MPa; temperature 423 K; raw data).

The transmitted signal of the diode laser beam traversing the combustion chamber fluctuates strongly over time. As outlined earlier, these fluctuations are caused by non-resonant absorption and non-specific beam attenuation respectively such as partial blocking (e.g. due to soot) of the beam, scattering and beam steering due to refractive index gradients. The repetition rate of the diagnostic laser was 5 kHz corresponding to a 0.2 ms time resolution with a total recording time of 264 ms. In Fig. IV.2-25 (a) the absorbance of water vapor is shown generated during the ignition process.

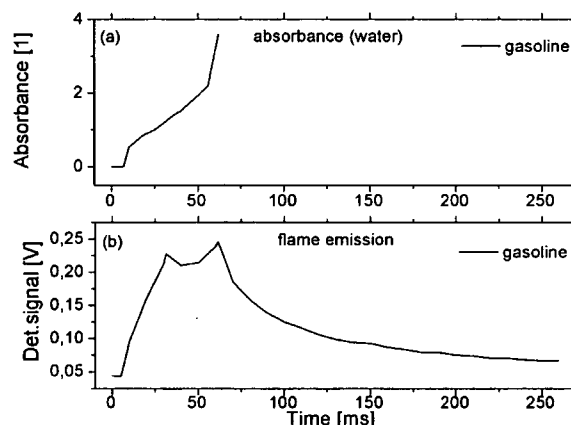


Fig. Fig. IV.2-25: Data evaluation of laser-induced ignition of the fuel rich gasoline/air mixture in Fig. IV.2-24. (a) depicts the water absorbance and (b) the flame emissions with a double peak. It might be the result of a two stage ignition process.

The water absorbance at  $2.55 \mu\text{m}$  increases sharply with time because of a rapid combustion process of the fuel rich gasoline/air mixture. After approximately 70 ms, it could not be

determined any more because the transmission became too low. During the ignition of a fuel lean gasoline/air mixture a slow rise of the water absorbance is observed due to a decelerated oxidation of the gasoline. An absorbance value of two was reached 200 ms after the laser set the mixture on fire.

Observing the flame emission signal in Fig. IV.2-25 (b) of a fuel rich mixture two peaks occur during the ignition process. As mentioned before the investigations were performed at 423 K and 1 MPa. Under these conditions (high pressure) the boiling point increases and the injected fuel does not completely evaporate in the combustion chamber.

The flame emissions show two peaks. An explanation for this curve progression is a two-stage ignition process. In [186] HCCI (homogeneously charged compression ignition) combustion of hydrocarbons was investigated. It was found that fuels which contained the structure  $-\text{CH}_2-\text{CH}_2-\text{CH}_2-$  showed two-stage ignition (also compare Fig. II.7-4; Note, however, that HCCI cannot be readily compared to the laser ignition test runs done here, since these tests are on induced ignition rather than on auto ignition). Gasoline is a complicated mixture of a large number of hydrocarbons including  $-\text{CH}_2-\text{CH}_2-\text{CH}_2-$  structures such as alkanes (e.g. n-heptane, iso-octane), cyclo-alkanes (e.g. cyclohexane), aromatics (xylene, toluene) and additives (e.g. MTBE). It is impossible to create a reaction mechanism for the oxidation of gasoline including all species. In the following chapters gasoline ingredients were ignited separately and the combustion process analysed. In this way information on the oxidation process of gasoline can be obtained.

### Saturated hydrocarbons

In Fig. IV.2-26 the water absorbance of several saturated hydrocarbons contained in gasoline are presented. Note that  $\lambda$  is also varied.

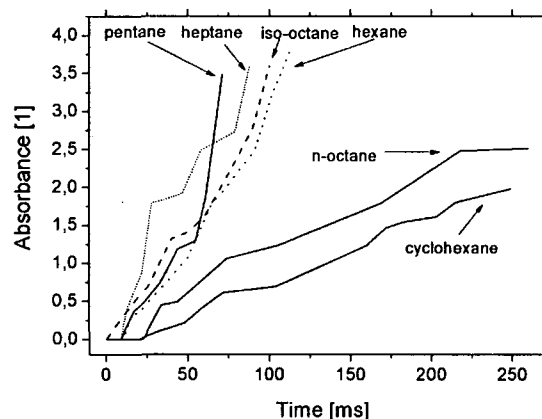


Fig. IV.2-26: Water absorbance of the saturated hydrocarbon/air mixtures at an initial pressure of 1 MPa and 423 K. Pentane (air to fuel equivalence ratio  $\lambda = 0.75$ ), hexane ( $\lambda = 0.81$ ), heptane ( $\lambda = 0.78$ ), iso-octane ( $\lambda = 0.78$ ), cyclohexane ( $\lambda = 1.1$ ) and octane ( $\lambda = 1.2$ ). Note that  $\lambda$  was not held constant.

Fuel rich hydrocarbon/air mixtures including pentane, hexane, heptane and iso-octane showed a similar rise in the water absorbance due to a fast burning velocity. Within 120 ms the absorbance values of the aforementioned hydrocarbons reached 3.5 (see Fig. IV.2-26). An absorbance of 3.5 corresponds to a transmission of approximately  $\exp(-3.5) \sim 3\%$ . In other words, only a small fraction of the initial laser light intensity is not absorbed. For cyclohexane and n-octane only a slow rise in the water absorbance was seen due to a fuel lean hydrocarbon/air mixture resulting in a slower combustion process and flame kernel propagation, respectively. Within a time span of 264 ms the water absorbance reached only a value of about 2 which corresponds to a transmission of about 13.5%. In Fig. IV.2-27 the corresponding flame emissions captured by the detector are illustrated.

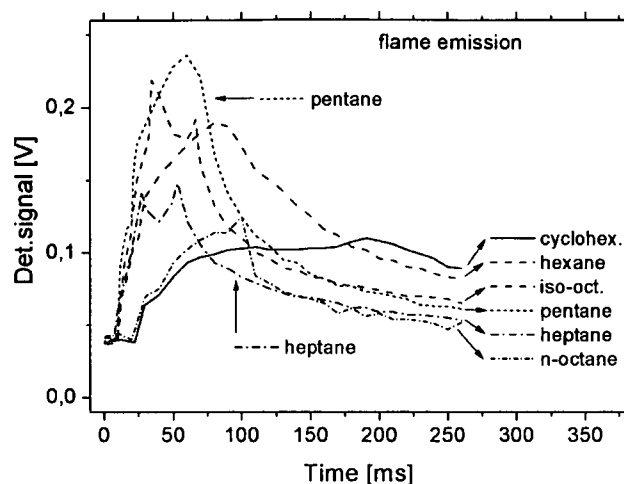
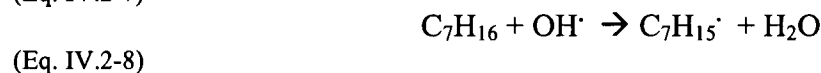
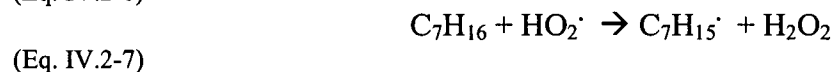
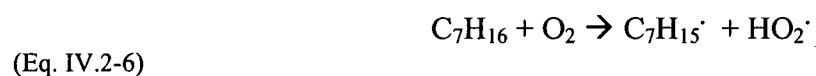


Fig. IV.2-27: Flame emission from test runs with saturated hydrocarbon/air mixtures. The fuels ignite in a two stage ignition process. Remarkable flame emission peaks were obtained for iso-octane, heptane and n-octane. For pentane, hexane and cyclohexane only slight bends in the curve progression were observed.

One can deduce the ignition delay time from the difference of the start in emission to the trigger signal of the laser pulse. Fuel rich hydrocarbon/air mixtures (pentane, hexane, heptane and iso-octane) show an ignition delay of approximately 10 ms whereas the fuel lean octane/air and cyclohexane/air mixtures depict an induction time of about 25 ms before the mixture was set on fire. As mentioned in the section on gasoline hydrocarbons containing the chemical structure  $-\text{CH}_2-\text{CH}_2-\text{CH}_2-$  show a two stage ignition process. This might be the reason for the remarkable peaks for n-heptane and iso-octane. The curve progression of pentane and hexane also depicts a two stage combustion process due to a small bend of the flame emission after approximately 25 ms. n-octane also reacts in a two stage oxidation process whereas the first bend occurs after 40 ms and the second peak is situated 100 ms after the laser pulse was initiated. By regarding the flame emissions in Fig. IV.2-27, one can see that the combustion process of cyclohexane is the slowest one which is also confirmed by the water absorbance (Fig. IV.2-28).

The interest in oxidation processes of hydrocarbons (especially the model substances n-heptane and iso-octane) lies in the possibility of a better understanding of the unwanted knocking behaviour in internal combustion engines.

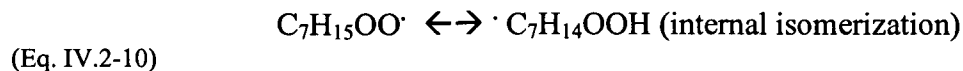
The two stage ignition process involves a low temperature followed by a high temperature cycle. At low temperatures the oxidation of n-heptane is initiated by the reaction with  $\text{O}_2$  to produce an alkyl radical and  $\text{HO}_2$  which in turn reacts with the fuel, forming  $\text{H}_2\text{O}_2$ . Another initiation step is the reaction with  $\text{OH}$  [185]:



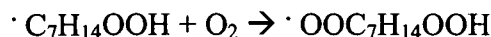
Eq. IV.2-6 is not an important route to the formation of the n-heptyl radical  $\text{C}_7\text{H}_{15}^\cdot$  but Eq. IV.2-7 and Eq. IV.2-8 are the main reactions to form the alkyl radical. During the low temperature regime the n-heptyl radical reacts with  $\text{O}_2$ :



At low temperatures the reaction rate is high forming a heptylperoxy radical whereas with rising temperature the formation of the n-heptyl radical is preferred. Further the heptylperoxy radical  $C_7H_{15}OO\cdot$  isomerize to a heptylhydroperoxy radical  $\cdot C_7H_{14}OOH$  by internal H-abstraction followed by second  $O_2$  addition forming a hydroperoxyheptylperoxy radical:



(Eq. IV.2-10)



(Eq. IV.2-11)

The hydroperoxyheptylperoxy radical can then isomerize and decompose into a relatively stable ketohydroperoxide species and  $OH\cdot$ . This cycle continuous (Eq. IV.2-9 to Eq. IV.2-11) until temperature rises ( $>800$  K) and the reaction



(Eq. IV.2-12)

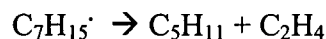
becomes more and more important competing with Eq. IV.2-9. This is the termination of the first stage of combustion resulting in the formation of the first peak of the n-heptane flame emission. Further the reaction rate of Eq. IV.2-7 becomes higher and the stable species  $H_2O_2$  is formed slowing down the oxidation. This is the beginning of the second stage process where slight exothermic reactions take place and the temperature rise drops sharply. At 900-1000 K  $H_2O_2$  is relatively stable but once the temperature is high enough  $H_2O_2$  quickly decompose according to



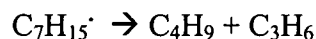
(Eq. IV.2-13)

This is the termination of the second stage and branched thermal explosion occurs. As a result the second flame emission peak of n-heptane is formed after approximately 60 ms.

For higher temperatures the heptyl radical do not react with oxygen, as presented in Eq. IV.2-9 but will decompose instead via  $\beta$ -scission to a smaller olefin and other species such as

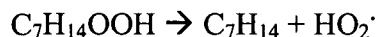


(Eq. IV.2-14)

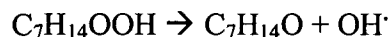


(Eq. IV.2-15)

The heptylhydroperoxy radical formed in Eq. IV.2-10 forms a stable olefin and a hydroperoxy radical at high temperatures or reacts to a cyclic ether and a hydroxy radical

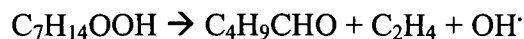


(Eq. IV.2-16)



(Eq. IV.2-17)

Another possibility is the formation of a hydroxyl radical an olefin and an aldehyde:



(Eq. IV.2-18)

The iso-octane oxidation scheme is very similar to the n-heptane reaction path. Iso-octane has got a highly branched chemical structure compared with n-heptane having a higher amount of primary H-atoms. These primary H-atoms are less reactive than the secondary ones, slowing down H-abstraction and isomerizations. During the iso-octane oxidation process mainly less



reactive species are formed such as olefins and cyclic ethers whereas the production rate of highly reactive peroxide species is decreased. As a result the flame emission peaks of the two stage ignition process of iso-octane are delayed compared to n-heptane. The increase in water generation of iso-octane is also delayed which confirms a slower combustion process.

A detailed reaction scheme of higher hydrocarbons becomes very complex. [187] contains a scheme of iso-octane oxidation involving 324 species and 1303 reactions. A dramatic simplification of the oxidation mechanism of n-heptane was published by [188] where the kinetic mechanism was reduced to 4 global steps. Further information on n-heptane and iso-octane oxidation processes and mechanisms are discussed in [189]-[193].

### Aromatic hydrocarbons

Aromatic hydrocarbons such as xylene and toluene are also important constituents of gasoline. The oxidation behaviour is rather different compared to saturated hydrocarbons. The water absorbance of both xylene and toluene shows a slow ignition process compared to pentane, hexane, iso-octane and n-heptane as shown in Fig. IV.2-28.

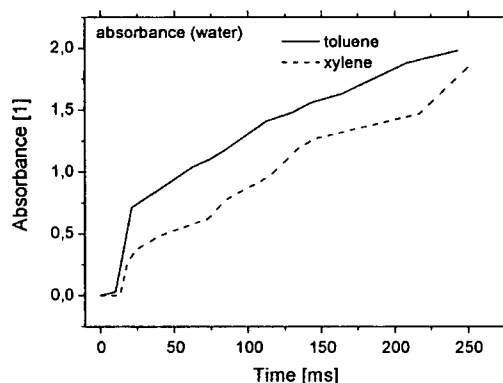


Fig. IV.2-28: Water absorbance of aromatic hydrocarbon/air mixtures at an initial pressure of 1 MPa and 423 K. Toluene (air to fuel equivalence ratio  $\lambda$  0.7), xylene ( $\lambda$  0.69)

In Fig. IV.2-29, the flame emission of the aromatic fuels is shown. One can assume a single stage ignition process due to the absence of the double peaks.

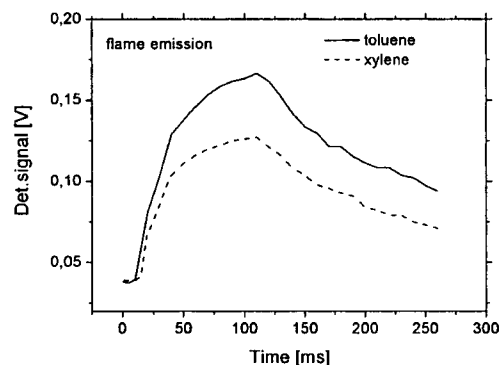
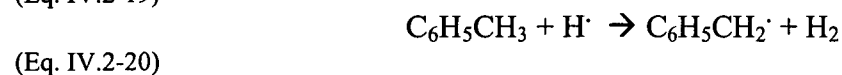
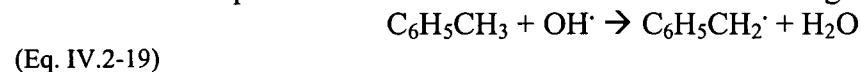
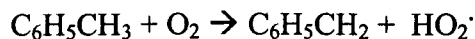


Fig. IV.2-29: Flame emission of aromatic hydrocarbon/air mixtures. Toluene and xylene ignite in a single stage ignition process (no double peaks were observed).

The initiation steps of toluene oxidation consist of the following reactions [185]:





(Eq. IV.2-21)



(Eq. IV.2-22)

Since the reaction of toluene with  $\text{O}_2$  is quite slow the main benzyl radical producer is the reaction of toluene with the hydroxyl radical  $\text{OH}^\cdot$  and the  $\text{H}^\cdot$  radical. Though it might be unexpected, Eq. IV.2-19 and Eq. IV.2-20 are inhibition reactions because the benzyl radicals formed during these reactions are less reactive than  $\text{OH}^\cdot$  and  $\text{H}^\cdot$  radicals. As a result of this poor reactivity of benzyl radicals the oxidation process is slowed down.

Toluene oxidation is continued by the reaction of benzyl radicals with  $\text{HO}_2^\cdot$  and  $\text{O}^\cdot$  forming benzaldehyde. Decomposition of the benzaldehyde follows generating  $\text{C}_6\text{H}_5\text{CO}$ . The next step is the formation of the phenyl radical  $\text{C}_6\text{H}_5^\cdot$  after CO abstraction. From this point,  $\text{C}_6\text{H}_5^\cdot$  most likely reacts with  $\text{O}_2$  to yield phenoxy radicals  $\text{C}_6\text{H}_5\text{O}^\cdot$ . Further CO abstraction leads to the generation of cyclopentadienyl radicals  $\text{C}_5\text{H}_5^\cdot$ . The cyclopentadienyl radical can finally yield  $\text{C}_2\text{H}_3^\cdot$  and acetylene  $\text{C}_2\text{H}_2$  or another branching path might lead to the formation of CO and acetylene. The reaction paths of xylene are comparable but the reaction rates of the oxidation processes are slower, which is consistent with the flame emission and the water absorbance of xylene measured here.

### MTBE

MTBE has a high reactivity which is illustrated in the steep increase of water absorbance in Fig. IV.2-30 reaching an absorbance value of 4 within 70 ms. Toluene has been plotted for comparison.

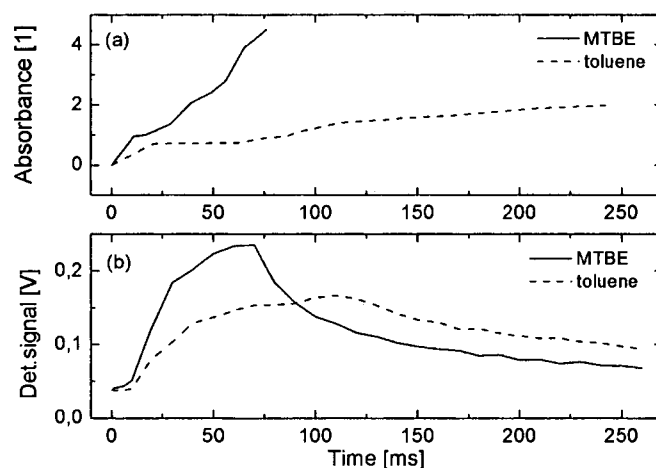
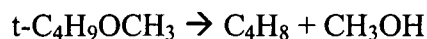


Fig. IV.2-30: Data evaluation of laser-induced ignition of the fuel rich MTBE/air mixture. (a) depicts the water absorbance and (b) the flame emission (implying a single step ignition process). Toluene (dashed line) has been plotted for comparison.

The high intensity in flame emission implies a fast and complete combustion process of the MTBE/air mixture. The curve progression of the MTBE flame emission resembles the curves of xylene and toluene. Here, too, a one stage combustion process can be assumed. The oxidation of MTBE can be described by a unimolecular decomposition yielding iso-butene and methanol [194]:



(Eq. IV.2-23)

Since the principal product of the MTBE consumption is iso-butene the reactions involved in the iso-butene oxidation are also important in the MTBE oxidation. For further information the reader is referred to [195] to [196].

### Conclusions (laser ignition of higher hydrocarbon/air mixtures)

Laser-induced ignition of vaporized liquid hydrocarbon/air mixtures was investigated including gasoline and its several main constituents (saturated and aromatic hydrocarbons as well as MTBE). Two characterization parameters were utilized to judge the combustion process of the hydrocarbon/air fuels namely water absorbance and flame emission. Two stage ignition occurred in the combustion of gasoline, pentane, hexane, heptane, n-octane, iso-octane and cyclohexane marked by two flame emission peaks during the ignition process. The aromatic hydrocarbons toluene and xylene and MTBE seem to be consumed in a single stage ignition process. To gain a better understanding of knocking behavior in internal combustion engines the focus of this work lies in the investigation of especially n-heptane, iso-octane, toluene and MTBE.

A single stage oxidation process seems to occur for toluene generating radicals such as benzyl, phenyl, phenoxy and cyclopentadienyl. Xylene also reacts in a single stage ignition process but the combustion of toluene is faster resulting in a decreased water absorbance.

MTBE with its high reactivity which is seen in the steep increase of water absorbance is decomposed in a single stage combustion process. During the oxidation process MTBE generates mainly iso-butene and methanol.

A two stage ignition process also occurs in the combustion of gasoline having two flame emission peaks. The ignition processes are described by formulae from the literature.

### Conclusions (all diagnostics on laser ignition: CH<sub>4</sub>, biogas, higher hydrocarbons)

The main goal of this thesis was to gain a deeper understanding of laser-induced ignition. Tunable diode laser absorption spectroscopy (TDLAS) was selected as the method best suited to address the problem. Most of the additional work presented here was done in preparation for this. The *in-situ* species concentration measurements in the laboratory scale fluidized bed combustor (see chapter IV.1) were, more or less, a by product of the absorption line selection and temperature calibration procedures needed for the subsequent use of the 2.55  $\mu\text{m}$  laser in the laser ignition test runs. The extensive work on vertical-cavity surface-emitting lasers (VCSELs) (see chapter III.4) was primarily done to obtain a laser source that is better suited for the investigation of high pressure environments as encountered in the laser ignition test setup.

Most of the work was done in the characterization of laser induced ignition of CH<sub>4</sub>/air mixtures at high pressures. Biogas/air mixtures and vaporized higher hydrocarbon/air mixtures were also investigated.

The probing laser beam (2.55  $\mu\text{m}$  or 3920  $\text{cm}^{-1}$ ) traversed the combustion vessel at the height of the ignition spark perpendicularly to the radiation of the pulsed Nd:YAG laser for ignition. It was wavelength tuned at 5 kHz (0.2 ms time resolution) in order to track the formation of water vapor formed in the vicinity of the igniting laser spark.

The formation of H<sub>2</sub>O was used to judge the quality of the ignition process.

In addition, the emissions from the flame were recorded. They allow the determination of ignition delay time, flame growth and flame quenching.

The fluctuations in the transmission of the probing diode laser beam can be correlated with properties of the developing flame and the effect the plasma and the shock wave have generated. A gas inhomogeneity index is introduced by extracting a frequency variable from the envelope curve in the raw data and performing its derivation.

The developed technique based on the three parameters (i.e. water absorption, flame emissions, gas inhomogeneity index) was found to adequately characterize fuel rich, stoichiometric, fuel lean and failed ignition attempts (see the conclusions in the respective subchapters for details).

Limitations include the adverse effect of pressure broadening on the quantification of the absorbance signal and the ignorance of temperature.

### Outlook

By using VCSELs instead of edge emitting diode lasers, species concentration measurements at higher pressures can be done in a better way. Especially H<sub>2</sub>O absorption lines in the 1.96 to 2.0 μm wavelength range that increase with temperature and show only weak pressure broadening coefficients would be very useful in continued tests.

The following Fig. IV.2-31 shows calculated absorption spectra of H<sub>2</sub>O (1cm path length, pressure 30 bar, 10% H<sub>2</sub>O (CH<sub>4</sub> + 2 O<sub>2</sub> → 2 H<sub>2</sub>O + CO<sub>2</sub>, ~ 5 % CH<sub>4</sub> at lambda = 2), temperature 296 –1500 K in 300K steps). CH<sub>4</sub> shows broad, negligible absorbance in this spectral region. Depicted are overview spectra (b) and in (a) 2 nm broad detailed spectra. One can see that the absorbance increases with temperature in the range of 300K – 1500K. At 296 K (room temperature), there is only negligible absorbance. By doing spectroscopy based on one of these lines, one would not have to purge the region outside the combustion vessel.

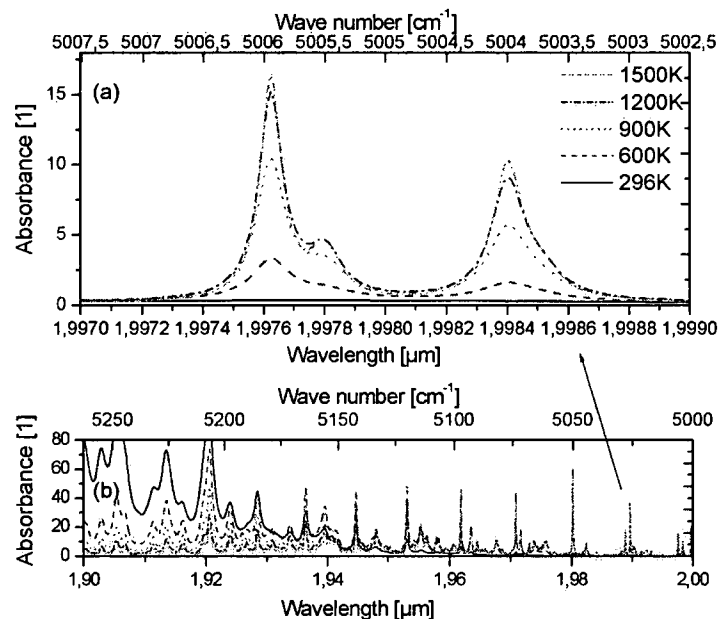


Fig. IV.2-31: Calculated absorption spectra of H<sub>2</sub>O for 1cm path length, 30 bar pressure, 10% H<sub>2</sub>O (CH<sub>4</sub> + 2 O<sub>2</sub> → 2 H<sub>2</sub>O + CO<sub>2</sub>, ~ 5 % CH<sub>4</sub> at lambda = 2) and temperatures of 296K, 600K, 900K, 1200K and 1500 K. (b) shows overview spectra. In (a), a 2 nm (5 cm<sup>-1</sup>) broad range showing two suitable H<sub>2</sub>O absorption features is depicted.

This work was published:

M. Lackner, Ch. Forsich, F. Winter, H. Kopecek, E. Wintner, *In-situ* Investigation of Laser-induced Ignition and the Early Stages of Methane-Air Combustion at High Pressures Using a Rapidly Tuned Diode Laser at 2.55 μm, *Spectrochimica Acta A*, in press (2003).

M. Lackner, Ch. Forsich, F. Winter, H. Kopecek, E. Wintner, Characterization of Laser Ignition of Hydrocarbon/Air Mixtures using a tunable InGaAsSb/AlGaAsSb diode laser at 2.55μm, poster presentation at CLEO/Europe (conference on lasers and electro optics), Munich, Germany, June 25<sup>th</sup> (2003).

### IV.3 Trace gas sensing in biogas and biomass steam gasification gas

A GaAs-based quantum cascade laser (QCL) capable of sensing  $C_2H_4$  and  $NH_3$  was used to investigate biogas and the product gas from a biomass steam gasification plant for their content of  $C_2H_4$  and  $NH_3$ . Details in the laser can be found in chapter III.2. This work was carried out in cooperation with Prof. Dr. Strasser and Dr. Solveig Anders from the Institut für Festkörperelektronik, Vienna University of Technology. The biogas was obtained from the municipal sewage purification plant in Bad Voeslau/Lower Austria (for the composition, see table IV.2-1 in the previous chapter on the laser-induced ignition of biogas/air mixtures). The second set of gas samples was obtained from the biomass steam gasification plant in Guessing, Austria, and provided by Prof. Dr. Hermann Hofbauer and Dr. Reinhard Rauch from the Institute of Chemical Engineering, Vienna University of Technology.

Both  $C_2H_4$  [116], [197]-[198] and  $NH_3$  [199]-[201] have already been measured by laser absorption spectroscopy, however the latter predominantly in the near-infrared. Here, we describe direct absorption spectroscopy as a tool to probe rovibrational transitions of  $C_2H_4$  and  $NH_3$  in the  $\nu_7$  and  $\nu_2$  fundamental bands, respectively.

#### Experimental

The experimental setup is depicted in Fig. IV.3-1. The laser light passes a gas cell (0.44 m long, wedged ZnSe windows) containing the absorber. It is then focused onto a mercury-cadmium-telluride detector. The pressure of the absorbing gas was 1.013 bar. It was measured at room temperature. The baseline was recorded at atmospheric pressure (gas cell filled with air) to avoid distortions of the cell (with respect to a evacuated cell).

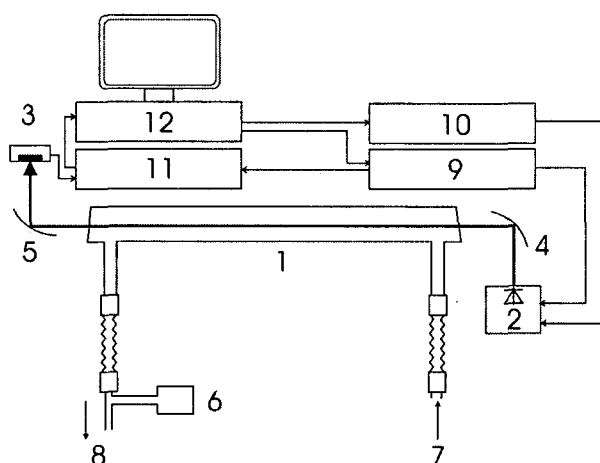


Fig. IV.3-1: Experimental setup. 1: gas cell (length 0.44 m); 2: quantum cascade laser in thermostated housing; 3: photodetector; 4, 5: parabolic mirrors; 6: pressure gauge; 7: gas inlet; 8: gas outlet, cryotrap and vacuum pump; 9: pulse generator; 10: thermostat; 11: lock-in amplifier; 12: personal computer.

Fig. IV.3-2 shows a picture taken during the measurements.

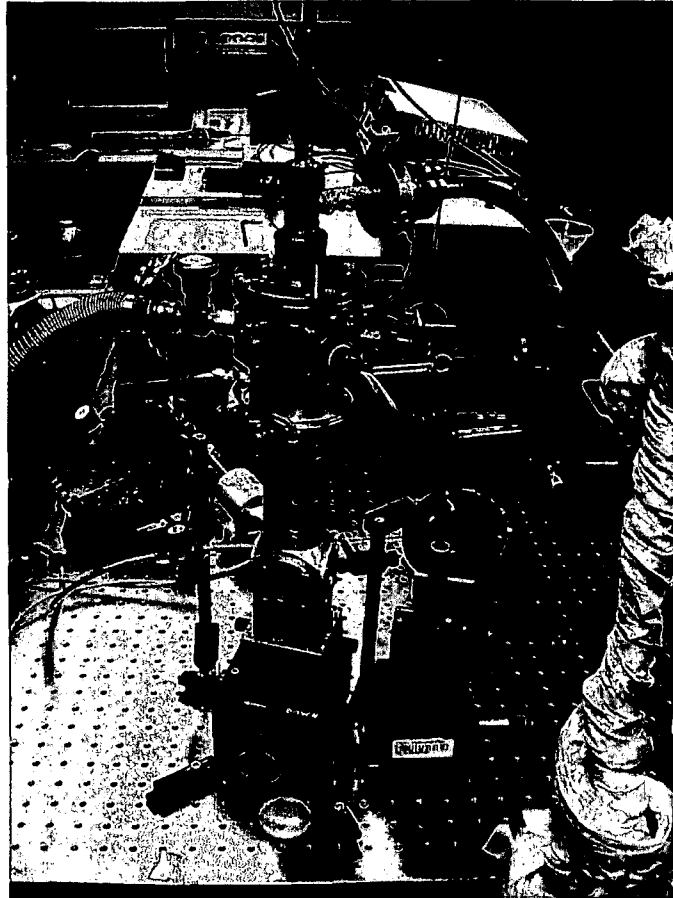


Fig. IV.3-2: Picture of the experimental setup. At its bottom, the metallic upright tube contains the QCL.

### Results and Discussion

To demonstrate the use of a QCL for sensitive absorption spectroscopy, diluted  $\text{NH}_3$  (1500 ppm in nitrogen) and  $\text{C}_2\text{H}_4$  (2.00 % in nitrogen) were filled into the gas cell. The measurement was performed at a total pressure of 1.013 bar and at room temperature. Figs. IV.3-3 and IV.3-4 show spectra of  $\text{NH}_3$  and  $\text{C}_2\text{H}_4$ , respectively, as obtained with the QCL.

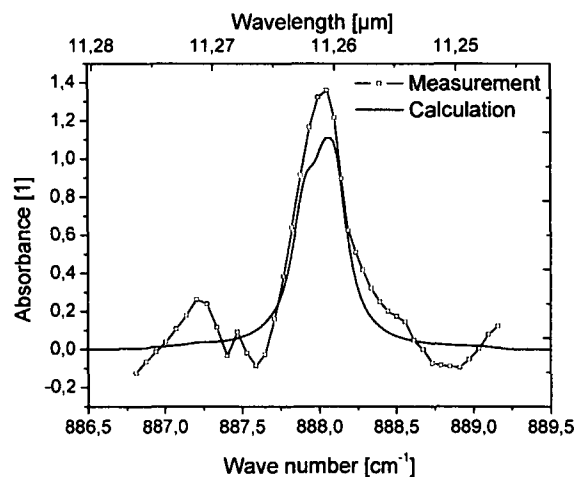


Fig. IV.3-3: Measurement of  $\text{NH}_3$  in the laboratory glass cell. Adequate agreement was found with the calculated spectra from the HITRAN 2000 database. Experimental parameters were 0.44 m path length, room temperature, 1.013 bar total pressure, 1500 ppm  $\text{NH}_3$  in air.

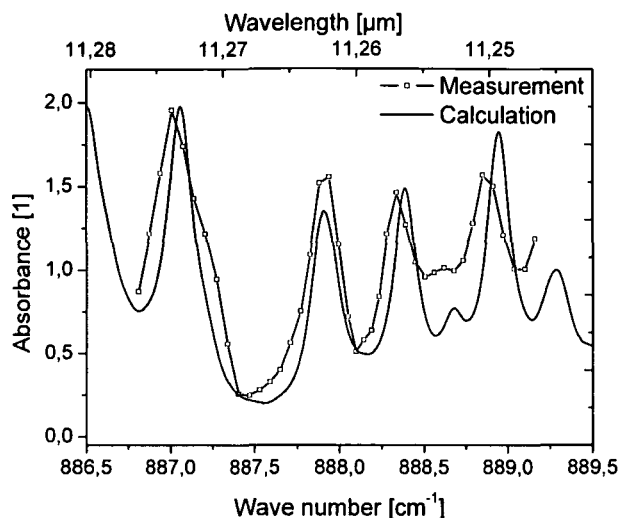


Fig. IV.3-4: Measurement of  $C_2H_4$  in the laboratory glass cell. Adequate agreement was found with the calculated spectra from the HITRAN 2000 database. Experimental parameters were 0.44 m path length, room temperature, 1.013 bar total pressure, 2.00 %  $C_2H_4$  in nitrogen.

The absorbance  $A(\nu)$  is defined as  $A(\nu)=\ln(I_0/I)(\nu)$  with  $\nu$  being the frequency,  $I_0$  the laser output intensity (baseline) and  $I$  the transmitted laser intensity (signal). The absorbance is directly proportional to the number density (concentration times path length) of the absorber. The major absorption feature of  $NH_3$ , centered at approximately  $888\text{ cm}^{-1}$  ( $11.26\text{ }\mu\text{m}$ ), consists of several absorption lines that cannot be resolved at the pressure of 1.013 bar. For the  $C_2H_4$  spectrum, the laser was tuned over four absorption lines.

The solid lines are calculated reference spectra based on line parameters from the HITRAN 2000 spectroscopic database [4]. The spectra measured with the QCL show adequate resemblance to the HITRAN 2000 database spectra. The detection limits for the current experimental setup, are 0.5% for  $C_2H_4$  ( $= 2200\text{ ppm}\cdot\text{m}$ ) and 500 ppm for  $NH_3$  ( $220\text{ ppm}\cdot\text{m}$ ). Further, we investigated biogas from a municipal sewage plant. The biogas contained approximately 50.5 %  $CH_4$  and 31.7 %  $CO_2$ . Biogas is produced by anaerobic digestion of organic material in the sewage. Its composition varies strongly with process parameters. The gas has to be disposed of for safety reasons and can be used for energy generation. The spectra taken with the QCL showed neither  $C_2H_4$  nor  $NH_3$ .

We will now discuss the investigation of product gas from a biomass steam gasification pilot-plant. Instead of directly burning biomass fuels, one can produce thermal energy more efficiently and cleaner by converting the solid fuels to a combustible gas. If the conversion process utilizes steam as the gasification agent, a high grade synthesis gas that is nearly nitrogen free can be obtained (calorific value of  $12\text{ MJ/m}^3$ ) [202].

The composition of the investigated gasification gas is given in table IV.3-1.

Compound	Concentration
$H_2$	35%
CO	25%
$CO_2$	20%
$CH_4$	10%

Table IV.3-1: Composition of the biomass steam gasification gas.

Fig. IV.3.-5 presents a spectrum obtained from the gasification gas, together with a spectrum of  $C_2H_4$ . All were taken with the QCL. The concentration of  $C_2H_4$  was determined to be approximately 2 %, in agreement with conventional methods.  $NH_3$  could not be detected.

Conventional methods determine the  $\text{NH}_3$  content as  $< 200$  ppm. Note that around  $11 \mu\text{m}$ , none of the other constituents in the gasification gas exhibits absorption lines.

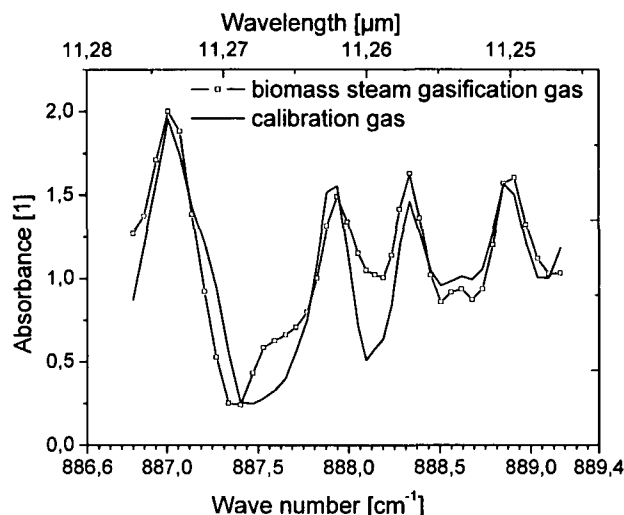


Fig. IV.3.-5: Examination of product gas from biomass steam gasification. The gas was found to contain approximately 2% of  $\text{C}_2\text{H}_4$ .  $\text{NH}_3$  was not detected. For comparison, a measured spectrum for  $\text{C}_2\text{H}_4$  (2.0%) is overlaid. Experimental parameters were 0.44 m path length, room temperature, 1.013 bar total pressure, pure biomass steam gasification gas.

### Conclusions

To summarize, we have used a quantum cascade laser emitting in the mid-infrared to measure the spectra of  $\text{NH}_3$ ,  $\text{C}_2\text{H}_4$ , biogas and biomass steam gasification gas. The measured spectra of  $\text{NH}_3$  and  $\text{C}_2\text{H}_4$  agree well with the HITRAN 2000 database, both for the bottled reference gases and  $\text{C}_2\text{H}_4$  as found in the investigated gases. The  $\text{C}_2\text{H}_4$  and  $\text{NH}_3$  levels in the biogas were below detection limits (0.5% (= 2200 ppm\*m) and 500 ppm (= 220 ppm\*m) respectively), and these findings were confirmed for  $\text{NH}_3$  by conventional methods, which indicated that  $\text{NH}_3$  levels were below 200 ppm. The biomass product gas was shown to contain approximately 2 %  $\text{C}_2\text{H}_4$ , in agreement with conventional methods. We conclude that the use of a quantum cascade laser is a reliable and relatively quick method to measure spectra of gases in the mid-infrared.

This work was published:

M. Lackner , Ch. Forsich, F. Winter, S. Anders, G. Strasser, Investigation of biomass steam gasification gas using GaAs based quantum cascade laser emitting at  $11 \mu\text{m}$ , Optics Communications 216 (4-6), 357 - 360 (2003).



## IV.4 Rapid absorption spectroscopy using VCSELs

In this work, vertical-cavity surface-emitting lasers (VCSELs) were used in absorption spectroscopic demonstration experiments.

Details of the lasers can be found in chapter III.3 (761 nm VCSEL) and III.4 (novel long wavelength VCSELs, 1.54 – 1.81  $\mu\text{m}$ ). This work was carried out in cooperation with Prof. Dr. Markus-Christian Amann, Dr. Markus Ortsiefer and Dipl.-Phys. Robert Shau from the Walter Schottky Institute (WSI), Munich University of Technology (Germany).

The 1.54  $\mu\text{m}$  VCSEL was used for high temperature spectroscopic investigations of  $\text{NH}_3$ .

The measurements using 1.68 and 1.81  $\mu\text{m}$  VCSELs for rapid and high resolution spectroscopy of  $\text{CH}_4$ ,  $\text{H}_2\text{O}$  and  $\text{HCl}$  were carried out during a research stay at the WSI in Munich.

In the second part of this chapter, results from measurements under difficult conditions are presented. A 761 nm VCSEL for the detection of  $\text{O}_2$  was used for measurements at high temperatures (i.e. in flames up to 1 m length and in particle laden flows), at high pressures and in a wavelength modulation spectroscopy setup. For the measurements in flames and particle laden flows, the rapid tuning is essential.

The lower detection limit was not determined experimentally.

If a minimum detectable absorbance of 0.01 is assumed, the approximate detection limit for  $\text{NH}_3$  (1540 nm) is 17500 ppm\*m, for  $\text{CH}_4$  (1680 nm) 2200 ppm\*m, for  $\text{HCl}$  and  $\text{H}_2\text{O}$  (1810 nm) 320 and 290 ppm\*m, respectively. For  $\text{O}_2$  (760 nm), it is 150000 ppm\*m (all calculated for 1 bar and 296K).

### IV.4.1 High speed and high resolution molecular absorption spectroscopy using long wavelength InP based VCSELs

#### IV.4.1.1 1540 nm VCSEL

$\text{NH}_3$  is an important gas needed in various industrial processes and products ranging from the organic chemistry and chemical synthesis to fertilizers, refrigerators, chemical fiber production and  $\text{NO}_x$  removal in combustion processes. The widespread use and the toxic nature of ammonia results in a need for an adequate gas sensor, which helps to reduce costs by optimizing processes control and to avoid pollution risks and potential health hazards. Diode lasers for process control [203] might be used as ammonia sensors in industrial SNCR (selective non-catalytic reduction) and SCR (selective catalytic reduction)  $\text{DeNO}_x$  processes [204]. One main advantage of diode laser based gas sensors is the ability to measure reactants and intermediates *in-situ* and non-intrusively directly in the reaction chamber without the need for sampling and recalibration and with high time resolution. Up to now vertical-cavity surface-emitting lasers (VCSELs) have been used for absorption spectroscopy of  $\text{O}_2$  near 760 nm [42], [117], [124], [205] -[208] and for  $\text{H}_2\text{O}$  measurements near 962 nm [209]. [208] reported that they achieved unsatisfactory results using VCSELs as compared to DFB lasers. None of these papers reports highly resolved low pressure spectra and [117], [209] state that their VCSEL systems are unsuitable to perform low pressure measurements. Only recently long wavelength VCSEL have been developed (see chapter III.4 and [119], [121]-[123], [210]-[211]). The results presented in this paper show that VCSELs are very well suited not only to measure spectra at high pressures, but also for high resolution spectroscopy at low pressures. A 1.5 $\mu\text{m}$  VCSEL is used to measure highly resolved spectra of  $\text{NH}_3$  at various pressure ranging from 9.6 mbar to 1 bar. For the first time the high speed tuning capabilities of near IR VCSELs are investigated and used for high speed (within 2  $\mu\text{s}$ ) gas sensing.

More information about the  $\text{NH}_3$  absorption lines in the 1496-1582 nm range which are best suited for diode laser combustion-emission and air-quality monitoring can be found in [212]. The 1.5  $\mu\text{m}$  wavelength region is also a very well suited for the measurement of a variety of other species ranging from OH,  $\text{N}_2\text{O}$ , HCN, HI,  $\text{H}_2\text{S}$  to CO and  $\text{CO}_2$  ([213], compare [4]).

### Experimental

The 1.54  $\mu\text{m}$  VCSEL, supplied in a TO-46 case, was mounted on a copper heat sink with integrated thermistor and a small Peltier cooler for temperature control. The laser emission was collimated using an anti-reflection coated aspheric lens with 4.5 mm focal length and <0.25% nominal reflectivity at 1.5  $\mu\text{m}$ . The temperature controller and laser diode driver were the HTC-3000 (Wavelength Electronics Inc.) and the LDX-3220 (ILX Lightwave Inc.), respectively. The 0-7 mA current needed to drive the VCSEL was only a fraction of the laser driver output current range of 0-200mA, but despite this fact the laser driver was sufficiently low noise to record clean spectra. The laser beam was directed with mirrors twice through the 43.7 cm long sampling cell (total absorption path length 87.4 cm) and onto the DC-10 MHz InGaAs photo detector (PDA400-EC, Thorlabs Inc.) with 1 mm active diameter and a 800-1750 nm response (see Fig.IV.4-1).

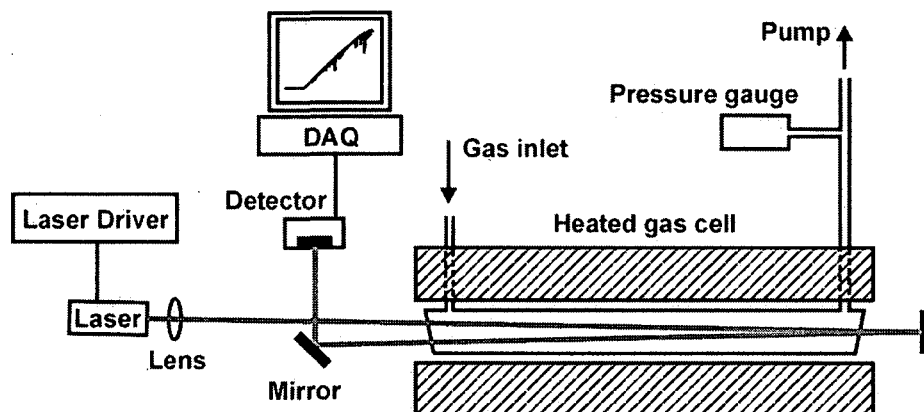


Fig. IV.4-1: Experimental schematic of the 1.5  $\mu\text{m}$  VCSEL absorption spectroscopy setup (DAQ = data acquisition board).

The quartz glass measurement cell which had 25 mm diameter wedged fused silica windows could be heated to 1300 K using electric heating shells and could be evacuated using a roughing pump in series with a cold trap to 2 mbar. The pressure was measured using a Varian VCMT 13T capacitive pressure transducer. The data shown in the figures was recorded at 31.25 MS/s sampling rate with a 12 bit Signatec PDA12A data acquisition board mounted in personal computer. Only for the high speed measurements (Fig IV.4-7) a different sampling rate of 125 MS/s was used. A 5 mm thick sapphire window (etalon) was positioned in the beam path before each series of experiments. The sapphire window generated an interference signal (etalon trace) which was used to convert the time scale of the measurement into a linearized wavelength scale (see Fig. IV.4-2). The  $\text{NH}_3$  line list by Lundsberg-Nielsen et al. [214], [215] was then used to shift this relative wavelength scale to the correct absolute wavelength/wave number.

## Results and Discussion

No data averaging or smoothing was applied in any of the figures presented in this chapter. The spectra shown are single scan raw data. In the top window of Fig. IV.4-2 the detector signal is shown for the laser beam passing twice through the 43.7 cm long gas cell filled with 9.6 mbar of pure  $\text{NH}_3$  at room temperature.

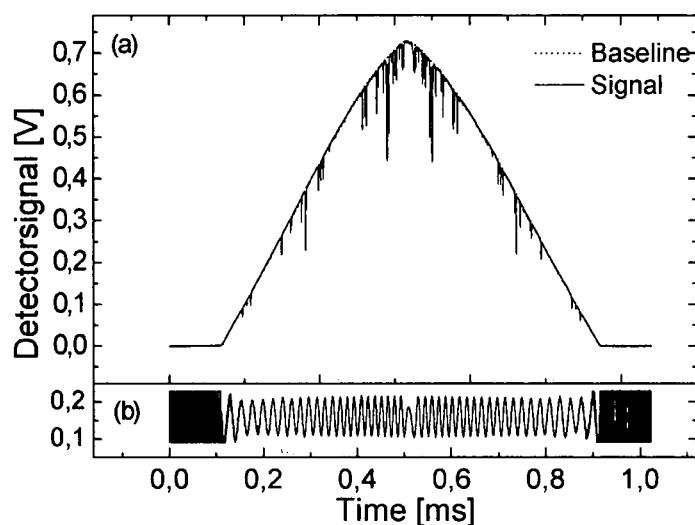


Fig. IV.4-2: In the top window (a) the detector signal of a laser absorption experiment is given for the gas cell being filled with 9.6 mbar of pure  $\text{NH}_3$ . Also shown in (a) is the baseline. In the bottom window (b), one can see the etalon trace.

The laser injection current was modulated by a 1 kHz 0-5.8 mA triangular ramp at a laser temperature of 15.2 °C. Also shown in the top window is the used baseline and in the bottom window the etalon interference trace (in units of absorbance) used to measure the wavelength tuning of the laser during a scan. The frequency jitter of the laser emission between different scans (most likely caused by the noise of the laser driver) was up to 0.01-0.03  $\text{cm}^{-1}$ . Therefore for very high precision measurements three detectors and beam splitters and an etalon with a small free spectral range should be used to measure simultaneously the laser power, the etalon transmission and the absorption signal. Since the purpose of this work was to demonstrate the measurement capabilities of the 1.5  $\mu\text{m}$  VCSEL and not to propose corrections to the HITRAN2000 database the different traces were measured sequentially. In the top window of Fig. IV.4-3(a) a measured absorbance spectrum of 9.6 mbar of pure  $\text{NH}_3$  is shown.

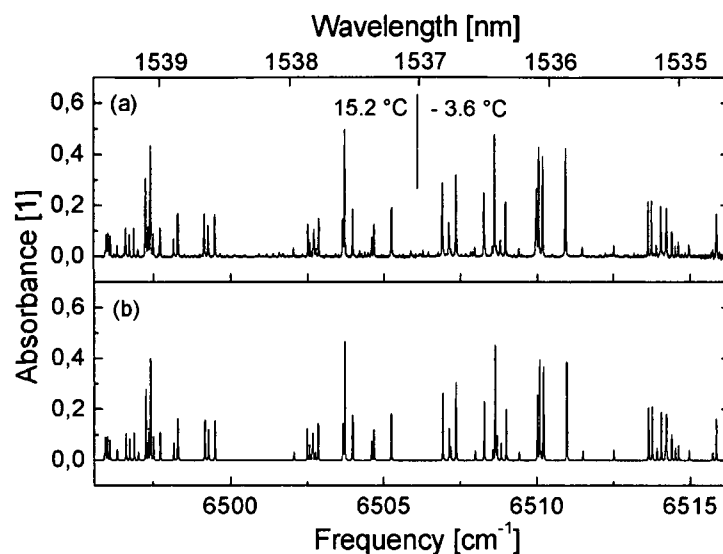


Fig. IV.4-3: The absorbance spectrum of 9.6 mbar of pure  $\text{NH}_3$  at 296K and 87.4 cm absorption path length, measured with the 1.5 $\mu\text{m}$  VCSEL, is shown in the top window (a). The calculated spectrum using the Lundsberg-Nielsen  $\text{NH}_3$  line list is shown in the bottom window (b).

The spectrum in Fig. IV.4-3(a) is a combination of two overlapping spectra, each recorded by tuning the laser with a triangular 0-5.8 mA current ramp, but at two different laser temperatures. The left part of the spectrum was measured at a laser temperature of 15.2°C and is actually the evaluation of the data shown in Fig. IV.4-2. The right part of the spectrum was recorded at a laser temperature of -3.6°C. The tuning range of the laser at 15.2°C, 1 kHz and 0-5.8 mA current modulation was 12.162  $\text{cm}^{-1}$  (2.9 nm). The range covered by the two overlapping spectra was 20.4  $\text{cm}^{-1}$  (4.8 nm). In the bottom window (Fig. IV.4-3 (a)) a calculated spectrum of pure  $\text{NH}_3$  is shown for 296 K gas temperature and 9.6 mbar pressure. The spectrum was calculated assuming a uniform pressure broadening coefficient of  $\gamma_s = 0.3 \text{ cm}^{-1}\text{atm}^{-1}$  and Voigt line shapes. The line list of Lundsberg-Nielsen et al. [214], [215] was used for the calculation, but unfortunately no individual self broadening coefficients  $\gamma_s$  are given for the lines listed. Lundsberg-Nielsen [215] suggests a representative value of  $\gamma_s = 0.3 \text{ cm}^{-1}\text{atm}^{-1}$ , which was used in the calculation. The  $\gamma_s$  of individual  $\text{NH}_3$  lines typically vary between 0.1 and 0.6  $\text{cm}^{-1}\text{atm}^{-1}$  and because of this uncertainty in the self broadening coefficients, the calculated spectrum (bottom window of Fig. IV.4-3) is accurate only for the line positions. It can be seen from Fig. IV.4-3(a) that all the measured strong lines are listed in the Lundsberg-Nielsen line list, but many weaker lines are missing. The line strengths listed in Lundsberg-Nielsen et al. [214], [215] are on average 23% lower than the line strengths measured from the data shown in Fig. IV.4-3(a). This relates well to the work by Webber et al. [212], which states that the line strengths listed in Lundsberg-Nielsen are on average by 10-20 % too low compared to their own measurements. The spectrum of the isolated 6510.986  $\text{cm}^{-1}$  (1.53587  $\mu\text{m}$ ) peak from Fig. IV.4-3(a), also shown again in Fig. IV.4-4(a), is redrawn in Fig. IV.4-4 (b) and compared to a calculated Voigt profile. Good agreement can be observed.

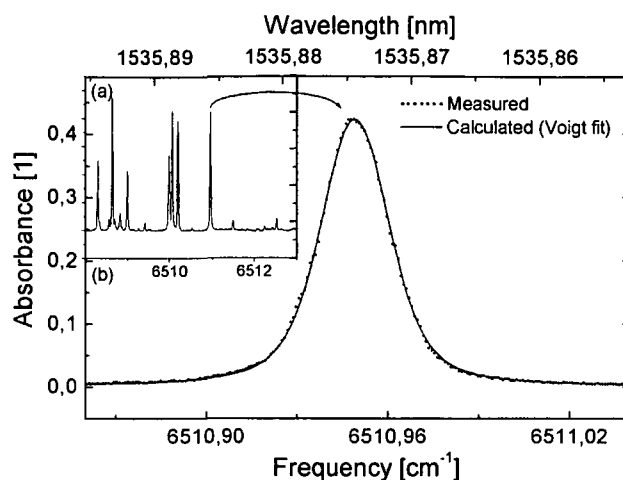


Fig. IV.4-4. Enlarged part of Fig. IV.4-3 (a) and individual peak compared to a Voigt fit (b).

The Voigt fit gives a shape parameter  $a=(\ln(2))^{1/2} \Delta\nu_C/\Delta\nu_D$  of 0.5, a Doppler line width  $\Delta\nu_D$  (FWHM) of  $0.01997 \text{ cm}^{-1}$  and a collision broadened Lorentzian line width  $\Delta\nu_C$  (FWHM) of  $0.0119 \text{ cm}^{-1}$ . The measured Doppler line width of  $0.01997 \text{ cm}^{-1}$  agrees within 3 % with the theoretical value calculated by Eq. II.1-30:  $\Delta\nu_D=7.1623 \times 10^{-7} \nu_0 (T/m)^{1/2}$  ( $T$ ...temperature [K],  $m$ ... molecular mass [amu]). The measured Lorentzian line width of  $0.0119 \text{ cm}^{-1}$  agrees within 6 % with the value calculated from the measured self broadening coefficient  $\gamma_S$ . This demonstrates the ability of the  $1.537 \mu\text{m}$  VCSEL to accurately measure highly resolved low pressure spectra. The self broadening coefficient  $\gamma_S$  of the isolated  $6510.986 \text{ cm}^{-1}$  line was measured to be  $\gamma_S=0.6 \text{ cm}^{-1}\text{atm}^{-1}$  by acquiring a series of spectra of pure  $\text{NH}_3$  in the gas cell with the pressure varying from 9-145 mbar. In order to further illustrate the ability to measure highly resolved low pressure spectra, spectra of  $\text{NH}_3$  were measured at pressures of 9.6, 67.5, 134, 273, 543 mbar and 1 bar. In order to allow better visual inspection a representative section of the whole measured spectrum is shown in Fig. IV.4-5 in an enlarged fashion.

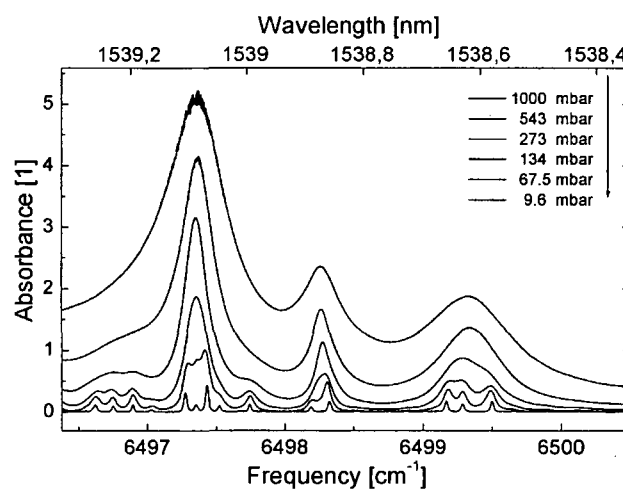


Fig. IV.4-5: Spectra of pure  $\text{NH}_3$  measured with the  $1.5 \mu\text{m}$  VCSEL for gas pressures of 9.6, 67.5, 134, 273, 543 mbar and 1 bar (order: bottom to top of graph).

It can be seen that the strong pressure broadening and the close spacing of the different  $\text{NH}_3$  lines result in a blending of lines for the pressures above 60 mbar. Only at 9.6 mbar the pressured broadening is reduced to a level where the individual lines can be resolved. For the very strong absorption feature near  $6497.36 \text{ cm}^{-1}$  ( $1.53909 \mu\text{m}$ ) the measurement points with absorbance values of more than 3 are rather noisy, since at these high absorbances almost no light ( $I/I_0=\exp(-3)=0.05$ , i.e. the transmission is less than 5%) is transmitted to the detector

and the detection noise and the 12 bit data acquisition limit the accuracy. The  $12.2 \text{ cm}^{-1}$  ( $2.9 \text{ nm}$ ) tuning range of the VCSEL at  $15.2^\circ\text{C}$  was used to test if some strong high temperature  $\text{NH}_3$  lines, useable for combustion monitoring, were accessible by the laser. Fig. IV.4-6 shows spectra of pure  $\text{NH}_3$  measured at 40 mbar and at 296, 468, 606, 1020 and 1173 K gas temperature.

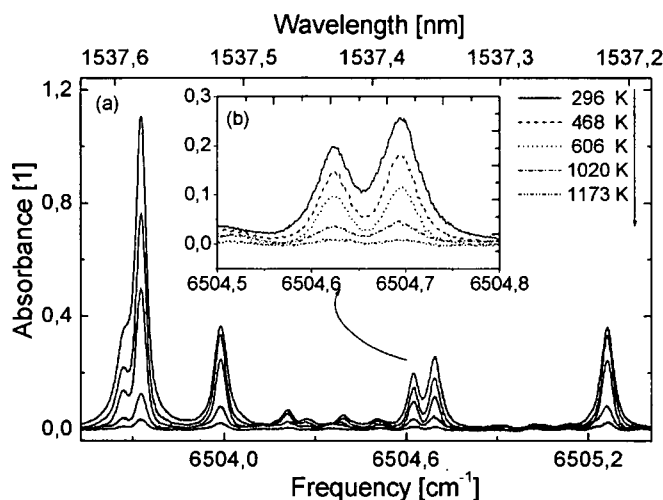


Fig. IV.4-6: Spectra of 40 mbar pure  $\text{NH}_3$  measured with the  $1.5 \mu\text{m}$  VCSEL at gas cell temperatures of 296, 468, 606, 1020 and 1173 K (order: top to bottom of graph). The insert (b) shows a magnification.

The insert in Fig. IV.4-6 (b) is a magnification of the double peak feature at  $6504.65 \text{ cm}^{-1}$  where the individual traces are better resolved.

Only a small part of the acquired spectrum is shown in order to allow better visual inspection. It can be seen that the peak absorption of some features (at  $6503.7 \text{ cm}^{-1}$  and at  $6504.7 \text{ cm}^{-1}$ ) strongly decrease with increasing temperature while other absorption features (at  $6504 \text{ cm}^{-1}$  and at  $6505.3 \text{ cm}^{-1}$ ) show almost no decrease between 296 and 468K, but decrease strongly for temperature above 600K. In the  $12.16 \text{ cm}^{-1}$  tuning range no absorption feature was found which absorbs strongly for temperatures above 600K. One main interest point of this work was to investigate the high speed tuning and measurement capabilities of  $1.54 \mu\text{m}$  near infrared VCSELs.

In order to further demonstrate the high speed measurement capability of the  $1.537 \mu\text{m}$  VCSEL, a  $4.5 \text{ cm}^{-1}$  wide  $\text{NH}_3$  spectrum measured in  $2 \mu\text{s}$  (200 kHz triangular current modulation) is shown in Fig. IV.4-7.

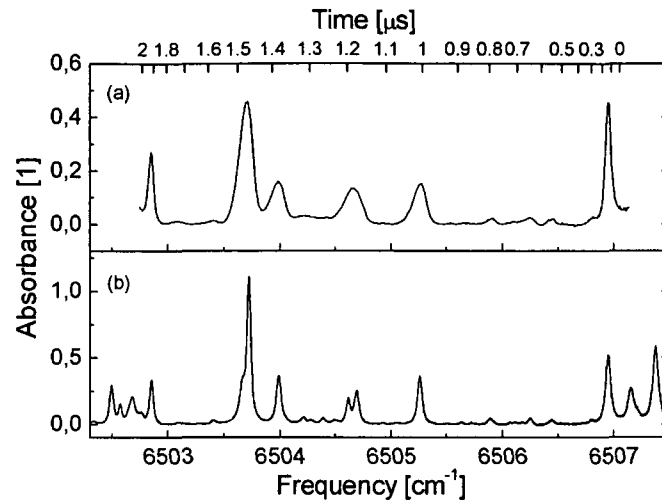


Fig. IV.4-7: In (a) a  $4.5 \text{ cm}^{-1}$  wide spectrum of 40 mbar of pure  $\text{NH}_3$ , measured with the  $1.5 \text{ }\mu\text{s}$  VCSEL in  $2 \text{ }\mu\text{s}$ , is displayed. In (b) the same gas sample is measured with the  $1.5 \text{ }\mu\text{s}$  VCSEL at  $1 \text{ kHz}$  tuning frequency. The frequency scale applies to both windows, the time scale applies only to the top window. The  $10 \text{ MHz}$  bandwidth limitation of the detector results in a smoothed high speed spectrum.

The measured high speed spectrum (top window) is compared with a spectrum measured at  $1 \text{ kHz}$  (bottom window). The frequency scale is valid for both windows. The time scale applies only to the top window displaying the high speed measurement. In Fig. IV.4-7, the laser tunes from the right to the left. By comparing the time scale and the  $1 \text{ kHz}$  spectrum (bottom window) one can see that the laser scans so fast that it tunes over the  $6505.262 \text{ cm}^{-1}$  line in less than  $50 \text{ ns}$ . The peak tuning speed in the middle of the scan was about  $3.5 \text{ cm}^{-1}/\mu\text{s}$ . The  $10 \text{ MHz}$  bandwidth detector can not follow the sharp absorption spikes at this speed and as a consequence the high speed spectrum is broadened by the insufficient bandwidth detector. At the beginning and at the end of the tuning, when the laser tunes slower (compare Fig. IV.4-2 (b)), the detector smoothing is reduced and the measured peaks sharpen. Using a higher bandwidth detector the accurate measurement of a  $4.5 \text{ cm}^{-1}$  wide spectrum in  $2 \text{ }\mu\text{s}$  should be possible. Very high time resolution and measurement rates are therefore possible with near infrared VCSEL absorption spectroscopy.

### Conclusions (1540 nm VCSEL)

For the first time the high speed tuning capabilities of a  $1.5 \text{ }\mu\text{s}$  VCSEL was investigated and used for high speed gas sensing. The measured peak tuning speed was  $3.5 \text{ cm}^{-1}/\mu\text{s}$  and a  $4.5 \text{ cm}^{-1}$  wide  $\text{NH}_3$  spectrum was recorded in  $2 \text{ }\mu\text{s}$ . At  $200 \text{ Hz}$  triangular current modulation the tuning range was  $13.5 \text{ cm}^{-1}$  ( $3.2 \text{ nm}$ ). A  $1.5 \text{ }\mu\text{s}$  VCSEL was used to measure highly resolved spectra of  $\text{NH}_3$  at various pressures ranging from  $9.6 \text{ mbar}$  to  $1 \text{ bar}$ . The measured Doppler linewidth of  $0.02 \text{ cm}^{-1}$  for the  $6510.986 \text{ cm}^{-1}$  line at  $9.6 \text{ mbar}$  agreed within  $3 \%$  with the theoretical value. A  $20.4 \text{ cm}^{-1}$  ( $4.8 \text{ nm}$ ) wide  $\text{NH}_3$  spectrum was recorded and compared to a  $\text{NH}_3$  line list from the literature. It was found that, in contrast to indications in the referenced literature, VCSELs are very well suited for high resolution spectroscopy even at low pressures.

Main advantages of  $1.54 \text{ }\mu\text{s}$  near IR VCSELs for industrial gas sensing applications are the large tuning range by laser injection current ( $>10 \text{ cm}^{-1}$  as compared to  $1\text{-}2 \text{ cm}^{-1}$  for typical distributed feedback (DFB) diode lasers) and the very high tuning rates ( $>3 \text{ cm}^{-1}/\mu\text{s}$ ). The broad tuning range facilitates multiple species measurements, temperature measurements (by

measuring a high and a low temperature line in one laser scan) and high pressure measurements (up to more than 100 bar, compare Fig. IV.5-8 and IV.5-9).

#### IV.4.1.2

#### 1680 nm VCSEL

Methane ( $\text{CH}_4$ ) is known to be an important infrared active trace gas in the atmosphere with a significant global warming potential [216]. Therefore, considerable effort is made to monitor the atmospheric concentration of this gas [217]–[222]. Not only environmental monitoring, but also applications in process control [203], leak detection and medicine [223] need adequate sensors for probing methane. Laser spectroscopic techniques provide a convenient way of conducting *in-situ* measurements, especially in a non-intrusive manner, that is without disturbing the investigated system. In a method relying on a single fixed wavelength, the signal beam is attenuated by resonant absorption of the species under investigation, but also by non-resonant processes such as scattering. It is not possible to determine to which extent the attenuation can be attributed to the influence of the absorber. However, when the light source is tuned over the absorption feature of interest, resonant absorption that is linked to the concentration of the molecule can be discerned from unspecific attenuation of the light. The signal and its background (to both sides of the absorption feature) are recorded simultaneously. The emission wavelength of certain diode lasers can be tuned with the temperature and the injection current. Fast real-time measurements without perturbing the system, a large dynamic range, selectivity and sensitivity are some of the merits associated with tunable diode laser absorption spectroscopy (TDLAS).

Various tunable diode lasers have successfully been used to measure methane by different research groups. For these applications, laser devices with stable single-mode emission across a continuous tuning range are essential. Lead salt diode lasers have been used to probe the  $\nu_3$  band of methane at  $3.3 \mu\text{m}$  [222], [224]–[225] and rovibrational transitions at  $7.9 \mu\text{m}$  [217]–[218]. The main drawback of these lasers is the need for cryogenic cooling. The transitions in the mid-infrared (MIR), however, are strong, since these are fundamental ones. Difference frequency mixing of a distributed feedback (DFB) laser at  $1.066 \mu\text{m}$  and one at  $1.574 \mu\text{m}$  in periodically poled lithium niobate (PPLN) has also been used to access the  $\nu_3$  band at  $3.3 \mu\text{m}$  [226]. At  $1.33 \mu\text{m}$ , the  $\nu_2+2\nu_3$  combination band has been investigated using room temperature InGaAsP telecommunication lasers [203], [227]. The  $2\nu_3$  band around  $1.65 \mu\text{m}$  has been accessed using room temperature InGaAsP DFB lasers [219] and GaInPAs diodes [228]. Also, the low frequency side of this band has been probed at  $1.73 \mu\text{m}$  [26].

In the near infrared (NIR) the transitions, overtone and combination bands are by two orders of magnitude weaker than the fundamental ones in the MIR (compare Fig. III.2-3). Yet the availability and the easy handling of room temperature laser diodes makes these lasers favorable candidates for molecular spectroscopy. DFB lasers, for example, have been designed for telecommunication purposes, hence they are compact, robust devices suitable for fiber coupling with output powers in the lower mW range and available at good quality.

Another type of lasers are vertical-cavity surface-emitting lasers (VCSELs). Their use for spectroscopy instead of conventional edge emitting lasers has been discussed previously by Weldon [117]. In that paper, it was concluded that VCSELs were inferior spectroscopic tools at that time. Up to now, VCSELs have not extensively been used for molecular spectroscopy ( $\text{O}_2$  near  $760 \text{ nm}$  [117], [124], [205]–[208] and  $\text{H}_2\text{O}$  near  $962 \text{ nm}$  [209]).

In this work, measurements with a novel type of VCSELs employing a buried tunnel junction (BTJ) (see chapter III.4 and [119], [121]–[123]) are presented. The suitability of VCSELs for spectroscopy is reassessed and it is concluded that they have superior properties over



conventional edge emitting lasers with respect to certain applications. A couple of problems can solely be satisfactorily dealt with by using VCSELs.

### Experimental

The setup of the experiments is depicted in Fig. IV.4-8.

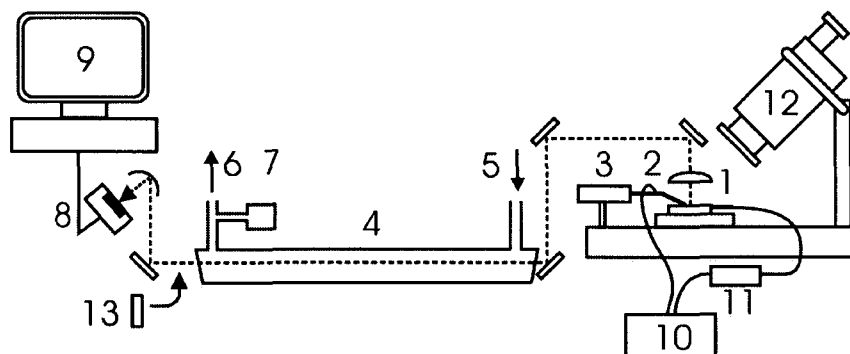


Figure IV.4-8: Experimental setup. 1: section of VCSEL wafer; 2: lens; 3: needle for contacting; 4: gas cell; 5: methane inlet; 6: methane outlet, to vacuum pump; 7: pressure gauge; 8: photo detector and focusing mirror; 9: computer and waveform digitizer; 10: function generator; 11: 2kOhms resistance; 12: microscope; 13: etalon (not permanently in beam path);

An electrically pumped InP-based vertical-cavity surface-emitting laser (VCSEL) emitting at  $1.685 \mu\text{m}$  ( $5935 \text{ cm}^{-1}$ ) was used for direct absorption spectroscopy of methane.

A single-pass setup was chosen. A sector of a wafer containing hundreds of VCSELs was deployed. The VCSEL array was positioned on a thermo stated ( $\pm 0.1 \text{ }^\circ\text{C}$ ) copper block under a microscope. Controlling the temperature of the VCSEL is not as stringent a demand as with conventional diode lasers, since the current tuning range of vertical cavity surface emitting lasers is much larger than that of edge-emitting lasers ( $10$  to  $30 \text{ cm}^{-1}$  for VCSELs as compared to  $1$  to  $2 \text{ cm}^{-1}$  for DFB lasers). In chapter IV.4.2, a VCSEL ( $761 \text{ nm}$  for oxygen) housed in a copper heat sink was operated without any thermostatisation at all. The heat sink temperature was set between  $10$  and  $40 \text{ }^\circ\text{C}$  in order not to have water condense on the chip or to loose output power, respectively. A needle attached to an optical stage adjustable in three directions was used to contact a single laser diode of the wafer. The laser array was held in its position solely by the pressure of the needle. The laser drive current was provided by a function generator (GFG-8050, output impedance  $50 \text{ Ohms}$ ) in conjunction with an Ohmic resistance ( $2\text{kOhms}$ ). This setup was chosen to overcome bandwidth limitations of commercially available laser diode current sources.

The injection current was ramped linearly from  $0$  to typically  $5 \text{ mA}$  to tune the VCSEL in its emission frequency. To track the frequency tuning, an etalon ( $5.0 \text{ mm}$  thick sapphire,  $\text{FSR} = 0.574 \text{ cm}^{-1} = 0.16 \text{ nm}$ , see Fig. III.4-7) was used. The etalon was inserted into the beam path between the (empty) gas cell and the detector between the absorption measurements. For sake of simplicity, no beam splitters which would have allowed the simultaneous recording of tuning properties and absorption were used. The baseline was also obtained between the measurements. A beam splitter to create signal beam and reference beam in conjunction with two detectors could have been used to record the base line in the same scan and to avoid drifts in the wavelength calibration. For the demonstration experiments presented here, a setup using beam splitters was not considered necessary.

An aspheric collimating lens ( $f = 4.5 \text{ mm}$ ) was positioned above the selected laser. To facilitate the handling of the infrared beam, an alignment laser (laser diode module at  $650 \text{ nm}$ ) was used. The beams were superimposed and the alignment laser was used to align the setup.

The collimated VCSEL beam was directed through a gas cell onto the detector. An amplified InGaAs detector (PDA400, Thorlabs Inc.) was used. A focusing mirror ( $f = 25.4$  mm) was placed before the detector. The gas cell had a length of 44 cm and was made of quartz. The entrance and exit windows were wedged to prevent etaloning. Etaloning is an unwanted interference effect and manifests itself by a wavelength dependent variation of the transmission. The appearance of these unwanted fringes is caused by inadvertent multiple reflections between parallel optical surfaces. A vacuum pump was placed behind the cell. The pressure was recorded using a Varian CDG pressure gauge (operating range 0-1316 mbar). The cell was filled with methane (99.5%) at varying pressures. The detector signal was digitized at 60 MSamples/s using a data acquisition (DAQ) board (SignaTec PDA12A) in a desktop computer.

## Results and discussions

VCSELs with a new device architecture, the buried tunnel junction (BTJ), were demonstrated to work with a new wavelength for gas sensing (1.68 micron range).

All experimental data in the following figures represent single measurements (no averaging, no smoothing).

In Figure IV.4-9 the wide temperature tuning properties of the VCSEL are demonstrated. One can see two strong absorption features of methane at 136 mbar that are approximately  $12\text{ cm}^{-1}$  ( $3.39\text{ nm}$ ) apart.

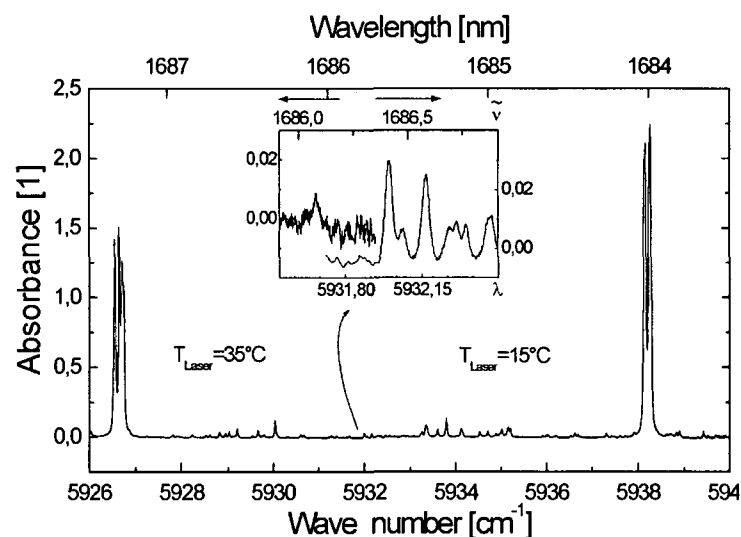


Fig. IV.4-9: Temperature tuning of the VCSEL. This figure is composed of two spectra, one recorded at a laser heat sink temperature of  $15^{\circ}\text{C}$  (right), the other at  $35^{\circ}\text{C}$  (left). The pressure was 140.8 mbar (pure methane) at 296 K, the path length 44 cm. The insert shows a magnification of the overlapping region.

The left part of the spectrum was covered by current tuning 0-5.1 mA of the VCSEL at a heat sink temperature of  $15^{\circ}\text{C}$ . The right part of the spectrum was obtained by current modulation from 0-5.1 mA at a heat sink temperature of  $35^{\circ}\text{C}$ . Since there is an overlap of the two scans (depicted in the insert of Fig. IV.4-9), it is possible to record both absorption features in a continuous scan using a single VCSEL. The temperature tuning coefficient was determined to be  $-0.40\text{ cm}^{-1}/\text{K}$  ( $+0.11\text{ nm}/\text{K}$ ).

Fig. IV.4-10 shows a measured absorption spectrum of methane near  $1.685\text{ }\mu\text{m}$  ( $5935\text{ cm}^{-1}$ ). The path length was 44 cm, the methane partial and total pressure 140.8 mbar, the ambient

temperature 296K, and the laser heat sink temperature 15.0 °C. The laser drive current was ramped from 0 to 5.1 mA at a repetition rate of 706 Hz.

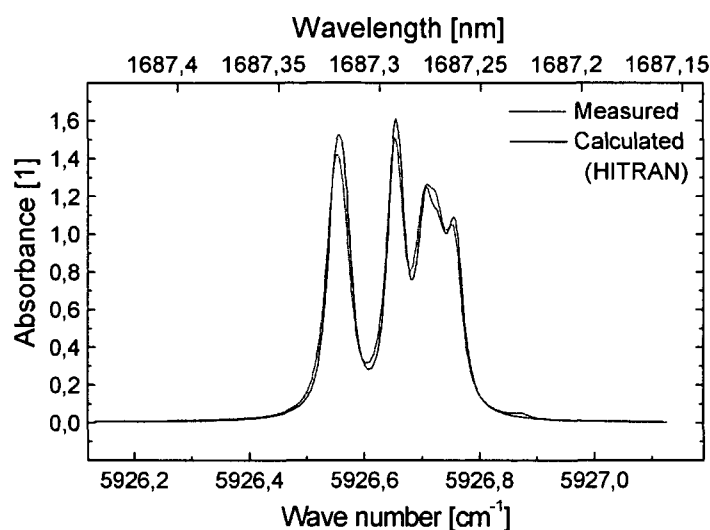


Figure IV.4-10: Comparison of an absorption spectrum of 140.8 mbar methane measured with the 1.68 $\mu\text{m}$  VCSEL and a calculated spectrum using the HITRAN2000 database. The temperature was 296 K, the path length 44 cm.

The reference spectrum was calculated using the HITRAN2000 spectroscopic database [4]. The exact wavelength was also obtained from comparison of the experimental data with the HITRAN2000 database. The mismatch between the measured and calculated spectrum was as low as 0.8% (determined by integration).

As one can see, there are several distinct absorption features. They are composed of several individual lines that, for the chosen pressure, have been blended. It is this spectral congestion leading to broad absorption features that usually limit the range of operation when higher pressures are encountered. A laser that can be tuned continuously in a single mode regime over several wave numbers comes in handy, though. Numerous different approaches have been followed to obtain lasers with good tuning characteristics. Setups using external cavity diode lasers (ECDL) permit extending the tuning ranges of diode lasers. However, since mechanical parts are involved, repetition rates are low. For example, ECDLs could be continuously scanned over  $1\text{ cm}^{-1}$  (at  $1.73\text{ }\mu\text{m}$ ) [26] at 20-30 Hz. Repetition rates of 500 Hz using a multi mode diode laser at  $3.3\text{ }\mu\text{m}$  were achieved by [10]. A DFB laser at  $1.5\text{ }\mu\text{m}$  was successfully deployed for species concentration measurements at 200 Hz in [226]. A tuning range of  $0.7\text{ cm}^{-1}$  (single mode) using an InSbAs/InAs diode laser is reported in [223]. [228] demonstrated a GaInPAs Fabry Perot laser at  $1.65\text{ }\mu\text{m}$  that was continuously scanned over 1 to  $3\text{ cm}^{-1}$  in one laser mode at repetition rates of 10 Hz to 1 kHz.

The pressure broadened line width is on the order of  $0.1 - 0.6\text{ cm}^{-1}/\text{atm}$  ( $0.03 - 0.17\text{ nm}/\text{atm}$  at  $1680\text{ nm}$ ). This implies that with the above cited diode lasers of conventional setup, TDLAS can only be conducted up to pressures of several bars. (Temperature narrowing allows accessing higher pressures at elevated temperatures, though). VCSELs exhibit large tuning ranges within an order of magnitude of more than  $10\text{ cm}^{-1}$  (cf. Fig. III.4-5 in chapter III.4) and are thus very suitable for high pressure environments (see Fig. IV.5-8 and IV.5-9).

High speed absorption measurements are demonstrated in Fig. IV.4-11 and Fig. IV.4-12.

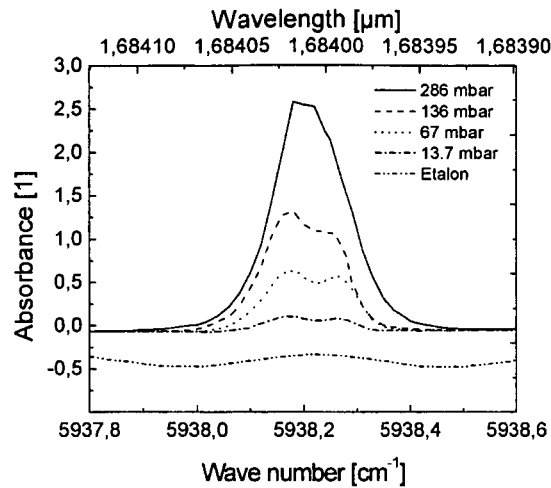


Figure IV.4-11: Variation of the methane partial pressure at 200 kHz. Depicted are four curves at pressures of 286, 136, 67 and 13.7 mbar respectively. The lowest curve is the recorded etalon trace (FSR =  $0.574 \text{ cm}^{-1} = 0.16 \text{ nm}$ ). The temperature was 296 K, the path length 44 cm.

Fig. IV.4-11 shows measurements of methane at several pressures (13.7 to 286 mbar) where the laser was scanned with repetition rates of 200.9 kHz with a 0-5.1 mA triangular modulation at 15°C laser temperature. For better visual inspection only a part of the measured  $6.2 \text{ cm}^{-1}$  broad spectra is shown. The sinusoidal curve at the bottom is the recorded etalon trace (FSR =  $0.574 \text{ cm}^{-1} = 0.16 \text{ nm}$ ).

The lower detection limit was not determined experimentally. The major noise sources were not localized, either, because the focus of this work lies on the demonstration of a novel laser used in a novel wavelength range.

In Fig. IV.4-12 the laser is tuned at 5.0 MHz repetition rate over an absorption feature of pure methane at 397 mbar around  $5938 \text{ cm}^{-1}$ .

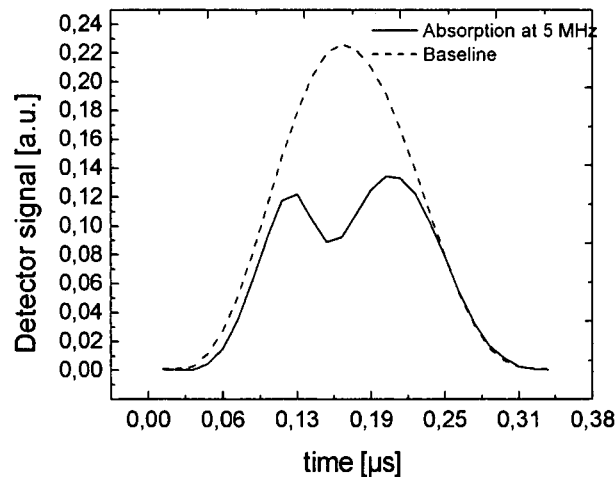


Figure IV.4-12: Absorption measurements of methane at 5 MHz. The upper (dotted) curve represents the baseline. The lower (solid) curve contains an absorption feature. The measurement was done at a partial pressure of methane of 394 mbar. A triangular current ramp was imposed on the VCSEL.

The resolution is limited by the sampling rate of the data acquisition board (60 MSamples/s) and the bandwidth of the detector (10 MHz). The output of a function generator, limited by a 2 kOhms resistance in series with the VCSEL was used to drive the laser with such high frequencies. These measurements are the first absorption spectroscopic studies where a VCSEL is frequency tuned at repetition rates as high as 5 MHz.

This is the first demonstration of absorption spectroscopy at scan rates  $\gg 100$  kHz. The absorption feature is composed of several individual lines that appear as a double peak at this pressure (peak absorbance 5.3,  $0.2\text{cm}^{-1}$  line width (FWHM)).

The tuning range at 5 MHz was about  $0.36\text{ cm}^{-1}$  (0.21 nm). This was estimated by temperature tuning of the laser over the absorption line (visible from 13.8 to 15.7°C). Limiting factors for the resolution in our experiments were the bandwidth of the detector used (10MHz) and the sampling rate of the data acquisition (DAQ) board (60 MSamples/s). Since the bandwidth of the detection system was not matched to the scan rate, significant instrument broadening can be seen in Fig. IV.4-12. Using a detector with a sufficiently high bandwidth, accurate high speed absorption measurements should be feasible. These measurements are the first absorption spectroscopic studies where a VCSEL is frequency tuned at repetition rates on the order of several MHz.

Besides the far wavelength tuning, their rapid tuning ability is a key advantage of VCSELs. By scanning over an entire absorption feature, the specific absorption signal can be discerned from the background attenuation. When the scanning is done faster than the typical time scale of the noise, unspecific and misleading attenuation by scattering, etc, can be efficiently eliminated. Speaking of combustion diagnostics for instance, typically encountered experimental noise sources are emissions from flickering flames and particles passing the beam. TDLAS measurements conducted on the order of  $\mu\text{s}$  do not experience trouble with these noise sources.

In order to obtain a good time resolution in TDLAS experiments, rapid scanning is also desirable when noise is not that big an issue. VCSEL based gas monitoring sensors exploiting the rapid tuning properties of these lasers can be used to obtain a superior time response.

### Conclusions (1680 nm VCSEL)

The feasibility of conducting tunable diode laser absorption spectroscopy of  $\text{CH}_4$  at  $1.68\ \mu\text{m}$  has been demonstrated for the first time using a VCSEL. VCSELs with new device architecture, the buried tunnel junction (BTJ), were demonstrated to work with a new wavelength for gas sensing (1.68 micron range). A single VCSEL was contacted directly on a wafer to demonstrate the ability of device performance testing prior to singularizing and mounting the laser. A 44 cm long gas cell was used in a single pass arrangement. Rovibrational transitions of pure  $\text{CH}_4$  at 300K and 10 mbar to 1.3 bar were probed at high repetition rates (500 Hz to 5 MHz, corresponding to a time resolution of 2 ms to  $0.2\ \mu\text{s}$  respectively). The laser was driven with a triangular waveform of a function generator in series with a  $2\ \text{k}\Omega$  resistor. The peak tuning rate was  $5.2\ \text{cm}^{-1}/\mu\text{s}$ . The measured tuning rates of the VCSEL were  $-3.05\ \text{cm}^{-1}/\text{mA}$  ( $+0.86\ \text{nm}/\text{mA}$ ) and  $-0.40\ \text{cm}^{-1}/\text{K}$  ( $+0.11\ \text{nm}/\text{K}$ ).

The maximum continuous current tuning range was more than  $16\ \text{cm}^{-1}$  (4.5 nm). At 1 MHz the tuning range was as large as  $2.6\ \text{cm}^{-1}$  (1.5 nm), and at 5 MHz it was still approximately  $0.36\ \text{cm}^{-1}$  (0.21 nm).

The outstanding advantages of VCSELs for spectroscopy are the ability of fast (several MHz) and far ( $>10\ \text{cm}^{-1}$ ) wavelength tuning without mode-hops. Further benefits are on wafer testing and wavelength selection, low power consumption, less susceptibility to optical feed back, single mode emission and low cost. VCSELs as used in this work are particularly suitable for numerous applications in spectroscopy, e.g. where high pressures ( $\gg 1$  bar) significantly broaden the absorption features or where a good time resolution ( $\ll$  ms) is needed.

## IV.4.1.3

## 1810 nm VCSEL

Diode laser based gas sensors are ideally suited for the control of a variety of industrial processes ranging from CVD (chemical vapor deposition), DeNO<sub>x</sub> SNCR/SCR processes, combustion and electro- and bag-house filter applications to process control in the aluminum industry and emission monitoring (see e.g. [203] and [229]). One main advantage of diode laser based gas sensors is the ability to measure reactants and intermediates *in-situ* and non-intrusively directly in the reaction chamber without the need for sampling and recalibration. Only recently long wavelength electrically pumped single frequency vertical cavity surface emitting lasers (VCSELs) have been developed (see chapter III.4 and [119], [121]-[123], [210]-[211]). This is a very promising development, since VCSELs offer a variety of advantages when compared to other diode lasers for absorption spectroscopy and real world gas sensing applications. They typically have a much higher continuous single frequency tuning range with laser current (up to 37 cm<sup>-1</sup> or 2.1 nm for VCSELs [124], 1-2 cm<sup>-1</sup> typically for standard distributed feedback back (DFB) diode lasers). This enables to measure multiple lines in one high speed current scan (e.g. [124] and this work) and can be utilized for multi-species measurements or for the determination of the gas temperature by measuring simultaneously a high and a low temperature line in one current scan. Also, gas temperature distributions can be measured by scanning over more than two lines with known temperature dependence simultaneously [42]. The broad continuous tuning range can also be used to measure absorption spectra of gases at very high pressures [124] (up to more than 100 bar, depending on the specific line, gas composition and temperature). VCSELs can be tuned at much higher repetition rates (up to MHz) and tuning speeds (more than 5 cm<sup>-1</sup>/μs) over an absorption line (see e.g. [124] and the previous chapter (methane VCSEL at 1.68 μm)). This allows very high time resolution (μs). Also, it enables makes measurements of the concentration of the target species possible even under very difficult experimental conditions as in flickering flames, in particle laden gas streams or in a turbulent hot gas stream causing beam steering. Particles or aerosols passing through the beam or refractive index gradients of a hot gas stream causing beam steering can result in strong high frequency fluctuations of the laser intensity collected by the detector. Flickering flame emission and glowing particles can cause additional signal on the detector. All these effects may be highly dynamical and time varying, but if the laser (VCSEL) is able to scan over a absorption line in a time (e.g. less than 1 μs) which is short compared to the fluctuations then it is possible to discriminate between the wavelength dependent absorption by the target species and the wavelength independent and on this short time scale stationary experimental effects (compare Fig. II.3-3 and Fig. IV.4-21).

In this work the ability of 1.8 μm VCSELs to measure highly resolved low pressure spectra is demonstrated and compared to calculations based on the HITRAN database. The results from this work show that 1.8 μm VCSELs are very well suited not only to measure spectra at high pressures, but also for high resolution spectroscopy at low pressures. The newly developed electrically pumped long wavelength (λ=1-2 μm) VCSELs open up the field for VCSEL based gas sensors for a variety of species [213], compare [4].

## Experimental

In Fig. IV.4-13 the experimental setup of the 1.8  $\mu\text{m}$  VCSEL tests is shown.

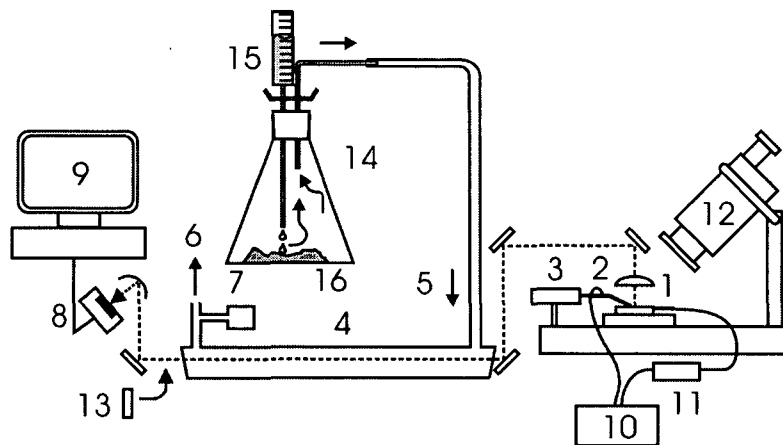


Fig. IV.4-13: Experimental setup. 1: section of VCSEL wafer; 2: lens; 3: needle for contacting; 4: gas cell; 5: methane inlet; 6: methane outlet, to vacuum pump; 7: pressure gauge; 8: photo detector and focusing mirror; 9: computer and waveform digitizer; 10: function generator; 11: 2kOhms resistance; 12: microscope; 13: etalon (not permanently in beam path); 14: Kipp's apparatus; 15:  $\text{H}_2\text{SO}_4$  reservoir; 16: NaCl.

A sector of a wafer containing hundreds of 1.8  $\mu\text{m}$  VCSELs was placed on top of a temperature controlled ( $\pm 0.1$   $^\circ\text{C}$ ) copper plate. A fine needle, attached to a three axis positioning tool, was used to contact the 250  $\mu\text{m}$  x 250  $\mu\text{m}$  gold metalized cathode of a single laser and a microscope was used to control the placement of the needle. As a result of inhomogeneities of the epitaxial crystal growth, the VCSELs had different wavelength at different positions of the wafer. A VCSEL with the desired wavelength was selected on the wafer using a wave meter. The needle pressed the wafer on the copper cooling plate, which functioned as anode for all lasers on the wafer. The emission wavelength of a VCSEL can be changed by tuning the laser temperature and by tuning the laser injection current. The center wavelength of the selected VCSEL was set to the position of the very strong HCl lines near 1810 nm by tuning the temperature of the cooling plate to 30 $^\circ\text{C}$  with a Peltier element and a temperature controller. A 0-4.1 mA current ramp was used to tune the laser wavelength over the desired absorption features and to measure the absorption spectra. An aspheric lens (Geltech C230TM) with 4.5 mm focal length, attached to a 3 axis positioning stage, was used to collimate the laser output radiation. The lens had a standard antireflection coating from 1 to 1.8  $\mu\text{m}$  with a nominal reflectivity of  $R=1\%$  at 1.8  $\mu\text{m}$ . With several mirrors the collimated laser beam was directed through the 44 cm long measurement cell and onto the detector. The total path length between laser wafer and the detector was 130 cm. 86 cm of the laser beam path went through room air. The humidity of the room air resulted in a background water vapor absorption present in all the measurements. The laser beam path outside of the sampling cell was not purged with a inert gas, since these experiments are intended as demonstrations of the multi species measurement capability of the 1.8  $\mu\text{m}$  VCSEL. The measurement cell was made out of quartz glass and had 25 mm diameter wedged fused silica windows. The measurement cell could be evacuated using a roughing pump in series with a cold trap to 2 mbar. The cold trap was used to capture the HCl before the vacuum pump (The freezing point of HCl is 159 K, the temperature of liquid nitrogen (boiling point) 77 K). The pressure was measured using a Varian VCMT 13T capacitive pressure transducer. The laser beam was focused on an extended InGaAs detector (J18-18I-R01M-2.2 from EG&G JUDSON) with a 1 mm active area diameter and a cut off wavelength of 2.2  $\mu\text{m}$ . A homemade detector amplifier

was used and the bandwidth of the detector-amplifier combination was 250 kHz. The signal was recorded at 12.5 MS/s sampling rate with a 12 bit Signatec PDA12A data acquisition board mounted in a personal computer. Since there are no infrared indicator cards for 1.8  $\mu\text{m}$  radiation and in order to simplify the alignment, the collimation lens, the mirrors and the detector were first aligned using a wafer with 1.55  $\mu\text{m}$  VCSELs and a 1.55  $\mu\text{m}$  viewing card. The needle was then lifted off the 1.5  $\mu\text{m}$  wafer, the wafer was replaced by a 1.8  $\mu\text{m}$  wafer and the alignment of the wafer was optimized again. An analog function generator was used as laser driver. The 5 MHz analog function generator was set to supply a 0 – 10.8 V triangular voltage ramp which was applied to a 2 k $\Omega$  resistor in series with the laser diode. This results in a laser current of about 0 - 4.1 mA. The resistor was chosen rather large so that it was easy to adjust the laser current with the function generator. The ramping frequency was chosen rather low (505 Hz) so that the 250 kHz bandwidth detector could also follow the transmission signal generated by very sharp low pressure absorption peaks (see Fig. IV.4-14 and Fig. IV.4-17). This simple and cheap way to drive a VCSEL seems to have superior performance as compared to expensive commercial laser diode driver. For the etalon trace a 5 mm thick sapphire window was positioned in the beam path to measure the wavelength tuning of the VCSEL. The interference signal (etalon trace) is used to convert the time scale of the measurement into a linearized wavelength scale. The HITRAN2000 database was then used to shift this etalon generated relative wavelength scale to the correct absolute wavelength/wave number. For very high precision measurements typically three detectors and beam splitters are used to measure simultaneously the laser power, the etalon transmission and the absorption signal (compare Fig. III-2). Since we did not have three extended InGaAs detectors available and since the purpose of this work was to demonstrate the measurement capabilities of the 1.8  $\mu\text{m}$  VCSEL and not to propose corrections to the HITRAN2000 database a sequential approach was used. For all the measurements in the paper the laser was operated under the same conditions. The room air temperature was 21°C.

## Results and discussion

No data averaging or smoothing was applied to any of the figures presented in this work. The curves shown are single scan raw data. Close to 1.8  $\mu\text{m}$  HCl, NO and hot H<sub>2</sub>O vapor (>1000 K) have the strongest absorption lines in the near infrared below 2  $\mu\text{m}$ . CH<sub>4</sub> has also some pretty strong lines close to 1.8  $\mu\text{m}$ , but even stronger lines at 1.65  $\mu\text{m}$  ( $S=1.280 \times 10^{-21}$  cm molecule<sup>-1</sup> at 1.65  $\mu\text{m}$ ). The following table IV.4-1 presents a compilation of the strongest line strengths at 296K accessible with the VCSEL (Taken from [4]).

Molecule	Wavelength	Line strength
HCl	1809.95 nm	$3.895 \times 10^{-21}$ cm molecule <sup>-1</sup>
NO	1811.44 nm	$4.3 \times 10^{-23}$ cm molecule <sup>-1</sup>
H <sub>2</sub> O	1811.22 nm	$1.57 \times 10^{-21}$ cm molecule <sup>-1</sup>
CH <sub>4</sub>	1810.50 nm	$1.69 \times 10^{-22}$ cm molecule <sup>-1</sup>

Table IV.4-1: Strong absorption lines accessible with the VCSEL (Data taken from [4], HITRAN2000).

The H<sub>2</sub>O lines in this region are very good for high temperature and high pressure measurements. There are lines which absorb strongly even at high temperatures and which have very small pressure broadening coefficients. Therefore the laser can scan over the whole line even when the line is highly pressure broadened. According to HITRAN2000 the collision broadening coefficient  $\gamma_a$  of H<sub>2</sub>O with air is for example only 0.0052 cm<sup>-1</sup> atm<sup>-1</sup> and



the line strength is  $2.78 \times 10^{-21}$  cm molecule<sup>-1</sup> for the  $5529.17 \text{ cm}^{-1}$  (1808.59 nm) line at 1300K [4]. Using this line and the 1.8  $\mu\text{m}$  VCSEL, measurements of an H<sub>2</sub>O spectrum at more than 200 bar should be feasible. NO was not measured, since we did not have NO available at the time of the measurements. In Fig. III.4-8 (chapter III.4) the laser output power and laser forward voltage versus current characteristics are given for a typical 1.8  $\mu\text{m}$  VCSEL with a 7  $\mu\text{m}$  BTJ at 20 °C. For the absorption measurements we used a different laser with had a wavelength very well suited for HCl, H<sub>2</sub>O and CH<sub>4</sub> measurements. For this laser the detection signal shown in Fig. IV.4-14 is a result of a 0 – 10.8 V voltage ramp applied to the laser in series with the 2 k $\Omega$  resistor. The wavelength tuning laser output was partly absorbed by 0.29 bar of gas containing HCl in the quartz glass cell and by water vapor in the room air.

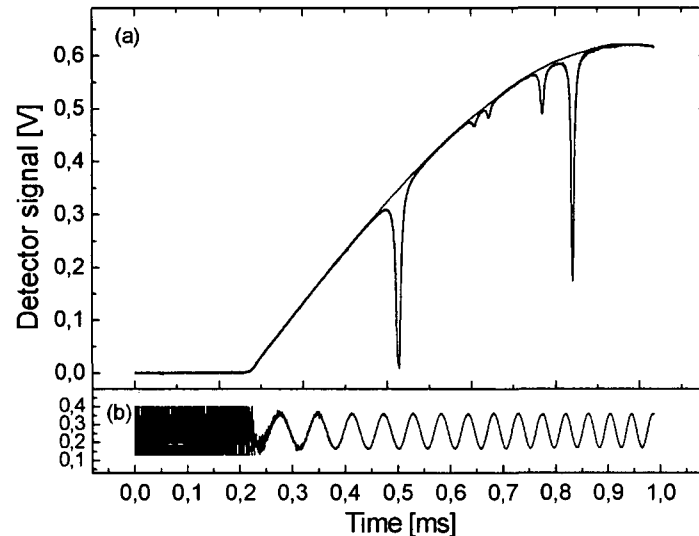


Fig. IV.4-14: 1.8  $\mu\text{m}$  VCSEL measurement of H<sub>2</sub>O and HCl. The top window (a) shows the measured detector signal generated by the laser beam after being partly absorbed by room air water vapor and by 0.29 bar of gas containing HCl in the measurement cell. Also shown is the baseline used to calculate the absorbance. The bottom window (b) displays the measured etalon trace. The tuning range in this measurement is  $8.4 \text{ cm}^{-1}$  (2.8 nm).

The HCl peaks are the two strongest peaks. For the measurement of the baseline the quartz glass cell was evacuated and the remaining 4 room air water vapor absorption peaks were removed on the computer. The absorbance is then calculated using the Beer-Lambert's law as negative natural logarithm of detection signal divided by the baseline. The bottom trace in Fig. IV.4-14 is the etalon signal generated by a 5 mm thick sapphire window. The free spectral range (FSR) of the etalon is  $0.574 \text{ cm}^{-1}$  (0.188 nm). From the etalon trace it can be seen that the wavelength tuning speed of the laser increases towards the end of the ramp, i.e. with increasing currents (see also Fig. IV.4-2(b)). The total tuning range in this measurement is about  $8.4 \text{ cm}^{-1}$  (2.8 nm). As said above, the ramping frequency was chosen low (505 Hz) so that the 250 kHz bandwidth detector is able to resolve even the very sharp low pressure spectra. But even so, at sample gas pressures below 0.1 bar the detector started to broaden the spectra (compare Fig. IV.4-17).

For the room air water vapor measurement in Fig. IV.4-15 the quartz glass cell was filled with room air at ambient pressure (1 atm). The total absorption path length was 1.30 m.

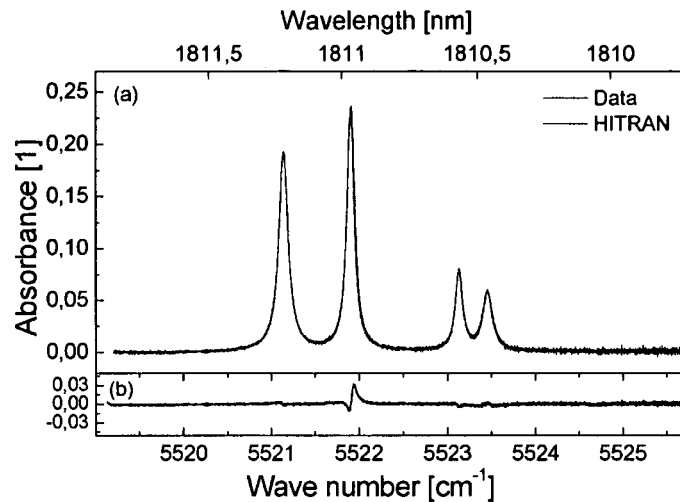


Fig. IV.4-15: Room air water vapor measurement. In the top window (a) the measured absorbance (thick line) is compared to the calculated absorbance (thin line) of  $\text{H}_2\text{O}$  based on the HITRAN2000 database. In the bottom the difference between the measured data and the HITRAN2000 calculations is given. All figures in this work show unfiltered single scan raw data.

In the top window the measured  $\text{H}_2\text{O}$  absorbance is compared to a calculated spectrum using the HITRAN2000 database. For the calculations a relative humidity of 31.4% was assumed (reading of a digital hygrometer) which corresponds to 0.75 vol % at 21°C room temperature. The difference between the measured data and the HITRAN2000 calculations is displayed in the bottom window. The line width of the  $5521.14 \text{ cm}^{-1}$  line agrees within 2% with the HITRAN value. The line width of the  $5521.91 \text{ cm}^{-1}$  is 10% larger than predicted by HITRAN. The measured ratio of the line strength of these two strongest  $\text{H}_2\text{O}$  lines is 1.02 as opposed to 1.11 as predicted by HITRAN.

In Fig. IV.4-16 the measured absorbance spectra of 1 bar and 0.07 bar methane in the 44 cm quartz glass cell are shown.

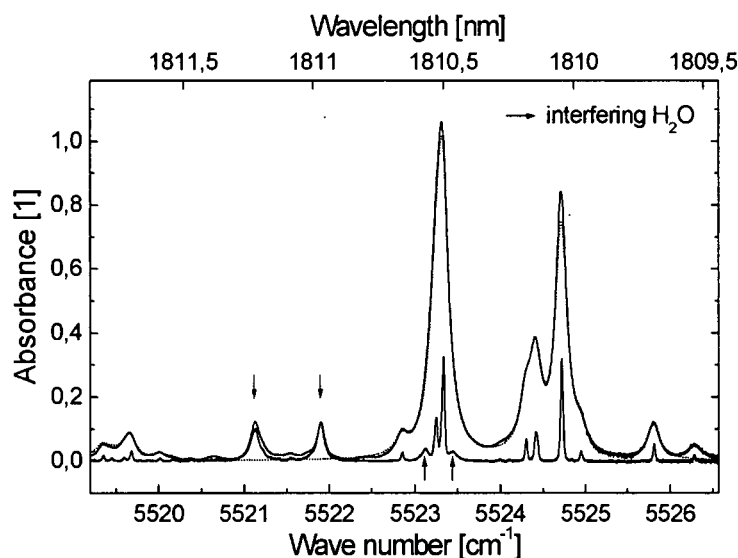


Fig. IV.4-16: Measured absorbance spectra of 1 bar (pressure broadened spectra) and 0.07 bar (spectra with the sharp peaks) of pure methane in the 44 cm long measurement cell. Additionally a calculated spectrum of pure methane at 1 bar using the HITRAN2000 database is shown (thin line). The arrows indicate the absorption peaks originating from room air water vapor.

The measured 1 bar spectrum is compared to a calculated spectrum of pure methane at 1 bar using the HITRAN2000 database. Since the laser setup was not purged with nitrogen, the

laser beam outside of the measurement cell was exposed to room air humidity on 86 cm path length between laser and detector. The arrows in Fig. IV.4-16 indicate the position of the room air water vapor absorption peaks. The calculated spectra of pure methane do not include these water peaks. It can be seen that, overall, the calculated spectrum agrees pretty well with the measured data, but especially the peak absorbance of the two strongest peaks at  $5523.34\text{ cm}^{-1}$  and  $5524.72\text{ cm}^{-1}$  are predicted by 4 % and 12 % too low and some  $\text{CH}_4$  lines are completely missing in the HITRAN2000 database. For example the right most peak in Fig. IV.4-16 at  $5526.29\text{ cm}^{-1}$  is missing, but also other smaller peaks for example at  $5520.17$ ,  $5520.38$ ,  $5521.55$ ,  $5522.41$ ,  $5523.99$  and  $5524.11\text{ cm}^{-1}$ .

In order to be able to compare the measured and the calculated spectra for various pressures, the data from Fig. IV.4-16 (methane) is displayed again in Fig. IV.4-17 for a smaller wavelength range.

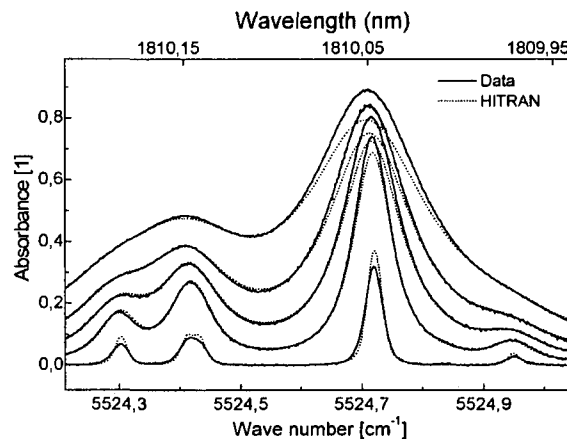


Fig. IV.4-17: Comparison of measured absorbance spectra (thick lines) of pure methane with calculated spectra (thin lines) based on the HITRAN2000 database for sample gas pressures of 1.48, 1.0, 0.71, 0.43 and 0.07 bar (order from top of the graph to the bottom).

The measured pressures were 1.48, 1.0, 0.71, 0.43 and 0.07 bar (from top to bottom). It can be seen that the HITRAN2000 calculations (using the Voigt line shape) are close but especially the absorbance peak at  $5524.72\text{ cm}^{-1}$  is predicted too low. The 0.07 bar spectrum is a special case, since the bandwidth of the detector plus amplifier (250 kHz) is too low to resolve the very sharp peaks sufficiently. As a consequence the peaks are smoothed.

In Fig. IV.4-18 measurements of HCl using the  $1.8\text{ }\mu\text{m}$  VCSEL are shown.

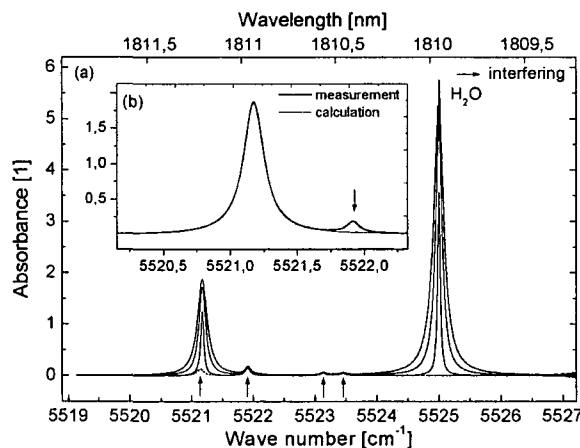
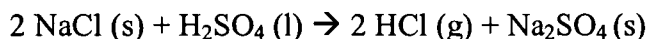


Fig. IV.4-18: Measurement of HCl using the  $1.8\text{ }\mu\text{m}$  VCSEL. The main window (a) shows measured absorbance spectra for sample gas pressures of 1.0, 0.74 and 0.29 bar (from top to bottom of the figure). The lowest trace is the water vapor background absorbance caused by the room air humidity. The arrows indicate the positions of the interfering water vapor lines. The inset (b) shows a comparison of the spectrum measured at 1 bar and the Lorentzian fit (thin line).

The HCl gas was produced on site using a Kipp's apparatus (see Fig. IV.4-13) and the reaction (Eq. IV.4-1):



Eq. IV.4-1

s... solid  
l... liquid  
g... gaseous

The produced gas flow, which should be pure HCl, was directed to the measurement cell. Absorbance spectra measured with the VCSEL are shown for sample gas pressures of 1.0, 0.74 and 0.29 bar. The lowest trace in Fig. IV.4-18 (dotted line) is the water vapor background absorbance caused by the room air humidity. It turned out that the gas composition of the measured samples was different for the different pressures. For the pressure range measured here and for a given gas mix the peak absorbance of an isolated line should not change noticeably with varying pressure. However, in these measurements the HCl peak height decreases for decreasing pressures. This may be caused by adsorption of HCl to the walls of the cell. Assuming that the HITRAN2000 line strength value is exact for the  $5521.17\text{cm}^{-1}$  line, the gas sample for the 1 bar spectrum contains only about 40% HCl. This was calculated by subtracting the water vapor background from the data and measuring the peak area of the  $5521.17\text{cm}^{-1}$  line. Further the ratio of the line strengths of the two HCl peaks was determined from the measured data. The measured ratio of 3.08 for the 1 bar spectrum shows very good agreement with the predicted ratio of 3.13 by the HITRAN2000 database. The measured ratio of the line width of the two lines was 1.04, which compares very well to the value 1.00 predicted by the HITRAN2000 database. The insert (b) in Fig. IV.4-18 compares the measured spectrum of the  $5521.17\text{cm}^{-1}$  line at 1 bar to a Lorentzian fit. It can be clearly seen that the measured line profile very nicely follows a pressure broadened Lorentzian line shape. For the very strong HCl line at  $5525.00\text{cm}^{-1}$  the measurement points with absorbance values of more than 3 are rather noisy, since at such high absorbances almost no light ( $I/I_0 = \exp(-3) = 0.05$ , i.e. the transmission is less than 5%) is transmitted to the detector and the detection noise and the 12 bit data acquisition limit the accuracy.

### Conclusions (1810 nm VCSEL)

In this work we demonstrated for the first time the application of a long wavelength  $1.8\ \mu\text{m}$  single frequency InP-based VCSEL to absorption spectroscopy and gas sensing. In the  $1.8\ \mu\text{m}$  region HCl, NO and hot  $\text{H}_2\text{O}$  ( $>1000\ \text{K}$ ) have the strongest absorption lines in the near infrared below  $2\ \mu\text{m}$  and there are also good absorption lines for  $\text{CH}_4$ . As demonstration for the multiple species measurement capabilities of the  $1.8\ \mu\text{m}$  VCSEL highly resolved spectra of HCl,  $\text{CH}_4$  and  $\text{H}_2\text{O}$  were measured at various pressures ranging from 0.07 to 1.5 bar and compared to HITRAN2000 database calculations. Generally very good agreement was found but some  $\text{CH}_4$  lines were missing and some other lines underestimated. A current tuning range of  $8.4\ \text{cm}^{-1}$  ( $2.8\ \text{nm}$ ) was demonstrated. The laser threshold was 0.9 mA, the temperature tuning rate was  $0.125\ \text{nm/K}$  ( $0.38\ \text{cm}^{-1}/\text{K}$ ) and the current tuning rate was  $0.9\ \text{nm/mA}$  ( $2.75\ \text{cm}^{-1}/\text{mA}$ ). In order to demonstrate the on wafer testing capability, the laser was selected, tested and used for the experiments by contacting the laser directly on the wafer. In contrast to  $760\ \text{nm}$  VCSELs, which are reported to operate multi mode at higher injection currents [124] the  $1.8\ \mu\text{m}$  VCSEL used in this work showed a mode-hop free continuous single frequency tuning over the whole laser driving current range. As high speed and sufficiently low noise current driver a 5 MHz analog function generator was used in combination with a  $2\ \text{k}\Omega$

resistor in series with the VCSEL. In conclusion it was shown that 1.8  $\mu\text{m}$  VCSELs are very well suited for high resolution spectroscopy and gas sensing.

### Conclusions (1.54, 1.68 and 1.81 $\mu\text{m}$ VCSEL)

In this work, novel, single frequency, long wavelength InP based vertical-cavity surface-emitting lasers (VCSELs) were used in tunable diode laser absorption spectroscopic measurements for the first time. A 1.54  $\mu\text{m}$  device was deployed to record high resolution spectra of  $\text{NH}_3$  at temperatures up to 1173K. Another VCSEL at 1.68  $\mu\text{m}$  was used to obtain spectra of  $\text{CH}_4$  at up to 5 MHz laser tuning frequency. This corresponds to a time resolution of 200 ns and is the fastest absorption spectroscopic measurement so far. A VCSEL at 1.81  $\mu\text{m}$  for the detection of  $\text{H}_2\text{O}$ ,  $\text{CH}_4$  and  $\text{HCl}$  was used to record high resolution spectra (see the conclusions in the three corresponding subchapters for further details).

The lower detection limit was not determined experimentally.

If a minimum detectable absorbance of 0.01 is assumed, the approximate detection limit for  $\text{NH}_3$  (1540 nm) is 17500 ppm\*m, for  $\text{CH}_4$  (1680 nm) 2200 ppm\*m, for  $\text{HCl}$  and  $\text{H}_2\text{O}$  (1810 nm) 320 and 290 ppm\*m, respectively (all calculated for 1 bar and 296K).

The tuning properties of the VCSELs were investigated. Besides the ability of extraordinary fast wavelength tuning, it was also discovered that the total continuous current tuning range of VCSELs is by approximately an order of magnitude larger than for conventional, edge emitting lasers, which makes them suitable for the investigation of high pressure environments.

Further advantages of VCSELs as compared to edge emitting diode lasers are on wafer testing capability, low manufacturing costs, low current operation and therefore low power consumption, less susceptibility to optical feedback (no optical isolator needed) and low beam divergence which eases fiber coupling. Two dimensional VCSEL arrays on a single chip mounted in a spectrometer device show the potential for easy and fast field replaceability. The low power consumption of VCSELs also gives them an edge for battery operated appliances. The availability of long wavelength, single frequency VCSELs should significantly expand the application fields for infrared diode laser gas sensors and make VCSELs a preferred choice for industrial diode laser based gas sensing applications.

The findings from this research were partly patented and published:

M. Lackner, G. Totschnig, F. Winter, R. Shau, J. Roskopf, M. Ortsiefer, M.C. Amann, Spektroskopischer Einsatz neuer, langwelliger (bis 2  $\mu\text{m}$ ) Diodenlaser (VCSEL) für schwierige Bedingungen, *Technisches Messen* 70 (6), 294-305 (2003).

M. Lackner, G. Totschnig, F. Winter, R. Shau, J. Roskopf, M. Ortsiefer, M.C. Amann, Demonstration of Methane Spectroscopy using a Vertical-Cavity Surface-Emitting Laser (VCSEL) at 1.68  $\mu\text{m}$  with up to 5 MHz repetition rate, *Science and Technology* 14 (1) 101-106 (2003).

G. Totschnig, M. Lackner, F. Winter, R. Shau, J. Roskopf, M. Ortsiefer, M.C. Amann, High speed vertical-cavity surface-emitting laser (VCSEL) absorption spectroscopy of ammonia ( $\text{NH}_3$ ) near 1.54  $\mu\text{m}$ , *Applied Physics B Lasers and Optics* 76 (5), 603-608 (2003).

G. Totschnig, M. Lackner, F. Winter, R. Shau, J. Roskopf, M. Ortsiefer, M.C. Amann, 1.8  $\mu\text{m}$  vertical-cavity surface-emitting laser absorption measurements of  $\text{HCl}$ ,  $\text{H}_2\text{O}$  and  $\text{CH}_4$ , *Meas. Sci. Technol.* 14 (4), 472-478 (2003).

#### IV.4.2 Demanding experimental environments probed with the 761 nm O<sub>2</sub> VCSEL

In this chapter, the 761 nm VCSEL described in chapter III.3 was used to probe rovibrational transitions of molecular oxygen in harsh environments.

A 0-8 V voltage ramp was applied to the VCSEL which was connected in series to a 1000 Ohm resistance (compare the high speed measurements using long wavelength VCSELs in the previous chapter). The VCSEL was not thermostated. It was housed in a copper heat sink at room temperature. This was done to demonstrate that temperature stabilisation is not as stringent a demand as with conventional edge emitting diode lasers. A silicon photodiode (Thorlabs PDA 55) was used to detect the laser light. The experimental setup is shown in Fig. IV.4-19.

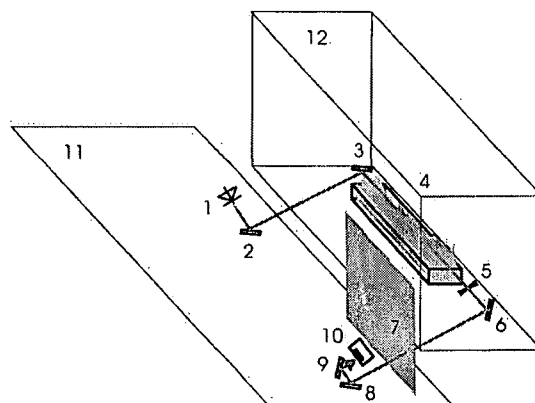


Fig. IV.4-19: Experimental setup: 1: VCSEL; 2, 3: mirror; 4: groove (0.50 m long); 6: mirror; 7: shield; 8, 9: mirror; 10: photodetector; 11: optical breadboard; 12: fume cupboard. The laser was sent through a flame to demonstrate the possibility of probing difficult environments. The VCSEL was frequency tuned at up to 25 kHz.

The laser beam was sent through the air and traversed a flame or region of particles falling down (silica sand, 80-500  $\mu\text{m}$ ) before being collected by the photodetector. The total path length was 2.75 to 4.85 m. The length of the flame was up to 1.00 m (groove filled with burning liquid fuel) and 2 cm (premixed and non-premixed torch lamp flame). In [230], comparable *in-situ* species concentration measurements in an industrial furnace were conducted (potassium atoms).

O<sub>2</sub> at 760 nm was detected by TDLAS using VCSELs in [117], [124], [205]-[208].

O<sub>2</sub> is a relatively weak absorber. So in order to be able to observe the absorption peaks without sensitive modulation techniques but by direct absorption spectroscopy instead, a long path length was chosen. The oxygen is therefore measured in the flame and outside concurrently. In this study, this fact does not disturb the investigations because the focus was on the necessity for rapid tuning in order to obtain undistorted signals.

A picture of the groove holding the liquid fuels is shown in Fig. IV.4-20.

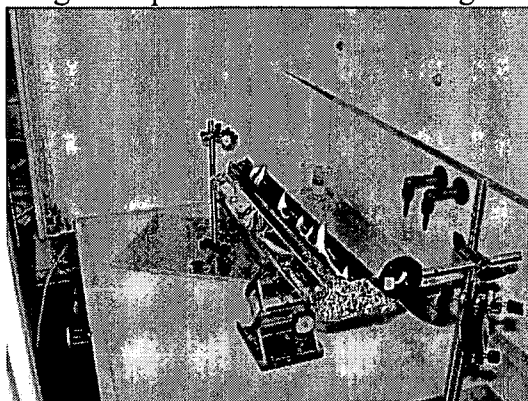


Fig. IV.4-20: Picture of the experimental setup: The groove is filled with liquid fuel (here: diesel) and can be varied in its relative height (compare Fig. IV.4-19).

In Fig. IV.4-21, the implication of the laser tuning frequency is addressed in a demonstrative way.

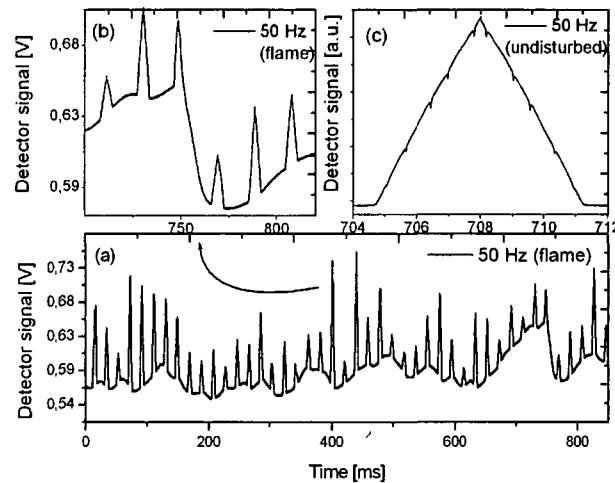


Fig. IV.4-21: The laser beam was sent through the air and traversed a propanol flame before hitting the photodetector. Experimental conditions: Total path length 4.85 m, length of the flame: 1.00 m. The laser was ramped at 50 Hz. Fig. IV.4-21 (b) shows the transmission over 850 ms. (b) is a magnification. On top of the flickering emissions by glowing soot particles, one can see the individual ramps. Their speed (50 Hz) is too low to deliver undistorted peaks (confer (c) for reference).

In this example, the laser was tuned at 50 Hz (frequency of the voltage ramps). The lowest data trace (a) shows the transmission in a time frame of 850 ms. The signal is composed of two parts: Broadband infrared emission resulting mainly from glowing soot particles and the laser signal (triangular ramps) atop of it. (b) is a magnification of (a). One can see that compared to the duration of the laser ramps, the fluctuations of the background occur on a short or at least comparable time scale. In order to obtain undistorted signals (i.e. ramps with absorption peaks as shown in the upper right picture (c)), it is necessary to tune the laser faster than the time scale of the encountered noise sources. By doing so, the systems virtually comes to a standstill where the adverse effects like broadband infrared emission and beam steering do not negatively affect the measurements. This was done in the experiment depicted in the next figure Fig. IV.4-22.

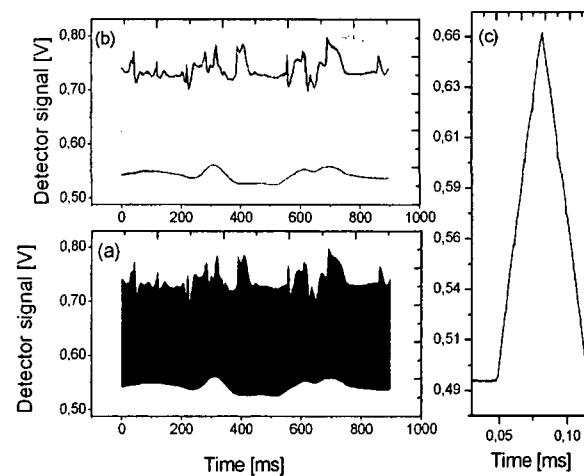


Fig. IV.4-22: The oxygen VCSEL is used to probe a 0.5 m long flame of kerosene. The transmission is shown in (a). An individual ramp of the laser is shown in (c). The tuning frequency was 5.0 kHz. This is fast enough to measure species concentrations in the flame despite beam steering and flickering emissions. (b) shows the "envelope curves" of data trace (a) (details see text).

In Fig. IV.4-22, the tuning speed was increased by two orders of magnitude from 50 Hz to 5.0 kHz. A 0.5 m long flame of kerosene was investigated. (a) is the transmission shown for a time duration of 900 ms. The resolution for printing is too low to display the individual ramps. One of these ramps can be seen on the right in (c). The tuning speed is fast enough for the accurate determination of the absorbance of the target species.

Fig. IV.4-22(b) in the upper left corner shows the "envelope curves" of the original data in (a). The lower curve would have been recorded without the presence of the laser beam. It shows the infrared emissions caused by the flame hitting the detector. The upper curve can be obtained by point-line measuring the peak transmission of each ramp. If the lower curve is subtracted from the upper envelope curve, one obtains the transmission of the laser beam through the flame.

One can see that the upper curve fluctuates stronger in time than the lower one. This is mainly due to two effects: Laser light scattering and beam steering.

Due to refractive index gradients caused by temperature gradients in the non-premixed kerosene/air flame, the probing laser beam does not traverse the sample volume (i.e. the flame) at the selfsame position during the entire experiment. Instead, it moves around and therefore more or less light is collected by the detector. Scattering of laser light on soot particles also causes fluctuations of the laser beam transmission.

The following seven figures address this issue more thoroughly, yet also in a more qualitative and descriptive way.

Fig. IV.4-23 shows the transmission of the laser beam through the 0.02 m long flame of a torch lamp (total path length 4.85 m).

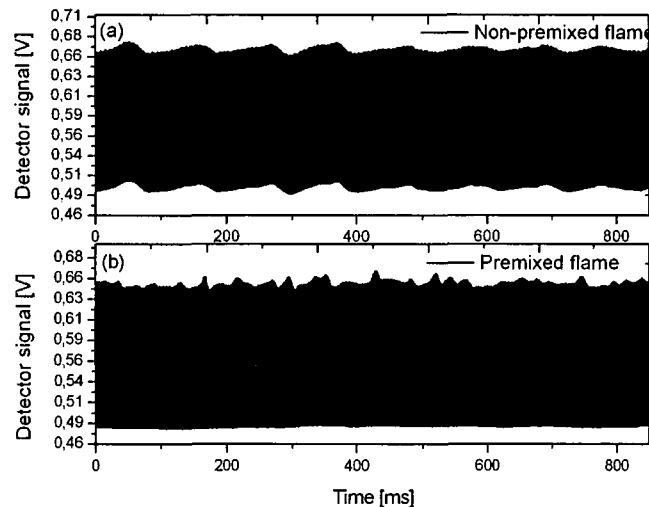


Fig. IV.4-23: Investigation of a non-premixed (a) and premixed (b) propane/butane flame (torch lamp). The total path length was 4.85 m, the path length in the flame 0.02 m. The laser was ramped at 5 kHz. For details, see the succeeding Fig. IV.4-24.

In Fig. IV.4-23(a), the diffusion flame was probed, in (b), the premixed (blue) flame. The time duration of the depicted measurement was 850 ms. The non-premixed flame does not burn as smoothly as the premixed one (see the lower envelope curve). As the figure shows, the premixed flame causes more beam steering than the non-premixed one.

In Fig. IV.4-24, two magnifications of Fig. IV.4-23(a) are shown.



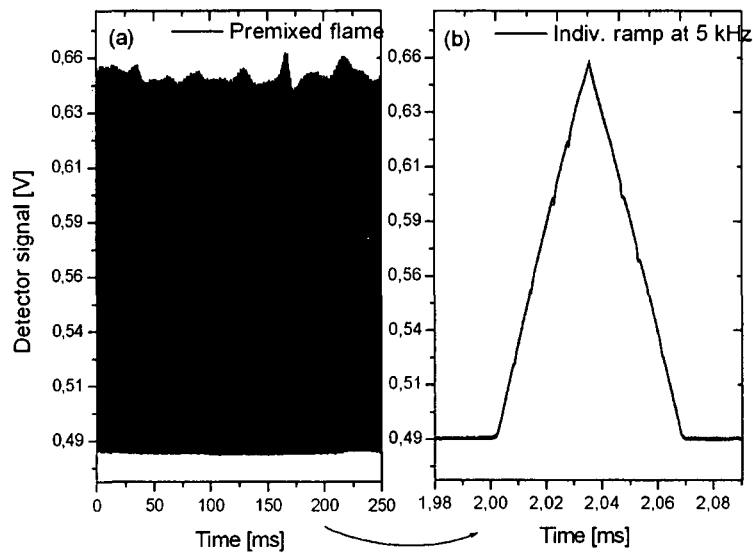


Fig. IV.4-24: Closer look at the preceding figure Fig. IV.4-23: (a) is a magnification of the transmission curve, in (b) an individual laser ramp where four absorption peaks can be seen on each side is shown. The tuning speed of the laser (5 kHz) is fast enough to allow undistorted signal recording.

Fig. IV.4-24(b) shows an individual laser ramp. At 5 kHz tuning speed, the experimental noise does not adversely affect the measurements any more. Note that VCSELs can be operated at tuning speeds far beyond the kHz range!

The fluctuations in the laser light transmission caused by particles are visually investigated in the succeeding Fig. IV.4-25 and Fig. IV.4-26.

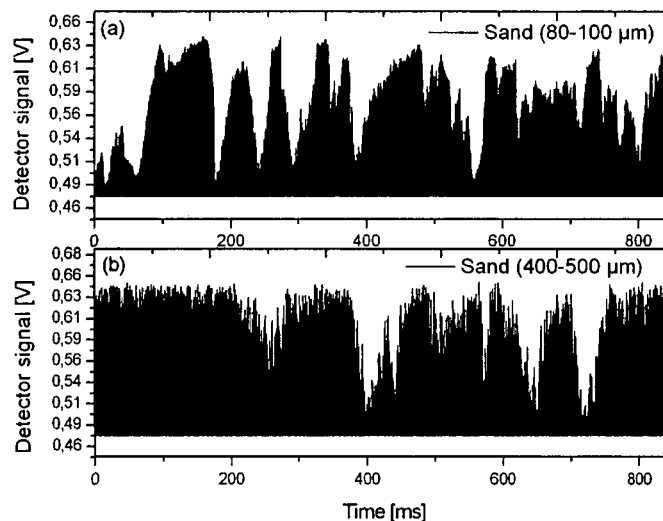


Fig. IV.4-25: Investigation of the transmission of the laser through a particle laden flow (5 mm broad area of silica sand trickling out of a funnel). In (a), silica sand from 80-100  $\mu\text{m}$  was used, in (b), the diameter was 400-500  $\mu\text{m}$ . The total path length was 4.85 m. The laser was ramped at 5 kHz. For details, see the succeeding Fig. IV.4-26.

In Fig. IV.4-25(a), 80-100  $\mu\text{m}$  silica sand was used, in (b), the grain size was 400-500  $\mu\text{m}$ . The total path length of the laser beam was 4.85 m. The sand was filled into a funnel and allowed to trickle through the laser beam path (5 mm broad section). The difference can be seen more clearly in Fig. IV.4-26.

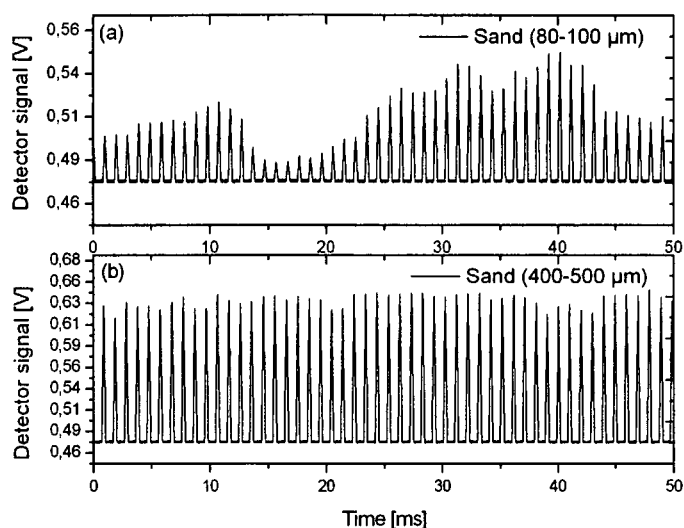


Fig. IV.4-26: Closer look at the preceding Fig. IV.4-25: (a) is a magnification of the transmission curve with 80-100  $\mu\text{m}$  sand particles, (b) shows the case for 400-500  $\mu\text{m}$  sand. The tuning speed of the laser (5 kHz) is fast enough to allow undistorted signal recording. The smaller particles cause faster fluctuations.

This figure is a magnification of Fig. IV.4-25 where approximately 50 individual ramps can be seen. The “lower envelope curve” does not fluctuate. It is mainly caused by sunlight falling onto the photodetector (the experiments were carried out by day). The transmission of the probing laser beam (laser ramped again at 5.0 kHz) was disturbed more strongly by the smaller sand particles.

Fig. IV.4-27 to Fig. IV.4-29, 0.5 m long flames of liquid fuels are compared (gasoline and octane, kerosene and diesel). The path length was changed from 4.85 to 2.75 m because the groove holding the liquid fuels had to be positioned in the fume cupboard.

Fig. IV.4-27 shows the transmission of the probing 761 nm VCSEL through an octane flame (a) and a gasoline flame (b). Gasoline with octane number (ON) 95 obtained from a local petrol station was used.

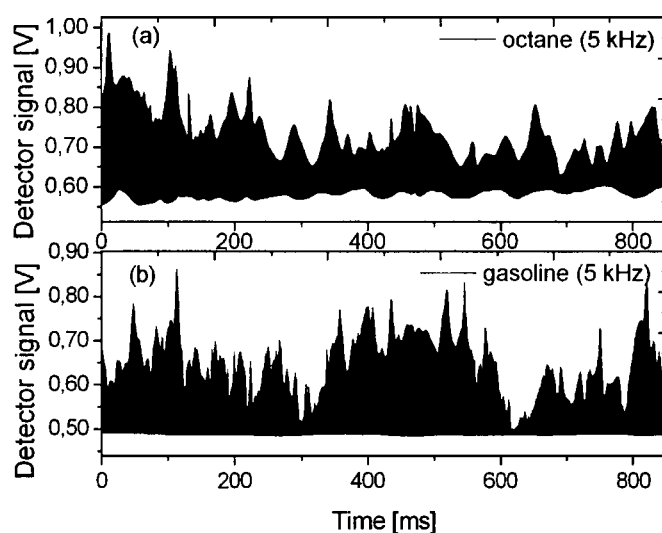


Fig. IV.4-27: Investigation of octane (a) and gasoline (ON 95, petrol station grade) (b) flames with the 761 nm VCSEL. The total path length was 2.75 m, the path length in the flame 0.50 m. The laser was ramped at 5 kHz. For details, see the succeeding Fig. IV.4-29.

From the lower envelope curves in Fig. IV.4-27(a, octane), and Fig. IV.4-27(b, gasoline), it can be seen that the emissions from the flame (predominantly glowing soot particles) show a qualitatively more transient behaviour for octane (compare Fig. IV.4-22 (b)). The upper envelope curve changes more rapidly for gasoline. This implies that beam steering is stronger in the gasoline flame.

Fig. IV.4-28 takes a closer look at the transmission through the gasoline flame.

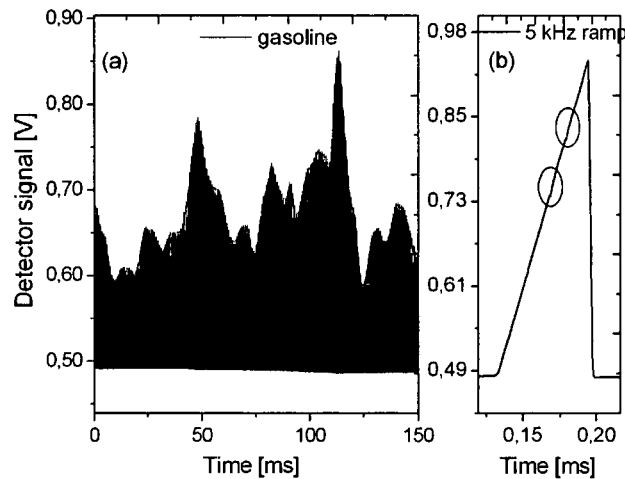


Fig. IV.4-28: Closer look at the preceding figure Fig. IV.4-27: (a) is a magnification of the transmission curve, in (b) an individual laser ramp where two absorption peaks can be seen on the ascending side of the ramp. The tuning speed of the laser (5 kHz) is fast enough to allow undistorted signal recording.

The 5 kHz ramp is fast enough in order to probe the oxygen peaks in an undistorted way.

Fig. IV.4-29 concludes this section with the depiction of a diesel (a) and kerosene (b) flame. The tuning speed of the VCSEL was 25 kHz.

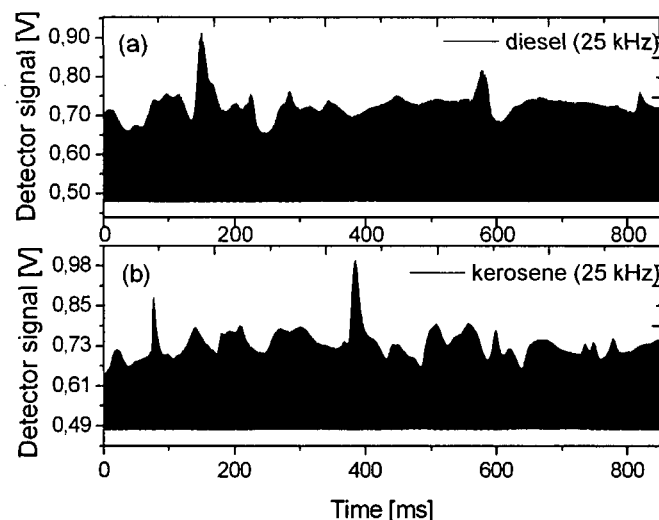


Fig. IV.4-29: Investigation of a diesel (a) and kerosene (b) flame. The total path length was 2.75 m, the path length in the flame 0.50 m. The laser was ramped at 25 kHz.

The transmission signal of the laser through the diesel (a) and kerosene (b) flames look very much alike. This is not surprising due to the chemical similarity of these two fuels.

As it could be seen in the previous figures,  $O_2$  is not a strong absorber. Relatively long path lengths are required in order to achieve detectable absorbencies. This chapter concludes with an illustration on how a sensitive detection scheme, here wavelength modulation spectroscopy (WMS), can alleviate this problem.

In Fig. IV.4.30, the experimental setup is shown. WMS is explained in more detail in chapter II.3.

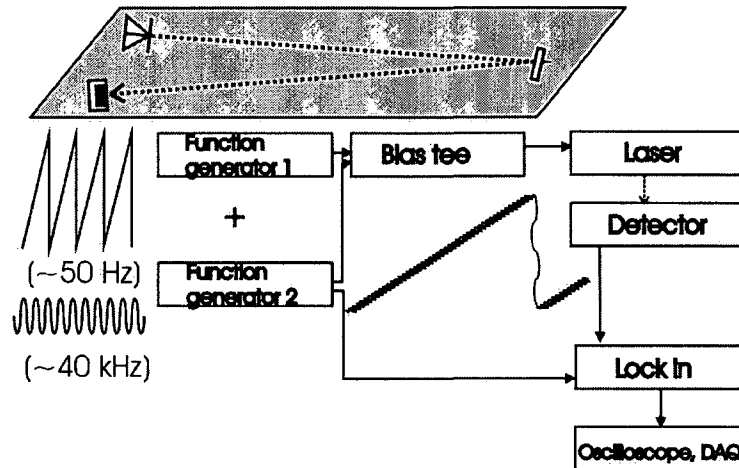


Fig. IV.4-30: Schematic setup of the sensitive concentration measurements using wavelength modulation spectroscopy (WMS). A sensitive detection scheme can be used for weak absorbers where path lengths are short. Instead of applying a triangular current ramp (function generator 1) to the laser, this current ramp is superimposed by a sinusoidal modulation of higher frequency (function generator 2). The outputs of the function generators 1 and 2 are combined in a circuit called bias tee. The lock-in amplifier is locked to the frequency of function generator 2. If resonant absorption occurs, the signal at the lock-in amplifier will be the first ( $1f$ ) or second ( $2f$ ) derivation of the initial absorption peak (see text and chapter II.3 for details). A SRS 510 lock-in amplifier (Stanford Research Systems, Inc.) was used, the bias tee was home made.

The frequency of the current ramp (saw tooth, approximately 50 Hz, 0-10 V) and a higher modulation frequency (sinusoidal, approximately 40 kHz) of smaller amplitude were mixed (home made bias tee) and applied to the laser. The band width of the available laser driver was too low, therefore the voltage ramp was applied directly to the laser. The upper limit of the sinusoidal modulation to the laser current ramp was close to 40 kHz because at  $2f$  detection (80kHz), the band width of the lock-in amplifier (SRS 510, Stanford Research Systems, Inc.) of 100 kHz was reached.

In Fig. IV.4.31 and Fig. IV.4.32, the results are shown. The path length was 2.40 m,  $O_2$  in room air was probed.

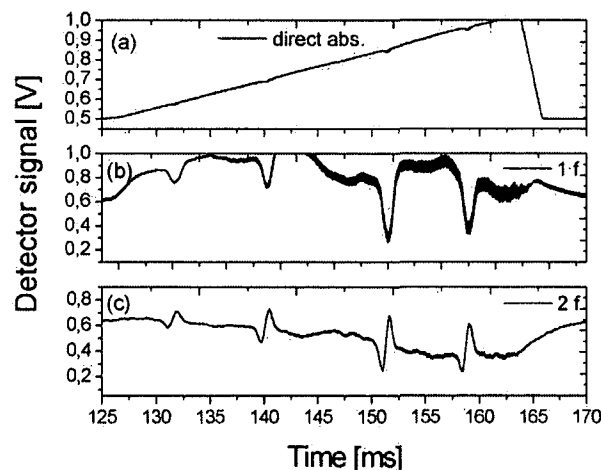


Fig. IV.4-31: Determination of  $O_2$  at 761 nm (path length 2.40 m in room air). (a) shows direct absorption where the peaks can scarcely be seen. (b) is the  $1f$  signal, (c) the  $2f$  signal using a lock-in amplifier and first and second harmonic detection, respectively.

In Fig. IV.4.31, direct absorption is compared to the  $1f$  and  $2f$  signal. For the direct absorption measurements, the fast sinusoidal modulation was not used, only the 50 Hz 0-10 V voltage ramp.

In Fig. IV.4.32, a closer look at the  $2f$  signal is taken.

In (a), one can see the original detector signal. The laser drive current applied to the laser was the 50 Hz 0-10 V voltage ramp (function generator 1) plus the 40 kHz sinusoidal modulation (function generator 2, both signals combined by the home made bias tee).

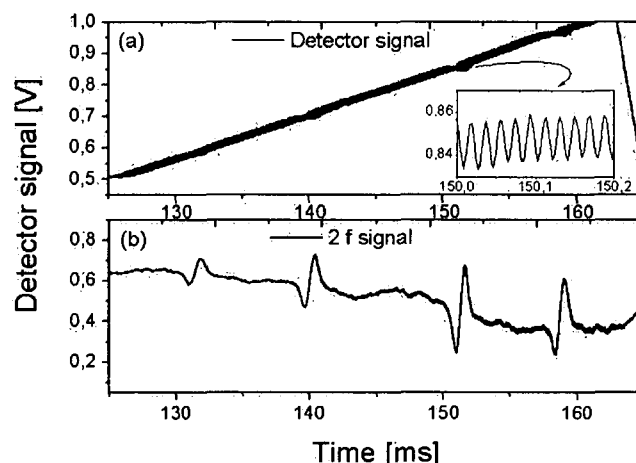


Fig. IV.4-32: Determination of  $O_2$  at 761 nm (path length 2.40 m in room air). (a) shows the original detector signal (current ramp plus modulation). The insert is a magnification. (b) shows the  $2f$  signal (compare the preceding figure Fig. IV.4-30).

The insert shows a magnification of the detector signal. One can see the modulation resulting from the input of the second function generator 2 (see Fig. IV.4-30). In Fig. IV.4-32 (b), the  $2f$  signal is shown.

Fig. II.3-10 in chapter II.3 (tunable diode laser absorption spectroscopy) shows calculated  $1f$  and  $2f$  signals. The  $2f$  signal in IV.4-32 (b) is distorted in respect to the theoretical signal. Note that the frequency of the current ramp to the laser was only 50 Hz. The small modulation frequency (40 kHz) was used in order to shift the detection from 50 Hz to 40 kHz (noise shows a  $1/f$  dependence with  $f$  being the frequency).

If you recall the measurement shown in Fig. IV.4-21 (probing of a 1 m long propanol flame with a tunable laser ramped at 50 Hz), the problem becomes obvious. In Fig. IV.4-21, the 50 Hz tuning was too slow to probe the flame.

Since the bandwidth of standard lock-in amplifiers is around 100 kHz, the modulation frequency cannot exceed 50 kHz ( $2f = 2 \cdot 50 \text{ kHz} = 100 \text{ kHz}$ ) in simple setups as shown here.

Higher ramping frequencies (kHz range) would require much higher modulation frequencies. In FMS, this is done by using equipment which is much more expensive than in WMS.

WMS is therefore only suitable for probing low absorbencies in environments that do not show a transient behaviour.

### Conclusions ( $O_2$ VCSEL)

In this chapter, a 761 nm VCSEL was used to probe rovibrational transitions of  $O_2$  under difficult conditions.

The laser which was housed in a copper heat sink was not thermostated. The total path length was 2.75 to 4.85 m. The laser beam was sent through the 0.5 to 1.0 m long flame of liquid fuels (propanol, octane, gasoline, diesel and kerosene). In a different test, it was directed through the premixed and non-premixed flame of a torch lamp (propane/butane). Finally, the

influence of a stream of sand particles (80-100 and 400-500  $\mu\text{m}$ ) was investigated. It was demonstrated that rapid tuning of the laser (several kHz) enables undistorted recording of the absorption peaks despite scattering, heavy beam steering and flickering emissions from the flames. The investigations were conducted in a qualitative way.

Since  $\text{O}_2$  is a comparatively weak absorber, either long path lengths or sensitive detection methods have to be used. Wavelength modulation spectroscopy (WMS) was used. The frequency of the current ramp was 50 Hz, the modulation frequency 40 kHz. The 1f and 2f signals were compared to the direct absorption signal.

The findings from this research ( $\text{O}_2$  VCSEL) were accepted for a poster presentation:

M. Lackner, G. Totschnig, F. Winter, Rapid absorption spectroscopy for *in-situ*  $\text{O}_2$  measurements in hostile environments (multi-phase and flames) using a 761 nm vertical-cavity surface-emitting laser (VCSEL), accepted for poster presentation at TDLS 2003 (4<sup>th</sup> international conference of tunable diode laser spectroscopy), Zermatt, Switzerland, July 14-18 (2003).

## IV.5 Absorption spectroscopy at elevated pressures using VCSELs

Absorption spectra of  $O_2$  at pressures of 1 bar, 5 bar and 10 bar were recorded using the 761 nm VCSEL (see chapter III.3).

TDLAS experiments at elevated pressures were reported in [124] and [230]. A fixed wavelength technique using two diode lasers to cope with high pressures was elaborated in [231].

A triangular voltage ramp rising from 0.0 – 10.0 V was applied to the VCSEL which was connected in series to a 1000 Ohm resistance. This was done to overcome bandwidth limitations of commercially available laser drivers as in the previous chapter IV.4. The VCSEL was not thermostated. It was housed in a copper heat sink at room temperature. This was done to demonstrate that temperature stabilisation is not always essential for VCSELs (compare chapter IV.2.4).

For edge emitting diode lasers used for spectroscopic purposes, it is an absolute must. A silicon photodiode (Thorlabs PDA 55) was used to detect the laser light.

The path length inside the pressurized cell was 0.30 m. A single pass setup was chosen. Prior to the experiments, the cell was flushed with oxygen.

The measurements were carried out with pure oxygen. The region outside the cell (approximately 0.15 m in air) was not purged for sake of simplicity. Therefore, approximately 10% of the absorption (at 1 bar) resulted from oxygen from outside. At higher cell pressures, the influence was correspondingly less.

Fig. IV.5-2 shows the detector signal for varying oxygen pressures. Two absorption peaks on the ascending side have been magnified in the small inserts on the right. Fig IV.5-2 (a) was recorded at 1 bar, (b) and (c) at 5 bar and 10 bar, respectively.

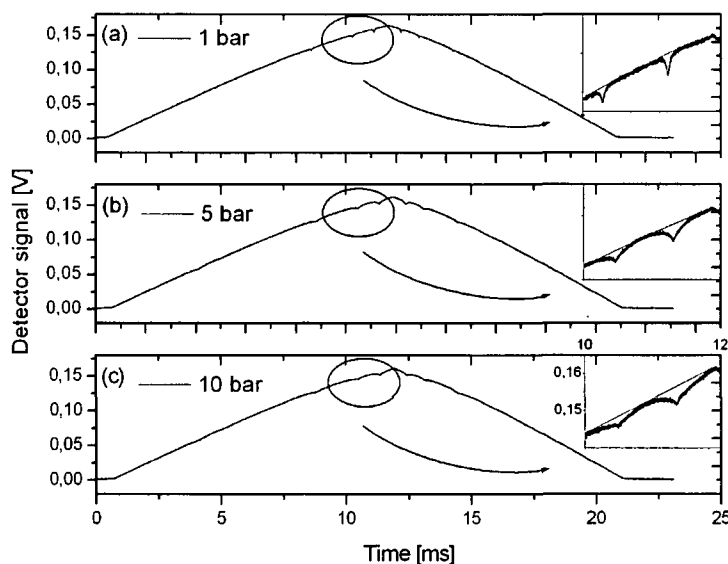


Fig. IV.5-1: Pressure broadened spectra of  $O_2$  at 1, 5 and 10 bar (0.30 m, 298K) recorded with the 761 nm VCSEL.

The following Fig. IV.5-2 is a magnification of the 1 bar and 10 bar data trace. The baseline is also shown.

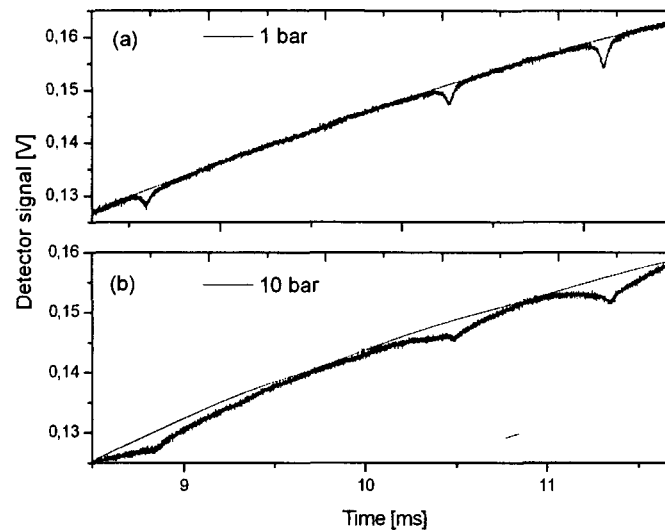


Fig. IV.5-2: Pressure broadened spectra of  $O_2$  at 1, 5 and 10 bar (0.30 m, 298K).

The absorbance is less than 0.025. In other words, the transmittance is approximately 97.5 %. With the detector signal being as small as 150 mV and a given resolution of the data acquisition board (SignaTec PDA 12A) of 12 bit, only a noisy spectrum could be recorded. Nonetheless, the effect of pressure broadening can be seen. The absorbance can be seen in Fig. IV.5-3 for 1 bar and Fig. IV.5-4 for 5 bar (both the second last peak on the ascending side of the ramp I Fig. IV.5-1(a) and (b)).

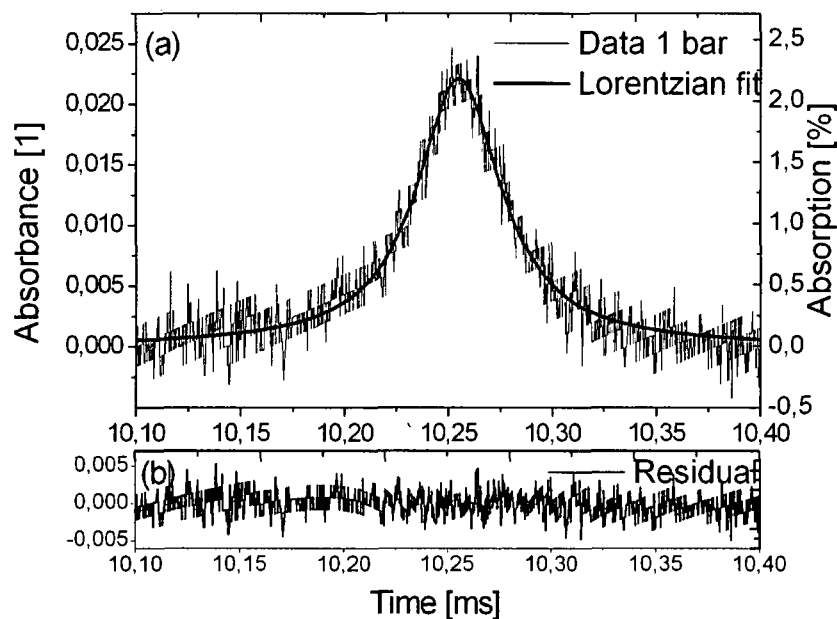


Fig. IV.5-3: Absorbance peak of  $O_2$  at 1 bar (0.30m, 298K). Using a linear computed baseline, good agreement with a Lorentzian fit can be observed (a). The residual is given in (b).

The baseline was calculated in a very simple approach. The peak was “cut out” and the empty section was replaced by a linear fit between the two bordering, truncated curve sections. A linear relationship between driving current (actually the voltage ramp limited by the 1000 Ohm resistance) and output power (more precisely: detector response) was assumed.



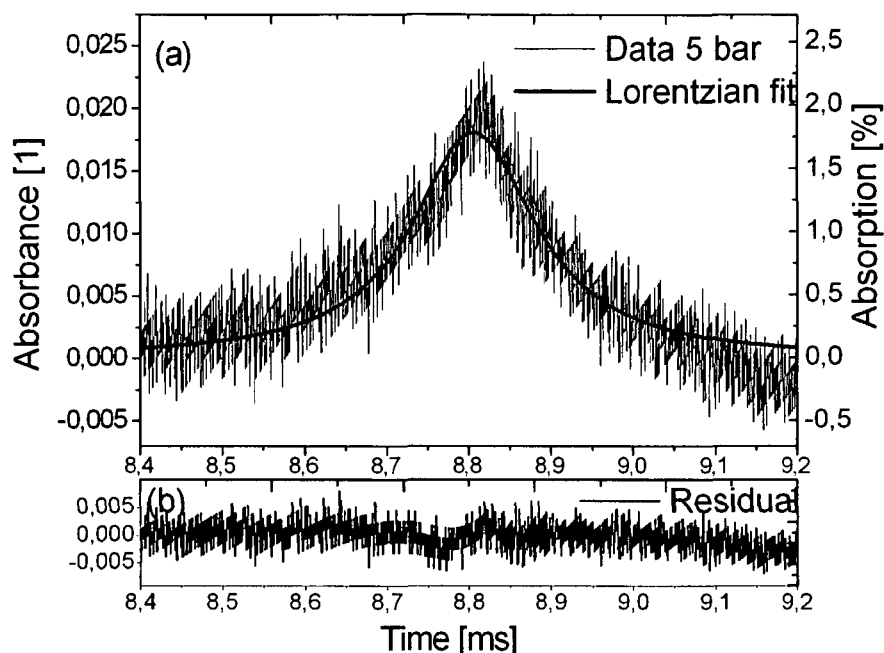


Fig. IV.5-4: Absorbance peak of  $O_2$  at 5 bar (0.30m, 298K). Using a linear computed baseline, good agreement with a Lorentzian fit can be observed (a). The residual is given in (b).

As the residual trace between measured curve and computed Lorentzian fit in Fig. IV.5-3(b) and Fig. IV.5-4(b) shows, the assumption of a linear baseline works well.

In Fig. IV.5-5, the Lorentzian fits for the measurements at 1 bar and 5 bar are shown separately.

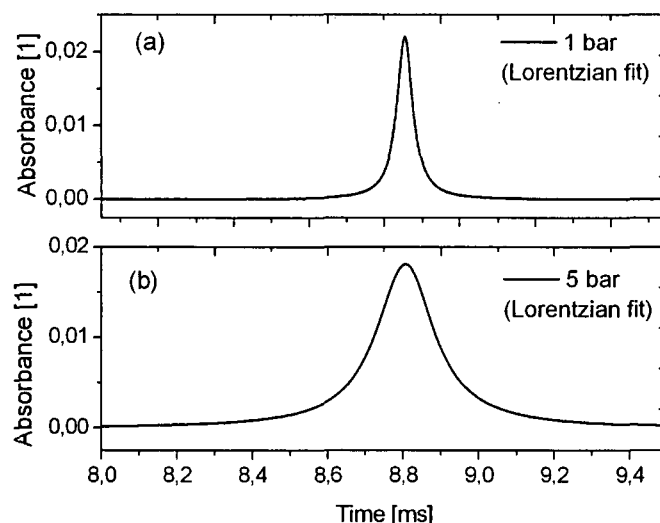


Fig. IV.5-5: Pressure broadening of the  $O_2$  absorption line at 1 bar (a) and 5 bar (b). Both traces are Lorentzian fits of the measurements in Fig. IV.5-3 and Fig. IV.5-4.

Fig. IV.5-6 shows a picture of the home made static cell that was constructed for line broadening measurements. The cell has got an inner path length of 0.30 m and is equipped with two wedged windows ( $2^\circ$ , 5 mm thick sapphire) that are fixed by copper compression rings. The vessel was constructed for rated peak pressures of 150 bar (based on the cell for laser ignition tests in chapter IV.2). Construction plans are given in the Appendix.

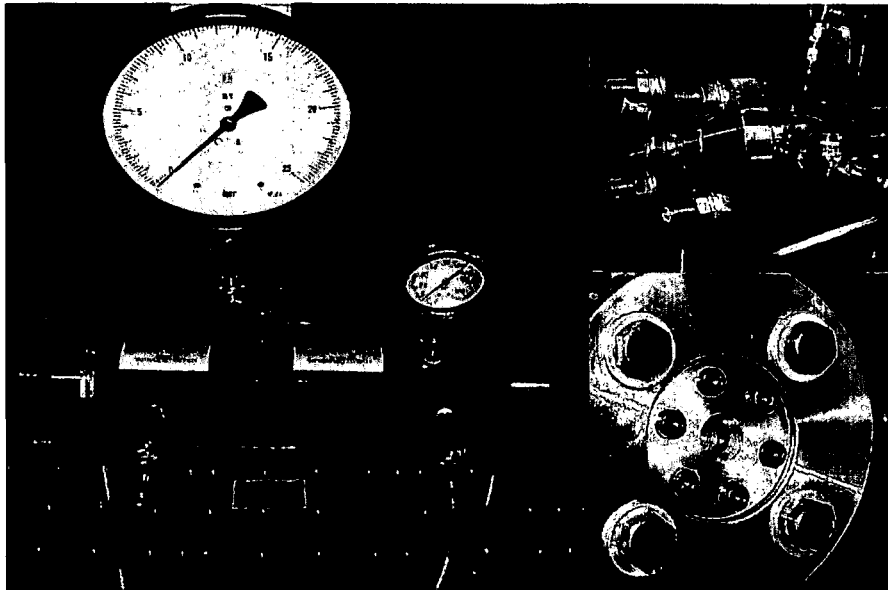


Fig. IV.5-6: High pressure static cell for spectral line broadening investigations.

In [231], high pressure spectroscopy of water vapour was investigated. The scanned wavelength method (TDLAS) was compared to a fixed wavelength method using two diode lasers (one at the center of the absorption feature, the second one in a non-absorbing region next to the absorption feature). It was concluded that in TDLAS the diode laser must be capable of wavelength tuning as far as approximately 12 times the half width (HWHM) of the chosen absorption peak (error <5%). Due to the limited tuning range of edge emitting lasers (EELs), TDLAS was found to be unsuitable for very high pressures. Instead, the wavelength method using two diode lasers was found to be more appropriate. This is shown in the following Fig. IV.5-7.

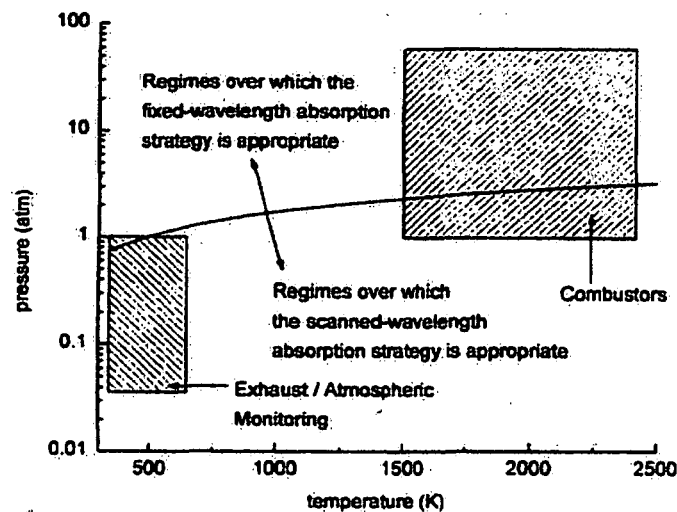


Fig. IV.5-7: The area beneath the solid curve was found to be appropriate for TDLAS (Taken from [231]).

Typical pressure/temperature regimes for combustors, atmospheric and exhaust gas monitoring are also marked in Fig. IV.5-7. It can be seen that for combustors operating above ambient pressure, TDLAS based on edge emitting lasers (as used in that study) is not applicable, even at high pressures.

The collisional width  $\gamma$  of an absorption peak depends on the temperature according to Eq. IV.5-1 (compare Eq.II.1-24):

$$\gamma(T) = \left(\frac{296}{T}\right)^n$$

(Eq. IV.5-1)

n... coefficient of the temperature dependence of the air-broadened half width [1]

T... temperature [K]

It depends on the pressure according to Ed. IV.5-2 (compare Eq.II.1-24):

$$\gamma(p) = (\gamma_{air} * p + \gamma_{self} * p)$$

(Eq. IV.5-2)

p... pressure [atm]

For calculating the curve in Fig. IV.5-7, the following assumptions were made:

- tuning range of the laser:  $2 \text{ cm}^{-1}$  (at  $1.4 \mu\text{m}$ )
- necessity of wavelength tunability 12 times the half width of the absorption peak
- $n = 0.9$
- $\gamma_{\text{H}_2\text{O}, \text{H}_2\text{O}} = 0.4 \text{ cm}^{-1}/\text{atm}$
- $\gamma_{\text{H}_2\text{O}, \text{N}_2} = 0.1 \text{ cm}^{-1}/\text{atm}$
- mole fraction  $\text{H}_2\text{O} = 10\%$

In the following Fig. IV.5-8 and Fig. IV.5-9, the range of operation for the scanned wavelength regime, i.e. TDLAS, is reassessed for VCSEL based sensors.

A tuning range of  $20 \text{ cm}^{-1}$  instead of  $2 \text{ cm}^{-1}$  is assumed (compare the previous chapter IV.4).

At  $1.4 \mu\text{m}$ ,  $2 \text{ cm}^{-1}$  correspond to  $0.4 \text{ nm}$ .

The coefficient of the temperature dependence of the line width  $\gamma_n$ , was assumed to be 0.1 and 0.9, the broadening coefficient was assumed to be 0.1 and  $0.4 \text{ cm}^{-1}/\text{atm}$  (compare [231]).

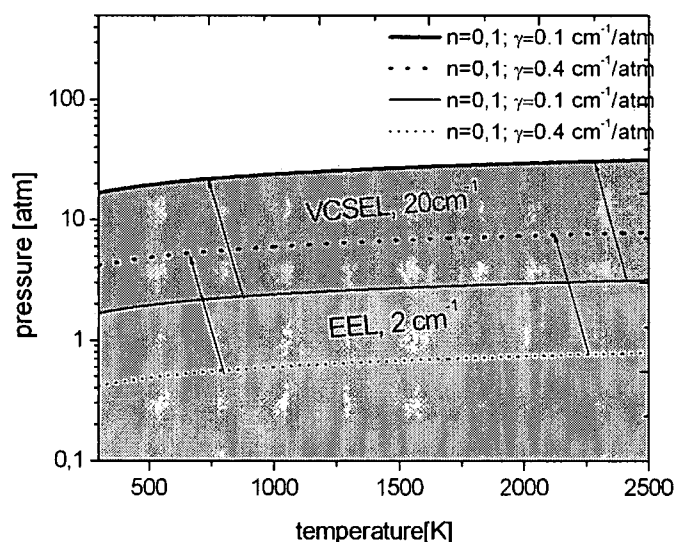


Fig. IV.5-8: Reassessment of the range of operation for TDLAS derived in [231] with VCSEL based sensors;  $n=0.1$ ,  $\gamma=0.1$  and  $0.4 \text{ cm}^{-1}/\text{atm}$ . In the shaded areas, TDLAS might be used successfully.

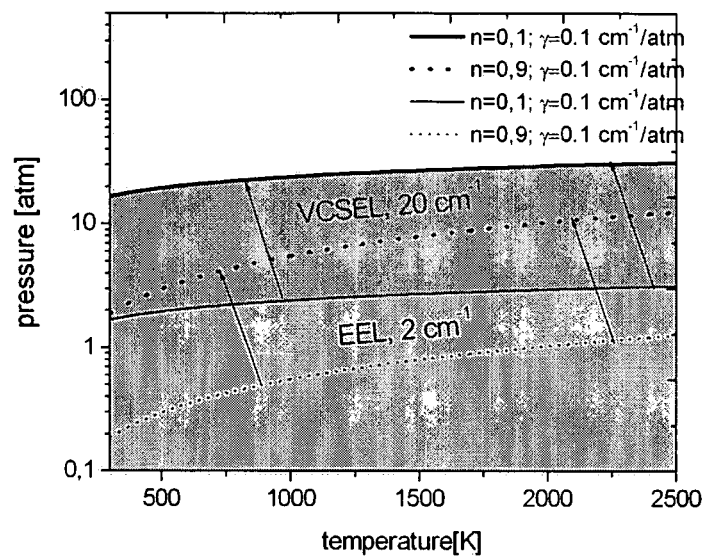


Fig. IV.5-9: Reassessment of the range of operation for TDLAS derived in [231] with VCSEL based sensors;  $n=0.1$  and  $0.9$ ,  $\gamma=0.1 \text{ cm}^{-1}/\text{atm}$ . In the shaded areas, TDLAS might be used successfully.

The shaded areas in Fig. IV.5-8 and IV.5-9 show the range of operation for sensors based on the scanned wavelength technique (TDLAS). The area in light grey gives the range of operation for edge emitting lasers (EELs, assumed tuning range  $2 \text{ cm}^{-1}$ ), the area in dark grey (above) denotes the pressure/temperature regime that can be accessed in addition by using a laser that can be far wavelength tuned (VCSEL, assumed tuning range  $20 \text{ cm}^{-1}$ ).

It can be seen from the preceding Figures IV.5-8 and IV.5-9 that for the conditions assumed in [231], VCSELs can extend the range of operation for TDLAS sensors by an order of magnitude towards higher pressures. Even at ambient temperatures around  $296 \text{ K}$ , species concentrations measurements are feasible above  $10 \text{ bar}$ . At higher temperatures, line narrowing enables measuring at higher pressures at a given tuning range. The temperature/pressure field for combustors marked in Fig. IV.5-7 can hence be accessed using VCSELs instead of edge emitting lasers.

Fig. IV.5-7, IV.5-8 and IV.5-9 are based on general assumptions.

The true and precise upper limit for a given application depends on the experimental conditions. Depending on the temperature, wavelength, mole fractions of present species and path length, TDLAS measurements are feasible at pressures up to  $100 \text{ bar}$  and more. A proper choice of the transition to be monitored and the laser (preferably VCSEL) is therefore essential. In Fig. IV.5-10, a calculated spectrum of water vapour ( $10\%$  in air),  $1 \text{ cm}$  path length,  $50 \text{ atm}$  total pressure, is shown.

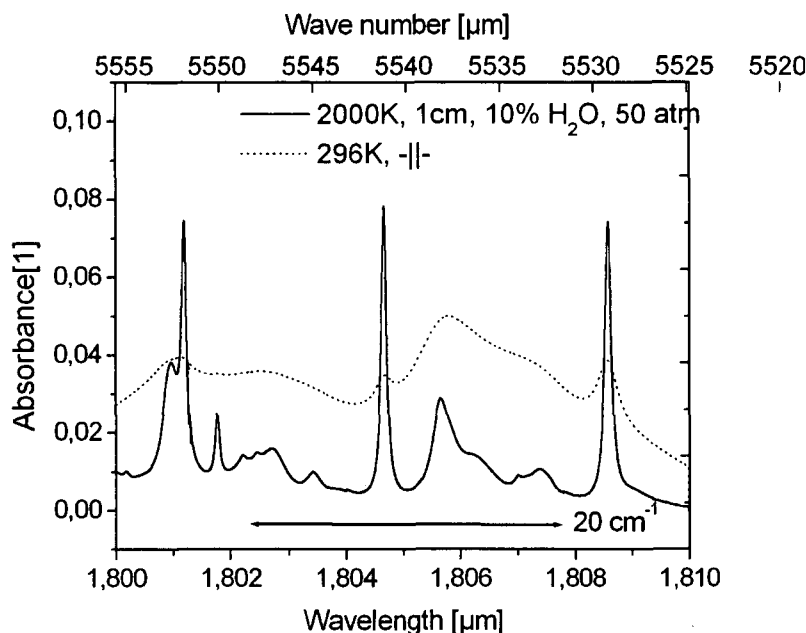


Fig. IV.5-10: Comparison of calculated water vapour spectra at 50 atm for temperatures of 296K and 2000K. At 2000K, TDLAS based on a suitable VCSEL is able to determine the mole fraction.

The solid trace was calculated for 2000K, the dotted line for 296K. At 296K, spectral broadening leads to line mixing and interferences that are too strong for a quantitative determination of the H<sub>2</sub>O mole fraction.

At 2000K, the tuning range of a suitable VCSEL is sufficient to tune over an entire absorption peak for quantitative results.

### Conclusions

In this work, absorption spectra of O<sub>2</sub> at 1, 5 and 10 bar (100% O<sub>2</sub>, 30 cm path length, 298K) were recorded using a 761 nm VCSEL. The peaks were compared to a calculated Lorentzian fit, good agreement was found. Tunable diode laser absorption spectroscopy (TDLAS) requires that the laser wavelength is tuned over the absorption peak of interest in order to discern resonant absorption from non-specific effects (compare Fig. II.3-3). Due to the finite tuning range of diode lasers and the effect of pressure broadening of absorption peaks, the range of operation of TDLAS is limited towards higher pressures. In the pertinent literature, a pressure vs. temperature plot was published where the regime of TDLAS (typical conditions) was marked. This plot was reassessed for VCSEL based systems.

The findings from this research (O<sub>2</sub> VCSEL) were accepted for a poster presentation:

M. Lackner, G. Totschnig, F. Winter, Rapid absorption spectroscopy for *in-situ* O<sub>2</sub> measurements in hostile environments (multi-phase and flames) using a 761 nm vertical-cavity surface-emitting laser (VCSEL), accepted for poster presentation at TDLAS 2003 (4<sup>th</sup> international conference of tunable diode laser spectroscopy), Zermatt, Switzerland, July 14-18 (2003).

## IV.6 Species concentration measurements in an internal combustion engine

### Introduction

The Large Scale Facility (LSF) at the Combustion Center at Lund University (Sweden) is a European research infrastructure that was initiated within the EU Fifth Framework (IHP, improving human potential, contract period 2001-2004). The LSF comprises a high pressure combustor facility, a gas turbine laboratory and, among others, optical engine facilities (<http://www.forbrf.lth.se/lst/intro.htm>). A proposal was submitted to the European Union in autumn 2002. The aim of the submitted project was to conduct *in-situ* species concentration measurements in one of the optical engines using VCSELs.

In spring 2003, a research stay of one month duration was granted.

It was decided to split the whole campaign into two parts of two weeks each. In April 2003, the author made a preparatory visit to the LSF in order to meet the local scientists and to plan the experiments. Prof. Anders Hultqvist was responsible for the tests in Sweden. It was decided to run several experiments for *in-situ* species concentration measurements and to investigate laser aided HCCI. A modified Volvo TD100 engine equipped with four suprasil windows was to be used.

The first experiments were carried out in May 2003 by the author and Dipl.-Ing. Herbert Kopecek. Dr. Hultqvist and the mechanic Bertil Andersson prepared and operated the engine.

### Experimental

The experimental setup is depicted in Fig. IV.6-1. (a) shows a vertical cross section, (b) a horizontal one.

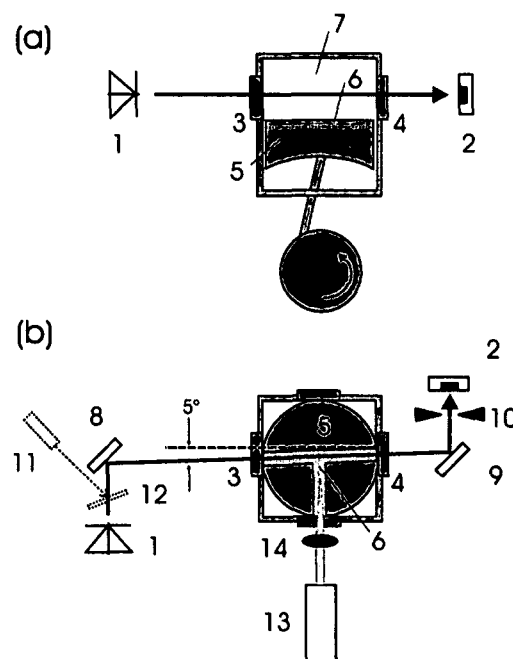


Fig. IV.6-1: Experimental setup for the *in-situ* species concentration measurements in the VOLVO TD 100 optical engine; (a): vertical cross section; (b): horizontal cross section; 1: VCSEL; 2: photo detector; 3, 4: 5x5cm<sup>2</sup> suprasil window; 5: piston; 6: groove (T shape); 7: cylinder; 8, 9: mirror; 10: slit; 11: visible alignment laser; 12: removable mirror; 13: diode pumped Q-switched Nd:YAG laser; 14: focusing lens. 13 and 14 were only used in the experiments for laser aided HCCI (see end of this chapter).

The engine, a Volvo TD100, is a modified six-cylinder truck size engine that operates on one (optical access) cylinder only. The remaining cylinders are fed by air and merely serve to balance the engine.

The following Fig. IV.6-2 shows a picture of the engine. The cylinder with optical access is the one on the left (indicated by an arrow).



Fig. IV.6-2: Picture of the engine. The cylinder with optical access is situated on the left (arrow).

The optical access cylinder has two valves, port fuel injection and an electric intake air heater (up to 400°C). The volume is 1.6 liters, the bore 120.6 mm and the stroke 140.0 mm.

The engine can be operated in CI (original), SI and HCCI mode. The fuel delivery system can supply two fuels simultaneously. There are four fuel injectors that can handle gaseous and liquid fuels. The compression ratio can be varied from 10:1 to 28:1. For optical access a spacer is placed between cylinder head and the main engine block. Four rectangular windows made of suprasil (38x38 mm<sup>2</sup>, thickness 22 mm) that are contained in the spacer (graphite sealing) allow good optical access into the combustion chamber. Suprasil is an isotropic material (fused silica) with a transmission of 90% from 0.2 to 2 μm. The transmission then falls off to zero around 2.8 μm. The spacer is shown in the following Fig. IV.6.3.



Fig. IV.6-3: Spacer containing the four suprasil windows.

Graphite sealings had to be used instead of copper compression rings for the harder sapphire (compare combustion bomb in chapter IV.2 and static pressure cell in chapter IV.5).

The engine is equipped with an EGR system and can be motored externally or fired in the speed range of 600 to 2000 rpm. The cylinder pressure is measured alongside the main exhaust gas constituents. A piezo-electric transducer (Kistler 7061B) was mounted in the middle of the cylinder head. From the pressure trace, using the ideal gas law, the average temperature is estimated. This means that far away from the cylinder walls (in the bulk) it could be roughly 50 K hotter than estimated and close to the walls 50 K cooler than estimated. In the test runs, isooctane and CH<sub>4</sub> were used as fuels. The engine was operated in HCCI mode at 1000 rpm only. When running on CH<sub>4</sub>, at least 3% of isooctane had to be added (i.e. 97 parts CH<sub>4</sub> and 3 parts isooctane). Here, tests were done with the following fuel mixtures: CH<sub>4</sub>/isooctane = 0/100, 25/75, 50/50, 75/25 and 95/5.

A special piston was used. It had a T shaped groove. As indicated in Fig. IV.6-1, the main groove was tilted 5°. The laser beam of the VCSEL for diagnostics (see later) was sent through this groove (in upper position = top dead center (TDC)). The 5° angle was chosen in order to prevent unwanted etaloning of the laser beam (compare Fig. II.3-5). The short groove in the middle was used for the test runs with the Nd:YAG laser (laser aided HCCI, see end of this chapter). The following Fig. IV.6-4 shows the piston with a laser spark inside (the engine was taken apart).



Fig. IV.6-4: Laser spark inside the groove of the piston (spacer and cylinder head are missing).

The width of the groove was 25 mm, the depth 12.5 mm.

As shown in Fig. IV.6-1, a single pass setup was chosen. It proved more advantageous than sending the laser through the engine twice. The laser and the detector unit were positioned on two small, three legged racks to both sides of the engine. The engine was placed on a damping scaffold. Vibrations made the two pass setup more prone to misalignment when running the engine.

The following Fig. IV.6-5 shows the VCSEL mounted in front of the engine (left side in Fig. IV.6-1). The piston is in TDC position in the picture.



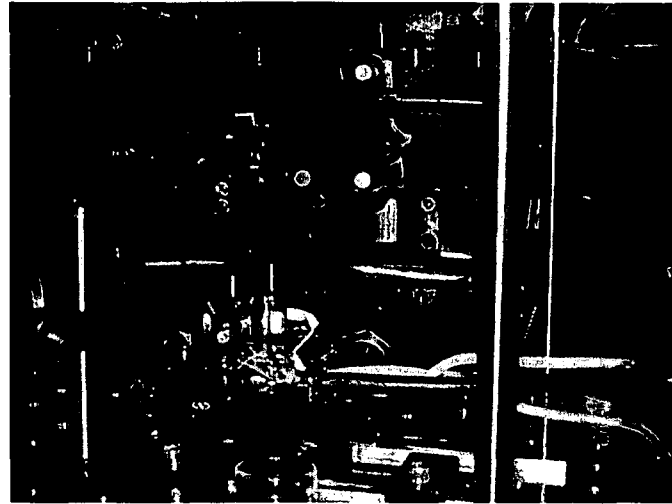


Fig. IV.6-5: VCSEL measurement system mounted in front of the engine.

The following Fig. IV.6-6 shows the photo detector unit (right side in Fig IV.6-1).

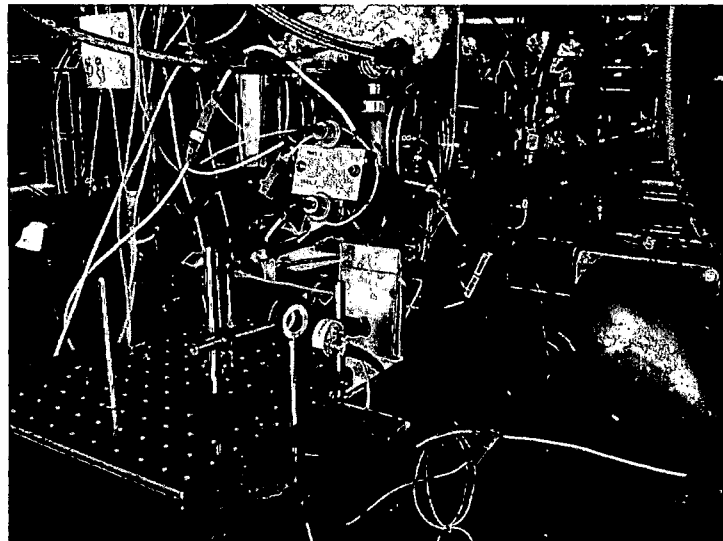


Fig. IV.6-6: Second part of the setup (photo detector behind the engine).

An iris was used in order to prevent too much emissions from the flame from reaching and saturating the detector.

A 1690 nm VCSEL for the detection of  $\text{CH}_4$  and a 2015 nm VCSEL for the detection of  $\text{CO}_2$  were used. For the 1690 nm VCSEL, a PDA 400 photo detector (Thorlabs Inc.) was used. The response of this device was from 800 to 1800 nm. For the 2015 nm VCSEL, a liquid nitrogen cooled infrared InSb photo detector (EG&G Judson, Inc.) in conjunction with a home-made transimpedance amplifier was used (response 1 -10  $\mu\text{m}$ ). Since the 1690 nm VCSEL could be seen on a detector card, handling was much easier.

More pictures of the engine are presented in the Appendix.

The VCSELs were first tuned at 10 kHz and later at 25 kHz (40  $\mu\text{s}$  time resolution). At 1000 rpm, 1 degree crank angle (CA) corresponds to 167  $\mu\text{s}$ . Therefore, a sampling rate of  $\sim 4$  measurements per CA was achieved. In the following Fig. IV.6-7 a sampling rate (laser tuning frequency) of 10 kHz (a) is compared to one of 25 kHz (b). Because of the very fast, explosion-like HCCI combustion, the 10 kHz ramping frequency is too low.

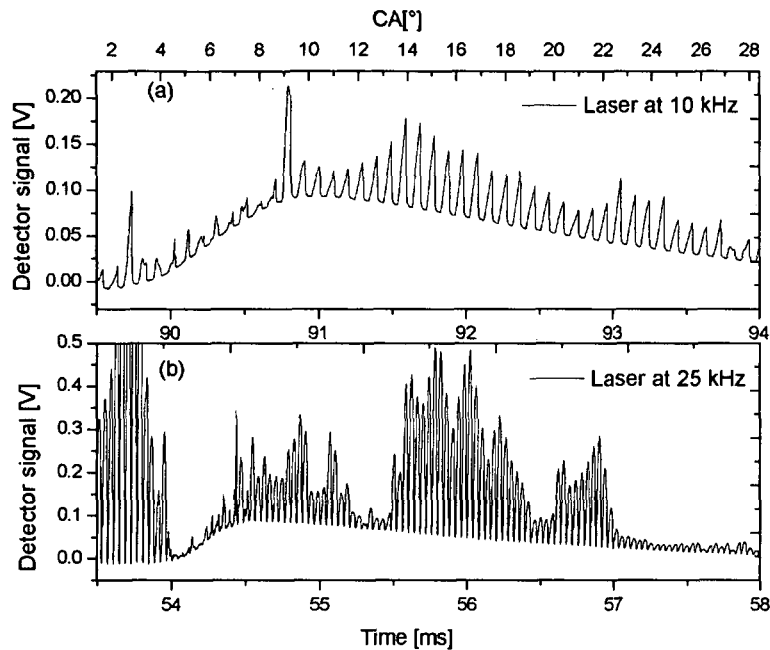


Fig. IV.6-7: Comparison of a laser scanning frequency of 10 kHz (a) and 25 kHz (b). 25 kHz is better suited to the investigation of the very fast combustion. The convex, hilly part that the individual laser ramps are sitting on is caused by the emissions from the flame (800-1800 nm wavelength range, compare raw data of the laser-ignition tests in chapter IV.2, e.g. Fig. IV.2-2).

The lasers were driven by a 0-4 and 0-10 V triangular voltage ramp. A 1 kOhm resistance was connected in series to the laser (compare high speed measurements in chapter III.4 and IV.6). This was done in order to overcome the bandwidth limitations of the available low noise laser drivers. First, a 0-5 V voltage ramp was applied to the laser. Then more aggressive tuning was performed. The wavelength tuning properties were characterized by a 5.0 mm thick sapphire etalon ( $FSR = 0.574 \text{ cm}^{-1}$ ). Data acquisition was done by a SignaTec PDA 12A high speed waveform digitizer (12 bit). A sampling rate of 0.98 MHz was used. Up to 65.5 Msamples/s were possible. However, to be able to measure for a full cycle ( $720^\circ \text{ CA}$ ), a tradeoff between high resolution and duration of the measurement had to be coped with. The detector signal was recorded on one channel. On the second channel, the trigger signal ( $-10^\circ \text{ CA}$ , measured from TDC) was recorded. This was needed in order to correctly correlate the laser signal to the pressure and temperature traces. In Fig. IV.6-8, these two traces are shown. In (a), one can see the detector signal on channel one (laser signal plus emissions from the combustion). (b) gives the trigger signal recorded on channel two. One can see two ignition events (separated by  $720^\circ \text{ CA}$  or 120 ms). The graphs on the right hand side (c) and (d) show a magnification. The trigger signal (left falling edge) is given  $10^\circ$  before TDC of the piston which is at  $0^\circ \text{ CA}$ . Also marked in Fig. IV.6-8 (c) are the two contributions to the detector signal: laser ramps (boxed) and emissions from the flame (hatched area).

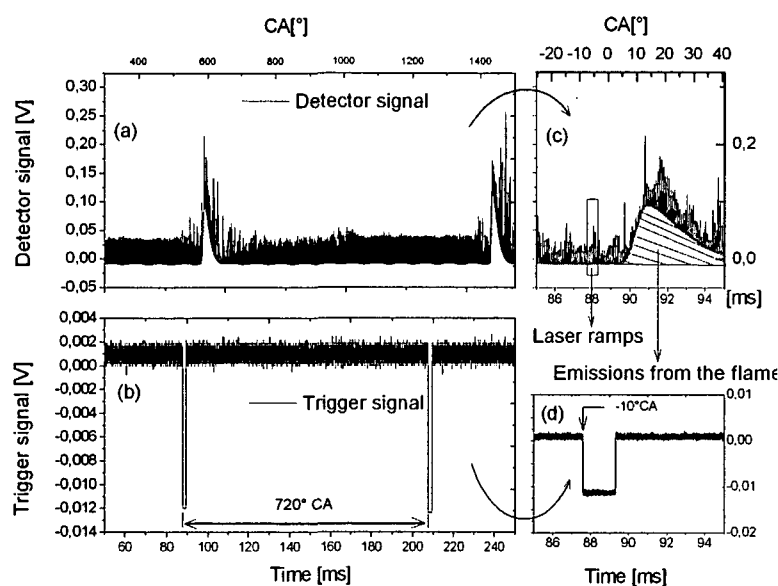


Fig. IV.6-8: Matching of the two different time scales (ms for the detector signal capturing the laser, °CA for pressure and temperature trace). The temperature and pressure traces from the engine were recorded in terms of degrees crank angle (° CA). The laser signal was recorded by a different computer in terms of time [ms]. The figure shows how the two time scales were correlated. (a) is the laser signal, (b) the trigger signal (trigger given at  $-10^{\circ}$  CA,  $720^{\circ}$  CA = 120 ms). (c) and (d) are magnifications. In (c), the box contains several laser ramps. The hatched area shows the detector signal originating from emissions from the flame.

The hatched area in Fig. IV.6-8 (c) (compare (a)) is a detector offset caused by emissions from the flame. Because of the use of an iris in front of the detector, the signal from the flame emissions is not very strong. The flame emissions show the duration of combustion in each cycle.

In Fig. IV.6-9, typical data from an engine test run in HCCI mode are shown. Depicted are the measured pressure and the calculated temperature traces for a motored (a) and fired (b) engine operated at 1000 rpm. “Motored” means that the engine was driven externally. Either no fuel was supplied or the inlet temperature was too low for auto ignition. “Fired” means that auto ignition occurred. The pressure was measured by a piezo-electric transducer (Kistler 7061B) mounted in the middle of the cylinder head. From the pressure trace, using the ideal gas law, the average temperature is estimated.

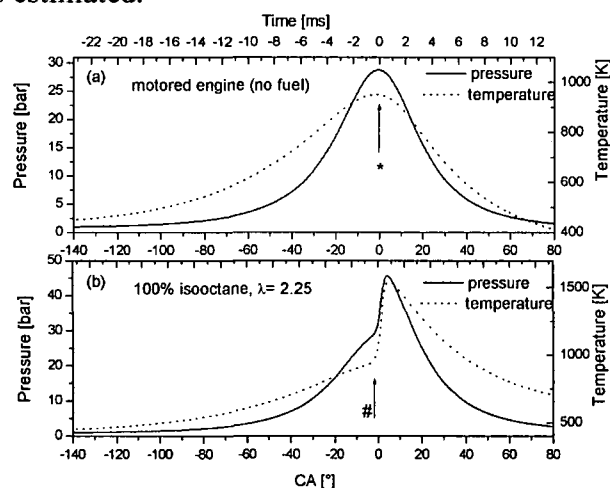


Fig. IV.6-9: Typical temperature and pressure traces during HCCI combustion. \* denotes the top position of the piston ( $0^{\circ}$  CA), # the onset of auto ignition ( $\lambda=2.25$ , isooctane as fuel). In (a), no ignition occurred (engine externally motored, no fuel supplied), In (b), auto ignition took place. (a) and (b) are both at an engine speed of 1000 rpm. The pressure was measured by a piezo-electric transducer (Kistler 7061B) mounted in the middle of the cylinder head. From the pressure trace, using the ideal gas law, the average temperature is estimated.

## Results and discussion

The tests will be described in the order that they were carried out in. First, the CH<sub>4</sub> VCSEL (1690 nm) was used in a single pass setup. It was ramped from 0-4 V (plus 1 kOhm resistance) at 10 kHz. The results were not satisfying, so the voltage ramp was raised to 0-10 V (plus 1 kOhm resistance) still at 10 kHz. After that, the laser was ramped from 0-10 V (plus 1 kOhm resistance) at an increased tuning frequency of 25 kHz. Finally, the laser was sent through the engine twice with the same settings (ramp 0-10 V (plus 1 kOhm resistance), 25 kHz) for increased sensitivity.

Then tests were done with the CO<sub>2</sub> VCSEL (2015 nm). The laser was deployed in a single pass setup and ramped from 0-5 V (plus 1 kOhm resistance) at 25 kHz. After the first series, both available CO<sub>2</sub> VCSELs were destroyed.

Laser aided HCCI was also investigated using the CH<sub>4</sub> VCSEL (optimum settings of 0-10 V ramp and 25 kHz tuning frequency).

### A) CH<sub>4</sub> VCSEL for HCCI diagnostics

The following Fig. IV.6-10 depicts calculated absorption spectra for the CH<sub>4</sub> VCSEL. The range shown fully covers the wavelength tuning range of the laser.

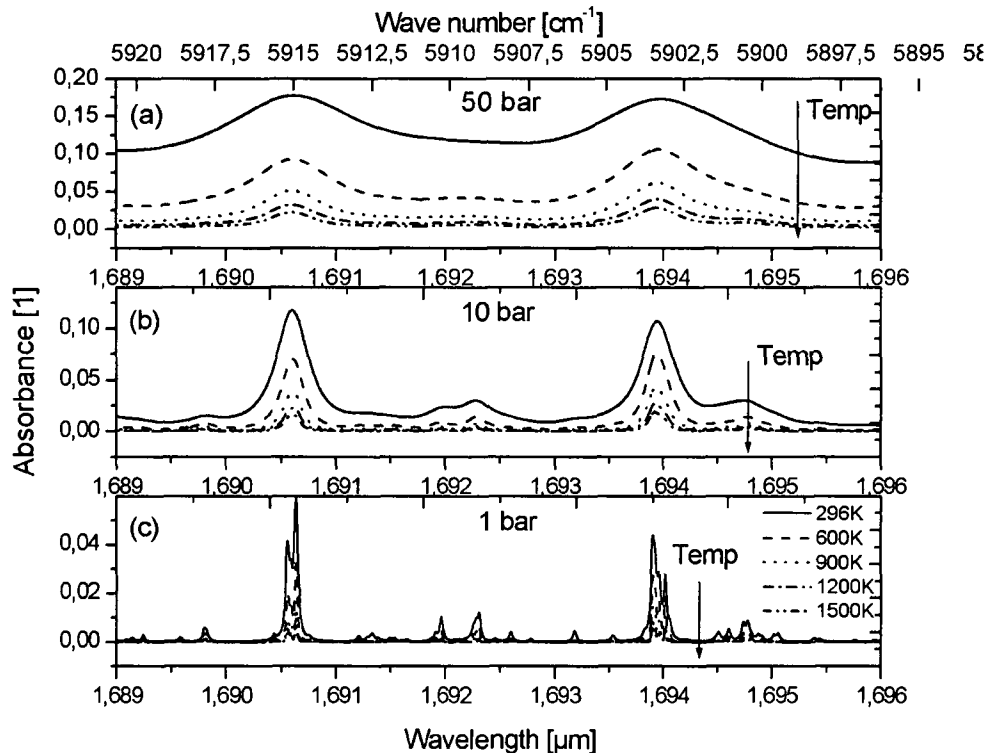


Fig. IV.6-10: Calculated spectra of CH<sub>4</sub> for varying temperatures and pressures (for conditions encountered in the HCCI engine: path length 12 cm, 10 % CH<sub>4</sub>). (a) is for 50 bar, (b) for 10 bar and (c) for 1 bar pressure.

One can see two distinct peaks that are composed of several individual lines (overlapping at elevated pressures). The height of the peaks recedes with increasing temperature. The tuning range of the VCSEL is as high as 5.9 nm ( $20.66 \text{ cm}^{-1}$ ) at 10 kHz tuning frequency (0-10V, 27°C). Therefore, the laser should be capable of measuring CH<sub>4</sub> at pressures > 10 bar. The spectra were calculated for the conditions likely to be encountered inside the engine: path length 12 cm,  $\lambda = 1$  (10% CH<sub>4</sub>).

The following two Fig. IV.6-11 and Fig. IV.6-12 demonstrate the tuning properties of the VCSEL. It was ramped aggressively by a 0-10V asymmetric triangular voltage function (plus

1 kOhm resistance). Fig. IV.6-11 shows the etalon trace of the VCSEL at 25 kHz. The FSR of the etalon (5.0 mm thick sapphire) is  $0.574 \text{ cm}^{-1}$  (0.286 nm).

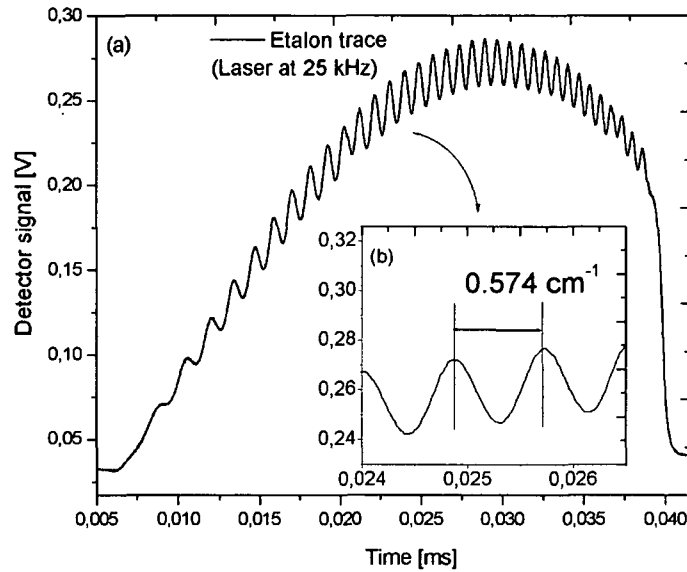


Fig. IV.6-11: Aggressive current tuning of the VCSEL at 25 kHz. The insert (b) is a magnification to show the FSR ( $0.574 \text{ cm}^{-1} = 0.286 \text{ nm}$ ).

The tuning range is as large as 6.07 nm ( $21.27 \text{ cm}^{-1}$ ) at 100 Hz and still 2.62 nm ( $9.18 \text{ cm}^{-1}$ ) at 340 kHz (see Fig. IV.6-12). (a) shows a linear, (b) a logarithmic x-axis (tuning frequency).

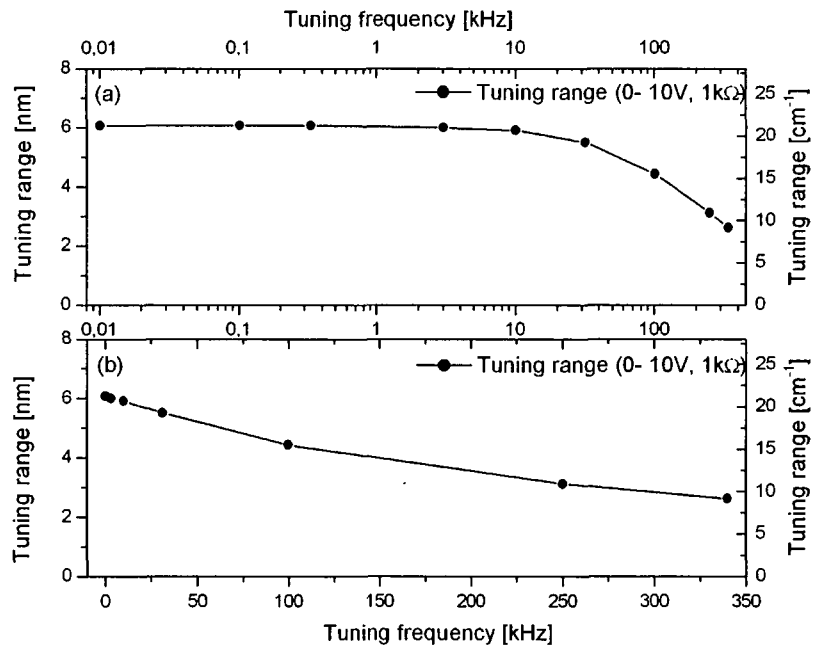


Fig. IV.6-12: Aggressive current tuning of the VCSEL. The continuous current tuning range obtained by aggressive tuning (0-10V in conjunction with a 1000 Ohm resistance) is as large as 6.07 nm ( $21.27 \text{ cm}^{-1}$ ) at low tuning speeds. (a) shows a linear, (b) a logarithmic x-axis (tuning frequency).

### Tuning of the laser at 10 kHz and 0-4 V (VCSEL in series with a 1 kOhms resistance)

The following five figures show reference measurements of CH<sub>4</sub>. The engine was motored at 1000 rpm, the lambda was set at 1.0 (i.e. approximately 10% CH<sub>4</sub>). No ignition took place (inlet temperature intentionally too low). The aim was to get as much CH<sub>4</sub> into the engine as possible in order to obtain strong absorption signals. Fig. IV.6-13 shows the transmission of the laser through the engine (a). The lower graph (b) depicts the pressure trace and the calculated temperature trace.

The laser was ramped at 0-4V at 10 kHz (1 kOhms resistance connected in series to the laser).

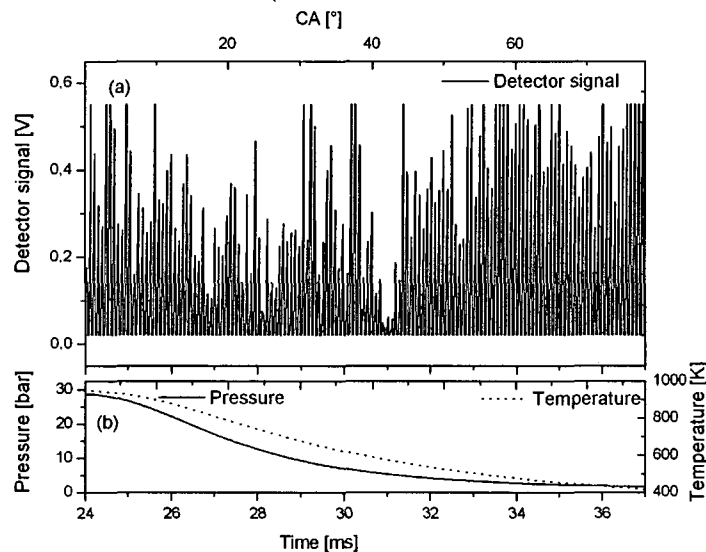


Fig. IV.6-13: Reference measurements in the motored engine (engine running at 1000 rpm, 10% CH<sub>4</sub>, not firing because the inlet temperature was intentionally too low for auto ignition).

The printing resolution of Fig. IV.6-13 (a) is again too low to display the individual ramps (compare the previous chapters). This one and all upcoming figures show the time scale at the bottom [ms] and additionally the crank angle reading at the top [° CA]. The pressure in the piston goes from ambient to approximately 29 bars at TDC. The temperature goes from 450 to 950 K.

The next Fig. IV.6-14 depicts an individual ramp recorded close to TDC position of the piston (pressure and temperature are given below: 21.2 bar, 865K). The baseline has also been plotted (dashed line).

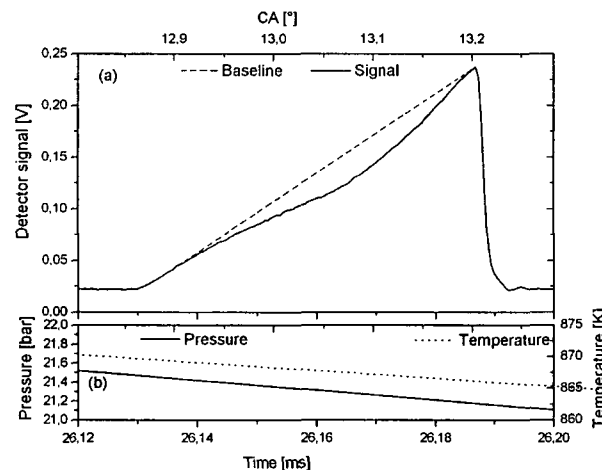


Fig. IV.6-14: Absorption peak of CH<sub>4</sub> at 21.4 bar (engine running at 1000 rpm, 10% CH<sub>4</sub>, not firing because the inlet temperature was intentionally too low for auto ignition). In (b), pressure and temperature trace are given. Compare Fig. IV.6-15 (2 bar).

One can see that the absorption peak is so broad that it almost spans over the entire tuning range of the VCSEL. The next Fig. IV.6-15 shows the CH<sub>4</sub> peak at 2 bar and 445 K. One can see that it is much narrower now. The CH<sub>4</sub> peak is actually composed of two peaks that have convoluted to a double peak. Compare the calculated absorbance spectra in Fig. IV.6-10.

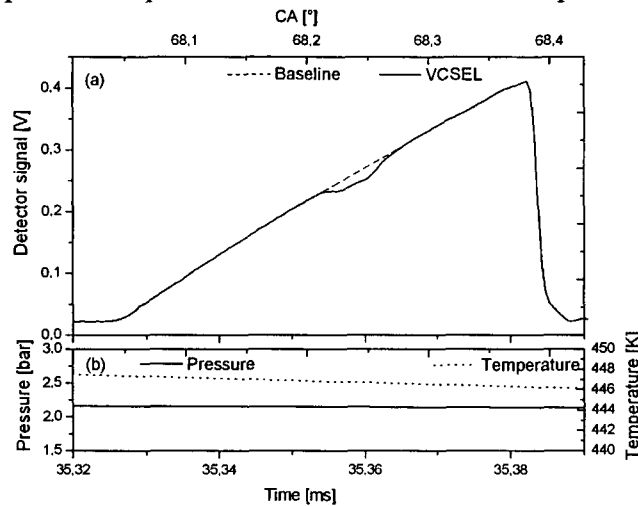


Fig. IV.6-15: Peak of CH<sub>4</sub> at 2 bar (engine running at 1000 rpm, 10% CH<sub>4</sub>, not firing because the inlet temperature was intentionally too low for auto ignition). Compare Fig. IV.6-14 (21.4 bar).

Fig. IV.6-16 shows the baseline (engine running at 1000 rpm on air).

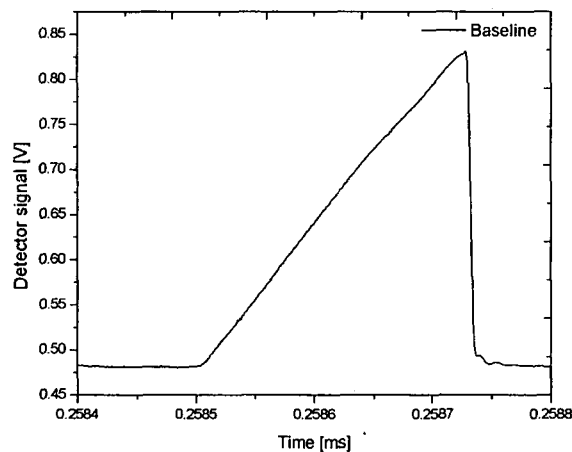


Fig. IV.6-16: Reference measurements (baseline) in the motored engine (no fuel, engine externally driven at 1000 rpm).

One can see that the slope is perfectly linear for the low modulation (0-4V, 1000 kOhms resistance in series with the laser).

However, also several disturbances were encountered. The upcoming Fig. IV.6-17 is also a magnification from Fig. IV.6-13 (engine motored at 1000 rpm, 10% CH<sub>4</sub>, not firing). One can see 22 laser ramps recorded upon expansion of the piston (24-36 ° CA, pressure decreasing from 12 to 8 bar). Several of the ramps exhibit strong distortions that resemble absorption peaks.

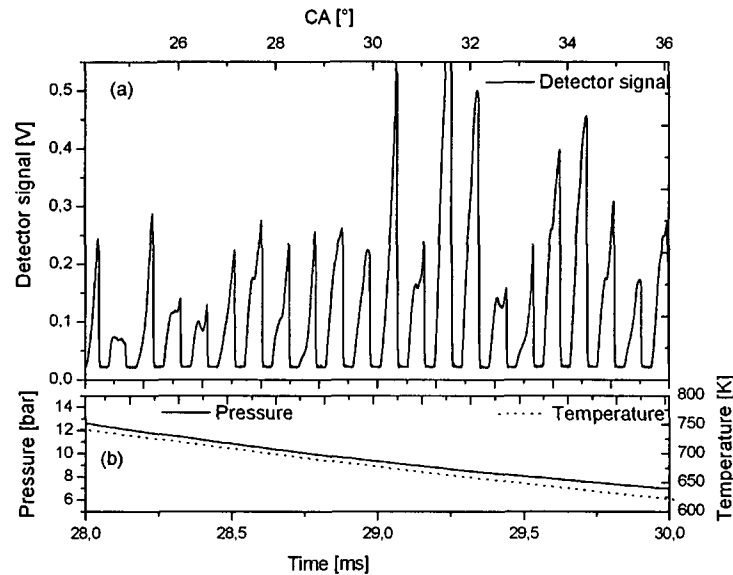


Fig. IV.6-17: Interference signals of unknown origin on the laser ramps (magnified from Fig. IV.6-13).

These disturbances only affect individual ramps at random occurrence. They were also encountered when recording the laser transmission through the unfired engine with no  $\text{CH}_4$  present at all (i.e. only air) and in the test runs (successful auto ignitions) with  $\text{CH}_4$  and isoctane fuel.

It might be that these peaks/disturbances are related to polarization issues of the laser device. It is not expected that resonant absorption by species other than  $\text{CH}_4$  leads to this signal shape. It is also possible that the laser encounters optical feedback or is disturbed by the engine (leak current, etc). As it can be seen in several upcoming figures, these disturbances occur randomly at all crank angles but more often upon the onset of auto ignition.

Therefore, very fast deflections of the probing laser beam caused by refractive index gradients (developing flame kernels) might also be the reason for the distortions. Further investigation is needed here.

The following eight figures show engine tests at  $\lambda = 1.85$  ( $\text{CH}_4/\text{isoctane} = 95/5$ ). 13000 ppm  $\text{CH}_4$  were measured in the exhaust gas. In Fig. IV.6-18 one can see three consecutive auto ignition events. The trigger signal is displayed at the bottom (timing also  $-10^\circ \text{CA}$ ).

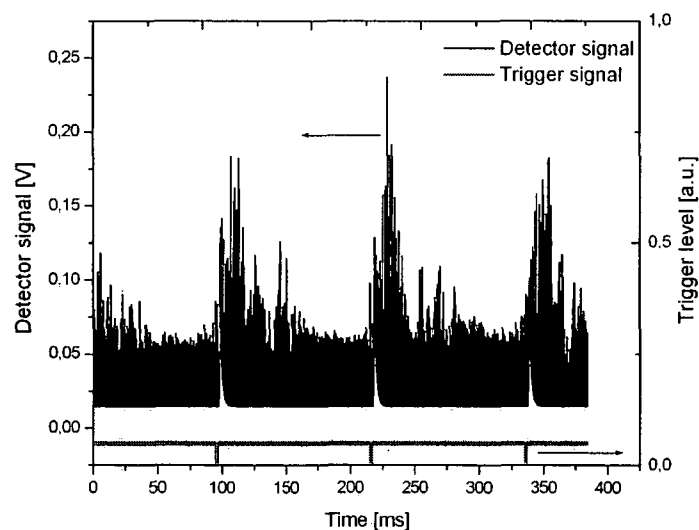


Fig. IV.6-18: HCCI combustion at  $\lambda = 1.85$  ( $\text{CH}_4/\text{isoctane} = 95/5$ ). One can see three full cycles.



In Fig. IV.6-19 one of these cycles is displayed in more detail. In (a), one can see the laser signal on top of the emissions from the flame. In (b), the pressure and temperature traces are given. The peak pressure is approximately 40 bar, the peak temperature 1600 K.

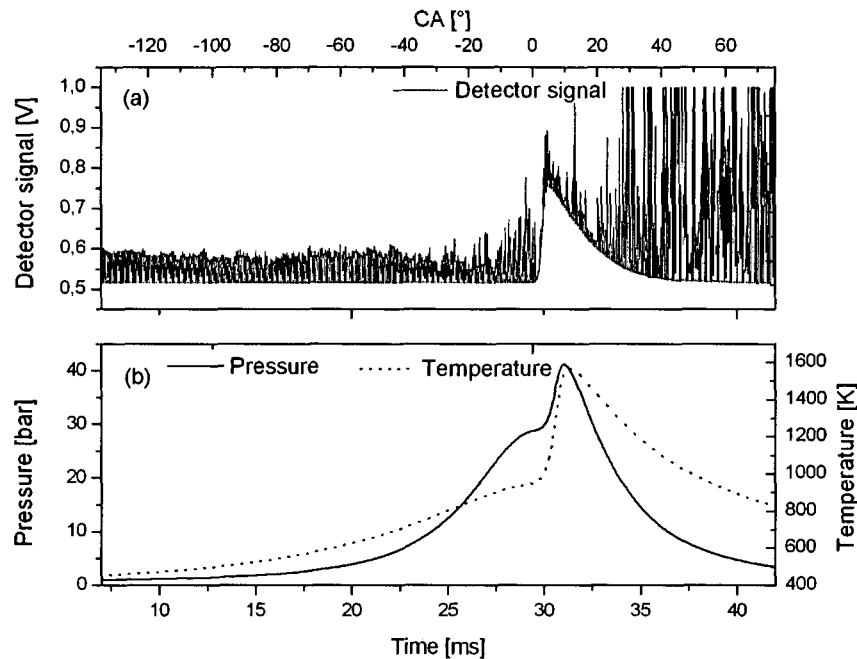


Fig. IV.6-19: Laser signal and emissions from the flame [800-1800 nm] (a), pressure and temperature trace (b). See also Fig. IV.6-52.

The response of the photo detector was 800 to 1800 nm. One can see that the emissions from the flame in this spectral region show a progression similar to the temperature trace. A more detailed discussion is given later (Fig. IV.6-52 and Fig. IV.6-53).

The next six Fig. IV.6-20 to IV.6-25 show consecutive intervals (each 2 ms or approximately 12 ° CA) of this ignition event. They are all a magnification of Fig. IV.6-19 above (-11 to +1 °CA, 1°CA to 13°C, 13°CA to 25°C and so on). Fig IV.6-20 starts with an interval recorded shortly before the onset of auto ignition. One can see a gradual rise in temperature and pressure due to the compression of the gas inside the cylinder (b).

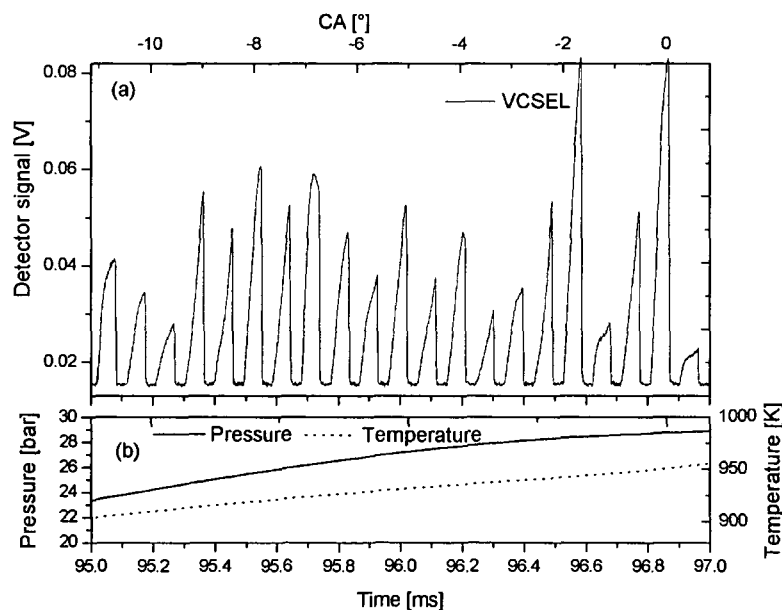


Fig. IV.6-20: 1<sup>st</sup> interval (duration 2 ms or 12°C) of the ignition test run depicted in Fig. IV.6-19: Shortly before auto ignition.

At a lambda of 1.85 the content of CH<sub>4</sub> inside the cylinder is approximately 5% (the ratio of CH<sub>4</sub>/isooctane being 95/5 since pure CH<sub>4</sub> as fuel was not possible). Judging from the calibration runs shown in Fig. IV.6-14 and Fig. IV.6-15, one should be able to determine CH<sub>4</sub> before auto ignition. However, no peaks could be seen on the laser ramps in Fig. IV.6-20 or in comparable test runs.

Fig. IV.6-21 below shows the start of combustion in the HCCI engine.

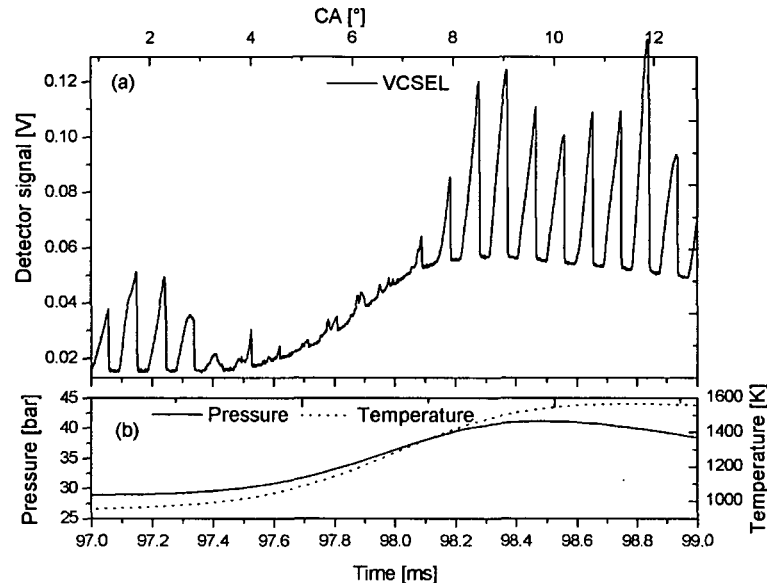


Fig. IV.6-21: 2<sup>nd</sup> interval (duration 2 ms or 12°CA) of the ignition test run depicted in Fig. IV.6-19: Onset of auto ignition.

A steep rise in temperature and pressure occur on a short time scale (b). The laser ramps (a) show strong distortions when the ignition takes place. As suggested above, these disturbances on the laser signal are not likely to stem from resonant absorption. None of the species except for CH<sub>4</sub> present in sufficient concentration (H<sub>2</sub>O, CO, CO<sub>2</sub>, OH) shows strong absorption lines at the wavelength of the VCSEL (1690 nm). Very fast deflections due to refractive index gradients introduced by developing flame kernels seem to be the most plausible explanation (Note, however, that the disturbances were also encountered in the unfired engine (see Fig. IV.6-17)).

Below Fig. IV.6-22 shows the next 2 ms interval of the test run.

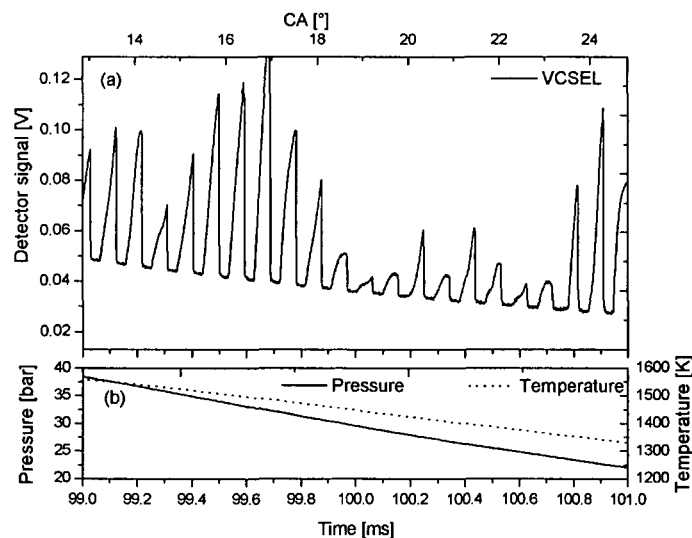


Fig. IV.6-22: 3<sup>rd</sup> interval (duration 2 ms or 12°CA) of the ignition test run depicted in Fig. IV.6-19: Expansion of the piston after auto ignition.

Combustion is already over. The temperature and pressure drop are accompanied by less expressed disturbances of the VCSEL ramps  
Below in Fig. IV.6-23, the next consecutive interval is shown.

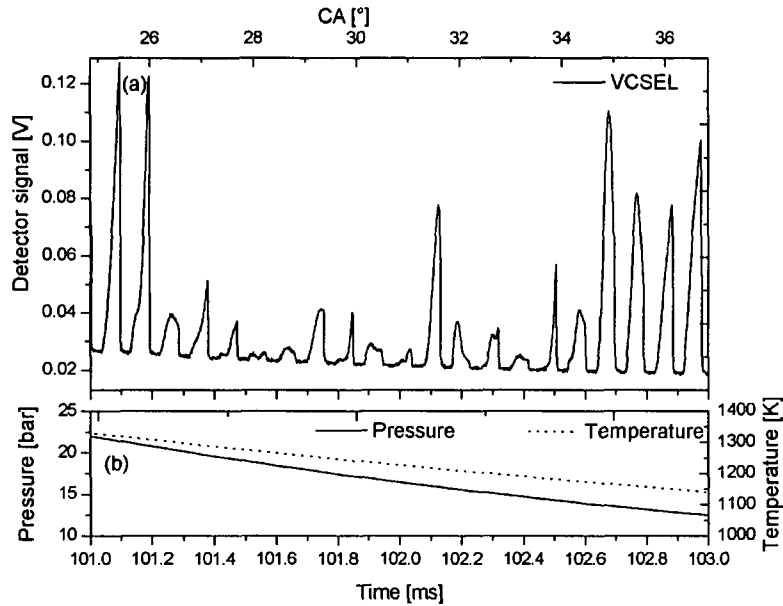


Fig. IV.6-23: 4<sup>th</sup> interval (duration 2 ms or 12°CA) of the ignition test run depicted in Fig. IV.6-19: Further expansion of the piston.

Fig. IV.6-24 and Fig. IV.6-25 are the last figures in this series. Although they show the laser signal at a rather late time in the cycle, again several laser ramps show distortions (marked below in Fig. IV.6-24 by two circles).

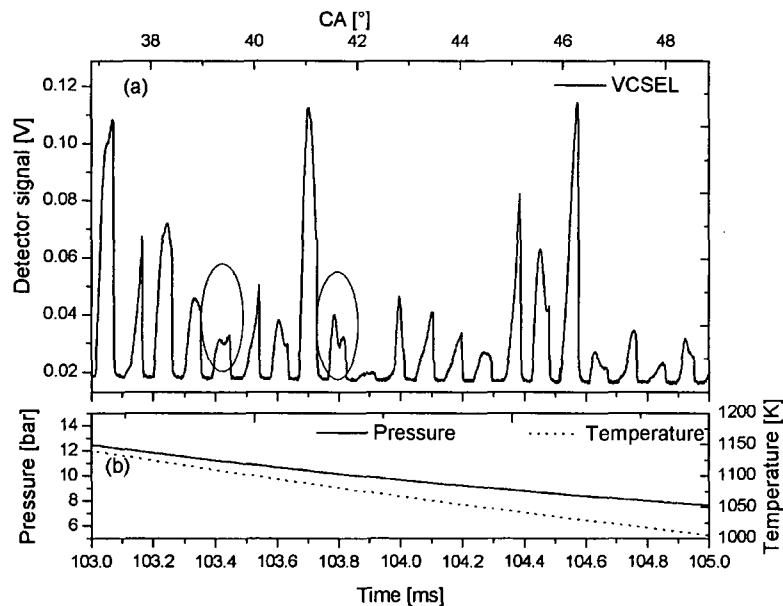


Fig. IV.6-24: 5<sup>th</sup> interval (duration 2 ms or 12°CA) of the ignition test run depicted in Fig. IV.6-19: Continued expansion and gas cooling. The two circles show ramps with strong distortions).

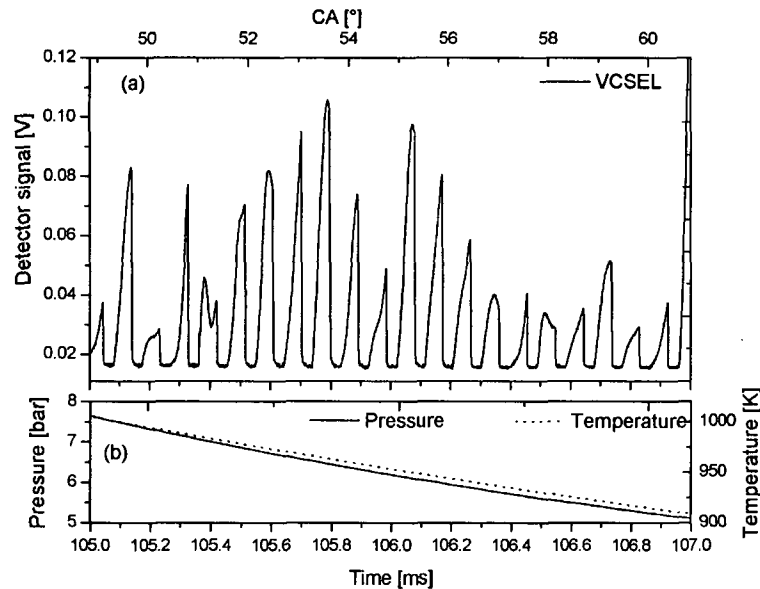


Fig. IV.6-25: 6<sup>th</sup> interval (duration 2 ms or 12°CA) of the ignition test run depicted in Fig. IV.6-19: The expansion is almost finished.

The preceding figures showed a single ignition test run. Experiments were made with various lambdas and fuel compositions ( $\text{CH}_4/\text{isooctane} = 97/3$  up to 0/100). A lambda of 1.85 was the lowest air/fuel ratio that could be used with the Volvo engine. The engine was capable of running on lambda >2 (lean operation is intended with HCCI!), however, since there was trouble with the sensitivity of the laser in lean mixtures, the lowest lambda possible (i.e. 1.85) was used.

For the next series, the laser was ramped more aggressively. A 0-10 V (instead of 0- 4 V) voltage ramp was applied to the laser still connected in series with a 1 kOhms resistance. The tuning frequency was 10.8 kHz.

#### Tuning of the laser at 10 kHz and 0-10 V (VCSEL in series with a 1 kOhms resistance)

The first figures show calibration (reference) test runs (lambda 1, engine motored at 1000 rpm but not fired). A full cycle starting at 0 °CA (TDC) is shown in Fig. IV.6-26.

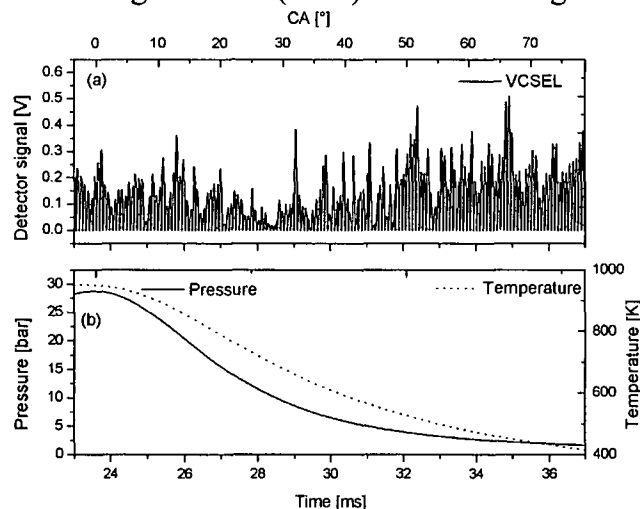


Fig. IV.6-26: Reference test runs in the motored engine (engine running at 1000 rpm, 10%  $\text{CH}_4$ , not firing because the inlet temperature was intentionally too low for auto ignition).

Fig. IV.6-27 and Fig. IV.6-27 show individual ramps at high and low pressure, respectively.

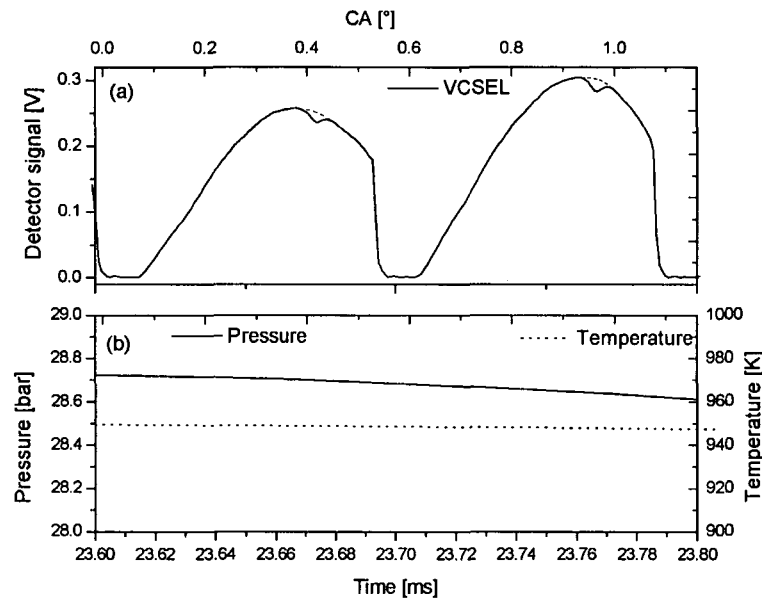


Fig. IV.6-27: Reference test runs in the motored engine (engine running at 1000 rpm, 10% CH<sub>4</sub>, not firing because the inlet temperature was intentionally too low for auto ignition); Two laser ramps close to TDC.

One can see that the laser, due to the more aggressive ramping, exhibits a roll over. The peak is now centered at the highest point of the ramp so that the absorption signal is strongest (laser heat sink temperature still 27°C). The ratio  $I_0/I$  is naturally the same no matter where on the ramp the peak is situated. At a higher position, however, noise is lower. This strategy was chosen because no CH<sub>4</sub> could be seen in the preceding engine test runs.

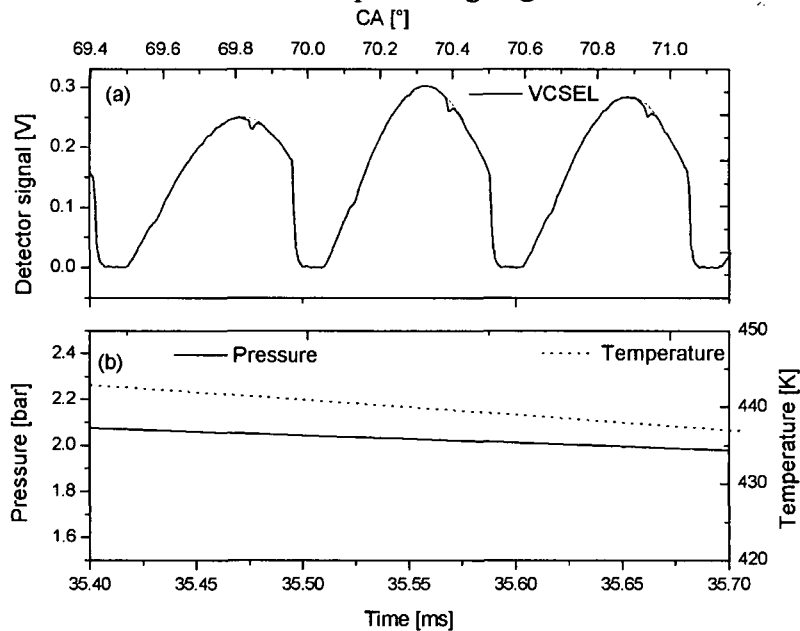


Fig. IV.6-28: Reference test runs in the motored engine (engine running at 1000 rpm, 10% CH<sub>4</sub>, not firing because the inlet temperature was intentionally too low for auto ignition); Three laser ramps at the end of the expansion phase (low pressure).

The next figures show data from an engine test run. The conditions are the same as before ( $\lambda$  1.85, CH<sub>4</sub>/isooctane = 95/5). 12000 ppm CH<sub>4</sub> were measured in the exhaust gas.

Fig. IV.6-29 gives an overview of a complete auto ignition event with laser signal and emissions from the flame (800-1800 nm) in (a) and pressure plus temperature trace in (b).

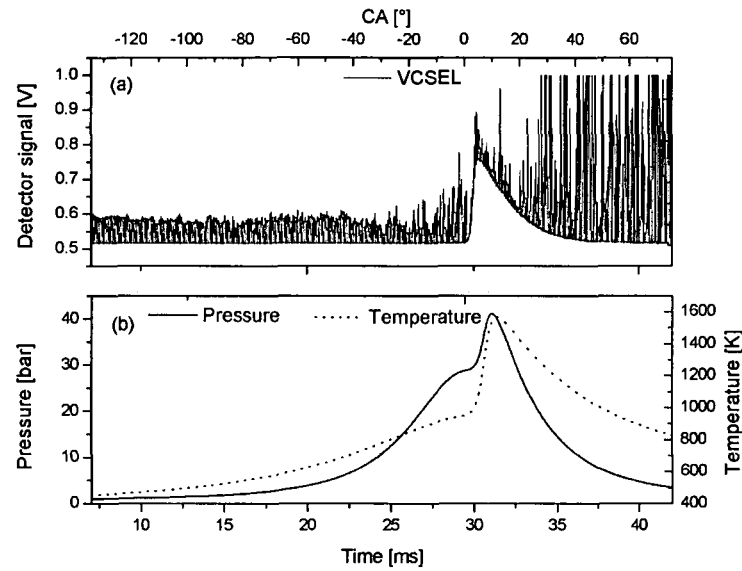


Fig. IV.6-29: HCCI combustion of a  $\text{CH}_4/\text{isooctane}$  mixture (95/5),  $\lambda = 1.85$ . (a) shows the transmitted laser signal on top of the emissions from the flame [800-1800 nm], (b) gives the pressure and temperature traces.

The following Fig. IV.6-30 shows two laser ramps recorded shortly before auto ignition. No  $\text{CH}_4$  could be detected.

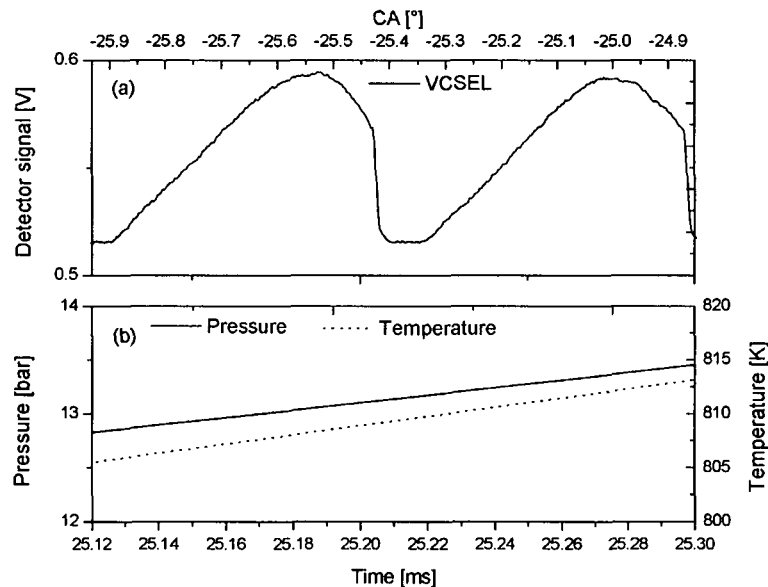


Fig. IV.6-30: Detail of Fig. IV.6-29, shortly before auto ignition. Two laser ramps are shown. No  $\text{CH}_4$  peak can be spotted.

The following Fig. IV.6-31 shows the onset of combustion accompanied by a step rise in pressure and temperature.

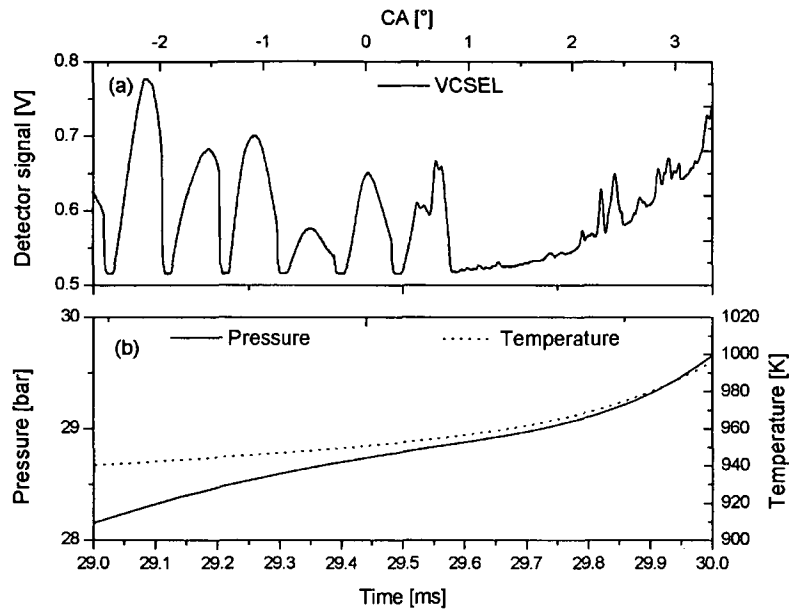


Fig. IV.6-31: Onset of ignition (detail of Fig. IV.6-29). Note the strong distortions on the laser ramps (a). Temperature and pressure rise steeply (b).

Again one can see these strong distortions on the laser ramp signals. The next Fig. IV.6-32 presents the data trace during the entire combustion (5 °CA rising emissions of the flame, then approximately 7 °CA of the receding luminosity).

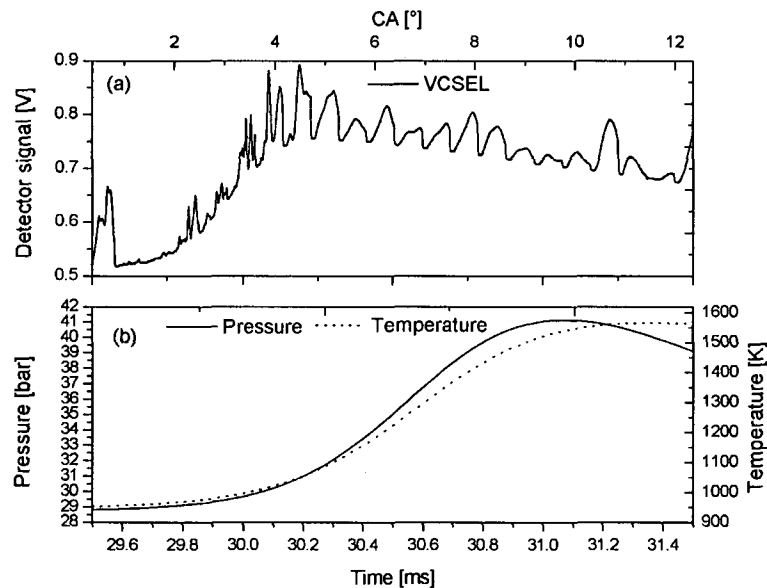


Fig. IV.6-32: Complete depiction of the auto ignition event (detail of Fig. IV.6-29). Combustion lasts approximately 5 °CA (0.8 ms).

The start of auto ignition already displayed in Fig. IV.6-31 and Fig. IV.6-32 is replotted below in Fig. IV.6-33.

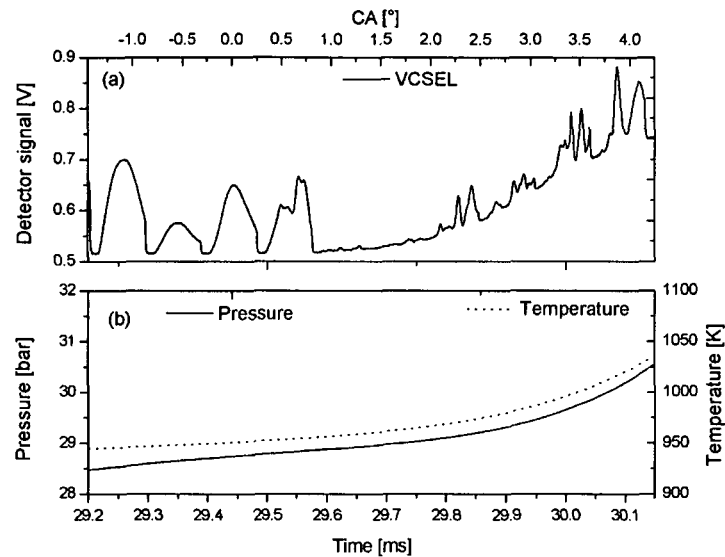


Fig. IV.6-33: Closer look at the start of ignition.

One can see extremely strong signal distortions. The individual ramps have been placed in boxes in Fig. IV.6-34 below (same data as in Fig IV.6-34).

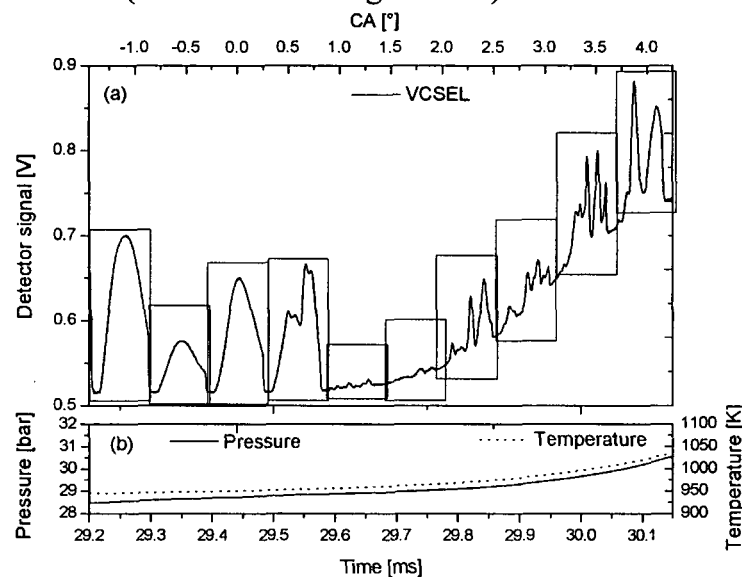


Fig. IV.6-34: The individual laser ramps are surrounded by boxes (same data as in Fig IV.6-33) to show the original laser ramps and their distortions.

There seems to be no correlation between the shapes of the distortions on the different ramps. Strong beam steering might actually be the reason.

This question could be resolved by ramping the laser faster than it was done here (10 kHz). By scanning the laser wavelength faster than the time scale of all noise sources, (compare the previous chapters) one could alleviate beam steering (provided this is the reason for the encountered effect).

In order to sustain a sufficiently large tuning range, the VCSELs were not ramped faster than 25 kHz within these studies.

IV.6-35 and IV.6-36 finally show two sections of Fig. IV.6-29 as the gas further expands and cools down.



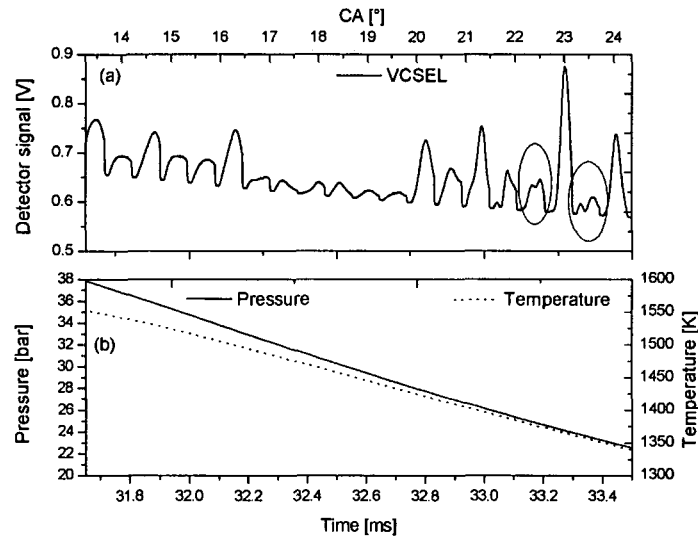


Fig. IV.6-35: Expansion of the gas volume after combustion (detail of Fig. IV.6-29).

In Fig. IV.6-35, too, one can see distortions on several ramps (marked by the two rings).

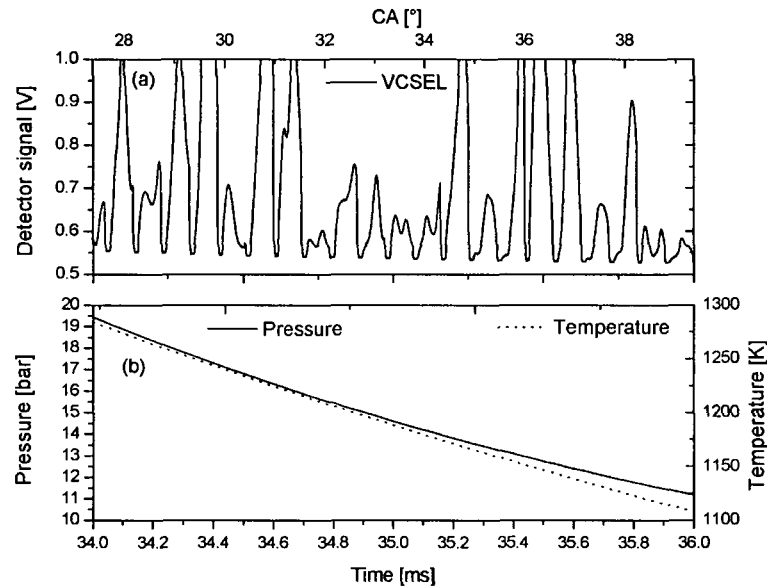


Fig. IV.6-36: Further expansion of the gas volume after combustion (detail of Fig. IV.6-29).

In Fig. IV.6-36, too, the distortions on some ramps are present.

#### Tuning of the laser at 25 kHz and 0-10 V (VCSEL in series with a 1 kOhms resistance) in double pass alignment for increased sensitivity

The laser ramping was raised from 0-4 V to 0-10 V in order to allow further wavelength tuning and to place the absorption peak on top of the ramp (increased signal/noise ratio, preceding subchapter). However, no CH<sub>4</sub> could be detected either. Running fatter (i.e. closer to  $\lambda = 1$ ) was not viable. Therefore, the setup was modified from single pass (12 cm path length inside the engine) to double pass (24 cm path length). Fig. IV.6-37 to Fig. IV.6-41 present results from calibration (reference) test runs (unfired engine flushed with 10% CH<sub>4</sub> again).

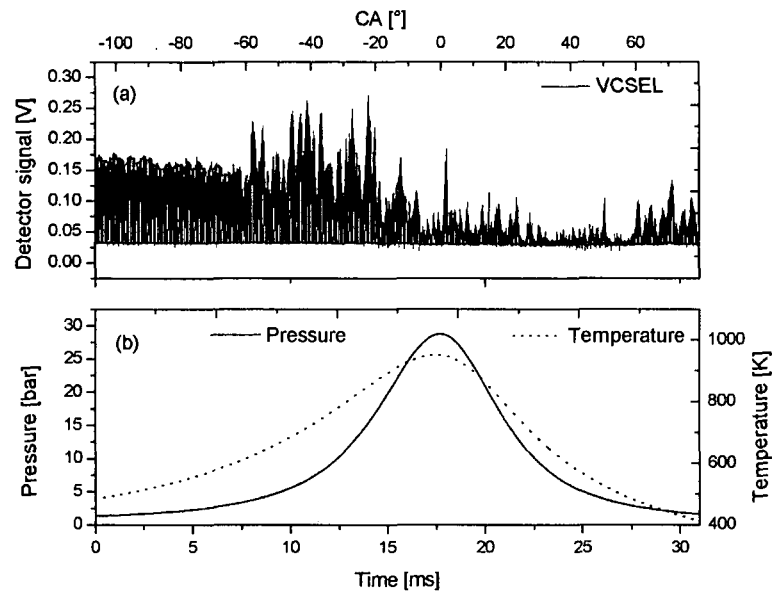


Fig. IV.6-37: Calibration (reference) test run in double pass alignment for increased sensitivity. (a) shows the laser signal, (b) gives pressure and temperature trace (path length 0.24 m, 10% CH<sub>4</sub>).

In Fig. IV.6-38, a magnification of the right most part of the preceding Fig. IV.6-37 is shown (low pressure side).

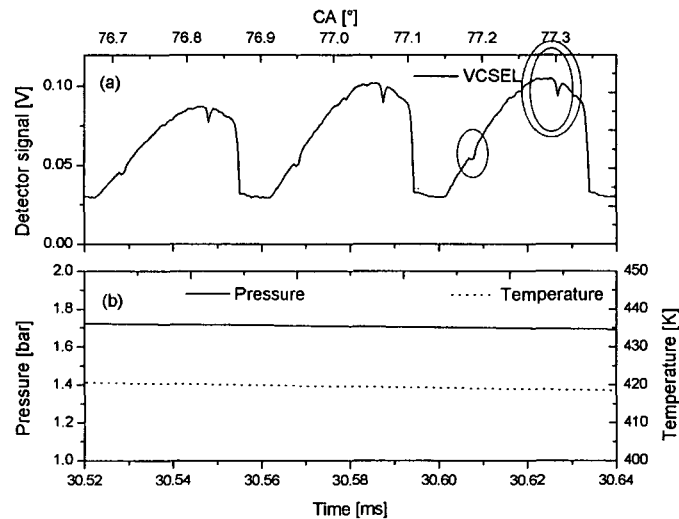


Fig. IV.6-38: Reference signal (three ramps) in the motored, unfired engine (10% CH<sub>4</sub>, two passes of the laser beam). At low pressures (here 1.7 bar), one can see a second peak (one circle). The main peak is highlighted by two circles. No auto ignition occurred because the inlet temperature was intentionally too low. Compare the strong absorption peaks on top of the ramps to those in Fig. IV.6-15 and Fig. IV.6-18 (single pass setup).

One can see three laser ramps. The CH<sub>4</sub> absorption peak can be seen more clearly than in the single pass setup (engine also motored in an unfired way,  $\lambda = 1$ ). Also, a second absorption peak can be seen on each ramp (the strong peak is circled by two rings, the second, smaller one by one ring).

Fig. IV.6-39 shows a section at higher pressures (28.5 bar). The smaller peak can hardly be seen any more due to pressure broadening.

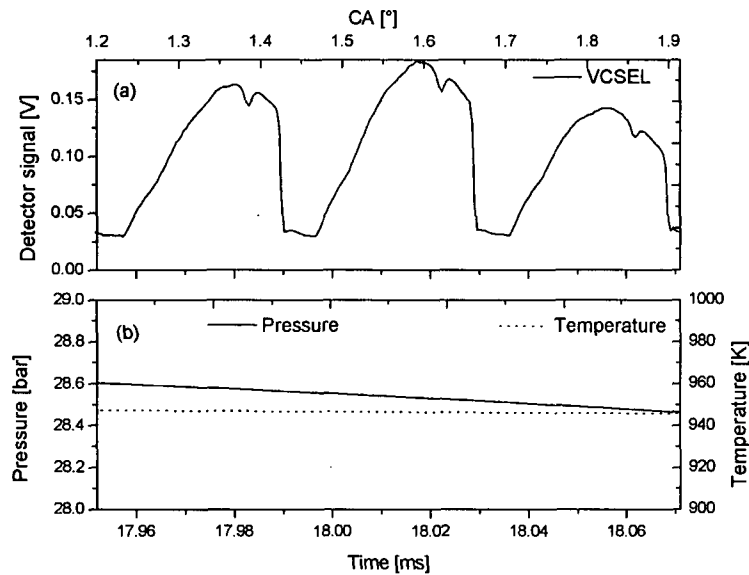


Fig. IV.6-39: Reference signal (three ramps) in the motored, unfired engine (10 % CH<sub>4</sub>, two passes of the laser beam) at high pressures (here 28.5 bar). The inlet temperature was intentionally too low for auto ignition. Compare the strong absorption peaks on top of the ramps to those in Fig. IV.6-14 and Fig. IV.6-27 (single pass setup).

Fig. IV.6-40 shows five successive laser ramps displaying the CH<sub>4</sub> absorption peak on top at intermediate pressures (15.5 bar).

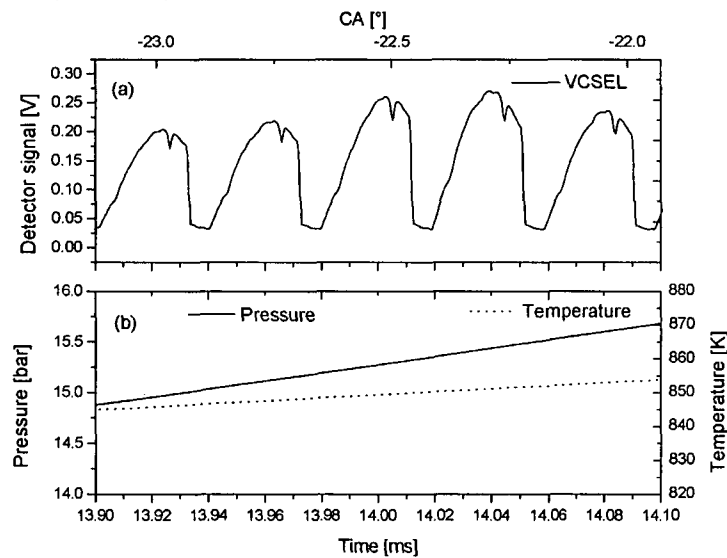


Fig. IV.6-40: Reference signal (five ramps) in the motored, unfired engine (10 % CH<sub>4</sub>, two passes of the laser beam) at intermediate pressures (here 15.5 bar). The inlet temperature was intentionally too low for auto ignition.

A slight frequency jitter could be observed. In chapter IV.6, the frequency jitter of the laser emission between different scans of a comparable VCSEL was up to  $1 \cdot 10^{-2} - 3 \cdot 10^{-2} \text{ cm}^{-1}$  ( $3 \cdot 10^{-3} - 9 \cdot 10^{-3} \text{ nm}$ ). It is most likely caused by the noise of the laser driver (i.e. the function generator used here). The following Fig. IV.6-41 shows the absorbance of the CH<sub>4</sub> peak on two neighboring laser ramps (strong jitter displayed, not always as large as here).

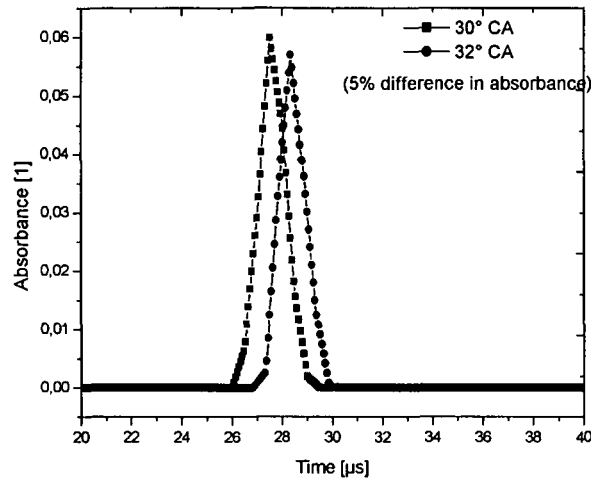


Fig. IV.6-41: Frequency jitter of the VCSEL (absorbance of two consecutive ramps).

The following four Fig. IV.6-42 to Fig. IV.6-45 show engine tests using the CH<sub>4</sub> VCSEL in double pass alignment.

14000 ppm CH<sub>4</sub> were measured in the exhaust gas.

Fig. IV.6-42 presents the overall ignition and combustion (laser signal and emissions in the 800 – 1800 nm wavelength range in (a), pressure and temperature trace in (b)). Lambda was 1.85 (CH<sub>4</sub>/isooctane = 95/5).

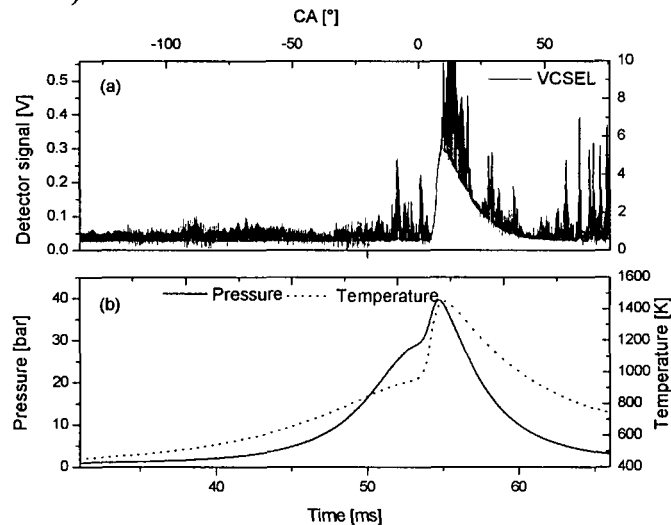


Fig. IV.6-42: Test run at lambda = 1.85 (CH<sub>4</sub>/isooctane = 95/5). (a) depicts the transmitted laser light and the emissions from the flame, (b) pressure and temperature trace.

The following Fig. IV.6-43 depicts three laser ramps recorded shortly before auto ignition. One can see slight absorption peaks resulting from CH<sub>4</sub> absorption. The absorbance is approximately 0.03. Data averaging is not possible.

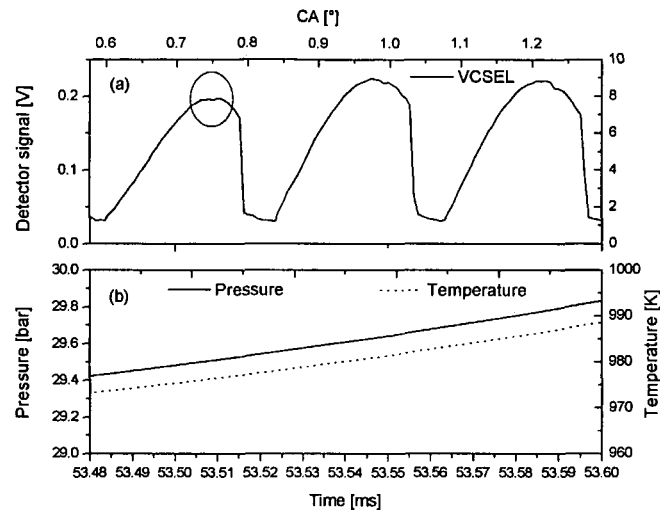


Fig. IV.6-43: Depiction of three laser ramps (detail of the preceding Fig. IV.6-42). Thanks to the more sensitive double pass setup, a slight dip (circle on the first ramp) resulting from resonant  $\text{CH}_4$  absorption can be seen (29.5 bar, shortly before auto ignition).

Unfortunately, the absorbance is very weak right from the start, and the signal is rather noisy. Therefore, even in the two pass setup, no concentration history of  $\text{CH}_4$  (i.e. the decrease upon combustion) could be obtained.

The formation of  $\text{CH}_4$  from the isooctane (combustion intermediate) could not be observed either.

Fig. IV.6-43 shows auto ignition and combustion.

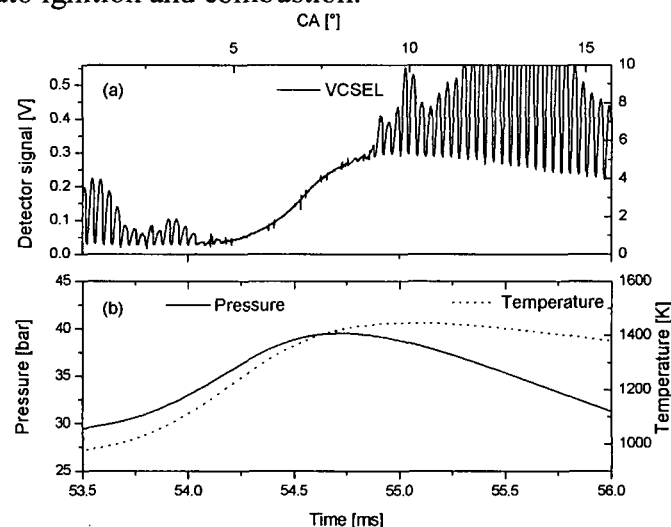


Fig. IV.6-44: Auto ignition of the  $\text{CH}_4$  and isooctane/air mixture. The two pass setup is much more sensitive to misalignment and beam steering (almost no transmission upon combustion, approx. 4-9 °CA).

The transmitted laser signal falls off to almost zero upon combustion. Heavy beam steering and the long path length proved disadvantageous on the stability of the laser signal. Also, the laser beam became misaligned very fast. After several minutes of engine operation, the experiments had to be stopped to realign the laser beam.

For this reason, no triple or higher pass setups were experimented with. Instead, after this test series, the single pass setup which was much more robust against vibrations from the engine was reinstalled.

Fig. IV.6-44 presents four laser ramps recorded shortly after ignition. The peaks on two of the ramps are most likely to stem from noise (compare similar spikes between the ramps).

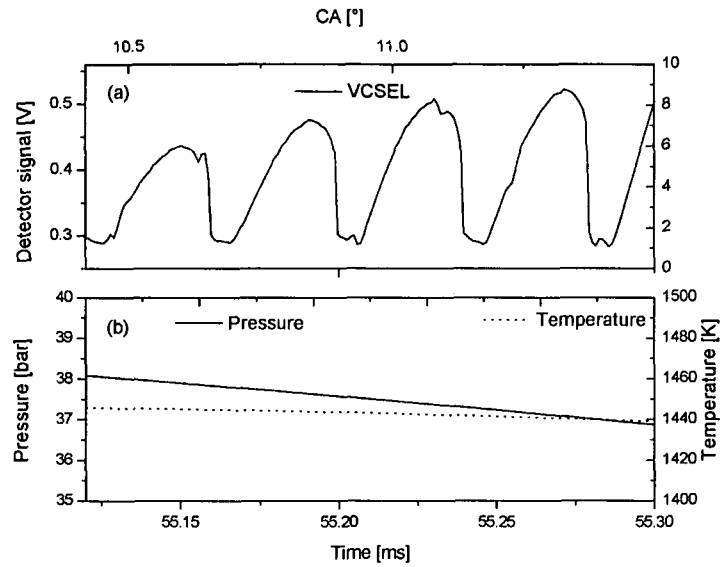


Fig. IV.6-45: Detail of the preceding Fig. IV.6-44, time shortly after combustion. See text for details.

The next section shows measurements with the 2.015  $\mu\text{m}$  VCSEL for  $\text{CO}_2$  detection.

### B) $\text{CO}_2$ VCSEL for HCCI diagnostics

Besides the  $\text{CH}_4$  VCSEL, another laser was used in the engine experiments. Two VCSELs at 2.015  $\mu\text{m}$  designed for the detection of  $\text{CO}_2$  were deployed.

Fig. IV.6-46 shows calculated spectra of  $\text{CO}_2$  in the tuning range of the VCSELs for various temperatures and pressures.

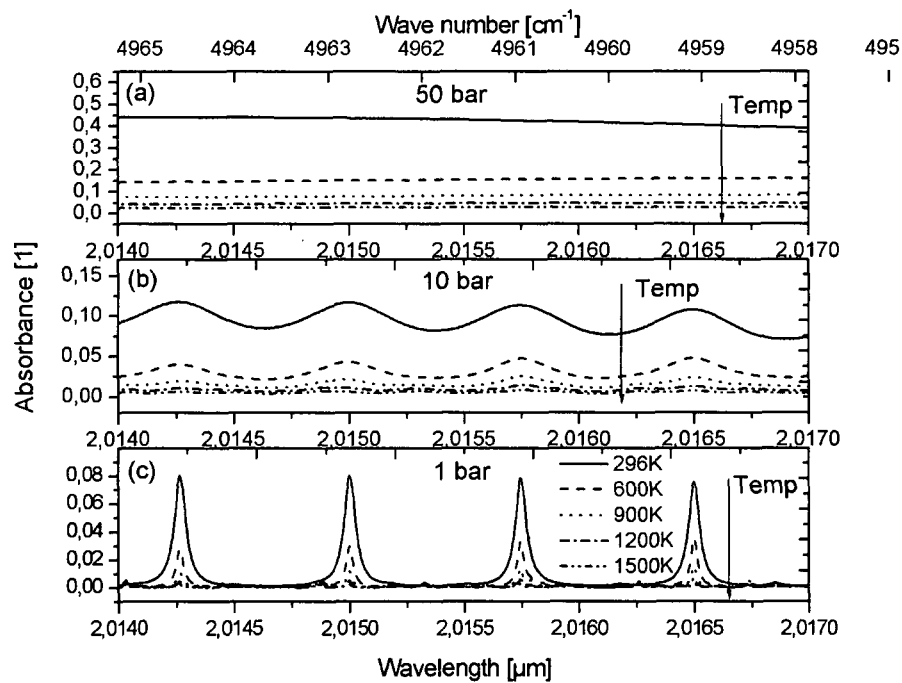


Fig. IV.6-46: Calculated spectra of  $\text{CO}_2$  for varying temperatures and pressures (conditions encountered in the HCCI engine: path length 12 cm, 10 %  $\text{CO}_2$ ). (a) is for 50 bar, (b) for 10 bar and (c) for 1 bar pressure.

Compared to  $\text{CH}_4$  at 1690 nm (see Fig. IV.6-10),  $\text{CO}_2$  at 2015 nm is subject to more severe pressure broadening which should make sensing more difficult.

Below in Fig. IV.6-47 one can see the etalon trace of  $\text{CO}_2$  recorded at 10 kHz.

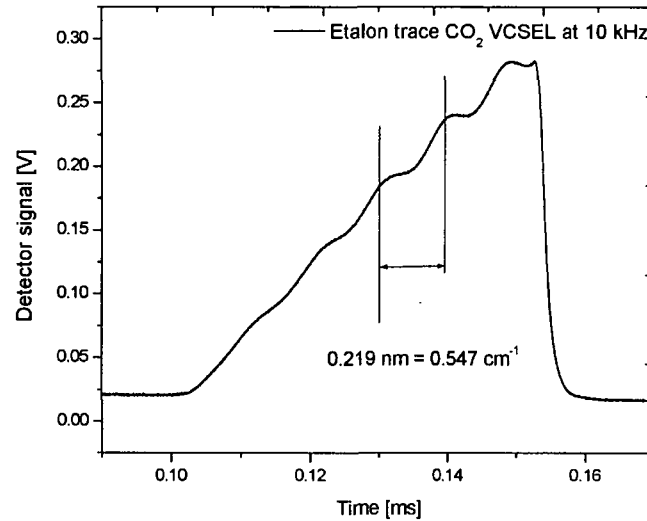


Fig. IV.6-47: Etalon trace of the VCSEL (0-5 V voltage ramp, 1 kOhms resistance, 20°C, 10 kHz). The FSR of the etalon was  $0.547 \text{ cm}^{-1}$  (0.219 nm).

The laser was ramped smoothly by a 0-5 V ramp at 25 kHz (laser in series with a 1 kOhms resistance). The temperature of the laser heat sink was 20°C.

Fig. IV.6-47 shows a test run ( $\text{CH}_4/\text{isooctane} = 50/50$ ) probed with the  $\text{CO}_2$  VCSEL. Lambda was 1.85. The laser signal is shown in (a), pressure and temperature traces are given below in (b).

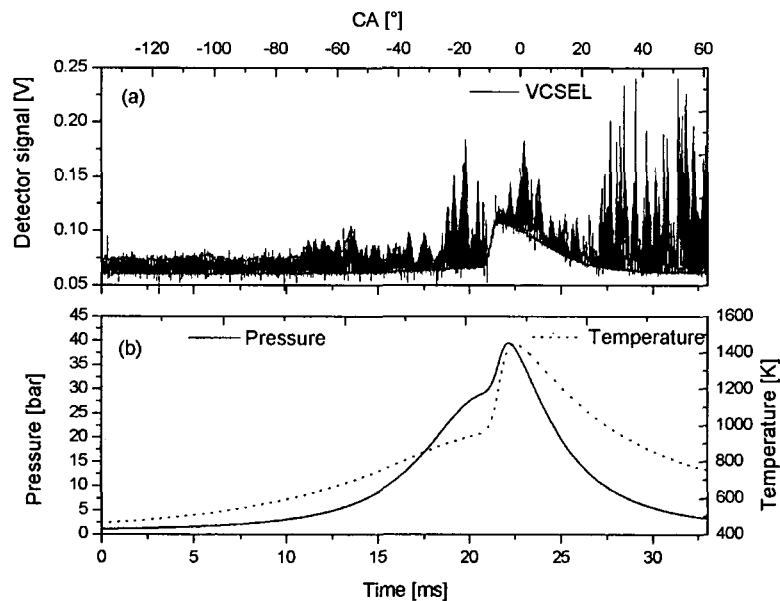


Fig. IV.6-48: Test run with the  $\text{CO}_2$  VCSEL ( $\text{CH}_4/\text{isooctane} = 50/50$ ), lambda = 1.85. See also Fig. IV.6-53.

For the  $2.015 \mu\text{m}$  VCSEL, a different photo detector had to be used. The liquid nitrogen cooled InSb detector (response from 1 – 10  $\mu\text{m}$ ) was taken (compare previous chapters). One

can see that the emissions from the flame in this spectral region show a progression similar to the temperature trace. A more detailed discussion on the emissions from the flame is given later (Fig. IV.6-52 and Fig. IV.6-53).

The band width of the necessary amplifier (home made transimpedance device) was rather low compared to the tuning speed. In the detector signal in Fig. IV.6-49 (a), one can therefore see that no sharp bends could be recorded. This smoothing also adversely affects the measured line shapes and sensitivity.

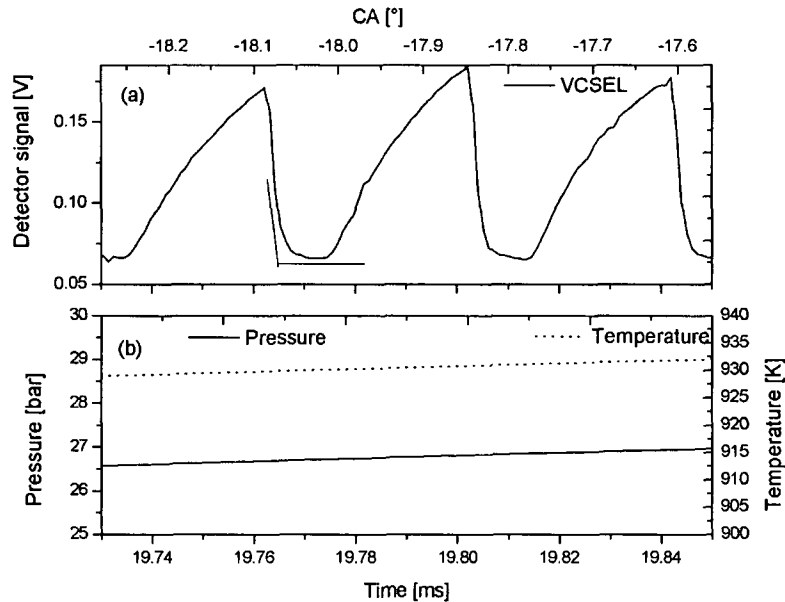


Fig. IV.6-49: Detail of the preceding Fig. IV.6-48 (shortly before auto ignition). One can see that the electronics cannot follow the 25 kHz tuning too well (see corner at the first ramp). It is the home made amplifier that has a limiting bandwidth.

In Fig. IV.6-50 below the magnification of ignition and combustion is shown. The signal is rather noisy.

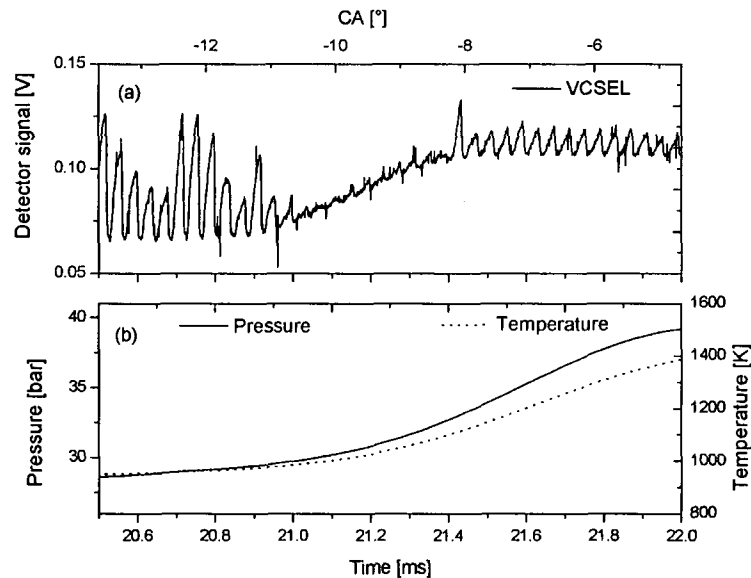


Fig. IV.6-50: Auto ignition part (enlarged from Fig. IV.6-48). The sharp downward spikes on the laser signal stem from the home made amplifier. The transmission of the laser beam is very low ( $< 50$  mV signal).

Fig. IV.6-51 shows four laser ramps after combustion.



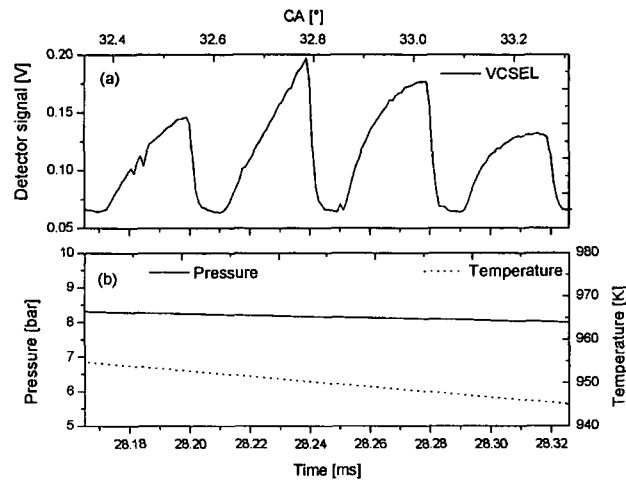


Fig. IV.6-51: Section of Fig. IV.6-48 after combustion. No  $\text{CO}_2$  can be spotted. 4 %  $\text{CO}_2$  were measured in the exhaust gas by a conventional analyzer.

No  $\text{CO}_2$  absorption peaks could be detected. The  $\text{CO}_2$  content of the exhaust gas was determined to be approximately 4 % (conventional analyzer).

Unfortunately, both  $\text{CO}_2$  VCSELs were destroyed after the very first experiments. Neither more aggressive current tuning nor a two pass setup could hence be tried.

### C) Evaluation of the emissions form the flame

The following two Fig. IV.6-52 and Fig. IV.6-53 take a closer look at the emissions from the flame. Lambda was 1.85. Fig. IV.6-52, modified from Fig. IV.6-19, depicts a test run with  $\text{CH}_4/\text{isooctane} = 95/5$ . The emissions from the flame were recorded in the wavelength range of 800-1800 nm.

Fig. IV.6-53, modified from Fig. IV.6-48, depicts a test run with  $\text{CH}_4/\text{isooctane} = 50/50$ . The emissions from the flame were recorded in the wavelength range of 1-10  $\mu\text{m}$ . The cylinder pressure is measured alongside the main exhaust gas constituents. The pressure trace was measured using a piezo-electric transducer mounted in the middle of the cylinder head. From the pressure trace, using the ideal gas law, the average temperature was estimated ( $\pm 50$  K in the bulk and close to the walls).

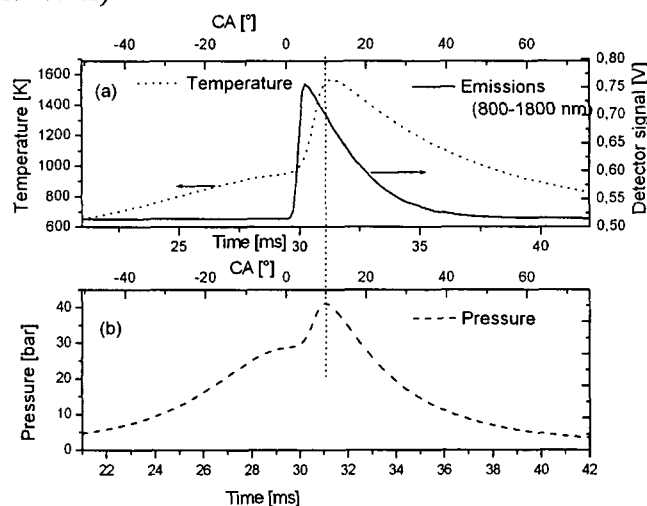


Fig. IV.6-52: Emissions from the flame in the 800-1800 nm range and temperature trace (a). (b) shows the measured pressure history (Modified from Fig. IV.6-19). Depicted is an HCCI combustion of a  $\text{CH}_4/\text{isooctane}$  mixture (95/5) at  $\lambda = 1.85$ . The pressure trace was measured using a piezo-electric transducer mounted in the middle of the cylinder head. From the pressure trace, using the ideal gas law, the average temperature was estimated ( $\pm 50$  K in the bulk and close to the walls).

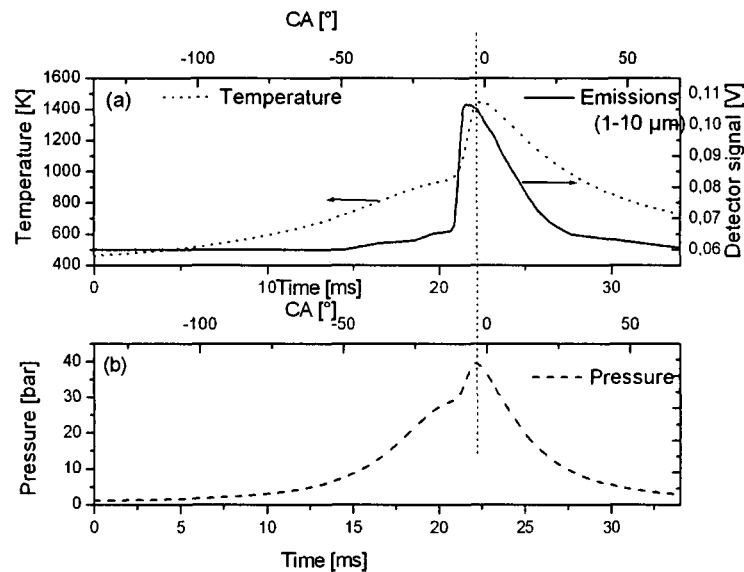


Fig. IV.6-53: Emissions from the flame in the 1-10  $\mu\text{m}$  range and temperature trace (a). (b) shows the measured pressure history (Modified from Fig. IV.6-48). Depicted is an HCCI combustion of a  $\text{CH}_4/\text{isooctane}$  mixture (50/50) at  $\lambda = 1.85$ . The pressure trace was measured using a piezo-electric transducer mounted in the middle of the cylinder head. From the pressure trace, using the ideal gas law, the average temperature was estimated ( $\pm 50$  K in the bulk and close to the walls).

One can see that the shape of all three curves is similar (pressure, temperature and flame). The optical signal, that is the emissions from the flame, rise and decay fastest. Temperature and pressure trace exhibit a time lag (as expected, the pressure transducer cannot follow the steep rise so fast). Both signals (800-1800 nm and 1-10  $\mu\text{m}$ ) show the same qualitative curve progression. The emissions in the 1-10  $\mu\text{m}$  wavelength range start rising earlier. This is due to thermal radiation of the compressing (hot) gas.

It was planned to use an additional SiC photo diode (UV region) to monitor OH emission. The UV range is much more selective than the broad 1-10  $\mu\text{m}$  wavelength region where also radiation from soot particles and walls contributes to the signal [103]. Unfortunately, the signal captured by the SiC photodiode (OEC GmbH) was too weak and no proper amplification circuit could be obtained or made during the measurement campaign.

### D) Laser aided HCCI plus diagnostics – Preliminary results

Control and stabilization of the HCCI ignition process have been known and recognized as two major problems with this promising new engine concept (see also chapter II.7).

In these preliminary experiments, the suitability of a pulsed laser source for HCCI ignition control was investigated.

The idea was to provide the mixture, shortly before auto ignition, with an additional (small) amount of energy in order to trigger the auto ignition.

Auto ignition and laser ignition sounds like an inconsistency; However, the laser is solely used to provide a small amount of energy (as such not able to ignite) at a very precise timing.

A crank angle encoder in conjunction with a delay time generator was used to trigger the shot of the laser. A pulsed Nd:YAG laser (10 ns pulse duration, several mJ pulse energy) was focused into the short groove (compare Fig. IV.6-1 and Fig IV.6-4). The optimum location of the focal spot would have been in the middle of the T shaped groove, but this could not be realized with the available optics.

The laser was used to generate optical breakdown several degrees before TDC.

Cycle to cycle variations of “ordinary” and “laser aided” HCCI test runs at various CA positions were recorded. A marked influence of the laser could be observed. This has got strong implications on potential control mechanisms in future HCCI engines. The whole work can be found in [232].

Within this thesis, only two exemplary graphs are presented.

In the depicted experiment, the inlet gas temperature of the running HCCI engine (approximately 200 °C) was slowly reduced. Every 10<sup>th</sup> cycle was recorded in terms of the pressure trace (this means that there is approximately one second between each trace).

Fig. IV.6-54 (a) shows the 11 relevant pressure traces (all overlaid). They are denoted “c. 0” to c. 100” (c for cycle). In (b), the upper parts of these graphs are shown in an enlarged fashion.

One can see that the peak pressure goes down from cycle 0 to cycle 40. This is because the inlet temperature decreases. Ignition takes place later. Cycles 50, 60 and 70 show an even stronger, progressive decrease.

By not intervening at that point, the engine would have stopped firing.

Now laser pulses were sent into the engine before TDC. One can see (cycles 80, 90 and 100) that the ignition was instantaneously advanced and that the peak pressure rose again.

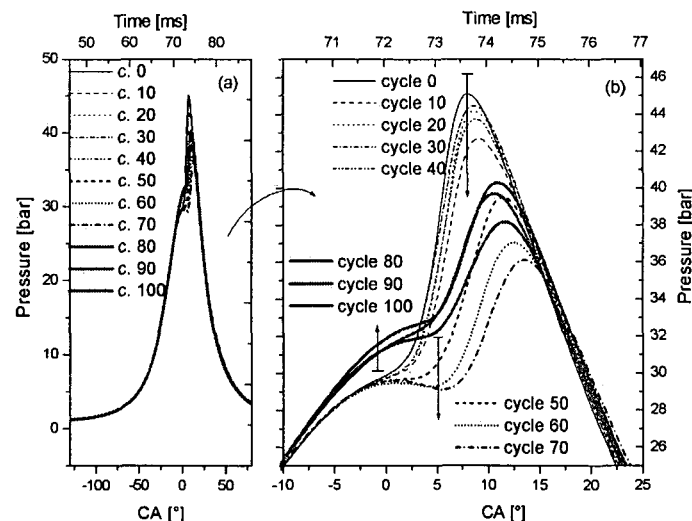


Fig. IV.6-54: Laser aided HCCI. (a) shows 11 pressure traces (each approximately 1 second apart). Every 10<sup>th</sup> cycle out of 1000 is shown (labeled c. 0 to c. 100). (b) is a magnification of the most relevant part. The inlet temperature was lowered as the curves were recorded (see decline in the pressure form cycle 0 to cycle 40 and from cycle 50 to cycle 70. At cycle 70, combustion is almost dead). Then, after cycle 70, the Nd:YAG laser was fired into the engine before TDC. The combustion could be stabilized and ignition was advanced. Note that the mixture ( $\lambda$  2.3) was too lean to be ignitable by the laser! The experiments are the first to show laser aided HCCI combustion.

Note that at the chosen  $\lambda$  of 2.3, the laser beam as such is not capable of igniting the mixture.

In Fig. IV.6-55 below the overlaid data traces from the preceding Fig. IV.6-54 (b) are shown in a different way; For better visual inspection and to stress the progressive behavior, the 11 curves have been annexed (cycle 0 most left one , cycle 100 most right one).

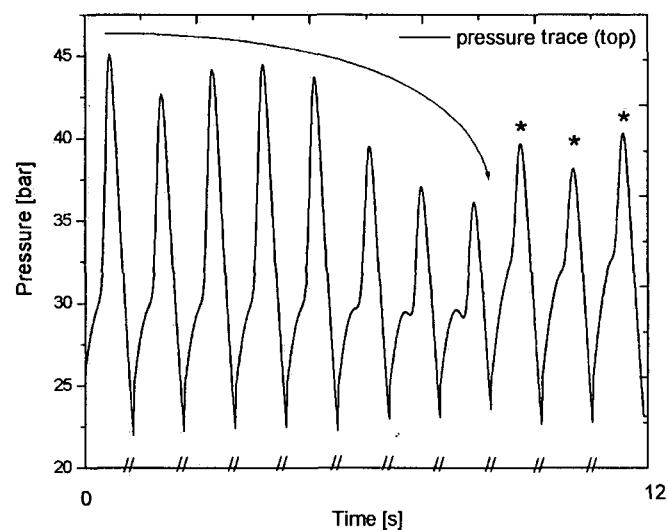


Fig. IV.6-55: Juxtaposition of the partial pressure traces from the preceding Fig. IV.6-54 for better visual inspection. The pressure traces where the pulsed Nd:YAG laser was used are marked by a \*.

One can see a steady decline in the peak pressures until the laser (firing marked with a \*) is used to revive and stabilize the auto ignition.

More information on the work related to laser aided HCCI can be found in Dipl.-Ing. Herbert Kopecek's PhD thesis [232].

Optical diagnostics using the CH<sub>4</sub> VCSEL (ramped from 0-10 V at 25 kHz, connected in series to a 1 kOhm resistance) was carried out concurrently to the test runs on laser aided HCCI. Since no specific results could be obtained (similar disturbances as described above in the "ordinary" HCCI experiments), no curves are presented.

## Conclusions

In this work, TDLAS was applied to species concentration measurements in an internal combustion engine. VCSELs at 1690 nm (CH<sub>4</sub> detection) and 2015 nm (CO<sub>2</sub> detection), two devices of each wavelength, were used.

Preparatory work (compare chapter III.4, IV.6 and IV.5) showed that VCSELs should be superior tools for the investigation of high pressure transient environments. The experiments in Lund were the most challenging ones ("real" engine, high temperatures and pressures).

First, the CH<sub>4</sub> VCSEL (1690 nm) was sent through the optical engine, a modified Volvo TD100, in a single pass setup. The laser was ramped from 0-4 V (plus 1 kOhm resistance) at 10 kHz. The results were not satisfying, so the voltage ramp was raised to 0-10 V (plus 1 kOhm resistance) still at 10 kHz. After that, the laser was ramped from 0-10 V (plus 1 kOhm resistance) at an increased tuning frequency (25 kHz). Finally, the laser was sent through the engine twice with the same settings (ramp 0-10 V (plus 1 kOhm resistance), 25 kHz) for increased sensitivity.

Then tests were done with the CO<sub>2</sub> VCSEL (2015 nm). The laser was deployed in a single pass setup and ramped from 0-5 V (plus 1 kOhm resistance) at 25 kHz. After the first series, both available CO<sub>2</sub> VCSELs were destroyed.

Two major problems were encountered:

- Due to the very fuel lean operation of the HCCI engine, the detection limit of CH<sub>4</sub> and CO<sub>2</sub> was too low (a lambda of 2.0 corresponds to approximately 5 vol% CH<sub>4</sub>).
- Severe signal distortions possibly resulting from heavy beam steering.

CH<sub>4</sub> could be measured in the unfired engine where the highest temperatures and pressures were 1000 K and 30 bar, respectively (10% CH<sub>4</sub>, temperature too low for auto ignition). In the running engine, no lambda below 1.85 could be used, which was too lean for the laser.

CO<sub>2</sub> was not detected. Before proper optimization could be carried out, both VCSELs were destroyed (possibly by leak currents or coupling effects).

Laser aided HCCI was also investigated using the CH<sub>4</sub> VCSEL (optimum settings of 0-10 V ramp and 25 kHz tuning frequency). The spectroscopy did not produce any useful results (severe distortions).

The concept of influencing a HCCI engine by a pulsed Nd:YAG laser, however, provided some preliminary, yet remarkable results: The laser could be used to stabilize and advance auto ignition.

This work was partly submitted for conference presentation:

F. Winter, M. Lackner, A. Hultqvist, Laser diagnostics applied to an internal combustion engine operating in HCCI mode, submitted to the Scandinavian Nordic – Italian Sections of the Combustion Institute Joint Meeting 2003, Ischia, Italy, September 18-21 (2003).

H. Kopecek, M. Lackner, E. Wintner, F. Winter, A. Hultqvist, Laser-Stimulated Ignition in a Homogeneous Charge Compression Ignition Engine, submitted to the 2004 SAE World Congress, Detroit, USA, March 8 – 11 (2004).

## IV.7 Summary of all applications

The following table IV.7-1 is a compilation of all applications where measurements were conducted. The laser systems that were used are tabulated in table III.5-1.

Experiments were made in room air, laboratory installations (quartz cell, pressurized cells, fluidized bed combustor) and in an internal combustion engine. The pressure range was 10 mbar – approx. 50 bar, the temperature range 25 – 1200°C, the concentration range 0.15 – 100 vol%. Some experiments served demonstration purposes, others were compared to modeling results and used to deduct information from the system under investigation.

Application/ experimental installation	Laser used	Measured species	Concentration range	Achievements	Tuning speed (path length)	Temperature range	Pressure range	Chapter
Solid fuel combustion/ laboratory- scale FBC	FP EEL at 2.3 and 2.55 $\mu\text{m}$	CO, CH <sub>4</sub> , H <sub>2</sub> O	0.2%-10 vol%	Particle laden gas flow, high temperatures	300 Hz (4*7cm)	700- 1000°C	1.013 bar (ambient)	IV.1
Laser ignition/ constant volume vessel	FP EEL at 2.55 $\mu\text{m}$	H <sub>2</sub> O	Semi quantitative, absorbance 0-4	High pressure, characterization of laser ignition	5 kHz (approx. 1 cm to 10 cm)	150°C- approx. 1200°C (estimated)	10-30 bar (initial pressure)	IV.2
Quartz cell	QCL at 11.4 $\mu\text{m}$	C <sub>2</sub> H <sub>4</sub> , NH <sub>3</sub>	2 vol% C <sub>2</sub> H <sub>4</sub> , 1500 ppm NH <sub>3</sub>	Trace gas sensing	5 kHz pulsed (44 cm)	25°C (ambient)	1.013 bar (ambient)	IV.3
Quartz cell (heated)	VCSEL at 1.540 $\mu\text{m}$	NH <sub>3</sub>	100%	High temperature measurements, high resolution spectroscopy	1-200 kHz (88 cm)	25°C- 900°C	9.6 mbar – 1bar	IV.4.1.1
Quartz cell	VCSEL at 1.680 $\mu\text{m}$	CH <sub>4</sub>	100%	Rapid tuning	25 kHz – 5 MHz (44 cm)	25°C (ambient)	13.7 mbar – 286 mbar	IV.4.1.2
Atmosphere and quartz cell	VCSEL at 1.810 $\mu\text{m}$	H <sub>2</sub> O, HCl, CH <sub>4</sub>	0.75% (H <sub>2</sub> O at 21°C), ~40% HCl 100% (CH <sub>4</sub> )	Multiple species, high resolution spectroscopy	505 Hz (44 cm for HCl and CH <sub>4</sub> , 86 cm for H <sub>2</sub> O)	21°C (ambient)	7 mbar - 1.48 bar	IV.4.1.3
Flames and atmosphere	VCSEL at 0.761 $\mu\text{m}$	O <sub>2</sub>	Up to 21 vol%	WMS, harsh conditions (flames up to 1.0 m long)	50 Hz – 25 kHz <sup>#</sup> (2.4 m – 4.85 m)	25°C (ambient)	1.013 bar	IV.4.2
Small constant volume vessel	VCSEL at 0.761 $\mu\text{m}$	O <sub>2</sub>	100 vol%	pressure broadening	50 Hz – 25 kHz <sup>#</sup> (30 cm)	25°C (ambient)	1– 10 bar	IV.5
Internal combustion engine (HCCI)	VCSEL at 1.690 and 2.015 $\mu\text{m}$	CH <sub>4</sub> , CO <sub>2</sub>	0-10% (CH <sub>4</sub> ), 0-4% (CO <sub>2</sub> )	<i>In-situ</i> laser spectroscopy in an engine	10 – 25 kHz (12 – 24 cm)	~25°C - 1200 °C	1-50 bar	IV.6

Table IV.7-1: Summary of all applications where the laser systems (compilation in chapter III.5) were used (FBC = fluidized bed combustor, WMS = wavelength modulation spectroscopy, FP = Fabry Perot, EEL = edge emitting laser, QCL = quantum cascade laser, VCSEL = vertical-cavity surface-emitting laser, , HCCI = homogeneously charged compression ignition).

<sup>#</sup> up to 5 MHz in [118].

## V. Conclusions

In the studies of the presented PhD thesis, laser-induced ignition of gaseous fuel/air mixtures was to be investigated in order to gain an understanding on the quality of the ignition. Tunable diode laser absorption spectroscopy (TDLAS), a non-intrusive optical diagnostic technique with high temporal and spatial resolution, was deployed.

Suitable laser sources were selected, tested and used in laser ignition experiments. The laser measurement systems were home made.

Accompanying experiments where the various laser systems were applied to the investigation of different aspects of combustion were carried out.

Two InGaAsSb/AlGaAsSb diode lasers emitting at 2.3 and 2.55  $\mu\text{m}$  (4348 and 3922  $\text{cm}^{-1}$ ) were used for the *in-situ* measurement of concentration histories of CO, CH<sub>4</sub> (2.3  $\mu\text{m}$  device) and H<sub>2</sub>O (2.55  $\mu\text{m}$  device) close to the surface of single burning particles in conjunction with accompanying conventional determinations of CO<sub>2</sub> and O<sub>2</sub>. CO, CH<sub>4</sub> and H<sub>2</sub>O could be measured *in-situ* and real-time in the freeboard section of a laboratory-scale fluidized bed combustor (FBC, superficial velocity 0.3 m/s) in a distance of 4, 10, 21 and 31 mm to the surface of burning particles. The corresponding residence times were 12, 30 60 and 90 ms. The laser was ramped at 300 Hz.

The lower detection limit (800°C, 1 bar) was 500 ppm\*m for CO and CH<sub>4</sub> and 50 ppm\*m for H<sub>2</sub>O. Bituminous coal, fir wood (softwood) and beech wood (hardwood) were investigated during devolatilization and char combustion. The O<sub>2</sub> partial pressure was 5, 10, 15 and 21 kPa, the bed temperature 700, 800 and 900°C. Biomass was found to produce four times as much CO as coal. The CO/CO<sub>2</sub> ratio was found to be about five times higher for beech wood than for fir wood. The *in-situ* results of CO were compared to data obtained by conventional methods. It was found that conventional methods overestimate the concentrations during char combustion and underestimate those during devolatilization. The results were compared to a chemical kinetic model. Good agreement was found.

*The FBC was an experimentally challenging (hot and multi phase) environment where species concentration measurements could be carried out successfully.*

Laser-induced ignition was investigated using the 2.55  $\mu\text{m}$  InGaAsSb/AlGaAsSb diode laser. The beam of the diode laser (ramped at 5 kHz) was sent through the constant volume vessel perpendicularly to the igniting laser spark. The initial pressure was up to 3 MPa (473 K). The formation of H<sub>2</sub>O in the vicinity of the ignition spot was tracked in a semi-quantitative manner.

In addition, the emissions from the flame were recorded. They allow the determination of ignition delay time, flame growth and flame quenching.

The fluctuations in the transmission over time of the probing diode laser beam onto the detector were found to result mainly from refractive index gradients inside the combustion vessel. These can be correlated with properties of the developing flame and the effect the plasma and the shock wave have generated. A gas inhomogeneity index was introduced. The developed technique based on the three parameters (i.e. water absorption, flame emissions, gas inhomogeneity index) was found to adequately characterize fuel rich, stoichiometric, fuel lean and failed ignition attempts of methane/air mixtures in the constant volume vessel.

Limitations include the adverse effect of pressure broadening on the quantification of the absorbance signal and the ignorance of temperature.

Laser ignition of biogas/air mixtures (CH<sub>4</sub>/CO<sub>2</sub> =50.5%/31.7%) was also investigated. Preliminary tests of diagnostics on vaporized higher hydrocarbon/air mixtures were conducted, too.

*Tunable diode laser absorption spectroscopy could be successfully applied to the investigation of a high pressure, transient process (laser-induced ignition).*

A novel DFB quantum cascade laser (QCL) emitting at  $11.4\ \mu\text{m}$  ( $877\ \text{cm}^{-1}$ ) was used to record spectra of  $\text{NH}_3$ ,  $\text{C}_2\text{H}_4$ , biogas and biomass steam gasification gas (pulsed operation at 5 kHz). The  $\text{C}_2\text{H}_4$  and  $\text{NH}_3$  levels in the biogas were below the detection limits ( $2200\ \text{ppm}\cdot\text{m}$  and  $220\ \text{ppm}\cdot\text{m}$ , respectively). These findings were confirmed for  $\text{NH}_3$  by conventional methods, which indicated that  $\text{NH}_3$  levels were below 200 ppm. The biomass product gas was shown to contain approximately 2 %  $\text{C}_2\text{H}_4$ , in agreement with conventional methods.

*Due to its emission in the mid infrared, the QCL device is much more sensitive than telecommunication diode lasers in the 1-2  $\mu\text{m}$  near infrared spectral region. A main drawback are the sophisticated cooling requirements.*

Novel InP based vertical-cavity surface-emitting lasers (VCSELs) in the  $1.54$  to  $1.81\ \mu\text{m}$  wavelength range were characterized with respect to their spectroscopic properties and used in a series of demonstration experiments.

A  $1.54\ \mu\text{m}$  ( $6494\ \text{cm}^{-1}$ ) VCSEL was used to measure highly resolved spectra of  $\text{NH}_3$  at various pressures ranging from 9.6 mbar to 1 bar and temperatures up to 1173 K. The measured Doppler linewidth of  $0.02\ \text{cm}^{-1}$  for the  $6510.986\ \text{cm}^{-1}$  line at 9.6 mbar agreed within 3 % with the theoretical value. A  $20.4\ \text{cm}^{-1}$  (4.8 nm) wide  $\text{NH}_3$  spectrum was recorded and compared to a  $\text{NH}_3$  line list from the literature. It was found that, in contrast to indications in the referenced literature, VCSELs are very well suited for high resolution spectroscopy even at low pressures. The measured peak tuning speed was  $3.5\ \text{cm}^{-1}/\mu\text{s}$  and a  $4.5\ \text{cm}^{-1}$  wide  $\text{NH}_3$  spectrum was recorded in 2  $\mu\text{s}$ . At 200 Hz triangular current modulation the tuning range was  $13.5\ \text{cm}^{-1}$  (3.2 nm).

A  $1.68\ \mu\text{m}$  ( $5952\ \text{cm}^{-1}$ ) VCSEL was used for rapid absorption spectroscopy of  $\text{CH}_4$ . A single VCSEL was contacted directly on a wafer to demonstrate the ability of device performance testing prior to singularizing and mounting the laser. Rovibrational transitions of pure  $\text{CH}_4$  at 300K and 10 mbar to 1.3 bar were probed at high repetition rates (500 Hz to 5 MHz, corresponding to a time resolution of 2 ms to 0.2  $\mu\text{s}$ , respectively). The laser was driven by a triangular waveform of a function generator in series with a 2 k $\Omega$  resistor. The peak tuning rate was  $5.2\ \text{cm}^{-1}/\mu\text{s}$  (1.5 nm/ $\mu\text{s}$ ). The measured tuning rates of the VCSEL were  $-3.05\ \text{cm}^{-1}/\text{mA}$  (+0.86 nm/mA) and  $-0.40\ \text{cm}^{-1}/\text{K}$  (+0.11 nm/K).

The maximum continuous current tuning range was more than  $16\ \text{cm}^{-1}$  (4.5 nm). At 1 MHz the tuning range was as large as  $2.6\ \text{cm}^{-1}$  (1.5 nm), and at 5 MHz it was still approximately  $0.36\ \text{cm}^{-1}$  (0.21 nm).

A  $1.81\ \mu\text{m}$  ( $5525\ \text{cm}^{-1}$ ) VCSEL was used to record high resolution spectra of HCl,  $\text{CH}_4$  and  $\text{H}_2\text{O}$  at pressures ranging from 0.07 to 1.5 bar. The measurements were compared to calculated spectra based on the HITRAN2000 database. Good agreement was found.

A current tuning range of  $8.4\ \text{cm}^{-1}$  (2.8 nm) was demonstrated. The laser threshold was 0.9 mA, the temperature tuning rate  $0.125\ \text{nm}/\text{K}$  ( $0.38\ \text{cm}^{-1}/\text{K}$ ) and the current tuning rate  $0.9\ \text{nm}/\text{mA}$  ( $2.75\ \text{cm}^{-1}/\text{mA}$ ).

*It was discovered that the outstanding advantages of VCSELs for spectroscopy are the ability of fast (several MHz) and far ( $>10\ \text{cm}^{-1}$ ) wavelength tuning without mode-hops. Further benefits are on wafer testing and wavelength selection ability, low power consumption, less susceptibility to optical feed back, single mode emission and low cost. VCSELs as used in this work are particularly suitable for numerous applications in spectroscopy, e.g. where high pressures ( $> 1\ \text{bar}$ ) significantly broaden the absorption features or where a good time*



*resolution ( $< 1$  ms) is needed. It is therefore expected that the availability of long wavelength, single frequency VCSELs should significantly expand the application fields for infrared diode laser gas sensors and make VCSELs a preferred choice for industrial diode laser based gas sensing applications.*

A  $0.761 \mu\text{m}$  ( $13141 \text{ cm}^{-1}$ ) VCSEL (detection of  $\text{O}_2$ ) was used to probe harsh environments: liquid fuel flames of up to 1.0 m length and heavily particle laden gas streams (silica sand). *It was demonstrated that by rapidly (i.e. faster than the time scale of the disturbing effects) tuning the laser wavelength over an absorption peak, undistorted signal recording is possible despite strong beam steering, scattering, partial blocking of the beam and luminosity from flames.*

The  $0.761 \mu\text{m}$  VCSEL was also deployed to measure absorption spectra of  $\text{O}_2$  at 1, 5 and 10 bar (100%  $\text{O}_2$ , 30 cm path length, 298K). The peaks were compared to a calculated Lorentzian fit. Good agreement was found. In the pertinent literature, a pressure vs. temperature plot was published where the regime of TDLAS (typical conditions) was marked. This plot was reassessed for VCSEL based systems.

*It was concluded and demonstrated that VCSELs are superior laser sources for the investigation of high pressure environments.*

A  $1.690 \mu\text{m}$  ( $5917 \text{ cm}^{-1}$ ) and a  $2.015 \mu\text{m}$  ( $4963 \text{ cm}^{-1}$ ) VCSEL for the detection of  $\text{CH}_4$  and  $\text{CO}_2$  were used for *in-situ* optical diagnostics in an internal combustion engine.

Preparatory work showed that VCSELs should be superior tools for such demanding high pressure transient environments.

The engine, a modified Volvo TD100 truck size engine, which was equipped with four windows for optical access was operated in HCCI (homogeneously charged compression ignition) mode on  $\text{CH}_4$  and isooctane.

Also, the influence of a pulsed Nd:YAG laser on the control of an HCCI engine was investigated (laser aided HCCI). Promising preliminary results regarding laser aided HCCI were obtained.

*Strong signal distortions, possibly caused by heavy beam steering in the cylinder, were encountered. The engine tests showed the limitations of the VCSELs.*

*It was found that a laser pulse which as such would not ignite the engine (too lean mixture) was capable of advancing the timing and stabilizing the ignition.*

To summarize, *in-situ* species concentration measurements were conducted using tunable diode laser absorption spectroscopy (TDLAS) in the temperature and pressure range of  $25^\circ\text{C}$  to  $1200^\circ\text{C}$  and 10 mbar to 50 bar. Laser measurement systems were constructed based on edge emitting lasers at  $2.3$  and  $2.55 \mu\text{m}$ , VCSELs at  $0.761$  and  $1.540$  to  $2.015 \mu\text{m}$  and a quantum cascade laser at  $11.4 \mu\text{m}$  to measure  $\text{CO}$ ,  $\text{CH}_4$ ,  $\text{H}_2\text{O}$ ,  $\text{O}_2$ ,  $\text{NH}_3$ ,  $\text{HCl}$ ,  $\text{NH}_3$ ,  $\text{C}_2\text{H}_4$  and  $\text{CO}_2$  in static cells, a laboratory-scale fluidized bed combustor, the atmosphere and an internal combustion engine. The path length was 1 cm to 4.85 m. Transient, hostile environments were probed in the concentration range of 0.15 – 100% (detection limit of the laser systems  $50 \text{ ppm}\cdot\text{m}$  ( $\text{H}_2\text{O}$  at  $2.55 \mu\text{m}$ ) to  $17500 \text{ ppm}\cdot\text{m}$  ( $\text{NH}_3$  at  $1.540 \mu\text{m}$ )). Besides rapid absorption spectroscopic demonstration experiments, solid fuel combustion and laser-induced ignition of gaseous fuel/air mixtures at high pressures were investigated by these newly developed laser systems.

## VI. Outlook

Embedded in the research field of the work group, Reaction Engineering & Combustion, the focus of the laser diagnostics subgroup has been to develop laser based measurement systems for *in-situ* combustion and ignition diagnostics. Tunable diode laser absorption spectroscopy (TDLAS) was found to be the best suited technique for the given problem in terms of handling, performance and costs. The author's forerunner, Dr. Gerhard Totschnig, who started experimental work in this area in the work group, initially encountered a severe lack in suitable lasers. One of the first ideas was to build a tunable laser of a suitable wavelength himself. Also, different types of diode lasers were experimented with. Continuous wave, room temperature edge emitting diode lasers at 2.3 and 2.55  $\mu\text{m}$  (4348 and 3922  $\text{cm}^{-1}$ ) and short wavelength vertical cavity surface emitting lasers (VCSELs) at 0.761  $\mu\text{m}$  (13141  $\text{cm}^{-1}$ ) were used besides a quantum cascade device. VCSELs were discovered to show advantageous properties for spectroscopy, however, they were only available at wavelengths below 1  $\mu\text{m}$ . The lasers were used for rapid *in-situ* species concentration measurements in difficult environments such as particle laden gases and flames. When the author started, the situation had already improved considerably. Long wavelength VCSELs had just appeared and were obtained from a Munich based research group. Gerhard's work was finished with joint demonstration experiments of long wavelength VCSEL spectroscopy. The unique and very promising properties of these lasers in the 1.54 to 1.81  $\mu\text{m}$  (6494 – 5525  $\text{cm}^{-1}$ ) wavelength range were investigated and presented.

The work of the author was mainly focused on two directions of impact:

- Progress in understanding and characterizing laser ignition
- Advancement of TDLAS for combustion and ignition research

The author used the existing laser measurement systems (2.3 and 2.55  $\mu\text{m}$  edge emitters for CO, CH<sub>4</sub> and H<sub>2</sub>O determination plus the 0.761  $\mu\text{m}$  VCSEL) that had been devised by Gerhard to apply them to novel applications. The laser-induced ignition of gaseous fuel/air mixtures was thoroughly investigated by tracking the generation of water in the vicinity of the spark location (2.55  $\mu\text{m}$  laser). The 0.761  $\mu\text{m}$  VCSEL was used to investigate flames and particle laden gas streams. It was also used to study pressure broadening. A novel quantum cascade laser at 11.4  $\mu\text{m}$  was tested, too.

New VCSELs were obtained from our German partners (1.690  $\mu\text{m}$  for CH<sub>4</sub> and 2.015  $\mu\text{m}$  for CO<sub>2</sub> sensing).

The laser measurement systems were continuously improved in terms of size and functionality. They were used during a research stay at Lund Institute of Technology to conduct *in-situ* species concentration measurements in an internal combustion engine.

In the outlook of Gerhard's thesis the search for novel laser sources is mentioned besides the need to bring the laser based sensors closer to a marketable product.

Both issues were advanced, however not completely fulfilled, within the scope of this thesis.

All ambitious work packages offered to our industrial partner within the FFF project could be fulfilled.

The following listing shows the most important achievements:

- Characterization of laser-induced ignition using TDLAS: a set of three parameters was derived to adequately judge the quality of the ignition
- Species were measured *in-situ* an internal combustion engine
- Demonstration of the feasibility of laser aided HCCI and concurrent diagnostics

The question arises of which are the next steps.

The following two listings comprise issues that should be addressed next.

### **Outlook I - Characterization of laser-induced ignition**

- Combination of TDLAS with laser induced fluorescence to yield quantitative, two dimensional results. This can probably not be put into practice in the short run.
- Deploying VCSELs (e.g. to measure H<sub>2</sub>O at 1.96 – 2.00 μm) instead of edge emitting devices.
- Use of an imaging technique like Schlieren (shadowgraph) images. This step is already under discussion.
- Proper injection of liquid fuels. A diploma thesis (Martin Tesch) was devoted to this issue which will be realized in the near future.
- Accompanying modeling of laser-induced ignition.
- Investigation of laser aided HCCI and optical diagnostics.

### **Outlook II - TDLAS using VCSELs**

Based on our findings, it is strongly believed that VCSELs are superior lasers for spectroscopic applications over DFB, external cavity or quantum cascade laser devices in terms of costs, handling and wavelength tuning properties. Therefore, research in this area should be fostered.

- Continued sensor development in terms of size and functionality towards a prototype suitable for industrial use (VCSEL based gas sensors with a section of an array installed have the potential of fast and convenient in field laser replaceability. The low power consumption of VCSELs gives these lasers an edge for battery operated appliances).
- Profound investigation of pressure broadening. This was only started in this thesis. A START and an FWF project have already been submitted to pursue this way.
- Search for alternative VCSELs (not InP based ones).
- Search for alternative laser sources (e.g. tunable twin guide lasers as indicated in Gerhard's outlook [118]).
- Application of VCSEL based gas monitoring systems to real world applications. A project of measuring pollutants in an urban road tunnel was granted and will be worked on in the near future.

**VII. Publications and patents****Journals**

1)

M. Lackner, G. Totschnig, F. Winter, R. Shau, J. Rosskopf, M. Ortsiefer, M.C. Amann, Spektroskopischer Einsatz neuer, langwelliger (bis 2  $\mu\text{m}$ ) Diodenlaser (VCSEL) für schwierige Bedingungen, *Technisches Messen* 70 (6), 294-305 (2003).

2)

M. Lackner, Ch. Forsich, F. Winter, H. Kopecek, E. Wintner, *In-situ* Investigation of Laser-induced Ignition and the Early Stages of Methane-Air Combustion at High Pressures Using a Rapidly Tuned Diode Laser at 2.55  $\mu\text{m}$ , *Spectrochimica Acta A*, in press (2003).

3)

M. Lackner, Ch. Forsich, F. Winter, S. Anders, G. Strasser, Investigation of biomass steam gasification gas using GaAs based quantum cascade laser emitting at 11  $\mu\text{m}$ , *Optics Communications* 216 (4-6), 357 - 360 (2003).

4)

M. Lackner, G. Totschnig, G. Loeffler, H. Hofbauer, F. Winter, *In-situ* laser spectroscopy of CO, CH<sub>4</sub> and H<sub>2</sub>O at 2.3 - 2.55  $\mu\text{m}$  in a particle laden laboratory-scale fluidized bed combustor (FBC), *Thermal Science* 6 (2), 13-27 (2002).

5)

M. Lackner, G. Totschnig, F. Winter, *In-situ* laser measurements of CO and CH<sub>4</sub> close to the surface of a burning single fuel particle, *Measurement Science and Technology* 13 (10), 1545-1551 (2002).

6)

M. Lackner, G. Totschnig, F. Winter, R. Shau, J. Rosskopf, M. Ortsiefer, M.C. Amann, Demonstration of Methane Spectroscopy using a Vertical-Cavity Surface-Emitting Laser (VCSEL) at 1.68  $\mu\text{m}$  with up to 5 MHz repetition rate, *Measurement Science and Technology* 14 (1) 101-106 (2003).

7)

G. Totschnig, M. Lackner, F. Winter, R. Shau, J. Rosskopf, M. Ortsiefer, M.C. Amann, High speed vertical-cavity surface-emitting laser (VCSEL) absorption spectroscopy of ammonia (NH<sub>3</sub>) near 1.54  $\mu\text{m}$ , *Applied Physics B Lasers and Optics* 76 (5), 603-608 (2003).

8)

G. Totschnig, M. Lackner, F. Winter, R. Shau, J. Rosskopf, M. Ortsiefer, M.C. Amann, 1.8  $\mu\text{m}$  vertical-cavity surface-emitting laser absorption measurements of HCl, H<sub>2</sub>O and CH<sub>4</sub>, *Measurement Science and Technology* 14 (4), 472-478 (2003).

9)

H. Kopecek, E. Wintner, M. Lackner, F. Winter, Laser-Induced Ignition of Methane-Air Mixtures at Pressures up to 4 MPa, *Journal of Laser Physics*, accepted for publication (2002).

**Book chapters**

- 1)  
M. Lackner, F. Winter, What is tuneable diode laser spectroscopy for combustion applications? Combustion File 185, IFRF (International Flame Research Foundation) Online Combustion Handbook, ISSN 1607-9116 (2002).  
<http://www.handbook.ifrf.net/handbook/>
- 2)  
M. Lackner, F. Winter, How can gas species be measured in high pressure combustion systems using tuneable diode lasers? Combustion File 187, IFRF (International Flame Research Foundation) Online Combustion Handbook, ISSN 1607-9116, 2002.  
<http://www.handbook.ifrf.net/handbook/>

**Conferences**

- 1)  
M. Lackner, G. Totschnig, F. Winter, *In-situ* Laser Measurements of CO and CH<sub>4</sub> Close to the Surface of a Single Fuel Particle in a Fluidized Bed Combustor, oral presentation at 44<sup>th</sup> IEA-FBC Meeting, Vienna, Austria, May 27<sup>th</sup> (2002).
- 2)  
M. Lackner, G. Totschnig, G. Löffler, H. Hofbauer, F. Winter, *In-situ* laser spectroscopy and modeling of bituminous coal in a laboratory-scale FBC, oral presentation at 45<sup>th</sup> IEA-FBC Meeting, Prague, Czech Republic, November 18<sup>th</sup> (2002).
- 3)  
M. Lackner, G. Totschnig, F. Winter, R. Shau, J. Roskopf, M. Ortsiefer, M.C. Amann, Rapid high resolution absorption spectroscopy using long wavelength InP-based VCSELs at 1.54  $\mu\text{m}$  (NH<sub>3</sub>), 1.68  $\mu\text{m}$  (CH<sub>4</sub>) and 1.80  $\mu\text{m}$  (H<sub>2</sub>O, HCl), oral presentation at CLEO/QUELS (conference on lasers and electro optics), Baltimore, USA, June 6<sup>th</sup> (2003).
- 4)  
M. Lackner, Ch. Forsich, F. Winter, H. Kopecek, E. Wintner, Characterization of Laser Ignition of Hydrocarbon/Air Mixtures using a tunable InGaAsSb/AlGaAsSb diode laser at 2.55 $\mu\text{m}$ , poster presentation at CLEO/Europe (conference on lasers and electro optics), Munich, Germany, June 25<sup>th</sup> (2003).
- 5)  
H. Kopecek, M. Lackner, K. Iskra, Ch. Forsich, D. Rüdissler, T. Neger, F. Winter, E. Wintner, Laser ignition of methane air mixtures at high pressures and optical diagnostics, Proceedings of the SPIE (2002).
- 6)  
H. Kopecek, S. Charareh, M. Lackner, C. Forsich, F. Winter, E. Wintner, Laser ignition of methane air mixtures at high pressures and diagnostics, oral presentation at ASME conference, Proceedings of Spring Technical Conference of the ASME International Combustion Engine Division, ICES2003-614, Salzburg, Austria, May 11-14 (2003).

7)

M. Lackner, F. Winter, Laserspektroskopie- Spezienmessung bei hohen Temperaturen und Drücken, oral presentation at Minisymposium Angewandte Schwingungsspektroskopie, Österreichische Gesellschaft für Analytische Chemie – AG Schwingungsspektroskopie, Vienna University of Technology, Vienna, Austria, June 26<sup>th</sup> (2003).

**Patents**

1)

M. Lackner, G. Totschnig, F. Winter, Innovationsagentur, Verfahren zur raschen spektroskopischen Konzentrations-, Temperatur- und Druckmessung von gasförmigem Wasser, PCT filing, A210/2002 (status pending), February (2003).

2)

M. Lackner, J. Klausner, F. Winter, Verfahren zu einer berührungslosen Druckmessung, A859/2002 (status pending) (2002).

**Press reports**

1)

Michael Hatcher (editor), Fast-tuning VCSEL detects methane, Opto & Lasers Europe, Volume 2, <http://optics.org/articles/news/9/2/4/1> (2003)

**Submitted publications (status pending)**

1)

M. Lackner, Ch. Forsich, F. Winter, K. Iskra, T. Neger, H. Kopecek, E. Wintner, Diagnostic tools for laser-induced ignition of hydrocarbon/air mixtures: *In-situ* tunable diode laser absorption and LIF spectroscopies, submitted to OpticsExpress (2003).

2)

Ch. Forsich, M. Lackner, F. Winter, H. Kopecek, E. Wintner, Characterization of Laser-Induced Ignition of Biogas-Air Mixtures, submitted to Biomass & Bioenergy (2003).

3)

Ch. Forsich, M. Lackner, F. Winter, H. Kopecek, E. Wintner, Laser-induced Ignition of Vaporized Liquid Fuel-Air Mixtures, submitted to Combustion and Flame (2003).

**Upcoming conferences (accepted for presentation)**

1)

M. Lackner, G. Totschnig, F. Winter, Rapid absorption spectroscopy for *in-situ* O<sub>2</sub> measurements in hostile environments (multi-phase and flames) using a 761 nm vertical-cavity surface-emitting laser (VCSEL), accepted for poster presentation at TDLS 2003 (4<sup>th</sup> international conference of tunable diode laser spectroscopy), Zermatt, Switzerland, July 14-18 (2003).

2)

M. Ortsiefer, R. Shau, M. Lackner, G. Totschnig, F. Winter, J. Rosskopf, C. Lauer, M.C. Amann, Long-wavelength vertical-cavity surface-emitting lasers for molecular absorption spectroscopy in the 1.5-1.8  $\mu\text{m}$  range, accepted for oral presentation at TDLS 2003 (4<sup>th</sup> international conference of tunable diode laser spectroscopy), Zermatt, Switzerland, July 14-18 (2003).

3)

M. Lackner, G. Totschnig, F. Winter, R. Shau, J. Rosskopf, M. Ortsiefer, M.C. Amann, Pollutant reduction by *in-situ* combustion diagnostics at high pressures using a novel near infrared diode laser, the vertical-cavity surface-emitting laser (VCSEL), accepted for oral presentation at Clean Air 2003 (7<sup>th</sup> International Conference on Energy for a Clean Environment), Lisbon, Portugal, July 7-11 (2003).

4)

F. Winter, M. Lackner, G. Totschnig, R. Shau, J. Rosskopf, M. Ortsiefer, M.C. Amann, *In-situ* Verbrennungsdiagnostik bei hohen Drücken mittels neuartiger (VCSEL) Diodenlaser, accepted for oral presentation at 21<sup>st</sup> German Flameday, Cottbus, Germany, September 9-10 (2003).

5)

H. Kopecek, M. Lackner, F. Winter, E. Wintner, Laser ignition of methane air mixtures at high pressures, accepted for oral presentation at 21<sup>st</sup> German Flameday, Cottbus, Germany, September 9-10 (2003).

6)

M. Weinrotter, M. Lackner, F. Winter, H. Kopecek, E. Wintner, Laser ignition of hydrogen/air mixtures, accepted for presentation at the conference European Combustion Meeting, Orleans, France, October 25-28 (2003).

### Planned publications

1)

M. Lackner, G. Loeffler, G. Totschnig, F. Winter, H. Hofbauer, Carbon conversion of solid fuels in the freeboard of a laboratory-scale fluidized bed combustor (FBC) - Application of *in-situ* laser spectroscopy, to be submitted to Fuel (2003).

2)

H. Kopecek, M. Lackner, E. Wintner, F. Winter, A. Hultqvist, Laser-Stimulated Ignition in a Homogeneous Charge Compression Ignition Engine, submitted to the 2004 SAE World Congress, Detroit, USA, March 8 – 11 (2004).

3)

F. Winter, M. Lackner, A. Hultqvist, Laser diagnostics applied to an internal combustion engine operating in HCCI mode, submitted to the Scandinavian Nordic – Italian Sections of the Combustion Institute Joint Meeting 2003, Ischia, Italy, September 18-21 (2003).

## VIII. Collaborations

In the course of the research activities carried out and presented in this thesis several national and international cooperations were started and continued.

1)

Institute: Institut für Festkörperelektronik, Vienna University of Technology,  
Floragasse 7 / 362, A-1040 Wien, Austria

Professor: Dr. Gottfried Strasser

Homepage: <http://www.fke.tuwien.ac.at/>

Duration: Summer 2002

Description: A quantum cascade laser (QCL) at 11.4  $\mu\text{m}$  provided by the partner institute was used for spectroscopic investigations. A joint journal publication was made. Due to the need for cryogenic cooling of the QCL, which restricts its use to controlled laboratory environments, the program was finished.

2)

Institute: Sarnoff Corporation, Inc., Princeton Lightwave, Inc. 2601 Route 130 South  
Cranbury, NJ 08512, USA

Contact: Dr. D. Z. Garbuzow, Dr. M. A. Maiorow

Homepage: <http://www.princetonlightwave.com/>

Duration: Summer 1999 - summer 2002

Description: Edge emitting diode lasers (2.3 and 2.55  $\mu\text{m}$ ) were obtained from the partner institute. Several joint publications were made. The cooperation was started by Dr. Gerhard Totschnig, the lasers are still in use.

3)

Institute: Institut für Photonik, Vienna University of Technology, Gußhausstr. 25-29,  
A-1040 Wien, Austria

Professor: Dr. Ernst Wintner

Homepage: <http://info.tuwien.ac.at/photonik/>

Duration: Autumn 2000 -

Description: A joint FFF funded research project (grant 803050) on laser-induced ignition was carried out successfully. The project terminated in April 2003, however, a new, bigger project (A3) was annexed (running at the time being). The cooperation was started by Prof. Dr. Winter. The partner institute is responsible for laser-induced ignition, our institute does concurrent laser diagnostics for understanding the ignition process.

4)

Company: Jenbacher AG, Achenseestraße 1-3, 6200 Jenbach, Austria

Contact: Dr. Günther Herdin, Dipl.-Ing. Johann Klausner

Homepage: <http://www.jenbacher.com/>

Duration: Autumn 2000 -

Description: Based on the FFF research project (grant 803050) and the continuing A3 project mentioned in 3) Jenbacher AG was an industrial partner for whom research on laser diagnostics for laser-induced ignition was done. The main goal was to develop a technique for *in-situ* species concentration measurements at high pressures in engines and under engine like conditions.



5)

Institute: Institut für Experimentalphysik, Technische Universität Graz  
Petersgasse 16, A-8010 Graz, Austria

Professor: Dr. Theo Neger

Homepage: <http://iep.tu-graz.ac.at/>

Duration: Summer 2002 -

Description: The partner institute is also involved in the joint FFF funded research project (grant 803050) and the A3 project. The main research interest is laser-induced fluorescence (LIF). Two joint publications (one journal (submitted), one conference) were made. In contrast to TDLAS, LIF is not quantitative. A potential idea for the future is to combine our TDLAS with their LIF to obtain two dimensional, quantitative results.

6)

Institute: Walter Schottky Institute, Munich University of Technology

Professor: Dr.-Ing. Markus-Christian Amann

Homepage: <http://www.wsi.tu-muenchen.de/E26/index.htm>

Start: Spring 2001 -

The research group of Prof. Amann is leading in the development of long wavelength VCSELs. VCSELs from the partner institute have been obtained for TDLAS test setups. Also, a research stay in Munich took place in autumn 2001. Several joint publications have been written.

7)

Institute: Department of heat and power generation, Lund Institute of Technology, Box 118, S22100 Lund, Sweden

Professor: Dr. Anders Hultqvist

Homepage: <http://www.vok.lth.se/en/index.htm>

<http://www.forbrf.lth.se/lsf/facilities.htm>

<http://www.forbrf.lth.se/combustion-center/ice.htm>

Start: Spring 2003 -

In autumn 2002, a research proposal was submitted to the EU for the funding of a research stay at the Lund combustion center where optical diagnostics can be performed in internal combustion engines. The proposal was accepted. In May 2003, VCSELs were deployed for *in-situ* species concentration measurements ( $\text{CH}_4$ ,  $\text{CO}_2$ ) in an internal combustion engine. A continuing cooperation and joint publications are planned.

8)

Institute: Paul Scherrer Institute (PSI), Villigen, Switzerland.

Professor: Dr. Wolfgang Kreutner

Homepage: <http://cdg.web.psi.ch/>

Start: Summer 2002 -

Based in the research in this thesis, a START and an FWF proposal were submitted in autumn 2003 concerning fundamental combustion and pollutant formation research in a high pressure flat flame burner installation. A similar unit is located at the PSI. The project was discussed at the PSI with Dr. Kreutner who gave valuable advice concerning the planned installations. Joint measurements are planned.

## IX. Nomenclature

### Acronyms

ACC	active combustion control
ACE	active combustion enhancement
AIC	active instability control
AIT	auto ignition temperature
BTJ	buried tunnel junction
CA	crank angle
CB	conduction band
CCD	charged coupled device
CEAS	cavity enhanced absorption spectroscopy
CFT	cool flame temperature
CI	compression ignition
CR	compression ratio
CRD	cavity ring-down spectroscopy
CVD	chemical vapor deposition
cw	continuous wave
DBR	distributed Bragg reflector
DFB	distributed feed back
ECDL	external cavity diode laser
EEL	edge emitting laser
EGR	exhaust gas recirculation
EOM	electro optic modulator
FBC	fluidized bed combustion
FBC	fluidized bed combustor
FIR	far infrared
FT	Fourier transform
FMS	frequency modulation spectroscopy
FP	Fabry Perot
FSI	fuel stratified injection
FSR	free spectral range [ $s^{-1}$ ]
FTIR	Fourier transform infrared (spectroscopy)
FWHM	full width half maximum [ $cm^{-1}$ ]
GRI	Gas Research Institute
HCCI	homogeneously charged compression ignition
HITRAN	high resolution transmission (spectroscopic database)
HWHM	half width half maximum [ $cm^{-1}$ ]
ICOS	integrated cavity output spectroscopy
IR	infrared
LASER	light amplification by stimulated emission of radiation
LED	light emitting diode
LIF	laser-induced fluorescence
LPE	liquid phase epitaxy
MBE	molecular beam epitaxy
MIE	minimum ignition energy [mJ]
MIR	middle infrared
MOCVD	metal organic chemical vapor deposition
MPE	minimum pulse energy [mJ]
Nd:YAG	Yttrium Aluminum Garnet ( $Y_3Al_5O_{12}$ ) doped with $Nd^{3+}$

NICE-OHMS	noise-immune, cavity enhanced-optical heterodyne molecular spectroscopy
NIR	near infrared
ON	octane number
OPC	operating point control
OPO	optical parametric oscillator
PLIF	planar laser-induced fluorescence
PLL	phase-lock loop
PPLN	periodically poled lithium niobate
PSD	phase-sensitive detection
QCL	quantum cascade laser
SCR	selective catalytic reduction
SI	spark ignition
SNCR	selective non-catalytic reduction
TDLAS	tunable diode laser absorption spectroscopy
TDLS	tunable diode laser spectroscopy
TEM	transverse electromagnetic mode
UV	ultraviolet
VB	valance band
VCSEL	vertical-cavity surface-emitting laser
VIS	visible
VPE	vapor phase epitaxy
WMS	wavelength modulation spectroscopy

**Roman symbols**

[ ]	molar concentration		[molL <sup>-1</sup> ]
A	absorbance		[1]
A	pre-exponential factor		[Lkg <sup>-1</sup> ]
Abs	absorption		[1]
c	speed of light	3*10 <sup>8</sup>	[m/s]
C	concentration		[molL <sup>-1</sup> ]
d	distance		[m]
D	diffusion coefficient		[s <sup>-1</sup> ]
d	(electrode) gap		[mm]
e	elementary charge	1.602*10 <sup>-19</sup>	[C]
E	energy		[J], [eV]
E	activation energy		[Jmol <sup>-1</sup> ]
f	frequency		[s <sup>-1</sup> ]
F	fraction		[1]
g	degeneracy		[1]
h	Planck's constant	6.63*10 <sup>-34</sup>	[Js]
I	light intensity		[W/m <sup>2</sup> ]
I	current		[A]
J	concentration		[molL <sup>-1</sup> ]
k	Boltzmann constant	1.38*10 <sup>-23</sup>	[J/K]
k	velocity constant		[L <sup>2</sup> mol <sup>-2</sup> s <sup>-1</sup> ]
l, L	path length		[cm], [m]
M	molar mass		[kgmol <sup>-1</sup> ], [amu]
n	number		[1]
n	index of refraction		[1]
n	coefficient of temperature dependence of		

	the air-broadened half width	[1]
N	number population	[1]
P	(partial) pressure	[atm], [bar], [Pa]
Q	partition function	[1]
R	gas constant	8.314 / [J*K <sup>-1</sup> mol <sup>-1</sup> ]
R	reflectivity	[1]
rpm	rotations per minute	
s	speed	[m/s]
S	strength of a transition	[cm/molecule], [cm <sup>2</sup> /atm <sup>-1</sup> ]
T	temperature	[K], [°C]
T	transmittance	[1]
U	break through voltage, potential	[V]

**Greek symbols**

$\alpha_v$	spectral absorption coefficient	[1]
$\varphi$	angle	[°]
$\phi$	fuel equivalence ratio	[1]
$\phi$	line shape function	[cm]
$\gamma$	pressure broadened line half width	[cm <sup>-1</sup> ]
$\nu$	frequency	[s <sup>-1</sup> ], [Hz]
$\lambda$	wave length	[nm], [ $\mu$ m]
$\lambda$	air equivalence ratio (air number)	[1]
$\nu$	mole number	[1]
$\bar{\nu}$	wave number	[cm <sup>-1</sup> ]
$\rho$	density	[kgL <sup>-1</sup> ]
$\chi$	heat transfer coefficient	[Wm <sup>-2</sup> K <sup>-1</sup> ]
$\sigma_v$	absorption cross-section	[cm <sup>2</sup> /molecule]
$\sigma$	standard deviation	
$\tau$	lifetime	[s]
$\omega$	angular frequency	[s <sup>-1</sup> ]
$\Omega$	resistance	[V/A]

**Super- and subscripts**

$\nu$	dependent on the frequency $\nu$
0	initial
D	Doppler
elec	electric
i	i <sup>th</sup> level
ind	induction
L	Lorentzian
rot	rotational
thres	threshold
tot	total
vib	vibrational
V	Voigt
W	wall

**X. References****Introduction**

- [1] Douglas A. Skoog, F. James Holler, Timothy A. Nieman, Principles of Instrumental Analysis, Saunders College Publishing, Harcourt Brace College Publishers, Fifth edition, ISBN 0-03-002078-6 (1998).
- [2] Analytical Chemistry, Edited by R. Kellner, J.-M. Mermet, M. Otto, H. M. Widmer, Wiley-VCH, Weinheim ISBN 3-527-28881-3 (1998).
- [3] Q. V. Nguyen, B. L. Edgar, R. W. Dibble, Experimental and Numerical Comparison of Extractive and In Situ Laser Measurements of Non-Equilibrium Carbon Monoxide in Lean-Premixed Natural Gas Combustion, Combustion and Flame 100, 395-406 (1995).

**Fundamentals: Absorption spectroscopy**

- [4] L. S. Rothman, C. P. Rinsland, A. Goldman, S. T. Massie, D. P. Edwards, J.-M. Flaud, A. Perrin, C. Camy-Peyret, V. Dana, J.-Y. Mandin, J. Schroeder, A. McCann, R. R. Gamache, R. B. Wattson, K. Yoshino, K. V. Chance, K. W. Jucks, L. R. Brown, V. Nemtchinov, P. Varansi, The HITRAN molecular spectroscopic database and HAWKS (HITRAN atmospheric workstation): 1996 edition, J. Quant. Spectrosc. Radiat. Transfer, 60, 665-710 (1998).

<http://www.hitran.com>

<ftp://cfa-ftp.harvard.edu/pub/HITRAN/>

- [5] N. Jacquinet-Husson, E. Ariés, J. Ballard, A. Barbe, G. Bjoraker, B. Bonnet, L. R. Brown, C. Camy-Peyret, J.P. Champion, A. Chédin, A. Chursin, C. Clerbaux, G. Duxbury, J.-M. Flaud, N. Fourrié, A. Fayt, G. Graner, R. Gamache, A. Goldman, V. Golovko, G. Guelachvili, J.M. Hartmann, J.C. Hilico, J. Hillman, G. Lefèvre, E. Lellouch, S.N. Mikhailenko, O.V. Naumenko, V. Nemtchinov, D.A. Newnham, A. Nikitin, J. Orphal, A. Perrin, D.C. Reuter, C.P. Rinsland, L. Rosenmann, L.S. Rothman, N.A. Scott, J. Selby, L.N. Sinitza, J.M. Sirota, A.M. Smith, K.M. Smith, V. G. Tyuterev, R.H. Tipping, S. UrbanY, P. Varanasi, M. Weber, The 1997 spectroscopic GEISA databank, J. Quant. Spectroscopy and Radiative Transfer, 62, 205-254 (1999).

<http://ara.lmd.polytechnique.fr/>

- [6] Brendan M. Quine and James R. Drummond, GENSPECT: a line-by-line code with selectable interpolation error tolerance, Journal of Quantitative Spectroscopy and Radiative Transfer, Volume 74 (2), 147-165 (2002).

- [7] Brassington, D. J., Tunable diode laser absorption spectroscopy for the measurement of atmospheric trace species, Chapter in Advances in Spectroscopy Vol 24, R.E Hester ed., John Willey, 83-148 (1995).

<http://www.huxley.ic.ac.uk/research/AIRPOLL/TDL/adins/ADINS51.htm>

- [8] Peter W. Atkins, Physical Chemistry, sixth edition, Oxford University Press, ISBN: 0198792859 (1999).

[9] Manfred Hesse, Herbert Meier, Bernd Zeeh, Spektroskopische Methoden in der organischen Chemie, Georg Thieme Verlag, 5th edition, Stuttgart, ISBN 3-13-576105-3 (1995).

[10] Demtröder, Wolfgang, Laserspektroskopie, Grundlagen und Techniken, Springer, vierte Auflage, ISBN: 3540642196 (2000).

[11] M. Lackner, F. Winter: What is tuneable diode laser spectroscopy for combustion applications? Combustion File 185, IFRF Online Combustion Handbook, ISSN 1607-9116 (2002).

[12] M. Lackner, F. Winter: How can gas species be measured in high pressure combustion systems using tuneable diode lasers? Combustion File 187, IFRF Online Combustion Handbook, ISSN 1607-9116 (2002).

#### Fundamentals: Diode lasers

[13] Ezekiel, Shaoul (MIT), CLEO 2001 Short Course Notes, SC101, Understanding Lasers, Fiber Optics and the Broadband Revolution, Conference on Lasers and Electro Optics, Baltimore, USA (2001).

[14] Erwin Riedel, Anorganische Chemie, 3<sup>rd</sup> edition, deGryter, ISBN: 3110174391 (1994).

[15] ChemGlobe (Vereinigung der Chemiestudierenden an der ETH Zürich) (2000).  
<http://www.vcs.ethz.ch/chemglobe/ptoe/periodic.gif>

[16] Wintner, Ernst, Semiconductor Lasers, lecture notes, Vienna University of Technology, Vienna, Austria (1996).

[17] Kneubühl, F. K.; Sigrist, M. W., Laser, Teubner Studienbücher Physik, 2. Auflage, ISBN: 3519430320 (1989).

[18] F. Capasso, J. Faist, C. Sirtori and A. Y. Cho, Infrared (4–11  $\mu\text{m}$ ) quantum cascade lasers, Solid State Communications 102 (2-3), 231-236 (1997).

[19] Bahaa E. A. Saleh, Malvin C. Teich, Fundamentals of Photonics, John Wiley & Sons, ISBN: 0471839655 (1991).

[20] Ettenberg, Michael (Sarnoff Corp.), CLEO 2001 Short Course Notes, SC112, Fundamentals of Laser Diodes, Conference on Lasers and Electro Optics, Baltimore, USA (2001).

[21] Markus-Christian Amann, Jens Buus, Yasuharu Suematsu, Tunable Laser Diodes (Artech House Optoelectronics Library), Artech House ISBN: 0890069638 (1998).

#### Fundamentals: Tunable diode laser absorption spectroscopy

[22] Pawel Kluczynski, Åsa M. Lindberg and Ove Axner, Wavelength modulation diode laser absorption signals from Doppler broadened absorption profiles, Journal of Quantitative Spectroscopy and Radiative Transfer, in press (2003).

- [23] M. Gehrtz and G. C. Bjorklund, Quantum limited frequency modulation laser spectroscopy, *Journal of Molecular Structure*, Volume 141, 153-160 (1986).
- [24] G. Totschnig, D.S. Baer, J. Wang, F. Winter, H. Hofbauer and R.K. Hanson, Multiplexed Continuous-Wave Diode-Laser Cavity Ringdown Measurements of Multiple Species, *Appl. Optics* 39, 2009-2016 (2000).
- [25] A. S. -C. Cheung, Tongmei Ma and Hongbing Chen, High-resolution cavity enhanced absorption spectroscopy using an optical cavity with ultra-high reflectivity mirrors, *Chemical Physics Letters*, Volume 353( 3-4), 275-280 (2002).
- [26] H. R. Barry, L. Corner, G. Hancock, R. Peverall and G. A. D. Ritchie, Cavity-enhanced absorption spectroscopy of methane at 1.73  $\mu\text{m}$ , *Chemical Physics Letters*, Volume 333, Issues 3-4, 285-289 (2001).
- [27] Kurt L. Haller & Philip C. D. Hobbs, Double beam laser absorption spectroscopy: shot-noise limited performance at baseband with a novel electronic noise canceller, *Proc SPIE* 1435, 298-309 (1991).
- [28] J. Ye, L.-S. Ma, J. L. Hall, in *Cavity-Ringdown Spectroscopy*, ed. K. W. Busch and M. A. Busch, ACS Symposium Series 720 (1999).
- [29] Pavone, F. S., Inguscio, M., *Appl. Phys. B* 56, 118-122 (1993).
- [30] G. Modugno, C. Corsi, M. Gabrysch, F. Marin, M. Inguscio, Fundamental noise sources in a high-sensitivity two-tone frequency modulation spectrometer and detection of  $\text{CO}_2$  at 1.6  $\mu\text{m}$  and 2  $\mu\text{m}$ , *Applied Physics B (Lasers and Optics)* 67 (3), 289-296 (1998).
- [31] Pawel Kluczynski, Jörgen Gustafsson, Åsa M. Lindberg and Ove Axner, Wavelength modulation absorption spectrometry — an extensive scrutiny of the generation of signals, *Spectrochimica Acta Part B: Atomic Spectroscopy*, Volume 56 (8) 1277-1354 (2001).
- [32] Totaro Imasaka Diode lasers in analytical chemistry, *Talanta*, Volume 48(2), 305-320 (1999).
- [33] A. W. Mantz, A review of spectroscopic applications of tunable semiconductor lasers, *Spectrochimica Acta Part A: Molecular Spectroscopy*, Volume 51(13), 2211-2236 (1995).
- [34] Mantz A. W., A Review of the Applications of Tunable Diode Laser Spectroscopy at High Sensitivity, *Microchemical Journal*, Volume 50 (3), 351-364 (1994).
- [35] K. Uehara, K. Yamamoto, T. Kikugawa, S. Toyoda, K. Tsuji and N. Yoshida, Precise isotope abundance ratio measurement of nitrous oxide using diode lasers, *Sensors and Actuators B: Chemical*, Volume 90(1-3), 250-255 (2003).
- [36] Gary Kidd, An open path  $\text{H}_2\text{O}/\text{CO}_2$  gas analyzer for eddy correlation systems: theory and design, *Spectrochimica Acta Part A: Molecular and Biomolecular Spectroscopy*, Volume 58( 11), 2373-2388 (2002).
- [37] R. Kormann, H. Fischer, C. Gurk, F. Helleis, Th. Klüpfel, K. Kowalski, R. Königstedt, U. Parchatka and V. Wagner, Application of a multi-laser tunable diode laser absorption

spectrometer for atmospheric trace gas measurements at sub-ppbv levels, *Spectrochimica Acta Part A: Molecular and Biomolecular Spectroscopy*, Volume 58 (11), 2489-2498 (2002).

[38] G. Toci, P. Mazzinghi, B. Mielke and L. Stefanutti, An airborne diode laser spectrometer for the simultaneous measurement of H<sub>2</sub>O and HNO<sub>3</sub> content of stratospheric cirrus clouds, *Optics and Lasers in Engineering*, Volume 37 (5), 459-480 (2002).

[39] B. Hanoune, S. Dusanter, L. ElMaimouni, P. Devolder and B. Lemoine, Rate constant determinations by laser photolysis/diode laser infrared absorption: examples of HCO+O<sub>2</sub>→HO<sub>2</sub>+CO and CH<sub>2</sub>OH+O<sub>2</sub>→HCH(O)+HO<sub>2</sub> reactions at 294 K, *Chemical Physics Letters*, Volume 343( 5-6) 527-534 (2001).

[40] P. B. Davies, Diode laser absorption spectroscopy of free radicals, ions and transient molecules, *Spectrochimica Acta Part A: Molecular and Biomolecular Spectroscopy*, Volume 55(10), 1987-1997 (1999).

[41] Douglas S. Baer and Ronald K. Hanson, Tunable diode laser absorption diagnostics for atmospheric pressure plasmas, *Journal of Quantitative Spectroscopy and Radiative Transfer*, Volume 47(6) 455-475 (1992).

[42] S.T. Sanders, J. Wang, J.B. Jeffries, and R.K. Hanson, VCSEL Absorption Sensor for Line-of-sight Temperature Distributions, *Applied Optics* 40, 4404-4415 (2001).

[43] Lars Sandström and Donald Malmberg, On-line and in situ monitoring of oxygen concentration and gas temperature in a reheating furnace utilizing tunable diode-laser spectroscopy, *Spectrochimica Acta Part A: Molecular and Biomolecular Spectroscopy*, Volume 58( 11), 2449-2455 (2002).

[44] W. Gurlit, J. P. Burrows, H. Burkhard, R. Böhm, V. M. Baev and P. E. Toschek, Intracavity diode laser for atmospheric field measurements, *Infrared Physics & Technology*, Volume 37(1), 95-98 (1996).

#### Fundamentals: Combustion

[45] Warnatz, J.; Maas, U.; Dibble, R. W., *Combustion: Physical and Chemical Fundamentals, Modeling and Simulation, Experiments, Pollutant Formation*, Springer, Berlin, Third Edition (2001).

[46] Warnatz, J.; Maas, U.; Dibble, R. W., *Combustion: Physical and Chemical Fundamentals, Modeling and Simulation, Experiments, Pollutant Formation*, Springer, Berlin, Second Edition (1999).

[47] T.B. Hunter, H.Wang, T.A. Litzinger, and M. Frenklach, The Oxidation of Methane at Elevated Pressures: Experiments and Modeling, *Combust. Flame* 97:201 (1994).

[48] Gardiner, W. C., *Gas-Phase Combustion Chemistry*, Springer, ISBN: 0387988610 (2000).

[49] Hanna, M.; Karim, G. A., The Combustion of Lean Mixtures of Methane and Air-A Kinetic Investigation, *Transactions of the ASME*, Vol. 108, 336-342 (1986).



[50] M. Frenklach, H. Wang, C.-L. Yu, M. Goldenberg, C.T. Bowman, R.K. Hanson, D.F. Davidson, E.J. Chang, G.P. Smith, D.M. Golden, W.C. Gardiner and V. Lissianski, and Gas Research Institute Topical Report: M. Frenklach, H. Wang, M. Goldenberg, G.P. Smith, D.M. Golden, C.T. Bowman, R.K. Hanson, W.C. Gardiner and V. Lissianski, 'GRI-Mech---An Optimized Detailed Chemical Reaction Mechanism for Methane Combustion,' Report No. GRI-95/0058 (1995).

[http://www.me.berkeley.edu/gri\\_mech/](http://www.me.berkeley.edu/gri_mech/)

[51] Hughes, K. J.; Turányi, T.; Clague, A.; Pilling, M. J., Development and testing of a comprehensive chemical mechanism for the oxidation of methane; *Int. J. Chem. Kinet.*, 33, 9, 513-538 (2001).

[52] Sher, E.; Refael, S., Numerical Analysis of the early Phase Development of spark-ignited flames in CH<sub>4</sub>-air Mixture, Nineteenth Symposium (International) on Combustion/ The Combustion Institute, 251-257 (1982).

[53] Glarborg, P.; Lilleheie, N. I.; Byggstoyl, S.; Magnussen, B. F.; Kilpinen, P.; Hupa, M., A Reduced Mechanism for Nitrogen Chemistry in Methane Combustion, Twenty-Fourth Symposium (International) on Combustion/ The Combustion Institute, 889-898 (1992).

[54] Pfefferle, L.; Churchill, S., The constant-pressure ignition characteristics of ethane-methane-air mixtures; *Chem. Phys. Proc. Comb.*, 37-1 – 37-5 (1982).

[55] Ma, Jian X.; Alexander, D. R.; Poulain, D. E., Laser Spark Ignition and Combustion Characteristics of Methane-Air Mixtures, *Combustion and Flame* 112: 492-506 (1998).

[56] Bauerle, G. L.; Lott, J. L.; Slipecevic, C. M., Oxidation of methane at elevated pressures, ignition delay, *Fire & Flammability*, Vol. 5 (1974).

#### Fundamentals: Ignition

[57] Reid, I. A. B.; Robinson, C.; Smith, D. B., Spontaneous ignition of methane: Measurement and chemical model, Twentieth Symposium on Combustion/The Combustion Institute; 1833-1843 (1984).

[58] Caron, M.; Goethals, M.; De Smedt, G.; Berghmans, J.; Vliegen, S.; Van't Oost, E.; van den Aarssen, A., Pressure dependence of the auto-ignition temperature of methane/air mixtures, *Journal of Hazardous Materials A65*, 233-244 (1999).

[59] A. A. Pekalski, J. F. Zevenbergen, H. J. Pasman, S. M. Lemkowitz, A. E. Dahoe and B. Scarlett, The relation of cool flames and auto-ignition phenomena to process safety at elevated pressure and temperature, *Journal of Hazardous Material*, 93 (1), 93-105 (2002).

#### Fundamentals: Laser-induced ignition

[60] Phuoc, Tran X.; White, F. P., Laser-Induced Spark Ignition of CH<sub>4</sub>/Air Mixtures, *Combustion and Flame* 119: 203-216 (1999).

[61] Morsy, M. H.; Chung, S. H., Numerical Simulation of Front Lobe Formation in Laser-Induced Spark Ignition of CH<sub>4</sub>/Air Mixtures, The Twenty-ninth International Symposium on Combustion, July 2002, Sapporo, Japan, in press (2002).

[62] Rüdissler, D.; Iskra, K.; Neger, T., (Title of Rüdissler's diploma thesis: Raum- und zeitaufgelöste optische Diagnostik Laser-gezündeter Gasgemische mit planarer Laser-induzierter Fluoreszenz, Graz University of Technology) private communication (2002).

[63] Phuoc, Tran X., Laser spark ignition: experimental determination of laser-induced breakdown thresholds of combustion gases, *Optics Communications* 175, 419-423 (2000).

[64] Phuoc, Tran X., Single-Point Versus Multi-Point Laser Ignition: Experimental Measurements of Combustion Times and Pressures, *Combustion and Flame* 122: 508-510 (2000).

[65] Weinberg, F. J.; Wilson, J. R., A preliminary investigation of the use of focused laser beams for minimum ignition energy studies, *Proc. Roy. Soc. Lond. A.* 321, 41-52 (1971).

[66] Lewis, B.; Von Elbe, G., *Combustion, Flames and Explosions of Gases*, Academic Press Inc, Third edition (1987).

[67] Lee, Tae-Woo; Jain, V.; Kozola, S., Measurements of Minimum Ignition Energy By Using Laser Sparks for Hydrocarbon Fuels in Air: Propane, Dodecane, and Jet-A Fuel; *Combustion and Flame*, 125, 1320-1328 (2001).

[68] H. Kopecek, H. Maier, G. Reider, F. Winter and E. Wintner, Laser ignition of methane-air mixtures at high pressures, *Experimental Thermal and Fluid Science*, Volume 27(4), 499-503 (2003).

[69] Ballal, D. R.; Lefebvre, A. H, Ignition and flame quenching in flowing gaseous mixtures, *Proc. R. Soc. Lond. A.* 357, 163-181 (1977).

[70] Frendi, A., and Sibulkin, M., Dependence of Minimum Ignition Energy on the Ignition Parameters, *Combustion Science and Technology*, Vol. 73, 395 (1990).

[71] Morsy, M. H.; Ko, Y. S.; Chung, S. H.; Cho, P., Laser-Induced Two-point Ignition of Premixture with a Single-Shot Laser, *Combustion and Flame* 125: 724-727 (2001).

[72] Ronney, P. D., *Laser versus Conventional Ignition of Flames*, SPIE Symposium on Laser Applications in Combustion and Combustion Diagnostics, Los Angeles, USA (1992).

[73] Landolt-Börnstein, H., *Zahlenwerte und Funktionen aus Physik, Chemie, Astronomie, Geophysik und Technik*, Springer, Berlin, Sixth Edition (1957).

#### Fundamentals: Internal combustion engines

[74] X. Qin, H. Kobayashi, T. Niioka, *Experimental Thermal and Fluid Science* 21 58-63 (2000).

[75] H. Kobayashi, Experimental study of high-pressure turbulent premixed flames, *Experimental Thermal and Fluid Science* 26, 375-387 (2002).

[76] G. H. Abd Alla Computer simulation of a four stroke spark ignition engine, *Energy Conversion and Management* 43 (8), 1043-1061(2002).

- [77] F. N. Egofofopoulos, *Energy Conversion and Management* 42, 21-34 (2001).
- [78] Cornel Stan, *Direct Injection Systems for Spark-Ignition and Compression- Ignition Engines*, SAE International, ISBN Number: 0-7680-0610-4 (2000).
- [79] Tatsushi Nakashima, Masatoshi Basaki, Kimitaka Saito and Shigeo Furuno, *New concept of a direct injection SI gasoline engine: a study of stratified charge combustion characteristics by radical luminescence measurement*, *JSAE Review*, Volume 24 (1)17-23 (2003).
- [80] Shigeo Furuno, Satoshi Iguchi and Tokuta Inoue, *Lean combustion characteristics of locally stratified charge mixture: Basic studies of in-vessel combustion ignited by laser*, *JSAE Review*, Volume 16 (4) 357-361 (1995).
- [81] R. P. Roethlisberger and D. Favrat, *Comparison between direct and indirect (prechamber) spark ignition in the case of a cogeneration natural gas engine, part I: engine geometrical parameters*, *Applied Thermal Engineering*, Volume 22( 11) 1217-1229 (2002).
- [82] J. De Witt, *Development of gas engines for stationary applications (combined heat and power)*, *Fuel and Energy Abstracts*, Volume 37 (4) 292 (1996).
- [83] A. Henham and M. K. Makkar, *Combustion of simulated biogas in a dual-fuel diesel engine*, *Energy Conversion and Management*, Volume 39 (16-18), 2001-2009 (1998).
- [84] Michel Molière, *Stationary gas turbines and primary energies: A review of fuel influence on energy and combustion performances*, *International Journal of Thermal Sciences*, Volume 39 (2) 141-172 (2000).
- [85] P. A. Pilavachi, *Mini- and micro-gas turbines for combined heat and power*, *Applied Thermal Engineering*, Volume 22 (18), 2003-2014 (2002).
- [86] Anders Hultqvist, *Characterization of the Homogeneous Charge Compression Ignition Combustion Process*, Dissertation, Division of Combustion Engines, Lund Institute of Technology, Lund, Sweden (2002).
- [87] Mattias Richter, Axel Franke, Marcus Alden, Anders Hultqvist, Bengt Johansson, *Optical Diagnostics Applied to a Naturally Aspirated Homogeneous Charge Compression Ignition Engine*, SAE 1999-01-3649, SAE International Fall Fuels & Lubricants Meeting and Exposition, Toronto, Canada (1999).
- [88] Taichi Ando, Yusuke Isobe, Daisuke Sunohara, Yasuhiro Daisho and Jin Kusaka *Homogeneous charge compression ignition and combustion characteristics of natural gas mixtures: the visualization and analysis of combustion*, *JSAE Review*, Volume 24 (1) 33-40 (2003).
- [89] John E. Dec, Peter Kelly-Zion, *HCCI Combustion Fundamentals: In-Cylinder Diagnostics and Kinetic-Rate Computations*, Diesel Engine Emissions Reduction Workshop - DEER 2000, San Diego, USA (2000).
- [90] John B. Heywood, *Internal Combustion Engine Fundamentals*, McGraw-Hill, Inc., ISBN 007028637X (1988).

- [91] Mohamed Y. E. Selim, Effect of exhaust gas recirculation on some combustion characteristics of dual fuel engine, *Energy Conversion and Management*, Volume 44 (5), , 709-723 (2003).
- [92] G. H. Abd-Alla, Using exhaust gas recirculation in internal combustion engines: a review, *Energy Conversion and Management*, Volume 43 (8), 1027-1042 (2002).
- [93] Grigorios C. Koltsakis and Anastasios M. Stamatelos, Catalytic automotive exhaust aftertreatment, *Progress in Energy and Combustion Science*, Volume 23 (1), 1-39 (1997).
- [94] W. Marrecau, Diesel exhaust particulate filter system (patent WO 01 / 14696), *Membrane Technology*, Issue 136 (2001).
- [95] Eran Sher, *Handbook of Air Pollution from Internal Combustion Engines, Pollutant Formation and Control*, Academic Press Inc., ISBN: 0126398550 (1998).

#### Fundamentals: Combustion control

- [96] J. T. Woestman, E. M. Logothetis, *The Industrial Physicist*, 20-24 (1995).
- [97] Nicolas Docquier, Sébastien Candel, Combustion control and sensors: a review, *Progress in Energy and Combustion Science* 28, 107-150 (2002).
- [98] Wei Li, Xiaoguang Chang, A neuro-fuzzy controller for a stoker-fired boiler, based on behaviour modelling, *Control Engineering Practice* 7, 469-481 (1999).
- [99] Yuichi Miyamoto, Yoshimitsu Kurosaki, Hitoshi Fujiyama, Eiichiro Nanbu, Dynamic characteristic analysis and combustion control for a fluidized bed incinerator, *Control Engineering Practice* 6, 1559-1168 (1998).
- [100] Wei Li, Xiaoguang Chang, Application of hybrid fuzzy logic proportional plus conventional integral-derivative controller to combustion control of stoker-fired boilers, *Fuzzy Sets and Systems* 111, 267-284 (2000).
- [101] W. C. Chen, Ni-Bin Chang, Jeng-Chung Chen, GA-based fuzzy neural controller design for municipal incinerators, *Fuzzy Sets and Systems* 129, 343-369 (2002).
- [102] Ismael Prieto-Fernandez, J. Carlos Luengo-Garcia, Manuela Alfonso-Hidalgo, Daniel Ponte-Gutierrez, Generating a representative signal of coal moisture content to anticipate combustion control in thermal power stations, *Fuel Processing Technology* 76, 241-255 (2002).
- [103] Dale M. Brown, Evan Downey, Jim Kretchmer, Gerald Michon, Emily Shu, Don Schneider, SiC Flame Sensors for Gas Turbine Control Systems, *Solid-State Electronics Vol. 42(5)*, 755-761 (1998).
- [104] Edward R. Furlong, Douglas S. Baer, Ronald K. Hanson, Real-Time Adaptive Combustion Control Using Diode-Laser Absorption Sensors, 27<sup>th</sup> Symposium (International) on Combustion/The Combustion Institute, Boulder, 103-111 (1998).

- [105] M. G. Allen, Sensors and Actuator For Gas Turbine Combustion Control, MITE Workshop on Goals and Technologies for Future Gas Turbines, Georgia Institute of Technology, USA (2000).
- [106] Furlong, E. R., Baer, D. S., and Hanson, R. K., Combustion Control Using a Multiplexed Diode Laser Sensor System. Paper no. AIAA 96-0756 at the 34<sup>th</sup> Aerospace Sciences Meeting, January 15-18, Reno, NV, USA (1996).
- [107] Baer, D. S., Furlong, E. R., and Hanson, R. K., Combustion Control Using a Multiplexed Diode Laser Sensor System. presented at SPIE at Photonics West, January 1996, San Jose, CA. Sciences Meeting, January 15-18, Reno, NV, USA (1996).
- [108] Doug Hodgson, Bill Olsen (ILX Lightwave, Inc.), Laser diode protection strategies, Application note No. 3 (2000).  
<http://www.ilxlightwave.com/>
- [109] Wavelength Electronics, Inc., Optimizing thermoelectric temperature control systems, Technical note 201 (1995).  
<http://www.wavelengthelectronics.com>
- [110] IEC 60825-1: Safety of laser products - Part 1: Equipment classification, requirements and user's guide IEC, International Electrotechnical Commission (2001).  
<http://www.iec.ch/>

**Laser systems: Edge emitters 2.3 – 2.55  $\mu\text{m}$**

- [111] D. Garbuzov, R. Menna, M. Maiorov, H. Lee, V. Khalfin, L. DiMarco, D. Capewell, R. Martinelli, G. Gelenky, J. Connolly; 2.3 – 2.7  $\mu\text{m}$  Room Temperature CW-Operation of InGaAsSb/AlGaAsSb Broad-Contact and Single-Mode Ridge-Waveguide SCH-QW Diode Lasers, Proceedings of SPIE, vol. 3628, 124-129 (1999).
- [112] D. V. Donetsky, D. Westerfeld, G. L. Belenky, R. U. Martinelli, D. Z. Garbuzov, J. C. Connolly; Extraordinarily wide optical gain spectrum in 2.2-2.5  $\mu\text{m}$  In(Al)GaAsSb/GaSb quantum-well ridge-waveguide lasers, Journal of Applied Physics, Volume 90 (8) (2001).

**Laser systems: Quantum cascade laser at 11.4  $\mu\text{m}$**

- [113] J. Faist, F. Capasso, D. L. Sivco, C. Sirtori, A. L. Hutchinson, and A. Y. Cho, Science 264, 553 (1994).
- [114] S. Anders, W. Schrenk, E. Gornik, and G. Strasser, Appl. Phys. Lett. 80, 1864 (2002).
- [115] C. Pflügl, W. Schrenk, S. Anders, C. Becker, C. Sirtori, G. Strasser, High temperature performance of GaAs-based chirped superlattice quantum cascade lasers, to be published (2003).
- [116] Ghislain Blanquet, Jacques Walrand and Jean-Pierre Bouanich, Journal of Molecular Spectroscopy 201, 56 (2000).

**Laser systems: VCSEL at 761 nm**

[117] V. Weldon, J. O'Gorman, J. J. Pérez-Camacho, D. McDonald, J. Hegarty, J. C. Connolly, N. A. Morris, R. U. Martinelli and J. H. Abeles, Laser diode based oxygen sensing: A comparison of VCSEL and DFB laser diodes emitting in the 762 nm region, *Infrared Physics & Technology* 38, 325-329 (1997).

[118] G. Totschnig, Development of diode laser systems for *in-situ* combustion diagnostics and trace-gas sensing, PhD thesis, Vienna University of Technology, Vienna, Austria (2002).

**Laser systems: Long wavelength VCSELs**

[119] M. Ortsiefer, R. Shau, G. Böhm, F. Köhler, M.C. Amann, Low-threshold index-guided 1.5  $\mu\text{m}$  long-wavelength vertical-cavity surface-emitting laser with high efficiency, *Appl. Phys. Lett.* 76, 2179 (2000).

[120] M. Lackner, G. Totschnig, F. Winter, R. Shau, J. Roskopf, M. Ortsiefer, M.C. Amann, Spektroskopischer Einsatz neuer, langwelliger (bis 2  $\mu\text{m}$ ) Diodenlaser (VCSEL) für schwierige Bedingungen, *Technisches Messen* 70(6), 294-305 (2003).

[121] M. Ortsiefer, R. Shau, G. Böhm, F. Köhler, G. Abstreiter, M.-C. Amann, Low resistance InGa(Al)As tunnel junctions for long wavelength vertical-cavity surface-emitting lasers, *Jpn. J. Appl. Phys.* 39, 1727-1729 (2000).

[122] R. Shau, M. Ortsiefer, J. Roskopf, G. Bohm, F. Kohler, M.C. Amann, Vertical-cavity surface-emitting laser diodes at 1.55  $\mu\text{m}$  with large output power and high operation temperature, *Electron. Lett.* 37, 1295-1296 (2001).

[123] M. Ortsiefer, R. Shau, G. Bohm, M. Zigl drum, J. Roskopf, M.C. Amann, 90 degrees C continuous-wave operation of 1.83  $\mu\text{m}$  vertical-cavity surface-emitting lasers, *IEEE Photon. Technol. Lett.* 12, 1435-1437 (2000).

[124] J. Wang, S.T. Sanders, J.B. Jeffries, R.K. Hanson, Oxygen measurements at high pressures with vertical cavity surface emitting lasers, *Appl. Phys. B.* 72, 865 (2001).

[125] G. Modugno, C. Corsim M. Gabrysch, M. Inguscio, Detection of H<sub>2</sub>S at the ppm level using a telecommunication diode laser, *Optics communications* 4755, 76-80 (1998).

**Applications: Burning single fuel particle**

[126] J. Huang, A. P. Watkinson, Coal gasification in a stirred bed reactor, *Fuel and Energy Abstracts*, Volume 38, Issue 3, 152 (1997).

[127] H. Chen, Experimental research on combustion characteristics of pulverized-coal fluidized bed, *Fuel and Energy Abstracts*, Volume 38, Issue 6, 422 (1997).

[128] J. P. Jacobs, The future of fluidized-bed combustion, *Chemical Engineering Science* 54, 5559-5563 (1999).

[129] E.R. Furlong, R.M. Mihalcea, M.E. Webber, D.S. Baer and R.K. Hanson, Diode Laser Sensor System for Closed-Loop Control of a 50-kW Incinerator, paper AIAA-97-2833 at 33rd Joint Propulsion Conference, Seattle, WA (1997).

- [130] Löffler, G., Wartha, C., Winter, F., Hofbauer, H., NO<sub>x</sub> and N<sub>2</sub>O Formation Mechanisms – A Detailed Chemical kinetic Modeling Study on a Single Fuel Particle in a Laboratory-Scale Fluidized Bed, *J. Energy Res. Techn.* 123(3), 228-235 (2001).
- [131] Merrick, D., Mathematical Models of the Thermal Decomposition of Coal: 1. The Evolution of Volatile Matter, *Fuel*, 62, 534-539 (1983).
- [132] Loison, R., Chauvin, R., Pyrolyse Rapide Carbon, *Chem. Ind.*, 91, 269-275 (1964).
- [133] van den Bleek, C.M.; Brem, G.; Grubor, B.; Johnsson, J.E.; Jones, R.F.; Langer, V.; Verwey, N., Documentation of the IEA-AFBC model, Version 1.1, G. Brem, (Ed.), TNO Apeldorn, The Netherlands (1990).
- [134] Niksa, S., Kerstein, A.R., FLASHCHAIN Theory for Rapid Coal Devolatilization Kinetics. 1. Formulation, *Energy Fuels*, 5, 647-665 (1991).
- [135] Winter, F., Wartha C., Hofbauer H., *Bioresource Technology* 70, 39-49 (1999).
- [136] Hayhurst, A. N., Parmar, M. S., *Chem. Eng. Sci.* 53, 427-438 (1998).
- [137] Zeng, T., Fu, W. B., *Combustion and Flame* 107, 197-210 (1996).
- [138] Basu, P., Broughton, J., Elliott, D. E., Fluidized Combustion, *Inst. Fuel Symp.* 1, A3-1 to A3-10 (1975).
- [139] Di Blasi, C., Branca, C., Santoro, A., Perez Bermudez, P. A., *Journal of Analytical and Applied Pyrolysis* 57, 77-90 (2001).
- [140] Castaldi, M., Vincitore, A. M., Senkan, S. M., *Combustion Science and Technology* 107, 1-19 (1995).
- [141] Winter, F.; Prah, M.E.; Hofbauer, H., Intra-Particle Temperatures under Fluidized Bed Combustor Conditions: The Effect of Drying, Devolatilization and Char Combustion, *Combust. Flame*, Vol. 108, 302-314 (1997).
- [142] Löffler, G., Winter, F., Hofbauer, H.; Parametric Modeling Study of Volatile Nitrogen Conversion to NO and N<sub>2</sub>O during Biomass Combustion, *Progress in Thermochemical Biomass Conversion*, A.V. Bridgewater (Ed.), Blackwell Science, Oxford, UK, 641-655 (2001).
- [143] Wartha, C., An Experimental Study on Fuel-Nitrogen Conversion to NO and N<sub>2</sub>O and on Carbon Conversion under Fluidized Bed Conditions, Ph.D. Thesis, Vienna University of Technology, Vienna, Austria (1998).

**Applications: Laser ignition and diagnostics**

- [144] F. Grisch, P. Bouchardy and W. Clauss, CARS thermometry in high pressure rocket combustors, *Aerospace Science and Technology*, in press (2003).

- [145] Yukihiro Okumura, Yuriko Sugiyama and Ken Okazaki, Evolution prediction of coal-nitrogen in high pressure pyrolysis processes, *Fuel*, Volume 81(18), 2317-2324 (2002).
- [146] V. I. Vedeneev, V. S. Arutyunov, N. Yu. Krymov, P. M. Cherbakov and A. D. Sedykh, *Catalysis Today* 13 (4), 613-616 (1992).
- [147] U. E. Meier, D. Wolff-Gaßmann, W. Stricker, *Aerosp. Sci. Technol.* 4, 403-414 (2000).
- [148] C. Arcoumanis, H. G. Green, J. Whitelaw, *Expts Fluids*, 3, 270-276 (1985).
- [149] S. C. Johnston, SAE Paper, No. 790433 (1979).
- [150] P. Andresen, G. Meijer, H. Schluter, H. Voges, A. Koch, W. Hentschel, W. Oppermann, E. Rothe, *Applied Optics*, 29, 2392-2404 (1990).
- [151] T. A. Spiglanin, A. McIlroy, E. W. Fournier, R. B. Cohen, J. A. Syage, *Combustion and Flame*, 102, 310-328 (1995).
- [152] Sadami Yoshiyama, Yoshisuke Hamamoto, Eiji Tomita and Ken-Ichi Minami, *JSAE Review*, 17, 339-345 (1996).
- [153] Eiji Tomita, Nobuyuki Kawahara, Sadami Yoshiyama, Akihik Kakuho, Teruyuki Itoh and Yoshisuke Hamamoto, 29<sup>th</sup> International Symposium on Combustion, Sapporo, Japan, in press (2002).
- [154] Tran X. Phuoc, C. M. White, D. H. McNeill, *Optics and Lasers in Engineering* 38, 217-232 (2002).
- [155] T. Matsui, T. Tanaka, S. Ohigashi; SAE Paper, No. 790483 (1979).
- [156] U. Spicher, G. Schmitz, H. P. Kollmeiner; SAE Paper, No. 881637 (1988).
- [157] H. Shoji, T. Shimizu, K. Toshida, A. Saima, SAE Paper, No. 952407 (1995).
- [158] D. Sauvage, A. Breskin and R. Chechik, A systematic study of the emission of light from electron avalanches in low-pressure TEA and TMAE gas mixtures, *Nuclear Instruments and Methods in Physics Research Section A: Accelerators, Spectrometers, Detectors and Associated Equipment*, Volume 275(2), 15, 351-363 (1989).
- [159] J. D. Dale, M. D. Checkel, P. R. Smy, *Prog. Energy Combust. Sci.* 23, 379-398 (1997).
- [160] C. Robinson and D. B. Smith, *Journal of Hazardous Materials* 8 (3), 199-203 (1984).
- [161] M. Caron, M. Goethals, G. De Smedt, J. Berghmans, S. Vliegen, E. Van't Oost and A. van den Aarssen, *Journal of Hazardous Materials* 65 (3), 233-244 (1999).
- [162] M. Jazbec, D. F. Fletcher and B. S. Haynes, *Applied Mathematical Modelling* 24 (8-9), 689-696 (2000).
- [163] C. M. Ho, *Chem. Phys. Proc. Comb.*, 78, 1-4 (1989).



- [164] H. Östmark, M. Carlson and K. Ekvall, *Combustion and Flame*, 105, 381-390 (1996).
- [165] J. D. Dale, P. R. Smy, R. M. Clements, SAE Paper, No. 780329 (1978).
- [166] H. Östmark, H. Bergman and K. Ekvall, *Journal of Analytical and Applied Pyrolysis*, 24, 163-178 (1992).
- [167] C. Domingo, T. de los Arcos, A. Ainetschian, M. M. Sanz and I. Tanarro, *Vibrational Spectroscopy*, in press (2002).
- [168] I. Tanarro, M. M. Sanz, C. Domingo, D. Bermejo, J. Santos, and J. L. Domenech, *The Journal of Physical Chemistry*, 98, 5862 – 5866 (1994).
- [169] B. Raffel, J. Wolfrum, *Ber. Bunsenges. Phys. Chem.* 90, 997-1001 (1986).
- [170] S. T. Sanders, D. W. Mattison, J. B. Jeffries, and R. K. Hanson, *Optics Letters*, 26, 1568-1570 (2001).
- [171] S. T. Sanders, D. W. Mattison, J. B. Jeffries, R. K. Hanson, 29<sup>th</sup> International Symposium on Combustion, Sapporo, Japan, in press (2002).
- [172] J. P. Chen, X. W. Ni, J. Lu, B. M. Bian, *Optics Communications*, 176, 437-440 (2000).
- [173] Tran X. Phuoc, Fredrick P. White, 29<sup>th</sup> International Symposium on Combustion, Sapporo, Japan, in press (2002).
- [174] Chiaramonti D, Bonini M, Fratini E, Tondi G, Gartner K, Bridgwater AV, Grimm HP, Soldaini I, Webster A, Baglioni P. Development of emulsions from biomass pyrolysis liquid and diesel and their use in engines – Part 1: emulsion production. *Biomass and Bioenergy*, in press (2003).
- [175] Chiaramonti D, Bonini M, Fratini E, Tondi G, Gartner K, Bridgwater AV, Grimm HP, Soldaini I, Webster A, Baglioni P. Development of emulsions from biomass pyrolysis liquid and diesel and their use in engines – Part 2: tests in diesel engines. *Biomass and Bioenergy*, in press (2003).
- [176] Rubab S, Kandpal C. A methodology for financial evaluation of biogas technology in India using cost functions. *Biomass and Bioenergy* 10(1), 11-23 (1996).
- [177] Van den Broek R, Faaij A, Van Wijk A. Biomass combustion for power generation. *Biomass and Bioenergy*, 11(4), 271-281 (1996).
- [178] Yoshida Y, Dowaki K, Matsumura Y, Matsushashi R, Li D, Ishitani H, Komiyama H. Comprehensive comparison of efficiency and CO<sub>2</sub> emissions between biomass energy conversion technologies – position of supercritical water gasification in biomass technologies. *Biomass and Bioenergy*, in press (2003).
- [179] Omer AM, Fadalla Y. Biogas energy technology in Sudan. *Renewable Energy* 28, 499-507 (2003).

- [180] Kaygusuz K, Türker MF. Biomass energy potential in Turkey. *Renewable Energy* 26, 661-678 (2002).
- [181] Akinbami JFK, Ilori MO, Oyebisi TO, Akinwumi IO, Adeoti O. Biogas energy use in Nigeria: current status, future prospects and policy implications. *Renewable and Sustainable Energy Reviews* 5, 97-112 (2001).
- [182] Ni JQ, Nyns EJ. New concept for the evaluation of rural biogas management in developing countries. *Energy Conversion and Management* 37(10), 1525-1534 (1996).
- [183] Löffler G, Wargadalam VJ, Winter F, Hofbauer H. Effect of SO<sub>2</sub> on Homogeneous Nitrogen Chemistry under FBC Conditions. 10<sup>th</sup> Int. Conf. on Coal Science, Taiyuan, China (1999).
- [184] Miccio F, Löffler G, Wargadalam VJ, Winter F. The influence of SO<sub>2</sub> level and operating conditions on NO<sub>x</sub> and N<sub>2</sub>O emissions during fluidised bed combustion of coals. *Fuel* 80, 1555-1566 (2001).
- [185] Ogink, R., Gasoline HCCI Modeling: An Engine Cycle Simulation Code with a Detailed-Chemistry, Multi-Zone Combustion Model, Licentiate Thesis (Licentiate Thesis = Report written at some universities in Sweden when approximately half of the Ph.D. study has been carried out), Chalmers University of Technology, Gothenburg, Sweden (2002).
- [186] Tanaka S, Ayala F., Keck J. C., Heywood J. B.; Two-stage ignition in HCCI combustion and HCCI control by fuels and additives; *Combustion and Flame* 132, 219-239 (2003).
- [187] Westbrook C. K., Warnatz J., Pitz W. J.; A Detailed Chemical Kinetic Reaction Mechanism For The Oxidation Of Iso-Octane And n-Heptane Over An Extended Temperature Range And Its Application To Analysis Of Engine Knock; Twenty-Second Symposium (International) on Combustion, The Combustion Institute, Pittsburgh, 893-901 (1988).
- [188] Müller U. C., Peters N., Linan A.; Global Kinetics For n-Heptane Ignition At High Pressures; Twenty-Fourth Symposium (International) on Combustion, The Combustion Institute, Pittsburgh, 777-784 (1992).
- [189] Ranzi E., Faravelli T., Gaffuri P., Sogaro A., D'Anna A., Ciajolo A.; A Wide-Range Modeling Study of Iso-Octane Oxidation; *Combustion and Flame* 108, 24-42 (1997).
- [190] Dagaut P., Reuillon M., Cathonnet M.; Experimental Study of the Oxidation of n-Heptane in a Jet Stirred Reactor from Low to High Temperature and Pressures up to 40 Atm ; *Combustion and Flame* 101, 132-140 (1995).
- [191] Curran H. J., Gaffuri P., Pitz W. J., Westbrook C. K.; A Comprehensive Modeling Study of n-Heptane Oxidation; *Combustion and Flame* 114, 149-177 (1998).
- [192] Curran H. J., Gaffuri P., Pitz W. J., Westbrook C. K.; A Comprehensive Modeling Study of iso-Octane Oxidation; *Combustion and Flame* 129, 253-280 (2002).
- [193] Ranzi E., Gaffuri P., Faravelli T., Dagaut P.; A Wide-Range Modeling Study of n-Heptane Oxidation; *Combustion and Flame* 103, 91-106 (1995).

- [194] Curran H. J., Dunphy M. P., Simmie J. M., Westbrook C. K., Pitz W. J.; Shock Tube Ignition Of Ethanol, Isobutene And MTBE: Experiments And Modeling; Twenty-Fourth Symposium (International) on Combustion, The Combustion Institute, Pittsburgh, 769-776 (1992).
- [195] Brocard J. C., Baronnet F., O'Neal H. E.; Chemical kinetics of the oxidation of methyl-tert-butyl-ether (MTBE); *Combustion and Flame* 52, 25 (1983).
- [196] Brezinsky K., Dryer F. L.; A flow reactor study of the oxidation of iso-butylene and an iso-butylene/n-octane mixture; *Combust. Sci. Tech.* 45, 225 (1986).
- [197] W. E. Blass, J. J. Hillman, A. Fayt, S. J. Daunt, L. R. Senesac, A. C. Ewing, L. W. Jennings, J. S. Hager, S. L. Mahan, D. C. Reuter and M. Sirota, *Journal of Quantitative Spectroscopy and Radiative Transfer* 71, 47 (2001).
- [198] Stéphane Schilt, Luc Thévenaz, E. Courtois and Philippe A. Robert, *Spectrochimica Acta Part A: Molecular and Biomolecular Spectroscopy* 58, 2533 (2002).
- [199] P. Cancio, C. Corsi, F. S. Pavone, R. U. Martinelli, R. J. Menna, *Infrared Physics and Technology* 36, 87 (1995).
- [200] A. Popov, V. Sherstnev, Yu. Yakovlev, S. Civis, Z. Zelinger, *Spectrochimica Acta Part A* 54, 821 (1998).
- [201] Schmohl, Andreas; Miklós, András; Hess, Peter, *Applied Optics* 41, 1815 (2002).
- [202] H. Hofbauer, R. Rauch, G. Loeffler, S. Kaiser, E. Fercher, H. Tremmel, 12<sup>th</sup> European Conference and Technology Exhibition on Biomass for Energy, Industry and Climate Protection, Amsterdam, The Netherlands (2002).
- [203] Y. Zaatar, J. Bechara, A. Khoury, D. Zaouk and J. -P. Charles, Diode laser sensor for process control and environmental monitoring, *Applied Energy*, Volume 65, Issues 1-4, 107-113 (2000).
- [204] Miroslav Radojevic, Reduction of nitrogen oxides in flue gases, *Environmental Pollution*, 102(1), Supplement 1, 685-689 (1998).
- [205] P. Vogel, V. Ebert, Near shot noise detection of oxygen in the A-band with vertical cavity surface-emitting lasers, *Appl. Phys. B* 72, 127 (2001).
- [206] H. P. Zappe, M. Hess, M. Moser, R. Hövel, K. Gulden, H. Gauggel, F. Monti di Sopra, Narrow-linewidth vertical-cavity surface-emitting laser for oxygen detection, *Appl. Opt.* 39, 2475 (2000).
- [207] Sanders, S.T., Baldwin, J.A., Jenkins, T.P., Baer, D.S., and Hanson, R.K., Diode-Laser Sensor for Monitoring Multiple Combustion Parameters in Pulse Detonation Engines, *Proceedings of the Combustion Institute* 28, 587-594 (2000).
- [208] V. Weldon, J. O'Gorman, J.J. Pérez-Camacho, J. Hegarty, Oxygen sensing using single frequency GaAs-AlGaAs DFB laser diodes and VCSELs, *Electron. Lett.* 32, 219 (1996).

- [209] D. C. Hovde, C. A. Parsons, Wavelength modulation detection of water vapor with a vertical cavity surface-emitting laser, *Appl. Opt.* 36, 1135 (1997).
- [210] W. Yuen, G. S. Li, R.F. Nabiev, J. Boucart, P. Kner, R.J. Stone, D. Zhang, M. Beaudoin, T. Zheng, C. He, K. Yu, M. Jansen, D.P. Worland, C. J. Cang-Hasnain, High-performance 1.6  $\mu\text{m}$  single epitaxy top emitting VCSEL, *Electron. Lett.* 36, 1121 (2000).
- [211] C. J. Hepburn, R. Sceats, D. Ramoo, A. Boland-Thoms, N. Balkan, M. J. Adams, A. J. Dann, S. D. Perrin, I. Reid, J. Reed et al., Temperature dependent operation of 1.5  $\mu\text{m}$  GaInAsP/InP VCSELs, Superlattices and Microstructures, in press (2003).
- [212] M.E. Webber, D.S. Baer, R.K. Hanson, Ammonia monitoring near 1.5  $\mu\text{m}$  with diode-laser absorption sensors, *Appl. Opt.* 40, 2031 (2001).
- [213] D.E. Cooper, R.U. Martinelli, Near-infrared diode lasers monitor molecular species, *Laser Focus-World* 28, 133 (1992).
- [214] L. Lundsberg-Nielsen, F. Hegelund, F.M. Nicolaisen, Analysis of the High Resolution Spectrum of Ammonia ( $^{14}\text{NH}_3$ ) in the Near-Infrared Region, 6400-6900  $\text{cm}^{-1}$ , *J. Mol. Spectrosc.* 162, 230 (1993).
- [215] L. Lundsberg-Nielsen, Molecular overtone spectroscopy on ammonia, Ph.D. thesis, Department of Chemistry, University of Copenhagen, Copenhagen, Denmark (1995).
- [216] World Meteorological Organization (WMO), 1992, Scientific Assessment of Ozone Depletion: 1991, WMO/UNEP, WMO Global Research and Monitoring Project, Rep. 25, Geneva (1992).
- [217] P. Wiesen, J. Kleffann, R. Kurtenbach, K. H. Becker, *Infrared Physics and Technology* 37, 75-81 (1996).
- [218] Robert Kormann, Hans Müller, Peter Werle, *Atmospheric Environment* 35, 2533-2544 (2001).
- [219] Georges Durry, *Spectrochimica Acta Part A* 5, 1855-1863 (2001).
- [220] I. J. Simpson, G. C. Edwards, G. W. Thurtell, *Atmospheric Environment* 33, 1141-1150 (1999).
- [221] K. M. Beswick, T. W. Simpson, D. Fowler, T. W. Choularton, M. W. Gallagher, K. J. Hargreaves, M. A. Sutton, A. Kaye, *Atmospheric Environment* 19, 3283-3291 (1998).
- [222] K. J. Hargreaves, D. Fowler, *Atmospheric Environment* 19, 3275-3282 (1998).
- [223] Konstantin L. Moskalenko, Alexander I. Nadezhdinskii, Inna A. Adamovskaya, *Infrared Physics and Technology* 37, 181-192 (1996).
- [224] M. Aidaraliev, N. V. Zotova, S. A. Karandashov, B. A. Matveev, N. M. Stus', G. N. Talalakin, *Infrared Physics and Technology* 37, 83-86 (1996).

- [225] N. V. Zozova, S. A. Karandashov, B. A. Matveev, N. M. Stus', G. N. Talalakin, M. A. Remennyi, *Spectrochimica Acta Part A* 52, 852-862 (1996).
- [226] D. G. Lancaster, R. Weidner, D. Richter, F. K. Tittel, J. Limpert, *Optics Communications* 175, 461-468 (2000).
- [227] Michael Hippler, Martin Quack, *Chemical Physics Letters* 314, 273-281 (1999).
- [228] A. Nadezhdinskii, A. Berezin, S. Chernin, O. Ershov, V. Kutnaya, *Spectrochimica Acta Part A* 55, 2083-2089 (1999).
- [229] V. Hopfe, D. W. Sheel, W. Graehlert and O. Throl , NIR laser diode and FTIR based process control for industrial CVD reactors, *Surface and Coatings Technology*, 142-144, 328-332 (2001).
- [230] E. Schlosser, T. Fernholz, H. Teichert and V. Ebert, In situ detection of potassium atoms in high-temperature coal-combustion systems using near-infrared-diode lasers, *Spectrochimica Acta Part A: Molecular and Biomolecular Spectroscopy* 58(11), 2347-2359 (2002).
- [231] Venu Nagali, Diode laser study of high-pressure water-vapor spectroscopy, PhD thesis, Stanford University, USA, UMI microform 9924469(1998).  
<http://wwwlib.umi.com/dxweb/gateway>
- [232] Herbert Kopecek, Laser ignition for gas engines (working title), PhD thesis, Vienna University of Technology, Vienna, Austria, to be published (2003).

**XI. Appendix 1: Pictures**

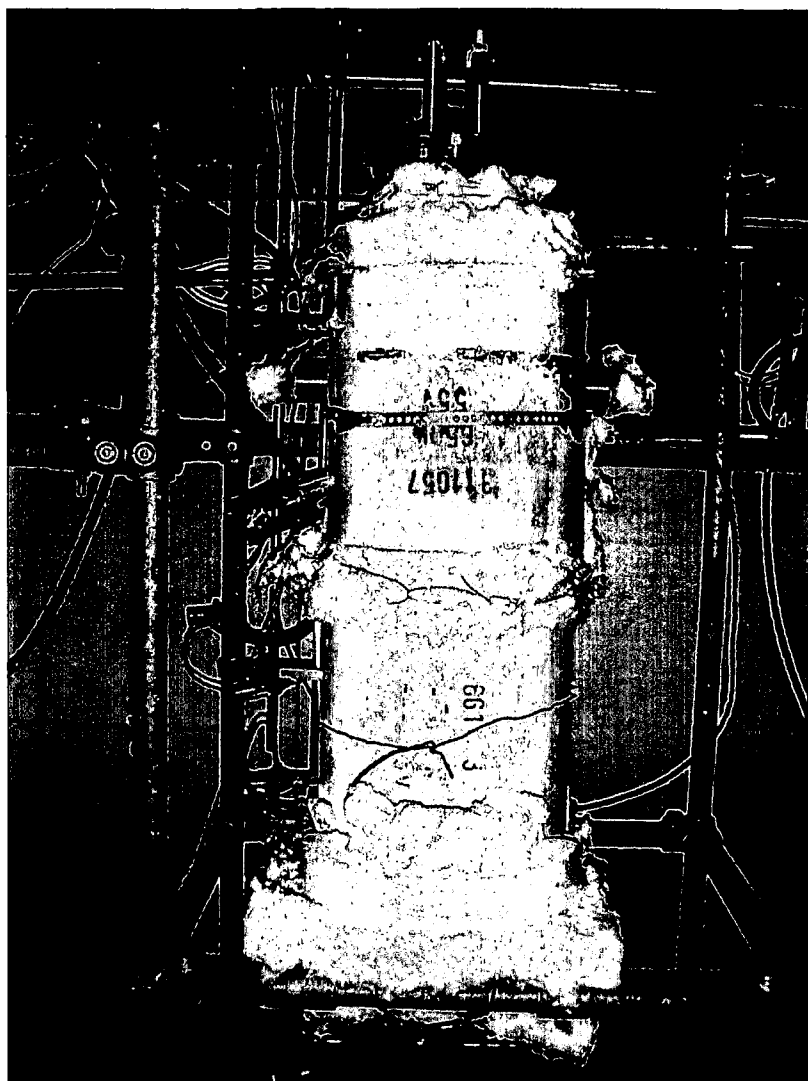


Fig. XI-1: Image of the laboratory-scale fluidized bed combustor (chapter IV.1).

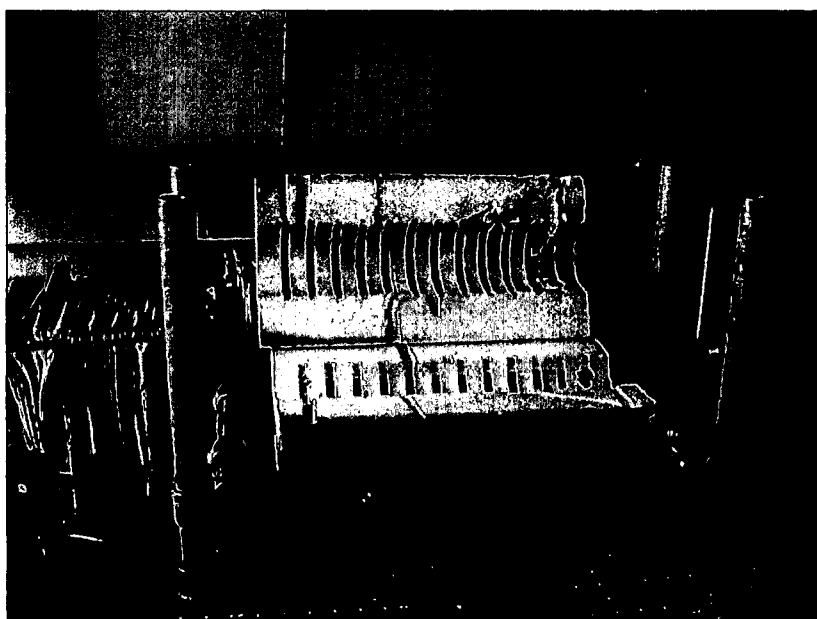


Fig. XI-2: Heating shells that house the quartz cell for high temperature spectroscopy (chapter IV.1).

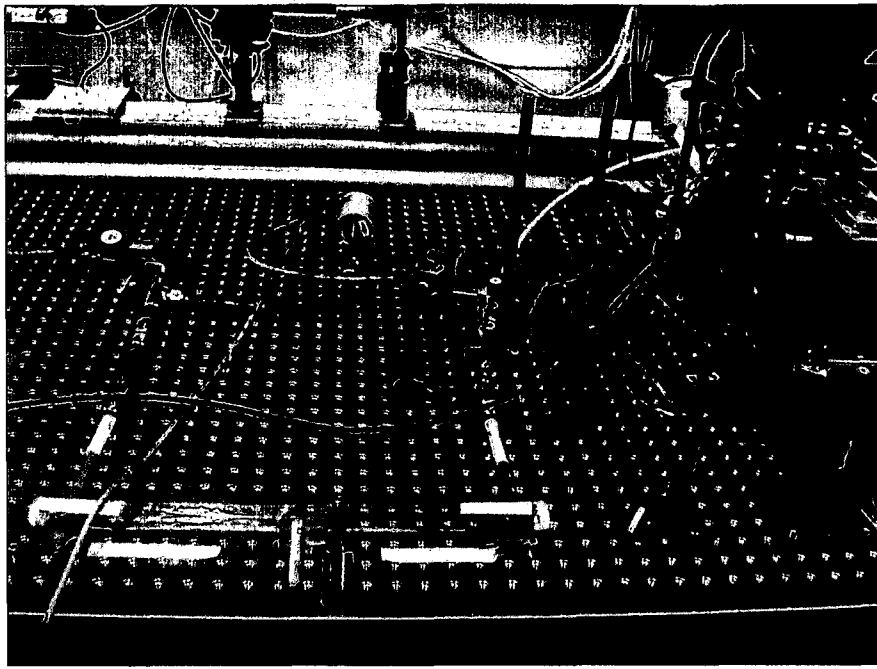


Fig. XI-3: Rapid absorption spectroscopy of  $\text{CH}_4$  ( $1.68 \mu\text{m}$ ),  $\text{HCl}$  and  $\text{H}_2\text{O}$  ( $1.81 \mu\text{m}$ ), Munich University of Technology (Germany), (chapter IV.4).

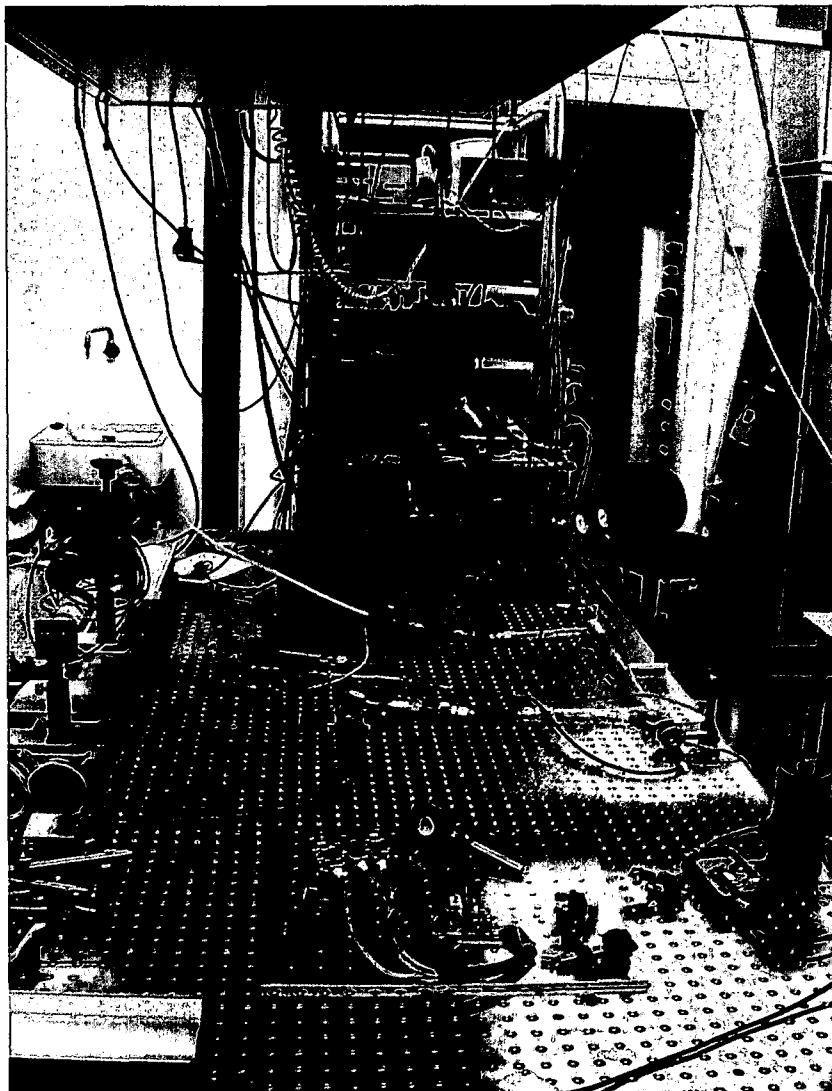


Fig. XI-4: Experimental setup at Munich University of Technology (Germany), (chapter IV.4).

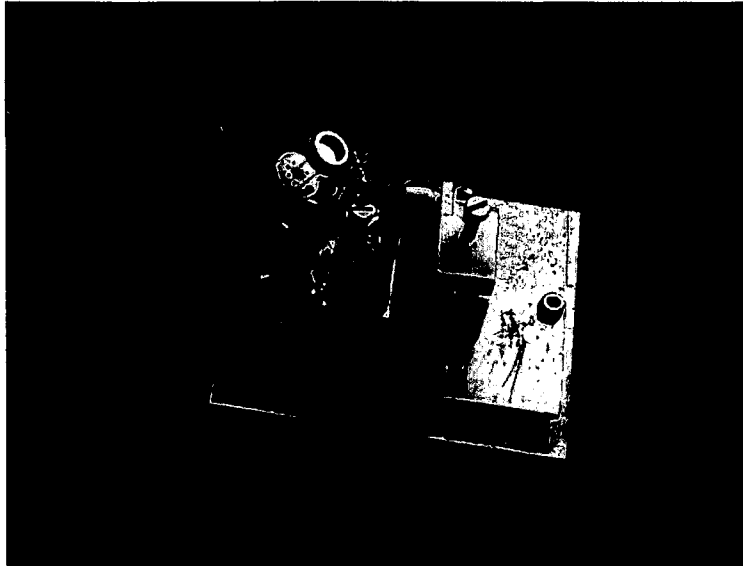


Fig. XI-5: Semi-finished VCSEL based laser measurement system (chapter III.4).



Fig. XI-6: Q-switched Nd:YAG laser for laser ignition tests (chapter IV.2).

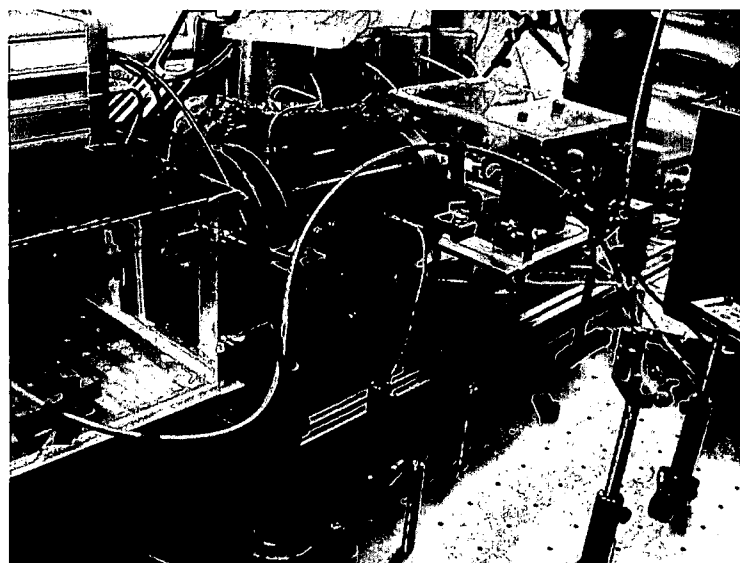


Fig. XI-7: Setup for laser ignition tests and optical diagnostics (chapter IV.2).





Fig. XI-8: Setup for laser ignition tests and optical diagnostics (chapter IV.2).

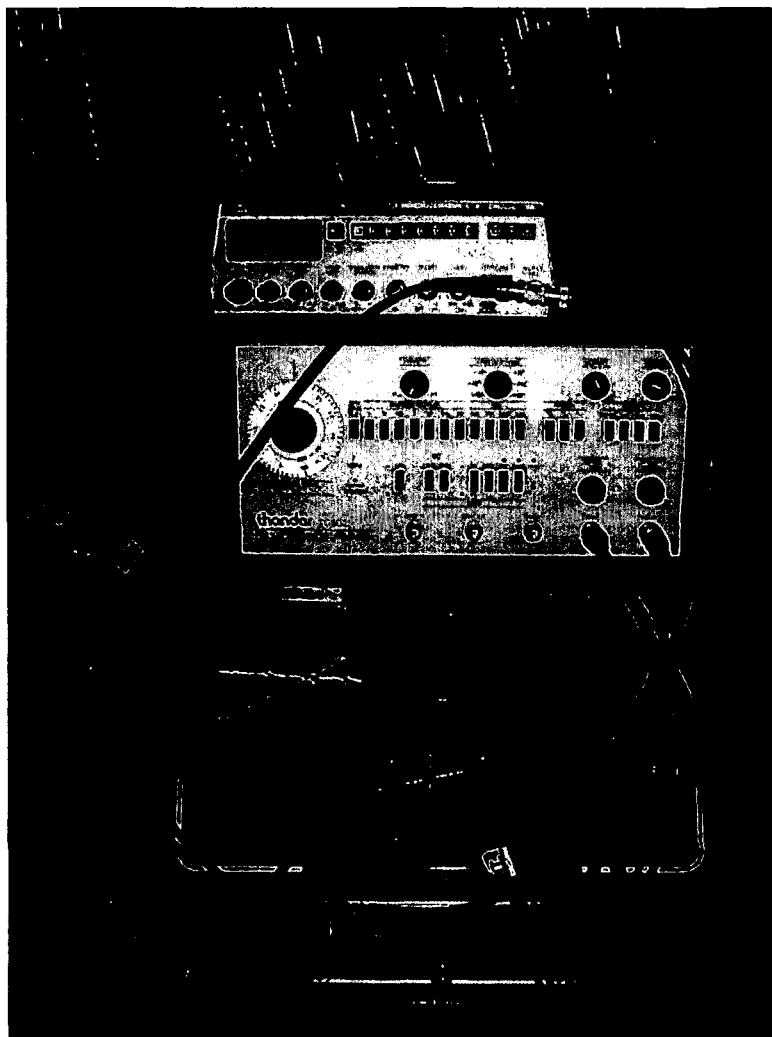


Fig. XI-9: Wavelength modulation spectroscopy (WMS); From top to bottom: function generator 1, function generator 2, oscilloscope, lock-in amplifier (chapter IV.4).

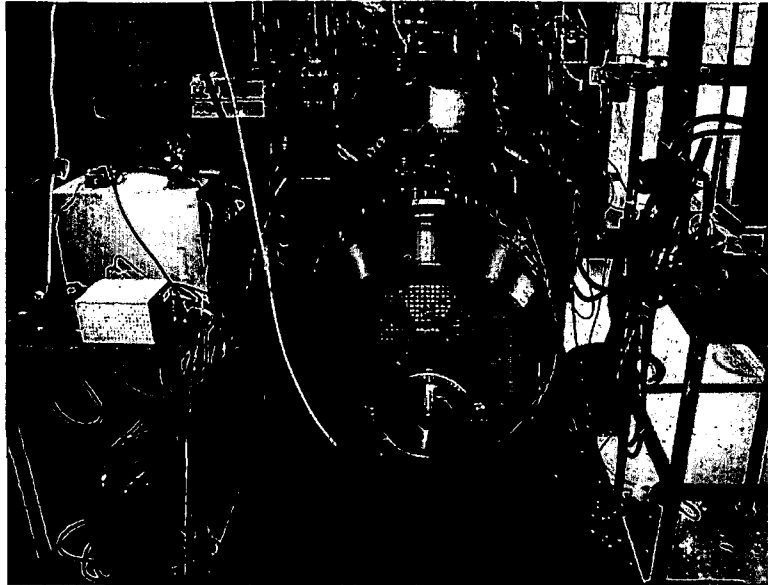


Fig. XI-10: Optical engine, front view, Lund Institute of Technology (Sweden), (chapter IV.6).



Fig. XI-11: Optical engine, control room, Lund Institute of Technology (Sweden), (chapter IV.6).



Fig. XI-12: Optical engine, peripheral equipment for spectroscopy, Lund Inst. of Technology, (chapter IV.6).

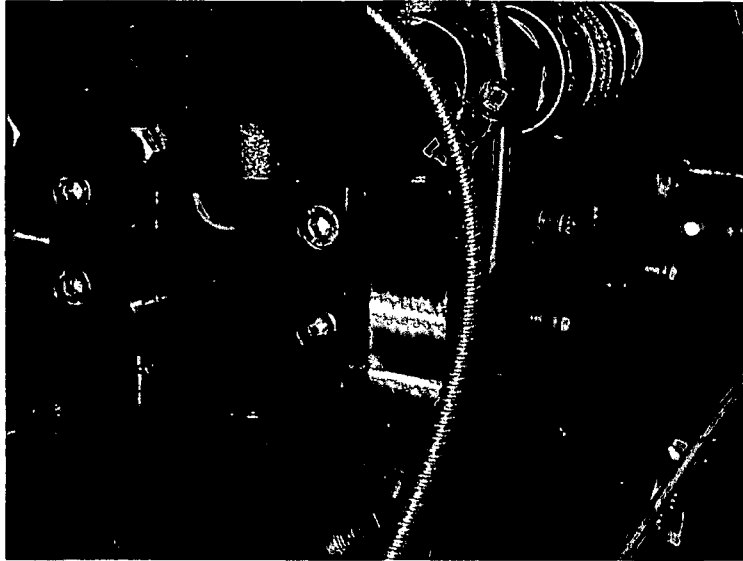


Fig. XI-13: Optical engine, piston in top position, Lund Institute of Technology (Sweden), (chapter IV.6).

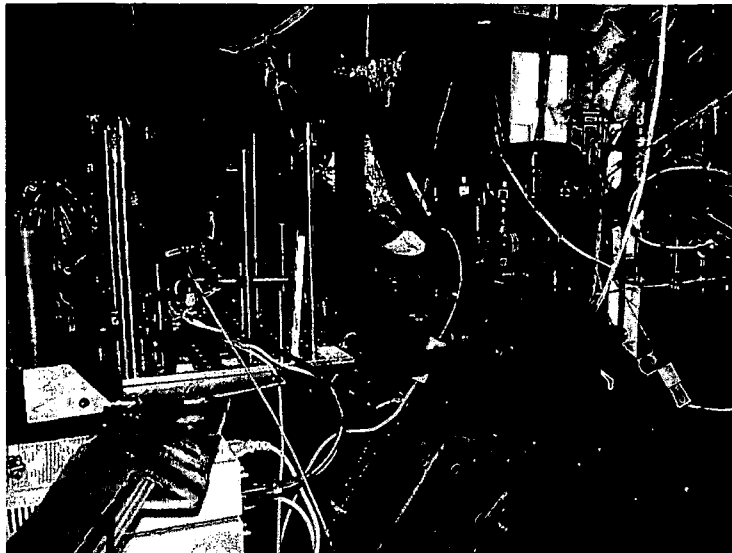


Fig. XI-14: Optical engine, single pass setup, Lund Institute of Technology (Sweden), (chapter IV.6).

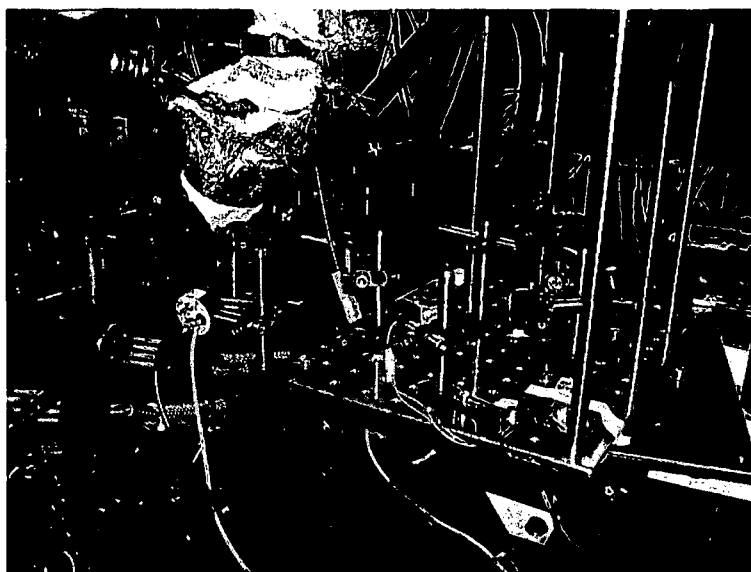
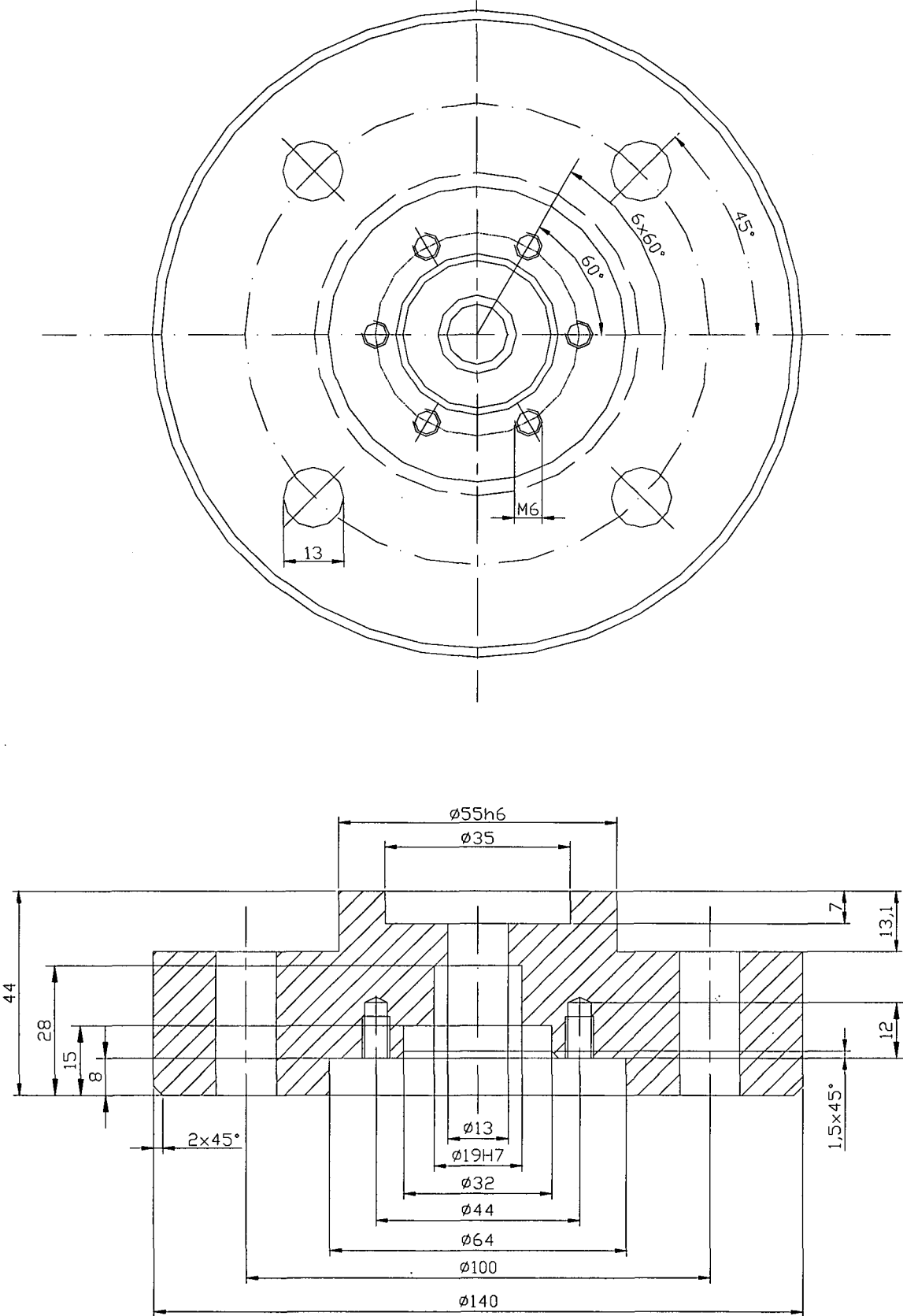
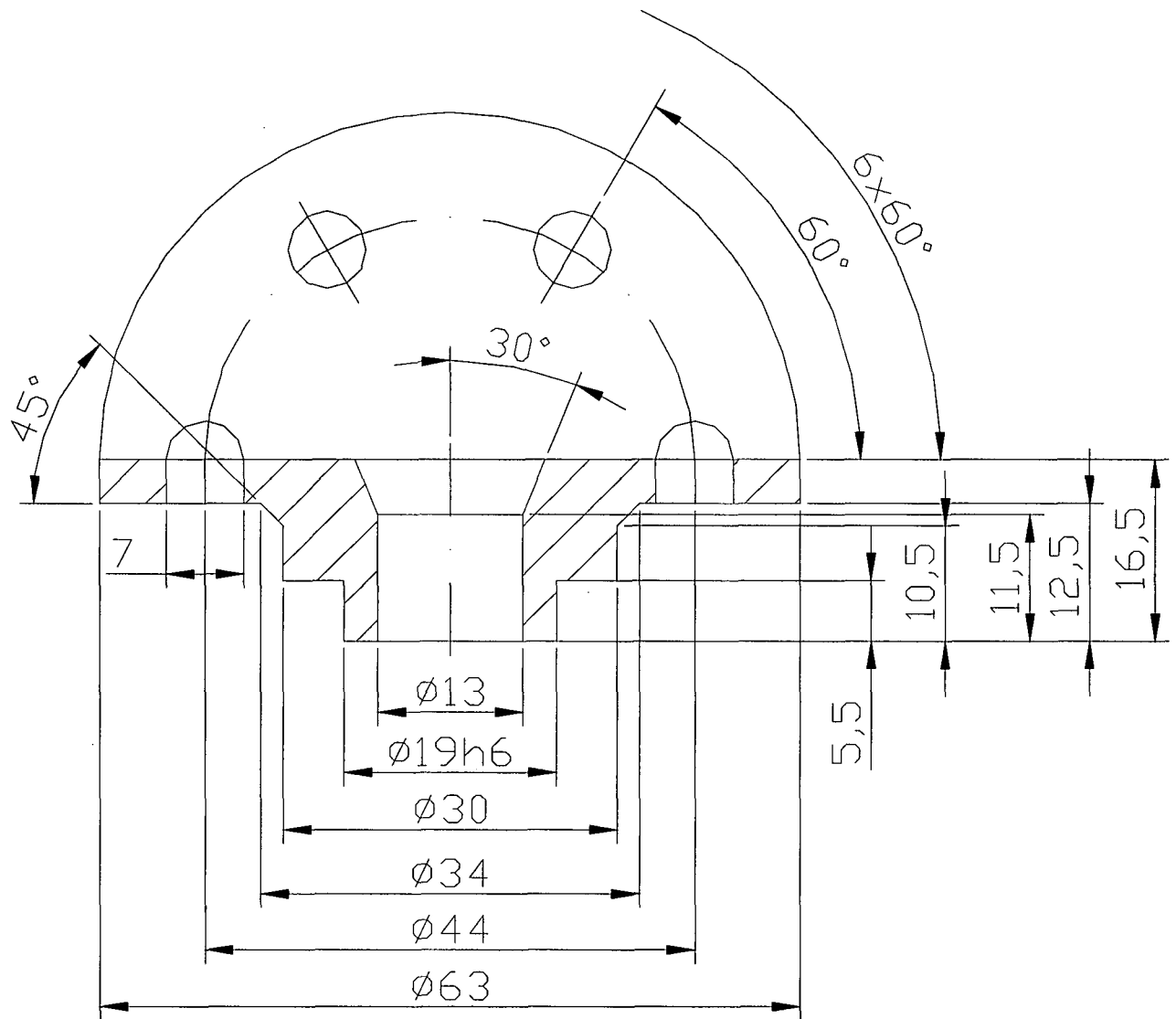
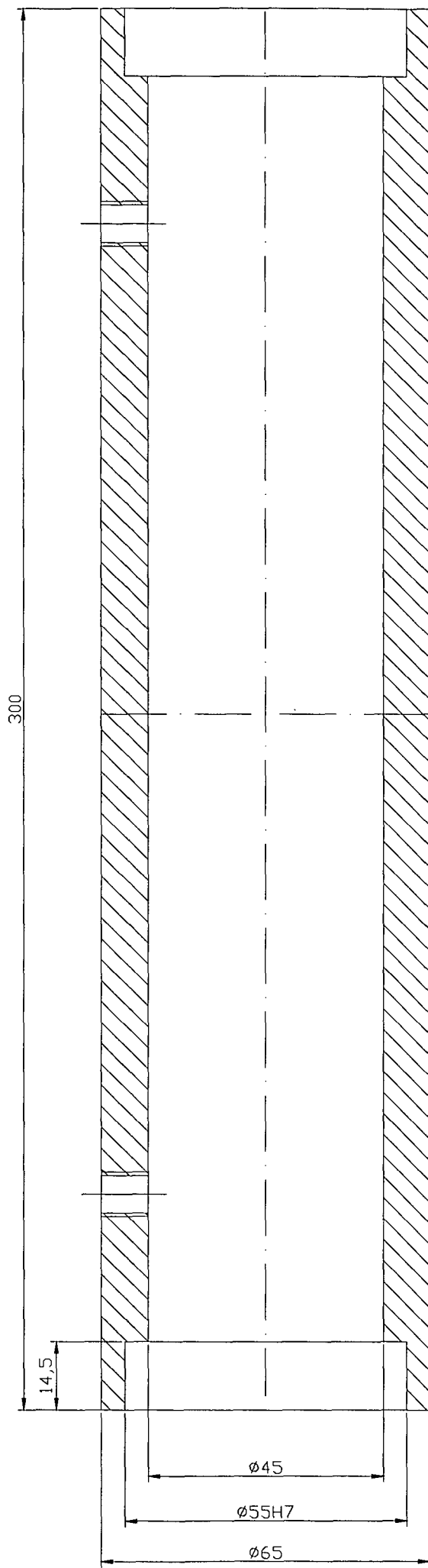


Fig. XI-15: Optical engine, two pass setup, Lund Institute of Technology (Sweden), (chapter IV.6).

**XI. Appendix 2: Drawings of the high pressure static cell**







278

**XIII. Curriculum vitae**Contact

Dipl.-Ing. Maximilian Lackner  
 Langegasse 8/30, A-2540 Bad Vöslau, Austria  
 Email: [maxlackner@gmx.at](mailto:maxlackner@gmx.at)  
 Internet: <http://www.maxlackner.com>

Personal data

Born: Mödling/Lower Austria, December 15<sup>th</sup>, 1977  
 Nationality: Austrian

Education

1984-1988 Elementary school in Gainfarn  
 1988-1996 Humanistic secondary school in Baden  
 6/1996 School leaving examination with excellence  
 10/1996- Military service in Eisenstadt, thereof 3 months at  
 5/1997 the Eastern Austrian border in Lackenbach and Halbturn

Foreign language skills

English and French fluently

Language courses

1994	Paignton/England	(2 weeks)
1995	Saint Malo/France	(4 weeks)
1995	Feurs/France	(3 weeks)
1996	Mandelieu/France	(2 weeks)

Academic studies

10/1997- 11/2001	Diploma study of technical chemistry at Vienna University of Technology, specialisation in physical and analytical chemistry Graduation with excellence two semesters under regular duration Diploma thesis at the Institute of Chemical Engineering, Vienna University of Technology, with Prof. Dr. Franz Winter entitled „ <i>In-situ</i> laser spectroscopy for combustion processes“
11/2001- 6/2003	Doctoral studies at the Institute of Chemical Engineering, Vienna University of Technology, with Prof. Dr. Franz Winter Main research interest: tunable diode laser absorption spectroscopy for combustion and ignition diagnostics, key researcher of an FFF funded project, 7 diploma students
11/2001	Research stay at Munich University of Technology (Germany)
05/2003	Research stay at Lund University of Technology (Sweden)

Additional courses

- 2000 Typewriting course, driving licence (B), glassblower course, blasting course
- 2001 3 short courses (lasers), CLEO 2001 conference (Baltimore/USA)
- 2002 3 short courses (lasers), CLEO 2002 conference (Los Angeles/USA)
- 2003 Management for executives (1 semester training course in 6 modules, BFI Wien)
- 2003 Concession for running a technical consultancy (Technisches Büro/Ingenieurbüro)

Internships

- 7/1998 Herberts Austria, now DuPont (testing of barrel coatings)
- 1999-2000 Sanochemia Pharmazeutika AG (investigation of scientific literature)
- 7/1999 Polycollege Sprachferien GmbH (guide and local organiser for language course holidays for teenagers in Antibes/France)
- 8/1999 OMV AG (analysis of water and sewage)
- 8/2000 Polycollege Sprachferien GmbH (guide and local organiser for language course holidays for teenagers in London/England)
- 10/2000-6/2001 Institute of Physical Chemistry, Vienna University of Technology, Vienna (tutor)

Working experience

- 07/2001 Lackner & Partner OEG (foundation of the general partnership as a team of four, line of business: internet information services, termination in 2002)
- 09/2001- Institute of Chemical Engineering, Vienna University of Technology (research assistant)
- 07/2002 ProcessEng Engineering GmbH (foundation of the company amongst three shareholders)
- 07/2002- ProcessEng Engineering GmbH (managing director: building up the company, operational and strategic tasks)

Prizes and awards

- 03/2001 Scholarship awarded by Vienna University of Technology (denary of natural sciences and informatics, Förderstipendium)
- 10/2002 Scholarship awarded by Vienna University of Technology (denary of natural sciences and informatics, Förderstipendium)
- 11/2002 Award for appreciation by the Austrian federal Ministry for Education, Science and Arts (Würdigungspreis 2002)
- 10/2002 Scholarship by the municipality of Vienna (Hochschuljubiläumsstiftung 2002)
- 6/2003 Rank 4 at the Austrian i2b business plan competition (laser spectroscopic tunnel sensor for pollutant and temperature measurements)